Analysis of Complex Flows in Safety Valves Using CFD

PhD Thesis

Christopher James John Doyle

James Weir Fluids Laboratory

Department of Mechanical and Aerospace Engineering

University of Strathclyde, Glasgow

15 April 2022

DECLARATION

This thesis is the result of the author's original research. It has been composed by the author and has not been previously submitted for examination which has led to the award of a degree.

Signed: 

Date: 15/04/2022

ACKNOWLEDGEMENTS

In completing this thesis, it has been the greatest academic challenge of my career to date. However, the research that I conducted would not have been possible without the guidance and support of a select few individuals and organisations in addition to the financial support provided by the Engineering and Physical Sciences Research Council (EPSRC).

Primarily, I would like to thank my supervisor Dr. William Dempster for his resolute technical guidance and confidence in me to deliver the objectives of this thesis. He enabled me to challenge myself, drive my research further and taught me many lessons which I'll continue to carry forward with me in my career. I would also like to express my thanks to Steven Taggart and Jordan Gronkowski who provided me with an important link of my research to industry and supplied me with critical manufacturing data which I required. In addition, I would like to thank the many technicians within the mechanical engineering laboratories as well as the support staff from the regional supercomputer centre at ARCHIE WeSt for their expertise and technical support.

Finally on a personal note, I would like to thank my family and friends. I would specifically like to thank my Mum and Dad who throughout my life have provided me with the love and support required for me to achieve my best. I will be forever grateful to them and I hope this thesis will make them proud. I would also like to recognise my partner Heather who has been with me throughout my PhD journey and always ensured that I was determined and supported when I needed it most.

ABSTRACT

The aim of this thesis was to utilise Computational Fluid Dynamics (CFD) tools available to industry - primarily ANSYS FLUENT and ANSYS Workbench - to develop a modelling methodology which could allow CFD to be relied upon and be used as an analysis/design tool within the Pressure Relief Valve (PRV) industry. This work will also investigate the capability and resilience of modern day CFD solvers to accurately capture the array of complex flow dynamics which exist during the operation of various types of PRV's. Furthermore, to achieve confidence in the capability of the CFD models developed; it was required for experimental validation work to be performed. Initially a 3D single phase (air only) steady state CFD model was developed for a right-angled type 3511E PRV manufactured by Broady Flow Control and validated against experimental results generated at an industrial testing facility. In addition, by developing upon previous 2D CFD work at the University of Strathclyde for a smaller through flow type PRV geometry; the lessons learned from the Broady PRV research allowed a 3D CFD model to be developed for a 5231BX through flow type PRV manufactured by Henry Group Industries. Experimental validation for the 5231BX PRV was performed at a testing facility developed within the flow laboratory at Strathclyde. For both cases, good correlation for air mass flow rate and disc/piston aerodynamic force with experimental results was achieved. Furthermore, from the validation analysis performed for the Henry PRV it was highlighted that a significant improvement in CFD modelling accuracy could be achieved by adopting a 3D CFD model when compared with 2D. This was due to a significant variation in complex flow features found at the piston surface and presence of symmetry breaking flow phenomena.

Due to the success of the 3D steady state CFD models to accurately capture flow features for both the Broady and Henry PRV's, a transient single phase CFD model was developed to enable the use of a dynamic moving mesh to capture each PRV's operational characteristics. The experimental facilities

developed for both PRV's allowed a validation of the CFD model's prediction for overpressure, blowdown and overall dynamic characteristics (disc lift vs time). For both cases it was found that overpressure and blowdown could be predicted closely as well as a general consensus being achieved for lift vs time behaviour. Therefore, it was concluded that for both types of PRV geometry, a moving mesh was capable to accurately capture the dynamic PRV response. For the Henry case however there was vibration in the CFD results which was attributed due to numerical errors induced by the RANS CFD numerical model. Following the dynamic mesh analysis for the Henry PRV; a study of the validity of the commonly used quasi steady design approach to PRV's was examined by comparing results from steady state to dynamic operating conditions. The conclusion from this study highlighted a potentially significant issue with current typical PRV design practices as different magnitudes of disc force could be attributed with disc velocity when compared with steady state results. This would therefore cause a difference in expected performance from quasi steady based simple dynamic models often used in initial valve design.

In addition, two-phase (air-water) 3D CFD analysis was performed for the Henry 5231BX PRV to extend previous 2D CFD research at Strathclyde. Both steady state and transient experimental testing was performed for a range of water injection rates; however only two-phase steady state CFD validation was undertaken due to computational restrictions. The two-phase steady state validation results highlighted that a 3D CFD model, which utilised the homogenous mixture model, was capable of achieving a reasonably accurate correlation to experimental data across the full lift range when subjected to a water injection rate of 0.96 L/min and 2.1 L/min. Degradation in accuracy could be found for two-phase CFD modelling when compared to single phase modelling; however correlation was generally within acceptable limits. Furthermore, from two phase transient experimental testing; it was possible to establish a direct trend of water injection rate/water mass fraction to the dynamic characteristics of the Henry PRV as well as blowdown pressure. The effect of two-phase operation on dynamic stability was also established.

CONTENTS

PRV TERMINOLOGY [1] [2]

Back Pressure – Static pressure existing at the outlet of a PRV device due to outlet pressure. It is a sum of superimposed and built up backpressure. Built up backpressure is caused by flow through the PRV whereas superimposed backpressure caused by pressure in the discharge system external from PRV.

Blowdown – The difference between popping pressure of a PRV and reseating pressure. Expressed as a percentage of set pressure.

Chatter – Rapid oscillating movement of moving PRV components such as the disc which violently contacts the seat at a high frequency.

Closing Pressure – The value of inlet static pressure at which the disc establishes a seal with the seat after blowdown.

Disc – Otherwise known as a “Piston” which is a moving part within the PRV which is subject to aerodynamic, spring and damping forces.

Lift – Displacement of the disc from the PRV’s sealed position at the seat.

Over Pressure – The pressure increase over the set pressure of the PRV at which maximum discharge capacity and lift is reached. Expressed as a percentage of set pressure.

Popping Pressure – Value of increasing inlet static pressure above set pressure at which the disc moves in a rapid motion in the direction of opening.

Rated Lift – The design lift at which the PRV achieves rated discharge capacity.

Safety Valve – A pressure relief valve (PRV) actuated by inlet static pressure and characterized by rapid opening or pop action which provides overpressure protection for pressurized equipment.

Set Pressure – Value of increasing static pressure at which the PRV begins to simmer and is in equilibrium with resistive forces. The definition of set pressure can vary between manufacturers with various techniques used in practice such as first audible point or a bubble test to identify initial leakage.

Seat – Contact point between the fixed geometry of the PRV body and moving disc. When the PRV is not in operation, the seat and disc interface provides a seal for the system to prevent discharge of contained fluid.

Simmer – The audible or visible escape of fluid between the seat and disc at an inlet static pressure below the popping pressure and at no measurable flowing capacity.

CHAPTER 1

INTRODUCTION

Within this chapter an overview of the project in which this thesis is based upon is provided to establish the overall context for this body of work in terms of technical and philosophical background. In addition, the research objectives that this thesis will address and refer upon throughout will be identified alongside a description of the structural outline of the thesis.

1.1 Project Overview

Pressure relief valves (PRV) and their reliable performance is crucial for ensuring the safety of pressurized infrastructure across a variety of engineering industries. In a substantial number of applications such as within nuclear power plants and industrial refrigeration units, the installation of a PRV is a legal requirement to guarantee the integrity of a pressurized system during a non-standard operating condition [2-4]. Such an emergency condition would occur due to a range of circumstances such as external heating of a pressure vessel during fire, a runaway chemical reaction or loss of cooling mechanisms. An example of the typical operation of a PRV installed on a pressure vessel in a two-phase (air/water) environment is shown within figure 1.1.

It is crucial for valve designers to fully understand the flow regimes and dynamics involved in the operation of a PRV to achieve the desired performance. The use of Computational Fluid Dynamics (CFD) within the PRV industry would therefore seem to be natural fit due to the complex flow phenomenon involved during its operation and ability to visualize flow fields and report forces. Research studies utilizing CFD for application within the PRV industry have been developed over the course of many years and have

been found to be effective at providing an insight into the complex flows involved during the operation of a PRV [5-9]. It has been observed during such research that flow characteristics such as flowrate and forces correlate reasonably well with experimental values. Much of the work however was performed within a 2-dimensional (2D) domain to reduce computational cost and using steady state RANS (Reynolds Averaged Navier-Stokes) equations and quasi steady assumptions. However due to the ever increasing computing power available, the capability of CFD to achieve greater accuracy and use more complex models has enabled the requirement to develop new sophisticated and modern three dimensional (3D) models for PRV's. Noting this, the application of advanced modelling techniques such as the use of URANS (Unsteady Reynolds Averages Navier Stokes Equations), multiphase analysis and dynamic meshing will be explored within this thesis.

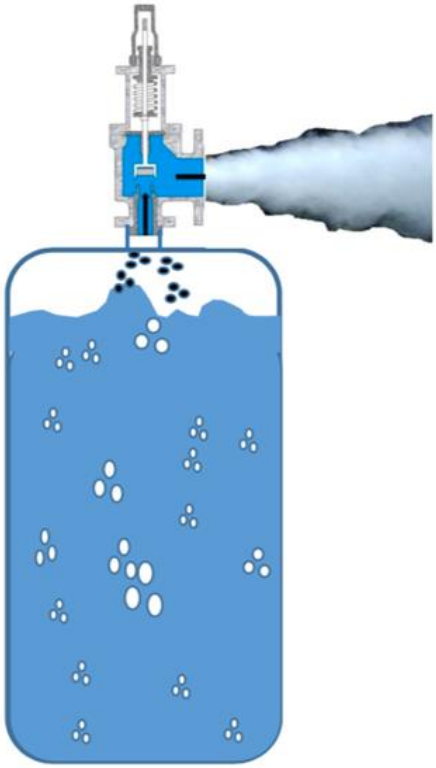

Figure 1.1 – Illustration of Right Angled PRV Mounted on Pressure Vessel

With the development of industrial CFD solvers such as ANSYS FLUENT, it could be proposed that a PRV model, once validated to an acceptable degree of accuracy, could provide valve manufacturers with an inexpensive theoretical solution when compared to experimental testing. This is especially true during the initial design stages of PRV design which is often the most time consuming stage of the development process. Historically, pressure relief valves are designed and developed using an iterative trial and error based method to achieve the performance required. As a result, such a method is costly to the manufacturer; this difficulty is heightened further when designing PRV's for high pressure application where testing is prohibitive or two phase flow where the complexity of the phase interaction makes it difficult to predict fluid behavior and interaction with the PRV. It has been successfully demonstrated in previous research performed by Taggart [9] that by combining validated steady state CFD models with Genetic Algorithm based optimization techniques that CFD can be used to achieve improved designs with reduced development times. Therefore, the basic premise of this thesis is that the use of transient CFD could provide manufacturers with a cost effective solution to identify systematic design flaws and instability. By doing so, other than capital costs, the manufacturer would achieve additional assurance regarding the safe and desired operation of the PRV. It is hoped therefore that within this thesis that sophisticated transient PRV modelling techniques such as dynamic meshing could be developed for manufacturers to adopt within their design processes.

In operation, a PRV is required to self-actuate in order to manage the system pressure and to prevent the possibility of structural failure of a vessel potentially leading to a sudden rupture and uncontrolled mass loss. Failure of such a pressurized system could also result in the release of energy which would cause significant destruction of property, exposure to dangerous chemicals and possibly injury or loss of life; therefore the reliable operation of a PRV is of paramount importance [10] . It has been found however in previous research that the appropriate design and installation of PRV's is often

overlooked and is not included during the early stages of a pressurized system's design. As a result, it could be suggested that there is a significant risk of PRV's currently in operation being inappropriately sized, having undesirable dynamic characteristics or installed incorrectly which could prevent the device from operating as desired. Therefore, the use of CFD methods, particularly for the more complex flow conditions proposed within this thesis could enhance the ability of manufacturers and operators to understand further the limitations of their device and optimize the use of PRV's within various systems thus reducing the risk of catastrophic PRV failure events.

1.2 Research Objectives

The primary objective of the thesis is an analysis of the complex flow regimes found in safety valves (PRV's in particular) using CFD modelling techniques available within the commercial CFD package ANSYS FLUENT. Following previous research at the University of Strathclyde as well as work by many other institutions a series of research objectives has been established. These objectives were inspired from recommendations made by previous researchers as well as a need to advance previous achievements by utilizing ever increasing computational capabilities.

By achieving these objectives within this thesis, it is hoped that the results can provide insight of the capability of CFD to provide a potentially cost-effective design tool. This could be particularly effective during the early development of a PRV design. In addition it could be postulated that well validated CFD methods should be included in design standards as is the case with Finite Element Analysis (FEA) tools.

The major research objectives of this thesis are as follows;

- To revisit previous research in literature and evaluate the capability of CFD to model single phase flow for various types of PRV geometry for both 2D and 3D simulation. Within this study two distinctly different PRV types will be studied: an ASME Section VIII/API right angled PRV from Broady Flow Control and an ISO 4126 through flow PRV supplied by Henry Technologies. By developing a CFD model for both steady state and transient analysis it is hoped that a resilient modelling technique could be developed; capable of being implemented to capture flow effects for a variety of PRV geometry. A transient dynamic mesh CFD model will be developed for both geometries to allow an assessment of the ability of CFD to capture the dynamics of PRV operation and provide an understanding towards the flow behaviour. Improvements in the use of CFD models will be pursued by undertaking the following steps;

    - Development of a single phase experimental rig and procedure which will allow validation of both steady state and transient simulation by capturing flow force, mass flow rate and lift vs time.

    - Development of a CFD modelling procedure which closely matches experimental results by undertaking a validation study investigating the roles of turbulence model, mesh density, numerical discretization methods, use of symmetry and 2D/3D approaches. In addition, the time dependency of each solution will be analysed by comparing steady state and transient results. Furthermore, development of an effective dynamic mesh method for transient fluid structure interaction analysis will be achieved.

    - Following the validation of single-phase models, an investigation will take place to identify any source of symmetry breaking flow phenomena which would result in the result of a 3D CFD

simulation to differ from the results of a 2D CFD simulation in an axisymmetric domain. In addition, the analysis could also help to identify any time dependent flow features which would result in a difference between steady state and transient solutions. The effect of mesh density and turbulence model selection will also be explored to understand the challenges posed for using CFD in complex PRV geometry.

    - To investigate using validated dynamic mesh CFD techniques and with comparison to experimental data any observed instability mechanisms and identify likely causation.

- Once a transient dynamic mesh model for single phase has been developed and validated, an assessment of the validity of the commonly used quasi steady assumption during the design of PRV's will take place. This will enable a greater understanding towards the effectiveness of the assumption and help to identify any flow features/behaviour which could cause the assumption to break down. Furthermore, an appreciation of the use of dynamic meshing and a fluid structure interaction approach to understand PRV dynamics and flow instability features such as vortex generation which is absent during steady state simulation could be achieved.

- To revisit previous research in literature and perform an investigation of the capability of CFD to model two phase flow in steady state. This work will initially build upon previous research performed at Strathclyde using a through flow PRV supplied by Henry Technologies [11, 12]. An accurate CFD model will be sought by undertaking the following steps;

    - Development of a two-phase experimental rig and procedure for air and water which will allow measurement of both steady state

and transient flow characteristics in a similar manner to single phase. Additional modifications will be required to the experimental rig to allow injection of water as well as a method of separating, sealing and returning water to a closed system.

- Development of a steady state two-phase CFD modelling procedure by undertaking a validation study (similar to single-phase) to achieve an accurate but computationally efficient model. The homogeneous mixture model previously developed at the University of Strathclyde will also be extended to a 3D domain from previous 2D work. Justification will be provided within the literature review (chapter 3.2).

1.3 Thesis Outline

The thesis presents the pursuit of these objectives in three main themes; background and literature review to establish current relevant knowledge, models and methods to present the theoretical modelling approach and the results of single phase and two-phase modelling and experimental case studies. The thesis is thus structured in the following chapters as follows;

1. **Introduction**

   The introduction provides context and highlights the objectives of the research as well as identifying an outline of the thesis to follow.

2. **Background**

   To provide context and sufficient knowledge for the general reader, chapter 2 provides an understanding of the typical operational principles and characteristics of a PRV as well as reviewing current

design methodology and industry standards. Furthermore, issues such as dynamic instability and general best practices are introduced.

3. Literature Review

The focus of the study is justified in Chapter 3 where an in-depth literature review of previously conducted PRV research for single phase and two-phase flow is discussed. An overview of previously utilized numerical, CFD and experimental techniques for PRV analysis will be established and reviewed.

4. Overview of CFD Numerical Methods Required to Capture PRV Flow Physics

A description of the numerical models and methods required to be used within CFD over the course of the thesis will be established for both single and two-phase flow. Fluid structure interaction and dynamic meshing techniques are also described for the PRV geometries studied. The utilization of an HPC cluster ARCHIE WeSt will also be described.

5. Validation of CFD PRV Models for Steady State Single Phase Flow

Within chapter 5, single phase steady state experimental and CFD techniques will be presented for both the Henry and Broady PRV's. The experimental results will be compared with those generated within CFD to determine the degree of correlation and establish the appropriate CFD modelling techniques to achieve a validated CFD model. The results from both 2D and 3D computational domains will be compared. A study will also be performed following steady state CFD validation to identify and establish the effect of symmetry breaking phenomena on

the modelling capability of CFD to achieve accurate results. In addition, any 3-Dimensional flow effects will also be identified and explored.

6. Validation of Transient Moving Mesh PRV CFD Models for Single Phase Flow

In addition to the work within chapter 5, a transient dynamic mesh CFD approach for single phase flow will be established where the results of CFD analysis will be compared with experimental results. This will allow an appreciation to be achieved towards the effectiveness of CFD to capture the dynamics of PRV operation and determine the required modelling parameters to obtain a validated/accurate model. Furthermore, sources of dynamic instability predicted by the transient CFD models will be analyzed and compared with experimental data.

7. An Assessment of the Validity of Quasi-Steady Based Analysis of PRV's

The validity of the commonly used quasi-steady design approach to PRV's is examined by comparing detailed steady state conditions of valve behavior directly with transient conditions generated within CFD. A low order Matlab model will be used with steady state results from CFD and compared with transient CFD results and transient experimental data. This will allow any differences to be observed.

8. Two Phase Flow Analysis of Henry 5231BX PRV

In a similar nature to the work performed within chapter 5, a two phase experimental procedure to measure steady state values will be developed and compared to two phase CFD modelling techniques both

in 2D and 3D. Comparison will allow an accurate two phase CFD model to be developed in 3D in conjunction with lessons learned from previous 2D work in literature. Furthermore, a transient two phase experimental study will be developed to allow an evaluation of the dynamic performance of the Henry 5231BX PRV in two phase air-water operation to be achieved.

9. Conclusions and Future Recommendations

This chapter will identify the conclusions which have been determined over the course of the study and review the effectiveness of the research performed to meet the initial research objectives. Furthermore, any future recommendations will be established which would help to complement the work performed and provide a route to further contribute knowledge to the PRV industry.

10. Appendix

Within the appendix, CFD animations, experimental drawings, representative UDF used for dynamic meshing within CFD and matlab type 1 model for the Henry 5231BX PRV used for quasi steady analysis will be provided.

CHAPTER 2

BACKGROUND

In accordance with the research objectives established within the previous chapter, it is necessary to achieve a deeper appreciation towards the background of the PRV industry. Therefore, within this chapter a range of topics will be introduced such as the general operating principles of a PRV and associated design methodology. Furthermore, an overview of the plethora of industrial standards and sizing practices will be described to establish current design regulations. Finally, the dynamic operation of a PRV and the resultant challenges which PRV designers are required to overcome will be described with respect to the most up to date literature to highlight the opportunities which the development of robust and accurate PRV CFD models would offer to the wider industry.

2.1 Operation of a Typical Pressure Relief Valve [3]

Pressure relief valves operate on the principle that the device provides passive fail safe protection when the system pressure exceeds system design pressure. The typical geometry of a spring loaded PRV is shown in figure 2.1.

The inlet of the device is often directly connected to a system such as a pressure vessel where in the event of an emergency, pressure and temperature in the vessel would increase. In this safety critical scenario, pressure would be relieved to ensure that the pressurized system would remain within safe pressure limits and maintain integrity. Figure 2.1 highlights the typical components found within a spring loaded PRV with the flow path identified by the black/yellow arrows.

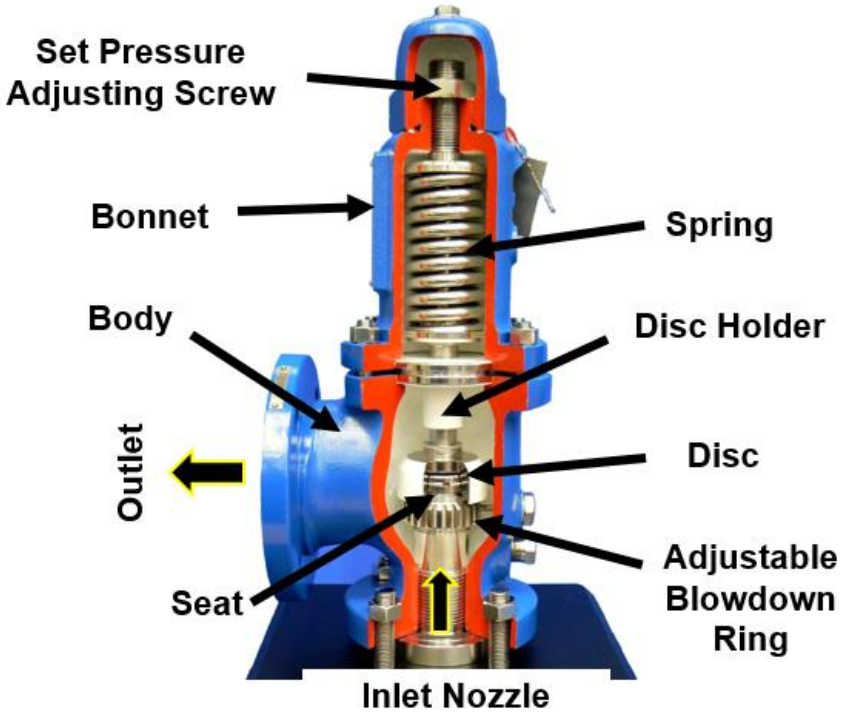

Figure 2.1 – Illustrated PRV diagram of 3511E Broady PRV

In normal operation, the spring which is set by a pressure test during the manufacturing stage, provides a suitable compression force to seal the system until a critical point, known as the set pressure is reached. This can be typically adjusted using a set pressure adjusting screw. The sealing surface exists between the disc and seat, where the disc surface is subjected to the system pressure at its lower surface. The seat itself is typically metal however depending on the sealing arrangements the disc can have metal or elastomer elements. The disc holder typically ensures alignment of the disc on to the seat, as shown in figure 2.1. The overall body and bonnet assembly ensures that the pressure and components are contained and provides geometry for the fluid to exhaust from the valve. The effect of components such as the spring and piston on the dynamic operation of a PRV is shown in the free body diagram in figure 2.2.

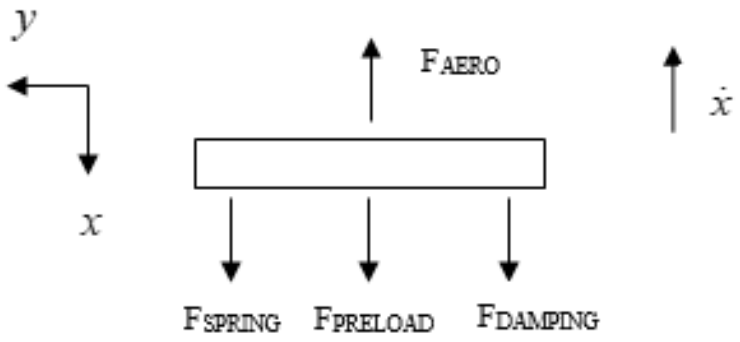

Figure 2.2 – Free Body Diagram of PRV Disc

The force balance on the PRV disc consists of several fundamental forces;

- Aerodynamic force due to static pressure distribution acting on the piston surface (F_{AERO}). Shear forces are generally small. [N]
- Spring force at displacement x_n from the datum position when closed (F_{SPRING}) and preload ($F_{PRELOAD}$) at displacement x_0 determined during the valve setting process at set pressure with spring constant k. [N]
- Weight due to mass of moving parts, m (W_{MOVING}). This force is taken into account within $F_{PRELOAD} = F_{AERO} - W_{MOVING}$ at set pressure. [N]
- Damping force ($F_{DAMPING}$) due to frictional contact and inherent spring damping with damping constant, c. [N]

Historically, pressure relief valves are designed and developed using an iterative trial and error based method to achieve the specified specification required from the customer's system. There are however codes and design practices available for selection and sizing purposes, however the resilience of such methods has been shown to be questionable and do not as of yet include the widespread use of CFD as a design tool or for use on two phase flow. In addition, during PRV operation a complex fluid structure interaction exists between the aerodynamic surfaces of the PRV and working fluid which

as a result generates significant pressure gradients, high velocity flow, shock structures and expansion due to compressibility effects. Such complex flow characteristics highlight the modelling challenge which CFD must overcome and capture to achieve an accurate solution. Supersonic and multiple choked flow regions, where the Mach number of the flow is equivalent to unity, exists during the normal operation of a PRV for a compressible fluid as the geometry is designed such that the pressure ratio between the inlet and outlet exceeds the critical pressure ratio. As the supersonic flow is deflected across the geometry of the seat and disc (otherwise known as a piston), strong separation regions and vortices are produced as a result of distinct pressure gradients across the PRV surface. During the dynamic operation of the PRV, the movement of the choking points allow the total mass flow rate through the device to be passively controlled and the aerodynamic force to vary.

During PRV operation [13], it is common to encounter either single phase (eg, air or water) or multiphase flow where various flow regimes have an effect on the flow structure and pressure distribution. An example of multiphase flow for the case of steam results from the various acceleration and subsequent expansion processes rapidly decreasing the temperature and pressure producing condensation and droplets in the vapour flow. Two phase flow at the valve inlet can also be generated due to the level swell in a vessel containing saturated liquid leading to droplet entrainment. In general, cavitation or boiling processes for liquid PRV operation are common for operating PRV’s due to the subsequent reduction in pressure experienced as the valve opens.

The operating behavior of a typical pressure relief valve with respect to pressure can be understood from the pressure vs lift plot shown within figure 2.3. Lift is defined as the piston displacement from the seat and will increase as the unbalanced force due to the increasing aerodynamic force against the spring force causes the piston to accelerate in a linear motion. Such behavior

represents PRV movement as pressure increases during a non-standard event within the pressure vessel on which the PRV is installed.

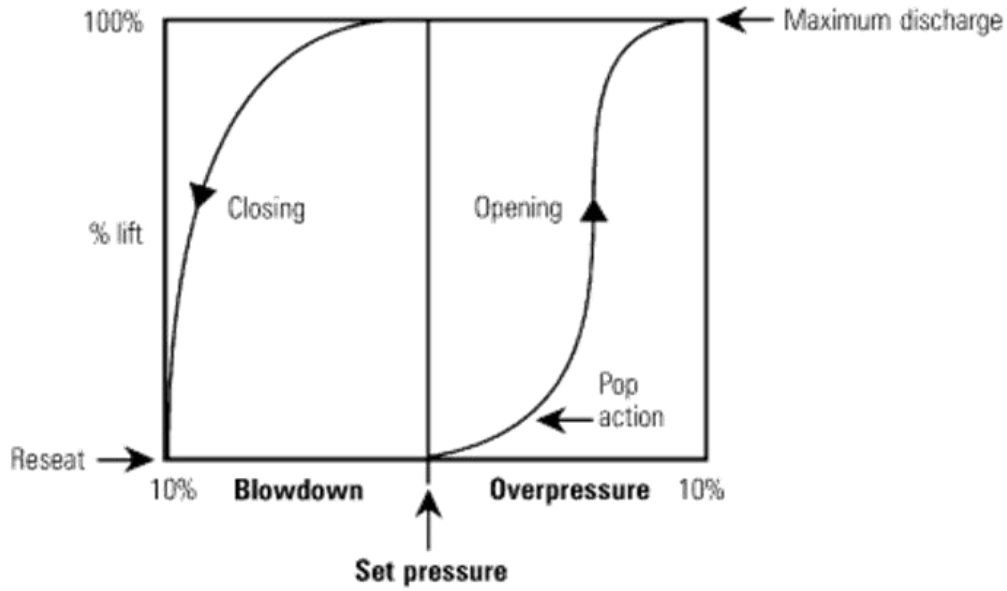

Figure 2.3 – Typical Operating Principle of PRV With Respect to Pressure

The **set pressure** of the PRV represents the critical system pressure at which the valve starts to open and is indicated by an initial flow leakage from the valve due to the disc lifting from its seated position [13]. As the pressure continues to increase the valve will lift further until an **overpressure** value (relative to set pressure) is reached leading to a rapid opening of the valve. This pop action occurs at the pop pressure and will lead to a fully open valve and the PRV's peak flow relieving capacity to reduce system pressure. At overpressure, the increasing back pressure within this system reduces the overall aerodynamic force to allow equilibrium with the spring force; as a result the acceleration of the piston is arrested. Typically, the value of overpressure for a PRV is approximately 10% however it is dependent on the certified rating of the valve and performance requirements; for example, steam applications typically require tighter tolerances when compared to refrigeration systems. In

addition, the value is dependent on the working medium as the typical overpressure range for compressible fluids tends to be 3%-10% and for liquids 10%-25%. It should be noted that the use of a PRV is only effective when the pressure increases in a uniform manner and at a measurable rate throughout the pressurized equipment.

Figure 2.3 also illustrates that for a predetermined decrease in pressure, the disc returns to its closed position during a process called blowdown in which the pressure of reseating (reseat pressure) compared to the set pressure is known as the **blowdown pressure**. This is due to the spring force overcoming the decreasing aerodynamic pressure force due to system pressure reduction and causing a net closing force and acceleration. As a result, the now re-sealed system reaches its original state given the emergency event has been resolved. Similarly to overpressure, the value of blowdown pressure also varies given the performance requirements of the system. For example, it may be desirable to limit the egress of environmentally harmful fluids or if the vessel contains a valued asset. In such cases the blowdown pressure tolerance will be closer to the set pressure. The characteristics of blowdown and overpressure for a selection of PRV's can be modified through the use of adjustable blowdown rings which modify the geometry of the flow path and flow forces. This allows the manufacturer to provide a tailored pressure relief solution to meet the customer's specification.

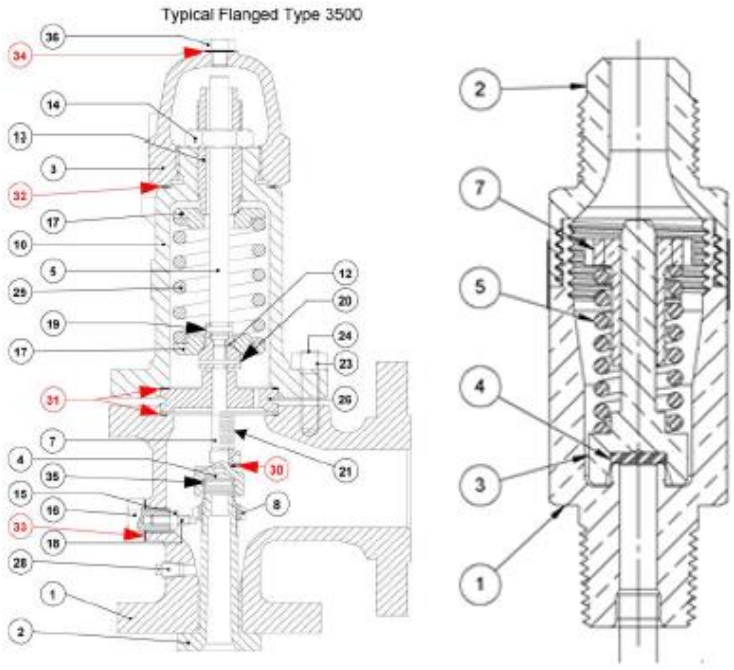

Figure 2.4 – Broady 3511E PRV (left) and Henry 5231BX PRV (right)

For PRV's to meet the requirements of various scales and complexity of pressurized systems, as well as cost reduction, there are two distinct pressure relief valve types available based on geometry and flow direction; both of which will be analyzed in detail within this study. The most common type consists of a right angle flow deflection between the inlet and outlet of the valve. Such a configuration is required when dealing with very high flowrates and strict performance constraints such as those found within the nuclear industry. In addition, due to the isolation of the flow from components such as the spring, gland and adjusting screw the expected lifetime of a right angled PRV is much higher when used in harsh, corrosive environments. During this study a Broady Flow Control 3511E pressure relief has been used (figure 2.4) as an example of a right angle PRV. Alternatively, a through flow PRV can be used in applications with tight geometrical constraints with a lower flow requirement such as the refrigeration industry. In the case of a through flow PRV, the flow is more constrained and a greater coupling arises between the flow and piston motion, however both the inlet and outlet directions are aligned. As a result, the performance of a through flow PRV is strongly dependent on the geometry

of various valve components and is heavily influenced by the effect of backpressure. During this study a Henry 5231BX through flow valve (figure 2.4) has been used as a case study for this valve type.

2.2 PRV Design Methodology and Industrial Standards

The design process of a pressure relief valve and its integration within a pressurized system has been developed over many years and must conform to the applicable codes and standards at the facility in which it is being installed. The development of design codes such as ASME VIII was motivated by proliferation of steam boilers in which a large number of fatal accidents was recorded due to explosions within the pressurized equipment. Accidents in particular were caused by inadequate boiler design and/or lack of stringent use of overpressure protection devices. However, despite a widespread application of available design codes of pressurized equipment, accidents attributed in particular to PRV failure have occurred [2, 10]. Most famously in 1979 there was a significant nuclear accident at Three Mile Island Nuclear Power Station in the USA [14]. The release of radioactive material from the core which had suffered a partial meltdown was mainly attributed to the failure of one PRV. The PRV failed to reseal and lead to the loss of a large volume of reactor coolant, hence resulting in reactor meltdown. To this date, it is the most significant commercial nuclear incident in the USA and highlights the importance of such devices as a PRV in maintaining the integrity of a pressurised system [15].

To prevent such disasters and achieve conformity to the relevant design code, there are a variety of techniques used by manufacturers to develop an appropriate PRV design to meet the specification required from the customer. Especially due to the development of computational resources, sophisticated modelling approaches have been developed such as empirically based numerical models and CFD. Such techniques will be explored within this

section as well as the various codes, standards and guidelines available to valve manufacturers.

In general, the design of a pressure relief system requires a series of steps to achieve an inherently safe solution which is matched appropriately with the pressurized system and the local environmental conditions. Such a process allows designers to utilize a PRV and prevent the protected system from exceeding the maximum allowable accumulated pressure (MAAP) which could result in loss of structural integrity of the system. It is critical in the initial system design stage that there is identification of the worst possible pressure producing emergency event in order to establish the appropriate process conditions in which the relief valve will be required to operate within (ie pressure, temperature and discharge flowrate). By doing so the required worst case relief area could be determined from the necessary discharge capacity of the system to allow sizing and determination of the effectiveness of a pressure relief valve. Limitations in the current design methodology for PRV's however has been identified and is highlighted within the following section.

2.3 Standards and Sizing

As a result of various overpressure incidents the requirement of a pressure relief valve within a pressurized system is mandatory on most pressurized systems and must meet strict regulations set by local jurisdictions [2-4]. There are a wide range of international codes and standards which are applied. In Europe the European standard EN ISO 4126-1 and for the UK EN 1268 is often applied more recently in the form of a Pressure Equipment Directive (PED) required for all EU member countries to adhere to and in the U.S the regulatory bodies ASME and API apply similar regulation. In the case of some jurisdictions in which there is no legal requirements for a pressure relief valve then good engineering practice must be followed to avoid the danger of

pressurized equipment failure. The PRV's studied within this thesis were designed to adhere to the regulatory requirements of the ASME (American Society of Mechanical Engineers) code and API (American Petroleum Institute); therefore these codes will be covered in detail within this section. It should be noted that the requirements of the ASME, API and European Pressure Equipment Directive design codes are similar. The benefit of such standardization internationally allows the importation and exportation of devices to boost local economy and also provides geometrical consistency across the industry between various manufacturers. As a result the customer can acquire the most suitable valve for their requirements and allows inherent ability to swap out valves if required without substantial changes to pipework. In general, the regulations however enable manufacturers to maintain a unique identity in the use of bespoke internal components such as nozzle, disc, huddling chamber and blowdown adjustment rings. Therefore, competition can be achieved within the industry.

In the ASME code for boiler and pressure vessels (BPVC) both emergency relief requirements and equipment design are covered. Section VIII of the code is the most applicable for PRV's however it covers the requirements for performance rather than providing guidelines for the design of PRV's. Due to the similarity of the ASME and API design criteria, API publications regarding PRV design and development are generally used to meet ASME requirements. Pressure relief valves are then sized either by hand calculation using ASME and API provided formulas or by using a capacity chart according to the working fluid and valve type [16]. Computational programs have also been developed more recently based on ASME and API codes in order to check for ASME Section VIII compliance [7, 17] and provide the manufacturer with a much more time effective design tool. It is hoped that CFD could also provide a useful tool for manufacturers to achieve additional assurance on the effectiveness of the design and code compliance. As a result, costs such as inspection and testing could be kept to a minimum in the case of PRV compliance failure. Compliance with ASME code is verified by the National

Board of Boiler and Pressure Vessel Inspectors where the performance of the PRV design is verified by inspection of manufacturing processes and physical testing at an approved flow testing laboratory. This therefore provides assurance of the design and allows the resilience of the PRV to be tested across different conditions. For the purpose of the research within this thesis the flow related design issues such as overpressure, blowdown and discharge capacity will be studied in relation to the codes and standards.

The general provisions of the ASME BPVC code describe the performance of PRV's with a Maximum Allowable Working Pressure (MAWP) between 1 – 200 Barg where it is stated that all pressure vessels must be protected by a pressure relief device which would prevent pressure rise of more than 10% of set pressure or by 3 psi, whichever is greater. In the case of fire, the pressure accumulation is permitted to reach 20% that of set pressure. The value of blowdown for compressible flow is specified within the code as typically 10%.

It is important to note that set pressure within the ASME code is defined [3] as "the value of increasing inlet static pressure at which a pressure relief device displays one of the operational characteristics as defined by opening pressure, popping pressure, start to leak pressure, burst pressure or breaking pressure". This introduces a variability which is left to the valve manufacturers to select and make clear for their valve setting procedures. The code states that the set pressure when a single pressure relieving device is used should not exceed the maximum allowable working pressure of the vessel and shall not exceed 3% of the defined set pressure above 5 Barg. It is commonly found that pressurized plants and equipment can be operating at MAWP of between 200 and 2000 Barg, much higher than the earlier specified limits of 200 Barg; therefore valve sizing methods used during the design process are often required to be extrapolated as the discharge capacity is not defined. For the most stringent applications such as within the nuclear industry, ASME BPVC Section I highlights the tightest tolerances for both overpressure and blowdown

for pressure relief devices across a wide operational range of pressures. Overpressure values for such applications are stipulated to be 3% of set pressure and blowdown for pressures greater than 375 psi (25.8 bar) and less than 67psi (4.6bar) to be 4%. Such tolerances highlight the challenges posed to valve manufacturers to meet the required specification for a wide variety of applications and code compliance.

In general, PRV's are sized to achieve a required flow capacity to relieve pressure within a system to prevent significant overpressure. When sizing pressure relief valves, sizes are provided in terms of standard pipe sizes of the inlet and outlet as well as the letter designation of the nozzle. The letters associated with the nozzle are described within API RP 526 and range from a diameter of approximately 1cm to 15cm. These are commonly used by PRV manufacturers as design guidelines for flanged spring loaded pressure relief valves in which to conform to the requirements of ASME BPVC for gas, vapor and steam service. Selection and sizing of a PRV requires the use of a flow correction factor (discharge coefficient K) which is determined during ASME certification testing. However manufacturers tend to use a worst case value of K during early stages of design. API 526 and ASME codes utilize the value of K and the ideal gas law in order to size the PRV however Scuro [7] found ASME recommended calculations to over predict flow forces by approximately 20% compared to CFD calculations. This is due to the fact that the ASME standard considers that all static inlet pressure is converted into mechanical work in the disc area whereas CFD calculates the force as a function of disc lift. As a result, such an error could lead to inappropriate valve sizing and poor PRV performance. Further issues were found by Yang [18] where if compressed air was used as a test medium instead of high pressure high temperature steam, as is often done due to testing equipment limitations, the reseating pressure would be overestimated resulting in excessive steam discharge. Research documented by Beune [5, 19] has also shown limitations in API 526 and to be unsuitable for use at high pressure and temperature due to a break down in the ideal gas law as intermolecular forces change. As a

result, care must be taken by manufacturers when trusting the current standards and provides CFD with an opportunity to establish a more accurate approximation.

The design of a PRV requires several critical steps in order to appropriately size the device for the required system;

- Initially, it is crucial that the environmental conditions in which the PRV is operating within is well defined such as the physical properties of the flowing medium and the calculated set pressure depending on the MAWP of the system and design code in use.

- The size of the valve orifice is then selected for a given maximum expected discharge capacity when the system is operating at 10% above set pressure during an emergency event. The calculation of the required orifice area from an expected relieving capacity is given within API-520 Part 1.

- The sizing of the associated inlet and outlet piping is determined based on flowrate at 10% overpressure condition.

In the case of multiphase applications API-520 historically provided the recommendation to PRV manufacturers that each phase should be treated separately [2] with the total calculated orifice area representing the total required for all phases within the flow regime. However, more recent developments in modelling capability and numerical techniques has enabled the emergence of analytical techniques capable of calculating the interaction between each phase. Such methods are described within API RP 520 Part 1 Appendix D in order to size PRV's effectively for use within multiphase flow regimes. However currently within design codes there is no generally

recognized procedure for determining the relieving capacity of a PRV in a multiphase application.

2.4 Current PRV Design Methods and Numerical Modelling

In contrast to the guidelines provided by the various codes and standards where calculations of flowrate are extensively provided, guidance for aerodynamic force is much less abundant. Information is available regarding the control of superimposed back pressure which influences the total aerodynamic force however guidance on design for determining and controlling the aerodynamic pressure force acting on the moving disc surfaces is not. Manufacturers as a result have developed individual techniques and design methodologies to determine the dynamic behavior of their devices however such work is not openly available. Models not only have been developed for single phase compressible gas operation but also for incompressible liquid conditions and multiphase flow regimes. Such commonly used design methods will be described within this section.

The quasi-steady assumption, which is commonly used by manufacturers especially during the early stages of design, relies on a premise that the influence of disc velocity on the flow is negligible and that the flow is not coupled with the opening time of the valve. This assumption then allows a series of steady state experiments or CFD simulations at pre-defined values of piston/disc displacement (lift) to determine the aerodynamic force acting on the piston and to determine a valve characteristic force vs lift curve at a constant inlet pressure. As described in previous research by Beune [20], Song [21] and Darby [22, 23] the results are converted to the time domain by solving equations of motion for the disc using a numerical solver package such as MATLAB which represents a simplified low order dynamic model of the PRV. Such algebraic models to predict transient behavior using quasi steady

assumptions will be described as being type 1 models in this thesis. In addition, as the force lift curve is determined at a fixed pressure, the assumption of linear pressure scaling is also used to determine the flow forces at alternative pressures. Once the data has been input to a numerical solver, curve fitting is used to interpolate the force vs lift relationship generated, where in combination with constraints such as the ramp required for inlet pressure, initial disc velocity, spring preload and maximum allowable lift; a pseudo dynamic piston position vs time relationship can be created. Such a low order one degree of freedom (1 DOF) numerical type 1 model however does not provide information to the designer regarding flow physics or flow instability mechanisms as well as important features such as surface pressure acting on the disc. This is in contrast to the ability of CFD to provide such information however the low order type 1 model is able to achieve a solution at a fraction of the computational cost and time of that required for CFD.

Once a manufacturer completes steady state flow force measurement of a PRV it is possible to generate a force vs lift curve and mass flow rate vs lift curve similar to figure 2.5. The results are often obtained within a flow testing laboratory using custom components to enable the flow force acting on the piston to be recorded by a device such as a load cell and disc lift to be measured by a laser, LVDT or dial gauge. Flow rate is measured using a flowmeter and components such as the spring and bonnet is often removed. The inlet pressure is set and managed using an upstream pressure gauge in which it is held at a constant value whilst disc lift is incrementally increased to allow disc force and flow rate measurement to be determined. Such an approach however requires significant dedication of time and design effort as well as manufacturing and material cost of the bespoke equipment. In addition, the capital investment required for the flow testing facility itself would be required to be large and is often only used at low pressures due to equipment limitations such as a compressor capacity and pressure vessel/piping rating. Therefore, due to the substantial commercial cost required CFD could, once

properly validated, provide manufacturers with a much more cost effective and useful theoretical method.

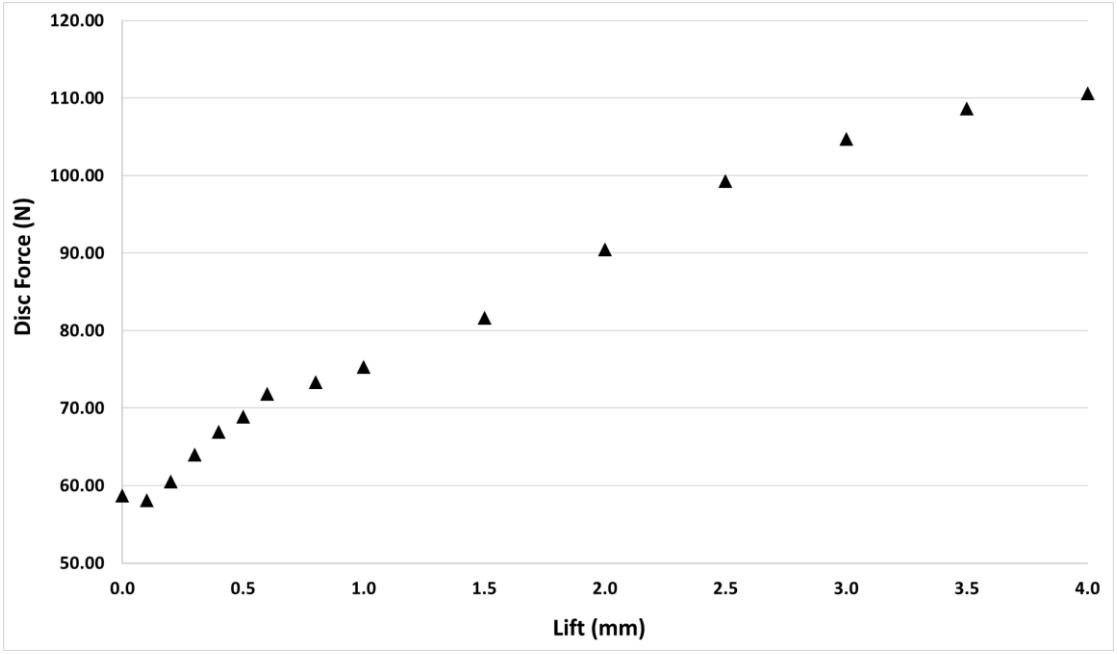

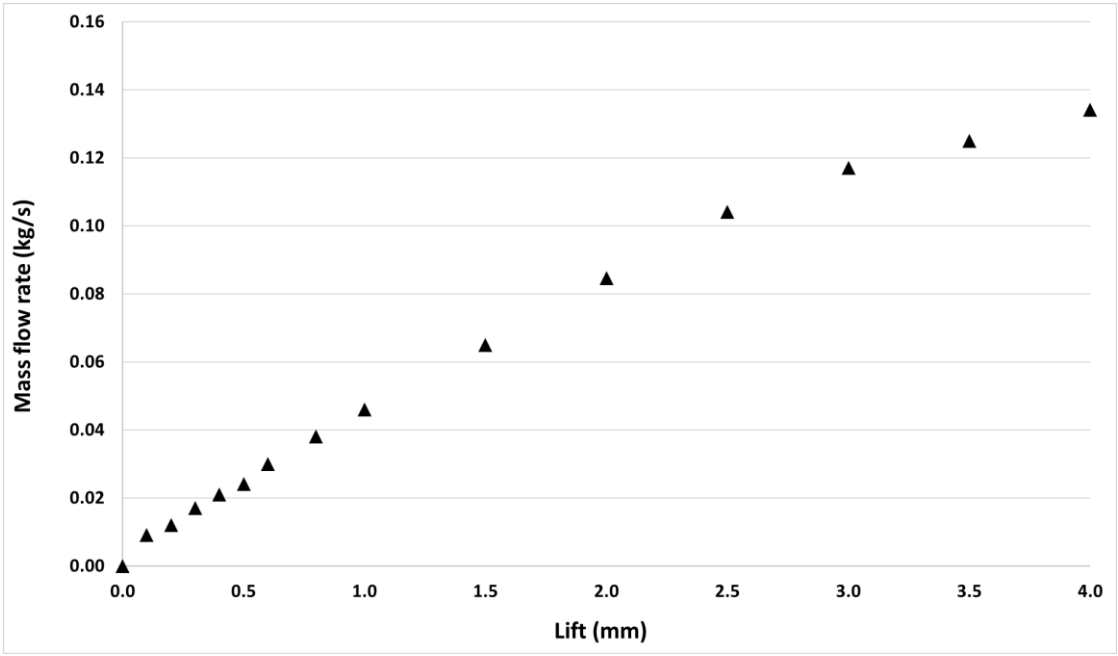

Figure 2.5 – Typical Experimental PRV Disc Force and Mass Flow vs Lift Curves for Broady 3511E PRV at an inlet pressure of 3.3 Barg.

Assuming that the quasi-steady assumption is valid then designers can use the force lift curve to understand the operational characteristics of the valve during the valve opening and closing stages and undertake any design changes required to achieve the desired performance. Design changes, which was investigated by Taggart [9], highlighted the influence in adjustment of disc/seat geometry and the successful use of optimization techniques to achieve tolerances required, in particular to meet ASME I requirements. Manufacturers also make use of a blowdown adjustment ring, in particular for larger right angled PRV's, which provides the functionality to adjust the force lift curve to achieve the desired overpressure and blowdown performance at different pressure operating conditions. A force lift curve such as that shown within figure 2.5 and the use of pressure scaling for a normalized (n) aerodynamic disc force (equation 2.1) allows designers to appreciate the forces involved at various pressures when the flow is assumed to be choked (Ma = 1). This as a result allows engineers to select a suitable spring stiffness and orifice size required to achieve force equilibrium at set pressure and discharge rate. This approximation is shown within figure 2.6, where the relationship between the spring and force lift curve directly influence the unbalanced forces and hence disc acceleration during opening and closing.

$$F_n = \frac{F}{(P_0 - P_{atm})A_{seat}} \qquad \textbf{Equation 2.1}$$

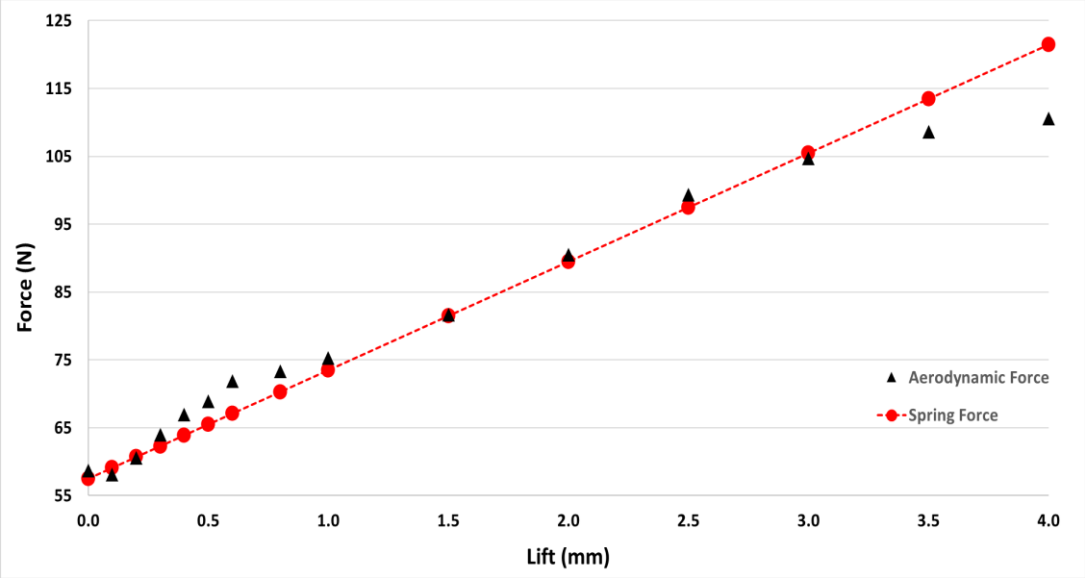

Figure 2.6 – Experimental Aerodynamic Force Lift Curve vs Spring Line

Following the initial spring setting selection, further refinement of the preload during initial pressure testing or shakedown of the PRV at the set pressure is required. It is important to note that most manufacturers have their own unique approach to setting valves. For example, some manufacturers use bubble tests whereas others use first audible techniques to detect initial leakage and identify the set pressure at which the disc has opened from the seat. Such testing is important in order to adhere to the 5% tolerance of the valve to be set at a pressure value close to the design pressure. This is due to the requirement of the PRV being able to operate for a range of spring specifications for a variety of applications and must be tested by the National Board in the case of ASME or equivalent regulatory body of inspectors.

In general, PRV designers use characteristic PRV curves such as figure 2.6 to achieve the required PRV opening and closing behavior based on a design approach known as the “high lift principle” [24]. Such a design feature prevents a slow opening and accumulation of pressure as it has the intention to allow the PRV to “pop” open and relieve flow at maximum discharge capacity as soon as possible once the critical value of system pressure is reached. In

addition, a slow opening PRV would likely result in an unstable motion which would cause oscillation of the disc known as simmering which could damage the sealing surfaces. Further to the aforementioned research by Taggart [9] the design of the disc and seat geometry as well as the outer recess formed between the disc and blowdown ring known as the huddling chamber significantly affect the ability of the valve to pop open and close firmly.

However, the use of assumptions such as pressure scaling and quasi steady assumptions without extensive validation would seem to be a potential design oversight. This is due to the fact that if the use of the assumptions for a given PRV geometry is incorrect then the desired performance would not be achieved. Interesting research performed recently by Dempster et al [25] highlighted a deficiency with utilizing a linear pressure scaling method for estimating flow force at various pressures using quasi steady state test data at lower pressure due to equipment limitations. It was found that for an API/ASME right angled type PRV, linear pressure scaling was invalid until a critical pressure ratio was achieved with uniform choked flow at the discharge area. This is evidence contrary to common design practice which involves linear pressure scaling, therefore in addition to the previous observations would result in a PRV to be designed inappropriately and not perform as expected. The research performed by Dempster [25] however didn't investigate the validity of the quasi steady assumption based on a decoupling between valve motion and flow physics. Therefore, in order to complement such work, it is proposed within this thesis to perform transient CFD analysis to predict the aerodynamic forces acting on the piston as the valve is in motion. As a result, a lift vs time curve will be generated and compared to the experimental and quasi steady based numerical type 1 model in order to identify and explain any differences between the approaches.

In addition to the quasi-steady design method described, an additional numerical modelling technique is required to provide a design tool for

multiphase applications. To date, a definitive design method for PRV's operating within a multiphase regime has not been established due to the complex flow regimes and modelling difficulty. API however have published recommendations for manufacturers to follow if they wish. As described earlier, two phase (multiphase) flow occurs where the flow stream through the PRV contains fluid in gaseous phase in combination with fluid in the liquid phase. The flow regime and relationship between both phases during dynamic operation of the valve is a transient process in which key parameters such as gas void fraction is changing. Therefore, the level of complexity to achieve a numerical model which approximates the process is significant. Traditionally a method was used which simply requires a calculation of the required discharge area for each phase where the results would be added together to achieve a mixture effective discharge area. This method is commonly known within older API recommendations as the 'added areas method' however it has been found to have significant shortcomings and errors such as under sizing and is no longer found within modern publications. Such work to define discharge area and disc forces for multiphase applications from an algebraic model will be described as type 2 models in this thesis whereas type 3 models will represent algebraic models to predict discharge area and disc forces in single phase.

Research performed by the Design Institute for Emergency Relief Systems (DIERS) enabled several multiphase modelling techniques to be developed which are based on the Homogeneous Equilibrium Model (HEM) and Homogeneous Non Equilibrium (HNE) models to determine the discharge area required. The homogeneous aspect of both type 2 models assume that the phases are well mixed and can be represented as a single phase fluid where individual phase properties are represented within volume or weight averaged properties. The HEM method also assumes that the phases are in mechanical and/or thermal equilibrium therefore a velocity slip term at the interface between the phases is not required. Whereas the HNE model requires terms to represent interfacial mass, momentum and energy transfer rates. Both approaches approximate the geometry of the PRV to represent a de-Laval,

converging/diverging type nozzle (figure 2.7) with an empirically derived discharge coefficient, K according to the model used [5]. A de-Laval nozzle operates on the principle of subsonic (Ma < 1) flow accelerating due to convergent geometry to a throat section in which flow is choked (Ma = 1). Following this critical point, as the sonic flow enters the divergent section; the gas expands to allow further acceleration of the flow to supersonic (Ma > 1). By using the de-Laval nozzle to represent a typical PRV geometry, the mass flow through the nozzle could be determined using the model and enable the required effective discharge area to be calculated by dividing the mass flow rate with the discharge coefficient. The complexity of deriving the discharge coefficient K however is the most significant challenge of any model development as it incorporates a correction factor for geometrical, numerical model and phase interface effects.

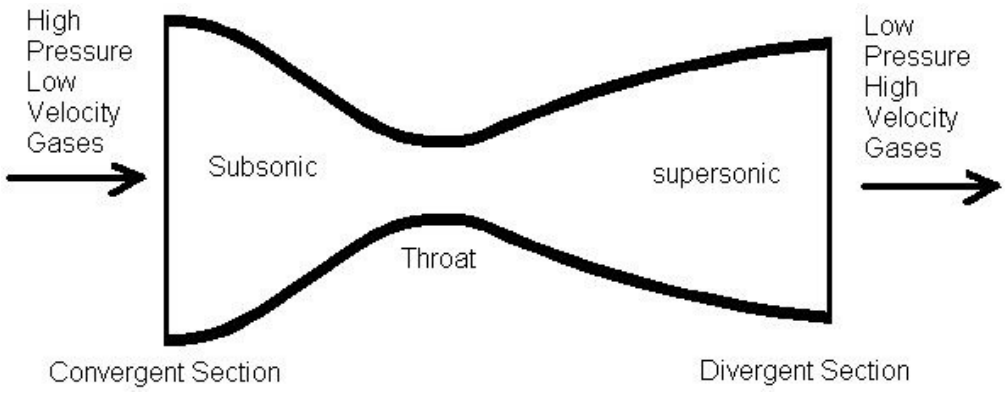

Figure 2.7 – Geometry of a Typical de-Laval Nozzle

A result of the work performed by DIERS was the development of a simplification of the full HEM method known as the “Omega Method”. The Omega method was developed as the HEM method was deemed to be too computational complex for PRV manufacturers to use. The Omega parameter introduced within the model is a compressibility factor which defines the equation of state for the multiphase flow. Extensive research of the method however has found that for multiphase flow with a lower ratio of gas/vapor to

liquid (mass quality), the Omega method would result in an undersized value of effective discharge area. Therefore, the development of the HNE model took place with a particular focus to improve correlation of the model at lower values of mass quality with terms to account for mechanical and thermal non-equilibrium. As a result, frictional and slip effects could be accounted for at the phase interface as well as the effects of boiling/condensation processes due to rapid expansion of the flow through the PRV. The results of the HNE type 2 model indicated much better correlation at low mass qualities however at higher mass qualities the results between HEM and HNE was similar. Therefore, due to the demonstrated accuracy of the HNE model and Omega simplification, ISO-4126 adopted the approach to recommend to manufacturers for sizing PRV's under two phase flow conditions.

The ISO 4126 HNE based type 2 model however still has limited accuracy and has a tendency to oversize the required discharge area. In addition, the type 2 model only has the capability to predict the mass flow rate of the PRV at maximum lift and does not provide the designer with detail regarding the force/mass flowrate vs lift characteristics and/or dynamic behavior. Therefore, manufacturers still require experimental testing in order to acquire such data regarding dynamic performance. Multiphase 2D CFD models have been developed [11, 12, 26-30] for PRV's however within this thesis 3D CFD transient capabilities will be explored and developed upon. As a result, valve manufacturers will have a design tool capable of providing designers with a much greater appreciation of flow physics and dynamic characteristics in a multiphase flow regime. This would provide a significant improvement in available design methods for multiphase flow especially for PRV dynamics and flow force as there are only discharge area calculations available.

2.5 PRV Dynamics, Instability and Operational Issues

The operation of a pressure relief valve is often captured within steady state measurements in the case of numerical models or experimental analysis through the use of the quasi steady assumption however the opening and closing process in reality is transient and subject to various transient phenomenon and instability mechanisms. In order to appreciate such effects, it is important to understand the “ideal” PRV dynamic behavior and fluid dynamic processes. Furthermore, it is critical for designers to identify potential damage mechanisms, system design and installation errors which could result in the PRV to not perform as designed. An example of the motion of the disc as the pressure changes, which is desirable for the previously described high lift design principle, is shown within figure 2.8 which represents a Broady 3511E PRV valve at notch position 4 and set pressure of 3.3 Barg.

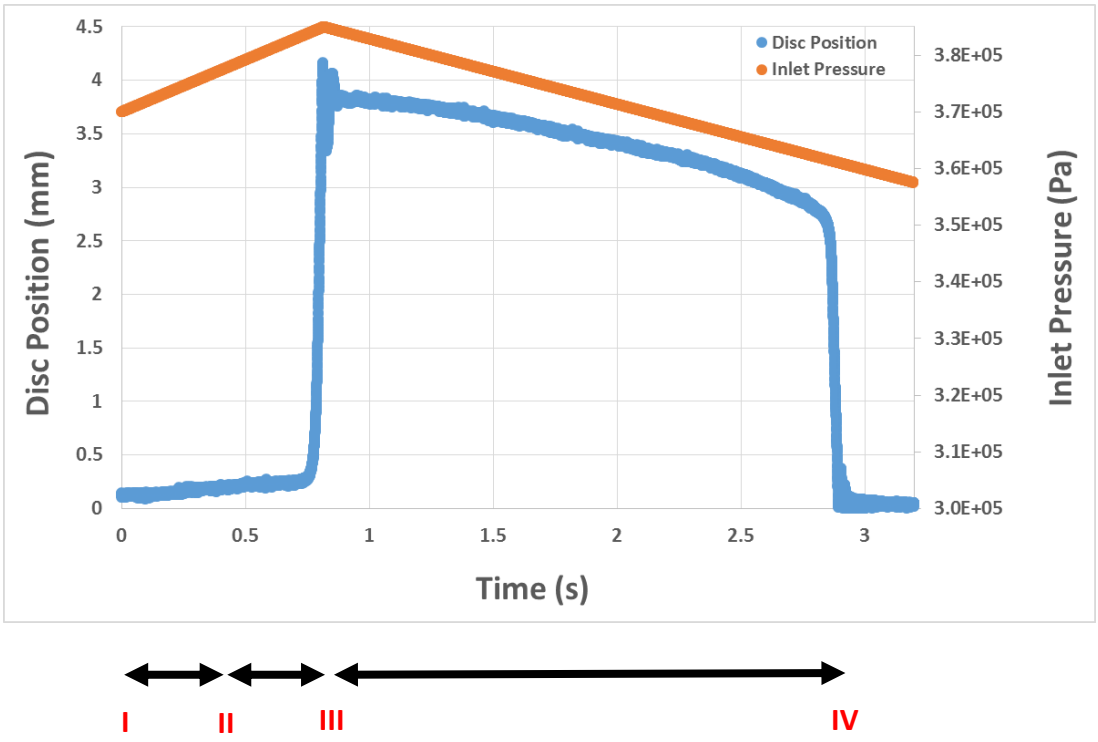

Figure 2.8 – Typical Dynamic Operation of a PRV With Respect to Time

It’s important to note that notch position refers to the adjustable position of the blowdown ring (described in chapter 2.1) and allows PRV performance to be tailored to the requirements of a given system.

The various stages of PRV operation are identified within figure 2.8 and can be understood by the following descriptions between time interval I to IV;

- **Time I –** The PRV is closed with no flow as the inlet static pressure of the vessel/system remains below set pressure.

- **Interval I to II -** Is known as the simmering stage when the inlet static pressure of the system is close to or just above the set pressure of the PRV where the aerodynamic force is in equilibrium with the closing force exerted by the spring and the weight of moving parts. As the inlet pressure continues to rise, the valve disc will lift which will cause an initial leakage through the system; in addition, this stage is often accompanied with aerodynamic force fluctuation and disc oscillation.

- **Interval II to III -** The high lift design principle described in section 1.2 is critical for stage 3 as fluid during the initial leakage and system pressure increase enters the huddling chamber and pressure acts on a larger area, causing a larger opening force to overcome the spring force. As a result, at a given point of lift, the PRV due to the previous combination of flow effects will result in a pop action and allow the PRV to reach its maximum discharge capacity.

- **Interval III to IV -** As the system pressure decreases and the mass of the pressurized system is vented, the effect of spring force and reduction in the aerodynamic force, the PRV will begin to close. Similar to opening, after a period of blowdown and incremental closure, a point

will be reached in which the PRV will rapidly close due to a significant closing force unbalance and reseal the system.

- **Time IV** - The PRV has returned to same state as at time I.

The equation of motion (equation 2.2) derived from the free body diagram shown in figure 2.2 (section 2.1) determines the dynamic response of the PRV and can be simplified to a simple spring mass damper system with an external applied force term. The external force applied exists in the form of the aerodynamic force applied to the disc, where if motion is opening, is opposed by spring force and damping force in the form of friction between the spindle and housing.

$$\sum F_x = kx_n + kx_0 + c\dot{x}_n - F_{AERO_n} = -m\ddot{x}_n$$
$$\sum F_x = F_{AERO_n} - kx_n - kx_0 - c\dot{x}_n = m\ddot{x}_n \qquad \text{Equation 2.2}$$

Where;

- F_x = Total unbalanced force on the disc of the PRV in the axial direction
- F_{AERO_n} = Aerodynamic force due to static pressure acting on the piston
- x_n = Displacement of disc from valve seat (closed datum position) (lift) at time n
- $\dot{x}_n$ = Velocity of disc
- $\ddot{x}_n$ = Acceleration of disc
- kx_0 = Preload force at displacement x_0 at set pressure
- kx_n = Spring force at displacement x_n with respect to x_0
- k = spring constant

- m = mass of moving parts
- c = damping constant due to frictional contact and spring damping

As the PRV dynamic system can be appreciated as a vibrating model then in the case where the system is not overdamped; instability mechanisms could influence the behaviour of the moving parts (disc). From research by Hos [31] it can be established that the PRV system should not be thought of as being intrinsically stable or unstable but dependant on various instability mechanisms. Each form of instability is due to a fluid structure interaction between valve components, fluid dynamics and connected piping/vessel arrangement. There is also an important difference between fundamental instability and the transient event which may initiate/trigger the instability. The various types of undesirable and/or unstable response for PRV's are defined as follows;

- **Chatter** – Is induced due to fluctuating aerodynamic/back forces. An unstable net force acts on the disc which results in large amplitude oscillation of the disc. If the amplitude oscillation is large then there will be a violent repetitive impact of the disc with the seat which would cause substantial damage to the disc/seat and hence integrity of the PRV.

- **Flutter** – Caused by unstable net force acting on the piston similarly to chatter however with a lower amplitude of oscillation. Frequency of oscillation due to this instability is typically high when the valve is open however the disc and seat do not impact with each other.

- **Cycling** – Cycling occurs when the net pressure acting on the disc falls below the blowdown pressure before the pressure in the vessels falls below set pressure. As a result, the disc will close as pressure is quickly relieved upon opening the valve, causing it to close however as

pressure continues to build in the vessel the PRV will reopen. A cyclic process therefore follows.

A primary focus of valve and pressurised system designers/engineers when installing PRV's is to ensure that the recommendations of API to avoid inlet piping causing unstable PRV behaviour, in particular chatter. The recommendation is commonly known as "the 3% rule" (designed to prevent an unstable response) by limiting the pressure drop in the inlet line to no more than 3% of valve set pressure. Therefore, if frictional pressure drop is always less than the blowdown the valve should not re-close and as a result would exhibit stable behaviour. The 3% guideline however is based upon steady state flow conditions (quasi steady) and has been found within the literature [19, 22, 32] to be inadequate as a reliable indicator of conditions for stability. By approximately 2010, the insufficiency of the 3% rule was recognized in a number of modern studies presented by Hos [31] and Darby [22]. Therefore it could be suggested that current standards are unable to provide robust recommendations to prevent instabilities early in the design process.

A significant amount of studies [23, 31, 33] have identified a number of factors which contribute to the instability of a PRV's operation. A range of factors from poor design to inadequate configuration of inlet/outlet piping as well as quality of installation can affect the PRV's dynamic stability. The major sources of instability can be described as follows;

- Pressure Waves - Due to acoustic coupling of the PRV dynamics with the pressure vessel/piping, a pressure surge associated with reflection of the expansion wave generated when the valve opens very quickly could occur. As a result, inlet pressure would fluctuate quickly after initial opening which could induce chatter and/or flutter. Both quarter wave and Helmholtz instability are related to pressure wave effects.

- Quarter Wave Instability – Quarter wave instability is the most common and most dangerous instability and is caused due to negative damping of the fundamental “organ pipe” acoustic mode in an excessively long inlet pipe. The instability can exist in the form of chatter or flutter.

- Helmholtz instability – Results in flutter or chatter due to interaction between the dynamic motion of the PRV and the Helmholtz resonator formed by the tank plus the inlet piping. A Helmholtz resonator can be represented as a pressure vessel with an open hole (or neck or port) where a volume of gas vibrates due to the elastic nature of the air contained within the vessel.

- Vortex shedding – Due to the geometry of the disc/seat arrangement; vortices are generated which directly affect the pressure distribution around the disc. If the vortices produced are unstable then the disc lift vs flow characteristics of the PRV could have hysteresis and result in instability.

- Oversizing/Under damping – Cycling or low amplitude chatter due to insufficient damping and/or the valve venting at a small portion of its rated discharge capacity would result in flutter to occur.

- Fluctuating Backpressure - The fluid dynamics and pressure drop in the valve discharge line, which affects the backpressure on the disc and re-closure conditions could result in a fluctuation of back pressure acting on the disc which would result in oscillation.

- Negative Gradient of Force Lift Curve – When studying the force lift curve of a given PRV, if there is a pronounced region of the curve where there is a negative gradient then inherent instability of the valve in that operating region should be expected. This represents the only form of

inherent instability from the literature and therefore does not agree with the aforementioned comment by Hos [31].

By avoiding such triggers of instability, PRV designers and operators could achieve a stable PRV response during operation. In addition, damage mechanisms such as corrosion, creep, fatigue, spindle misalignment and general seat erosion must be managed with regular maintenance and replacement programmes to prevent dynamic instability. In addition, frequent maintenance is required to check for signs of leakage and/or structural failure.

The dynamic nature of the PRV as a spring mass system with low damping will inherently oscillate and be prone to various forms of instability. For example, flutter during operation is not ideal however would not result in a destructive result such as when chatter occurs. Standards such as ASME PTC 25 however have been found to lag behind current research as they seem to indicate the oscillation is an indication of poor design or manufacturing flaw with the valve itself. Poor design can result in poor valve performance (e.g. with inappropriate body bowl shape) however instability can also occur for well-designed PRV's if used under the wrong operating conditions. It is recommended in research such as that by Hos [31] that standards should focus on preventing conditions for fundamental instabilities to occur than concerning themselves with triggering mechanisms. As a predictive tool, the use of transient CFD dynamic mesh models could therefore provide valve designers with a much greater insight towards the fluid dynamic causes and mechanisms to allow a solution to be found if instability occurs. This is due to the ability of CFD to simulate the complex unsteady transient effects formed during chatter to be captured.

CHAPTER 3

LITERATURE REVIEW

To appreciate the value of the research presented within this thesis, a literature review is required which encapsulates all publicly available research results regarding pressure relief valves. The review will directly address the research objectives previously presented for this thesis and identify where a valuable contribution could be achieved. In particular, both single and multiphase numerical modelling and experimental validation will be evaluated for both steady state and transient analysis. Furthermore, previously utilised transient modelling techniques such as dynamic meshing will also be introduced and discussed in order to establish a firm starting point for further development. A review of previous numerical modelling approaches will also take place with a particular focus towards the techniques such as the quasi-steady assumption and use of symmetry/geometrical simplification for CFD models. This will allow the effectiveness of such numerical techniques to be examined and discussed. Operational and design induced instability research will also be reviewed to identify time dependant instability phenomena which could be encountered during transient dynamic mesh modelling. An overview of research regarding fluid dynamic phenomenon which could cause instability and/or symmetry breaking flow behaviour for geometry similar to PRV's will also be presented.

3.1 Single Phase PRV Research

This section of the literature review will assess previously adopted research methods used to achieve steady state and transient models for single phase applications. The effectiveness of previous modelling and experimental work to accurately capture PRV characteristics such as mass flow rate and flow forces as disc position changes as well as the ability to capture the dynamic motion of the valve for single phase conditions will be evaluated.

Over the past 20 years CFD has increasingly been used for understanding the single-phase steady state and dynamic behaviour of PRV's as well as gaining an appreciation towards the interdependence of valve geometry on flowrate and aerodynamic forces. The development of CFD analysis techniques has been found to be attributed to the desire to minimize high costs involved with early valve development in terms of financial capital and development time. It is also very difficult to achieve the required high pressure necessary for some industrial applications of PRV's to be tested within a manufacturing facility and can only be achieved with limited success at well-funded national testing laboratories [5, 18, 20, 25]. In modern day engineering offices where there is readily available extensively validated industrial computer aided design (CAD) and finite element analysis (FEA) software, the use of CFD provides a much more time and cost-efficient method for early design work; providing appropriate validation has been performed and continuously reviewed. Dempster [25] proposed that due to the accuracy of CFD presented within his study and available literature, CFD should be utilized as a design tool during the initial stages of product development. Such a reduction in initial design effort is desired by manufacturers to allow products to reach market quickly and reduce the number of iterations required to achieve the required PRV performance.

The industrial CFD codes ANSYS FLUENT and ANSYS CFX have been numerically validated for single phase conditions to ensure the appropriate flow physics expected to occur during PRV operation are accurately captured for use within industrial design studies. Scuro [7] conducted research regarding the capability of ANSYS CFX to model a traditional flow scenario of transonic air flow through a converging diverging diffuser. It was found that the code was in agreement to published literature in terms of predicting the position and intensity of shocks formed within the geometry. Furthermore, Beune [19] also validated the solver within ANSYS CFX as well as the use of the k-ω SST turbulence model by using benchmark tests such as modelling flow cases for a 1D shock tube, a 2D supersonic ramp and a axisymmetric

valve geometry for both 2D and 3D computational domains. The axi symmetric geometry was used to investigate if the PRV domain could be simplified to reduce computational demands. Beune [19] concluded that the flow physics involved for each case, which represent similar physical flow characteristics of a PRV such as real gas effects, choking points and flow separation were sufficiently captured. Elmayyah [34] extended this work to ANSYS FLUENT where theoretical calculations relating to predicting shock prediction and intensity were compared to CFD results using a RANS solver and the k-epsilon turbulence model. Elmayyah stated that FLUENT was capable of predicting shock characteristics accurately compared to theoretical calculations and therefore would be suitable for further computational analysis on PRV's. However the accuracy of the capture of shock wave characteristics such as exact location, thickness and diffusion could not be guaranteed. In addition, to accurately model the flow physics involved for PRV operation; regions with the largest flow gradients such as expansion zones and near disc/seat area require a sufficiently dense mesh in order to limit truncation error and improve the robustness of the numerical model. Beune [5, 19] also stated that for both steady state and transient numerical analysis, the appropriate mesh quality to capture flow gradients and features must be sufficient at every time step. Furthermore, Beune [20] also highlighted the importance of mesh independence as results for flow force was found to be significantly different between coarse and fine meshes.

The literature indicated the existence of experimental studies to support the validation data of the numerical schemes and turbulence models to experimental data; however, the number of detailed validation studies available were found to be small. For steady state analysis, Elmayyah [11] and Alshaikh [12] performed work on a PRV used within the refrigeration industry using air as a compressible fluid within ANSYS FLUENT, (similar to one of the valves chosen in this study). They both used a 2D RANS modelling approach with use of the k-ϵ turbulence model. Elmayyah [11] initially found reasonable agreement with experimental force measurements to within 13% however he

also recommends that for prediction of aerodynamic disc forces, a 3D CFD model may be required to ensure accurate prediction of backpressure acting on the disc. Alshaikh [12] also found good correlation between experimental results and 2D axisymmetric simulation using the k-epsilon model; however a large outlet was used in order to simplify exit geometry. As well as research for through flow valves, Beune [5], Dempster [25], Song [8] and Taggart [9] also conducted validation studies with 3D geometry for ASME type right angled valves. All studies adopted RANS modelling using the k-ω SST turbulence model which was said to provide the highest accuracy with acceptable calculation times and numerical stability. Beune [19] found mass flow rates to correlate to within 3.6% for all valve lift points and forces to within 11% at low pressure. The study by Dempster [25] however showed improved results using second order numerical discretization and half symmetry to predict both mass flow rates and force at medium to high lifts to within 2%. The aforementioned validation studies by Dempster [25], Alshaikh [12], Elmayyah [11] and Beune [5] adopted a similar approach of using quasi steady state experimental techniques where the value of valve disc displacement was fixed and measured using a linear cross slide [5, 27, 35]. As the disc position was moved to predefined values, the value of disc force and flowrate at each position was measured and recorded using a load cell and flowmeter respectively. Constant upstream pressure conditions were achieved through the use of an upstream throttle valve within the main compressed air supply pipeline. As a result, a set of experimental results for disc force and mass flow rate vs disc position could be compared to CFD results to enable a comparison to be made and a determination of the accuracy of the CFD model to be achieved. While this provides good control and hence accuracy required for validation studies it is absent of all inherent transient effects and hence not a full validation of the phenomenon experienced by an operating valve.

Further to the previous validation work, research performed by Scuro [7] utilised ANSYS CFX and the k-epsilon turbulence model to generate a data set of 36 steady state CFD results for mass flow rate and disc force which

could be compared to hand calculations using the ASME 2011a section I standard. He found that in general, the mass flow rate prediction using both methods was consistent and both methods were in good agreement however maximum deviation in flow rate was found to occur at higher lifts. Scuro [7] also highlighted that for ASME standard calculations, an assumption is made for disc force where all of the work done by pressure at the inlet is converted into normal force applied on the disc. However the use of this approach is questionable as it is unlikely to be used by valve manufacturers due to its high degree of approximation of flow physics. By using CFD, Scuro [7] concludes that this assumption is invalid as there is evident 3-D phenomenon and vortex generation at the disc/seat region which would cause the theoretical calculation to be different to the value generated by CFD. It was identified that for the valve tested, the normal disc force for CFD was approximately 19% on average lower than the theoretical force from ASME calculation. As a result, PRV's if designed using the ASME standard assumption would be incorrectly sized as expected, therefore it is not commonly used by designers. However the work by Scuro [7] does identify that the use of CFD could help to prevent oversizing if used by manufacturers as a design tool.

For incompressible flows, Dossena [17] performed a numerical investigation by using a high order accurate discontinuous Galerkin CFD code with the k-omega turbulence model where the numerical results would be compared to experimental values in a similar manner to the processes performed by Elmayyah, Alshaikh and Taggart [9, 11, 12]. Results indicated that as fluid viscosity was changed, variations for disc force and flowing capacity was observed which would affect the operating performance of the PRV. Dossena [17] supports the previously mentioned work by Scuro [7] as he suggests that a modification of the sizing procedure proposed by the current reference standards should be made to account for viscosity effects. He states that for valves used in gas service, the choked flow conditions and negligible viscosity effects ensure that initial calculations are relatively accurate and allow a higher value of discharge coefficient to be achieved. Whereas in liquid service the

flow rate is affected considerably more by viscous pressure losses throughout the valve therefore the discharge coefficient is smaller than that of a valve in gas service. When valve selection needs to cater to various types of flowing mediums, the relieving case of gas flows is normally selected. This choice however results in an oversized valve for liquid case which will reduce disc lift and hence reduce liquid velocity at the orifice affecting discharge flowrate. The research described earlier by Scuro [7] and Dempster [25] confirm the suggestions by Dossena [17] that CFD could be used as a design tool and complement the standards.

Dossena [17] also performed a comparison study for both 3D and 2D numerical approaches; where an early 3D simulation of the valve operating in water at nominal disc height was compared with experimental measurements which would allow the effectiveness of a 2D approach to be determined. The 2D axisymmetric model neglected the valve body by assuming that the valve would discharge into an infinite space at ambient pressure. The effect of such an approximation was more pronounced at higher lifts where pressure losses due to the valve body and exit flange were not taken into account. However, Dossena [17] concludes that when comparing the results of the 3D simulation with 2D axisymmetric modelling that the assumption of axisymmetric flow through the PRV is “acceptable”. It is also important to note for this work that the outlet geometry is very simple, with little consideration for any built-up backpressure and body bowl effects. These results are also reminiscent of the conclusions achieved by Alshaikh [11] where a simpler outlet geometry was also used to achieve good validation.

Within the available literature, studies relating to the validation of transient moving mesh simulations for PRV’s and the capture of transient flow phenomena are evident. However, in depth validation research for dynamic CFD simulation has been found to be scarce [36-38]. In addition, studies to create or demonstrate a resilient dynamic mesh method have not been

established as each piece of work investigated required a slightly different meshing and modelling approach. Transient CFD for ASME type PRV's was first successfully performed by Song et al [8, 39], Yang [18] and Zhang [40] within ANSYS CFX using domain decomposition methods (DDM) and grid pre-deformation (GPM) to achieve a structured 3D dynamic mesh model using pre-defined motion input within the CFX expression langauge (CEL). Half symmetry models were generally used to reduce the size of the computational domain. Compressible air was used as the flow medium. The study by Yang [18] included computational and experimental steam conditions at high pressures of 70 bar and are rarely found in the literature. The influence of damping on the dynamic characteristics of the valve was studied to ensure that the dynamic motion of the PRV was accurately captured. This was found to be crucial in order to capture frictional effects and inherent damping of the spring mass system. Yang [18] also included a variable time step routine in order to minimize computational expense but maintain the integrity of the mesh volume and numerical stability. The k-ω SST turbulence model was used for the dynamic mesh studies of Yang [18] and Zhang [40], which is in agreement with the conclusions from Beune [19] and Taggart [9] for 3D simulation. Yang [18] found the model to be capable of predicting the value of blowdown to a relative error of 0.2% and Zhang to 0.6%. Song [8] used the k-ϵ turbulence model and also performed limited validation using historical data and confirmed that his model was validated to a relative error of 11% when predicting blowdown, therefore it would be apparent that the k-ω SST turbulence model is more accurate for transient blowdown studies. Song [8] also found that from his experimental research, assuming a large enough pressure vessel, that a linear pressure profile can be used to represent the pressure drop within the vessel; removing the requirement of modelling the vessel. It should be noted that from all studies it was found that there was a lack of validation data for opening processes and overpressure values.

Experimental measurements performed by both Yang et al [18] and Zhang et al [40] were performed at the same experimental facility, complying with ASME

PTC 25 guidelines, using high pressure steam provided by a super critical pressure boiler. During testing Yang [18] states that the pressure of the storage vessel was increased to 90% of valve set pressure then incrementally increased until the PRV popped open. At this point a pressure tapping sensor and laser-based displacement transducer recorded the transient response of the PRV. Such well-established and accurate experimental methods could therefore be used as inspiration for future validation studies of dynamic PRV systems; such as that which will be performed within this thesis.

Research performed by Iannetti [41] who developed a transient dynamic mesh CFD model of a positive displacement pump highlighted a hybrid dynamic meshing approach for the spring loaded valves which would incorporate fluid-structure interaction on ANSYS FLUENT. The model developed by Iannetti [41] was capable of using CFD solver results for the pressure field acting on the relevant valve surfaces to generate a force sufficient enough to overcome the preload of the valve spring and actuate the valve. Such an approach could be used to achieve a transient PRV model which utilises a similar novel meshing strategy to Iannetti [41] which would be perfectly suited for the complex geometry typical of a PRV; especially at the disc seat interface. The geometry of the CFD model for Iannetti [41] exactly replicated the design of the pump's test rig where a dynamic layering mesh methodology by means of structured cell creation/deletion technique was developed. When the dynamic layering process used within FLUENT is incorporated with a user defined function (UDF), the pump motion could be applied to the computational domain. To achieve the desired moving mesh geometry, Iannetti [41] decomposed the domain into static mesh zones, translating rigid mesh zones and structured deforming zones which either expanded/compressed to maintain the validity/integrity of the domain [41]. A hybrid mesh methodology was used due to the complex geometry, similar to PRV geometry, where tetrahedral cells were used for both static and translating zones and structured hexahedral cells used for layer generation. The forces were calculated at the end of each time step and entered into a force balance equation alongside the

spring force. From this, using a first order Eulerian numerical method, the valve displacement, velocity and acceleration could be calculated and used for the following time step and updated mesh. As a result, such work performed by Iannetti [41] could be used as a basis for developing a novel dynamic mesh, transient PRV fluid-structure interaction model. This work is distinct from other dynamic mesh models described in the literature as the hybrid nature of the mesh allows for complex geometry to be captured without simplifications.

From the literature, a similar technique was used by Budziszewski [42] to achieve a fluid structure interaction model for an ASME right angled type PRV with a dynamic layering approach to maintain mesh integrity across the full lift range. A significant difference however when compared to the Iannetti [41] approach, was that Budziszewski [42] was required to apply significant geometrical simplification to critical flow geometry to enable a structured mesh to be achieved which would allow dynamic layering. The hybrid meshing approach utilised by Iannetti [41] on the other hand would be capable of operating for a variety of complex disc/seat geometry arrangements which would be desirable for PRV designers in order to optimise performance. The purpose of the research performed by Budziszewski [42] was to investigate how a PRV could be dynamically modelled with CFD and to implement results in RELAP5 (a 1-D thermal hydraulic system code) to obtain realistic results of generated forces in the pipe systems as a result of PRV operation. An additional objective of the project was to also investigate and compare the results of 2D and 3D simulation for a PRV. Axisymmetry was used as a boundary condition in the 2D model, and in the 3D model mirror symmetry was used. The used turbulence model was SST k-ω. The fluid flowing through the safety relief valve is chosen to be liquid water, which is assumed to be incompressible in the CFD simulations. It’s also important to note that within this study only the opening process of the valve was considered, therefore a full dynamic analysis wasn’t established. Damping of the valve is also not considered during the simulations, which the author states is due to a lack of data. The UDF technique and dynamic mesh developed within this study in a

similar manner as Iannetti [41] could be used a basis for future research on ANSYS FLUENT using deforming mesh and rigid body fluid structure interaction modelling.

Budziszewski [42] also established interesting observations for both flow phenomena and PRV dynamics on the differences in 2D and 3D modelling. When the force lift curves for the 2D and the 3D simulations are compared Budziszewski [42] found that the hydraulic force acting on the shroud (outermost region of the disc) in the 2D model is lower than in the 3D model. This deviation in force between the two modelling approaches was found to occur due to a significant difference in the turbulent kinetic energy beneath the shroud of the disc; as the turbulent kinetic energy is larger beneath the shroud in the 2D model. As the turbulence generation is different between both 2D and 3D approaches, the resultant fluid pressure is different which affects the aerodynamic force prediction. As a simpler outlet was required for the 2D model, differences in back pressure were observed however in general it was found that the aerodynamic force values generated by each approach was similar in terms of order of magnitude. Budziszewski [42] concludes that the 2D model may be correct enough to be used for simpler applications such as determining the opening time of the valve. However, the 3D simulation performed where the inlet pressure was gradually increased showed a more realistic behaviour of the opening process than the 2D simulation, indicating that 3D simulations provide a more realistic solution for PRV dynamics. It is obvious therefore from the work conducted by Budziszewski [42] as well as that by Elmayyah [11] and Taggart [9] that care must be taken when comparing 2D and 3D modelling approaches and the resultant differences in accuracy.

In general, Budziszewski [42] established that the steady state and dynamic simulations in CFD showed that the 3D geometry model of the valve and the force calculations were deemed to be consistent with reality. However, it was found that for both 2D and 3D transient analysis that the PRV would open

faster than the safety relief valve does in reality. Budziszewski [42] states that the models could be said to be conservative which is often a requirement within engineering standards and nuclear engineering in particular; however the PRV opening early in CFD does not represent the worst case scenario therefore this statement seems to have been made in error. A potential source of inaccuracy which Budziszewski [42] highlights is that the valve cannot be completely closed at the start of the simulations, as a general mesh topology of at least one layer of cells for the dynamic mesh is required at all timesteps for dynamic layering to take place. Therefore, it is suggested by Budziszewski [42] that industry should attempt to find a meshing method for simulating a PRV from a fully closed position in order to accurately capture the popping process during opening. Alternatively, if not possible then it is suggested that the initial opening should be smaller than 5 % and a finer mesh should be used to achieve the required y plus value for the required turbulence model. Budziszewski [42] also suggests that the dynamic layering mesh approach should be applied to other types of PRV geometry in order to test the resilience of the method however the cost of 3D transient dynamic mesh simulation is very computationally expensive.

A study by Hos [31] assessed the ability of CFD to be used for PRV analysis and highlighted that the feasibility of using detailed fluid structure interaction simulations has become possible in the last decade due to the nature of Moore's Law. However, there is still a high computational price to pay in relation to time and computational resource; as shown in transient studies by Beune [5, 20], Iannetti [41] and Zhang [40] with computational times of several weeks with powerful desktop computers. Therefore, in the opinion of Hos [31], transient CFD should be used as a standalone virtual experiment to understand flow detail rather than as a quick parametric study. Hos [31] also postulated that CFD is used to enhance simple type 1 dynamic models by inputting flow detail gained from initial steady state CFD analysis.

It has been shown that geometrical simplifications can be used to reduce computational resource such as removing the spring geometry within the computational domain of a PRV was investigated in a study by Elmayyah [11, 34, 35]. In his work it was found that a significant reduction in mesh complexity with negligible effect on accuracy for steady state type simulations could be achieved. Elmayyah and Alshaikh also adopted the use of a modified gland [11, 12] to generate an axisymmetric experimental geometry to allow 2D simulation. Other studies on PRV's have shown that using quarter and half symmetry 3D models [7, 8, 18, 20, 25, 40, 42] have a significant effect on reducing the computational size of the PRV mesh and hence a reduction in simulation time. Therefore, such measures should be utilized in future studies to minimize computational expense.

3.2 Two Phase PRV Research

In recent years, there has been a number of two-phase flow regime studies for application in PRV modelling to enhance current design techniques used by the vast majority of PRV manufacturers. Approaches such as the HEM model which was described in detail earlier and defined as type 2 numerical models have been developed however such numerical techniques do not provide designers with as great an insight towards flow conditions as the flow visualisation possibilities provided by CFD. In a publication by Kourakos [6] he states that in standards such as ISO 4126, design methods for incompressible and compressible flow are well established when compared with current, unreliable two phase flow methods. This is supported in research by Couzinet [43] who highlights within his literature review that there is a significant lack of studies regarding two phase flow analysis for PRV's and the ability to capture flow effects such as cavitation which could significantly affect valve performance. Therefore, the requirement to achieve a CFD design tool for PRV's as suggested by Dempster [25] which extends to cover the two phase

flow regime is of critical importance to industry and academia to achieve a more accurate method for two phase flow PRV analysis.

In the work performed by Kourakos [6], the use of the quasi steady assumption allows a spring loaded PRV to be tested for two phase flow in order to determine the flow force acting on the aerodynamic surfaces and flow rate through the PRV. In addition, a plastic PRV body was used to enable flow visualisation of incompressible and/or two phase flow behaviour such as cavitation to further understand two phase flow characteristics through intricate PRV geometry. Kourakos [6] developed a numerical CFD model on ANSYS FLUENT using the k-omega SST turbulence model and pressure based coupled solver. The results of the CFD model were then validated against experimental results to determine the accuracy of the multiphase modelling techniques as well as the ability to capture both compressible and incompressible flow conditions. Air water flow mixtures of volumetric qualities up to 20% were tested where the most significant finding was that an interesting, inversed flow phenomenon was observed for aerodynamic force for both experimental and CFD solutions. It was found that at the lowest openings of the PRV, the force for predominantly air flow was higher than water flow. However, at larger openings, the water force was higher when compared to an air flow condition. In addition, two phase flow at higher lifts for 20% air water mixture tended towards compressible flow behaviour whereas at lower lifts the two-phase mixture was more similar in nature to incompressible flow. Kourakos [6] concluded that this observation was due to a change in the choked flow position as the disc position changes; a discovery only made through the help of CFD. Kourakos [6] also highlights the effectiveness of his validation efforts where he states that for compressible flow he was able to achieve correlation of 8% for flow force whereas for higher pressures the correlation changed to 22%. However, he states that the position of the adjustment ring for experimental tests and CFD comparison could be a source of error as geometrical similarity for ring position couldn’t be

guaranteed. For incompressible flow, however Kourakos [6] found much better correlation at 3% across the lift range above 1.5mm.

Research performed by Beune [5] further extended the use of a CFD model for incompressible liquid modelling to capture cavitation effects in which the accuracy of the CFD model was significantly improved. Beune [5] found that the results for both disc flow force and flow rate were much closer to experimental values when compared with a simplified CFD model without cavitation; in particular the results for the flow force were most improved. However, Beune [5] also suggests that to gain further accuracy, the cavitation model used in his research would need to be improved to account for heat transfer and compressibility effects of the vapour phase. Therefore it could be concluded from the work by Kourakos [6] and Beune [5] that CFD models need to be developed for both compressible and incompressible flow regimes to provide adequate flow force prediction in two phase regimes for PRV's.

Research was also conducted by Arnulfo et al [44] to analyse the simplified numerical type 2 models available within the literature at the time of his publication (2014) without utilising CFD and the resultant computational expense. The authors evaluated the effectiveness of several models to predict two phase flow mass flowrate through a nozzle such as the HEM, omega-method, SEMs, ERM, HDI as well as using the models developed by Lenzing, Darby and Leung [44] for two phase valve discharge coefficient. It was highlighted that for flashing flows in PRV's for two phase applications, the formulation for discharge coefficient developed by Lenzing when multiplied with the critical flow rate obtained by the Homogeneous Non-Equilibrium Direct Integration model provides good prediction [44]. Flashing flow often occurs during the operation of a PRV within a multiphase flow regime where due to a significant drop in flow pressure a substantial evaporation of liquid to vapour occurs causing a rapid change in phase interfaces within the flow. However in non-flashing flow conditions for air water mixtures, Arnulfo [44] determined that

the Leung/Darby formulation of the two phase valve discharge coefficient combined with the omega method is the most suitable for flow rate prediction. However, an obvious lack of flow visualisation and detailed analysis is obtained using such methods when compared with the capability of CFD.

A significant amount of work has been performed by a number of researchers at the University of Strathclyde to evaluate the capability of CFD to capture two phase flow accurately through a validation process. The objective of early research by Elmayyah [11, 29, 30] was to develop a generic CFD model to predict two phase flow conditions within a PRV, as a modelling solution could not be easily found within the literature at that time. In addition, Elmayyah intended the development of a two-phase model to provide manufacturers with a method of improving valve design in complex two-phase flow regimes. Elmayyah carried out both an experimental and CFD analysis of a PRV used most commonly within the refrigeration industry and manufactured in Glasgow by Henry Technologies. The pressure range tested was between 7-12 Barg and a mass fraction of 0-0.71 where the experimental and CFD results were compared to each other. Quasi steady based measurement techniques as described earlier were used which involved the recording of flow rate and force at predetermined values of valve lift. The experimental testing was performed within a pressure testing facility within the University of Strathclyde where a novel testing method, rig and geometrical simplifications were made to achieve an adequate result.

In publications by Elmayyah [29, 30] the computational and experimental techniques which were developed over the course of his research were described. The computational work was performed within ANSYS FLUENT where to achieve his CFD model, Elmayyah [29, 30] utilised a 2D axisymmetric approximation of the PRV domain. The mixture model was used alongside the standard k-epsilon turbulence model in addition to the homogeneous assumption of zero slip between the phases as well as thermal equilibrium. As

a result, the CFD model used in the research adopts a single temperature to represent the mixture temperature. From the results, Elmayyah [29, 30] found that the two-phase flow lift characteristics exhibit a similar trend to the single phase characteristics and at any fixed test pressure and lift the water and air flow rates have an inverse relationship to each other. Therefore, as could be intuitively expected, as water flow injection rates are increased the air flow rate through the system would decrease as air volume fraction decreases, for fixed upstream pressure. Elmayyah [29, 30] also concluded that the CFD mixture model could provide detailed information regarding the location of critical planes and overall distribution of flow properties however the flow details were not validated in order to ensure accuracy. Elmayyah [29, 30] was primarily focussed only on predicting flowrate using CFD and comparing results to other commonly used methods such as HEM. It was found that the CFD mixture based model was capable of showing good agreement with experimental results in particular at high lifts with low water mass fraction. For higher lifts the accuracy was found to be 0.5% at 0.11 water mass fraction however increased to 9% at 0.55 water mass fraction whereas at lower lifts the deviation was found to be as high as 16% from experimental values. Despite this however, Elmayyah [29, 30] concludes by stating that the mixture model has shown improved agreement with experimental results for mixture flowrate at fully open position when compared to the HEM and HNE-DS model which is adopted by ISO recommendations.

Elmayyah's PhD thesis [11] provides further application and analysis of his two phase flow CFD modelling and experimental techniques and results. The experimental test rig developed in house provided a variety of measurements of two phase flow conditions such as air and water flowrate, pressure, temperature and aerodynamic force was found to be "satisfactory" for obtaining simultaneously the valve flow lift and force lift characteristics at different test pressures and water mass fractions. Elmayyah [11] also develops his analysis on the fact that both the single phase and two phase flow and force lift curves share similar characteristics but establishes that the slopes for

each of the curves are slightly different. In particular, at higher lifts the two-phase flowrate vs lift curve has a lower slope when compared with single phase conditions. Due to the good agreement between CFD and experimental flow rate, Elmayyah [11] states that the assumption of zero slip between the water and air phases is valid for the high-speed flows existing in the valve and concludes that the flow could be considered homogeneous for lower water mass fractions. In addition, the ability of the 2D CFD model to describe shockwaves and critical plane position is accurate due to the strong correlation of flow rate to the experimental results. However, at higher mass fractions the results indicated that accuracy would reduce when using the homogeneous assumption within CFD. It was suggested that the higher mass fraction conditions leading to reductions in air flow for constant pressure testing also introduced greater slip between the phases indicating limitations in the use of homogeneous assumptions. In addition, Elmayyah [11] also identifies a further source of modelling error caused by 3D flow effects such as vortex generation and dissipation not being captured by the 2D modelling approach. This was an observation found during single phase compressible flow modelling by Elmayyah [11]; where the 3D model outperformed the 2D model by accurately modelling the pressure profile at the disc and hence aerodynamic force prediction. Therefore, it is recommended by Elmayyah [11] that for future work, a 3D computational domain should be used to evaluate the effectiveness of the mixture model and achieve a greater appreciation of the flow physics for two phase flow in PRV's.

In continuation of Elmayyah's [11, 29, 30] multiphase modelling research for PRV's on ANSYS FLUENT, Alshaikh published several papers [26-28] over the course of the development of his PhD studies [12] to provide further insight to the capability of CFD to capture two phase flow and to improve on previous modelling techniques. In a similar manner to Elmayyah [11], Alshaikh [12] performed a validation study for both single phase and two phase flow using the pressure testing facility already developed within Strathclyde. However as well as performing simulations assuming homogeneous conditions as before,

Alshaikh [12] utilised a two fluid model in order to help improve correlation at higher water mass fractions and where non equilibrium velocity differences between the phases would exist. Alshaikh [12] also used a 2D computational domain with the k-epsilon turbulence model, where a modified gland was used instead of the original in order to achieve geometry which could be represented by an axisymmetric 2D domain. At the time of Alshaikh's [12] research, a 3D model was used to represent the full valve geometry however convergence time using the computational resources was unfeasible for steady state calculation at a time of 17 days. As a result, Alshaikh [12] continued with the development of a 2D model. Furthermore, Alshaikh [12] verified the work by Elmayyah [11] that by removing the spring assembly within the PRV, significant geometrical simplification could be achieved with negligible effect on accuracy. Such a simplification was therefore deemed acceptable, allowing a much simpler mesh to be generated without impacting on capturing accurate flow effects. Alshaikh [12] also utilised a larger outlet in order to achieve a more simple exit flow path and to minimise disruption of experimental equipment on the operation of the valve as would be the case with a smaller outlet due to the size of the supporting rod required for force measurement.

Experimental results were generated by Alshaikh [12] at a variety of water mass fractions by using a spray nozzle which injected water at the inlet as an evenly distributed spray to ensure a good match with computational assumptions. As a result, the experimental conditions could be modelled as a mono dispersed flow where Alshaikh [12] performed a study to find the most appropriate Weber number which correlated well with experimental results. From the study, it was found that the validation results at lower water mass fractions agreed with the conclusions of Elmayyah [11] with similar force and flow lift characteristics and accuracy with CFD however at higher water mass fractions Alshaikh [12] utilised the two fluid Euler-Euler model. As a result the effectiveness of the Euler-Euler model could be compared with the homogeneous mixture model in CFD and also with the analytical homogeneous model developed by Darby [22]. At higher water mass fractions,

Alshaikh [12] demonstrated that the Euler-Euler CFD model was capable of providing a more detailed representations of the physical properties of the flow. It was found that the Euler-Euler model could predict flowrate with an uncertainty between 4-8% with the piston force being accurate enough to 19% at higher lifts and higher liquid mass fractions.

To investigate the difference in results between the Euler-Euler model and the mixture model at higher water mass fractions, Alshaikh [12] analysed the critical velocity of the flow through the PRV where it was found that there was a significant difference in velocity magnitude especially at higher lifts and water mass fractions. Therefore Alshaikh [12] concludes that the difference in critical velocity between the two modelling approaches is the reason for the differences in flow rate prediction. As a result of this research, for future two phase flow studies a better appreciation of which multiphase model to utilise given the flow conditions has been achieved. However, similarly to the conclusions from Elmayyah [11], Alshaikh [12] also suggests that a 3D model should be developed with the help of HPC clusters (High Performance Computer) to gain a better appreciation of the turbulence generated and identify if a difference exists between 2D and 3D modelling. Alshaikh [12] also suggests that alternative turbulence models other than the k-epsilon model should be looked at to see if an improved correlation can be achieved as well as transient modelling to identify any time dependent flow phenomena within the two phase flow regime through the PRV.

It also worth noting that in the previously described dynamic mesh work by Iannetti [41], the author utilised the two phase mixture model in tandem with a modified k-omega SST turbulence and cavitation model to achieve a transient, dynamic mesh model suitable for modelling transient two phase conditions within a pump. The mixture model was chosen by Iannetti [41] in a similar manner as Elmayyah [11] and Alshaikh [12] due to its lower computational cost when compared to other methods. Following experimental validation, it was

found to demonstrate sufficient accuracy for the transient dynamic mesh study. As a result, it could be suggested that the use of the mixture model for a transient dynamic mesh model for a PRV could be utilised to a sufficient degree of accuracy to capture two phase flow operating conditions, at least for lower liquid mass fractions.

3.3 Use of the Quasi-Steady Assumption for PRV Research and Design

In the literature described previously, the quasi-steady assumption has been used in a range of PRV research topics where the effect of disc motion was assumed negligible and aerodynamic force and mass flow rate was dependent only on the valve position. This is useful for validation purposes as has been demonstrated by Taggart [9], Alshaikh [12], Elmayyah [11], Song [21] and Beune [5, 20] where steady state computational models could be developed which are much less computationally expensive when compared to transient fluid structure interaction models. Steady state experimental data could then be generated at distinct lift points and compared directly with CFD. In addition, by using a quasi-steady data set generated from either experimental or CFD approaches, low order numerical type 1 models could be constructed to predict the dynamic behaviour of the PRV during opening and closing. When analysing previous research for type 1 models it is important to recognize that the PRV geometry for each of the validation cases were unique to each study. As a result, the flow paths from the inlet to the outlet would vary; causing the fluid interaction with the aerodynamic surfaces to be different and hence different force lift curves would exist. Care must be taken therefore to ensure that the conditions are met for the quasi-steady assumption to be valid for the specific PRV geometry; as highlighted in the work by Beune [5, 20].

Song et al [21] developed a type 1 model using the quasi steady assumption to predict blowdown and reclosing characteristics of the PRV based on a 1

degree of freedom valve dynamic model. Axisymmetric 2D steady state CFD simulations were used at several static lift points representing the transition of the valve from fully closed to fully open. This provides an opportunity to generate a force vs disc displacement (lift) curve which is input within a type 1 numerical model to represent the force behaviour of the valve across the lift range. The dynamic type 1 model would then use a set of boundary conditions and constraints to plot a dynamic valve displacement vs time curve. Song concluded that the quasi-steady based analytical model developed was reliable to predict the dynamic characteristics and blowdown of a conventional PRV. Research performed by Taggart [9] using a similar approach and PRV geometry to Song further confirms the capability of a quasi-steady based numerical type 1 model to accurately capture the dynamic characteristics of a valve during opening and closure. Dempster [25] also investigated the use of quasi steady techniques for pressure scaling which could be used in valve design to determine PRV performance over a range of pressures which are not feasibly possible to be experimentally tested and to also evaluate dynamic behaviour by relating aerodynamic force to spring forces. Therefore, if applied by manufacturers, a PRV would only be required to be tested at low pressure with force and flow measurements at various disc positions and scaled to the desired design pressure. This as a result helps manufacturers and national flow laboratories to overcome equipment limitations for either flow or pressure restrictions. Scaling for flowrate was found to be simple by using an empirically derived discharge coefficient however aerodynamic forces generally assumes a linear based pressure scaling method (type 3 model). It was found by Dempster et al [25] however that for ASME VIII conforming PRV's, at lower pressure ratios when the valve outlet is not choked that pressure scaling is not valid. At higher pressure ratios when the discharge flange is choked then pressure scaling would be valid. This therefore highlights that a minimum pressure must be identified to enable the outlet to be choked for the initial measurement of which pressure scaling could then be utilised. If not, then pressure scaling wouldn't be valid and could lead to incorrect sizing of PRV's and highlights an additional concern for the effectiveness of quasi steady

based modelling techniques due to the complex flow structure which interacts with the aerodynamic surfaces.

In the available literature, work performed by Beune [5, 19, 20] is the only research to date to dispute the validity and deficiencies of utilizing quasi steady state assumptions. In his article [20], Beune studied the difference in opening characteristics of a PRV in terms of flow structure and prediction of instabilities using a transient solver with 17 pre-defined grids across the full lift range compared to steady state fixed lift type 1 model analysis. It was found that steady state simulation was unable to take into account the effects of flow history due to significant unsteady bulk flow behaviour at a cavity on the valve disc surface. For steady state, a pair of recirculating vortices were generated within the cavity however, for transient modelling the bulk flow entered the cavity and required an increase in lift to generate the pair of rotating vortices. Such a difference significantly affected the pressure profile on the valve disc surface and hence a large rise and collapse in flow force was observed when compared to steady state results. In addition, it was also found that transient simulation damps oscillatory motion and is un-damped for quasi steady state simulation. Beune concluded that this effect was due to the transient CFD model being capable of accounting for the velocity of the valve disc and flow effects which result from the disc's motion. For steady state simulation however, the disc would be stationary. It is postulated [20, 45] that this error between quasi steady state and transient simulation would become larger with higher disc velocity where damping values due to flow effects would become more significant. On the contrary, at lower disc velocities where damping flow effects would be negligible; the validity of quasi steady assumptions would improve where it could be used for cases of slow blowdown conditions, for example.

Further work by Beune at higher pressures [19] displayed a constant deviation to experimental data between flow force prediction for quasi steady state

modelling which was corrected with use of the transient solver. Therefore, it was apparent in the work by Beune [19] that for dynamic simulation a flow history effect could be deduced which can't be identified by utilising static measurement techniques. An additional concern of Beune's [20] transient fluid structure interaction modelling was the effect of pressure waves on the flow structure which could lead to a redirection of the bulk flow path and induce unstable operation when the pressure wave occurs close to the resonant frequency of the valve. Static modelling approaches neglect the effect of pressure waves on the instability mechanisms and as a result could lead valve designers into a false sense of confidence regarding the operating characteristics of the PRV. This conclusion is confirmed in work performed by Borg [32] whereby using a series of stationary CFD simulations, operating characteristics of the valve could be compared to the dynamic opening of the valve. It was found that the transient opening of the valve could be predicted well using the steady state solutions however for longer inlet lines there are transient phenomena which are not captured by the stationary solutions. This is due to the effect of pressure wave propagation, which Borg [32] highlighted could be captured by transient dynamic mesh CFD techniques by using the transient moving mesh method described earlier by Budziszewski [42]. It could therefore be recognized that there is a significant discrepancy between the observations of Beune [20] and Borg [32] when compared with Song [21] and Taggart [9] which must be evaluated to identify the effectiveness and reliability of quasi steady type 1 modelling methods across various PRV geometries.

3.4 Dynamic Instability Research and Symmetry Breaking Phenomena

A number of studies have been performed within the available literature to identify the various mechanisms which would result in the unstable performance of a PRV and to try and capture those mechanisms within CFD. Such instability of a PRV during its operation could result in a complete failure

of the valve's pressure relieving capability and could lead to failure of the safety system. A clear example of such work was that performed by Borg [32], who by using a transient dynamic mesh CFD model was found to be able to capture the interaction between pressure wave propagation and PRV opening. Borg [32] evaluated the influence of various system parameters such as pressure drop across the inlet piping, effect of pipe length, system volume and friction on the opening behaviour of a conventional ASME VIII type PRV. In addition to Borg [32], a transient dynamic mesh model was developed by Zheng [33] which focussed particularly on the effect of design parameters on the instability of the PRV and to assess the effect of pressure waves on the connecting pipes to the valve. Yang also developed a transient CFD model [18] which allowed an accurate determination of the damping caused by friction and spring damping to predict the degree of instability experienced by a PRV during its operation. As a result, it can be established that using a transient dynamic mesh model within CFD could provide manufacturers with a valuable insight towards the triggers of instability and would help designers to optimise the installation/geometry of PRV's to enable a stable dynamic operation of the valve to be achieved.

In Borg's analysis [32], the typical force lift relationship is compared to the spring line typically applied by manufacturers when designing a valve. Three zones are identified as shown in figure 3.1 by the author as a typical PRV operation across the full lift range of the valve. Zone 1 is described by Borg as an unstable region as dictated by classical stability theory as the position of the disc is difficult to predict by the force balance. However, Borg [32] suggests that as the length of the inlet pipe affects the inertia of the system i.e. the system's responsiveness to pressure change then a longer pipe could stabilise the PRV's behaviour within zone 1. Zone 2 is described as the popping region where the valve can have two lift positions at the same pressure. During the popping process, the pressure within the system will rapidly decrease as mass is ejected from the valve which will cause a pressure wave to propagate. Zone 3 is of particular interest as Borg [32] claims that this region after the second

point of intersection between the force lift curve and the spring line is inherently unstable and should represent the maximum lift at which the PRV is allowed to operate at in order to prevent oscillation.

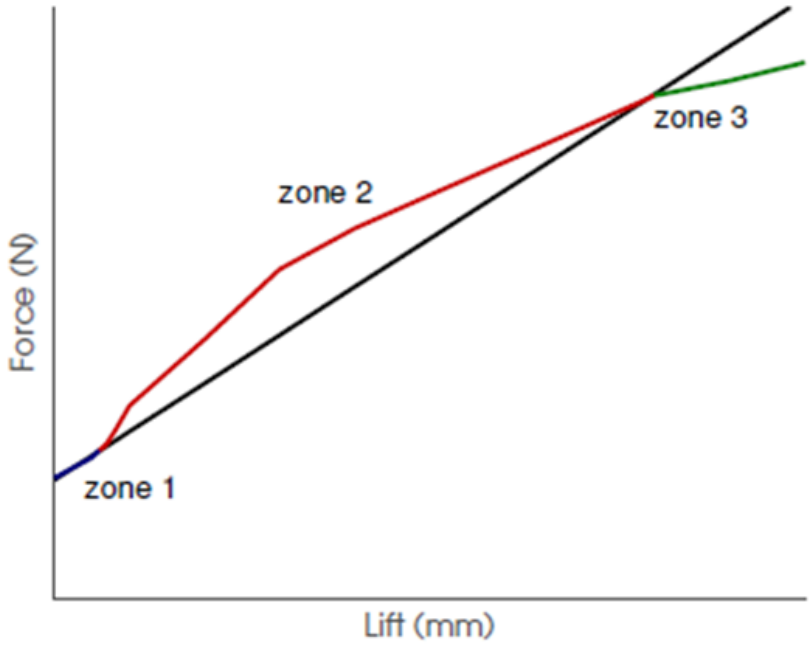

Figure 3.1 – Illustration of Force Lift Curve vs Spring Line and Corresponding Effect on Stability [32]

In addition to the research carried out by Borg [32], extensive work has by both Darby [22, 23] and Hos [31] has established an appreciation for the dynamic mechanisms of PRV instability and the use of computational models as tools for prediction. Darby [22, 23] describes the various modes and flow features of instability which affect PRV response such as chatter and cycling which is very destructive for the structural integrity of the PRV and low amplitude flutter which in some cases can exist within a stable valve response. Darby [22, 23] also describes the geometrical influence of devices such as the blowdown ring and local disc/seat geometry on the flow path such as flow deflection angle and how instability flow mechanisms can be generated. Hos [31] details that the ISO standards currently indicate that PRV instability is an indication of poor

design or manufacturing flaws and ignores the fact that oscillation can be due to the PRV being used under incorrect operating conditions. Inappropriate body bowl shape has been shown to promote instability however more importantly the effect of inlet pressure loss and quarter wave instability, are far more destructive and independent of the PRV design. Furthermore, Hos [31] states that the use of the 3% API rule for pressure inlet loss does not provide a robust and conclusive design method to prevent instability and an alternative means of determining instability should be developed. Hos [31] in particular encourages further discussion for industrial standards to produce more robust guidelines to prevent PRV instability as well as gaining a greater appreciation of the differences of instability mechanisms which occur between compressible and incompressible fluids. Beune [5, 20] states that the unstable flow behaviour in which he observed during his transient research indicates that instability can't always be avoided in valve design. However, the studies performed by both Darby [22, 23] and Hos [31] help to allow valve manufacturers identify the likely triggers and flow characteristics of unstable PRV operation which will be important throughout the remainder of this thesis.

In addition to PRV instability research it is also important to highlight any work which has been performed on flow induced instabilities which could be caused by the geometry of a PRV. In particular, research which was performed to describe and model annular and leakage flow induced instabilities [46] highlighted various mechanisms which could be of interest for annular type through flow PRV's. The study highlighted the effect of diffuser type annular geometry where a self excitation pressure force phenomena resulted in the instability of annular flow and significant vibration of the annular structure. It was found that there was a sensitive set of geometry for a diffuser if placed at the outlet of an annular flow region could result in a destabilizing flow structure causing an unstable system. Such a finding highlights the sensitivity of geometry, in particular diffusers, when used with annular flow and that such instability mechanisms for the flow should be considered for PRV's.

Furthermore, research was conducted by Padrón [47] to determine the factors which result in symmetry breaking flow instabilities in typically axisymmetric geometry. This is of particular importance to consider as a substantial amount of research has taken place by researchers such as Elmayyah [11] and Alshaikh [12] who utilised 2D axisymmetric CFD simulations but suggested enhanced accuracy could be achieved with 3D modelling. Hopf bifurcations in particular are described, which Padrón [47] highlights as being one of the more important types of bifurcations for flow geometry with symmetry as well as pitchfork bifurcations. Pitchfork bifurcations are described as being a state where several solutions can be achieved for the same geometry but at different flow conditions. Within the research, in particular planar sudden expansion geometry is investigated where there is obvious axisymmetric geometry. Such a domain is of particular relevance to the typical geometry found for a PRV where flow typically expands following the complex flow path around the disc/seat interface area. Padrón states that the development of asymmetrical flow with an axisymmetric planar expansion is dependent on both the value of Reynolds number and also on the expansion ratio of the downstream and upstream passage size [47]. Therefore, it's critical for PRV manufacturers to appreciate the likelihood of symmetry breaking flow phenomena from taking place within a PRV and the subsequent effect on CFD modelling. Padrón [47] establishes that the value of Reynolds number at which symmetry breaking occurs is different between 2D and 3D domains where symmetry breaking for 3D geometry can occur at Reynolds numbers above 1140. He identifies that the presence of the pitchfork bifurcation instability for asymmetrical flow constitutes a significant challenge for CFD to capture correctly and for CFD users to appreciate. The research also highlights that the ability of CFD to capture symmetry breaking flow phenomena is dependent on the quality of mesh used and instability of advection terms in the governing equations. Therefore, care must be taken in order to appreciate the possibility of symmetry breaking flow phenomena in axisymmetric geometry and to also recognise the limitations of CFD to capture it. In particular as discussed for PRV's, there is a risk of such phenomena where there is sharp expansion

caused by the geometry in which the bulk flow interacts with as it passes through the PRV structure.

When the high Reynolds number flow is combined with an expansion of the inner disc/seat interface to the outer cavity, the ratio of domain heights is approximately three and continues to rise as the disc opens further. Padrón states [47] that the combination of such flow and geometrical conditions can promote the generation of additional separation zones which are no longer symmetrical and exist within the turbulent flow regime.

3.5 Summary of Literature Review

Following an extensive literature review, it is possible to establish where the research objectives of this thesis could provide a useful contribution to the PRV research community and industry;

- It has been shown that a significant amount of work has been carried out to develop accurate single phase steady state CFD models of PRV's which achieve good correlation with experimental data. The experimental data has been generated by using novel measuring techniques. Some work, in particular for through flow type PRV's, have been limited to a 2D axisymmetric approximation therefore the development of 3D CFD models for such geometry would provide an even greater appreciation of the capability of CFD. Furthermore, extensive validation of turbulence models and numerical discretization methods has not been widely performed with both the k-epsilon and k-omega SST models being commonly used. Therefore, a greater understanding towards the benefits and limitations of each would provide CFD users with a better appreciation of the most appropriate turbulence model to use for PRV's. 3D modelling will also help to

identify any symmetry breaking flow phenomena or instability as suggested by the literature review which could prevent the safe operation of a PRV.

- In addition, there has been a development of transient dynamic mesh models for single phase in the literature however in a similar nature to steady state testing there has not been extensive validation performed. Furthermore, little work has been performed to validate a CFD dynamic mesh model which is capable of accurately capturing the full dynamic process of a PRV. In addition most models available required significant geometrical simplification of the PRV to be suitable for dynamic meshing in CFD. Therefore, there is an opportunity to develop a resilient, dynamic mesh modelling technique in CFD which is accurate to experimental data and can provide PRV manufacturers with a design tool which can predict the full opening and closing process of a PRV.

- There has been development of two phase experimental and modelling techniques in 2D for through flow PRV geometry in particular and the effectiveness of CFD has been compared to simpler analytical type 2 models suggested in standards. However little work has been performed for two phase analysis for 3D domains; therefore there is an opportunity to identify the difference between 2D and 3D CFD methods.

- In addition, extensive work has been achieved regarding understanding instability mechanisms related to the dynamic operation of a PRV. CFD has been utilised to some degree in order to capture and understand some instability mechanisms however only for an ASME VIII type geometry. Therefore, a validated 3D steady state and dynamic mesh model could be used to further appreciate instability mechanisms which affect the desired operation of a PRV and help to identify further sources of undesirable flow instability/characteristics. Furthermore, a 3D dynamic mesh model could help to further research the effectiveness of the quasi-steady assumption commonly used in early PRV design.

CHAPTER 4

OVERVIEW OF CFD NUMERICAL METHODS REQUIRED TO CAPTURE PRV FLOW PHYSICS

In accordance with the literature reviewed previously, a substantial amount of research has been performed to capture the fluid dynamic principles related to the operation of a PRV using CFD. Within this section therefore, the basic numerical CFD principles/models for single and two-phase flow will be established and examined to form the basis for study in this thesis. Following this chapter, the principles described will be used to construct CFD analysis of various types of PRV's for both steady state and transient dynamic mesh models for air only and air/water mixtures.

4.1 Governing Equations

Computational Fluid Dynamics (CFD) approximates physical flow conditions by providing a numerical technique of solving the governing equations of fluid flow known as the Navier-Stokes equations; which for single phase only, govern mass and momentum transfer and also describe the relationship between pressure, velocity, temperature and density [48-51]. To utilise the Navier Stokes equations, a continuum flow regime is required where the value of a non-dimensional term known as the Knudsen number is required to be less than 0.01. The Knudsen number relates the ratio of molecular mean free path to a representative characteristic length (L). Therefore, using equation 4.1, it was possible to determine the maximum Knudsen value (Kn) at minimum lifts for the PRV's which would be investigated over the course of this study. It was found that the Knudsen value was approximately $6x10^{-6}$ at a valve position of 0.1mm above the seat which established that continuum fluid mechanics could be utilised to model PRV's using RANS based CFD.

$$Kn = \frac{\text{molecular mean free path}}{L}$$ **Equation 4.1**

Equation 4.2 illustrates the mass conservation principle used in a cartesian coordinate system as part of the Navier-Stokes equations for 3D conditions. For 2D simulation, the terms which relate to the Z axis are neglected. In transient compressible simulation, variation in density (ρ) and time (t) are accounted for using the full form of equation 4.2. However for steady state incompressible flow simulation, the time dependant and density variation terms would equate to zero.

$$\frac{\partial \rho}{\partial t} + \frac{\partial (\rho u)}{\partial x} + \frac{\partial (\rho v)}{\partial y} + \frac{\partial (\rho w)}{\partial z} = \frac{\partial \rho}{\partial t} + \nabla . \rho \bar{u} = 0$$ **Equation 4.2**

By utilizing equation 4.2, the Navier-Stokes equations contain a set of three, time dependent equations for a 3-D spatial domain which govern conservation of momentum (eq 4.3). Velocity components in the x, y and z spatial coordinate system are shown as u, v and w whereas pressure and stress are represented respectively by p and τ in the Navier-Stokes equations alongside body forces (f). Equations 4.4 and 4.5 are also required to provide the necessary stress rate of strain relationships with μ associated to dynamic viscosity.

$$\rho \left[\frac{\partial u}{\partial t} + u \frac{\partial u}{\partial x} + v \frac{\partial u}{\partial y} + w \frac{\partial u}{\partial z} \right] = -\frac{\partial p}{\partial x} + \frac{\partial \sigma_{xx}}{\partial x} + \frac{\partial \tau_{xy}}{\partial y} + \frac{\partial \tau_{xz}}{\partial z} + \rho f_x$$

$$\rho \left[\frac{\partial v}{\partial t} + u \frac{\partial v}{\partial x} + v \frac{\partial v}{\partial y} + w \frac{\partial v}{\partial z} \right] = -\frac{\partial p}{\partial y} + \frac{\partial \tau_{xy}}{\partial x} + \frac{\partial \sigma_{yy}}{\partial y} + \frac{\partial \tau_{yz}}{\partial z} + \rho f_y$$

$$\rho \left[\frac{\partial w}{\partial t} + u \frac{\partial w}{\partial x} + v \frac{\partial w}{\partial y} + w \frac{\partial w}{\partial z} \right] = -\frac{\partial p}{\partial z} + \frac{\partial \tau_{xz}}{\partial x} + \frac{\partial \tau_{yz}}{\partial y} + \frac{\partial \sigma_{zz}}{\partial z} + \rho f_z$$

Equation 4.3

$$\sigma_{xx} = \lambda(\nabla.\bar{u}) + 2\mu\frac{\partial u}{\partial x}$$
$$\sigma_{yy} = \lambda(\nabla.\bar{u}) + 2\mu\frac{\partial v}{\partial y}$$
$$\sigma_{zz} = \lambda(\nabla.\bar{u}) + 2\mu\frac{\partial w}{\partial z}$$

Equation 4.4

$$\tau_{xy} = \mu\left[\frac{\partial u}{\partial y} + \frac{\partial v}{\partial x}\right]$$
$$\tau_{xz} = \mu\left[\frac{\partial u}{\partial z} + \frac{\partial w}{\partial x}\right]$$
$$\tau_{yz} = \mu\left[\frac{\partial v}{\partial z} + \frac{\partial w}{\partial y}\right]$$

Equation 4.5

Therefore to obtain a fully defined representation of the Navier-Stokes relations (λ = 2nd coefficient of bulk viscosity), the stress strain relationships (equations 4.4 and 4.5) are substituted into the momentum equations (equation 4.3). This provides the final fluid flow relation defined within equation 4.6 (representing the x momentum component only) which collects transient, convection, diffusion and source terms.

$$\rho\left[\frac{\partial u}{\partial t} + u\frac{\partial u}{\partial x} + v\frac{\partial u}{\partial y} + w\frac{\partial u}{\partial z}\right] = -\frac{\partial p}{\partial x} + \mu\left[\frac{d^2u}{dx^2} + \frac{d^2u}{dy^2} + \frac{d^2u}{dz^2}\right] + \rho f_x$$

Equation 4.6

However, as the flow required to be modelled is turbulent, equation 4.6 which represents instantaneous flow would require significant computational requirements to solve. Therefore eq. 4.6 can be modified to significantly ease such requirements to solve equations for high Reynolds number flows. This is achieved by decomposing the velocity field into a time average motion and turbulent fluctuation (equation 4.7). By substituting equation 4.7 into equation 4.6, the Reynolds Average Navier-Stokes (RANS) equations are generated which produce an additional tensor term to equation 4.6 known as divergence of the Reynolds stresses (equation 4.8). RANS equations are widely used as a reliable numerical solver when used with turbulence models which will be described in detail in the following section.

$$u = \bar{u} + u'$$

Equation 4.7

$$-\rho\left(\frac{\overline{\partial u'u'}}{dx}+\frac{\overline{\partial u'v'}}{dy}+\frac{\overline{\partial u'w'}}{dz}\right)$$ **Equation 4.8**

For the flow regimes within PRV's geometry, supersonic flow is typically expected to occur as the fluid expands through to the valve outlet. As a result, an accurate CFD model for use on PRV's must account for compressibility effects for Mach (Ma) numbers generally greater than approximately 0.3 [48, 49, 51] where changes in density due to flow velocity become significant. The Mach number of a flow can be determined by calculating the local speed of sound using equation 4.9 and substituting the result within equation 4.10 which determines a dimensionless ratio of the flow velocity with the local speed of sound. In equation 4.9, it should be noted that γ is the ratio of specific heats (C_p/C_v). When the Mach number is less than 1 the flow is considered to be subsonic whereas for Mach numbers greater than 1 the flow is supersonic and shocks and expansion fans are expected to exist which would severely impact flow structure within the regime.

$$c=\sqrt{\frac{\gamma p}{\rho}}$$ **Equation 4.9**

$$Ma=\frac{U}{c}$$ **Equation 4.10**

Furthermore, critically for equation 4.9 and the operational pressure for air which will be investigated within this study will remain below 150 Barg which allows intermolecular forces to be ignored and the ideal gas law to be valid. The ideal gas law is shown within equation 4.11 which uses the specific gas constant (R) to create a relationship between pressure (P), density (ρ), temperature (T) and molar mass (M). This is critical for modelling compressible

flow for a real gas whereas incompressible fluid such as water and low Mach number flows assume constant density and is independent to fluid velocity.

$$\frac{P}{\rho} = \frac{RT}{M}$$ **Equation 4.11**

For compressible flow, a relationship can be established between pressure and Mach number as shown within equation 4.12. A similar equation can is generated for temperature. The relationship describes the variation of static pressure in the flow as Mach number changes under isentropic flow conditions.

$$\frac{p_0}{P} = \left(1 + \frac{\gamma - 1}{2} Ma^2\right)^{\frac{\gamma}{(\gamma-1)}}$$ **Equation 4.12**

From equation 4.12 and the use of the ratio of specific heats for air, it is possible to determine a critical static pressure ratio which would result in choked flow where the Mach number is equivalent to unity. When considering flow through a converging nozzle for air, the pressure ratio between the exit of the nozzle and inlet/reservoir is equal to 0.5283 where the choked flow would occur at a point of minimum flow area. This area would typically be found in the near disc/seat area for a PRV. Following the critical choked area, there would be an expansion of the flow to allow the bulk flow Mach number to accelerate to supersonic conditions where pressure would continue to drop or would return to subsonic conditions where the flow would decelerate with a rise in pressure. It should be noted that if supersonic flow is subjected to an applied pressure increase, a shock would occur which provides the flow characteristics of a sudden pressure rise and flow deceleration across the shock geometry.

Since air is taken as the working fluid in this study and assumed to be an ideal gas, the density is a function of temperature and is determined through solution of the energy equation. The energy equation used by FLUENT is in the form shown within equation 4.13 where the value of k_{eff} represents the effective conductivity which is dependent on the sum of the conductivity of the flowing medium and turbulent thermal conductivity (dependent on the turbulence model used). E is determined by a relationship of enthalpy, h to temperature, T with J representing the diffusion flux of species j. The terms on the right-hand side represent energy transfer due to conduction, species diffusion and viscous dissipation in addition to any predefined heat source.

$$\frac{\partial}{\partial t}(\rho E) + \Delta \cdot \left(U\left(\rho E + p\right)\right) = \Delta \cdot \left(k_{eff} \Delta T - \sum_{j} h_j \vec{J}_j + \left(\overline{\overline{\tau}}_{eff} \cdot \vec{v} \right) \right) + S_h$$

Equation 4.13

4.2 Turbulence Modelling

As the flow velocity (U) and characteristic length (L) for a typical PRV are relatively large, the Reynolds number (Re) which can be determined using equation 4.14 highlights that the flow would generally operate in the turbulent flow regime. This is because the Reynolds number would be greater than $2x10^5$ and as such the turbulent flow characteristics is required to be modelled appropriately within CFD to achieve a model with a high degree of accuracy.

$$\mathrm{Re} = \frac{\rho U L}{\mu}$$

Equation 4.14

Turbulence typically manifests itself as fluctuating velocity fields in which transported terms such as momentum and energy also fluctuate. For industrial type flows, it is too computationally demanding to directly simulate turbulence therefore turbulence models are used by CFD engineers to solve ensemble

(time) averaged governing equations as described in the previous section. As a result of the random generation and dissipation of turbulence caused by the Reynolds stress terms, the RANS equations cannot be solved due to numerical closure problems. To overcome closure issues and solve the equations, turbulence models are widely used to achieve an approximate solution. For the purpose of the PRV simulations using CFD, isotropic eddy viscosity models were utilized which approximate the Reynolds stresses through the use of Boussinesq relations (equation 4.15); where the energy dissipating viscosity term represents the turbulent dynamic viscosity [48]. Turbulent transport of heat, mass and other scalar properties are modelled similarly as they share the same eddy mixing process, therefore turbulent viscosity is assumed to be close in value to turbulent diffusivity. This is commonly known as the Reynolds analogy with the ratio of turbulent viscosity and turbulent diffusivity describing the Prandtl number.

$$-\rho\overline{u'u'} = 2\mu_T \frac{\partial \bar{u}}{\partial x} - \frac{2}{3}\rho k$$

Equation 4.15 (x-component only)

For the present CFD investigation, the two equation turbulence models of K-Omega and K-Epsilon were used due to their reputation of providing good numerical stability and accuracy for a wide variety of turbulent flow conditions. In addition, the transition SST 4 equation model has also been utilised which is based on a coupling of the K-Omega SST model with two additional transport equations. However, to identify the most suitable model to use which would accurately simulate PRV performance to experimental conditions; background research and validation would be required for each PRV geometry and operating conditions. This is due to the fact that there is not a universal turbulence model which is suitable for every flow condition, therefore the expertise of the CFD engineer and compliance with CFD best practice [52] is required for the most appropriate RANS model to be achieved.

Standard K-Epsilon

The standard k-epsilon turbulence model is generally the most widely used approach for industrial applications and has been found to be robust and reasonably accurate for a variety of applications typically without separation. It has been used extensively in previous PRV research studies performed at Strathclyde by Alshaikh and Elmayyah to achieve an acceptable degree of accuracy for 2D simulation. The K-Epsilon model solves the transport equations for turbulent kinetic energy k and dissipation rate ε in which the turbulent energy is derived from an exact equation and dissipation rate obtained from empirical physical reasoning [48]. The model utilises the assumption that the effects of molecular viscosity are negligible therefore it can only be used for fully turbulent flows. The general transport equations for the standard k- ε model for both k and ε are shown within equations 4.16 and 4.17 respectively.

$$\frac{\partial}{\partial t}(\rho k)+\frac{\partial}{\partial x_i}(\rho k u_i)=\frac{\partial}{\partial x_j}\left[\left(\mu+\frac{\mu_t}{\sigma_k}\right)\frac{\partial k}{\partial x_j}\right]+G_k+G_b-\rho\varepsilon-Y_M+S_k$$

Equation 4.16

$$\frac{\partial}{\partial t}(\rho\varepsilon)+\frac{\partial}{\partial x_i}(\rho\varepsilon u_i)=\frac{\partial}{\partial x_j}\left[\left(\mu+\frac{\mu_t}{\sigma_\varepsilon}\right)\frac{\partial \varepsilon}{\partial x_j}\right]+C_{1\varepsilon}\frac{\varepsilon}{k}(G_k+C_{3\varepsilon}G_b)-C_{2\varepsilon}\rho\frac{\varepsilon^2}{k}+S_\varepsilon$$

Equation 4.17

The default model constant values are used as follows which are determined from experiments with air and water and have been found to work fairly well for a wide range of wall bounded and free shear flows [48];

$C_{1\varepsilon}$ =1.44, $C_{2\varepsilon}$ = 1.92, C_μ =0.09, σ_k = 1.0, σ_ε = 1.3 where σ represents the turbulent Prandtl number for both k and epsilon.

The turbulent viscosity term is shown within equation 4.18;

$$\mu_t = \rho C_\mu \frac{k^2}{\varepsilon}$$ **Equation 4.18**

The simplicity of the two equation K-Epsilon turbulence model and inherent affordability of the computational expense as well as its reasonable accuracy for a wide variety of flows offers CFD engineers with a robust solution suitable for an initial high level analysis of a turbulent flow regime. However there are numerous limitations for the application of the standard model which would prevent its effective use for certain flow types. The numerical model itself is known to be excessively diffusive where it performs poorly in particular for flow regimes with strong separation, large streamline curvature and significant pressure gradient [48, 51]. Such flow features are common during the operation of a PRV and typical seat/disc geometry therefore it is clear from literature and previous work that care should be taken when using the k-epsilon model in terms of capturing the correct flow physics. In addition, for near wall treatment the ε term can't be calculated at the wall therefore empirical wall functions are utilized to achieve an approximate solution at the wall. As a result, the use of approximate wall functions introduces an additional source of error to the model however can be beneficial to reduce mesh resolution at the wall when compared to more complex turbulence models.

K-Omega SST

An alternative to the standard k-epsilon turbulence model which could be appropriate to capture the flow regimes for PRV's using CFD is the K-omega SST model. The SST model is an adaption of the standard K-Omega turbulence model which is an empirical turbulence model based on the transport equations of turbulence kinetic energy (k) and specific dissipation rate omega (ω). The value of specific dissipation rate can be understood by the ratio of dissipation rate epsilon (ε) to turbulent kinetic energy k. The

FLUENT theory guide [48] states that the standard K-Omega model used in the solver is based on the Wilcox model which included modifications to capture flow effects due to compressibility and shear flow spreading. As a result, the model has been found to be in close agreement with experimental results for mixing layers, a variety of jet orientations and is generally applicable to wall bounded and free shear flows. The SST or shear stress transport model was derived by Menter which included a combination of the free stream independence of the k-epsilon model in the far field and use of the Wilcox K-Omega model in the near wall region which can be computed directly without the use of wall functions. To achieve this, Menter developed a transformation of the K-Epsilon model to allow both the standard K-Omega model and K-Epsilon model to be added together with use of a blending function to allow the K-Epsilon model to be used in the far field. As a result of the modifications which also include different model constant values, turbulent viscosity definition and diffusion terms when compared to the standard model, the K-Omega SST model is widely recognized as being more accurate and robust for a wider range of flow regimes such as adverse pressure gradient flows and supersonic conditions.

The general transport equations for the K-Omega SST model for both k and ω are shown within equations 4.19 and 4.20 respectively where further detail regarding additional terms and modified viscosity formulation can be found within the ANSYS FLUENT theory guide [48]. It should be noted that the G term for k represents the generation of turbulence kinetic energy due to mean velocity gradients whereas for ω, G represents the generation of ω.

$$\frac{\partial}{\partial t}(\rho k)+\frac{\partial}{\partial x_i}(\rho k u_i)=\frac{\partial}{\partial x_j}\left[\Gamma_k \frac{\partial k}{\partial x_j}\right]+\tilde{G}_k-Y_k+S_k$$

Equation 4.19

$$\frac{\partial}{\partial t}(\rho\omega)+\frac{\partial}{\partial x_i}(\rho\omega u_i)=\frac{\partial}{\partial x_j}\left[\Gamma_\omega\frac{\partial\omega}{\partial x_j}\right]+G_\omega-Y_\omega+D_\omega+S_\omega$$

Equation 4.20

The default model constant values are used as follows, which are identical to the standard K-Omega model.

It can be argued that there are limitations of the K-Omega SST turbulence model which exist as a result of the arbitrary location of the blending function between K-Omega and K-Epsilon which could interfere with the capture of turbulent flow features in the free stream. In addition, the k-omega model requires a much finer near wall mesh when compared with the k-epsilon turbulence model with a y^+ requirement of $1< y^+<10$. As a result, the K-Omega model could be considered computationally expensive when compared to K-Epsilon which may not be beneficial for certain industrial users where there are computational and/or time limitations. Furthermore K-Omega SST when compared with K-Epsilon has been found to be less computational robust with difficult convergence characteristics as well as increased sensitivity to initial conditions. However, given its proven ability to be able to accurately capture shockwave structures and position as well as strong performance for adverse pressure gradients, the K-Omega SST model would seem to be a suitable choice to capture the typical flow regimes found within a PRV.

Transition SST

In addition to the two equation K-Omega SST model, a 4 equation model is available within ANSYS FLUENT which was developed by Langtry and Menter [48] known as the Transition SST turbulence model. The Transition SST model is based on the coupling of the K-Omega SST model with two additional transport equations in order to improve the prediction of the transition point for

flow detachment from a surface. The model exhibits the same general behaviour and performance as the K-Omega SST turbulence model however requires a finer near wall mesh of $1< y^{+}<5$ in order to achieve an accurate prediction of the transition point. This model could therefore be feasible to use where computational resource and time is available. The general transport equation for the Transition SST model is shown within equation 4.21 for the modification of the equation for the generation of turbulent kinetic energy (k) however it should be noted that the production term for ω remains the same.

$$\frac{\partial}{\partial t}\left(\rho k\right)+\frac{\partial}{\partial x_j}\left(\rho k u_j\right)=\frac{\partial}{\partial x_j}\left[\left(\mu+\sigma_k\mu_t\right)\frac{\partial k}{\partial x_j}\right]+\tilde{P}_k-\tilde{D}_k$$

Equation 4.21

Wall Functions

As mentioned previously, due to the fact that the dissipation rate term ε can't be solved directly at the wall for the K-Epsilon turbulence model a wall function is required in order to achieve a numerical solution at the near wall region. The near wall region in particular provides a complex challenge for CFD models to capture due to the nature of the boundary layer which in a short distance transforms from a fully turbulent outer region (otherwise known as log-law) to a buffer layer then to a viscous sub layer. A term known as y^{+} is typically used to define the layer at which a corresponding mesh element is situated by using equation 4.22. For a y^{+} value of <5 then the viscous sublayer is captured however from $5<y^{+}<60$ the buffer layer is represented then above 60 represents the typical log law region of the boundary layer. The use of equation 4.22 allows CFD engineers to develop a mesh resolution which allows the required y^{+} value to be achieved. The wall functions used by the k-ε model, in particular the standard variant which is used with ANSYS FLUENT which was developed by Launder and Spalding [48] utilises a log law empirical correlation for fully turbulent boundary layers to achieve the necessary boundary

conditions for solution. As a result, the mesh density required for y^+ can be much higher (30-300) than that compared to viscous sublayer resolution for K-omega SST hence allowing a computationally cheaper model to be developed.

$$y^+ = \frac{U_\tau y_0}{\upsilon}$$ **Equation 4.22**

Care must be taken however if the wall functions are used in flow conditions in which the empirical correlation wasn't developed to model due to the limitations of the shear and local flow equilibrium assumptions which were used to derive them. Such conditions are when the near wall flow regime is subjected to severe adverse pressure gradients and non-equilibrium flow where it is suggested that "the quality of predictions is likely to be compromised" [48]. FLUENT offers several wall functions; standard, enhanced wall treatment and scalable. Each model has advantages, however the standard function is extensively used in industry and validated so will be used during the remainder of this study when the k-ε turbulence model is required.

4.3 Multiphase Flow Modelling

In addition to the single phase compressible governing equations described previously, it is required within this study to investigate the effectiveness of the multiphase extensions of the equations for the accurate capture of two phase flow physics within a PRV [48, 53, 54]. During the operation of a PRV, it is typical to observe two phase flow phenomena as a result of processes such as fluid entrainment and/or evaporation/condensation as the pressure within the system rapidly changes. As a result, it is critical for designers to be able to use CFD as a tool to improve understanding towards the two phase flow behaviour which occur within PRV's in order to optimise valve performance however the multiphase tools developed within CFD are very much in their infancy when compared to traditional single phase simulation. Furthermore,

various classifications can be applied to multiphase flows which is dependent on the boundary conditions of the system therefore the complexity of modelling such systems is much higher when compared to single phase. For the PRV boundary conditions examined in this study dispersed droplet-air two phase flow will dominate Such a flow regime can be understood by studying figure 4.1.

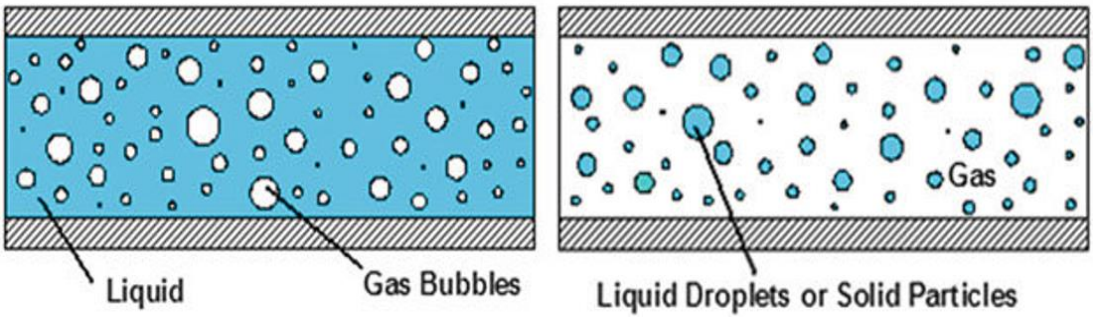

Figure 4.1 –Dispersed Droplet-Sir Two Phase Flow Regime [54]

In accordance with previous research of 2D multiphase modelling for a Henry manufactured PRV by both Elmayyah and Alshaikh [11, 12], it was concluded that for low liquid mass fraction flow, the homogenous mixture model could be utilised. The homogenous mixture model in particular uses the assumption of negligible slip velocity between the liquid and gas phases which significantly helps to reduce computational expense and improve convergence. This approximation was used as it was assumed that an equilibrium Weber number (ratio between the inertial force and the surface tension force) had been achieved leading to a fixed droplet size. As a result, the liquid droplets in the PRV would be mono dispersed as represented in figure 4.1. A range of droplet diameters of 1 to 10 µm were thought to exist with the droplets travelling at a similar velocity to the gas flow to achieve homogenous conditions. The volume fraction of the dispersed phase with subscript p and volume fraction of the continuous phase with subscript f could be calculated by using equations 4.23, 4.24 and 4.25 where V is the total volume, N_i is the number of all particles in the size fraction i with the particle volume of V_{p_i} [48]. Mass fraction of a phase

is determined using continuity with the ratio of the mass flow rate of the phase to the total mass flow rate of all phases.

$$\alpha_p = \frac{\sum_i N_i V_{p_i}}{V}$$ **Equation 4.23**

$$V_{p_i} = \frac{d_{p_i}^3 \pi}{6}$$ **Equation 4.24**

$$\alpha_f = \left(1 - \sum_i \alpha_{p_i}\right)$$ **Equation 4.25**

The mixture model treats the dispersed multiphase flow as two or more inter penetrating quasi fluids. The homogeneous mixture model which will be investigated however assumes the relative slip velocities can be neglected which further simplifies the governing equations. As a result of the fact that the flow treats the phases as interpenetrating, the volume fraction equations introduced previously are critical as it determines the quantity of each phase which is present at a given location at a given time.

The solutions provided by using such models provides an averaged representation of the fluid distribution within the domain. A key advantage of this averaged approach when compared to Lagrangian particle tracking methods is that the model doesn't depend on the number of particles within the system therefore it is common to use an averaged approach on industrial multiphase problems. This will continue to be the case until it becomes feasible to use particle tracking as computing power and memory capacity increases. A disadvantage of averaging however is the loss of detail regarding particle positioning when compared to direct particle tracking techniques. Furthermore the combination of the averaged form of particle interactions with the averaged

form of RANS turbulence models adds additional complexity and source of error to the computations when compared to single phase modelling. In addition, the closure relations required for droplet interactions act as the largest source of error compared to the use of the mixture model which requires less empirical based closure terms and models. Therefore the mixture model can provide a more accurate and computationally efficient model for lower dispersed volume fractions as was demonstrated by both Elmayyah and Alshaikh [11, 12] when compared with the full Eulerian multiphase model.

In the research previously conducted at Strathclyde, Elmayyah [11] also found that when using the homogenous mixture model that a single temperature could represent the thermal conditions of the mixture. Therefore at lower dispersed phase volume fractions, the continuous and dispersed phases could be assumed to be in thermal equilibrium with each other. As the homogeneous mixture model was explored in the past only for 2D modelling, the assumption will be extended within this thesis to investigate the effectiveness of the model for 3D flow as recommended in previous literature [12]. The 3D representations of the governing flow equations for the mixture model will be therefore be presented in the following section from the ANSYS FLUENT theory guide [48] and supplementary literature [53].

For the mixture model it is assumed that local equilibrium is achieved over short spatial length scales where for each phase it is possible to determine the governing equations of the flow such as the continuity, momentum, energy, volume fraction and relative velocity equations. Equation 4.26 illustrates the 3D mass conservation principle used by the mixture model. Equations 4.27 and 4.28 are supplementary equations which determine the mass averaged velocity and mixture density respectively;

$$\frac{\partial}{\partial t}\left(\rho_m\right)+\nabla\cdot\left(\rho_m\vec{v}_m\right)=0 \qquad \textbf{Equation 4.26}$$

$$\vec{v}_m = \frac{\sum_{k=1}^{n} \alpha_k \rho_k \vec{v}_k}{\rho_m}$$

Equation 4.27

$$\rho_m = \sum_{k=1}^{n} \alpha_k \rho_k$$

Equation 4.28

The momentum equation 4.29 is determined by using the sum of the momentum for each phase. It should be noted that the n term represents the number of phases, equation 4.30 calculates the viscosity of the mixture and equation 4.31 determines the drift velocity for the secondary phase;

$$\frac{\partial}{\partial t}\left(\rho_m \vec{U}_m\right) + \nabla \cdot \left(\rho_m \vec{U}_m \vec{U}_m\right)$$
$$= -\nabla p + \nabla \cdot \left[\mu_m \left(\nabla \vec{U}_m + \nabla \vec{U}_m^T\right)\right] + \rho_m \vec{g} + \vec{F} + \nabla \cdot \left(\sum_{k=1}^{n} \alpha_k \rho_k \vec{U}_{dr,k} \vec{U}_{dr,k}\right)$$

Equation 4.29

$$\mu_m = \sum_{k=1}^{n} \alpha_k \mu_k$$

Equation 4.30

$$\vec{U}_{dr,k} = \vec{U}_k - \vec{U}_m$$

Equation 4.31

The relative (slip) velocity can be calculated using equation 4.32. For homogenous flow the slip velocity is assumed to be zero to allow both phases to share the same velocity at the phase interface. Equation 4.33 represents the calculation which FLUENT performs to determine the mass fraction for any phase k. This solution is then input to equation 4.34 to provide a connection of the drift velocity to the relative velocity term.

$$\vec{U}_{pq} = \vec{U}_p - \vec{U}_q$$ **Equation 4.32**

$$c_k = \frac{\alpha_k \rho_k}{\rho_m}$$ **Equation 4.33**

$$\vec{U}_{dr,p} = \vec{U}_{pq} - \sum_{k=1}^{n} c_k \vec{U}_{qk}$$ **Equation 4.34**

From the continuity equation which was presented previously, the volume fraction of the secondary phase (p) can be determined from equation 4.35.

$$\frac{\partial}{\partial t}\left(\alpha_p \rho_p\right) + \nabla \cdot \left(\alpha_p \rho_p \vec{U}_m\right) = -\nabla \cdot \left(\alpha_p \rho_p \vec{U}_{dr,p}\right) + \sum_{q=1}^{n}\left(\dot{m}_{qp} - \dot{m}_{pq}\right)$$

Equation 4.35

Finally the energy equation for the mixture is obtained from equation 4.36; the term S_E represents any other volumetric heat source. Also it should be noted that the effective conductivity required for equation 4.36 is calculated using equation 4.37 where the K_t term is determined from the turbulence model used. The adaption required for the turbulence models such as K-Epsilon to be suitable for multiphase flow modelling can be understood in detail from the FLUENT theory guide [48].

Equation 4.38 is used when compressibility effects are taken into account or otherwise the E_k term would be equivalent to the enthalpy of phase k, h_k.

$$\frac{\partial}{\partial t}\sum_{k=1}^{n}\left(\alpha_k \rho_k E_k\right) + \nabla \cdot \sum_{k=1}^{n}\left(\alpha_k \vec{U}_k \left(\rho_k E_k + p\right)\right) = \nabla \cdot \left(k_{eff} \nabla T\right) + S_E$$

Equation 4.36

$$K_{eff} = \sum_{k=1}^{n} \alpha_k \left(K_k + K_t \right) \qquad \textbf{Equation 4.37}$$

$$E_k = h_k - \frac{p}{\rho_k} + \frac{U_k^2}{2} \qquad \textbf{Equation 4.38}$$

4.4 Transient Dynamic Meshing

To achieve a CFD model which is capable of capturing the transient processes of a PRV's dynamic operation from opening to closing, it is required to utilise the dynamic meshing capability within ANSYS FLUENT. In this study the piston motion, resulting in the requirement of a dynamic mesh is achieved in two ways; a force balance on the disc which results in acceleration as well as pre-prescribed linear velocity of the disc. To achieve a dynamic mesh, a suitable starting volume mesh is required to provide the topology and initial conditions as well as a prescription of the motion typically achieved using a user defined function (UDF). It should be noted that the mesh boundary between the various regions which are either moving, deforming or stationary is not required to be conformal therefore a sliding interface (non-conformal interface) can be used to reduce computational expense.

The FLUENT theory guide [48] allows an understanding of the various dynamic meshing strategies to be achieved. These meshing strategies enable the CFD model to generate a solution when the shape of the computational domain is changing with respect to time and in accordance with the motion prescribed on the domain boundaries. Care must be taken however when selecting an appropriate meshing strategy as each provide individual characteristics which affect the mesh quality and resilience with rate of change in the size of the computational domain. In addition, the meshing strategies can be used in

combination with each other or individually depending on the requirements of the CFD problem. The three meshing update methods which are available within ANSYS FLUENT which will be summarized below;

Smoothing Methods

There are various smoothing methods available for dynamic meshing within FLUENT such as spring based smoothing, Laplacian smoothing and boundary layer smoothing.

Laplacian smoothing is the most widely used technique where the solver adapts the mesh geometry to align the position of each mesh vertex to the centre of its neighbouring vertices. As a result of the simplistic method this process requires, the computational expense is relatively low compared to other methods however it doesn't guarantee an improvement on mesh quality. This is due to the fact that the repositioning of vertices during mesh motion could result in poor quality elements with unacceptable aspect ratio and/or skewness. FLUENT tackles this issue by applying smoothing where the vertex is only changed if an improvement in mesh quality is detected.

The fundamental process of the spring based smoothing method can be understood by evaluating the computational interior domains shown in figures 4.2 and 4.3. Figure 4.2 represents an interior zone before mesh motion is applied and figure 4.3 illustrates the nature of mesh deformation following mesh motion. It can be seen that the mesh is compressed in a similar manner to a spring, where the size of each cell is adjusted and compressed as the overall domain reduces in size.

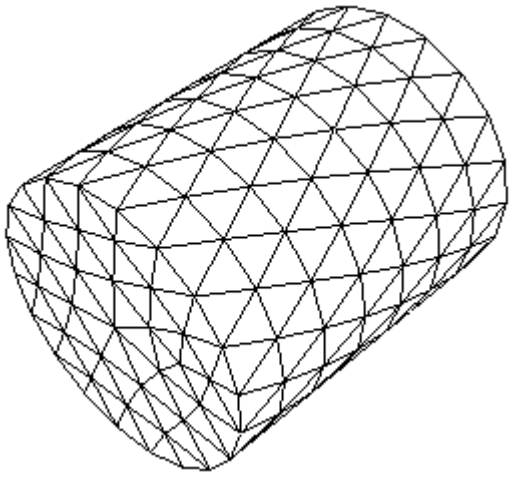

Figure 4.2 – Interior Spring Based Smoothing (Before Mesh Motion) [48]

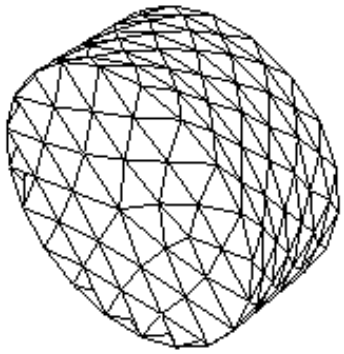

Figure 4.3 - Interior Spring Based Smoothing (After Mesh Motion) [48]

This is due to the connection of the edges between any two mesh nodes in the domain to create a network of interconnected springs [48]. Hooke's law (equation 4.39) can then be applied to each cell to determine the displacement of all interior nodes (x^{n+1}) where the positions are updated based on the force value of the previous iteration using equation 4.40. A key disadvantage of using this method however, is the fact that large mesh motion would result in significant mesh deformation as no new cell layers would be created/destroyed which could result in the generation of negative volumes. Therefore it is only suitable for dynamic mesh cases with small deformations.

$$\Delta\vec{x}_i^{m+1} = \frac{\sum_j^{n_i} k_{ij}\Delta\vec{x}_j^{-m}}{\sum_j^{n_i} k_{ij}}$$

Equation 4.39

$$x_i^{n+1} = x_i^{-n} + \Delta x_i^{-m,converged}$$

Equation 4.40

Dynamic Layering

Dynamic layering in principle provides the most robust dynamic meshing method when compared to the alternative strategies. This is because the method utilises structured meshing zones which preserve mesh quality by adhering to strict rules regarding the maximum cell height of each cell as the mesh is deformed. In addition, the strategy allows the creation and deletion of layers containing cells adjacent to the moving boundary based on the height of the layer adjacent to the moving surface [48]. During mesh expansion an ideal height of the cell layer adjacent to the moving boundary is required to be input by the user (h_{ideal}) as well as an allowable layer split factor (α_s) where by using equation 4.41 the solver can determine the critical value of cell height in which a cell layer (h) is required to be added or removed. When the value of h_{min} is greater than the value determined from equation 4.41 this deformation process occurs. The expansion dynamic layering process is highlighted within figure 4.4 where the layer of cells adjacent to the moving boundary j is split or merged with cells in layer i based on height h of the cells in layer j.

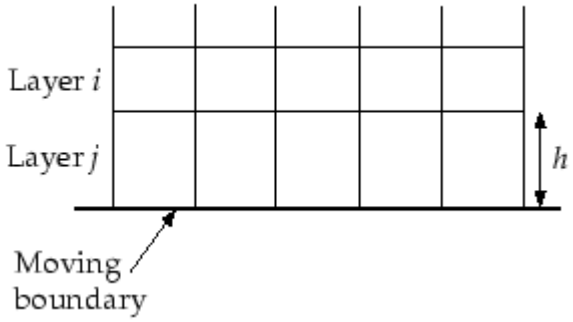

Figure 4.4 – Dynamic Layering Process [48]

$$h_{\min} > \left(1+\alpha_s\right) h_{ideal}$$ **Equation 4.41**

Importantly, a separate value for α_s is required to be set for a compression of the mesh zone known as the layer collapse factor (α_c). Using equation 4.42, when the conditions for minimum cell height are met the cells in layer j are merged with those in layer i to remove a cell layer.

$$h_{\min} < \alpha_c h_{ideal}$$ **Equation 4.42**

In addition, the application of equations 4.41 and 4.42 to add or remove a cell layer can be performed using either a height based or ratio based method. The height based method is illustrated within figure 4.5, where the cells are split to create a layer of cells with constant height h_{ideal} and a layer of cells equivalent to $h-h_{ideal}$. On the other hand, the ratio based approach is shown within figure 4.6 where the cells which are split so that locally the ratio of the new cell heights is exactly α_s everywhere. By comparing figures 4.5 and 4.6 for height and ratio approaches it is possible to appreciate the difference between both methods when comparing the structured mesh generated in both figures;

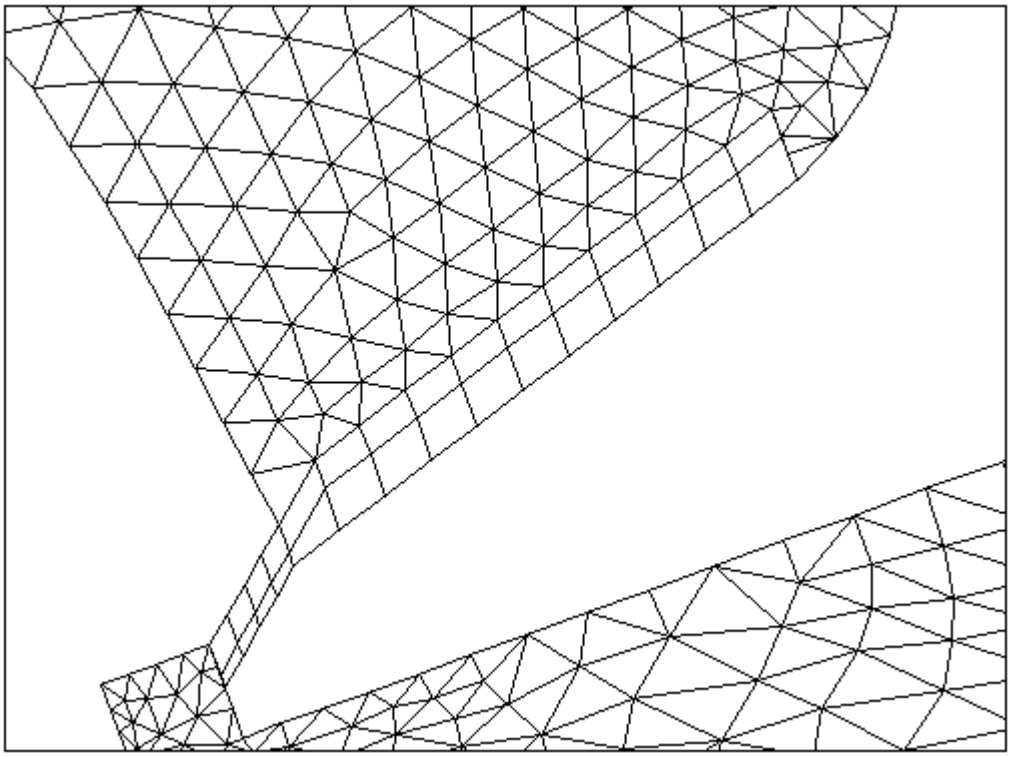

Figure 4.5 – Layer Generation Using Height Based Option [48]

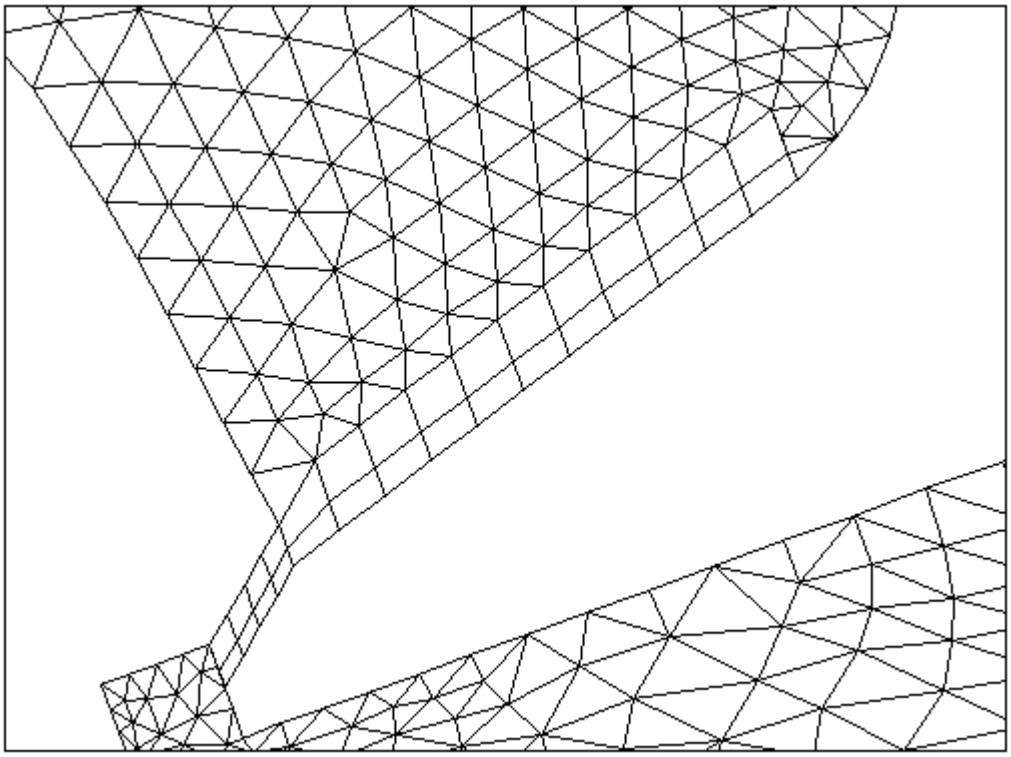

Figure 4.6 - Layer Generation Using Ratio Based Option [48]

Local Remeshing Methods

The remeshing dynamic mesh strategy is applicable to most meshing problems which consist of an unstructured mesh and generally works for a variety of problems. Its downside however is the high computational cost which is required to regenerate a computational mesh when the mesh quality deteriorates to an unacceptable value following mesh motion. The remeshing method is generally used in combination with the spring based smoothing method in order to prevent the generation of negative volumes during significant mesh deformation. A critical value of mesh skewness or a violation of the maximum and/or minimum length scale is required to achieve a criterion in which the mesh must be locally remeshed with the new cells where the solution is interpolated from the old cells. If the criterion is still not met then the new cells are deleted. Several remeshing methods are available to be used within FLUENT such as face region remeshing, and local face remeshing. For face region remeshing as shown in figure 4.7, FLUENT identifies the region of faces on the deforming boundaries at the moving boundary based on minimum and maximum length scales. Once marked, the solver remeshes the faces and the adjacent cells to produce a regular mesh on the deforming boundary at the moving boundary.

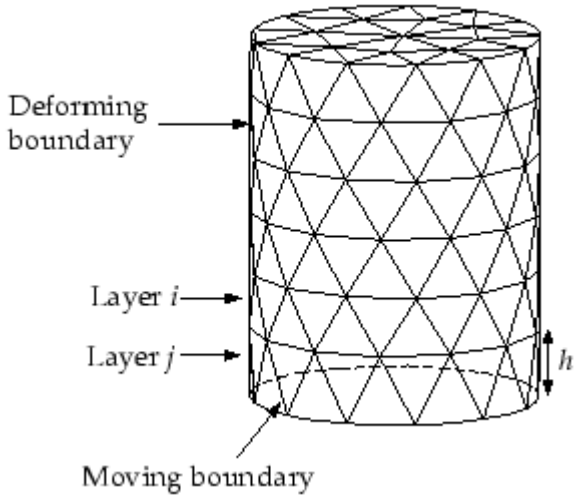

Figure 4.7 – Remeshing at deforming boundary [48]

During mesh movement it is necessary for the mesh at the face of a surface to deform. In a similar manner to the dynamic layering process, during an expansion of the zone due to mesh motion the faces in layer j are allowed to expand until the maximum length scale which was input prior to calculation is reached. Whereas for cell layer deletion, the faces are allowed to contract until the minimum length scale is reached where once the criterion is satisfied the compressed layer of faces is merged into the adjacent layer. The process for expansion using region face remeshing is shown within figures 4.8 and 4.9.

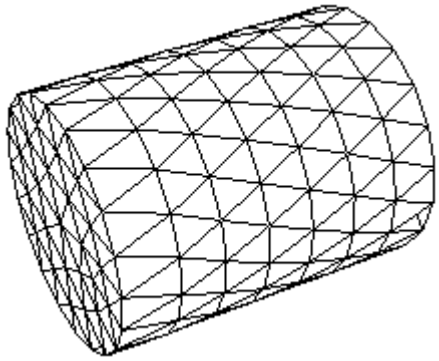

Figure 4.8 – Layer Generation Using Remeshing (Before) [48]

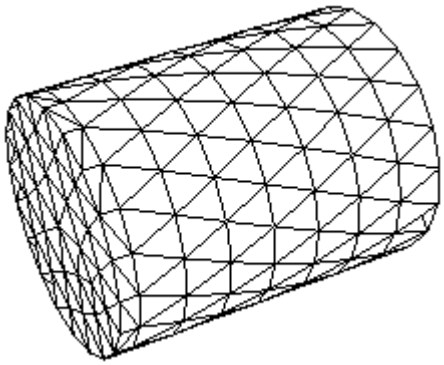

Figure 4.9 - Layer Generation Using Remeshing (After) [48]

The local remeshing methods available within FLUENT offer an alternative to the dynamic layering methods which is able to work for unstructured meshes and requires significantly less preparation of the mesh zones. However the process also requires a significant amount of computational resources for

remeshing in comparison and also provides significantly less control on maintain mesh quality for each time step during mesh motion.

Overview of Resilience for Dynamic Meshing

In general, it can be determined that in accordance with historical research and evaluating the operation characteristics of each method that the dynamic layering function would provide the solution which would maintain resilience across a range of PRV geometries. This was due to the fact that the greatest magnitude of velocities of the deforming interface and displacement range could be achieved when compared to local remeshing and smoothing methods to maintain sufficient control over mesh quality. It should be noted however that the use of dynamic layering requires significant preparation for meshing and knowledge of dynamic mesh settings to correctly define the mesh behaviour when subjected to interface motion.

A required preparation step during the meshing process is that for dynamic layering to be successful for the PRV geometries which will be explored during this thesis, the use of a sliding mesh interface is required. The sliding interface is achieved by ensuring that the mesh on both sides (zones) are non-conformal as shown within figure 4.10. At the non-conformal boundary, it is necessary for the FLUENT solver to compute the flux across the interface and enable the use of dynamic meshing for the mesh on each side of the interface to move relative to each other. A dynamic mesh can then be achieved to maintain the integrity of the solution as the mesh deforms where the interface is updated as the zone positions on either side of the boundary changes due to motion. It is critical however that the mesh zone is prescribed so that the zones remain in contact with each other over the duration of the simulation to allow the flow properties to be transferred across the boundary [48]. To maintain the conservation equations described previously for dynamic mesh processes the unsteady form of equation 4.2 is necessary. The use of a non-conformal interface is also beneficial in terms of mesh density as the mesh density can

be different on either side of the boundary. Care must be taken to avoid significant differences in mesh size which could lead to computational error.

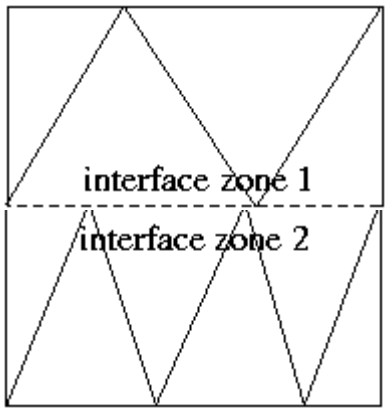

Figure 4.10 – Non-Conformal Interface

Critically to avoid the generation of negative volumes during dynamic meshing processes the velocity of the deforming interface (disc) is required to be less than the maximum allowable velocity value. This maximum velocity or V_{max} term is calculated using equation 4.43, where Δh represents the cell height at the interface and Δt is the time step. This is important for dynamic layering and spring based smoothing where if the time step used is not suitable for the maximum velocity of the system, negative mesh volumes would be generated. If such an event occurs, the simulation would catastrophically stop and not be able to recover therefore it is imperative for the CFD user to avoid negative volume generation.

$$V_{\max} = \frac{\Delta h}{\Delta t} \qquad \textbf{Equation 4.43}$$

The required settings and meshing procedures used within this study to achieve a working dynamic mesh model with layering will be described in detail within chapter 6. It should be noted that for all of the previously described

dynamic meshing methods, a small opening of at least one layer of cells is required to maintain mesh topology at the beginning of a simulation.

4.5 User Defined Functions

A user defined function (UDF) is required to be used in FLUENT to achieve customization within a simulation by using a series of macros. The ANSYS FLUENT customisation manual [55] provides guidance where the UDF is generally loaded in to FLUENT and then compiled however care must be taken to ensure that the appropriate compiling software is installed on the respective workstation for the compilation to complete successfully. The UDF is typically written in C programming langauge where for PRV transient dynamic mesh modelling it is required to define the movement of the disc and spindle based on the forces acting on. In addition the UDF is required to define the inlet pressure ramp where pressure increases until the valve is fully open where a corresponding drop in pressure will occur as well as allowing critical data to be saved to a text file.

The UDF developed by Budziszewski [42] was used as inspiration for the dynamic mesh PRV model in this project where it was improved and developed to suit requirements. The initial global variables/boundary conditions such as initial pre load, damping constant and spring constant are adjusted on an individual case by case basis. However the core principles are similar to the UDF created by Budziszewski with the utilisation of four variations of macros within the UDF and seven in total were used. The macros used in the UDF script are described in detail below [55];

DEFINE_ADJUST

The DEFINE_ADJUST macro is used in order to calculate the exact forces acting on the disc in 3D as the pressure in each cell as well as each respective area is multiplied together and summed together to achieve the total

aerodynamic force value. An additional DEFINE_ADJUST macro is used to calculate the mass flow rate through the PRV.

DEFINE_EXECUTE_AT_END

There are three DEFINE_EXECUTE_AT_END macros which are used in the UDF where the initial macro determines the displacement of the disc which is required to determine the spring force. The second macro calculates the total force acting on the spindle from the force balance and includes the aerodynamic force determines from the DEFINE_ADJUST function. From the value of the unbalanced force, the macro also calculates the velocity of the disc which can be used in the next time step. The final DEFINE_EXECUTE_AT_END writes critical data from the simulation at each time step such as disc position, unbalanced and aerodynamic force acting on the disc, disc velocity, inlet pressure and time. This is required for further analysis of the dynamic performance of the PRV to help to improve knowledge of operating characteristics and improve on the valve design.

DEFINE_CG_MOTION

The DEFINE_CG_MOTION macro is used in the UDF to specify the movement of the disc which in turn allows the solver to determine the mesh movement required for the dynamic mesh. The velocity which was determined in the previous time step using the DEFINE_EXECUTE_AT_END macro is used to define the linear motion of the PRV which is dependent on the force balance acting on the PRV at any given pressure and flow conditions.

DEFINE_PROFILE

The DEFINE_PROFILE macro is used to input the pressure ramp to the FLUENT solver by applying conditions which are dependent on the current time of the solution. In accordance with a pressure ramp generated

experimentally, an equivalent pressure ramp using a linear method dependent on time is used to allow the pressure to increase and decrease as it would for an external pressure vessel. An equivalent pressure vessel system is achieved using transient CFD and the response of the PRV to the applied inlet pressure is evaluated using dynamic meshing which requires the DEFINE_CG_MOTION macro.

The general process of the UDF when compiled on FLUENT is highlighted within the flowchart depicted in Figure 4.11;

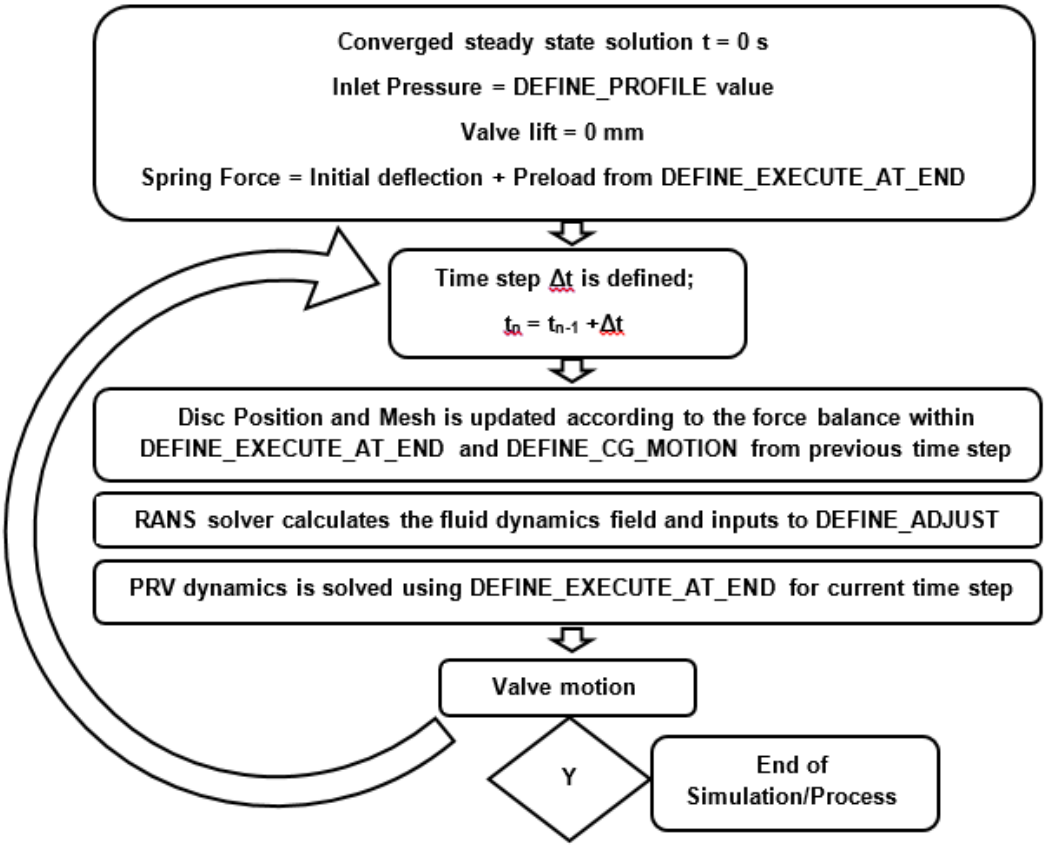

Figure 4.11 – UDF Flow Diagram for PRV Transient, Dynamic Mesh CFD Model

4.6 Solution Scheme and Discretisation Methods

In this study, FLUENT (ANSYS 17 and 18 workbench packages) has been used as a framework to examine the existing single phase and two phase flow flow models. It is implemented on both a workstation with 64GB of RAM and Intel Xeon Processor and an HPC. The HPC available at the University of Strathclyde ARCHIE-WeSt was used for the computationally demanding exercises such as transient, dynamic mesh problems using up to 280 Intel Xeon Gold 6138 cores with 192GB of RAM available per node (40 cores). This was identified to be the optimum configuration of cores/nodes to use on ARCHIE-WeSt following a scalability study in which the number of cores/nodes were increased until the gradient of speed up markedly plateaued. The simulations in general for both 2D and 3D analysis for PRV simulations are required to use the double precision version of FLUENT. This is due to the improved accuracy of the double precision solver when compared with the single precision version to accurately capture the flow physics for multiphase and high speed pressure driven flow with large pressure gradients. The boundary conditions which are used for each PRV case will be described later.

ANSYS FLUENT provides the choice of two numerical solvers in which to solve the flow physics of a given problem. The options are;

- Density based solver
- Pressure based solver

In general the pressure based solver is more suitable for low speed incompressible flows whilst the density based solver is more suited to high speed compressible flows [51, 56]. However numerical developments for both solvers allow them to operate for a wide range of flow conditions when compared to their initial focus. For both solvers the velocity field is determined from the momentum equation however for the pressure based solver the flow pressure field is determined by a pressure equation which uses a correlation

between the continuity and momentum equations. On the other hand for the density based model, the pressure field is obtained from the equation of state and the continuity equation is used to determine the density value.
Both the density and pressure based models use a finite volume based discretisation approach where the governing equations are solved by using a computational grid (mesh). However the solving approach used to solve the equations are different for both approaches as described previously. It is important to highlight that the pressure based solver is only suitable for use for multiphase based flow problems therefore in this thesis the pressure based solver will be mainly utilised in order to achieve a unified model with validated performance for both single phase and two phase flow simulation.

When using the Pressure based solver, Pressure-Velocity coupling is required to derive a condition for pressure from the continuity equation. There are two options which a user can select known as the Segregated Algorithm and Coupled Algorithm; these methods are illustrated with figure 4.12.

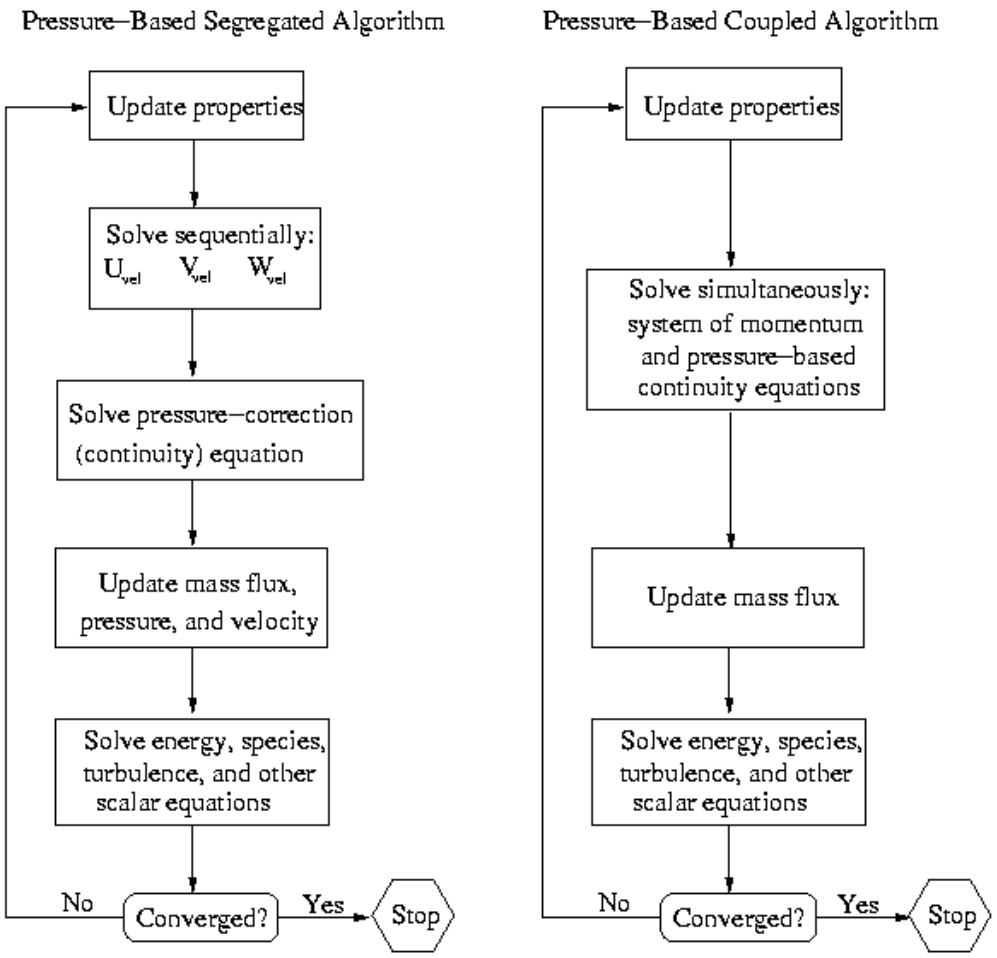

Figure 4.12 – Differences between Segregated and Coupled Solver [48]

As can be understood from figure 4.12, there are significant differences between the segregated and coupled algorithms. The segregated algorithm involves a sequential sequence where the governing equations are solved where the loop must be completed to move on to the next computational iteration until convergence is reached. Therefore, this approach is defined as being semi-implicit which could result in slower convergence. The advantage of this method is that its memory efficient and computationally less demanding due to the sequential manner in which calculations occur as each governing equation is segregated from the other. The Coupled algorithm for the pressure based solver however combine steps 2 and 3 from the segregated solver to generate a coupled system of equations for the momentum and continuity terms. The remaining equations are solved in a sequential fashion however as steps 2 and 3 are combined the resultant computational expense and memory requirement increase to double that of the segregated solver as additional

terms are required to be stored in memory (RAM). The coupled solver therefore represents a fully implicit method. The benefit of the coupled solver, if computational resources allow, is that the rate of convergence is significantly improved over the segregated algorithm.

Examples of the segregated algorithm which will be utilised in this study are SIMPLE which uses a relationship between velocity and pressure to achieve mass conservation and pressure field information and PISO which attempts to improve the computational efficiency of the SIMPLE algorithm by adding additional correction terms. Whereas the coupled solver will be used to determine if a more accurate solution or improved convergence characteristics could be achieved compared to the segregated solver. Under relaxation or implicit relaxation helps to improve stability and convergence of both the segregated and coupled solvers by using a non-dimensional factor to the discretized governing equations. The use of various values of under relaxation factors will be investigated during validation studies. For the pressure based coupled solver however, an additional under relaxation term is introduced known as the Courant number or CFL. The use of an appropriate Courant number is critical for stabilizing pressure based CFD simulations which experience high Mach number flow and significant pressure gradients.

The final numerical control which is available on ANSYS FLUENT is the spatial discretization terms available within the solution methods page. For the gradient term which discretises the convection and diffusion terms, Least Squares based is popularly used due to its proven accuracy on a variety of meshes and it's computational efficiency when compared to the node based approaches. For the pressure based solver, the second order pressure discretisation method is recommended for use for high speed compressible flow simulations as well as the QUICK scheme for all other terms such as density, momentum etc. This is due to the fact that the ANSYS user guide [56] recommends that "if you are calculating a compressible flow with shocks, the first-order upwind scheme may tend to smooth the shocks". In addition, it is

recommended that “for compressible flows with shocks, using the QUICK scheme for all variables, including density, is highly recommended for quadrilateral, hexahedral, or hybrid meshes”. The QUICK scheme will therefore be investigated during the validation process to check its performance.

For transient simulations, an implicit time integration is used which provides the advantage of unconditional stability with respect to time step size [48]. Equation 4.44 summarizes the approach which FLUENT uses to evaluate the term F(Φ) at a future time step;

$$\frac{\phi^{n+1}-\phi^{n}}{\Delta t}=F\left(\phi^{n+1}\right) \qquad \textbf{Equation 4.44}$$

CHAPTER 5

VALIDATION OF CFD PRV MODELS FOR STEADY STATE SINGLE PHASE FLOW

In order to achieve a CFD model capable of accurately capturing single phase transient flow phenomena by using transient dynamic meshing modelling, it was necessary to initially achieve a validated steady state solution. In this chapter an experimental testing procedure will be described alongside CFD modelling methodology to outline the steps required to achieve a validated CFD PRV model which could be utilised by valve manufactures to gain a greater insight towards PRV performance and flow characteristics. It is hoped that the modelling methodology outlined in this section could be widely applied by manufacturers to develop accurate CFD models for various geometries. The computational work performed in this chapter utilises Solidworks for CAD generation as well as ANSYS Workbench 17 and 18 for geometry modelling, meshing and for the industrial FLUENT CFD solver package.

Initially in this chapter, an ASME VIII certified right angled type PRV manufactured by Broady Flow Control Ltd will be validated using experimental data obtained by Taggart at the in house Broady flow testing facility [9]. The CFD work performed during this analysis will be 3D and will describe the steps required to achieve a meshing and CFD numerical modelling methodology capable of capturing flow features accurately such as mass flow rate and disc force when compared to experimental data. By achieving a validated single phase steady state model, a reference case model from which dynamic meshing can be used in chapter 6 will be established.

Following the Broady analysis in this chapter, an in-depth investigation will take place for an alternative type PRV consisting of a through flow valve

manufactured by Henry Technologies for typical use in the refrigeration industry. This study will help to extend previous 2D validation research performed at Strathclyde for a similar valve by Elmayyah [11] and Alshaikh [12] to 3D simulation. This builds upon the recommendations by both researchers to utilise a 3D computational domain as it was suggested that it could provide improved accuracy. In previous work, 3D modelling was not feasible due to practical limitations of computational equipment. Furthermore, by developing a validated 3D steady state simulation, a basis for transient dynamic mesh modelling will be achieved for the Henry valve. In addition, the development of a 3D CFD model will also allow an investigation towards identifying any differences between 2D and 3D modelling for a through flow type PRV.

By performing CFD validation work for both the Broady and Henry valves, it will be possible to test the resilience of numerical modelling methods developed for both problems. This will be able to identify if a general steady state CFD modelling procedure could be established for the vast majority of PRV geometries that are commercially available. This is of crucial importance as ASME VIII type PRV's share similar geometry, flow features and operational characteristics therefore would be expected to utilise similar modelling methods. However through flow and right angled type PRV's differ significantly, particularly due to the influence of built-up back pressure effects and to the degree of disc force coupling to local geometry thus representing a challenging comparative scenario to seek a general modelling procedure. If successful, this would represent a resilient CFD modelling solution for designers to generally adopt. The single phase validation work performed in this chapter will use air as the working gas due to experimental limitations and that air is predominantly used as a test medium in industry to provide a reference point. Therefore, by performing the single phase CFD validation analysis using air, manufacturers can similarly adopt such methods easily. Furthermore, since the overall interest in this work is the development of transient solution methods for multiphase applications, the CFD single phase analysis in this chapter will focus on using the pressure-based solver given

that ANSYS multiphase solution algorithms are restricted to pressure-based solvers only. This two-phase flow work will be described in chapter 8.

5.1 Broady 3511E PRV Validation

The purpose of this work was to extend the 2D CFD validation research by Alshaikh [12] and Elmayyah [11] from a through flow type PRV geometry to an ASME VIII certified device. In general, ANSYS Workbench 17 was used for the geometry modelling, meshing and FLUENT CFD package to perform 3D simulations. The test valve was the 3511E PRV which is developed and manufactured in house by Broady Flow Control Ltd. The 3511E PRV is a 1x2” E orifice relief valve from the 3500 series and is designed for gas service. It is typically found on unfired pressure vessels [9]. The 3511E was selected as the right angled geometry for the 3511E (shown in figure 5.1) is typical for an ASME section VIII certified PRV and is often used in safety critical industries.

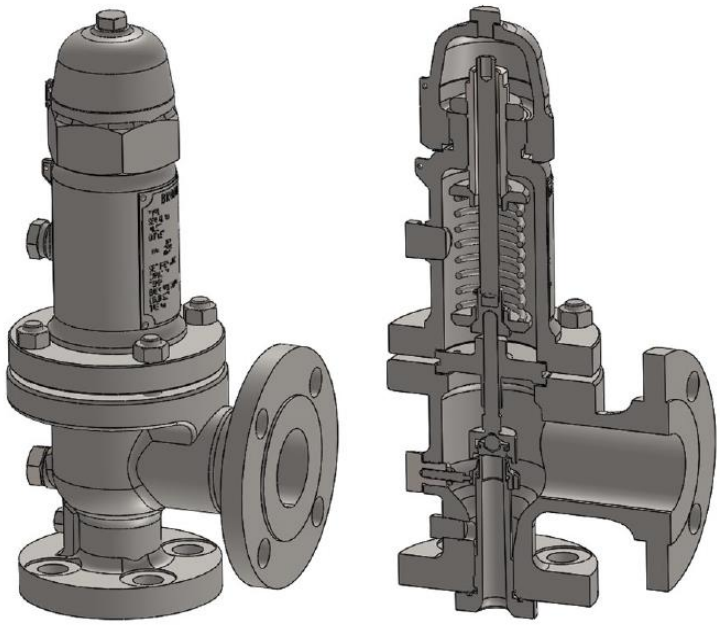

Figure 5.1 – Broady 3511E PRV Assembly from Solidworks [9]

Figure 5.2 highlights the components and flow path for the 3511E PRV. The valve consists of a flanged inlet and outlet area which can be attached to the necessary piping found in a pressurised system. There are various features shown in figure 5.2 which are consistent across every spring loaded PRV such as the disc, seat and body. However for the Broady PRV it's important to note the use of an adjustable blowdown ring. This device is used in order for manufacturers to tailor the performance of the PRV such as overpressure and blowdown values to the standard required by the customer. This is achieved by displacing the blowdown ring position (notch) using a form of adjustment such as a screw. In addition, to tailor the PRV to the desired system requirements, the set pressure adjusting screw found at the top of the spring allows the preload of the spring to be set to allow the PRV to activate when required at the system's set pressure value. The valve assembly is sealed using an external body piece with an attached flanged bonnet which houses the spring assembly.

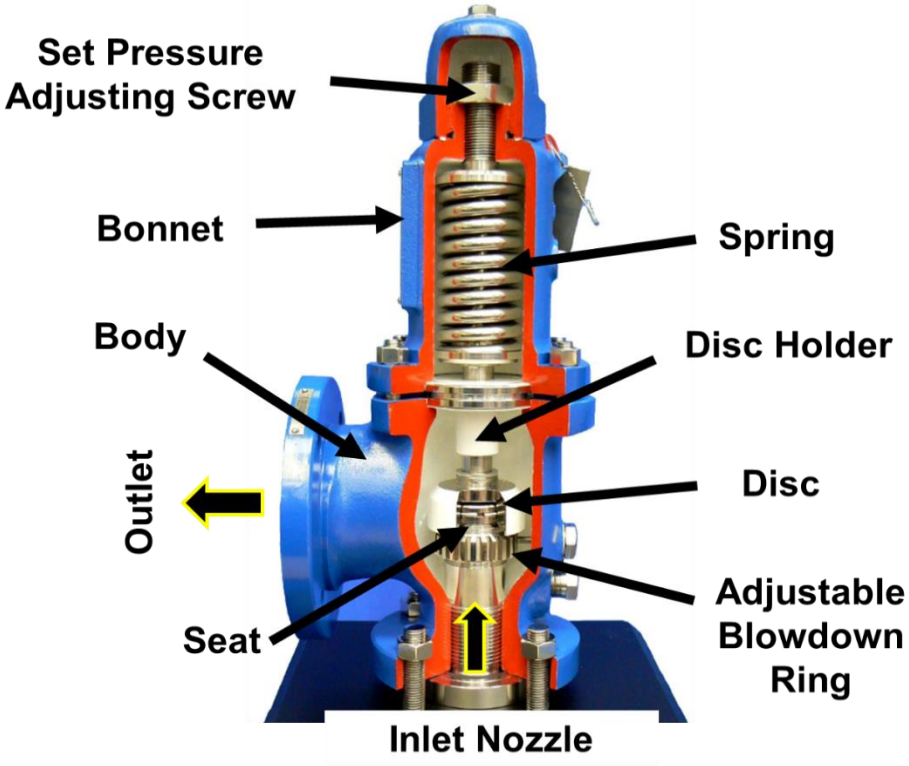

Figure 5.2 – Detailed Description of Broady 3511E PRV

Throughout the validation work for the Broady valve, the adjustable blowdown ring of the valve was set at 0.03mm above the datum seat height otherwise known as notch position 4. For validation it was required that the valve geometry was modelled at regular disc lift intervals from the seat to allow flow measurements to take place using the earlier described quasi steady assumption. This replicates the experimental procedure where flow measurement would take place at discrete values of disc lift to capture data. Experimental and CFD modelling will capture data points from 0.1mm to the valve's rated maximum rated lift of 4mm. Each data point will be subjected to an inlet pressure of 3.3 barg and will exhaust to atmosphere (0 barg) operating at typical room temperature.

By using the quasi steady principle described previously, a disc force vs lift and mass flow rate vs lift curve will be generated both experimentally and using CFD to enable easy comparison and validation. For CFD, surface monitors for force and flow rate will be measured from the simulation which is then compared to experimental values obtained by Taggart [9] at the Broady testing facility at the same pressure and temperature. Such a comparison would provide a method of validating the FLUENT model and allow future steady state and transient work to be performed with confidence.

By comparing CFD results with experimental results, it would be possible to perform investigations to improve the quality of the model and decide on the most appropriate boundary conditions, solver type and turbulence model settings. To allow future multiphase modelling of the Broady valve to take place, only models which use the pressure based solver will be developed. However the pressure based solver will be compared to the density based solver to identify the magnitude of difference in flow physics between the two approaches. It is critical however to investigate the accuracy of the pressure based solver rather than the density based solver which is recommended for use on high speed, compressible flow type problems.

In addition, during the validation study an investigation will take place to identify the most appropriate turbulence model which would provide a solution which accurately represent the flow physics within the PRV when using RANS CFD modelling. Furthermore the discretization methods and settings which would provide positive numerical stability and convergence will be determined. The turbulence models to be investigated for the Broady valve in particular were the 2 equation K-Omega SST and K-Epsilon models as well as the 4 equation Transition SST model. Furthermore, various iterations of mesh density and mesh arrangement were investigated to ensure that the required standard of mesh metrics (skewness, orthogonal quality, aspect ratio) were to be achieved with minimum computational intensity to obtain accurate results.

5.1.1 Experimental Testing for Broady PRV

As mentioned previously, for the Broady 3511E valve, experimental testing was conducted during research performed for the PhD thesis of Taggart [9] in which data was shared to allow validation of CFD models. The full details of the experimental uncertainty calculation and set up has been published by Taggart and will be summarised within this section of work. The experimental work was conducted assuming quasi steady state flow conditions to capture force vs lift and mass flow rate vs lift at a test pressure of 3.3 barg at room temperature. To do so it was necessary for a testing facility to be developed in order to provide measurement of pressure, flow rate, aerodynamic disc force across a range of lifts from closure to the fully open position (4mm).

The piping and instrumentation diagram (P&ID) for the test facility as well as a table of the measurement instrumentation which was used for experimental measurements is illustrated in figure 5.3 and table 5.1.

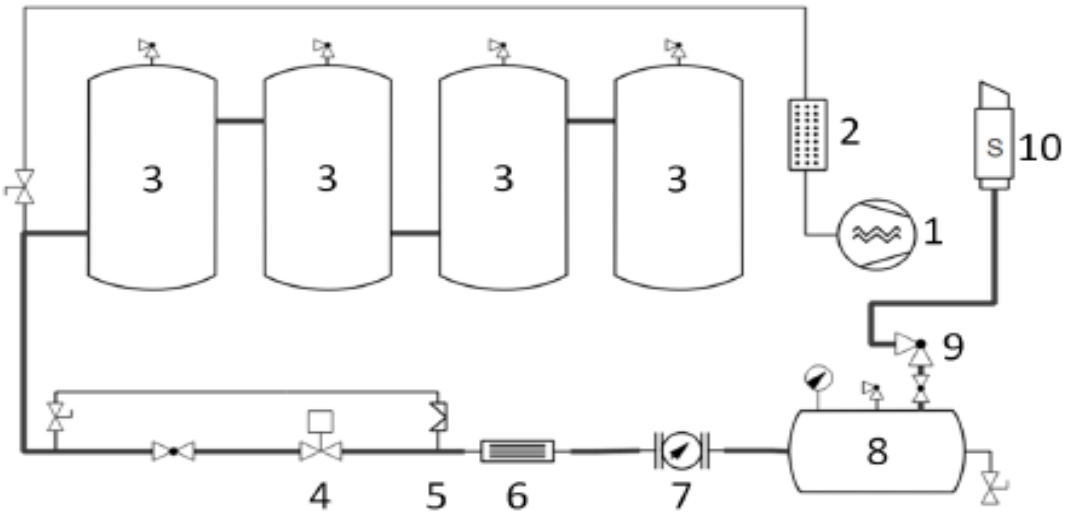

P&ID Number	Description of Corresponding Instrumentation
1	Small Feed Compressor
2	Ingersoll Rand Condensing Air Drier
3	4x Storage Vessels With Total Capacity of 10000L
4	Valvitalia Control Valve With Diaphragm Rotary Actuator
5	Broady C6 Diaphragm Valve
6	Straightening Vanes to Reduce Turbulence to Flow Meter
7	Emerson Coriolis Flow Rate Meter
8	Buffer Vessel (Max 10 Barg) with 1500L capacity
9	3511E PRV for Testing
10	Silencer

Figure 5.3 – P&ID of Broady Flow Testing Facility for 3511E PRV

Property	Transducer	Accuracy	Range
Pressure	Druck PTX 1400	0.25%	10bar
Pressure	Druck PTX	0.15%	10bar
Flow rate	Emerson Coriolis meter	0.1%	10kg/s
Disc force	Omega load cell	0.5%	200N
Displacement	LVDT	0.5%	0-10mm
Data acquisition	DT9813	0.1%	100kHz
Data acquisition	QuickDAQ	N/A	N/A

Table 5.1 – Measurement Instrumentation Required for 3511E PRV Testing

In addition to the measurement instrumentation listed in table 5.1, Taggart [9] used a dial gauge with a resolution of 10μm and a measurement accuracy of ±0.5%. This device was required to measure the displacement of the valve spindle from a datum position in order to determine the lift of the disc from the seat and allow the capture of aerodynamic force acting on the disc and mass flow rate to be recorded. It was possible for the lift of the disc to be finely adjusted by using a small pitch thread (M32x1mm) on a cross slide type device. By using a small pitch thread, play on the threads could be reduced and would allow greater control and stability of the disc position during testing. The aerodynamic force was measured using a load cell manufactured by Omega Engineering Ltd with a working range of 0-200N and a measurement accuracy of ±0.5% of range. An Emerson Coriolis flowmeter was used to measure the mass flow rate of the system with a measurement limit of 10kg/s. It was required from PTC 25 testing guidelines, as can be seen from figure 5.3, that upstream of the flowmeter there were flow conditioning vanes to allow accurate measurement. By doing so, the flowmeter was capable of achieving a repeatability of 0.02% [9] and rated to an accuracy of 0.1% of measurement. A pressure transducer was used in the buffer vessel, shown on figure 5.3 to measure the inlet pressure to the PRV with a maximum operating value of 10 Barg and a measurement accuracy of 0.25% of range. A PC connection was used for data acquisition of inlet pressure, flowrate and load cell using QuickDAQ software; an RDP transducer amplifier was also required for the load cell readings.

The measurement procedure used by Taggart was as follows;

1. The valve is set in a fully closed position with the disc in firm contact with the seat. This lift position will then be used as a datum point for where testing will occur as the PRV is gradually opened.

2. The required preload of the PRV is determined by compressing the spring (and disc) on the seat and slowly reducing the spring load until

the set point is reached. The setting process used as Broady Flow Control requires that the set point is identified as the first audible sign of leakage through the valve in which a clear hissing noise can be heard. The corresponding load and disc position is measured and referenced to as a datum position. Taggart [9] states that at the set point for the Broady 3511E valve and for a clear audible indication of air passing through the PRV, the disc and nozzle sealing faces are still in contact. Leakage is therefore occurring due to the roughness of the metallic sealing surfaces to provide small flow passages for air to escape which would otherwise be sealed due to the elastic deformation of the metal as a result of compressive forces. Such forces are relaxed as the degree of spring compression is reduced.

3. Once the set point is clearly defined as the datum point it is taken as 0 mm lift and the disc is gradually moved to pre described data capture points across the full lift range (0-4 mm lift). At each data point the displacement is recorded alongside the corresponding flow rate and force measurement. It is critical that the buffer vessel pressure is maintained at a constant value of 3.3 Barg to allow a constant inlet pressure to be achieved.

4. Following data collection, an aerodynamic force acting on the disc and flowrate vs lift relationship can be established to provide an insight towards the performance of the valve and allow validation of CFD.

Furthermore as can be seen in table 5.1, a linear variable differential transformer (LVDT) was available for use. The device operates using electromechanical principles where the linear motion of an object which is connected to the device is translated into an electrical signal for data capture using suitable data acquisition software. This device was necessary to measure the displacement of the disc for dynamic testing and when coupled with pressure measurement allowed the determination of overpressure and

blowdown. The validation process for this form of data capture alongside transient dynamic mesh CFD will be described in chapter 6.

Taggart [9] also conducted an investigation into the statistical errors and systematic errors which were present during his experimental study. The statistical error was reduced by Taggart conducting numerous tests in order to remove any random inaccuracies and obtain a Gaussian distribution for error analysis. He found that it was possible to establish an overall measurement uncertainty of 1.22%. This value was deemed acceptable for use during the validation of CFD models. Full details of the uncertainty calculation performed by Taggart can be found within his thesis [9].

Experimental data was captured by Taggart for the 3511E Broady PRV using a blowdown ring positioned at notch 4 at a constant inlet pressure of 3.3 barg [9]. The results from these measurements for both flow force and mass flow rate against lift are shown in figures 5.4 and 5.5. The measurement error for disc force data capture which was determined by Taggart is shown in the error bars in figure 5.4. It was deemed acceptable to select a single pressure and notch position for the Broady PRV due to computational time and to allow the method to be tested for alternative PRV's to allow the method to be validated in a universal manner.

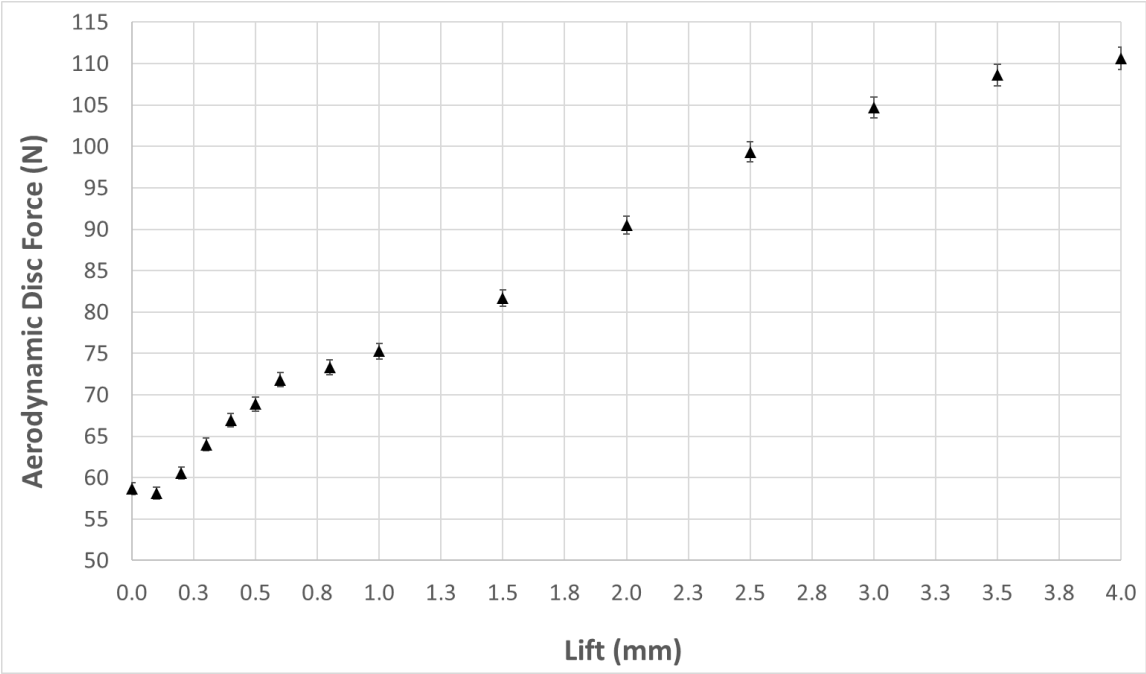

Figure 5.4 – Experimental Results of Aerodynamic Disc Force vs Lift for the 3511E PRV (4 Notches) at 3.3 barg with measurement error bars

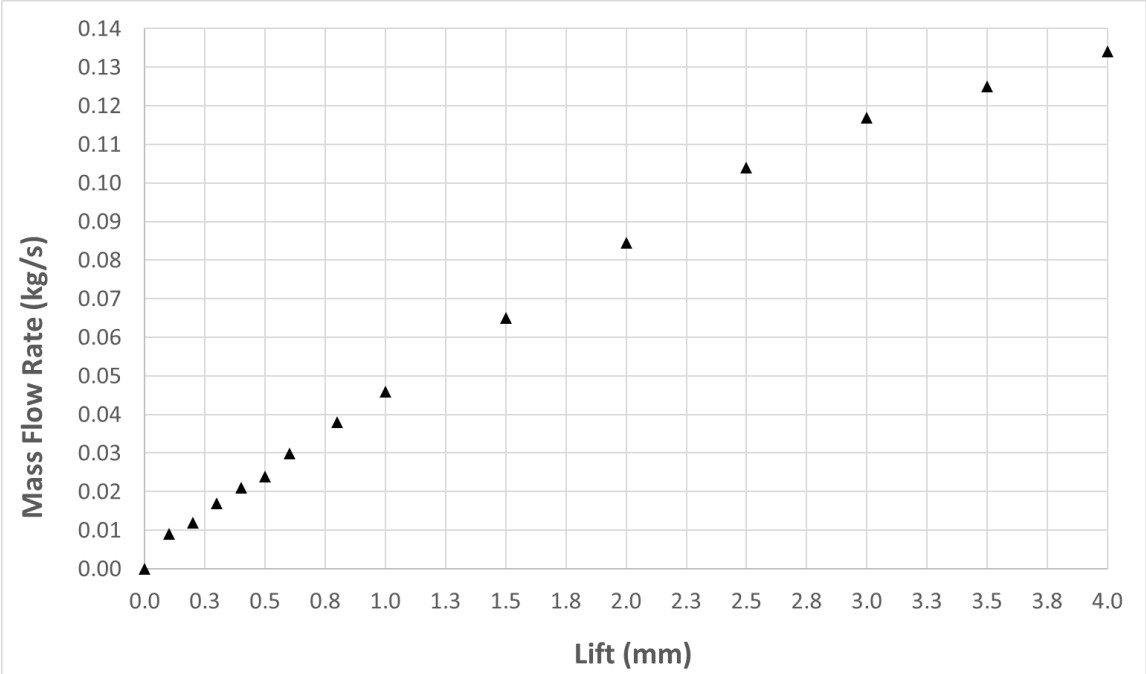

Figure 5.5 - Experimental Results of Mass Flow Rate vs Lift for the 3511E PRV (4 Notches) at 3.3 barg

5.1.2 Development of CFD Model for Broady PRV

To achieve an appropriate level of control over mesh refinement and reduce unnecessary computational expense within the CFD model it was important to split the PRV domain in to seven sub regions as can be seen in figure 5.6. This was achieved by using the slice and Boolean commands through a series of extrusions and projections within the ANSYS geometry modeller package. This was necessary as it was deemed important to capture the severe flow gradients expected in the flow area between the disc and seat therefore a dense mesh would be required. This is due to the series of expansions and redirection of the bulk flow through this region which would cause such complex flow characteristics. However on the other hand, a coarse mesh could be used at the outlet and lower section of the body bowl of the valve as flow gradients within those regions would be less severe due to a much simpler flow path. In addition, it was important to generate a mesh of sufficient density at the inlet nozzle to capture any high speed compressible flow effects, especially at higher lifts, and above the disc to capture back pressure if required which would become more apparent at higher inlet pressures. Through a series of iterations, the geometry shown within figure 5.6 was found to provide a suitable base for meshing to take place.

To further reduce computational expense, a 180 degree slice of the valve assembly was performed in preparation for using symmetry boundary conditions. It was determined that due to 3D effects of the flow interacting with the valve body bowl producing a non-uniform outlet flow, that half symmetry would be required instead of assuming axis-symmetry of the assembly to allow an accurate representation of the flow to be achieved.

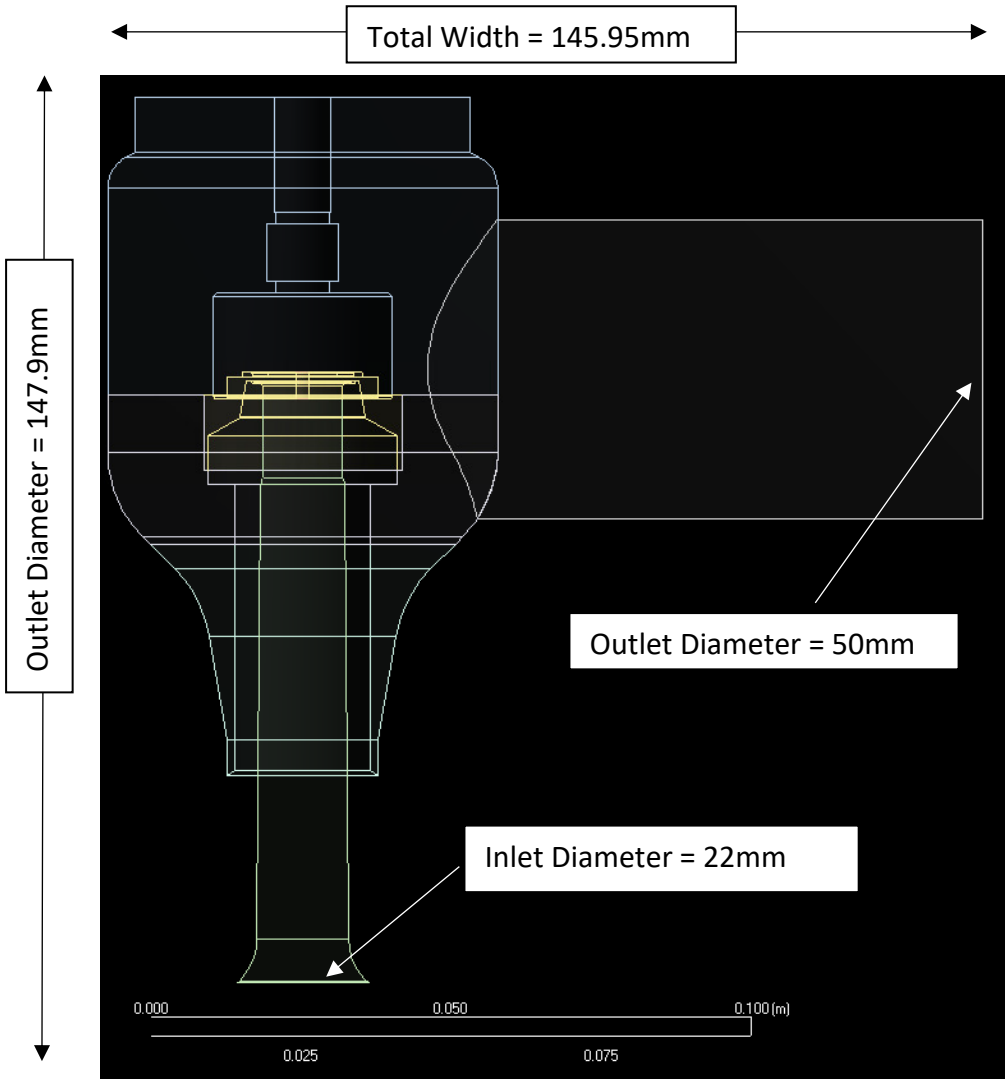

Figure 5.6 – 3511E FLUENT geometry model (zonal meshing)

Development of CFD Mesh for Broady PRV

Once the domain was split up into sub sections, it was then possible to mesh each sub section to the appropriate level of discretization. As mentioned previously, it was necessary to achieve a fine mesh at the disc/seat interface as flow gradients were expected to be high in this region due to the sharp changes in geometry; especially at lower lifts. In addition, due to the use of the Transition SST model which requires a y^+ value of approximately 1 [48, 51] to capture the boundary layer profile accurately, inflation was used from the

nozzle wall to the outer wall of the disc and blowdown ring. This would allow the separation points of the flow within the disc/seat area to be predicted more accurately which would affect the prediction of mass flow rate and flow characteristics across the valve. The method used for inflation was the First Layer Height method which required a calculation to be performed using equation 5.1;

$$y^+ = \frac{U_\tau y_0}{\upsilon}$$

Equation 5.1

From equation 5.1 it was found that using a first layer cell height of 1 µm would be sufficient across the full lift range to achieve the recommended y^+ value of approximately 1 when using the Transition SST turbulence model. This value was achieved using postprocessing available within fluent to calculate y^+ whereby cell height was adjusted by trial and error accordingly. Figure 5.7 illustrates the use of inflation at the seat area of the valve.

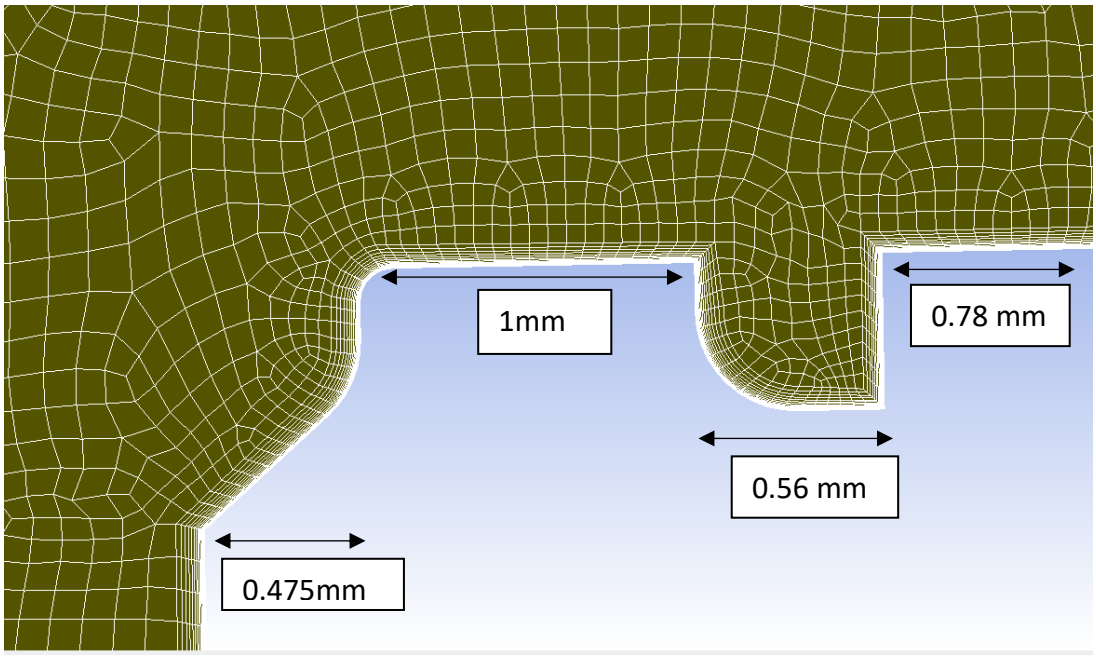

Figure 5.7 – Enlarged image of inflation across seat face

To achieve the desired level of discretization across the full domain and meet the recommended mesh metrics standard for the mesh [52], each domain was meshed using the patch independent MultiZone method. This method was suitable to use as it was required to automatically decompose the domain in preparation for generating a swept mesh within the structured regions of the domain. At this point the sweep element size was set to between 0.5 mm-0.75 mm in order to capture any circumferential 3D effects across the valve and reduce numerical diffusion/error. Once the meshing method was specified it was necessary to apply mesh sizing controls such as edge and body sizing. Figures 5.8 and 5.9 highlight the use of edge and body sizing to achieve a structured mesh with refinement achieved within the areas of interest such as the disc/seat interface and blowdown ring regions. It is likely that due to such sharp changes in flow direction and expanding to atmospheric pressure at the valve exit, expansion fans and shocks would be present which would require to be captured accurately to predict the force acting on the valve and mass flow rate. Figures 5.8 and 5.9 also highlight the critical surfaces of the 3511E PRV including the disc/seat interface and upper disc area.

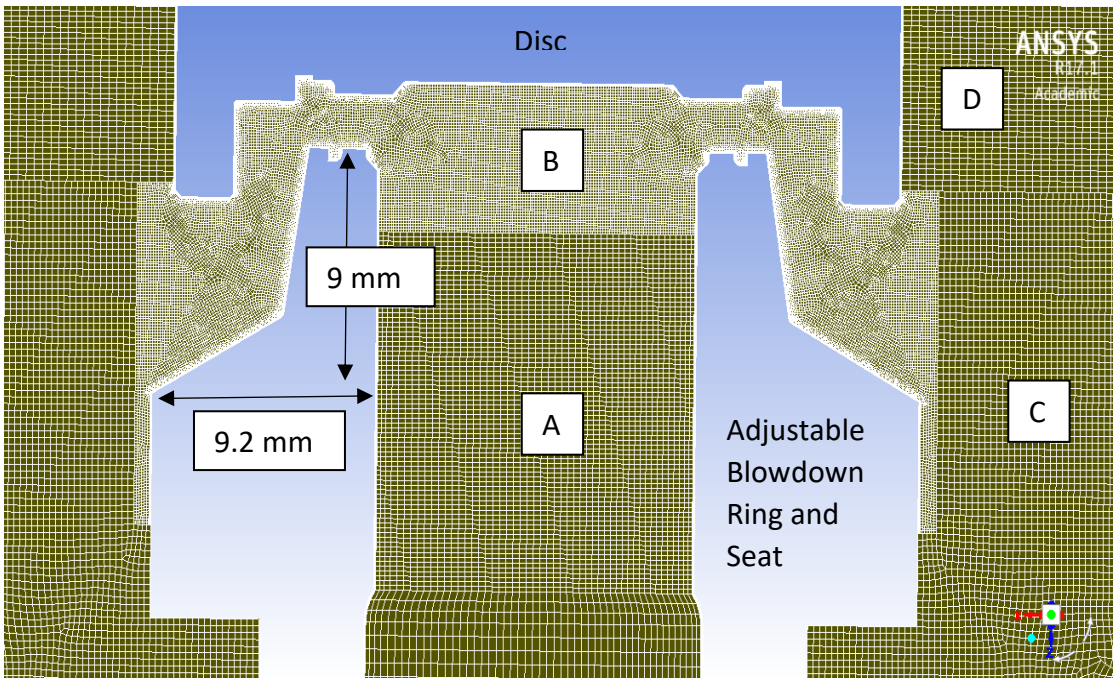

Figure 5.8 – Mesh structure at nozzle and disc/seat interface

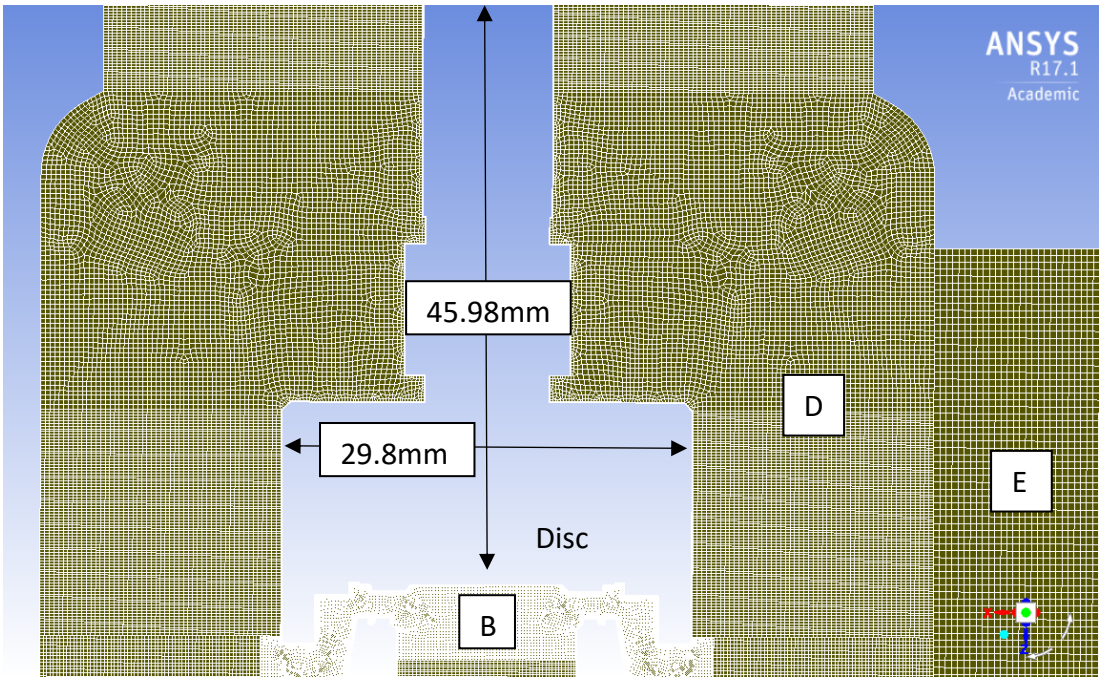

Figure 5.9 – Mesh Structure above disc and outlet

Figures 5.8 and 5.9 also illustrate that there are mesh regions across the domain with varying mesh density. This was necessary to reduce the computational expense of the mesh to decrease convergence time and memory requirements. However in order to determine the necessary balance between computational time and good correlation with experimental values, a mesh dependency study was performed by varying body sizing in particular at the near disc/seat region. Furthermore, as mentioned previously, it was important for the mesh to meet the required mesh metrics standards to help minimise any numerical errors [52, 56]. Table 5.2 highlights the average mesh metrics of the mesh across the lift range where figure 5.10 also demonstrates the structured nature of the mesh at the disk/seat interface which was achieved through the use of the aforementioned domain discretization and edge sizing. Figure 5.10 also shows the 16 layer inflation method used with 1.2 growth rate at an initial first cell height of 1µm across the walls of interest within the valve.

Mesh Zone and Description	**Mesh Independent Element Size**
Zone A –Region	500 Microns
Zone B –Region	75 Microns
Zone C –Region	250 Microns
Zone D –Region	350 Microns
Zone E –Region	500 Microns

Mesh Metric	**Value**
Average Orthogonal Quality	0.96
Average Aspect Ratio	29.5
Average Skewness	0.11
Total Number of Elements	9163858 Elements

Table 5.2 – Mesh independent element size and corresponding mesh metrics

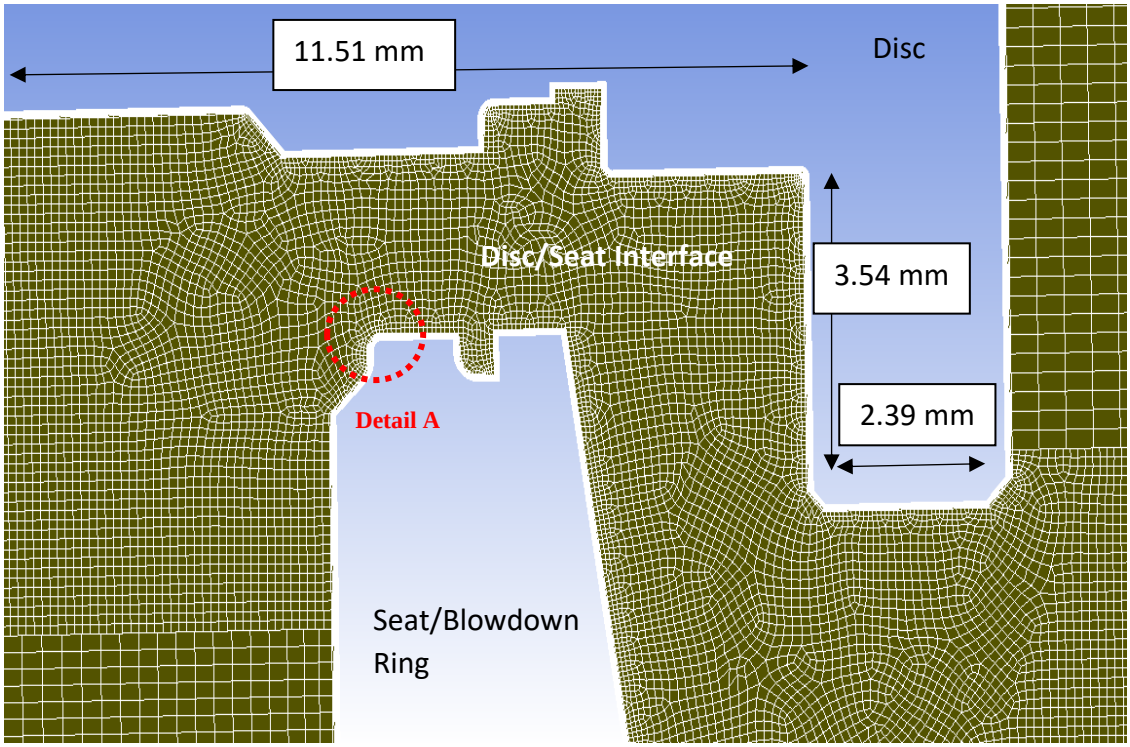

Figure 5.10 – Structure of mesh near the disc and detail of seat edge

Detail A within figure 5.10 highlights the inlet edge at the valve seat which has been highlighted as a geometrical feature which could significantly affect the mass flow rate and disc force correlation, due to flow separation effects. Initially the CAD model provided by Broady had no rounding at this edge which in reality is not the case as the part is required to be machined to a slight round. Therefore for comparison, a mesh was generated for both a sharp edge scenario and when the edge is rounded with a 0.1mm radius blend. During the meshing stage it was also required to establish named selections for the necessary boundary conditions to be applied within the FLUENT setup stage. As mentioned previously, due to the 3-D nature of the flow interacting with the bowl of the valve, half symmetry was used, as shown within figure 5.11; this arrangement would reduce the computational demands by 50% when compared to the full model and therefore shorten run times. Furthermore, it was necessary to highlight the disc area required by the FLUENT post processor to calculate the net force acting on the disc and establish a surface monitor to ensure convergence of the pressure values acting on the disc surfaces. The faces selected for surface monitoring are shown in figure 5.12.

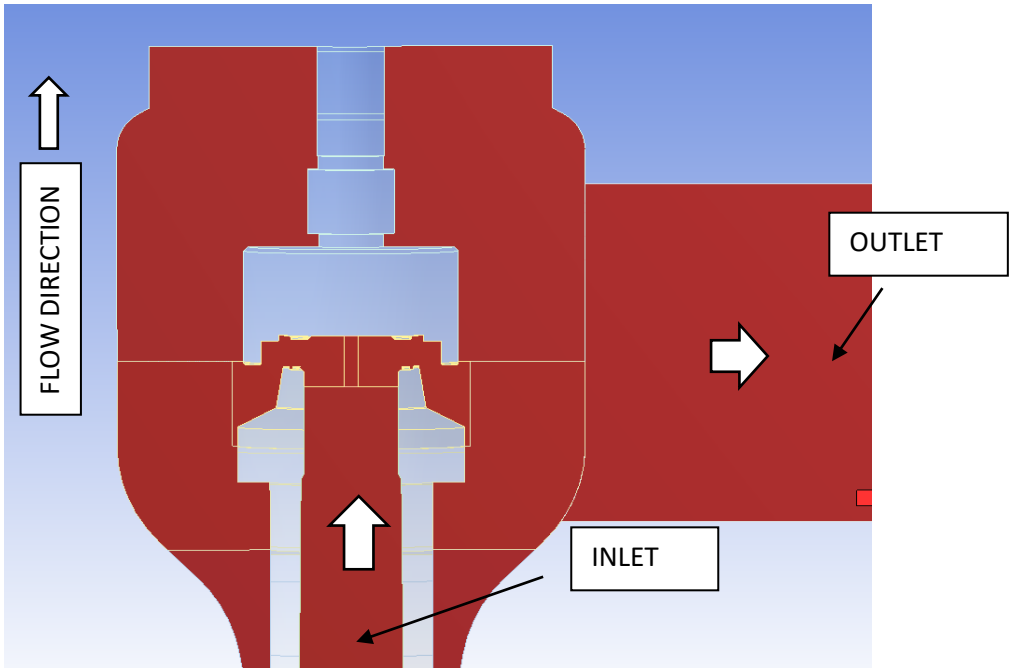

Figure 5.11 – Regions of symmetry and indication of flow direction

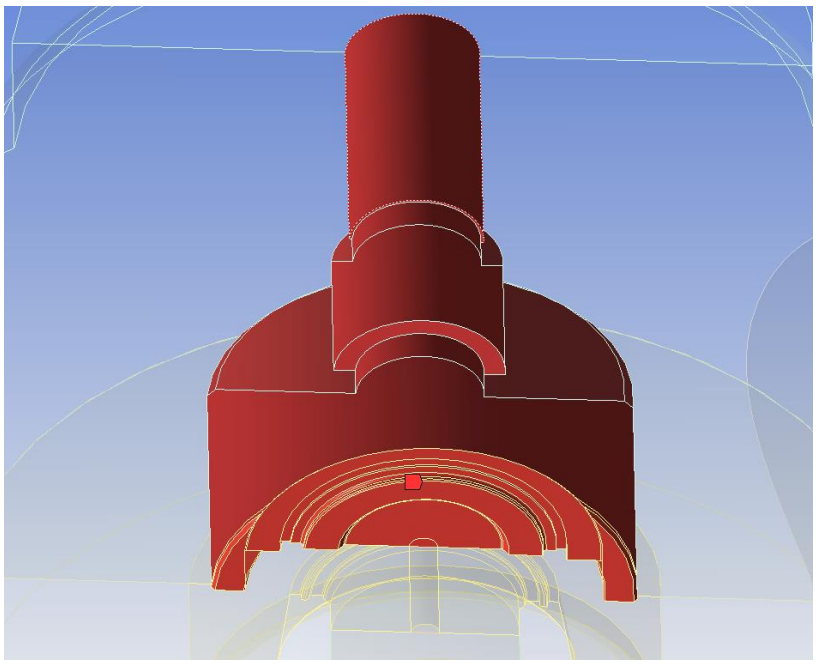

Figure 5.12 – Disc named selection surfaces (red)

CFD Numerical Procedure for Broady PRV

To model flow through the valve, the steady state form of the compressible RANS equations were used alongside the energy equation and air was assumed to be an ideal gas. Pressure boundary conditions were set at the inlet and outlet to drive flow across the valve from the pressurised inlet to the atmospheric exhaust at the outlet. For investigation, both the pressure based and density based solvers were utilised. This investigation was important to ensure that there were no significant differences in the results produced by both solvers. This would therefore allow future work involving multiphase flow as only the pressure based solver is available for use for such flow conditions. The pressure based solver is also suitable for the valve model as it represents an internal, pressure driven flow.

It was also important to investigate the most appropriate turbulence model to be used which would accurately capture the flow physics across the valve and achieve close correlation (acceptable within 5% or better) of the experimental data across the full lift range. For this investigation, the two equation K-Epsilon and K-Omega SST models were used as well as the 4 equation Transition SST turbulence model. A sensitivity study was performed using the turbulence models to determine the most suitable as well as with varying mesh qualities.

For all lift conditions, the boundary conditions applied were as follows;

- Gauge Total Pressure Inlet of 3.3 barg – which represented vessel pressure, with the zone positioned at the inlet face (figure 5.11).
- Gauge Total Pressure Outlet of 0 barg – which represented atmospheric exhaust, positioned at the outlet face of the valve (figure 5.11).
- Temperature at both inlet and outlet to represent experimental conditions – 295K or 22 ^{0}C
- No slip shear condition on stationary, adiabatic valve walls
- Half symmetry boundary condition applied (red faces on figure 5.11)
- Operating Conditions – 1 bar (to offset pressure bc's to gauge)

By applying the boundary conditions specified above it was possible to achieve an expected representation of the flow physics across the valve. It was also important to establish the solution methods required to achieve a stable yet accurate simulation. For all simulations, high order term under relaxation was used to provide stability during the initial stages of the simulation, especially when using higher order spatial discretisation terms which could lead to unphysical results, and to prevent divergence [56]. It was also important to

follow recommended CFD guidelines and initialise the solution with first order upwind spatial discretisation terms before switching to a higher order scheme after 100-200 iterations. This is effective in preventing convergence stalling through unrealistic flow physics due to poor initialisation; FLUENT's hybrid initialisation scheme was used for all cases.

For pressure velocity coupling; the SIMPLE, PISO and Coupled schemes were compared and investigated to determine the most computationally efficient and stable method to achieve accurate convergence. It was found that the Coupled scheme was more stable when compared with SIMPLE and PISO schemes as the residuals were non oscillatory (as observed with others) and achieved full convergence quickly in comparison.

For spatial discretisation; the least squares cell based method was used to capture the gradients as recommended from the FLUENT user guide for use on polyhedral meshes to achieve an accurate flow solution. For pressure discretisation, the standard, second order and PRESTO! methods were compared where it was found that the second order pressure method was the most stable and accurate option. For all other spatial discretisation terms, second order upwind and QUICK were compared where QUICK was finally selected as recommended by the FLUENT user guide for use on high speed compressible flows with strong shocks.

Furthermore, to achieve a stable start up and ensure convergence; the default FLUENT solution controls were altered. The Courant number which provides the primary control over the time stepping scheme used within the implicit coupled solver was changed from the default value of 200 to 10. This was found to provide stability across the full lift range for various inlet pressures so is recommended to adopt for future work. In addition the explicit relaxation

factors for momentum and pressure as well as the density and energy under relaxation factors were reduced to 0.25.

The final validated numerical procedure is shown within table 5.3;

Solver Type	**Pressure Based**
Turbulence Model	**Transition SST (4 equation)**
Air Density	**Ideal Gas (Energy equation On)**
Pressure-Velocity Coupling Scheme	**Coupled**
Spatial Discretisation - Gradient	**Least Squares Cell Based Scheme**
Spatial Discretisation (Pressure)	**Second Order Scheme**
Spatial Discretisation (Other Terms)	**QUICK Scheme**
Initial Flow Courant Number	**10**
Momentum, Pressure, Density and Energy URF's	**0.25**

Table 5.3 – Final solver settings for use across full lift range

The numerical stability and degree of convergence of the residuals at a snapshot of time during the calculation procedure using the validated numerical settings for the simulation is shown within figure 5.13. It should be noted that the residuals required for the simulation to be classified as converged required to be either below 10e-6 for the energy equation and 1e-3 for all other terms or exhibit residual stability. To achieve a fully converged solution it was also required to create surface monitors for disc force as well as mass flow rate at the PRV inlet in which constant values of each variable was needed.

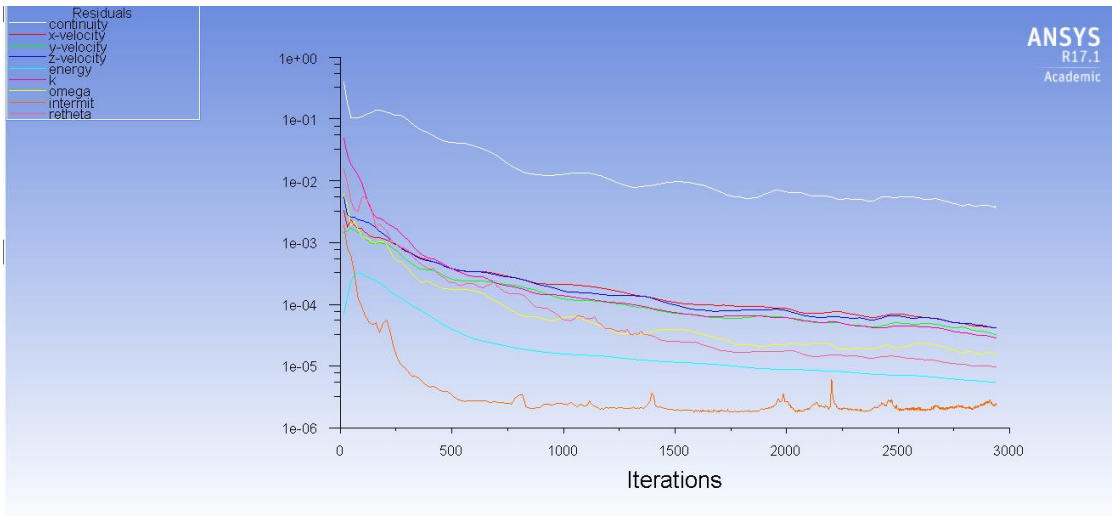

Figure 5.13 – Residuals after 3000 iterations using final solver settings

To ensure that the most suitable model was achieved within table 3, it was necessary to perform an investigation to determine the turbulence model, solver type and numerical schemes which would achieve closest correlation of CFD results with experimental data. In addition it was necessary to determine the most appropriate model settings which would be numerically stable and consistent across the full lift range; which would be challenging due to variation in flow structure and geometry across the range (0mm-4mm lift).

In addition, mesh density was investigated to determine the importance of a mesh independent solution within safety valve CFD modelling. As discussed previously, a dense mesh was selected as the most appropriate mesh density to capture the flow properties across the disc/seat interface due to the dramatic change in flow path. The downside of such a dense mesh however was the increase in computational demands in terms of memory usage and convergence time. This was improved through the use of domain splitting to achieve variable mesh density across the valve to maintain a dense mesh in areas of interest but coarser in areas which do not have an effect on the measured parameters/flow structure.

Geometrical effects were also considered, as the effect of rounding of the seat inlet edge indicated as detail A on figure 5.10 was investigated. Both cases where the edge was rounded with a blend radius of 0.1mm and where the edge wasn't rounded were analysed, where from tables 5.3-5.8 it was clear that there was a significant effect on both mass flow and disc force predictions. This therefore indicated the sensitivity of the inlet edge dimension on flow characteristics.

Table 5.4 illustrates the results of a comparison of mesh density, turbulence model and rounding of the inlet seat edge at 2 mm disc lift. It was found that the use of the round edge significantly improved the correlation of CFD mass flow rate prediction with experimental results. However there was a detrimental effect for force on disc prediction when using the round edge. This indicated the importance of capturing the seat geometry accurately as a small change caused a 2-3% change in force and mass flowrate values. From table 5.4 it was clear that when using a rounded inlet edge, a medium/dense mesh using either Transition SST or K-Omega SST turbulence models performed best. It could also be determined that for 2mm lift, the K-Epsilon turbulence model was not suitable as it was significantly less accurate in comparing disc force when compared to both the Transition SST and K-Omega SST models. In the following tables the mesh values defined as coarse, medium and fine/dense for the disc/seat interface area is as follows;

- Coarse – Element size within Disc Seat Interface = 300 Microns
- Medium - Element size within Disc Seat Interface = 150 Microns
- Fine/Dense - Element size within Disc Seat Interface = 75 Microns

	Mass flow rate (kg/s)	% Difference from experiment	Force on Disc (N)	% Difference from experiment
No round – Dense Mesh – Transition SST	0.0802	-5.35%	88.56	-2.17%
No round – Medium Mesh – Transition SST	0.08	-5.50%	88.21	-2.57%
No round – Coarse Mesh - Transition SST	0.0798	-5.89%	90.25	-0.26%
No round – Medium Mesh - K-Epsilon	0.0796	-6.16%	81.49	-11.03%
Round – Medium Mesh – Transition SST	0.0824	-2.56%	87.27	-3.67%
Round – Dense Mesh - Transition SST	0.0824	-2.60%	86.20	-4.96%
Round – Dense Mesh - K-Omega SST	0.0825	-2.48%	86.66	-4.41%

Table 5.4 – Mesh and Inlet Edge Investigation at 2 mm disc lift

Table 5.5 illustrates a similar study to table 5.4, however at the valve's maximum rated lift of 4 mm. It was obvious that the rounding at the seat inlet edge for the 4mm lift case, provided a substantial improvement in correlation for both mass flow rate and disc force. As the dense mesh along with the Transition SST turbulence model was capable of predicting both to within approximately 0.5% of the experimental values. Similarly to the 2 mm case, the K-Epsilon model wasn't suitable for use as it was substantially less accurate than the K-Omega SST and Transition SST models. Furthermore it was clear that mesh density was important in determining the correct mass flow rate at high lift but less so for predicting disc force.

	Mass flow rate (kg/s)	% Difference from experiment	Force on Disc (N)	% Difference from experiment
Round – Dense Mesh - Transition SST	0.1346	0.47%	110.00	-0.54%
Round – Dense Mesh - K-Omega SST	0.1304	-2.79%	112.35	1.57%
Round – Medium Mesh – Transition SST	0.1304	-2.76%	109.95	-0.58%
No round – Medium Mesh - Transition SST	0.1360	1.47%	108.78	-1.66%
No round – Medium Mesh - K-Epsilon	0.1298	-3.28%	101.38	-9.08%

Table 5.5 – Investigation at 4 mm disc lift

The results shown within table 5.6 represented the worst results across the full lift range in terms of both mass flow rate and disc force correlation. It was evident that the addition of a rounded seat inlet edge, as before, improves mass flow correlation and significantly changes the disc force value. It was found that the dense mesh using Transition SST provided the best possible correlation. The reason for such poor correlation is likely due to the fact that at lifts around 1mm, the flow chokes in the region between the disc and seat; therefore it's crucial to capture the geometry accurately in this region with the round edge dimensions now being nearly 10% of the lift. Furthermore, the trend of the K-Epsilon model being unsuitable for use is further shown within table 5.6. In addition, assurance for the accuracy of the flow rate measurement using the Coriolis flow meter which is a 80 mm diameter device at the low flow conditions is not provided in the work by Taggart [9] for lifts lower than 1 mm which could also result in poor correlation.

	Mass flow rate (kg/s)	% Difference from experiment	Force on Disc (N)	% Difference from experiment
Round – Dense Mesh – Transition SST	0.0419	-9.69%	78.38	3.97%
Round - Medium Mesh – Transition SST	0.0418	-9.92%	78.30	3.87%
No round – Medium Mesh - Transition SST	0.0396	-16.16%	74.48	-1.06%
No round – Medium Mesh - K-Epsilon	0.0398	-15.71%	70.83	-6.26%

Table 5.6 – Investigation at 1 mm disc lift

At 0.1 mm disc lift above the seat, as shown in table 5.7, mass flow rate correlation is very poor however the use of the round edge, dense mesh and Transition SST turbulence model is capable of predicting disc force to within 0.5%. Note that the edge radius is now of the same order as the lift and any uncertainty will have a major influence on the results. Interestingly, the K-Epsilon model is more suitable for use at low lift which is likely due to the change in flow physics and pressure gradients. Table 5.7 further highlights the need to accurately capture the disc/seat geometry as a radius of 0.1 mm was capable of producing a 30% change in mass flowrate prediction but less significant in affecting the disc force.

	Mass flow rate (kg/s)	% Difference from experiment	Force on Disc (N)	% Difference from experiment
Round – Dense Mesh – Transition SST	0.0043	-108.53%	57.86	-0.43%
Round - Medium Mesh - Transition SST	0.0043	-107.92%	59.64	2.58%
No round – Medium Mesh - Transition SST	0.0038	-139.36%	56.31	-3.19%
No round – Medium Mesh - K-Epsilon	0.0038	-136.84%	56.31	-3.19%

Table 5.7 – Investigation at 0.1 mm disc lift

Table 5.8 shows the results of the solver type study where both pressure and density based solvers were analysed for both seat inlet geometry using the medium density mesh at 1 mm disc lift. It's clear that the density based model was more accurate than the pressure based model when predicting disc force and also for mass flow rate with the rounded edge case. However the convergence time using the density based model was significantly longer and less stable than the pressure based solver. Therefore the correlation between the two models was close enough to allow the pressure based solver to be deemed acceptable to use. This is crucial for future work involving multiphase flow.

	Mass flow rate (kg/s)	% Difference from experiment	Force on Disc (N)	% Difference from experiment
No round – Pressure based	0.039594	-16.18%	75.88	0.81%
No round – Density based	0.0355588	-29.36%	75.42	0.20%
Round – Pressure based	0.0419182	-9.74%	78.21	3.75%
Round – Density based	0.0432862	-6.27%	77.39	2.73%

Table 5.8 – Investigation at 1 mm disc lift using transition SST/medium mesh

The results shown within table 5.9 represent a study of solver type and numerical schemes in an attempt to improve correlation of mass flow rate and disc force at 2 mm lift as well as to determine the most appropriate solver settings to use across the full lift range. It was found that the pressure based solver using the coupled pressure-velocity coupling scheme was the most accurate and stable option when compared to the SIMPLE scheme. It was also clear that using the coupled scheme with QUICK achieved similar results to the density based solver, further highlighting its relevance for use in modelling PRV's.

	Mass flow rate (kg/s)	% Difference from experiment	Force on Disc (N)	% Difference from experiment
No round – Pressure based SIMPLE with 2nd Order	0.08	-5.46%	87.86	-2.98%
No round – Density based	0.079	-6.92%	89.41	-1.19%
No round – Pressure based - SIMPLE with PRESTO	0.08	-5.46%	87.91	-2.92%
No round – Pressure based - Coupled	0.08	-5.49%	88.00	-2.82%
No round – Pressure based - Coupled with QUICK	0.08	-5.50%	88.21	-2.57%
Round - Pressure based - Coupled with QUICK	0.082	-2.56%	87.27	-3.67%
Round – Density based	0.082	-2.43%	88.51	-2.23%

Table 5.9 – Investigation at 2 mm disc lift using transition SST/medium mesh

5.1.3 Validated Results

Once the most appropriate solver, turbulence model and mesh settings as summarised within sections 4 and 5 were applied for the 3511E valve at an inlet pressure of 3.3 barg. A steady state analysis at 15 data points between 0-4 mm disc lift was performed where the results are shown in table 5.10. Force-lift curve and mass flow-lift curves were also produced as can be seen in figures 5.14 and 5.15 where the CFD results generated by the new model was compared to experimental values.

From table 5.10, it was clear that the disc force was captured accurately across the full lift range with an average error of 0.83% when compared to

experimental data. This was significantly below the general cut off of 4%, highlighting the ability of the model to predict the disc force reliably hence validating the model. Mass flow rate correlation was similarly accurately predicted with an average error of 1.6% for cases where disc lift was greater than 1.5mm. This is due to the inaccuracy of the disc/seat interface geometry, and in particular the seat inlet edge.

Figure's 5.14 and 5.15 highlight the quality of the correlation between the CFD model and experimental data and also shows the improvement of the CFD model by altering mesh density/quality/structure and solver settings. Further improvement however could be made in the 0.8 mm-2 mm range as the quality of disc force correlation deteriorates. This could be due to inaccuracy of the representation of the disc/seat geometry in CFD or measurement equipment.

In addition, from figures 5.14 and 5.15 it is possible to appreciate a significant difference in performance of the CFD model when using a rounded edge at the seat geometry compared to a sharp edge. It's clear that at lower lift values, the round edge geometry is more accurate than the sharp edge model when compared to the experimental data. However between 0.8 mm-2.5 mm there is a transition phase in which the sharp edge model provides better correlation with experimental data. This is likely due to the fact that the geometry is not perfectly captured in CFD as well as limitations with the RANS solver and turbulence models. At higher lifts greater than 2.5mm the round edge model provides best performance. Therefore the round edge CFD model is most appropriate. It should also be noted that as disc lift increases, mass flow rate subsequently increases due the movement of the choking point in the outlet direction. This is controlled by geometry of the disc and seat where it can be seen that at approximately 3 mm lift, the value of mass flow rate plateaus due to the choking point being fixed and no longer able to move.

Lift (mm)	Mass flow rate Experiment (kg/s)	Mass flow rate CFD (kg/s)	Percentage difference (%)	Force Experiment (N)	Force CFD (N)	Percentage difference (%)
0.00	0.0000	0.0000	0	58.70	58.7	0.00
0.10	0.0090	0.0043	-108.5	58.11	57.9	-0.4
0.20	0.0120	0.0087	-37.5	60.56	60.5	-0.1
0.30	0.0170	0.0130	-31.2	63.99	65.3	2
0.40	0.0210	0.0171	-22.7	66.94	67.5	0.8
0.50	0.0240	0.0212	-13.2	68.90	69.7	1.2
0.60	0.0299	0.0254	-17.7	71.84	72.6	1.1
0.80	0.0380	0.0337	-12.9	73.31	76.6	4.3
1.00	0.0460	0.0418	-9.9	75.28	78.3	3.9
1.50	0.0650	0.0624	-4.2	81.65	83.3	1.9
2.00	0.0845	0.0824	-2.6	90.48	87.3	-3.7
2.50	0.1040	0.1020	-2	99.31	99.8	0.5
3.00	0.1170	0.1170	0	104.71	105.4	0.7
3.50	0.1250	0.1234	-1.3	108.63	109.7	1
4.00	0.1340	0.1346	0.5	110.59	110	-0.6
			Average from 1.5mm lift = -1.6%			**Average = 0.8%**

Table 5.10 – Validated Results using Final Mesh and Solver Settings at 3.3 barg inlet pressure (notch position 4)

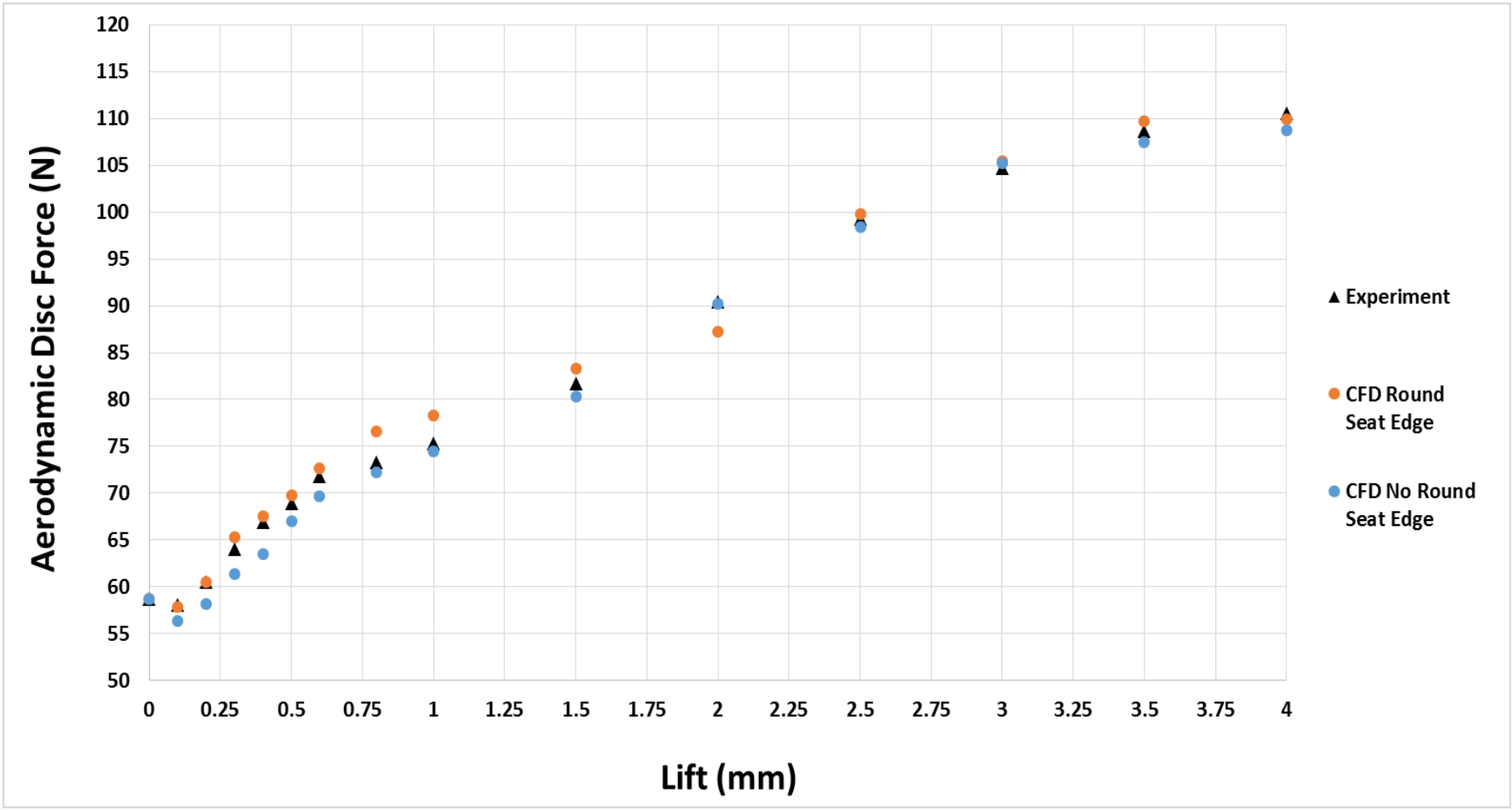

Figure 5.14 – Force-Lift Curve at 3.3 barg Inlet Pressure using final solver and mesh settings (notch position 4)

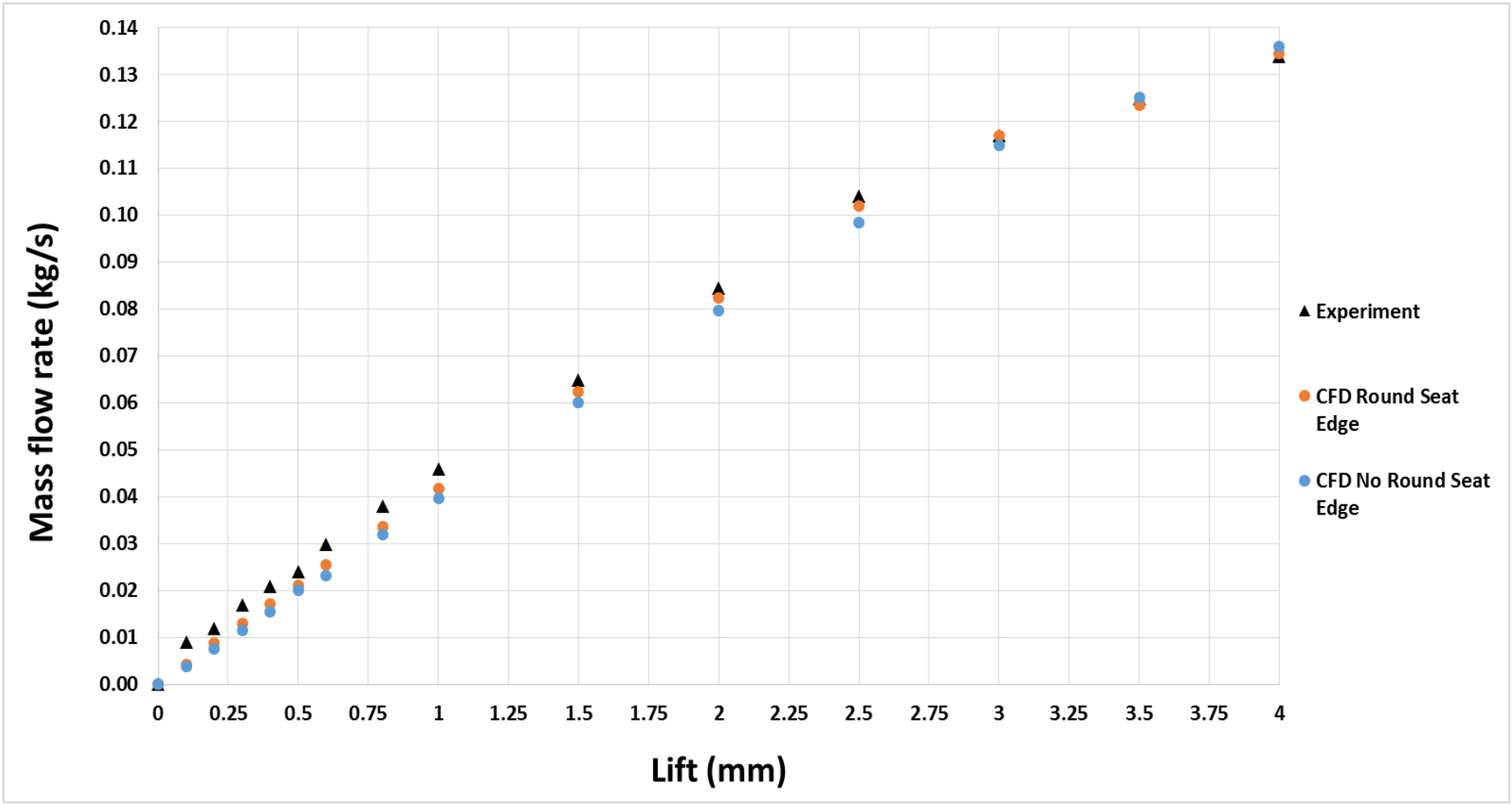

Figure 5.15 – Mass flowrate-Lift Curve at 3.3 Barg Inlet Pressure using final solver and mesh setting (notch position 4)

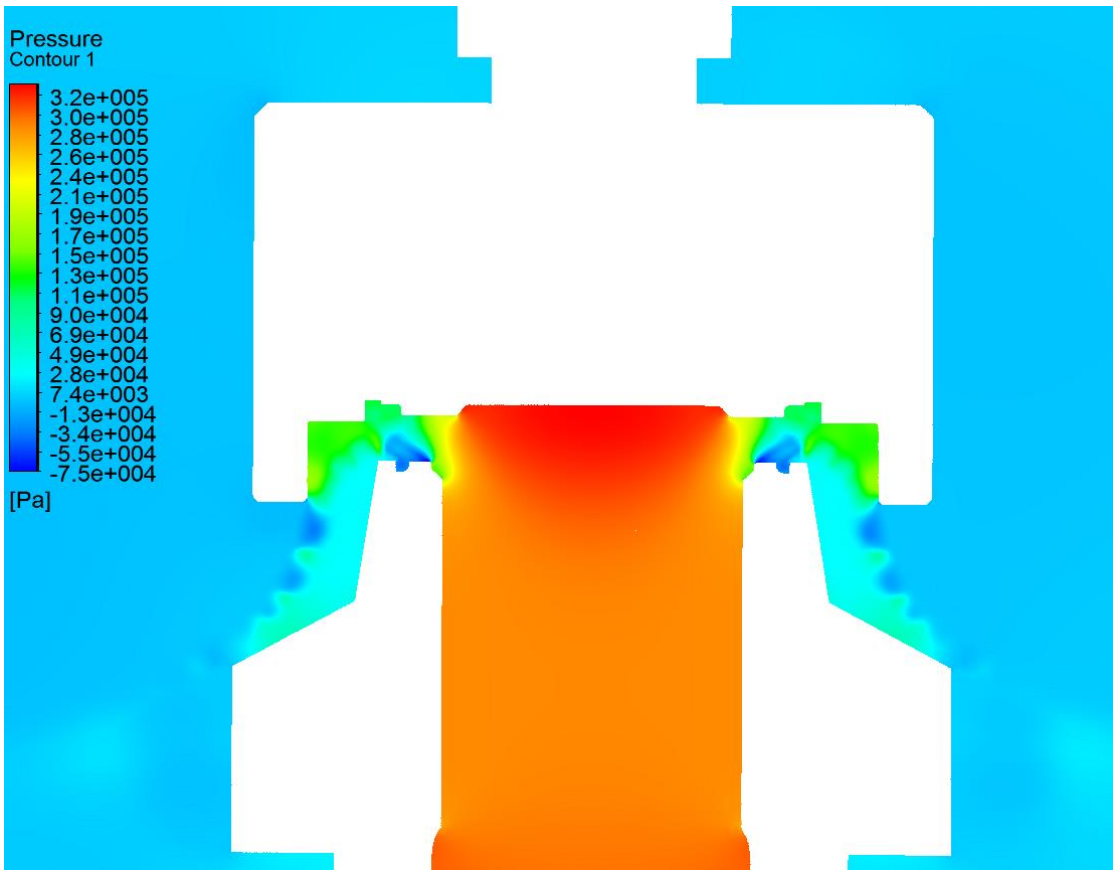

Figure 5.16 – Static Pressure Contour at 2mm disc lift, 3.3 barg inlet pressure

Figure 5.16 highlights the pressure gradients from the nozzle across the disc/seat interface in the valve and also indicates the proportion of pressure force acting on the disc. It can be seen that the greatest surface pressure occurs in the central region of the disc directly above the nozzle. Within the huddling chamber, the non-uniform values of static pressure highlights a region of shockwaves occurring as the flow expands through the channel. Figure 5.17 illustrates the overall Mach number flow behaviour across the valve where the flow leaves the nozzle and enters the huddling chamber where it is turned and expanded. Once leaving the blowdown ring/disc cover channel the flow interacts with the valve's body bowl where it can be seen that there are regions of recirculation and non-uniformity. This confirmed the justification of using 180 degree slice half symmetry boundary condition as 3D effects are apparent.

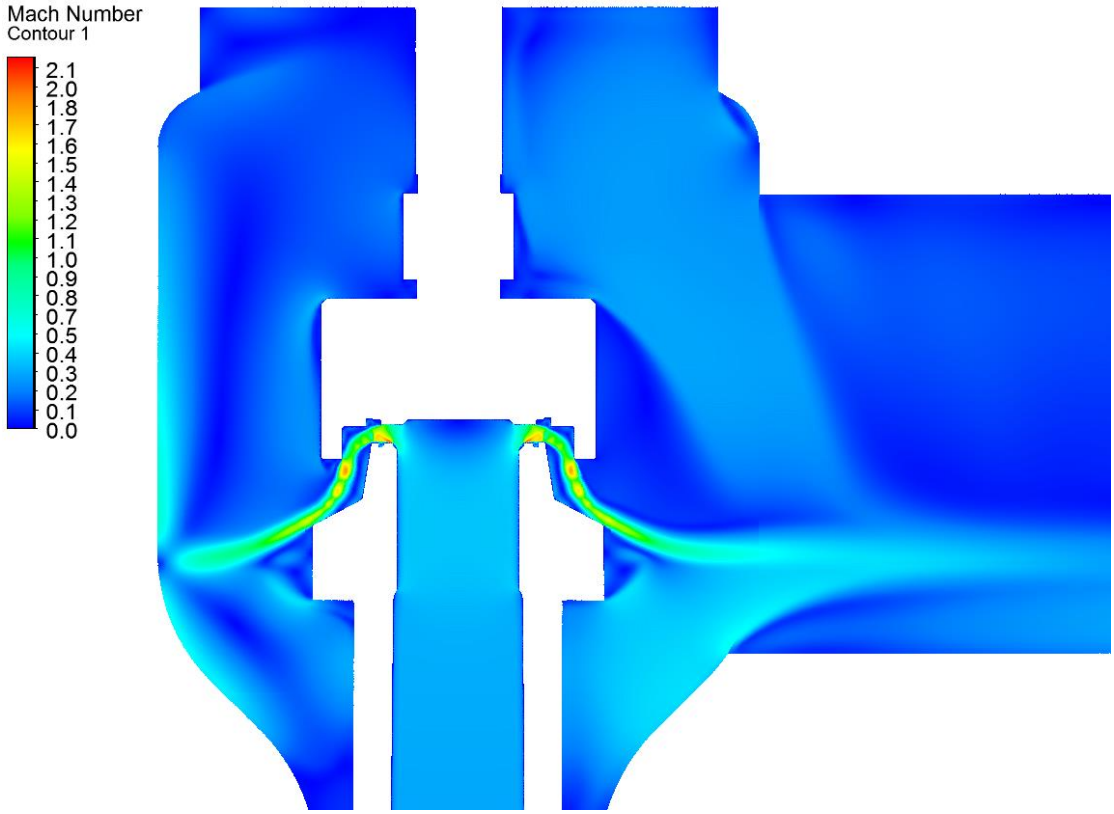

Figure 5.17 – Contour of Mach Number at 2 mm disc lift, 3.3 barg inlet pressure

Figure 5.18 represents an enlarged image of the flow channel between the disc/seat and blowdown ring. This is the area which required substantial mesh density to capture the severe pressure and velocity gradients throughout the geometry. Due to the turning effect of the flow, a series of Prandtl Meyer expansions occur resulting in the presence of strong shocks. A Prandtl-Meyer expansion fan represents an isentropic process in which Mach number increases and static pressure decreases with a constant total pressure. This is due to the supersonic flow undergoing an expansion fan process due to the presence of a sharp convex corner in which the bulk flow interacts with.

Furthermore, for the geometry shown at 2 mm lift, the flow becomes choked at the inlet edges of the disc/seat interface. This therefore highlights the

importance of capturing the geometry of the area accurately to predict the choking point which would affect the mass flow rate across the valve and disc force. In addition, recirculation regions can also be seen within the recesses generated at the disc and between the seat and blowdown ring. It can be observed that this interaction affects the structure of the expansion jet. The quality of the mesh and use of the Transition SST turbulence model is also apparent due to the contour resolution and clear indication of flow separation.

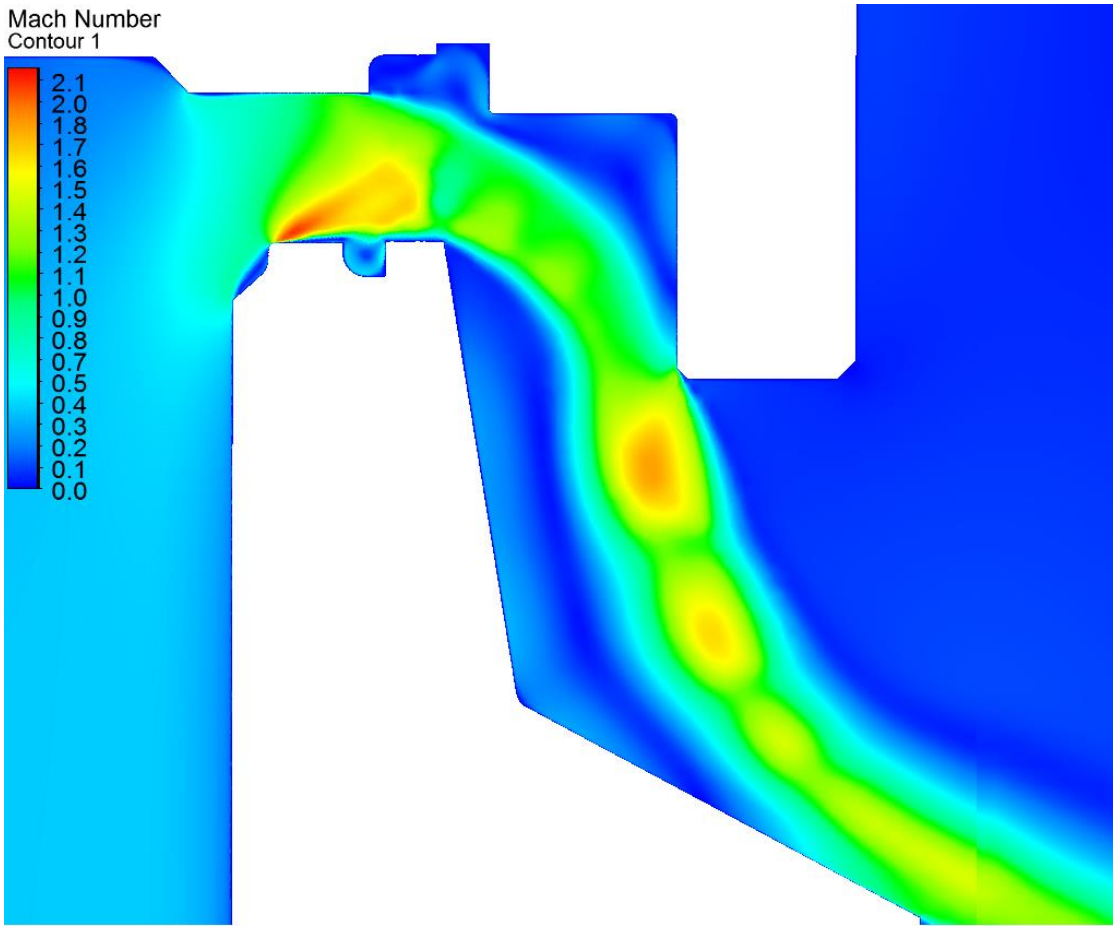

Figure 5.18 – Enlarged image of contour of Mach Number at 2mm disc lift, 3.3 barg inlet pressure

5.1.4 Discussion of Broady Steady State Validation

Through the use of CAD geometry supplied by Broady Flow Control Ltd it was possible to generate a CFD model alongside research by Taggart [9], to capture the steady state flow physics of pressure driven flow through a safety relief valve; in particular, the 3511E model designed and manufactured by Broady. The steady state performance of the valve was simulated using the fluid flow FLUENT module within ANSYS Workbench 17.1; where an inlet pressure of 3.3 barg was used as a boundary condition with the valve exhausting to atmospheric conditions. The CFD model was validated by measuring both the force acting on the disc and the mass flow rate to the inlet of the valve on CFD. This was achieved by using surface monitors and comparing the results to experimental values collected by Broady during steady state testing at similar pressure boundary conditions. This allowed the generation of a CFD disc force vs lift and mass flow rate vs lift curve which was compared to experimental curves. Following a study of appropriate numerical solvers and discretization terms, turbulence models and several mesh iterations, a steady state CFD model was produced with a capability of predicting the disc force across the full lift range (0-4 mm) with an average error of 0.83% and mass flow rate at high lift (1.5 mm-4 mm) with an average error of 1.6%. In addition it was found that the addition of curvature at the inlet edge of the seat provides better correlation compared to the sharp edge in the CAD file highlighting a strong sensitivity to the seat geometry, particularly at low lift and the need to consider as machined components. The sensitivity of seat and disc geometry for the 3511E valve was also observed in research by Taggart who utilised optimisation techniques to modify the geometry of the disc/seat in order to achieve the desired performance characteristics [9]. He also found it to be possible to validate his CFD models to within 1% of experimental data across the full lift range for disc force however accuracy of CFD to predict experimental mass flow rate was not presented [9].

5.2 Henry 5231BX PRV Validation

Following on from the Broady PRV validation work, it was important to revisit the CFD validation research performed by both Elmayyah [11] and Alshaikh [12] on through flow type PRV's manufactured by Henry Technologies. It would also be possible to analyse the robustness and suitability of the numerical methods used for the Broady right angled type PRV compared to the through flow Henry PRV to determine if a unified CFD modelling approach for most PRV geometries could be achieved. As mentioned previously, the work performed by both Elmayyah and Alshaikh used the 2D solver within FLUENT however both recommended that the use of 3D modelling should be investigated in future research. Elmayyah [11] initially hinted at a difference in accuracy between the two approaches in which 3D modelling was capable of achieving more accurate results. Although due to the large computational demands of running 3D simulations, Elmayyah recommended the use of 2D CFD modelling as a more practical solution at the time of publishing. Recent developments in computational power and memory however has enabled the development of larger meshes and complex 3D CFD models to be more commonly used. Therefore in this chapter a 2D validation will be performed alongside the development of a 3D model which utilizes similar modelling principles from the Broady PRV work. As a result a comparison will be made between the two approaches to determine their effectiveness at accurately capturing the flow physics of a through flow PRV and provide recommendations for future modelling by either researchers or industry.

The pressure relief valve modelled in this section was a 5231BX PRV manufactured by Henry Technologies in Glasgow and is shown within figure 5.19. In this study the PRV will be modelled in accordance with the specifications of the manufacturer for a set pressure of 10.3 barg with a 1/2" (12.7mm) NPTF inlet and 5/8" (15.875mm) SAE flare outlet.

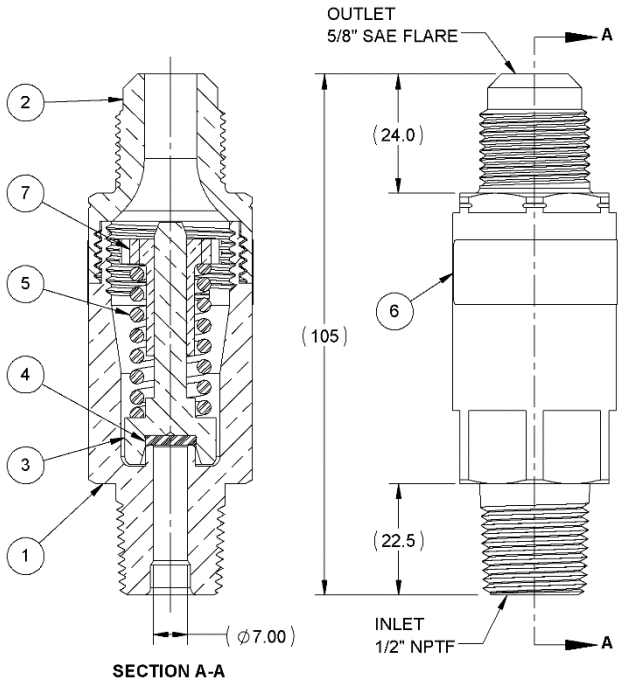

ITEM NO.	DESCRIPTION	QTY
1	Main Body	1
2	Outlet Connection	1
3	Piston	1
4	Seal	1
5	Spring	1
6	Tamper-Proof Seal	1
7	Adjusting Gland	1

Figure 5.19 – 5231BX PRV (dimensions in mm if not otherwise specified)

As can be appreciated from figure 5.19 the valve is a through flow type arrangement where the inlet and exit are inline. The PRV is designed primarily for use in the refrigeration industry to protect equipment to a pressure range of 10.3 – 46 barg. The shape of the geometry is advantageous for pressurized systems in which space is limited due to the small size of 5231BX. The PRV is assembled by various components with the primary elements being the bonded piston and LTFE (low temperature fluoro elastomer) seal arrangement; where the motion of the arrangement is governed by a preloaded spring (k=10.99 N/mm) set using a bubble test to a specified set pressure. This setting process varies between manufacturers where the Broady 3511E PRV is typically set using the first audible sign of leakage principle. From figure 5.19 it can be observed that the spring is held in place by a threaded positional

adjustment gland with vents to allow the PRV to exhaust through the outlet to atmosphere (7).

The Henry Technology 5231BX through flow valve has flow features that are quite distinct from the ASME type configuration of the Broady Valve. As shown in figure 5.19 the piston is more geometrically constrained and the exit flow is restricted due to the gland location. This results in a valve characteristic where the piston motion is more dependent on the built up back pressure behind the piston due to the gland restriction, which will generally be choked and the geometry of the outlet connection. Also the flow at the piston is more constrained due to the valve body and the potential for a greater flow-geometry coupling with this geometrical arrangement. Thus piston shape, gland geometry and end connector size are found to be much more integral to the valve performance than in an ASME type valve and potentially more challenging to model. It's critical to note however that the 5231BX geometry used in this study is also different to both of the through flow type valves used in research by both Elmayyah and Alshaikh. The differences were that Elmayyah in his work used a disc which used a square front face which is different to the circular front face for the 5231BX. The square faced geometry was suggested by Elmayyah to be a source of the differences observed between 2D and 3D modelling by comparing his 2D results to work performed by Gronkowski [57] who used 3D CFD modelling on Solidworks for the same valve. Therefore, it would be of interest to compare the use of 2D and 3D simulation for a disc with a circular front face to determine if the conclusions of Elmayyah were correct.

Alshaikh in his research however also used a 5231BX with a circular front face but he used a larger diameter outlet in order to house the experimental apparatus required for testing. This as a result did not provide a like for like comparison of the operational geometry of the 5231BX PRV therefore within this work the 5/8" SAE flare outlet will be used. It was found that the outlet

Alshaikh used had an internal diameter of 16 mm compared with the initial 5231BX value of 13.6 mm diameter for the 5/8” SAE flare outlet. The effect of this modelling change for the geometry will be analyzed to determine if such a change to the outlet geometry had an influence on the accuracy of the CFD model developed by Alshaikh.

Furthermore both Elmayyah and Alshaikh utilized the application of a modified gland to allow 2D simulations to take place as it would help to create an axisymmetric geometry compared to the original gland. However in this work a variation of the gland will be developed to allow an axisymmetric domain to be achieved and also one which replicates the flow path of the existing gland more accurately as well as allowing the spring to be mounted if required. In addition, it was extensively tested by both Elmayyah and Alshaikh that the spring shown in figure 5.19 could be removed without significantly affecting the valve performance in steady state. Therefore in addition to using a modified gland, the spring will be removed during both the CFD and experimental analysis of the 5231BX valve in this validation study.

The modified gland used in this study was designed in order to achieve an axisymmetric domain to reduce computational requirements and allow comparison between 2D and 3D simulation. The gland was designed to represent an equivalent annular area to the manufacturer’s specification which would allow the rated discharge rate of the PRV to remain consistent; this however would be verified during experimental testing. The key however was to allow an axisymmetric domain to be achieved by removing any non-uniformity in the geometry of the gland; this is true of the original gland shown in figure 5.20 as the geometry changes across each cross section of the geometry and only has quarter symmetry. Figure 5.20 also illustrates the modified gland which was designed for use in this study for the 5231BX valve as it allows a comparison of 2D and 3D simulation to take place as well as simplifying the outlet geometry without impacting on the expected flowrate

performance of the PRV. As can be seen from figure 5.20 for the modified gland, three thin supporting arms are used to support the central section of the gland which would hold the spring in place during transient work in the next chapter. Due to the small cross sectional area of the arms, the effect on the flow would be expected to be negligible in comparison with the original gland and therefore suitable for use as an axisymmetric domain once installed within the PRV. The full dimensions of the gland are shown within an engineering drawing in the appendix of this thesis.

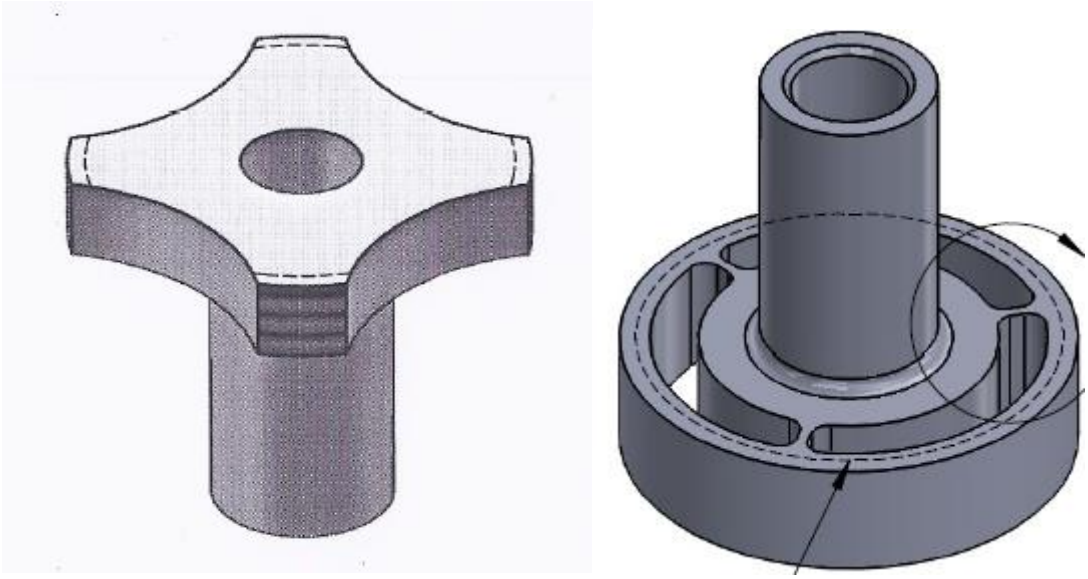

Figure 5.20 – Original Gland (left) and Modified Gland (right)

In a similar manner to the validation work performed for the Broady PRV, steady state testing of the Henry 5231BX valve would involve using measurement points at regular disc lift intervals from the fully closed to fully open position. Experimental data and CFD modelling will capture data points from 0.05mm to 5mm where each data point will be subjected to an inlet pressure of 10.3 barg and will exhaust to atmosphere (0 barg) operating at typical room temperature at both inlet and outlet. A disc force vs lift and mass flow rate vs lift curve will be generated both experimentally and using CFD to allow comparison and validation to take place to allow the most appropriate

solver settings to achieve an accurate modelling approach. This procedure will be performed for 2D using the modified gland as well as for 3D with and without the modified gland where each case will also be compared with each other to analyze and explain any differences. Furthermore, the pressure based solver will be used to allow development of a multiphase solver following single phase validation work; in previous Broady work the pressure based solver was proven to be effective when compared with the density solver. The validated models will then be carried forward to allow future steady state and transient dynamic mesh modelling to be performed with confidence.

5.2.1 Experimental Testing

To achieve a method of validating CFD results for the Henry 5231BX PRV it was necessary to develop an in house experimental rig which was located within the flow testing facility at the University of Strathclyde. The test fluid was air at a pressure of 10.3 barg at standard room temperature in order to meet the minimum recommended operating pressure of the PRV by the manufacturer. A method of measurement for inlet pressure, disc (piston) position, flow rate, backpressure and disc force was required to be developed to allow simultaneous measurement of each variable. The P&ID (pressure and instrumentation diagram) of the flow facility as well as a list of the measurement instrumentation used is shown respectively in figure 5.21 and table 5.11.

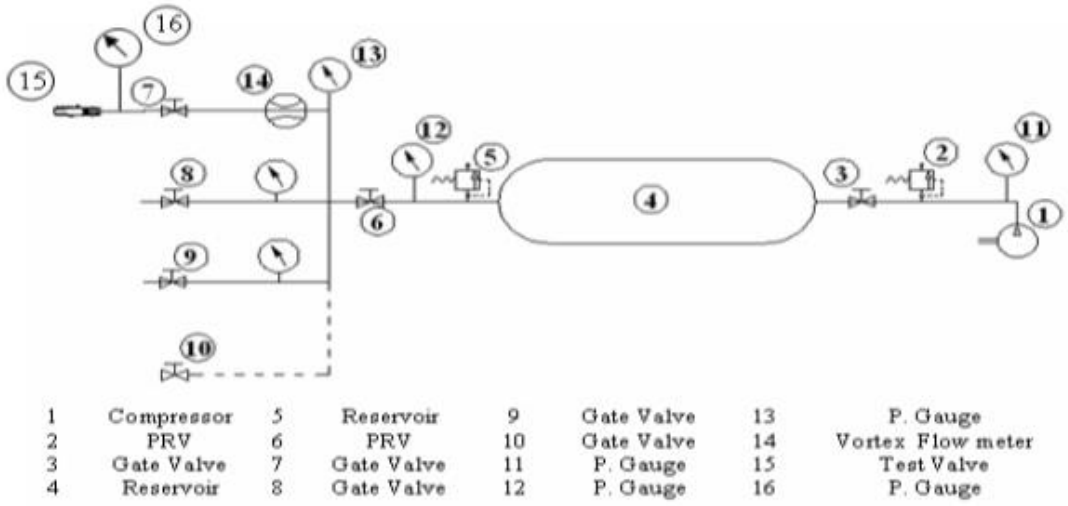

Figure 5.21 – P&ID of Strathclyde Flow Testing Facility for 5231BX PRV

Property	**Transducer (brand?)**	**Accuracy**	**Range**
Pressure	Bourdon Dial Pressure Gauge	2%	0- 20 barg
Pressure	BackPressure Digital Gauge	1%	0-5 barg
Flow Rate	Sierra Vortex Flow Meter	1%	0-0.6 kg/s
Disc Force	Omega Load cell	0.5-2%	1-500 N
Displacement	KEYENCE Laser Displacement	(0.1%) 0.001mm	+/- 15 mm
Data Acquisition	Inhouse Developed Software	N/A	N/A

Table 5.11 – Measurement Devices Required for 5231BX Testing

In addition to the instrumentation included shown on figure 5.21 and table 5.11, a linear cross slide device was required to adjust the displacement of the disc from the fully closed to the fully open position in discrete intervals. A high level illustration of the single phase steady state experimental rig is shown within figure 5.22 where the overall experimental rig is illustrated in further detail also within figures 5.22 and 5.23 where each component labelled in the figures is described in table 5.12.

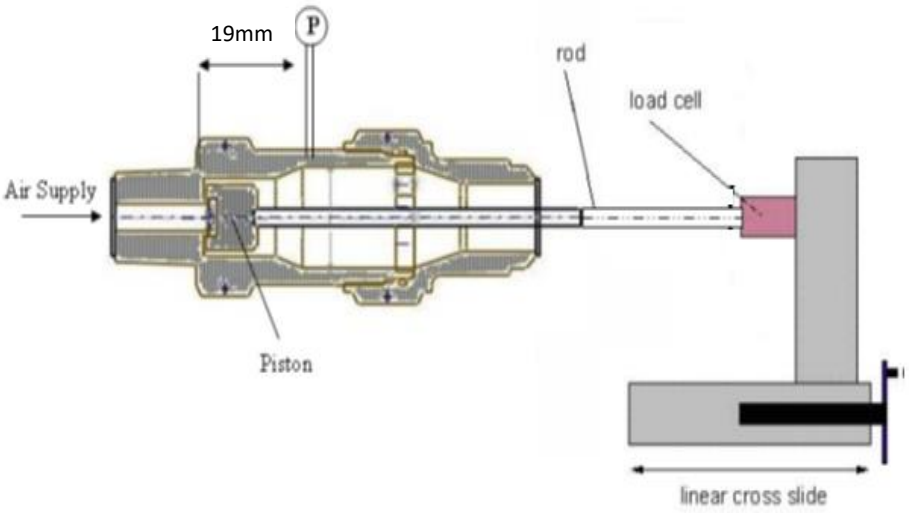

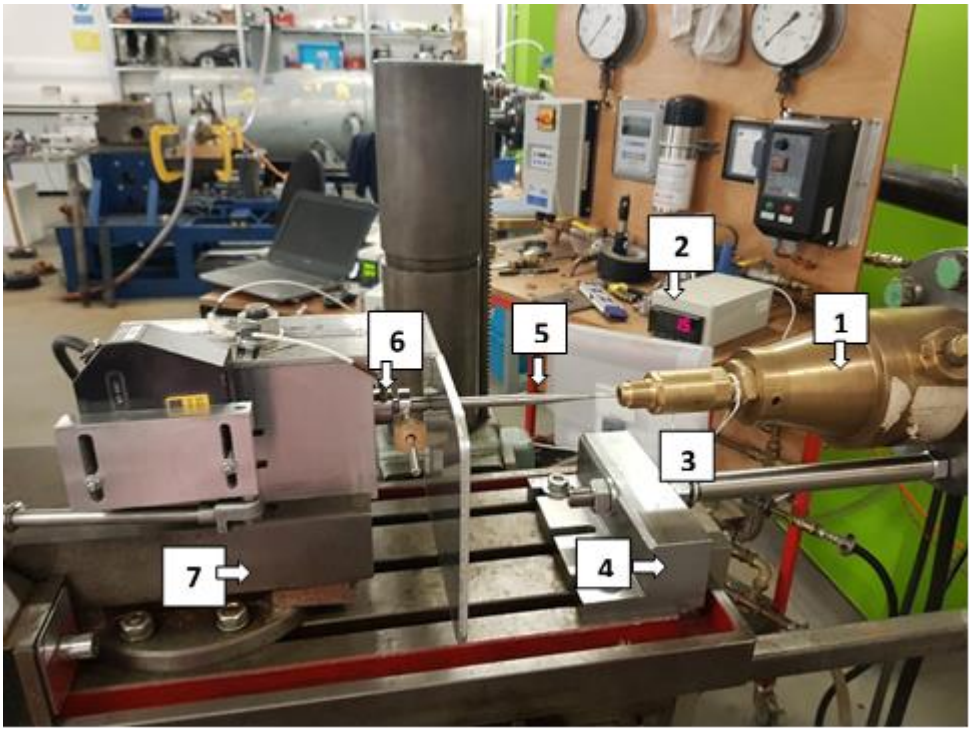

Figure 5.22 – High Level Overview of 5231BX Single Phase Steady State Experimental Rig (concept top, laboratory picture bottom)

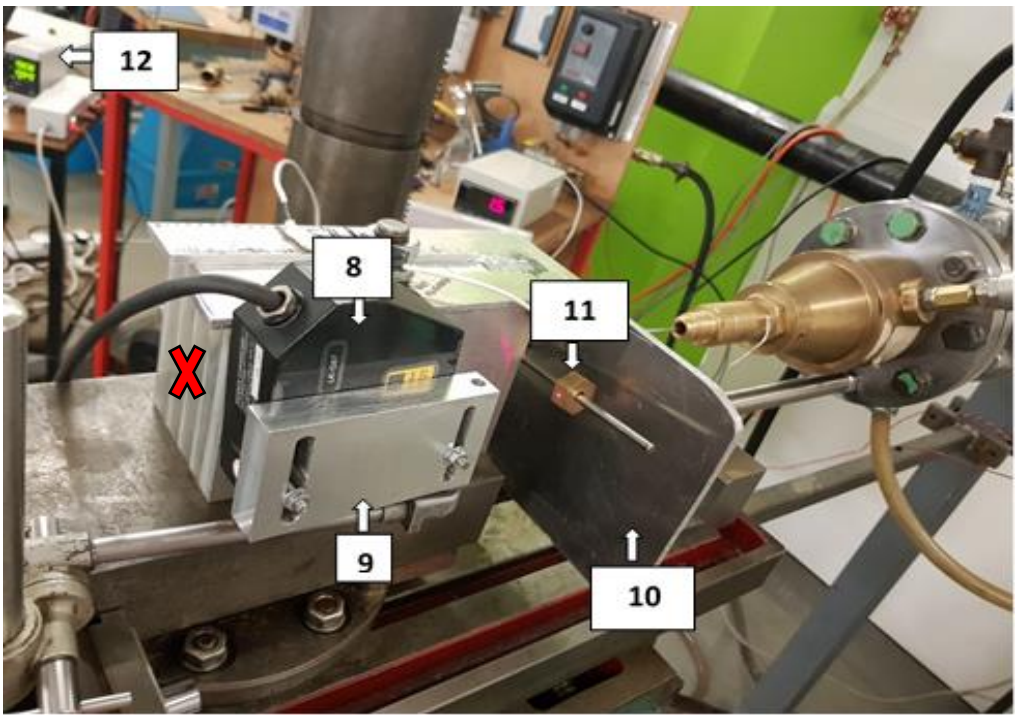

Figure 5.23 – Detailed View of Laser Assembly for 5231BX Experimental Rig

No.	**Experimental Part**	**Description**
1	Nozzle Inlet	Connection of PRV inlet to external piping
2	Load Cell Monitor	To provide reading of disc force from load cell
3	Henry 5231BX PRV	PRV used in this validation study
4	Horizontal Support Structure	Required to reduce error of disc position
5	Stainless Steel Rod	Connects disc to load cell to measure force
6	Load Cell	Determines the aerodynamic force on disc
7	Linear Traverse Table	Required to adjust disc displacement (lift)
8	Laser Displacement Sensor	Measures disc displacement for adjustment
9	Laser Mount	Necessary to position laser to reference point
10	Jet Deflection Shield	Shields load cell from PRV jet to prevent error
11	Laser Reference Structure	Provides a suitable surface for laser measurement
12	Laser Displacement Display	Provides a lift reading from the laser sensor.
13	Inlet Pressure Bourdon Gauge and Back Pressure Digital Gauge	Pressure devices required for measurement of inlet pressure and back pressure of PRV

Table 5.12 – Description of Experimental Components in Figures 5.24 - 25

The air compressor for the testing facility was capable of delivering an inlet pressure at 0-20 barg which was reduced to a 1-15 barg working range using the pressurized equipment in figure 5.21 and Bourdon dial pressure gauge (13). It was also possible to measure the back pressure acting on the upper surfaces of the disc by using a digital pressure gauge connected to a pressure tapping at a desired location of the PRV (Drawing provided in appendix A8). Once at a suitable inlet pressure, a flow was established through the PRV to allow measurement to take place (described later in this section). An upstream nozzle (1) was used to provide a connection between the inlet of the PRV and the pressurized equipment upstream in the flow testing laboratory. At the upstream section there is also a connection to the experimental rig via a horizontal support (4) which reduces the amount of play in the system to minimize any measurement error of the disc displacement (lift). The disc placed within the PRV is connected to the load cell (6) via a stainless steel connecting rod (5) which allows measurement of the flow force by displaying the value on a digital display (2). It was important to minimize the effect of the connecting rod on the flow and available surface area for backpressure to act on the disc. A stainless steel rod with minimum diameter which was capable of resisting buckling under typical loads was selected which would gradually increase in diameter with distance until the exit of the outlet in which a constant diameter would provide connection to the load cell. The connection between the rod and disc is highlighted in red (figure 5.24) alongside the modified gland where it can also be seen that the spring was removed for static testing.

The aerodynamic force acting on the piston was measured using a load cell (6). However offset from the load cell position was a custom made collar which was designed to be placed on the rod to allow the assembly of an attachment which would be suitable to provide a flat and reflective reference surface for the laser (11). The purpose of the laser was to provide a non-intrusive form of measurement for the lift which would remove the unknown deflection of the load cell from the reading. However to maintain the benefit of this approach when compared to work by Elmayyah [11] and Alshaikh [12] who used dial

gauges to measure displacement at the point marked ‘red X’ in figure 5.23; it was crucial at this stage to minimize any play in the laser reference structure.

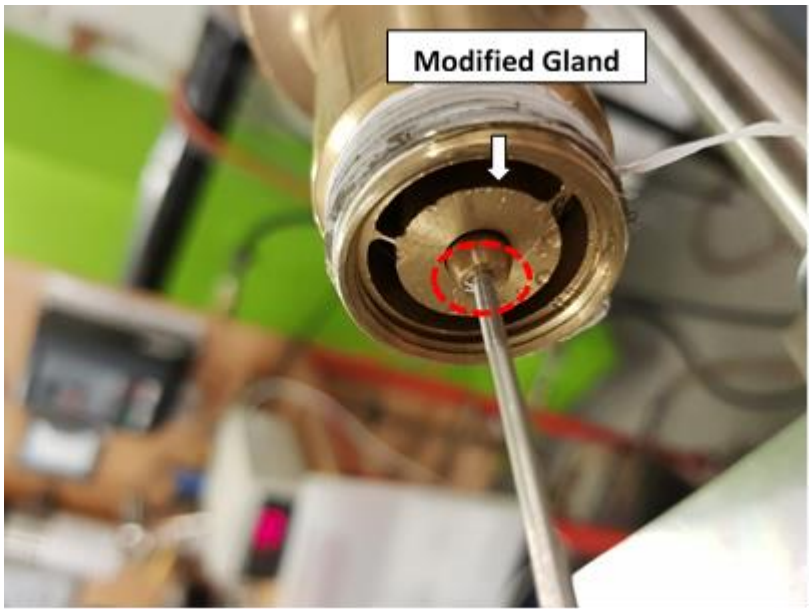

Figure 5.24 – Detailed View of Connection between the Disc and Rod

As a result the measurement error would be minimized and would provide a much more reliable form of measurement between the laser and piston position. The laser itself was held in place using a custom designed laser mount which would provide the necessary adjustment in the X, Y, Z axis to allow acceptable positioning of the laser to achieve the maximum working range and accuracy. The position of the disc was adjusted using a lead screw attached to a traverse table (7) to allow controlled linear adjustment of the valve lift to take place in which reading of the disc position was provided using the laser display (12). Finally, a deflection shield (10) was required to shield both the laser and load cell from the exhaust jet from the PRV; this was critical in order to prevent measurement inaccuracy for the load cell caused by changes in air pressure as well as avoiding debris damage. It should be noted that for all of the measurements which took place, the depth of both the original and modified glands from the top surface of the body to the top surface of the

gland was adjusted to be 3.2 mm which corresponded to the gland depth setting required for a set pressure of approximately 10.3 barg. The measurement procedure developed for the 5231BX PRV was as follows;

1. Before testing took place and flow was established it was crucial to ensure that the appropriate safety precautions were made within the laboratory such as securing of loose items in the vicinity of the jet, closing doors to public walking areas and wearing appropriate personal protection equipment (PPE) especially for ears, eyes and feet.

2. Initially by using the displacement reading from the laser display, the position of the disc was adjusted using the linear cross slide until a force increase (5N) is registered, indicating piston seat contact. At this point the laser position was zeroed and would be used as a datum point for where testing will occur at various lifts. Initially before flow is established however the disc is further compressed to be in firm contact with the seat with a sealing reaction force of approximately 100N to ensure zero leakage before testing can take place.

3. Once an appropriate sealing force is established, the lead screw is used on the linear traverse table to release the compression of the disc on the seat to the datum closed position at 0mm lift at the laser display. At this point, an audible hiss is often heard due to leakage across the disc/seat sealing interface due to imperfections in the sealing surfaces. The pressure is adjusted using the gate valve in the flow testing laboratory piping and maintained using the bourdon gauge. A measurement of force, pressure and disc displacement is taken at this stage once the test pressure is established and settled. Flowrate would be negligible and unable to be observed by the flowmeter as it would be out with the working range.

4. Step 2 was repeated at discrete lift intervals as required with recordings of disc lift, inlet pressure, back pressure and disc force until a noticeable reading of mass flow rate was available from the flow meter at approximately 0.3mm. From this point onwards mass flow rate would also be included in measurements once a stable value of pressure was achieved at the required value.

5. Measurements would then take place across the full lift range from 0-5mm in which care must be taken to adjust the gate valve position from the upstream piping to maintain 10.3 barg as flow rate increases with increasing lift and discharge rate of the PRV. At each lift position data would be recorded for the variables of disc displacement, disc force, mass flow rate, back pressure and inlet pressure.

6. Steps 1-5 of the experimental process were repeated numerous times in order to ensure repeatability of the results and tests were conducted using both the original gland and modified gland.

In a similar nature to the uncertainty analysis performed for the Broady valve, an evaluation was performed to quantify the measurement error during the experimental study. The statistical error was reduced by performing at least 20 repetitions of the experiment at a pressure of 10.3 barg at both a low disc lift value of 0.5 mm and high disc lift value of 3 mm. This would ensure confidence with the measurement equipment used and their positioning. At a low lift valve position of 0.5 mm for the 5231BX valve, a statistical error for flow force was determined for the modified gland experiment where the error was found to be 0.19%. For flow rate, a statistical error of 0.63% was found for the modified gland PRV assembly and a statistical error of 0.44% for backpressure measurement. At a high lift valve position of 3mm for the 5231BX valve with modified gland, a statistical error for flow force was found to be 0.44%. A statistical error of 0.14% was found for flow rate and 0.15% for backpressure

for the modified gland PRV assembly. The measurement uncertainty attributed to each device for measurement of disc force, mass flow rate and backpressure is highlighted in table 5.13 with statistical uncertainty shown for both low/high lifts in tables 5.14 and 5.15. The performance demonstrated was deemed acceptable and highlighted the effectiveness and repeatability of the test rig for the purpose of CFD validation.

Device Uncertainty	**Load Cell**	**Inlet Pressure**	**Laser**	**Flow Meter**	**Back Pressure**
Disc Force	0.5-2%	2%	0.1%	N/A	N/A
Mass Flow Rate	N/A	2%	0.1%	1%	N/A
BackPressure	N/A	2%	0.1%	N/A	1%

Table 5.13 – Measurement Uncertainty (Mod Gland)

	Statistical Uncertainty
Disc Force	0.19%
Mass Flow Rate	0.63%
BackPressure	0.44%

Table 5.14 - Statistical Uncertainty at 0.5mm (Mod Gland)

	Statistical Uncertainty
Disc Force	0.44%
Mass Flow Rate	0.14%
BackPressure	0.15%

Table 5.15 - Statistical Uncertainty at 3mm (Mod Gland)

From tables 5.14 and 5.15 it is therefore possible to appreciate the magnitude of error involved in the measurement of each variable at both low and high lift. It could be established that at higher lifts the statistical uncertainty for disc force was more significant than at lower lifts whereas the opposite was true for both mass flow rate and back pressure measurement. This was indicative of the likely flow phenomena occurring in the PRV's at each stage. Therefore, an appreciation of the total uncertainty variation between high lift and low lift should be included during analysis of the results. Table 5.14 and 5.15 however highlights that such error will be minimal to less than 1% across the full lift range therefore the worst case uncertainty should be used for each variable.

The experimental results captured at 10.3 Barg inlet pressure across a lift range of 0-5 mm for flow (disc) force, inlet mass flow rate and back pressure are shown in figures 5.25 and 5.26; note that the error bars correspond to the worst case uncertainty evaluated in tables 5.14 and 5.15.

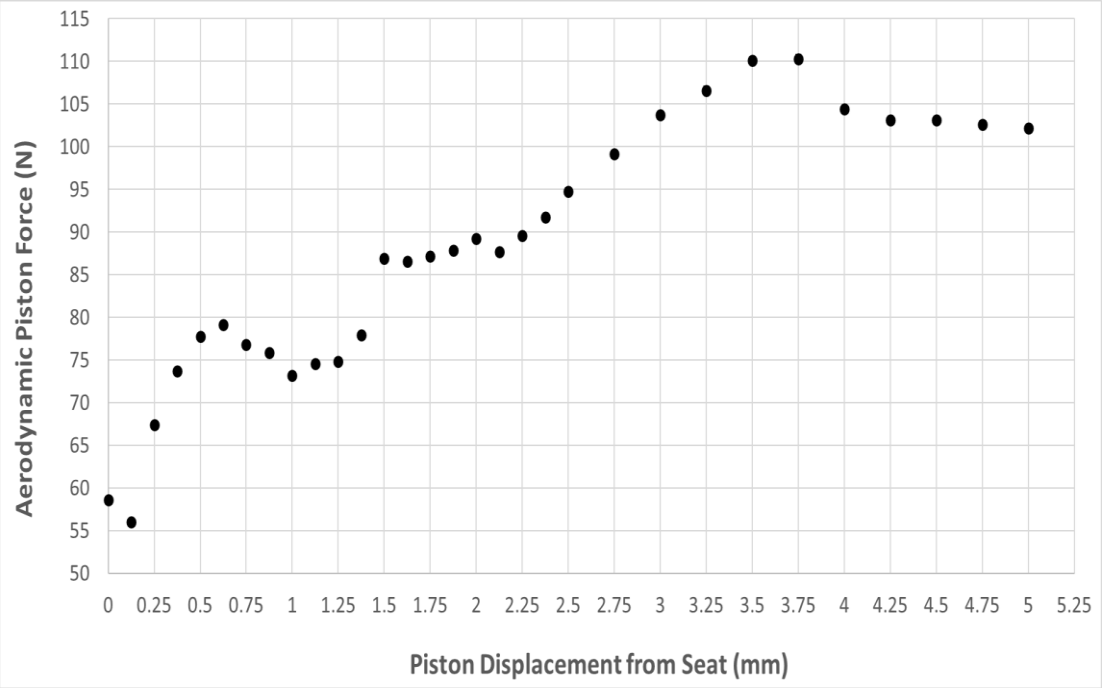

Figure 5.25 – Experimental Flow Force Results for 5231BX Modified Gland (10.3 barg)

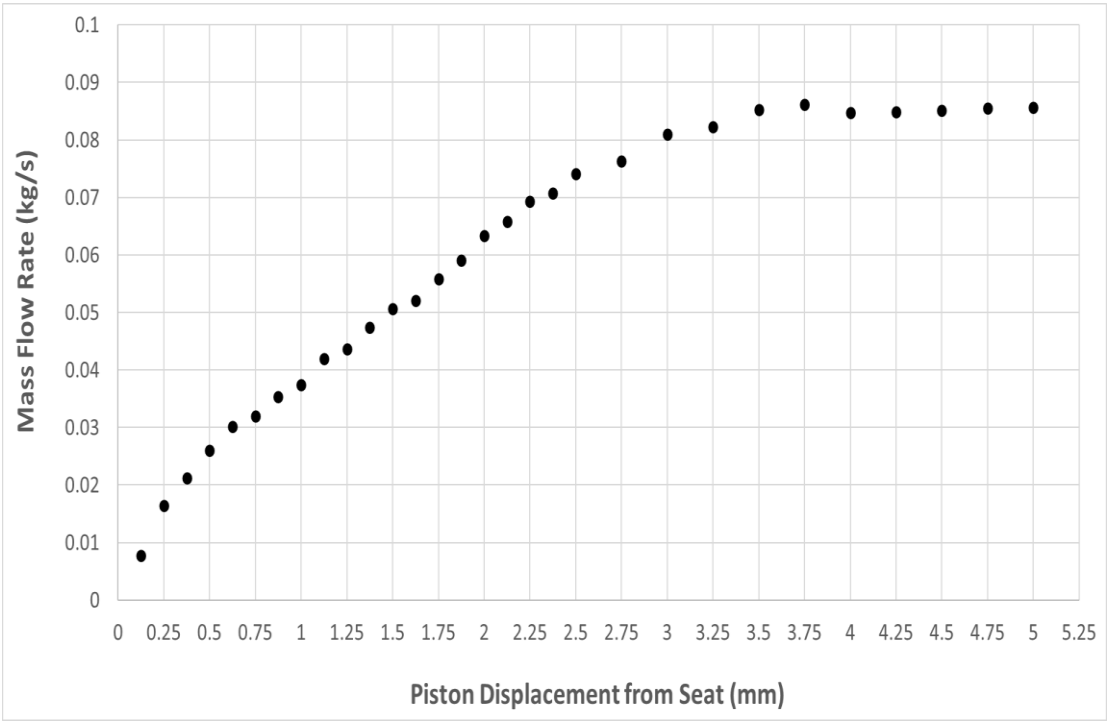

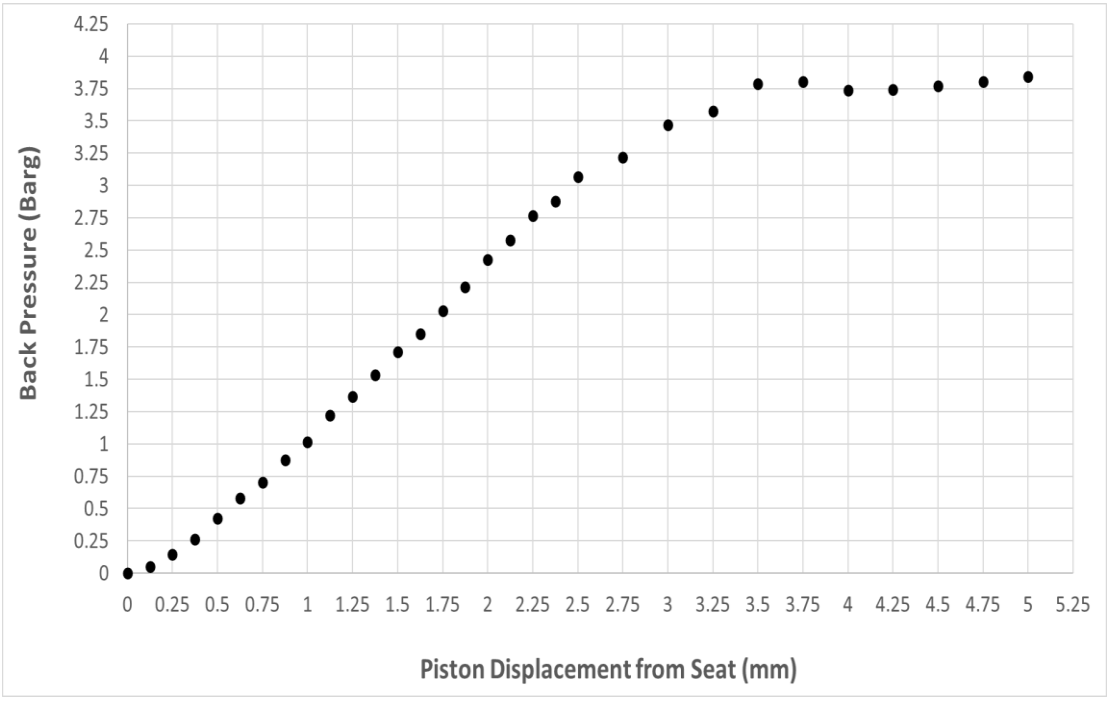

Figure 5.26 – Experimental Mass Flow Rate (top) and Back Pressure (bottom) Results for 5231BX Modified Gland (10.3 barg)

The typical force lift curve of the 5231BX PRV with modified gland shown within figure 5.25 highlighted the complex nature of the relationship between disc force and piston displacement from the seat (lift). It can be appreciated that there is initially a large increase in disc force with relatively small movement between 0 to 0.5 mm. It is likely this has been designed to allow a quick action pop to occur for the PRV in a bid to help to prevent valve instability during opening. Following 0.5 mm however there is a reduction in disc force from approximately 1-1.375 mm where the force once more increased to approximately 87N at 1.5 mm. This dip indicates that a transition in the flow regime and hence pressure distribution is likely to be occurring at the lower disc surface during these ranges of disc displacement. This will be investigated further during the CFD study in which visualization could provide more insight for what is occurring within the PRV. Following 1.5 mm a linear increase in disc force could be observed until a maximum value of 110 N is measured at 3.5 mm. From this point thereafter the disc force plateaus and reduces. With observation from figure 5.26 for mass flow rate and back pressure it can be realized that by approximately 3.5 mm the measurements also begin to plateau. This is likely due to a change of the choking positions within the PRV as disc lift is increased which eventually reaches a point in which the flow geometry can change no further. This hypothesis however will be investigated during the CFD study using visualization tools available within ANSYS FLUENT. Interestingly however, during the experimental study a hysteresis effect was observed during the likely transition phase of the PRV between 1-1.5 mm as the disc force dips before quickly increasing at 1.5 mm. The blue trace in figure 5.27 highlights the disc force results as the PRV is opened and steady state measurements are taken. The red trace on the other hand highlights the results of measurements taken during the closing of the PRV during steady state testing. It can be clearly observed that there is a significant difference in disc force observed highlighting a possible hysteresis effect due to flow history as the PRV enters the transition phase from either high lift or low lift.

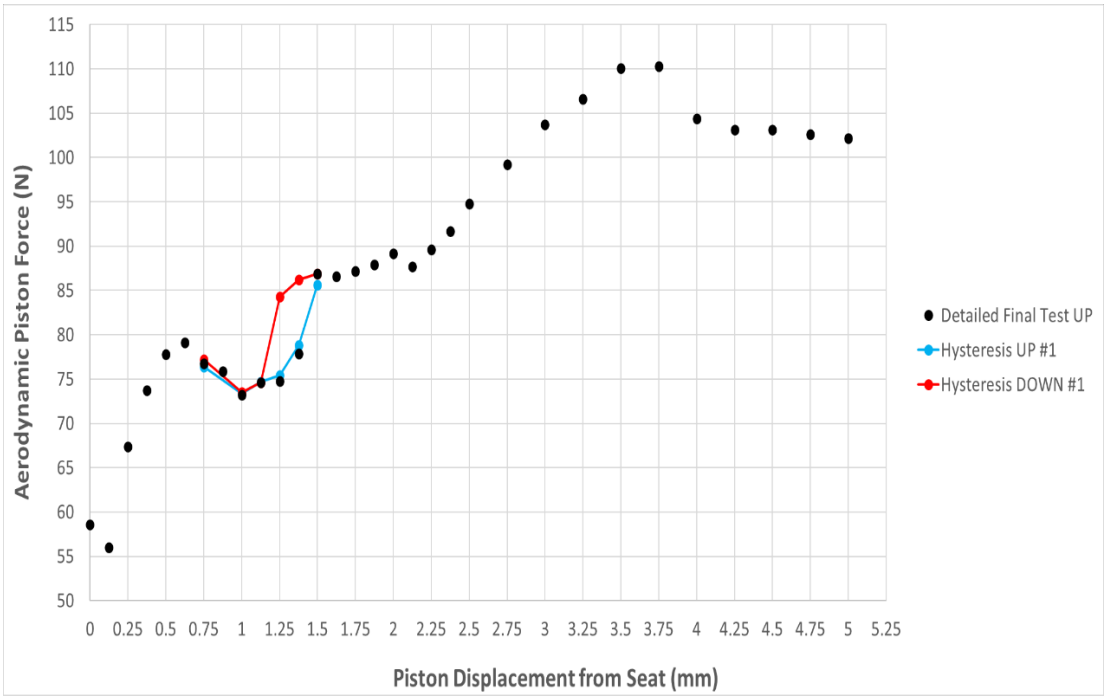

Figure 5.27 – Experimental Flow Force Hysteresis Observed for 5231BX Modified Gland (10.3 barg)

A comparison of the flow force and flowrate measurement for both the original and modified glands are shown in figures 5.28 and 5.29 in order to appreciate the impact of the gland shape on valve performance. It can easily be appreciated from the data in figure 5.29 that the modified gland provided the desired flow rate performance required as there was negligible change in the flow rate measurement. This is because of an almost identical linear increase in flowrate until the choking point at maximum lift is reached at 3.5 mm in which the flowrate plateaus to a near constant value of 0.09 kg/s. This is likely due to the maintenance of choking points and annular flow area therefore it could be proposed that the use of the modified gland would be appropriate for the remainder of the CFD validations for both 2D and 3D CFD analysis.

Worth noting is the differences in flow force between the original and modified gland, as shown in figure 5.28, where the flow force reported for the modified

gland was about 7% higher than that of the original gland at high lifts. At lower lifts, similar flow force values were reported for both glands with little variation. In agreement with the work performed by Alshaikh [12] who observed a similar phenomenon when using his modified gland this is caused by a reduction in backpressure at higher lifts which increase the aerodynamic flow force acting on the PRV when compared with the original gland. The effect of this change in flow force behavior across the valve lift range could result in a change in dynamic behavior however need not be to considered during steady state CFD validation.

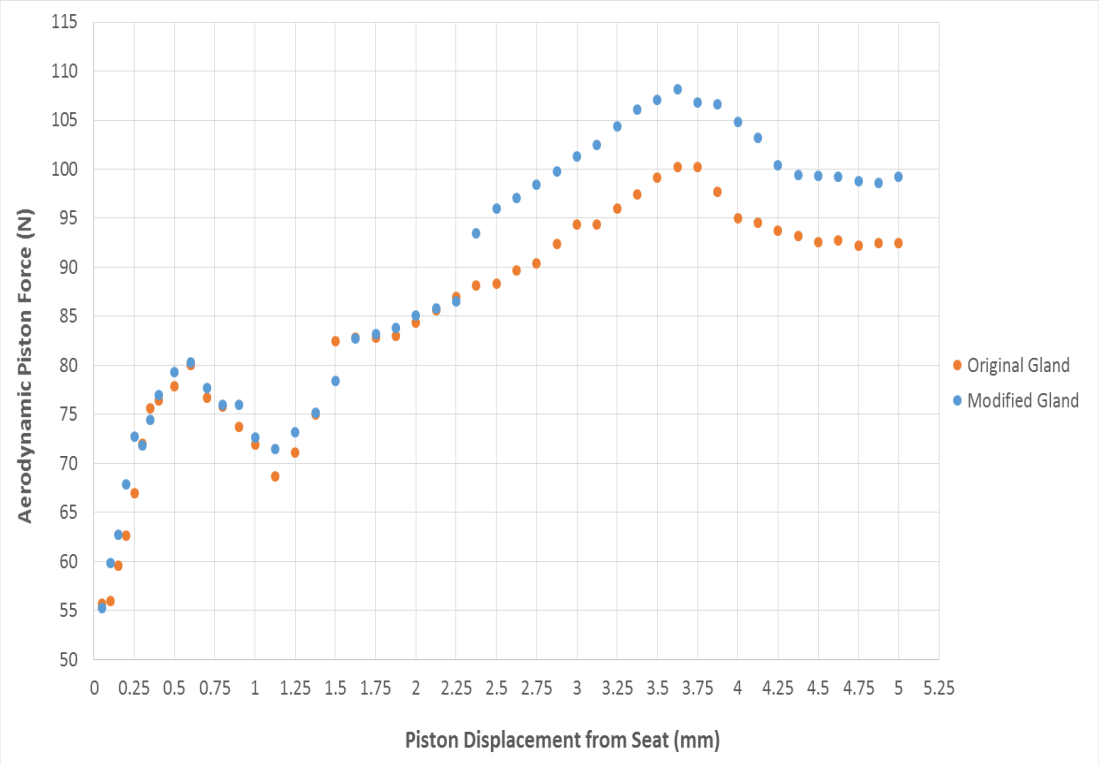

Figure 5.28 – Experimental Results of Piston Force for Both Glands at 10.3 barg

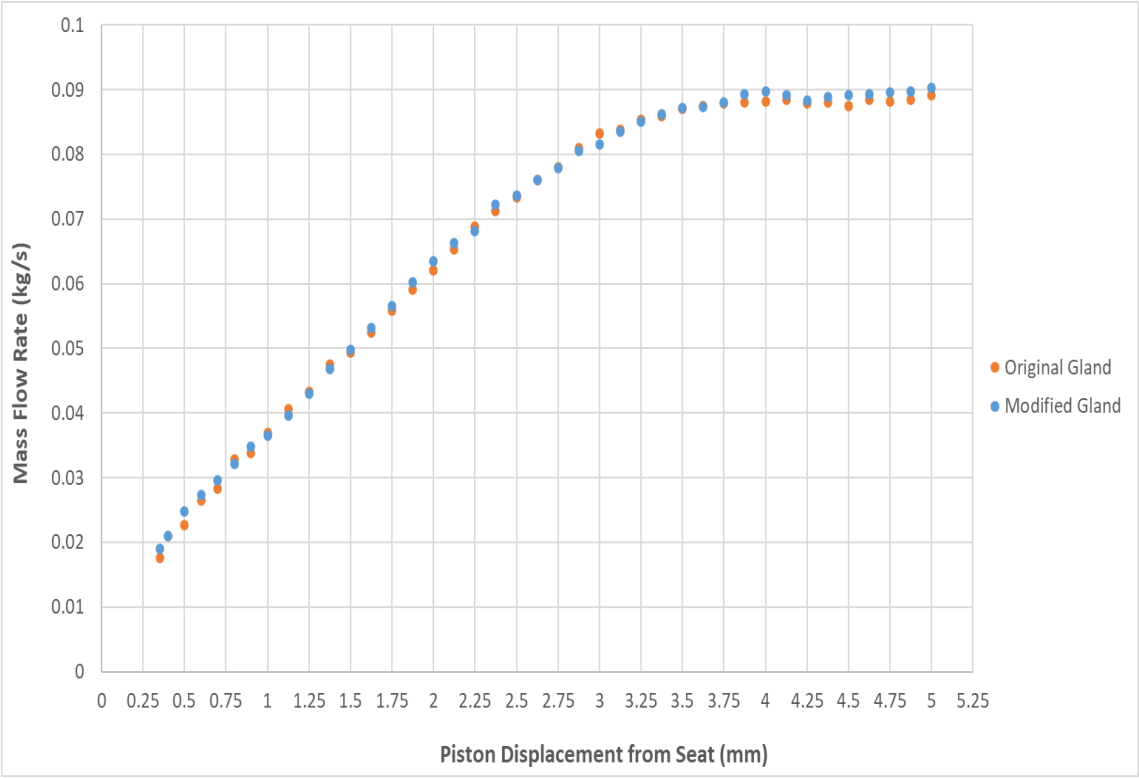

Figure 5.29 - Experimental Results of Flowrate for Both Glands at 10.3 barg

5.2.2 Development of 2D CFD Model for 5231BX PRV

As mentioned previously, extensive validation work has been performed for similar through flow valves by both Elmayyah and Alshaikh using 2D axisymmetric CFD modelling using ANSYS FLUENT. Therefore it was deemed appropriate for the 5231BX PRV that an initial 2D model should be developed and compare the performance to that determined in previously. By using ANSYS Workbench 18, it was possible to create a computational domain from a Solidworks CAD file of the Henry 5231BX PRV provided by the manufacturer. It was required however to swap the original gland geometry (figure 5.20) for the modified gland geometry (figure 5.21) within CAD in order to achieve an axisymmetric geometry suitable for 2D modelling. By utilizing 2D modelling it would be possible to minimize computational time and resources required for calculation however the effect of 3D flow behavior would not be captured. As

the domain was axisymmetric however, 3D flow effects were not expected however a comparison would be made to 3D modelling in order to ensure accuracy.

Figure 5.30 highlights the axisymmetric domain which was developed at a lift of 4mm. This domain was generated by creating a 2D surface from the face of a quarter symmetry 3D CAD model. The named selection tool was used for the edges shown in figure 5.30 in preparation for boundary condition assignment. The blue boundary represents the inlet edge for the pressure inlet boundary conditions to be applied whereas the red boundary represents the edge for pressure outlet conditions. The white edges represent the walls in which FLUENT will recognize as no slip walls whereas the yellow edges represent the boundaries for non-conformal mesh interface calculations to take place. Non-conformal interfaces are required to allow a greater variation of mesh density to be applied to minimize computational cost. Finally the yellow edge represents where axisymmetric conditions will be applied.

As can be seen within figure 5.30, for steady state CFD modelling of the 5231BX PRV it was decided to split the domain into 6 zones for greater mesh control. Zone 1's and 2 provided an opportunity for incremental mesh refinement to the disc/seat area in which the most significant mesh density would be required to capture the complex flow in this area. Areas 4, 5 and 6 also provided an opportunity to reduce overall mesh requirement as less mesh refinement would be required towards the outlet due to an expected stabilization of the flow due to choking. The modified gland area is marked in purple in figure 5.30.

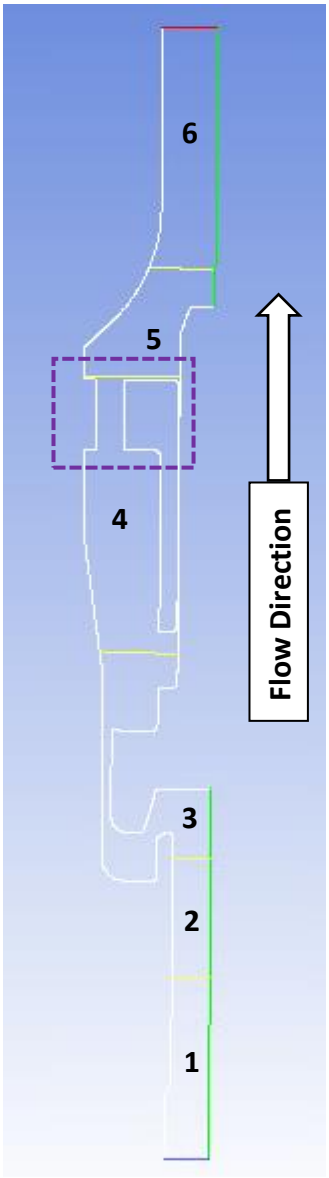

RED – Outlet boundary.

GREEN – Axis boundary for axisymmetry.

YELLOW – Mesh interface between zones.

WHITE – Wall boundary.

BLUE – Inlet boundary.

Figure 5.30 – 2D 5231BX Computational Domain used in FLUENT

2D CFD Modelling of 5231BX PRV – Meshing

Due to the more complex nature of the geometry of the Henry 5231BX, in particular in the flow area sandwiched between the disc and seat it was determined that the use of an unstructured tetrahedral mesh would be appropriate compared to the structured mesh developed for the Broady valve. The 2D mesh was generated in each of the six zones using the “All Triangles

Method"; where 5 contact regions were used to connect each zone using non conformal interfaces. Body sizing was used in each zone to achieve control over the mesh refinement required. The mesh generated for the Henry PRV domain at 4mm lift is shown in figure 5.31.

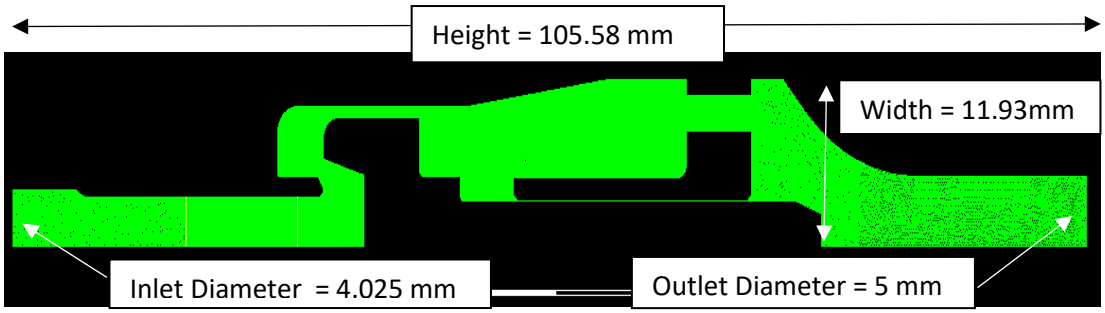

Figure 5.31 – Computational 2D Mesh Domain of 5231BX PRV at 4mm Lift

It was particularly necessary to create a dense mesh in zone 3, otherwise known as the disc/seat interface, to capture the significant flow and pressure gradients which would likely occur in this area due to significant redirection of the bulk flow as well as flow expansion and shocks critical for flowrate prediction. In addition, this area would require surface monitors for the disc force therefore the flow structures captured within this region are required to be as accurate as possible. In a similar manner to the Broady valve, the y^+ value was required to be approximately 1 in this region when using the k-omega SST turbulence model and to be $30 < y^+ < 300$ for use with the k-epsilon turbulence model. It was deemed particularly crucial to be able to accurately capture the separation points and boundary layer development of the flow across the disc/seat interface to model the correct flow path and predict both flow forces and flowrate. An example of the dense mesh required at the disc/seat interface is shown within figure 5.32 at a disc lift of 4mm which required a cell size of 50 microns. From figure 5.32 it is possible to appreciate the complex nature of the disc/seat interface geometry and also the meshing requirements to achieve the required y^+ of the turbulence model.

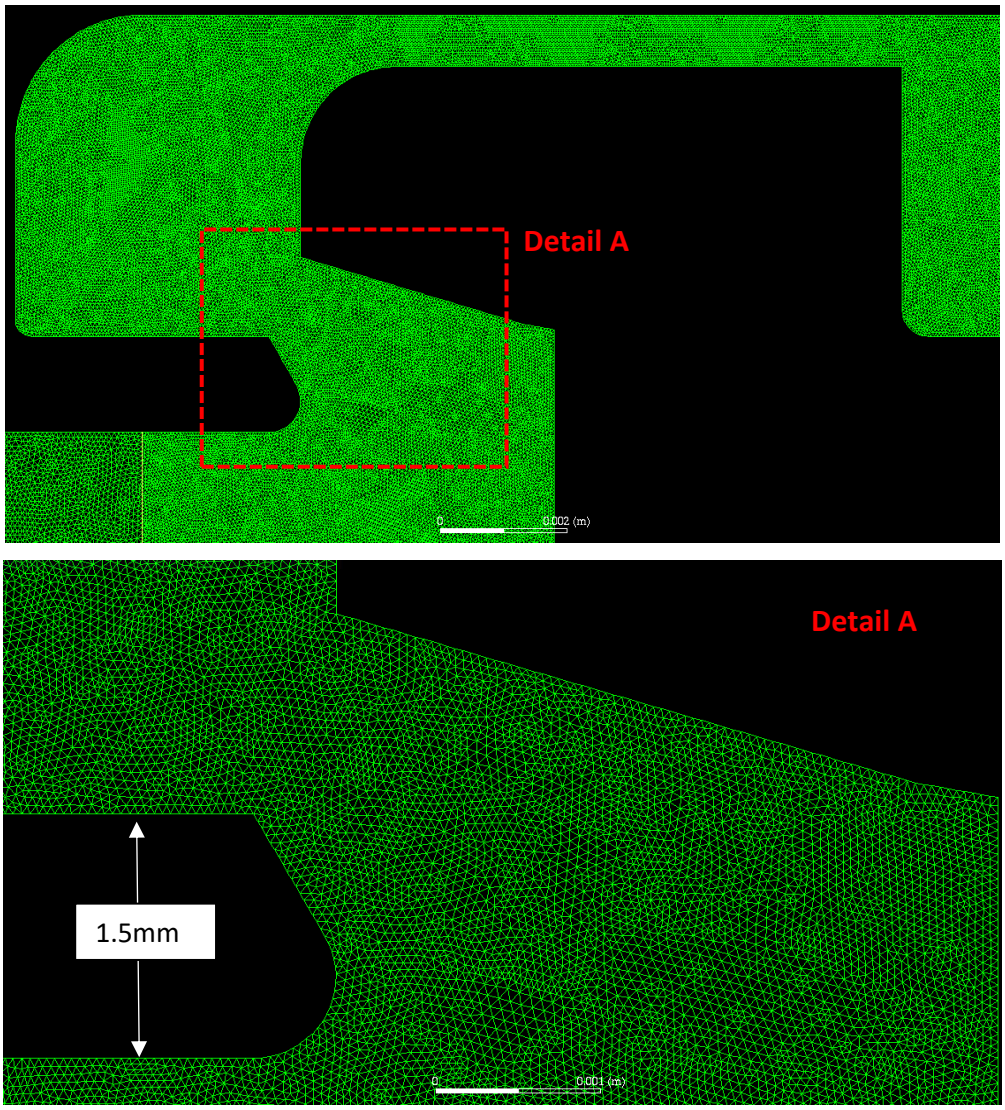

Figure 5.32 –2D Meshing for Zone 3 (Disc/Seat Interface) at 4mm

The incremental change of the mesh density across the domain is illustrated clearly within figures 5.33 and 5.34. Figure 5.33 highlights that in zones 1 and 2 the mesh increases in density in preparation with contact with the interface of zone 3. This was required for the CFD solver to capture the flow gradients at the inlet of the disc/seat interface as accurately as possible with minimal numerical diffusion across the zones. In addition, it was also important to capture the effect of pressure losses in the form of friction with the wall as the flow progressed through the initial inlet geometry of the PRV to the disc/seat.

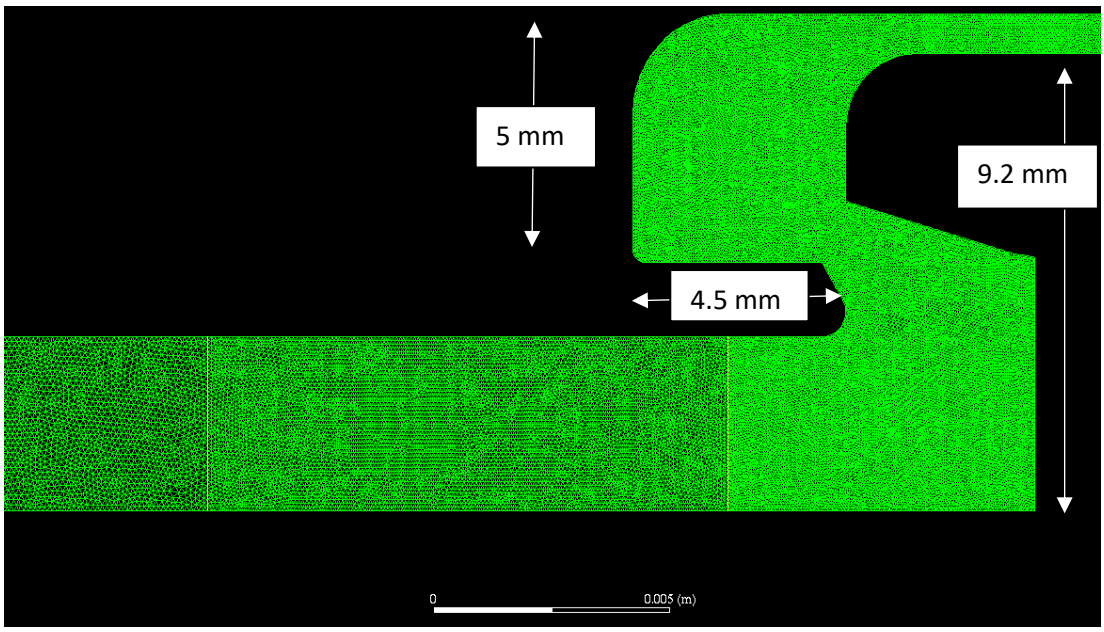

Figure 5.33 – 2D Mesh Density Progression for Zones 1, 2 and 3 at 4mm

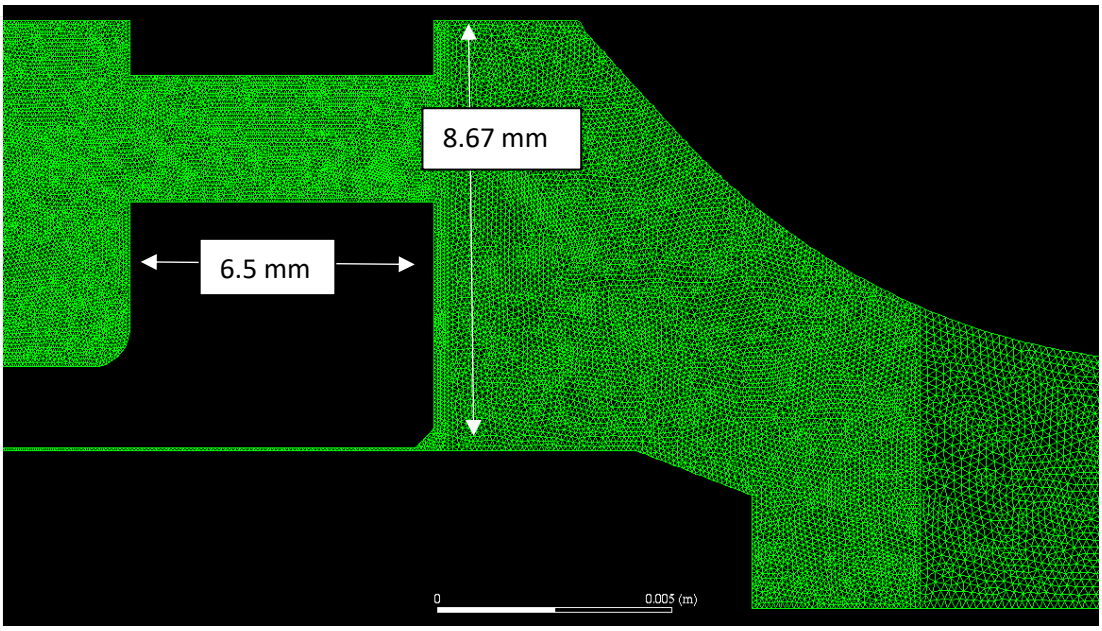

Figure 5.34 – 2D Mesh Density Progression for Zones 4, 5 and 6 at 4mm

Figure 5.34 highlights the mesh which generated for the 3 computational zones 4, 5 and 6 which include a gradual coarsening of the mesh from the modified gland geometry towards the outlet of the PRV. A finer mesh was selected for

the gland region due to the contraction of the flow area which would result in bulk flow redirection and generation of vortices which would affect backpressure prediction. Zones 5 and 6 towards the outlet however do not cause significant changes in the flow and only facilitate the passage of choked flow towards the outlet therefore a reduction in mesh density was applied.

During the meshing stage it was necessary to establish named selections for the appropriate boundary conditions to be applied within the FLUENT solver. For 2D simulation, symmetry is utilized by applying an axis condition shown earlier in figure 5.30, however in addition, it was required to select the disc surface which would be revolved in the solver to predict disc force and allow a surface monitor to be created. The 2D edges selected for the disc within the computational domain is shown in red within figure 5.35.

Figure 5.35 – 2D Edge Selection for the 5231BX PRV Disc (red) in FLUENT

To minimize computational expense, it was necessary to conduct a mesh independence study; in-particular for zone 3, as refinement in the other zones was found to have a negligible effect in comparison. The results from the mesh study is shown within table 5.16 for a range of element sizes for the disc/seat interface area. It should be noted that for this mesh independence study the K-Omega SST turbulence study was used for the PRV set at 4mm lift as it

offered the most conservative method of determining the minimum required mesh density to achieve a solution which is unaffected by mesh density.

Mesh Type	**Force (N)**	**Mass Flow Rate (kg/s)**
Coarse (113850 Elements)	87.97	0.09246
Medium (125291 Elements)	74.55	0.09142
Fine (150453 Elements)	75.1	0.09101
Finest (459177 Elements)	76.19	0.09102

Table 5.16 –Results of Mesh Convergence Study for PRV at 4 mm Lift

It could be seen that for the coarsest mesh, the force reported by the model was much higher than the value calculated by the finer meshes. A notable, but less significant difference was also found for the mass flow rate when comparing the coarse mesh with the higher mesh density alternatives. Since this region has a major influence on the piston face pressure distribution and hence the flow force, the detailed flow conditions were further examined and are indicated in figures 5.36 and 5.37.

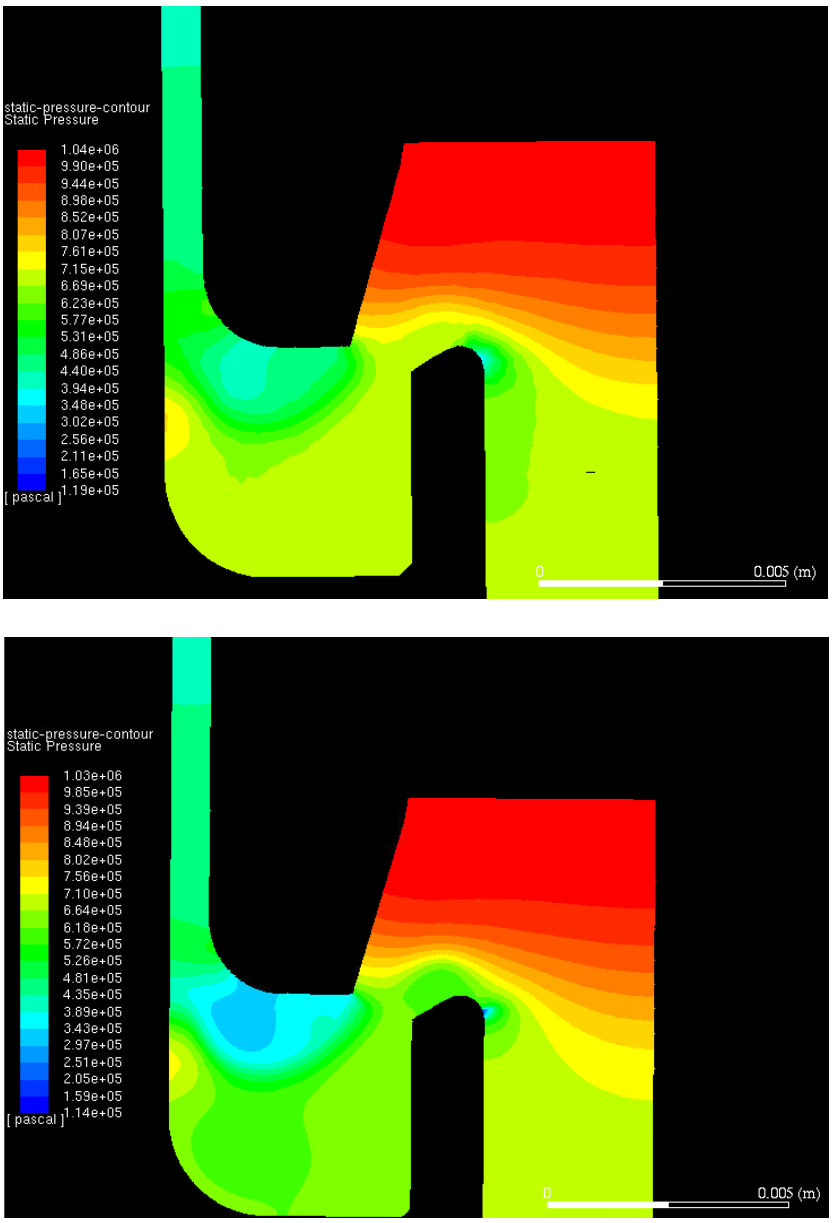

Figure 5.36 – 2D Contours of Static Pressure Comparison at 4 mm Disc Lift for Mesh Density of Coarse (Top) and Fine (Bottom) using K-Omega SST

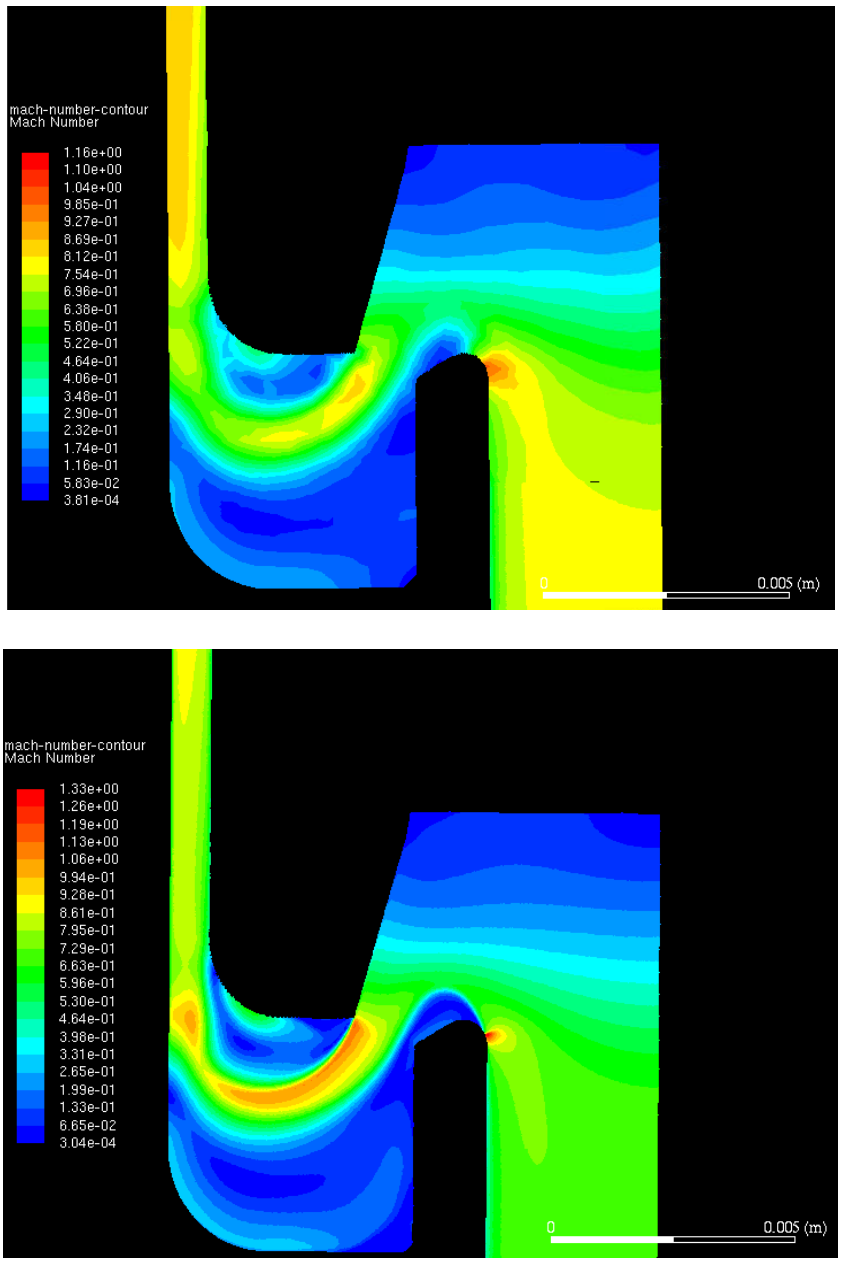

Figure 5.37 - 2D Contours of Mach Number Comparison at 4 mm Disc Lift for Mesh Density of Coarse (Top) and Fine (Bottom) using K-Omega SST

By comparing the static pressure contour plots between the “Coarse” mesh size to the “Fine” mesh size it was possible to identify key differences in the pressure profile between the two meshes. It was possible to appreciate a large difference in magnitude and size of the low pressure zone at the outer radial face of the disc. This would result in the coarser mesh predicting a higher

aerodynamic disc force when compared to the finer mesh where the force acting on the outer radial face of the disc would be noticeably lower as can be seen in table 5.16. This mesh based phenomenon can be further explained from figure 5.37, where it is clear that there was a significant reduction in resolution of the general bulk flow features calculated by the solver for the coarse mesh when compared with the fine mesh. This is especially true when observing the separation points of the jet in the disc/seat interface, where it can be seen that the separation point is delayed for the coarse mesh; causing a difference in sizes of the recirculation areas. As a result, the bulk flow pattern was much less structured for the coarser case which reduced the size of the recirculation zone beneath the outer face of the disc hence increasing the static pressure and disc force. On the other hand, the finer mesh exhibited a well-defined and expected bulk flow pattern and shape which in turn results in a larger recirculation and low pressure area beneath the outer region of the disc causing a lower disc force to be predicted.

From table 5.16, it was obvious that there was a dependency in predicting the low pressure region with mesh density and was the most significant factor in achieving a mesh independent model when using the K-Omega SST model in 2D. However, it was found that a mesh independent solution could be achieved with a “Fine” element size of 50 microns used in zone 3 with negligible effect on both disc force and mass flow rate with further increases in mesh density. As a result, for the remainder of 2D modelling research in this chapter an element size of 50 microns will be used for zone 3 alongside the mesh element sizes for the remaining zones which are shown in table 5.17.

This work however highlights a significant dependency of the mesh on the final solution which wasn’t an issue with the 3511E Broady PRV CFD research performed earlier. This is because the Broady PRV was sensitive to the disc geometry which would affect the shape of the jet and separation point however the Henry 5231BX PRV would appear to have significant numerical sensitivity

in the ability to predict the low pressure region. Therefore similarly to the Broady PRV, it would be crucial to correctly predict the flow physics in the disc/seat area in order to achieve an accurate solution.

Mesh Zone and Description	**Mesh Independent Element Size**
Zone 1 – Lower Inlet Region	100 Microns
Zone 2 – Upper Inlet Region	75 Microns
Zone 3 – Disc/Seat Interface Region	50 Microns
Zone 4 – Modified Gland Region	75 Microns
Zone 5 – Lower Outlet Region	100 Microns
Zone 6 – Upper Outlet Region	150 Microns

Table 5.17 – 2D 5231BX PRV Zonal Mesh Independent Element Sizes

In addition, it was necessary to report the mesh metrics for the mesh independent model to ensure that the mesh would be appropriate for CFD and not be vulnerable to excessive diffusion or instability during calculation. The mesh metrics for the 5231BX mesh independent solution is shown in table 5.18 where all metrics were to an appropriate standard for CFD modelling [52].

Mesh Metric	**Value**
Average Orthogonal Quality	0.97
Average Aspect Ratio	1.19
Average Skewness	0.051
Total Number of Elements	150453

Table 5.18 – 2D 5231BX PRV Final Mesh Independent Metrics at 4 mm Lift

5.2.3 2D CFD Modelling Procedure and Results of 5231BX PRV

By using the lessons learned during the development of the CFD modelling procedure for the Broady 3511E PRV validation the use of a similar numerical modelling procedure was to be followed for the 5231BX PRV study. Settings such as the use of the pressure based solver and coupled pressure-velocity coupling scheme were to be inherited from the Broady modelling methodology as their suitability were determined to meet similar flow characteristics between the two PRV's. Furthermore, the research performed previously at Strathclyde [11, 12] strongly indicated that the pressure based solver was capable of achieving an accuracy similar to the density based solver. In addition, for spatial discretization the QUICK Scheme as well as second order terms for pressure and least squares cell based scheme to capture gradients were used. Model settings however, such as choice of Courant number and Under Relaxation Factors (URF's) were investigated to determine the most appropriate values to achieve a good balance between numerical stability and convergence time. In addition, the use of both the K-Omega SST turbulence model and Standard K-Epsilon model allowed a comparison to be made between the two models as previous studies by both Alshaikh and Elmayyah adopted the K-Epsilon turbulence model.

The numerical settings which were applied within both the solution methods and controls tab within ANSYS FLUENT are given within table 5.19.

FLUENT Setting Type	**Recommended Setting**
Solver Type	Pressure Based
Turbulence Model	K-Omega SST and Standard K-Epsilon
Air Density	Ideal Gas Law (Energy Equation ON)
Pressure-Velocity Coupling Scheme	Coupled
Spatial Discretisation - Gradient	Least Squares Cell Based Scheme
Spatial Discretisation (Pressure)	Second Order
Spatial Discretisation (Other Terms)	QUICK
Initial Flow Courant Number	5
Momentum, Pressure, Density and Energy URF's	0.2

Table 5.19 – 2D Final solver settings for use across full lift range

In addition to the settings illustrated within table 5.19, it was necessary to determine a consistent set of boundary conditions to apply across all lift conditions for the 2D model. A significant variation for the 2D model when compared to the 3D model developed for the Broady PRV was that the use of an axis boundary condition was necessary as shown within figure 5.30 to mathematically revolve the bulk flow features by 360 degrees. However an obvious downside of such an approach would be the fact that 3D flow effects would be ignored which could cause significant modelling inaccuracy if not carefully reviewed. Both Alshaikh and Elmayyah found that the 2D model was satisfactory for achieving accurate CFD models however the 5231BX geometry used within this study is different to the through flow type PRV's in which they studied and represents an in production PRV at the time of writing.

For all lift conditions, the boundary conditions applied were as follows;

- Gauge Total Pressure Inlet of 10.3 Barg – which represented vessel pressure, with the zone positioned at the inlet face (figure 5.30)
- Gauge Pressure Outlet of 0 Barg – which represented atmospheric exhaust, positioned at the outlet face of the valve (figure 5.30).
- Temperature at both inlet and outlet – 295K or 22 ^{0}C
- No slip shear condition on stationary, adiabatic valve walls
- Axis boundary condition applied for 2D axisymmetry (figure 5.30)
- Operating Conditions – 1 Bar (to offset pressure bc's to gauge)

For all simulations, high order term under relaxation was used to provide stability during the initial stages of the simulation, especially when using higher order spatial discretisation terms which could lead to unphysical results, and help to prevent divergence [56]. It was also important to follow recommended CFD guidelines and initialise the solution with first order upwind spatial discretisation terms before switching to a higher order scheme after 100-200 iterations. As proven with the research for the Broady PRV, this was effective in preventing convergence stalling through due to poor numerical initialisation. It should be noted that FLUENT's hybrid initialisation was used for all cases due to its greater resilience when compared with the standard scheme. The residuals required for the simulation to be classified as converged required to be below 10e-6 for the energy equation and 1e-3 for all other terms and/or exhibit residual stability. To achieve a fully converged solution it was also required to create surface monitors for disc force as well as mass flow rate at the PRV inlet in which constant values of each variable was needed.

For turbulence model comparison between the standard K-Epsilon and K-Omega SST models it was necessary to produce 2D simulations at a range of lifts and compare with the experimental results for the modified gland. The results for both flow force prediction and mass flow rate with changes in lift is

shown within figures 5.38 and 5.39. It can be clearly seen that neither model was able to produce the accuracy which were indicated by earlier 2D work of both Elmayyah and Alshaikh. For flow force prediction at low lift, it can be determined that the K-Omega SST provided better performance than the K-Epsilon model however at higher lifts the K-Omega SST model reported significant under prediction of the disc force value. The K-Epsilon model on the other hand was able to remain at a similar peak force value however the data points from figure 5.38 remained significantly different from the experimental results and was not able to capture the flow force characteristics of the PRV.

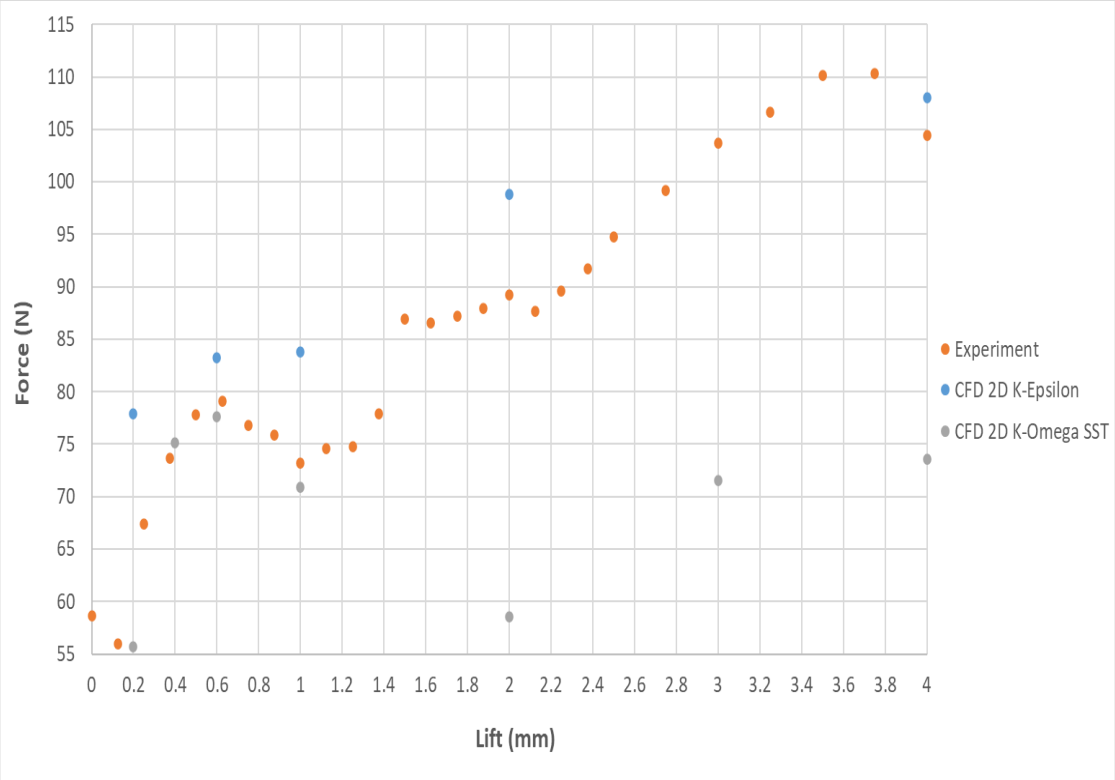

Figure 5.38 – 2D Disc Force vs Lift Turbulence Model Comparison

The mass flow rate prediction within figure 5.39 highlights that both turbulence models were capable however of producing approximately similar results to the experimental values which generally agreed with the findings of previous 2D CFD research for through flow PRV's.

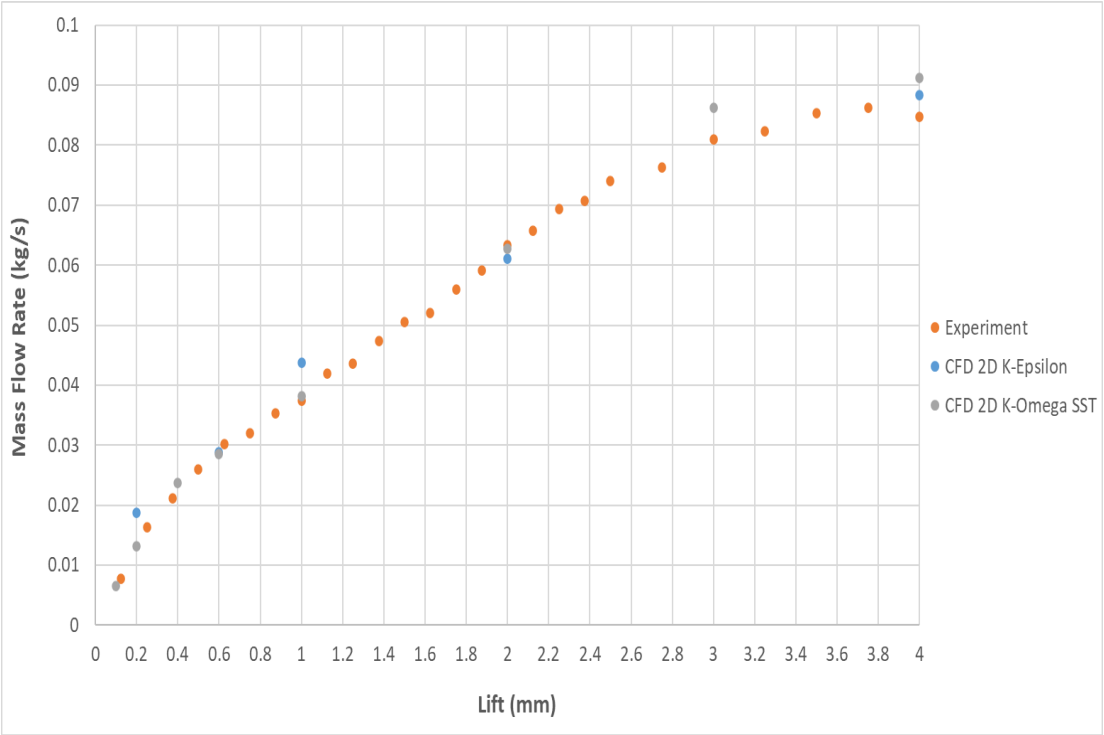

Figure 5.39 - 2D Mass Flow Rate vs Lift Turbulence Model Comparison

The surprisingly significant differences in the prediction of disc force however was of concern as it had not been previously observed. Therefore it was of critical importance to identify if the cause of the difference was due to experimental error and modelling error, or both. On the other hand it could also be a result of a physical flow phenomenon which was not identified in previous research. Initially the back pressure which acts on the outlet facing edges of the disc was studied as a significant variation in the back pressure would directly affect the predicted aerodynamic disc force; the results are shown within figure 5.40. The results shown however highlighted that the backpressure predicted by both turbulence models were generally similar in value and accurate to the experiment, especially at high lifts where the greatest difference in disc force was found.

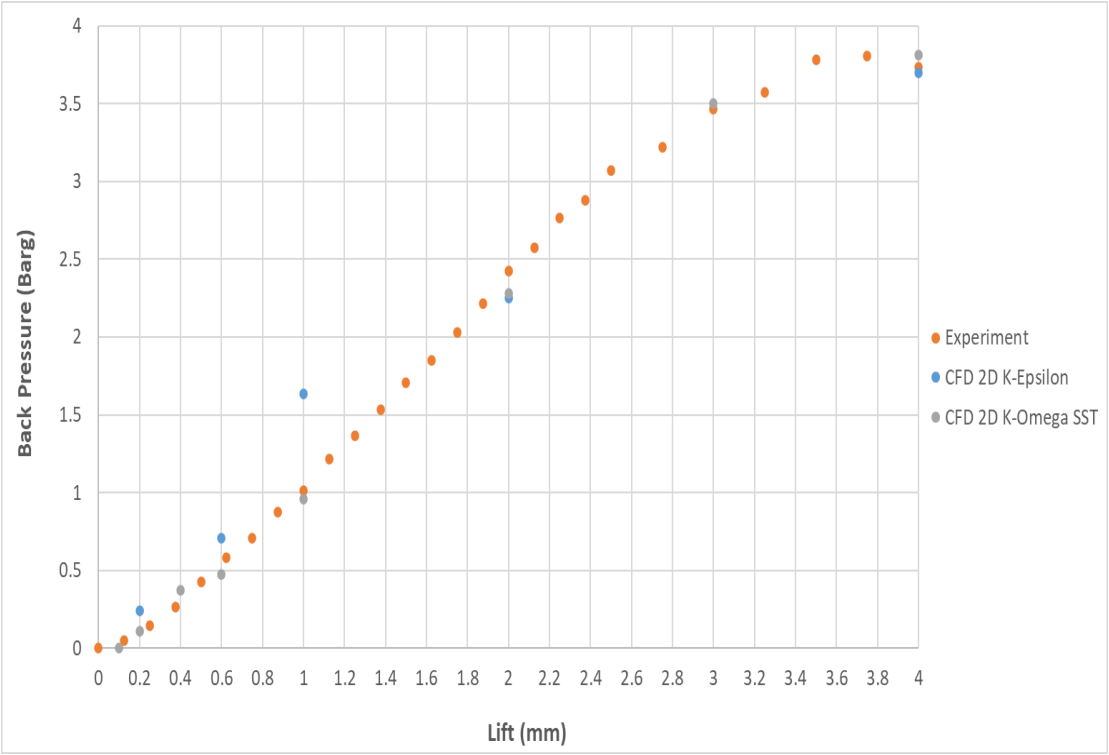

Figure 5.40 – 2D Back Pressure vs Lift Turbulence Model Comparison

A comparison shown in figures 5.41 and 5.42 was made regarding the pressure profile and Mach number around the modified gland and outlet geometry at 4 mm lift to ensure flow similarity between the turbulence models.

It can be established from figures 5.41 and 5.42 that both turbulence models were capable of predicting a similar flow pattern and back pressure profile which would produce the similarities shown within figure 5.40. This suggested that the issue was associated with the front face of the disc and disc/seat interface flow area. Thus, the prediction of the 2D pressure profile and flow structure produced by each turbulence model on the front face was compared at high lifts of 4mm, where the greatest differential between the two approaches occurred at this point.

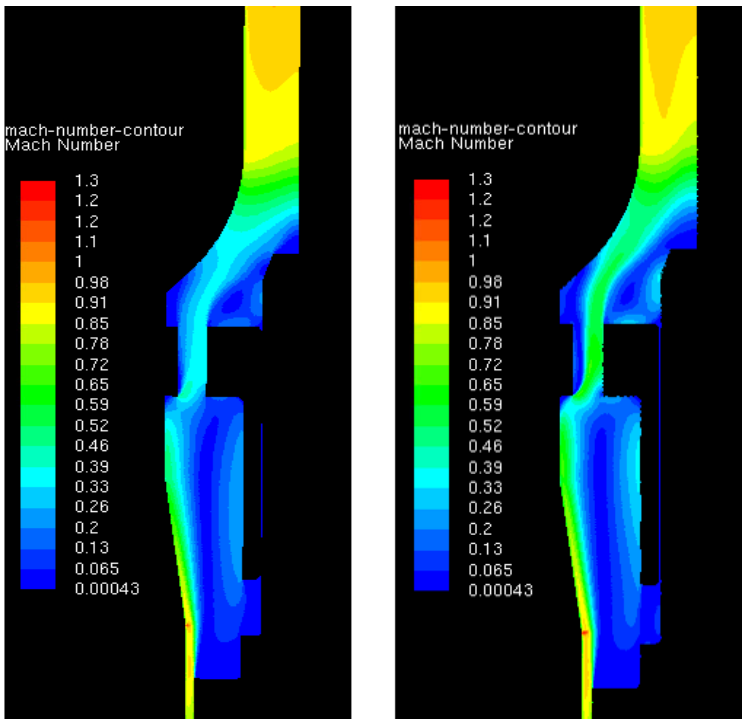

Figure 5.41 – 4 mm Mach Contour (K-Epsilon left, K-Omega SST right)

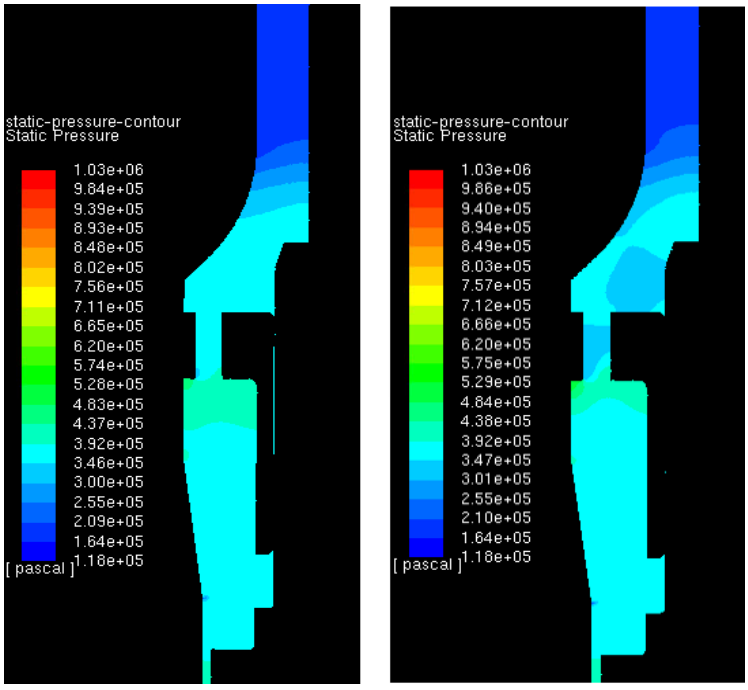

Figure 5.42 – 4 mm Static Pressure Contour (K-Epsilon left, K-Omega SST right)

In figures 5.43 and 5.44 a side by side comparison is shown with the results of the standard K-Epsilon model on the left and the K-Omega SST model on the right as before.

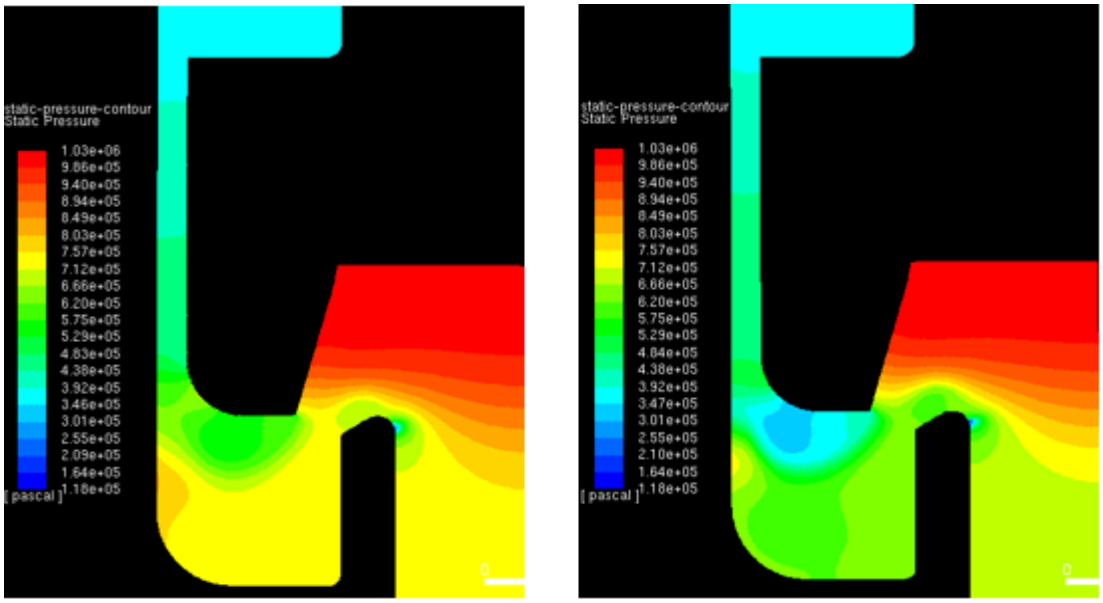

Figure 5.43 – 4 mm Static Pressure Contour (K-Epsilon, K-Omega SST)

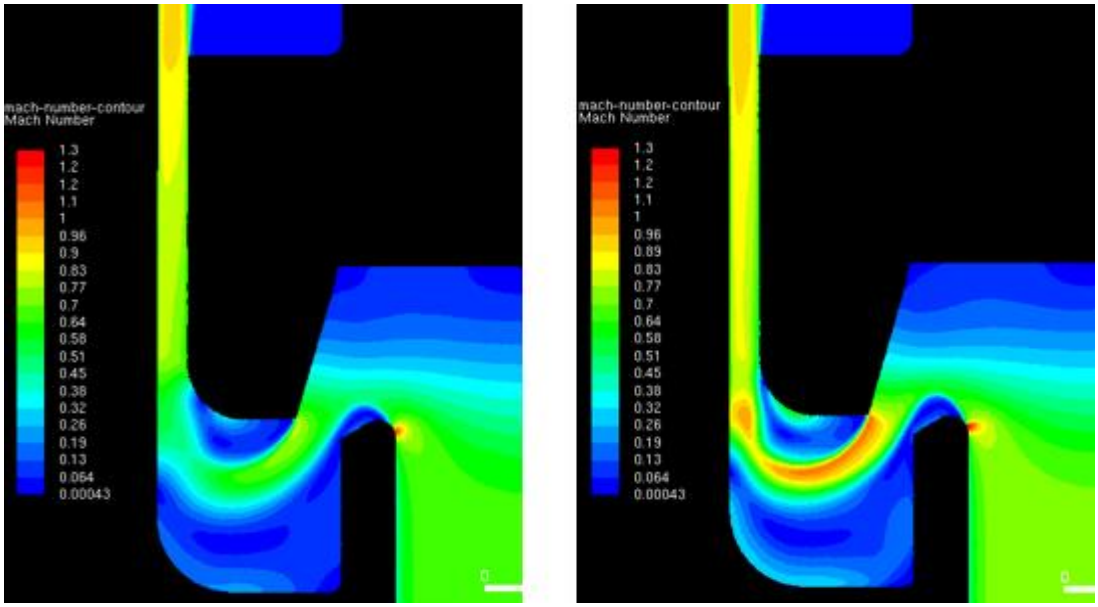

Figure 5.44 – 4 mm Mach Number Contour (K-Epsilon, K-Omega SST)

it can be observed from figure 5.43 that the low-pressure region mentioned earlier was produced at the outer region of the disc surface for the K-Omega SST turbulence model but was not produced to the same degree using the K-Epsilon turbulence model. Furthermore, the lower cavity pressure remained higher for the K-Epsilon model suggesting a difference in flow structure. On the other hand however, the pressure loss profile in the annulus of the disc and body was similar resulting in the backpressure value to be similar at the outlet side of the disc as was shown in figure 5.42.

As suggested in the differences within the static pressure contour plot in figure 5.43, a significant difference in flow structure can be observed for the Mach number contour plot in figure 5.44. The K-Omega SST model is capable of producing a much more defined jet structure as the flow is turned through the geometry of the disc/seat interface in which there are clear regions of separation and recirculation. There is a higher Mach number predicted across the lower cavity in the outer region for the K-Omega SST model which accounts for the difference in static pressure observed in figure 5.43. However, more importantly from a force prediction stand point, there is a noticeable difference in the Mach number of the recirculation region at the outer radial region of the disc for the K-Omega SST model as well as a difference in reattachment point of the flow as it is conditioned by the annulus region. This therefore would cause a substantial difference in aerodynamic disc force as was recorded in figure 5.38 where the K-Omega SST model reported a force decrease of 30N when compared to the K-Epsilon model at 4 mm lift. The results observed in figures 5.43 and 5.44 indicate either a deficiency of the 2D modelling or of the turbulence model to accurately capture the flow physics in the PRV correctly. As a result, it was deemed appropriate to develop a 3D model in which the performance of both turbulence models, and in particular the K-Omega SST model will be compared to their 2D equivalent. This work will be performed later in this chapter.

Before performing 3D CFD work however it was of critical importance to ensure the accuracy of both the experimental and 2D CFD modelling approaches. This was achieved by using the PRV used in previous research by Alshaikh [12] as a base model in which both the experimental equipment and method as well as 2D CFD meshing and modelling methodology would be applied to and compared to the accuracy and performance observed by Alshaikh. Alshaikh was generally able to predict air mass flow rate and piston force accurately across all lift ranges with his 2D CFD model to within 5%, however significantly he found that there was up to a 9% variation with experimental results when predicting back pressure at higher lifts. This is of critical importance, as if back-pressure is not captured correctly; the accuracy of overall piston force would be affected.

Furthermore, by comparing the production size outlet to Alshaikh's larger outlet it could be established if the use of the production size outlet was causing the differences in CFD performance which wasn't observed by Alshaikh. The key differences in geometry between Alshaikh's study and the current was the use of a different gland and a larger outlet by Alshaikh; 16mm internal diameter, compared with an internal diameter of 13.6mm.

The decision of Alshaikh to use a larger outlet was made due to the nature of the experimental rig he developed which is shown in figure 5.45. It can be observed the Alshaikh used a rod to connect the disc (piston) to the load cell however the rod and connection to the disc was of equivalent diameter to the disc in order to prevent buckling and maintain rigidity of the rig. However in work performed so far in this validation study, it has been demonstrated that the diameter of the rod can be substantially reduced and by using a tapered shape is capable of maintaining suitable strength and rigidity for testing. However due to the larger diameter of the rod used by Alshaikh, it was decided in his work to use a larger diameter outlet to achieve suitable clearance. Furthermore the gland in which he used is shown within detail A in figure 5.45

which is much simpler than the gland developed earlier. It is significantly different as the gland protrudes into the jet produced by the annulus of the disc and body causing the flow to deflect more substantially than the newly developed gland.

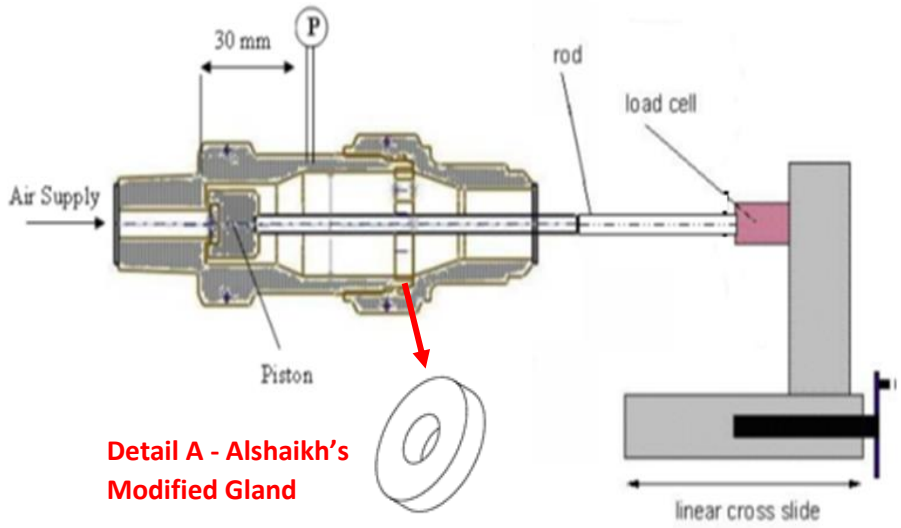

Figure 5.45 – Experimental Rig Used By Alshaikh with Modified Gland [12]

Experimental testing was carried out in this study using the previously developed experimental equipment and methods however the disc with larger rod connector, larger diameter rod and larger internal dimeter outlet of 16 mm will replace the previously used disc, rod and 13.6 mm internal diameter outlet.

In addition to modifying the experimental set up it was necessary to make the appropriate changes to the gland, rod and outlet within the CFD model using geometry modeler in ANSYS Workbench. The changes made can be clearly seen in figure 5.46 where it can be appreciated that the previous modelling methodology has been maintained with a zonal mesh discretization approach to increase computational efficiency. However an identical value of mesh sizing was used to the original geometry. Axisymmetry was achieved by using

the green edge highlighted within figure 5.46 and applying an axis boundary condition. The simplified gland geometry and larger outlet can also be appreciated by studying the 2D cross section below.

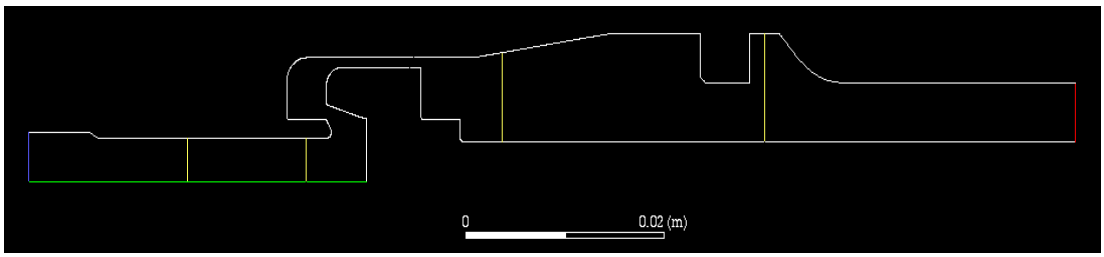

Figure 5.46 - Outline for FLUENT 2D 5231BX Computational Domain with Adaptions to Gland, Outlet and Rod to match work by Alshaikh [12]

The disc force and mass flow rate vs lift performance of the turbulence models for the Alshaikh style PRV as well as the corresponding experimental data using the modified set up is shown within figures 5.47 and 5.48.

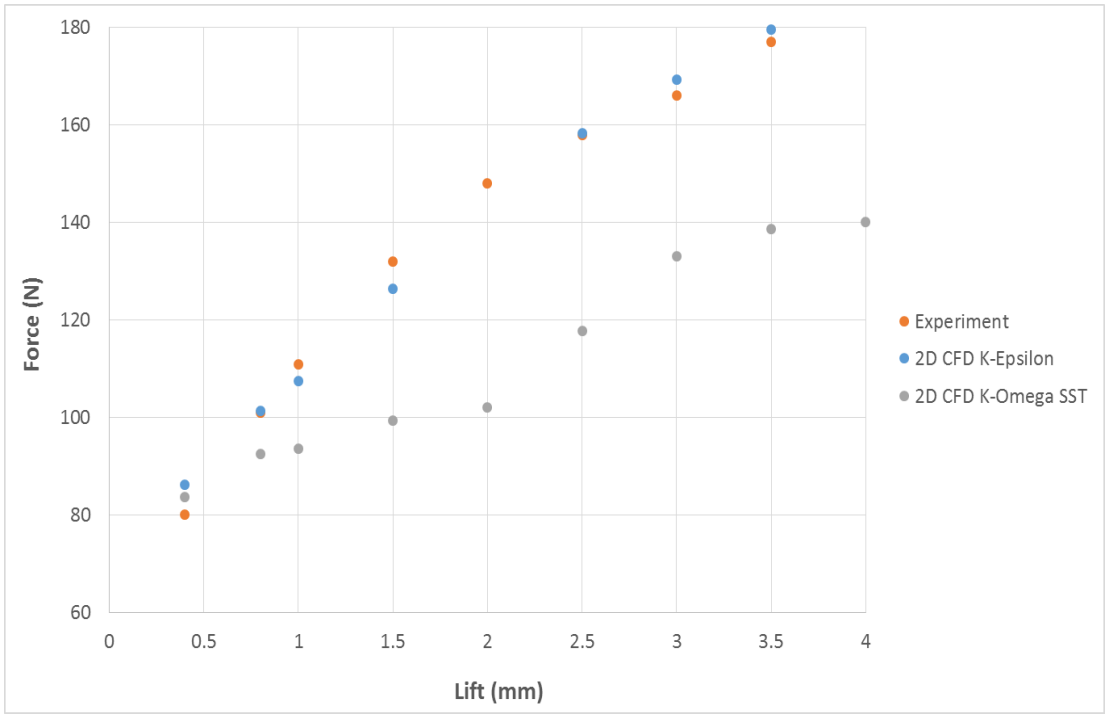

Figure 5.47 – Disc Force vs Lift Turbulence Model Comparison (Alshaikh geometry)

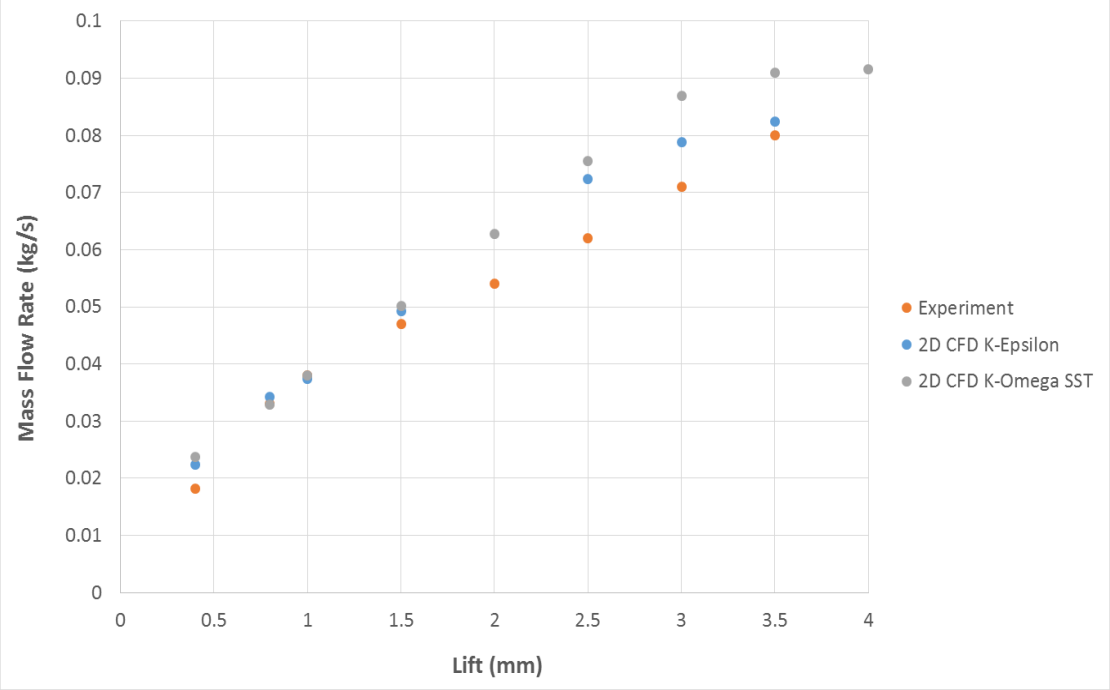

Figure 5.48 - Mass Flow Rate vs Lift Turbulence Model Comparison (Alshaikh geometry)

It can be clearly seen and as observed in the study performed by Alshaikh, the flow force prediction of the Standard K-Epsilon turbulence model was significantly better than the K-Omega SST turbulence model. The K-Epsilon model was capable of matching the experimental value well across the full lift range whereas the K-Omega SST significantly under predicted forces from 1 mm onwards. It can be also noticed that the change in gland and outlet geometry has significantly altered the flow force behavior of the PRV with a much higher peak disc force as well as a linear increase in disc force with lift when compared to the curves shown in figure 5.38 for the original geometry.

The mass flow rate comparison shown within figure 5.48 also highlights the strong performance of the 2D K-Epsilon model at predicting the flow rate performance of Alshaikh's modified geometry across the full lift range.

However interestingly, the predicted mass flow rate by both the K-Epsilon and K-Omega SST model over predicted the discharge rate at higher lift values above 2.5 mm. This effect was not noticed in the work by Alshaikh and could be due to slight differences in gland geometry and/or mesh effects as the mesh used by Alshaikh utilized less elements. In general though, the work performed in this study confirms the observation by Alshaikh for his modified geometry that the K-Epsilon model provided the best performance for predicting both mass flow rate and disc force when compared with the K-Omega model. It should be noted however that the difference in flow force predicted by the two turbulence models was greater across the full lift range for the Alshaikh type geometry, indicating that there was a dependency between geometry and turbulence model on the accurate prediction of the flow physics within the PRV. To achieve a better understanding, a comparison of backpressure took place in figure 5.49 to determine if a greater difference between turbulence models existed when compared to the study for the original geometry in figure 5.40.

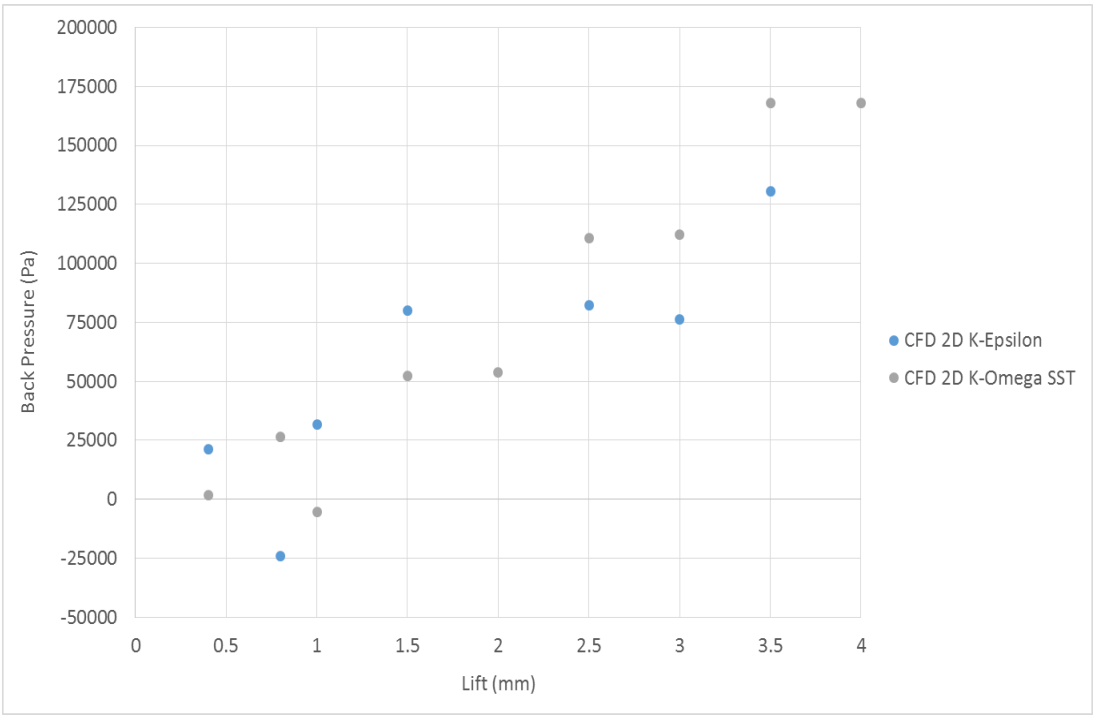

Figure 5.49 – Back Pressure vs Lift Turbulence Model Comparison (Alshaikh geometry)

Figure 5.49 indicates that there was a significantly higher variation in backpressure across the full lift range when compared with the variation shown for the original geometry (figure 5.40). By analyzing CFD contour plots of static pressure for both turbulence models within figure 5.50 it was further possible to visually appreciate the nature of the difference in pressure between both models. It can be clearly seen that in the middle section of the body in line with the end of the diverging section the static pressure for both models are similar. However a noticeable difference is clear in the region surrounding the disc in which the K-Omega SST model has a higher value of backpressure hence resulting in a lower total disc force.

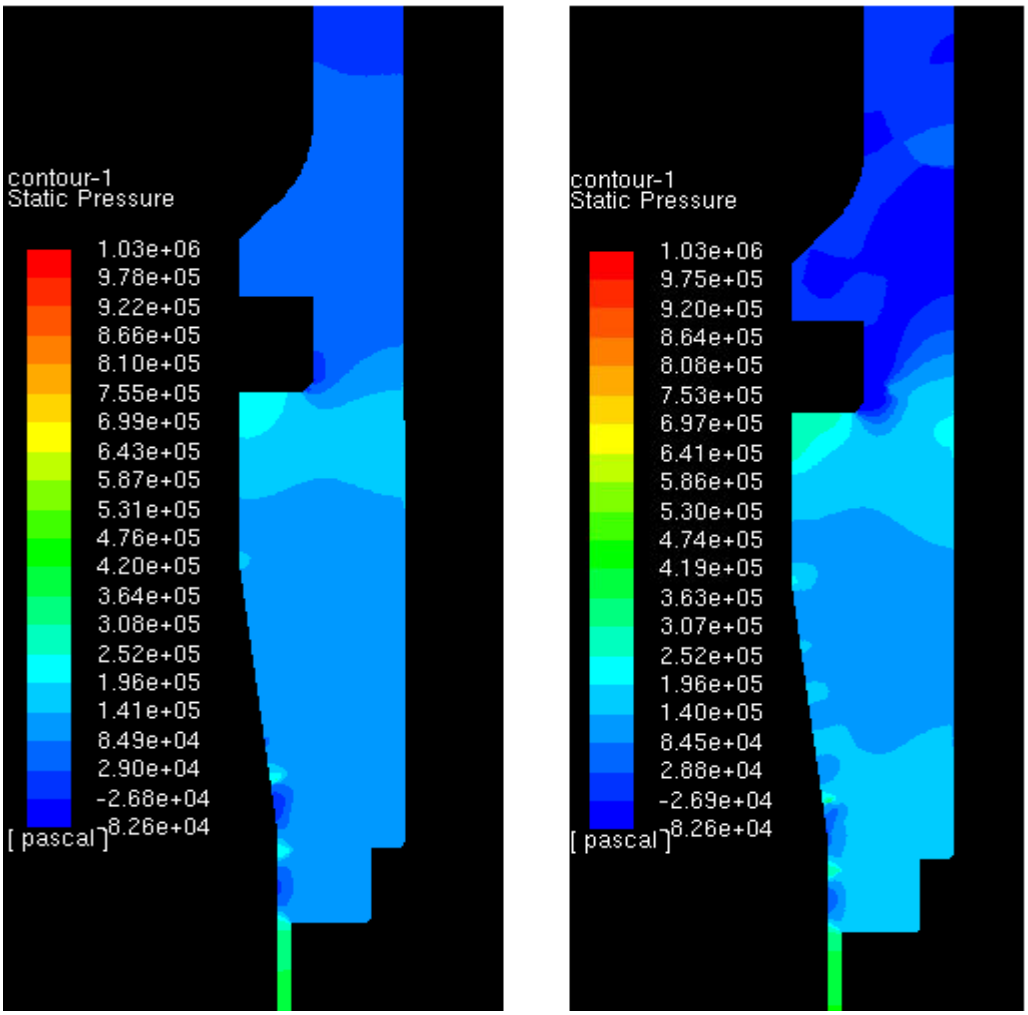

Figure 5.50 - 3.5 mm Static Pressure Contour (left- K-Epsilon, right- K-Omega SST) Alshaikh Geometry

A comparison of Mach number contours between the turbulence models is shown within figure 5.51 which helps to compliment understanding the results shown within figures 5.49 and 5.50. It can be seen that both turbulence models predict a difference in separation point and expansion as the flow passes through the gland geometry towards the outlet. As a result it can be seen in the right hand side of the PRV within figure 5.51 that the Mach number in this region is higher for the K-Omega SST model when compared to the K-Epsilon turbulence model. In addition to the contour plot, a vector plot of Mach number is shown in figure 5.52 for the highlighted region in red shown in figure 5.51 for the K-Omega SST turbulence model. This plot was produced in order to appreciate the degree of recirculation in this zone and to also understand the flow path at the right hand side of the PRV.

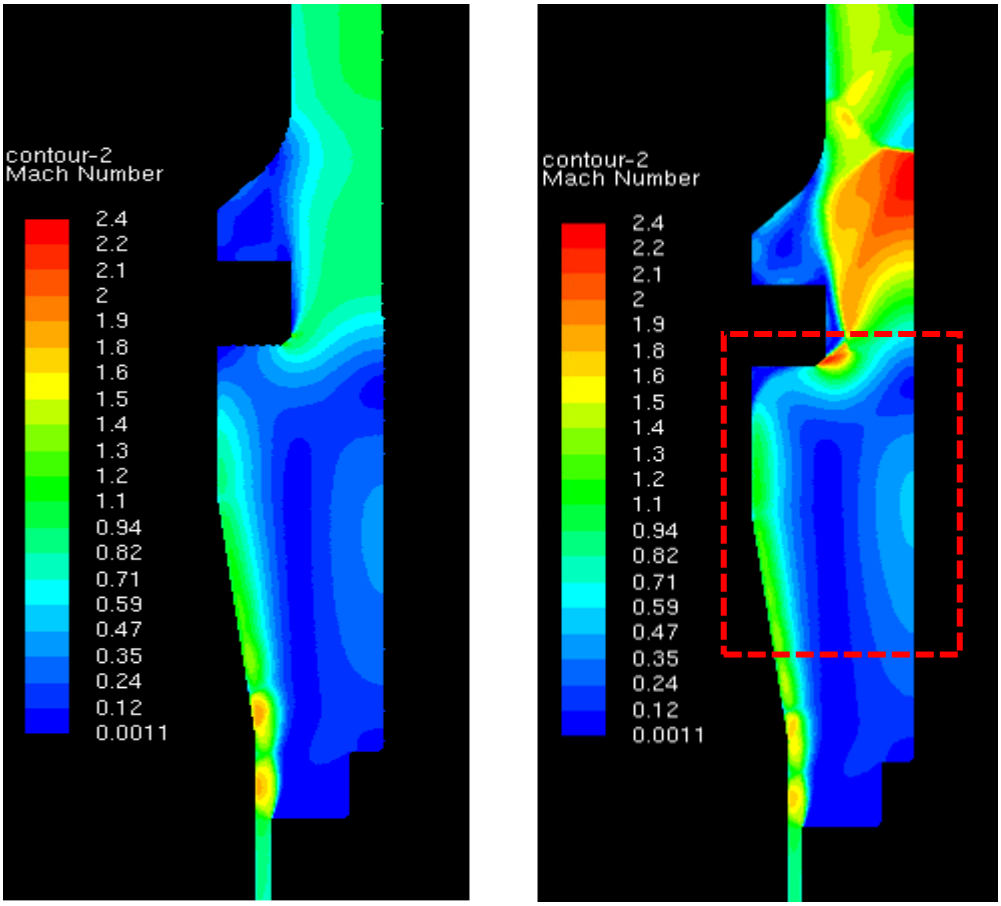

Figure 5.51 – 3.5 mm Mach Number Contour (K-Epsilon left, K-Omega SST right) Alshaikh Geometry

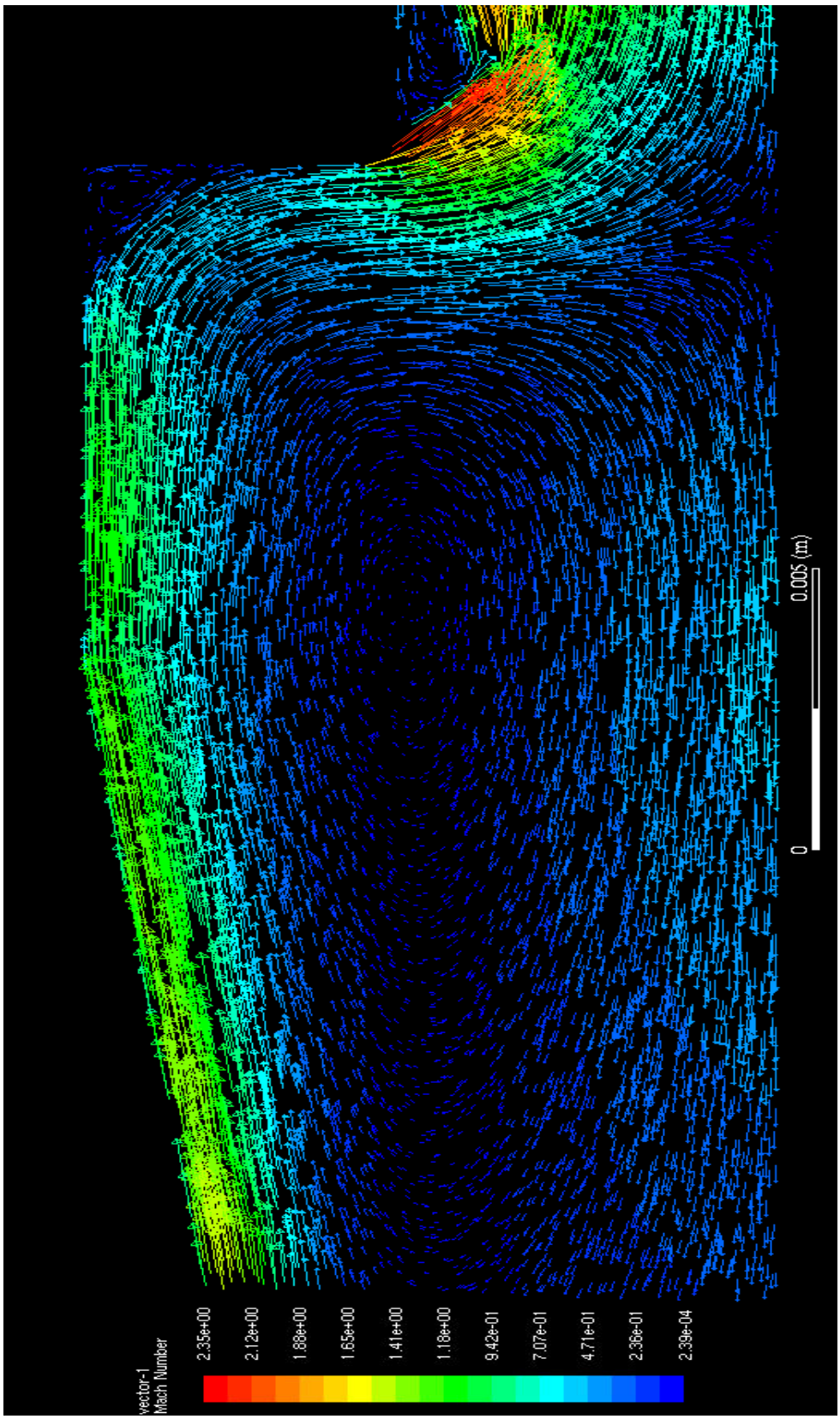

Figure 5.52 – 3.5mm Mach Number Vectors for Red section (K-Omega SST) Alshaikh Geometry

As can be appreciated from figure 5.52, on the right-hand side of the PRV the flow is travelling towards the disc surface. Therefore as the K-Omega SST model predicts a larger peak Mach number of the flow in this direction when compared with the K-Epsilon model, a higher back pressure and hence reduction in overall disc force as seen in figure 5.47. Furthermore, when studying both figures 5.51 and 5.52 it was clear that there is a noticeable difference in the expansion flow structure at the separation point near the inlet of the gland geometry. This highlights a critical difference in the ability of the K-Epsilon and K-Omega SST model in predicting separation points accurately and in detail. Typically the K-Omega SST model is known to perform much better at capturing such flow phenomena and also be more accurate for flows with strong pressure gradients as shown in figure 5.51. Therefore it could be proposed that in order to achieve confidence in the results, any inaccuracies caused by 2D modelling should be checked by performing a 3D validation study and comparing the performance of both turbulence models in a 3D domain. From figures 5.53 and 5.54, it was found that the effect of turbulence models on the flow prediction for the disc/seat interface zone was found to be similar in nature for Alshaikh's geometry as it was found in the original geometry.

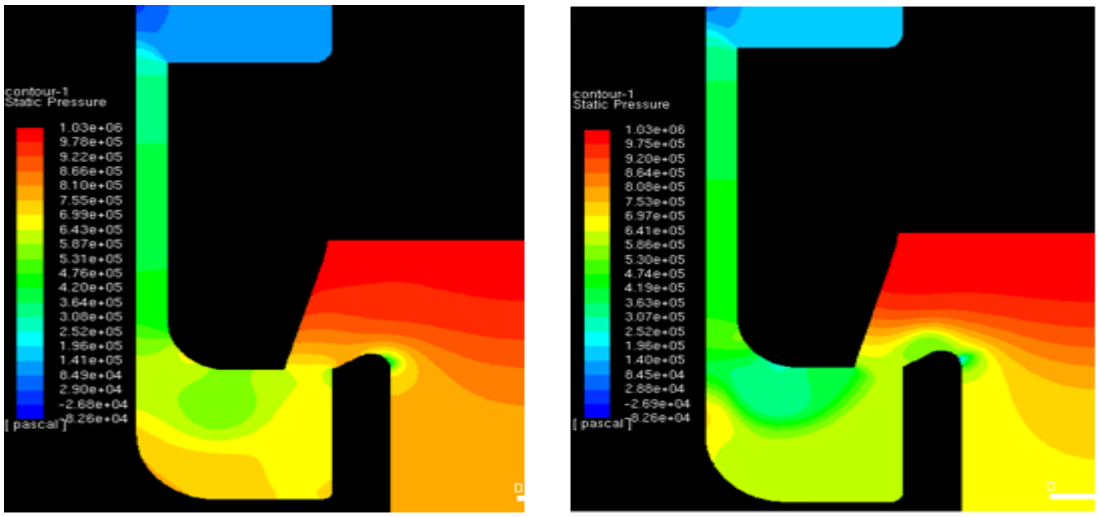

Figure 5.53 – 3.5mm Static Pressure Contour (K-Epsilon, K-Omega SST) Alshaikh Geometry

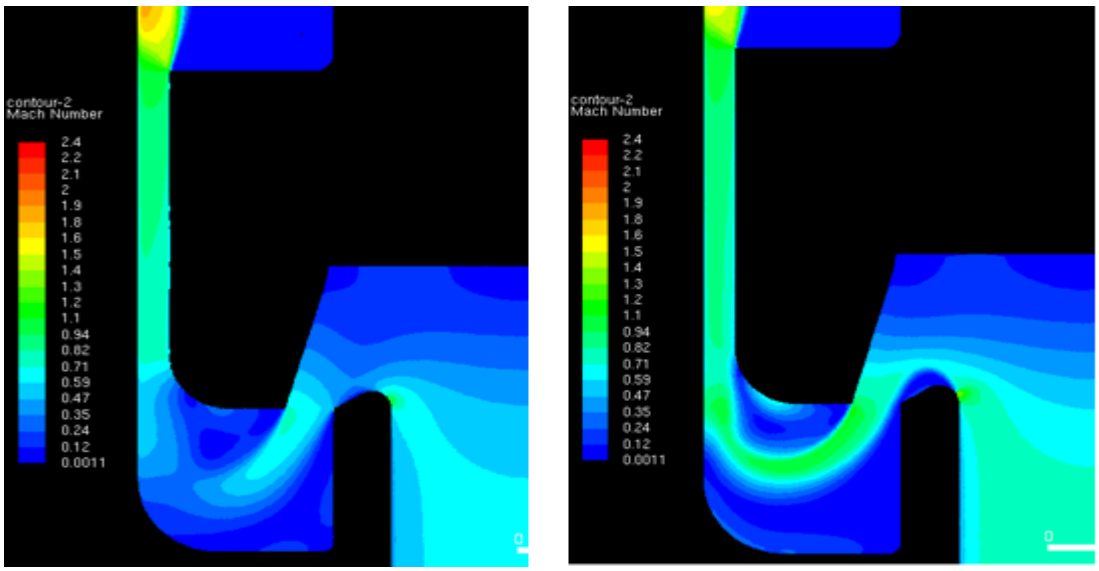

Figure 5.54 – 3.5mm Mach Number Contours (K-Epsilon, K-Omega SST) Alshaikh Geometry

It is indicated within these results that the changes of the gland, rod and outlet geometry for the Alshaikh style 5231BX PRV had a significant effect on the bulk flow features and the corresponding ability of the turbulence models to accurately predict aerodynamic disc force and mass flow rate. It was also determined that the accuracy of both the experimental facility and CFD modelling methodology were comparable with the observations found by Alshaikh for his geometry. This in turn validates the work which was performed for the original outlet geometry earlier in this study. As a result, a 3D validation study as recommended in the work of both Alshaikh and Elmayyah will be discussed in the next section in order to determine if the accuracy of the 2D model for the original 5231BX geometry with modified gland will improve when utilizing 3D modelling techniques. In addition, it will be important to compare the performance of both the standard K-Epsilon and K-Omega SST turbulence models to determine if any performance differences are caused by the change from a 2D computational domain to 3D. Furthermore, sensitivity to both turbulence modelling and mesh density has been shown for the low pressure zone at the lower outer disc region therefore it will be important to identify if the zone suffers any sensitivity to 3D modelling.

5.2.4 Development of 3D CFD Model for 5231BX PRV

As a result of the poor performance of the 2D CFD model to achieve an equivalent accuracy for the smaller, production sized outlet to the Elmayyah and Alshaikh results for simplified PRV geometries; a 3D CFD study was carried out to determine if an improvement in model prediction could be achieved. ANSYS FLUENT 18 was used alongside both a local desktop with 64GB of RAM and Intel Xeon E5-1620 processor as well as an HPC cluster called ARCHIE WeST at the University of Strathclyde. The HPC was required due to the significant mesh size required for Henry 5231BX when compared to only the local desktop for the Broady Valve which required a coarser structured mesh due to the simplicity of its geometrical and flow features. For all 3D simulations for the 5231BX on the ARCHIE WeST supercomputer, 280 Intel Xeon Gold 6138 cores with 192GB of RAM per node (40 cores) was utilized. A calculation time of approximately 10-22 hours depending on mesh size and lift was necessary for converged steady state solutions to be achieved.

In a similar manner to the 2D modelling performed earlier, initially a simulation was required to compare mesh densities to achieve a mesh independent solution. For this study the original gland will be used and compared with experimental data of the original gland for both the Standard K-Epsilon and K-Omega SST turbulence models. This will allow the most suitable choice of turbulence model to be selected for future modelling. As a starting point, once both a validated mesh density and turbulence model was selected for the original gland (figure 5.20) geometry, the mesh and numerical modeling procedure was extended to the modified gland geometry as well as the altered geometry for the Alshaikh validation. This would provide an opportunity for the performance of 3D modelling to be directly compared to 2D modelling results as well as gland geometry to identify if any differences could be observed. For all 3D cases it was decided to use quarter symmetry to minimize computational cost but maintain a sufficient 3D domain to capture the presence of any 3D

flow effects predicted within the simulation. The general 3D quarter symmetry CFD domain of the 5231BX PRV with modified gland (figure 5.32) is shown within figure 5.55 as within this thesis, the modified gland geometry will be predominantly used. However it should be noted that the form of both the original gland and Alshaikh modified geometry followed the general domain and mesh discretization as shown in the upcoming sections. The zones were created with a combination of extrusions, slicing and Boolean commands within the geometry modeler within ANSYS Workbench. The numbering structure shown within figure 5.55 corresponds to the zones described for the 2D model in figure 5.30.

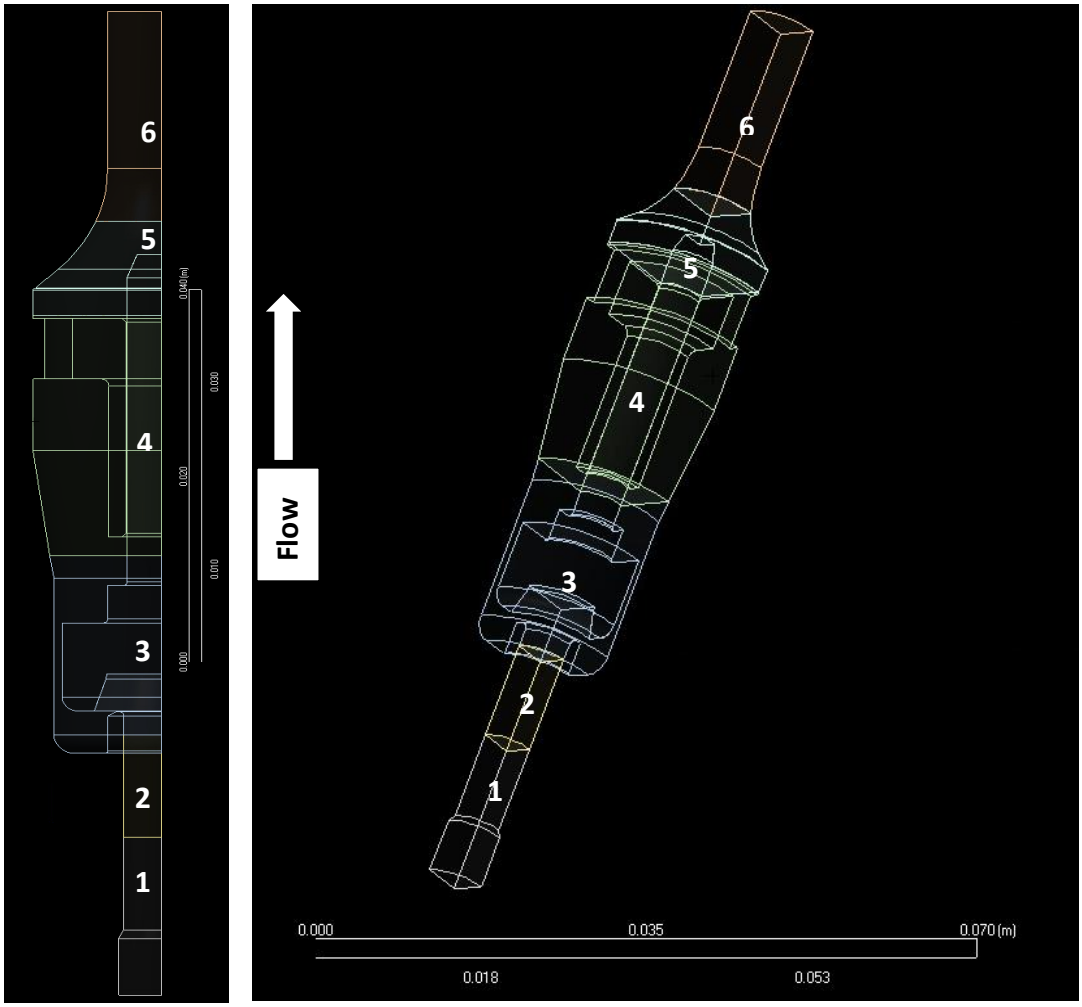

Figure 5.55 – Quarter Symmetry 3D CFD Domain (Mod Gland) at 4mm Lift

It can be clearly seen that a domain splitting method was adopted using inspiration from the 2D modelling procedure to improve computational efficiency by allowing greater control over mesh density with 6 discrete zones. Furthermore when meshing, additional refinement was added in order to further blend the dense mesh within zone 3 (disc/seat interface) to zone 4 (gland region). For 3D simulations, due to the significant increase in both computational and memory requirements when compared with 2D; a domain discretization approach such as this is critical to achieve a sensible 3D model which could be utilized by industry. The validated 2D principle for discretization density was similarly applied to the 3D geometry in deciding what refinement would be required for the disc/seat interface (zone 1) and least refinement required for the outlet (zone 6). However due to computational demands it was important to increase the local element size to feasible values where a mesh independency study could be performed to achieve a suitable density.

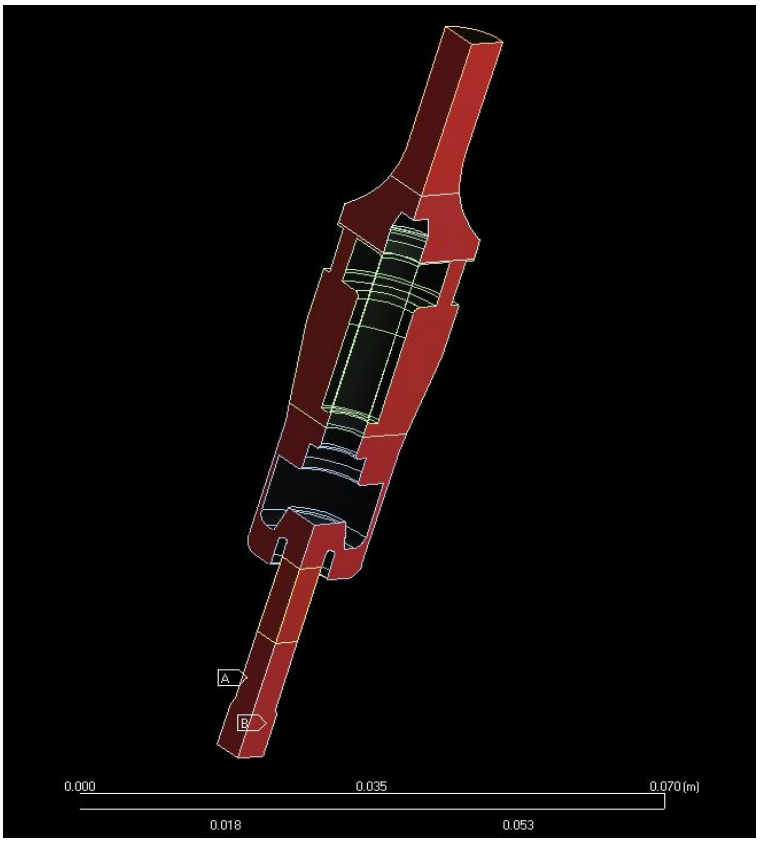

Figure 5.56 – Surface Selection for Quarter Symmetry on XZ and YZ Planes

Quarter symmetry was applied to the model by creating a symmetry named selection at the faces for both symmetry planes as shown in red within figure 5.56. By doing so it was simple to apply symmetry conditions within the FLUENT solver and would also provide 2 surfaces for post processing to occur which would provide insight towards the flow structures within the PRV.

In addition to the named selection of the symmetry faces it was necessary to identify the external and internal walls of the 3D domain for no slip boundary conditions to be applied. For the disc, it was important to identify the internal walls by using the wall selection shown in red within figure 5.57 whereby aerodynamic forces acting on the disc could be calculated easily by FLUENT.

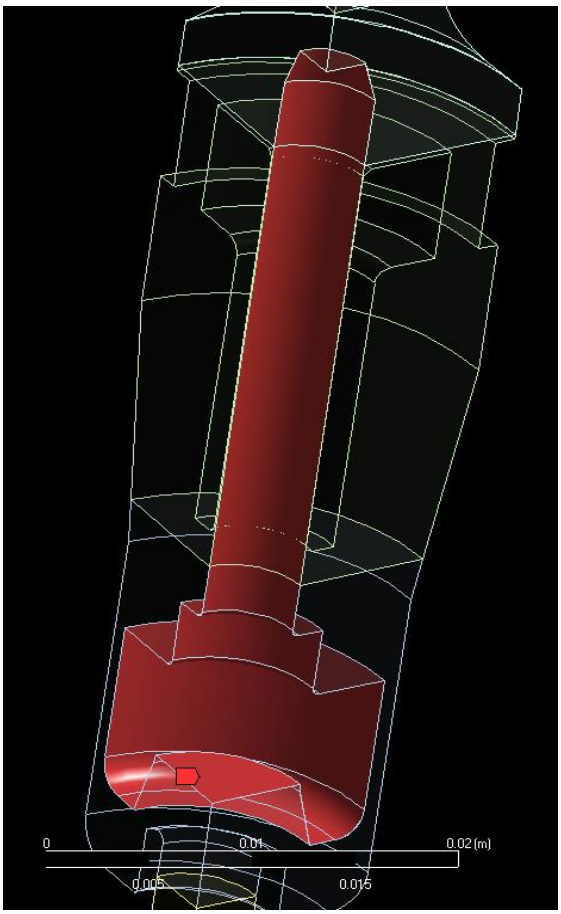

Figure 5.57 – Surface Selection for PRV Disc Force Monitor

It was also required to identify the inlet and outlet as surfaces for 3D modelling rather than edges which were necessary for 2D modelling. The inlet selection is shown on the left side within figure 5.58 and outlet selection is shown on the right side. It was important for computational stability during initialisation to simplify the inlet geometry by removing any curvature at the inlet walls and ensuring that both the inlet and outlet were of suitable distance from the disc/seat area and gland to avoid any unwanted boundary condition effects.

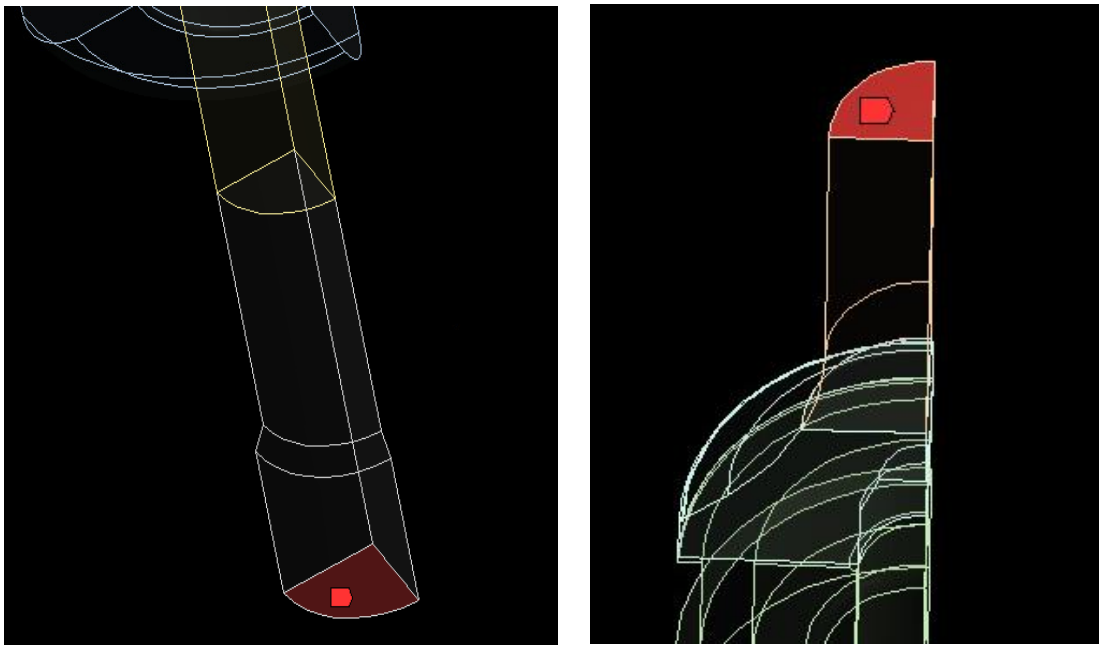

Figure 5.58 – Selection of Surfaces for Inlet (left) and Outlet (Right)

Once all zones were created and named according to the earlier convention established for 2D modelling as well as selecting the appropriate surfaces for boundary condiitions within the CFD solver; meshing of the quarter symmetry 3D domain could take place. The procedure and ideology for meshing of the 3D computational domain will be described within the following section.

3D CFD Modelling of 5231BX PRV – Meshing

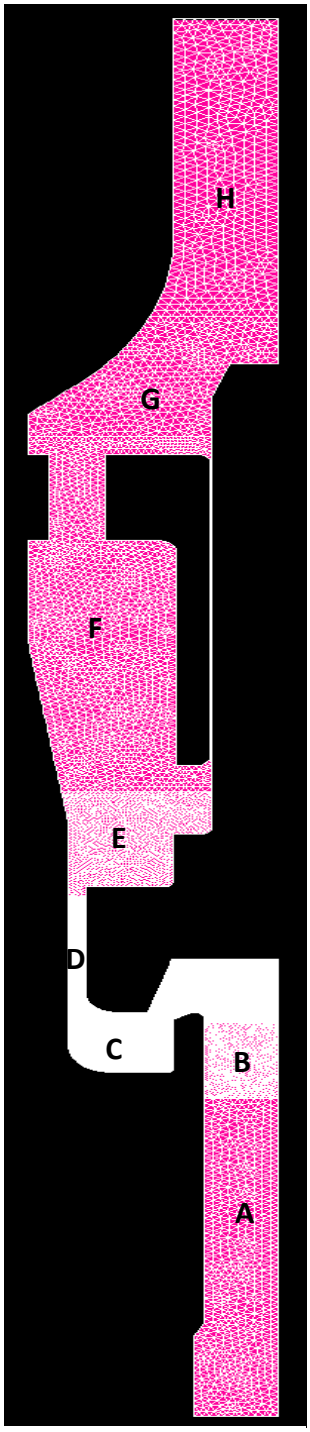

Figure 5.59 – 3D Mesh of Henry 5231BX PRV at 4 mm Disc Lift

Due to the complex nature of the geometry shown within figure 5.55, especially at the disc/seat inlet it was decided to use an unstructured meshing approach similar to the 2D approach. This approach would result in a greater number of elements however was justified to accurately capture the PRV geometry. ANSYS meshing was utilised within Workbench similar to 2D meshing however instead of using the 2D all triangles method in each zone, tetrahedrons were used within a patch conforming method across all zones in the 3D domain. The 3D unstructured, tetradahedral based mesh generated for the 5231BX modified gland geometry is shown within figure 5.59. Individual element sizes for each mesh zone was applied to allow discretisation to be controlled with a focus to acheving a dense mesh at the disc/seat interface relative to the surrounding zones. The domain discretisation methodology used is shown within figure 5.59 where each zone within the domain is labelled A-H. It should be noticed that two additional zones (D and E) were added to blend the dense mesh within zone C incrementally to the density shown within zone F. It was important to avoid creating an interface between each zone in which the mesh density was significantly different to avoid computational error.

From figure 5.59, the use of 7 non conformal interfaces can be identified which is an increase of 2 from the 2D model however in general there are no differences in terms of the approach between the meshes shown within figure 5.31 and that within figure 5.59. A more detailed overview of mesh zones A-F at 4 mm disc lift is provided within figure 5.60. It can be seen that an incremental increase in mesh density is used within zones A and B with the mesh density at an optimum value for zone C. Validated by the previous work for 2D simulation, this area is subjected to the most significant gradients for velocity and pressure as well as a strong sensitivity for mesh density. Therefore the ideology of using maximum possible mesh density in this zone was maintained. As mentioned previously, zones D and E highlighted in yellow within figure 5.60 provided a blending of mesh density towards zone F. However as can be seen within the 2D research, it was still very important to capture the significant gradients within the annular and expansion zone therefore a high value of mesh density was maintained in these regions.

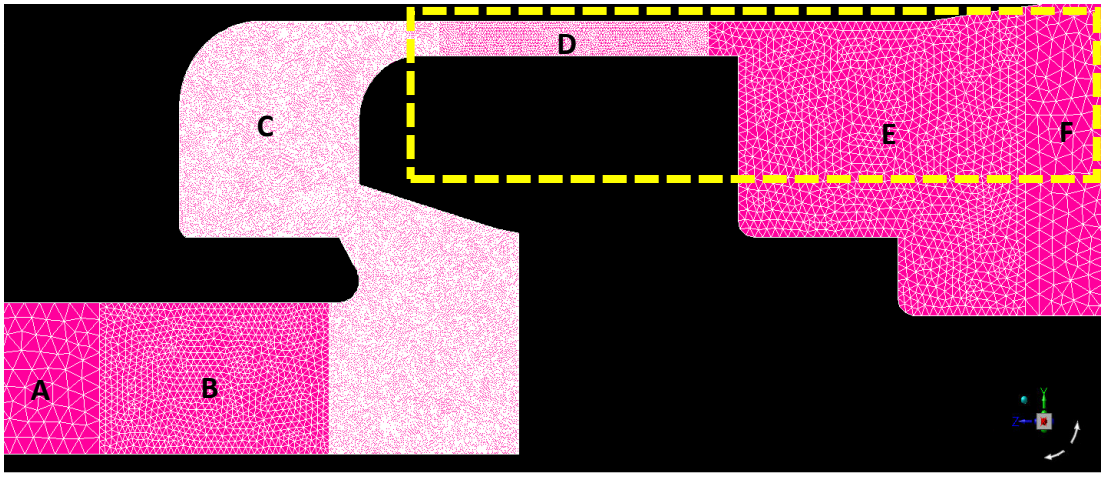

Figure 5.60 – 3D Mesh at Disc of Henry 5231BX PRV at 4 mm Lift

An expanded view of the dense mesh used in relation to the critical seat and disc geometry is also shown within figure 5.61. From the figure it can be understood that the tetrahedral mesh provides a good fit to capture the complex nature of the seat curvature and sharp changes in disc geometry.

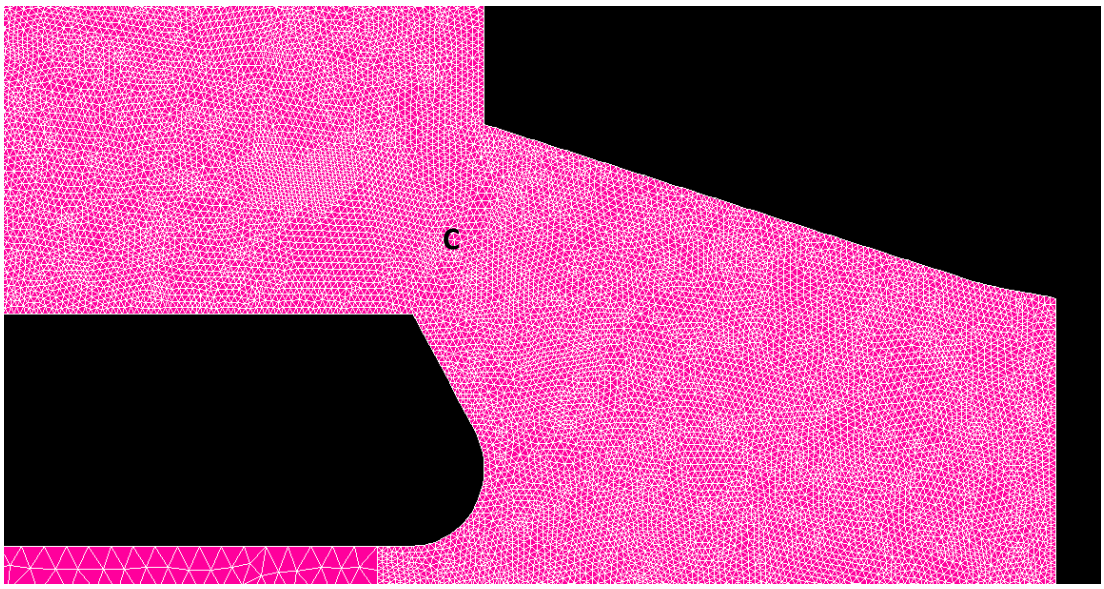

Figure 5.61 – 3D Mesh at Disc/Seat Interface at 4 mm Lift

The continous increase in mesh density from zones F to H is shown within figure 5.62 where it can be appreciated that mesh density was maintained in the proximity of the modified gland in order to capture the separation point and recirculation zone induced by the changes in bulk flow path. Mesh density is reduced towards the outlet however as the flow becomes choked in this region with lower gradients which in turn requires fewer elements. It should be noted that the small annulus between the modified gland and disc was maintained to achieve an accurate represenation of a potential leakage path which could affect flowrate and/or flow structures near the top of the disc.

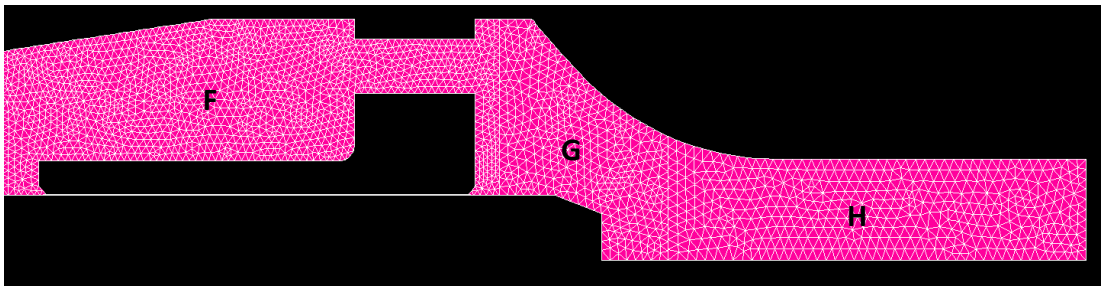

Figure 5.62 – 3D Mesh at Modified Gland/Outlet at 4 mm Lift

In a similar manner to the 2D mesh independence research, a study was focussed on reviewing the effect of mesh density within zone C (disc/seat interface) with other zones maintained to a similar ratio used for the 2D work in reference to zone C. This was done as it was shown earlier for the 2D work that the effect of mesh density in the surrounding zones have an almost negigible effect on both flowrate and flow force prediction when compared with the disc/seat interface zone. The original gland geometry was used for the mesh density comparison in zone C. Furthermore the study was performed at a disc lift of 4 mm alongside the K-Omega SST turbulence model to provide a conservative estimate of the mesh density which could be used across the full lift range during a validation study. For the K-Omega SST model it was important to maintain the y^+ value to be less than 10 and as close to 1 as possible if required. The results of the mesh convergence research is shown within table 5.20.

Mesh Type	**Force (N)**	**Mass Flow Rate (kg/s)**
Coarse (16 Million Elements)	98.64	0.0853
Medium (32 Million Elements)	95.96	0.08633
Fine (57 Million Elements)	91.08	0.08773
Finest (64 Million Elements)	91.39	0.08782

Table 5.20 –Mesh Convergence Results for PRV at 4 mm Lift (Original Gland)

From table 5.20 it was found that the fine mesh with 57 million computational elements in the quarter symmetry model provided the best balance between accuracy and computational performance. A noticeable difference of approximately 5N was found between a mesh size of 57 million elements compared to one with 32 million elements therefore it was decided that a finer mesh should be adopted in order to capture the flow force as accurately as

possible without the influence of mesh effects. In a similar manner to the 2D study it could be established that for a coarse mesh, the disc force value would be overpredicted when compared to the mesh independent value with the K-Omega SST turbulence model. Therefore in future modelling, care must be taken to ensure that a mesh independent solution is achieved; in particular by refining the disc/seat interface geometry within zone C. To provide further detail on the difference in flow features between the medium mesh size and fine mesh size a series of contour plots were produced for Mach number shown in figures 5.63 and 5.64. Both figures are based on the symmetry planes at either side of the quarter symmetry shown in figure 5.56. Contours plots of static pressure are also shown within figures 5.65 and 5.66 for their respective symmetry planes. In general a similar flow path is achieved for zones A-B and E-H for both mesh densities as focus was maintained on the mesh resolution within zones C and D.

The Mach number plots, in agreement with 2D observations in zone C, highlight a slight increase in definition of the bulk flow however most importantly differences can be found in the recirculation areas both above and under the jet at the outer radial area of the disc front face. As a result, there is a slight difference in jet positioning as well as magnitude of Mach number in these regions which affects the bulk flow path and hence mass flow rate prediction as choking points are altered slightly. The static pressure plots also highlight a difference as before for the low pressure zone at the outer radial region of the disc which in turn significantly affects the flow force predicition as shown within table 5.20. Critically however the magnitude of the pressure in this zone is higher than the 2D alternative which results in a higher disc force prediction. In addition it can be seen that variation in flow features can be seen across the two symmetry planes which suggests that the flow through the PRV in this section is not axisymmetric as was intially expected. These features with differences between 2D and 3D modelling as well as a breaking of axisymmetric flow behaviour will be explored later.

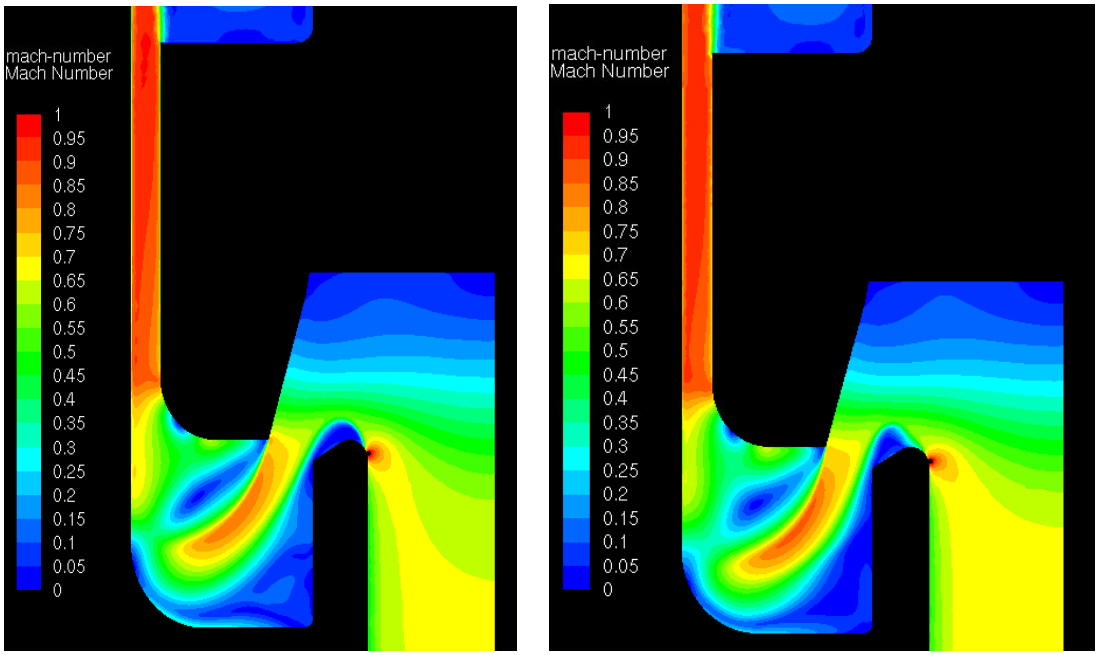

Figure 5.63 - 3D Contours of Mach Number Comparison (XZ Plane) at 4 mm Lift for Coarse Mesh Density (Left) and Fine (Right) using K-Omega SST

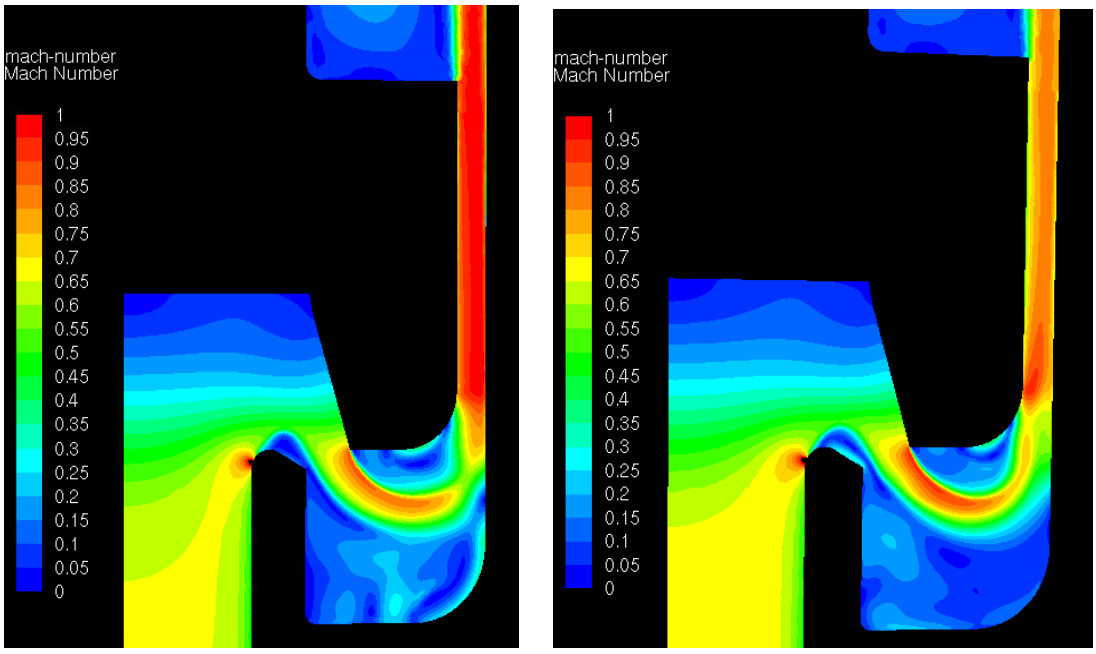

Figure 5.64 – 3D Contours of Mach Number Comparison (YZ Plane) at 4 mm Lift for Coarse Mesh Density (Left) and Fine (Right) using K-Omega SST

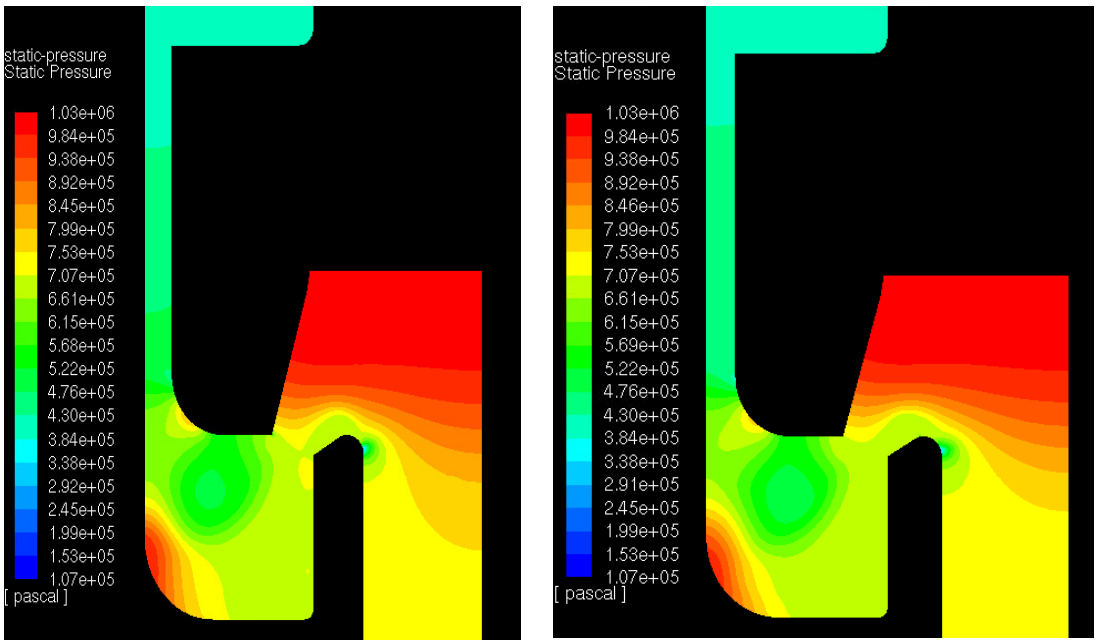

Figure 5.65 - 3D Contours of Static Pressure Comparison (XZ Plane) at 4 mm Lift for Coarse Mesh Density (Left) and Fine (Right) using K-Omega SST

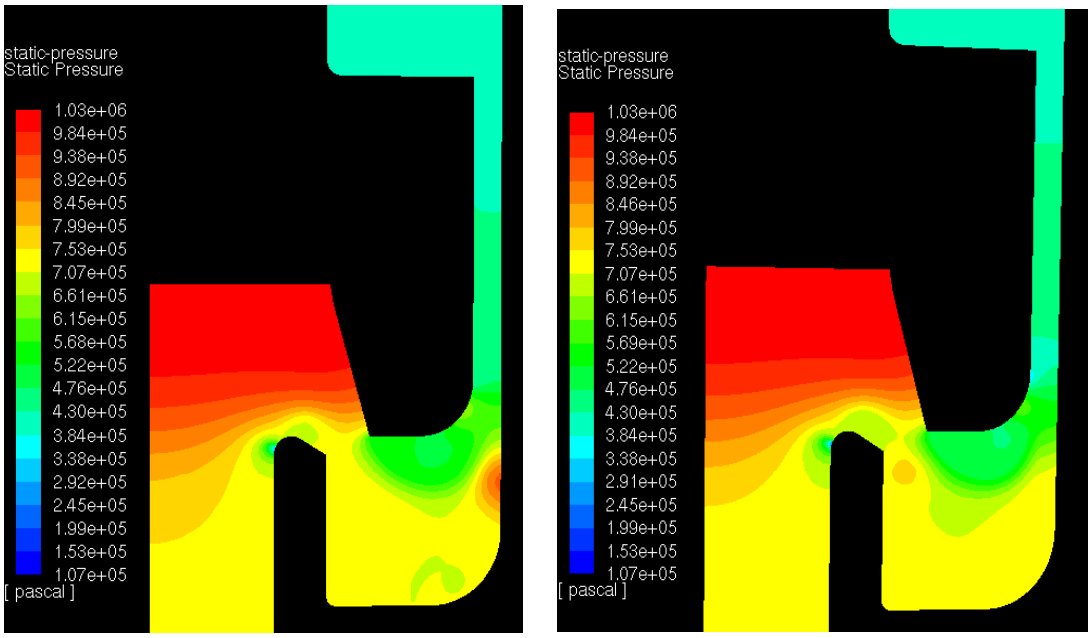

Figure 5.66 - 3D Contours of Static Pressure Comparison (YZ Plane) at 4 mm Lift for Coarse Mesh Density (Left) and Fine (Right) using K-Omega SST

The results of the 3D Mesh dependency study shown within table 5.20 and figures 5.63-66 are consistent with the theme shown from the 2D investigation; where in particular the outer radial region of the disc/seat interface is sensitive to mesh density. Both demonstrate a difference in recirculation features surrounding the bulk flow as well as slight differences in separation and choking points which affect mass flow rate predictions. In addition a difference in the magnitude of a low pressure region at the outer face of the disc causes substantial variation in disc force magnitude for different mesh densities until a density value is reached for mesh independence. The 2D model however demonstrated a larger variation in disc force for a similar ratio difference (approx 4x) in mesh density when compared with the 3D model. In addition the 3D model reported a higher pressure in this zone when compared with the 2D model which suggested the presence of 3D flow effects which also affect this recirculation area. It is therefore suggested that the mesh density values within table 5.21 for each zone is followed to ensure that a mesh independent solution for both aerodynamic disc force and mass flowrate is achieved.

Mesh Zone and Description	**Mesh Independent Element Size**
Zone A – Lower Inlet Region	375 Microns
Zone B – Upper Inlet Region	150 Microns
Zone C – Disc/Seat Interface Region	40 Microns
Zone D – Disc Annulus Region	60 Microns
Zone E – Upper Disc Surround Region	200 Microns
Zone F – Modified Gland Region	350 Microns
Zone G – Lower Outlet Region	425 Microns
Zone H – Upper Outlet Region	500 Microns

Table 5.21 – 3D 5231BX PRV Zonal Mesh Independent Element Sizes

For the mesh independent mesh densities shown within table 5.21 it was also necessary to evaluate the critical mesh metrics and compare to best practice guidelines [52] to reduce mesh induced computational error. The mesh metrics for the mesh independent solution is shown within table 5.22 where all metrics reach either a very good or excellent standard. In order to reach this standard it was required for the skewness to be as close to 0 as possible and orthogonal quality to be as close to 1 as possible. As a result of their desirable attributes the mesh densities and mesh methodology suggested will employed for a 3D validation study against experimental results across the full lift range. It should be noted that all mesh metrics for the 3D model are of a lower quality to the 2D model however this is expected due to the increased computational demands of 3D meshing and limitations for both CPU and memory.

Mesh Metric	**Value**
Average Orthogonal Quality	0.8
Average Aspect Ratio	1.79
Average Skewness	0.2
Total Number of Elements	57477621 Elements

Table 5.22 – 3D 5231BX PRV Final Mesh Independent Metrics at 4 mm Lift

5.2.5 3D CFD Modelling Procedure and Results of 5231BX PRV

Following the development of the 2D modelling procedure of the 5231BX PRV, a similar, robust group of FLUENT settings could be applied as shown within table 5.23. These settings would be used throughout the 3D validation study for all geometry variations of the 5231BX PRV; original gland, modified gland and Alshaikh modified outlet/gland.

FLUENT Setting Type	**Recommended Setting**
Solver Type	Pressure Based
Turbulence Model	K-Omega SST and Standard K-Epsilon
Air Density	Ideal Gas Law (Energy Equation ON)
Pressure-Velocity Coupling Scheme	Coupled
Spatial Discretisation - Gradient	Least Squares Cell Based Scheme
Spatial Discretisation (Pressure)	Second Order
Spatial Discretisation (Other Terms)	QUICK
Initial Flow Courant Number	5
Momentum and Pressure URF's	0.75
Density and Energy URF's	0.25

Table 5.23 – 3D Final solver settings for use across full lift range

The use of the pressure based solver was important to allow the future development of a 3D multiphase model as well as using the coupled pressure velocity coupling scheme to achieve computational stability and convergence. The QUICK scheme was used for spatial discretization due to it's ability to perform accurately for high Mach number flow with shocks [48, 56] as well as second order for pressure. The least squares cell based scheme to capture flow gradients accurately as validated in earlier work for the Broady PRV and 2D Henry geometry. Furthermore to improve computational stability both under relaxation factors and explicit relaxation factors as well as the flow courant number were adjusted to the intial values shown within table 5.23. As the computation advanced passed 1000 iterations for the 3D model it was then possible to increase each value to reduce computational time however care was required to prevent instability and/or calculation divergence.

In addition to the settings illustrated within table 5.23, it was necessary to determine a consistent set of boundary conditions to apply across all lift

conditions for the 3D model during the validation study. In general the boundary conditions selected for the 3D model were similar to those used for the 2D model with the omission of the axis boundary condition for a symmetry condition applied to both symmetry surfaces of the quarter symmetry PRV domain as shown earlier within figure 5.56. As a result, the 3D model will be able to capture any 3D flow effects which would not be picked up by the 2D model in the circumferential direction. For all lift conditions, the boundary conditions applied were as follows;

- Gauge Total Pressure Inlet of 10.3 barg – which represented vessel pressure, with the zone positioned at the inlet face of the nozzle (figure 5.58). A turbulence intensity of 5% and 8.05 mm hydraulic diameter were also input to allow calculation of the inlet turbulence conditions.
- Gauge Pressure Outlet of 0 barg – which represented atmospheric exhaust, positioned at the outlet face of the valve (figure 5.58). A turbulence intensity of 5% and 10mm hydraulic diameter were also input to allow calculation of the outlet turbulence conditions.
- Temperature at both inlet and outlet – 295 K or 22 ^{0}C
- No slip shear condition on stationary, adiabatic valve walls
- Symmetry boundary condition applied on both XZ and YZ planes as shown within figure 5.56
- Operating Conditions – 1 bar (to offset pressure bc's to gauge)

It should be noted here that the use of a pressure outlet condition for the outlet geometry shown within figure 5.55 is not an ideal case and for optimum accuracy a surrounding area with atmospheric pressure should be modelled to capture the effects of entrainment and to remove any possibility of boundary condition induced error. This could become important at higher lifts when the flow is choked or maginally supersonic where FLUENT uses the pressure

outlet input value for subsonic flow only. The user guide states that “should the flow become locally supersonic, the pressure will be extrapolated from the upstream conditions” [56]. In addition for the pressure inlet a similar possible source of error could be induced by ignoring modelling of the upstream piping and pressure vessel however the pressure inlet condition requires the total value (stagnation) pressure. Therefore in future work it is recommended that the use of these boundary conditions are revised in order to identify if any improvement in modelling accuracy can be found.

Similarly to the 2D procedure, for all 3D simulations high order term under relaxation was used to provide stability during the initial stages of the simulation. It was also important to follow CFD best practice guidelines by initialising the solution with first order upwind spatial discretisation terms before switching to a higher order scheme after 100-200 iterations. The hybrid initialisation scheme available within FLUENT was used for all cases. Residual requirements for a converged solution were to be below 10e-6 for the energy equation and 1e-3 for all other terms and/or exhibit residual stability. To achieve a fully converged solution it was also required to create surface monitors for disc force as well as mass flow rate at the PRV inlet in which constant values of each variable was needed for termination of the calculation.

The results of initial 3D simulations using the previously described mesh independent and model settings for the quarter symmetry modified gland simulations are shown within tables 5.24 and 5.25. Results for both 4 mm and 2 mm disc lifts were generated in order to compare the performance of each turbulence model at lifts greater than 2 mm as the 2D simulations highlighted that both share comparable performance at lower lifts. From table 5.24 for 4 mm disc lift it can clearly be seen that both models under predict the value of disc force however the K-Omega SST displays significant performance improvement when compared to the Standard K-Epsilon model. This characteristic is reinforced within the results in table 5.25 as the K-Omega SST

turbulence model is significantly closer to the experimental value. However it should be noted that the performance for both RANS turbulence models at 2 mm is poor, with a significant under prediction when compared with experimental disc force values. This observation will be discussed later within this section however it was clear than in contradiction to the 2D results, for 3D modelling the K-Omega SST turbulence model provided significant improvement for disc force. For mass flow rate, a similar trend can also be appreciated within tables 5.24 and 5.25 where the K-Omega SST out-performs the standard K-Epsilon model in terms of CFD correlation to experimental data; especially at 4mm lift. This is a strong indication of the inability of the standard 3D K-Epsilon turbulence model for high lifts to accurately capture the bulk flow path and choking points critical for the CFD model to achieve accuracy for mass flow rate predictions as shown in previous research [11, 12].

Turbulence Model	**Force (N)**	**Accuracy to Exp (%)**	**Mass Flow Rate (kg/s)**	**Accuracy to Exp (%)**
Standard K-Epsilon	90.86	-12.97	0.06578	-22.34
K-Omega SST	99.45	-4.74	0.08881	4.85

Table 5.24 – Results of 3D Turbulence Model Comparison at 4 mm Lift

Turbulence Model	**Force (N)**	**Accuracy to Exp (%)**	**Mass Flow Rate (kg/s)**	**Accuracy to Exp (%)**
Standard K-Epsilon	108.4	21.52	0.065779	3.92
K-Omega SST	70.78	-20.65	0.062036	-2.01

Table 5.25 - Results of 3D Turbulence Model Comparison at 2 mm Lift

To compliment the results shown in tables 5.24 and 5.25, a backpressure comparison was perfomed between the CFD results of both turbulence models and the experimental values at 4 mm and 2 mm disc lift. As indicated in Tables 5,26 and 5,27, at 4 mm it could be seen that the back pressure predicted for the two turbulence models was 2.6 barg for the K-Epsilon model and 3.6 barg for the K-Omega SST. This highlights a significant difference in the prediction of the backpressure which would allow a greater disc force to be generated for the K-Epsilon model compared to K-Omega SST. However at 2 mm disc lift the back pressure is greater for the K-Epsilon model when compared with the K-Omega SST model. It would therefore be expected that disc force would be less for the K-Epsilon case however it is not. This is likely due to a difference in prediction of static pressure at the disc/seat interface between the turbulence models (zone C), resulting in the K-Epsilon disc force to be higher.

Turbulence Model	**Force (N)**	**Accuracy to Exp (%)**	**Back Pressure (Barg)**	**Accuracy to Exp (%)**
Standard K-Epsilon	90.86	-12.97	2.62	-29.89
K-Omega SST	99.45	-4.74	3.59	-4.05

Table 5.26 – 3D CFD Turbulence Model Backpressure Comparison at 4 mm

Turbulence Model	**Force (N)**	**Accuracy to Exp (%)**	**Back Pressure (Barg)**	**Accuracy to Exp (%)**
Standard K-Epsilon	108.4	21.52	2.66	9.52
K-Omega SST	70.78	-20.65	2.16	-10.82

Table 5.27 - 3D CFD Turbulence Model Backpressure Comparison at 2 mm

Therefore due to the results of tables 5.26 and 5.27 which suggested significant flow differences at the disc seat interface (Zone C) both Mach number and static pressure contour plots for zone C are shown in figures 5.67 and 5.68 to establish any differences in flow regime at maximum lift.

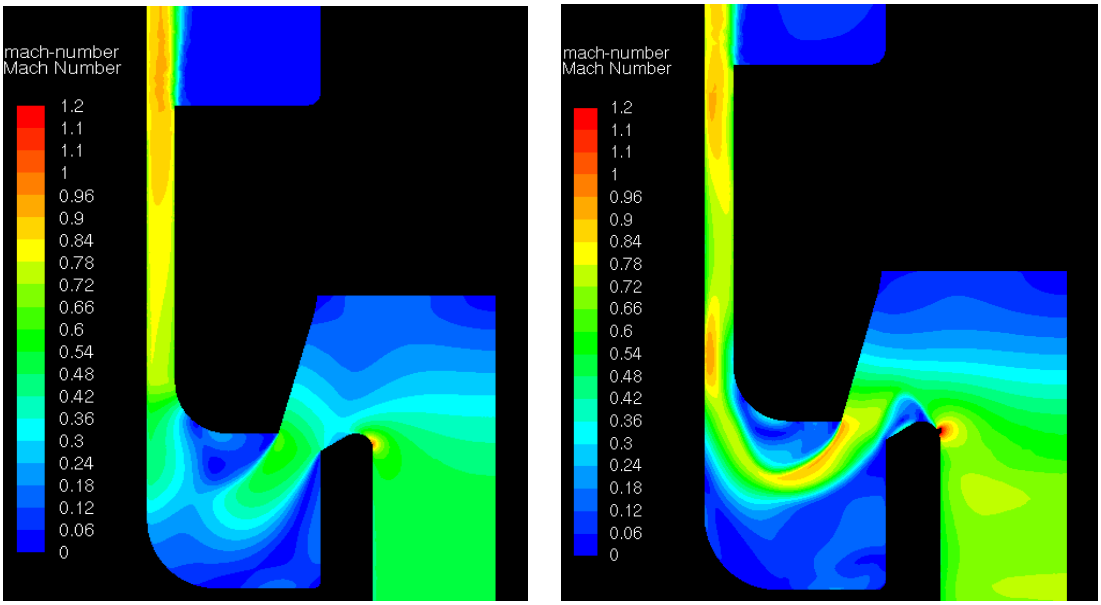

Figure 5.67 – Turbulence Model Comparison Mach Number at 4 mm (K-Epsilon left, K-Omega SST right)

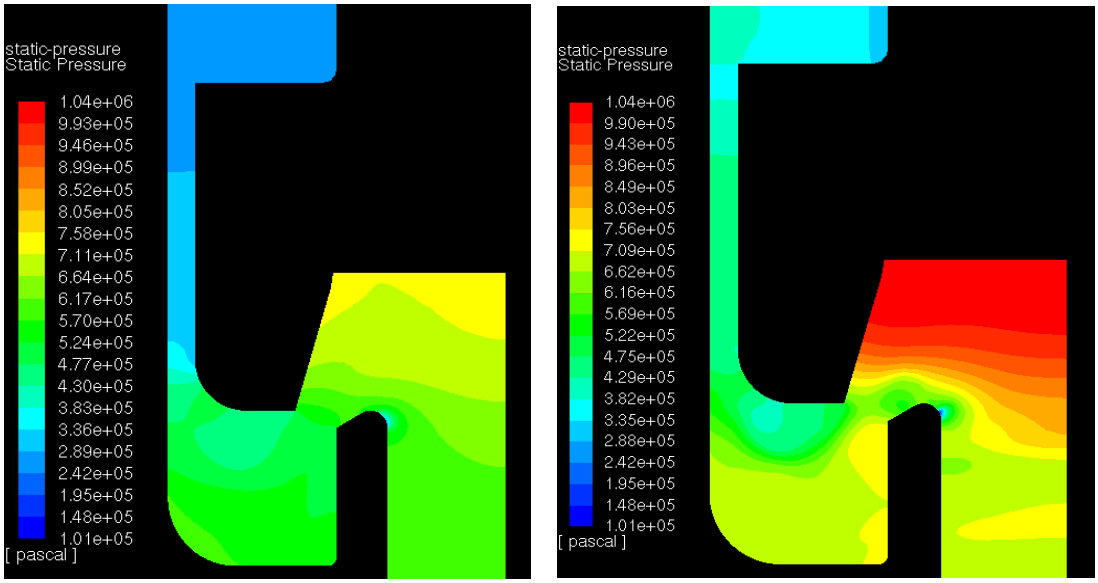

Figure 5.68 – Turbulence Model Comparison Static Pressure at 4 mm (K-Epsilon left, K-Omega SST right)

It can be clearly observed within figure 5.67 that for the Standard K-Epsilon model (left) there is an apparent lack of flow detail when compared with the K-Omega SST turbulence model (right). As a result of this the static pressure plots as shown within figure 5.68 highlight a substantial difference in pressure distribution at the lower surface of the disc across the full radial path of the disc. The aerodynamic disc forces predicted at the lower surfaces of the disc would be different which again provides a greater understanding for the force results observed in tables 5.24 and 5.25. Furthermore the variation in the nature of the jet curvature as well as choking points between the turbulence models as shown in figure 5.67 provide a clear illustration of differences noted for the mass flow rate predictions. It could therefore be established that the K-Omega SST turbulence model would be the most suitable choice for a 3D validation study across the full lift range of the 5231 PRV. It should be noted that the correlation of the K-Omega SST turbulence 3D model was significantly improved at both 2 mm and 4 mm disc lift when compared to the 2D results from earlier. This strongly suggests that the prediction for the disc force is sensitive to 2D and 3D modelling for the K-Omega SST turbulence model; this will be investigated in detail later.

Using the previously established mesh and modelling procedure, a 3D validation study was initially performed for the 5231BX Modified Gland geometry at 10.3 Barg for the lift range of 0-5 mm and the results shown in Table 5.28.. For 3D modelling the K-Omega SST turbulence model was used with the mesh meeting the required y^+ criteria to accurately capture wall shear stresses. The results of the validation study are displayed in terms of percentage error of the CFD relative to the experimental results and the disc force, mass flow rate and backpressure vs lift curves shown in figures 5.69,5.70 and 5.71 respectively. For figure 5.69, the CFD results are given with +/- 5% error bars to provide easy comparison of CFD values with experimental measurements. In the 3D validation study for the modified gland, disc lift from a small opening of 0.2 mm to 5 mm are studied over a total of 11 data capture

points using the quasi steady assumption to incrementally determine the flow force and flow rate across the lift range.

From table 5.28, it was shown that the 3D CFD methodology developed could achieve an averaged accuracy across the full lift ranges of 2.01% for mass flow rate and 7.24 % for disc force prediction compared to experimental values. Such a strong correlation across the full lift range highlights the ability of the CFD model to accurately capture the performance for a through flow valve and demonstrates a considerable improvement when compared with 2D modelling for the 5231BX PRV with modified gland. Figures 5.69, 5.70 and 5.71 visually highlight the strong performance of the CFD model for mass flow rate across the full lift range. However it should be noted that a low lift of <0.4 mm, the flowmeter was unable to provide a reading due to it's working range. In addition the flow correlation at 0.4 mm was likely affected by inaccuracy of the flowmeter which would be operating at the lower limits of it's design. Therefore the significant correlation difference of 11.51% at 0.4 mm was attributed to being caused by measurement error in a similar manner to the results shown during the Broady study at lower lifts. The performance for disc force prediction is shown in table 5.28 and figure 5.69 to be strong at both low and high lifts however at the transition phase from 2-3mm there appears to be a significant drop in accuracy as the disc force is significantly underpredicted by up to 18.5%.

Back pressure correlation of the CFD model with the experimental results, shown in figure 5.70, was also found to be very strong across the full lift range. This as a result provided a strong indication that the limitation of accuracy for capturing the disc force value was the flow regime prediction provided by the 3D RANS based CFD model using the K-Omega SST turbulence model. It could be suggested therefore that in order to improve correlation, more complex CFD models such as RSM or LES should be investigated if computationally possible to determine if the flow effects and turbulence

induced within the disc/seat interface region could be more accurately captured. In turn this would likely improve the disc force correlation as the static pressure distribution would be captured in a more realistic manner.

Lift (mm)	Experiment Mass Flow Rate (Kg/s)	CFD Mass flow rate (Kg/s)	Correlation of Mass Flow Rate (%)	Experiment Disc Force (N)	CFD Disc Force (N)	Correlation of Disc Force (%)
0.2	N/A	0.0132	N/A	67.4	59.3	-12.1
0.4	0.0212	0.0234	10.5	73.7	79.2	7.4
0.8	0.032	0.0330	3.1	76.8	77.8	1.3
1.125	0.042	0.0408	-2.9	74.6	73.5	-1.5
1.5	0.0506	0.0499	-1.3	86.9	76.7	-11.8
2	0.0633	0.0620	-2	89.2	70.8	-20.7
2.5	0.0741	0.0739	-0.3	94.8	78.2	-17.5
3	0.081	0.0822	1.5	103.7	94.3	-9.1
3.5	0.0853	0.0873	2.3	110.1	101.7	-7.7
4	0.0847	0.0888	4.9	104.4	99.5	-4.7
5	0.0857	0.0895	4.5	102.2	98.6	-3.5
			Average = 2			**Average = -7.2**

Table 5.28 - Validation Results for Henry 5231BX Modified Gland 3D CFD Model

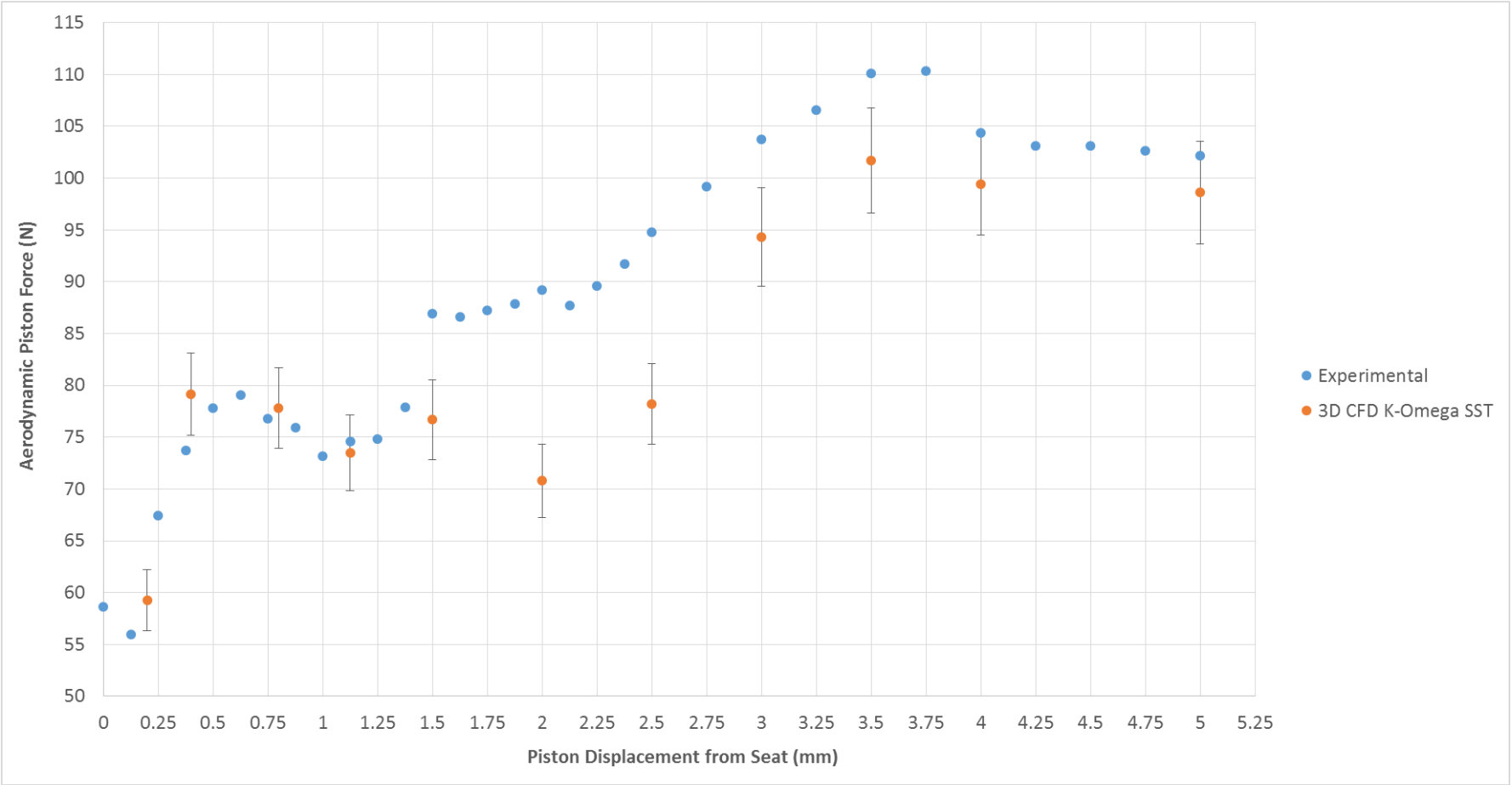

Figure 5.69 – Force vs Lift for Henry 5231BX Modified Gland 3D CFD Model with 5% Error Bars for CFD Values at 10.3 Barg

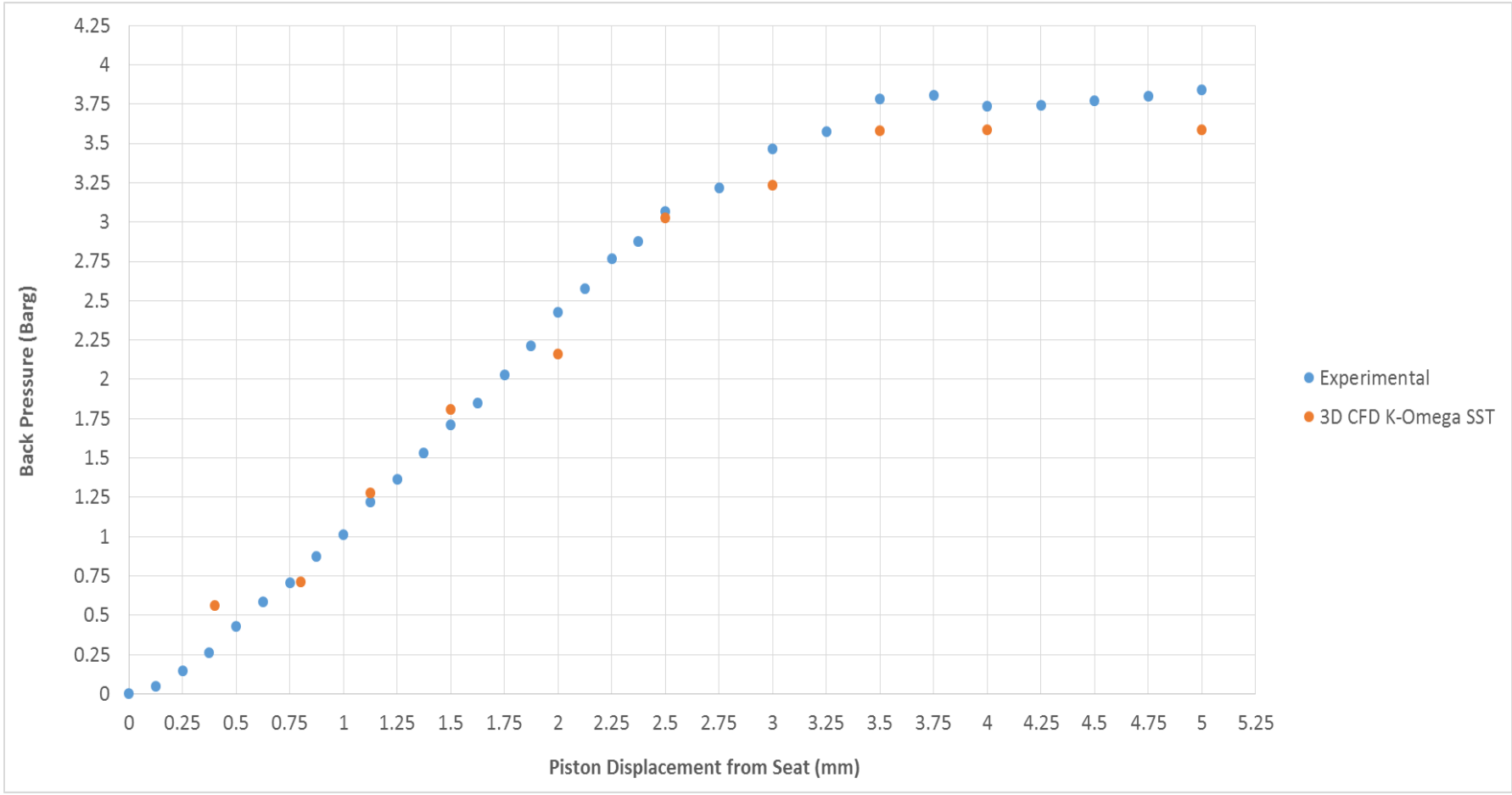

Figure 5.70 – Back Pressure vs Lift for Henry 5231BX Modified Gland 3D CFD Model at 10.3 Barg

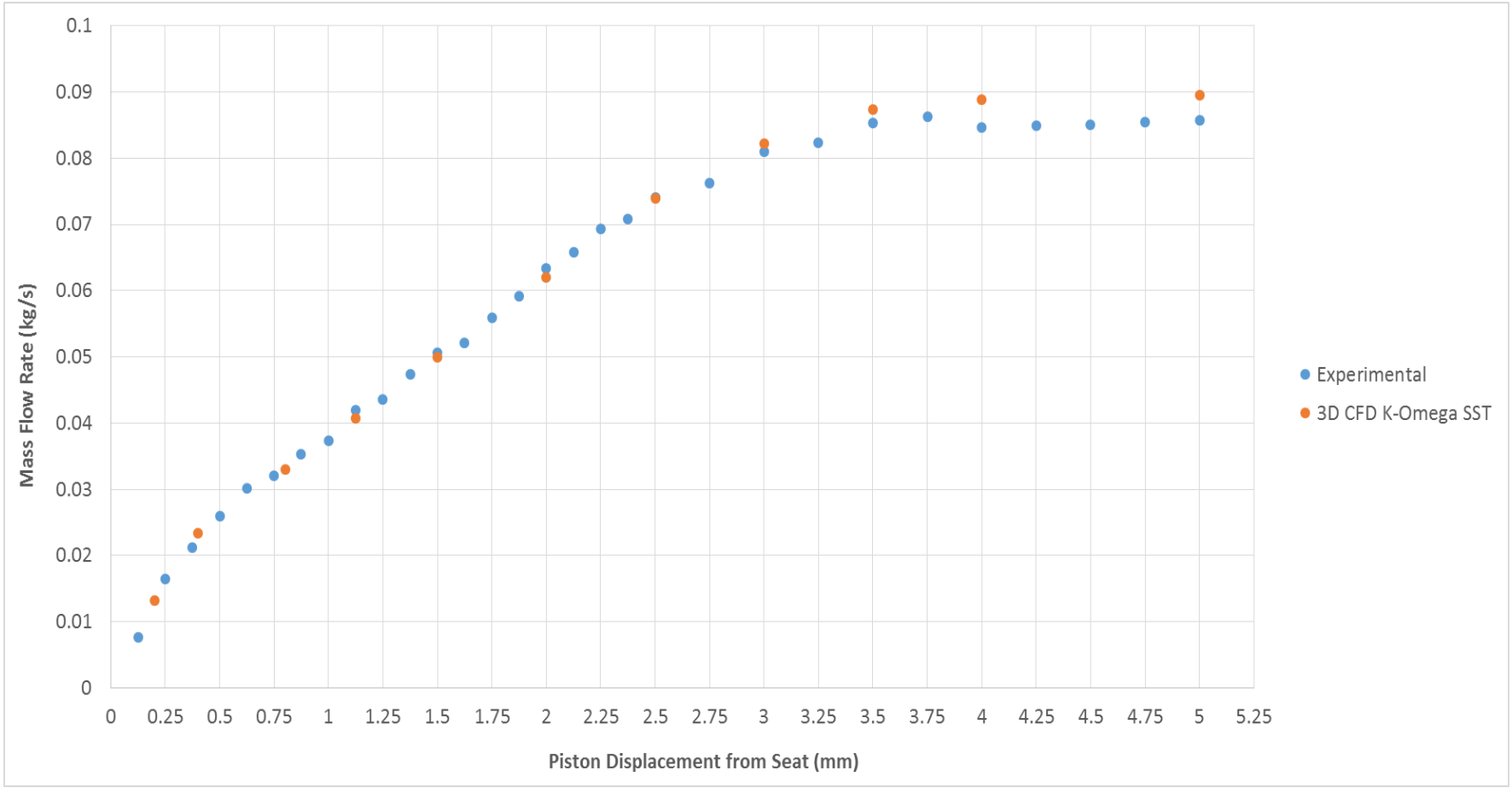

Figure 5.71 - Flowrate vs Lift for Henry 5231BX Modified Gland 3D CFD Model at 10.3 Barg

In addition to the reduction of quality for mass flow rate correlation at low lifts, a noticeable reduction in accuracy of the CFD model can be observed from figure 5.69 for disc force. By studying the experimental trend at low lift, a very steep gradient of disc force with disc lift can be appreciated which is required to provide the pop action opering of the PRV during operation. At the same points, the CFD disc force results also exhibit such behaviour however they would appear to be slightly lagging behind the experimental data with an inaccuracy of 12.7% at 0.2 mm which reduces to 2.82% at 0.4 mm. Therefore during the transition from 0.2 mm-0.4 mm the CFD model recovers to achieve good correlation with experimental results.

From figure 5.69 it could be easily observed that the disc force vs lift curve for the 3D K-Omega SST CFD model was significantly different to the 2D K-Omega SST model; especially at higher lifts. As a result the 3D model offers significant improvement in correlation with experimental results at higher lifts when compared to both the standard K-Epsilon and K-Omega SST 2D turbulence models. The 3D model was capable of capturing the peaks and troughs and general polynomial behaviour observed from the experimental results of the disc force which are vastly different to the linear nature of the disc force vs lift behaviour of the larger Alshaikh type outlet. This therefore suggests that the capability of 2D CFD to accurately capture the flow physics within the PRV is sensitive to the outlet design of the 5231BX. Peak force captured by CFD was consistent with experimental results to occur at 3.5mm lift as well as maximum flow rate.

The 3D modelling methodology developed was also applied for the 5231BX geometry at 10.3 Barg with the original gland; as it was not possible to model this geometry for 2D simulation as the gland geometry wasn’t axisymmetric. The results of the validation study are shown within table 5.29 and also figures 5.72 and 5.73 with 5% error bars for the disc force values. From table 5.29 it was apparent that the accuracy of the 3D CFD model for the original gland was

equivalent to that of the modified gland and that the K-Omega SST turbulence model was resilient for different gland geometries. The correlation on average across the operating lift range of the PRV was found to be 1.67% for mass flowrate and 5.11% for disc force prediction. The strengths and weaknesses of the CFD model were similar to those apparent for the modified gland geometry where the transition zone between 2 mm-3 mm exhibited the poorest correlation at 16% error from experimental values.

On the other hand however, accuracy of the CFD model was improved for the original gland at lower lifts from 0.1-0.2 mm but underpredicted disc forces by up to 9% at 0.4 mm with recovery of accuracy to 3% by 0.8 mm. This however would result in an underestimation of the initial pop action of the PRV if the results taken under quasi steady conditions are representative of actual opening performance. As mentioned previously the CFD model was also able to accurately capture the differences between the gland geometries as the CFD results indicate that the disc forces at the fully open position of 3.5 mm are signficantly lower for the original gland when compared to the modified gland. However CFD also predicts that the mass flow rate at maximum discharge for both glands are equivalent as was discovered during experimental testing. In addition, both the disc force and mass flowrate vs lift curves follow their experimental counterparts closely with similar gradients across the lift range.

As a result it could be concluded that for both the 5231BX original gland and modified gland models, it was possible to accurately capture disc force to within 5% and mass flow rate to within 1.5% across the operating range of the PRV's at an inlet pressure of 10.3 Barg. In addition, it was clear that the modified gland was effective in representing the actual gland in terms of maximum discharge rate therefore vindicating it as an appropriate axisymmetric representation of the actual geometry.

Lift (mm)	Experiment Mass Flow Rate (Kg/s)	CFD Mass flow rate (Kg/s)	Correlation of Mass Flow Rate (%)	Experiment Disc Force (N)	CFD Disc Force (N)	Correlation of Disc Force (%)
0.1	N/A	0.0068	N/A	56	54	-3.7
0.2	N/A	0.0134	N/A	62.6	59.8	-4.5
0.4	0.0209	0.0236	12.9	76.4	69.3	-9.3
0.8	0.0329	0.0336	2.3	75.8	73.2	-3.4
1	0.0370	0.0383	3.6	71.9	73.9	2.8
1.5	0.0494	0.0506	2.4	82.5	74.3	-9.9
2	0.062	0.0630	1.6	84.4	70.9	-16.1
2.5	0.0733	0.0742	1.2	88.3	75.6	-14.4
3	0.0833	0.0826	-0.8	94.4	89.1	-5.6
4	0.0882	0.0853	-3.3	95	98.6	3.8
5	0.0892	0.0881	-1.2	92.5	96.9	4.7
			Average = 1.7			**Average = -5.1**

Table 5.29 - Validation Results for Henry 5231BX Original Gland CFD Model at 10.3 Barg

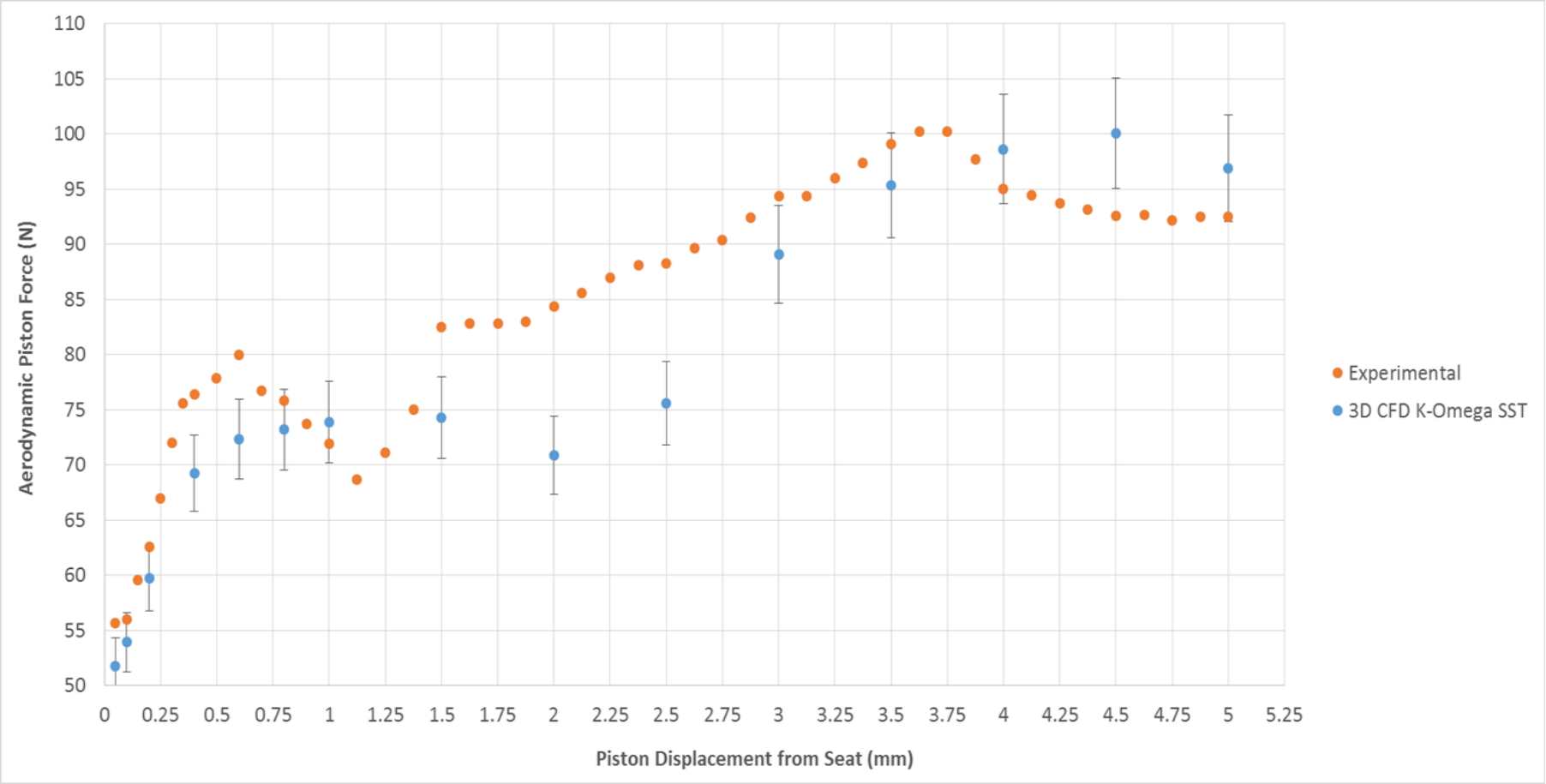

Figure 5.72 – Force vs Lift for Henry 5231BX Original Gland CFD Model at 10.3 Barg

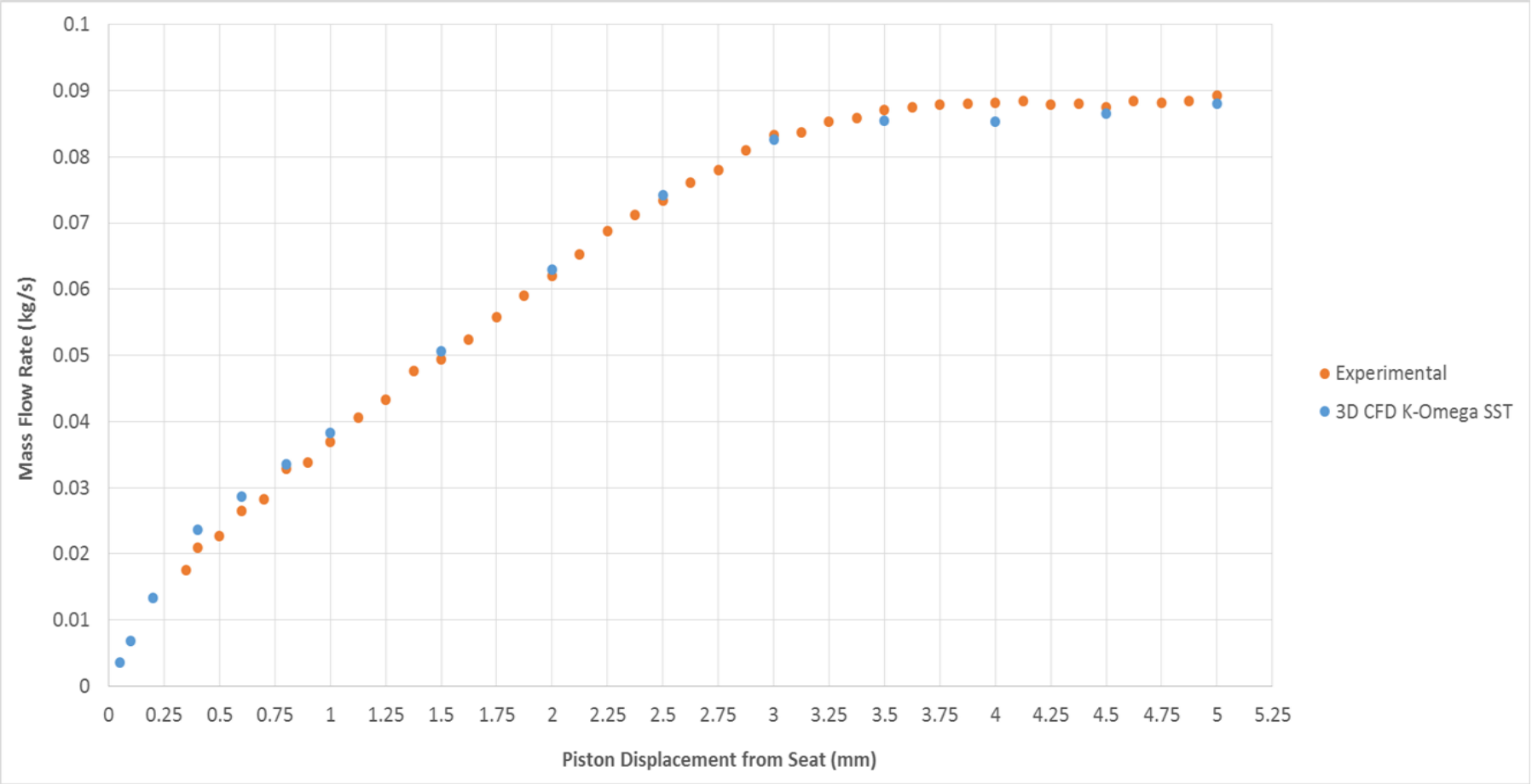

Figure 5.73 - Flowrate vs Lift for Henry 5231BX Original Gland CFD Model at 10.3 Barg

To further test the resilience of the developed 3D CFD K-Omega SST based PRV model it was important to compare the performance to the results of 2D models for the 5231BX with Alshaikh's modified outlet geometry at 10.3 barg inlet pressure. For this study 2 data points were selected at low disc lift (1 mm) and high disc lift (3.5 mm) to provide an opportunity for the 3D K-Omega SST turbulence model to be compared to the 2D variant. From table 5.30 at 1 mm disc lift, it is clear that the use of 3D modelling had significantly improved the performance of the disc force prediction as the error has been reduced from 15.6% to 7.6% and mass flow rate prediction has remained within 0.5% of each other. The backpressure for both models were similar which suggested that the main difference between 2D and 3D at 1 mm lift was due to pressure distribution acting on the lower face of the disc. Interestingly however, the 2D standard K-Epsilon remains to be the model with the best accuracy for disc force when compared with the 3D K-Omega SST model.

Turbulence Model	**Force (N)**	**Accuracy to Exp (%)**	**Mass Flow Rate (kg/s)**	**Accuracy to Exp (%)**	**BackPressure (Pa g)**
2D Standard K-Epsilon	107.6	-3.09	0.0374	-1.64	31605
2D K-Omega SST	93.7	-15.59	0.0379	-0.14	-5285
3D K-Omega SST	102.6	-7.61	0.0378	-0.61	-5733

Table 5.30 – Comparison of CFD Modelling for Alshaikh PRV: 1 mm Lift

Turbulence Model	**Force (N)**	**Accuracy to Exp (%)**	**Mass Flow Rate (kg/s)**	**Accuracy to Exp (%)**	**BackPressure (Pa g)**
2D Standard K-Epsilon	179.6	1.46	0.0825	3.07	130638
2D K-Omega SST	138.7	-21.64	0.0910	13.69	168030
3D K-Omega SST	160	-9.58	0.0881	10.13	115384

Table 5.31 - Comparison of CFD Modelling for Alshaikh PRV: 3.5 mm Lift

The theme observed from the 1 mm case is continued on to the 3.5 mm results shown in table 5.31 where it can be seen that the 2D standard K-Epsilon model achieves the best correlation with experimental (Exp) data. A significant difference is also observed between the 2D and 3D models using K-Omega SST for disc force. A higher value of back pressure is reported for the 2D model however as can be seen from figures 5.74 and 5.75; the bulk flow features and static pressure distribution were also different at the outer face of the disc.

As illustrated in figure 5.75, the magnitude of the low pressure zone as well as the size of the zone is substantially different for the 2D model when compared with the 3D K-Omega SST model. Therefore with a lower pressure acting on the lower surface of the disc and a higher back pressure acting on the upper surface; the disc force between the 2D and 3D models would be substantially different as is shown within table 5.31. Furthermore figure 5.74 indicates a small difference in the recirculation zones above and below the jet of the bulk flow which would affect the static pressure distribution and disc force.

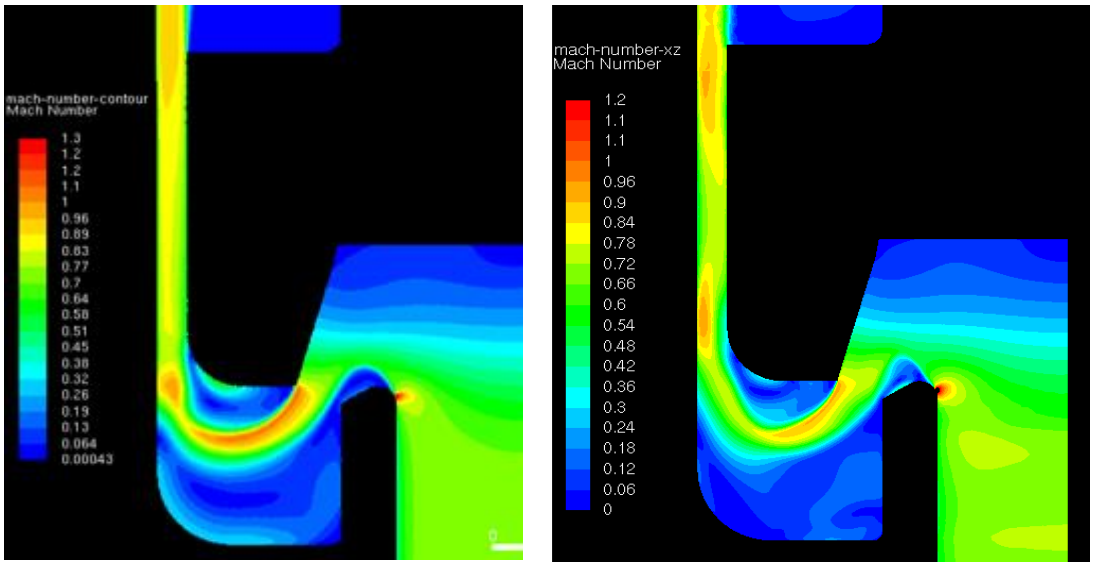

Figure 5.74 – Mach Number Comparison of 2D (left) and 3D (right) K-Omega SST Model at 3.5 mm for Alshaikh PRV

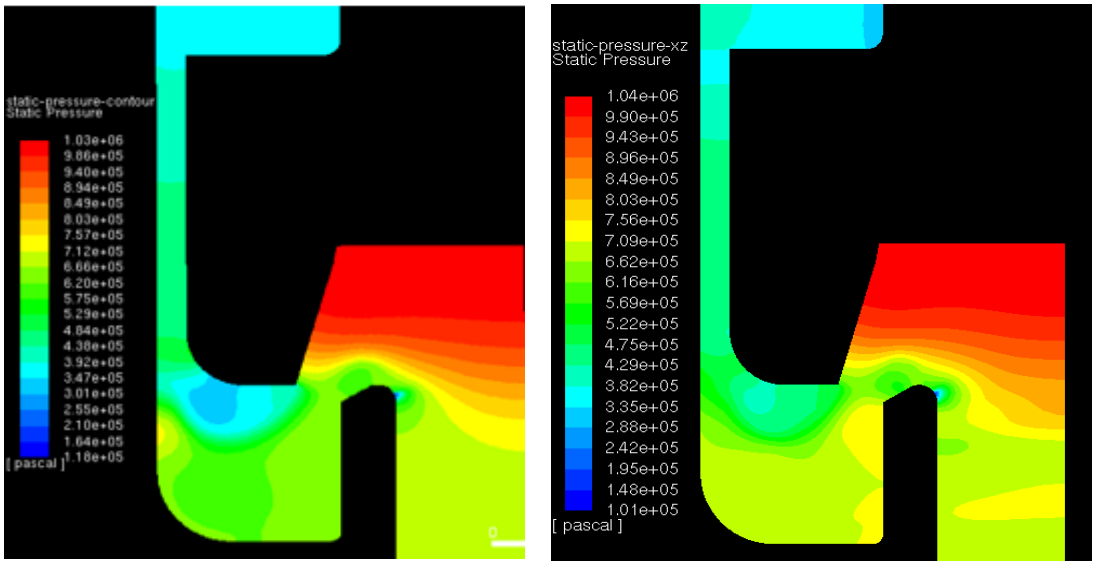

Figure 5.75 – Static Pressure Comparison of 2D (left) and 3D (right) K-Omega SST Model at 3.5 mm for Alshaikh PRV

An indication of the difference observed between the 2D and 3D K-Omega SST based CFD models is shown within figure 5.76 where a noticeable difference in turbulence intensity at the outer face of the disc can be observed. This in turn would affect the bulk flow features and pressure distribution shown in figures 5.74 and 5.75. For the 2D model it can be seen that the magnitude of turbulence intensity at the recirculation region near the outer surface of the disc is higher than the 3D model. Therefore, the flow in this region would deflect the main jet away causing a significantly larger low pressure region as can be observed in figure 5.75. In addition, the flow for the 2D flow could be identified as being more energetic than the 3D modelling case as the magnitude of turbulence for the 3D case is noticeably higher. This would help to explain the observations shown for both the magnitude and size difference of the low pressure zone at the outer face of the disc shown within figure 5.75.

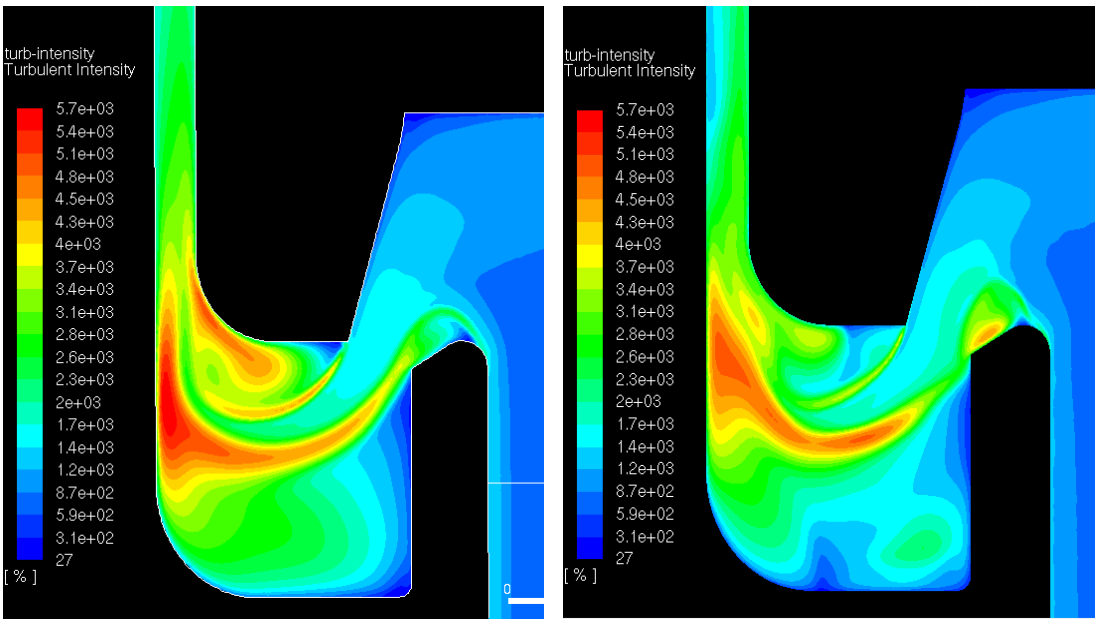

Figure 5.76 – Turbulence Intensity Comparison of 2D (left) and 3D (right) K-Omega SST Model at 3.5mm for Alshaikh PRV

From table 5.31, it can also be appreciated that the 2D standard K-Epsilon model predicts the flowrate more accurately than both the 2D and 3D K-Omega SST models. This is suspected to be caused by the different outlet geometry in which the flow becomes choked much earlier as seen within the 2D validation section where the K-Omega SST model is clearly not operating well within. Therefore the work performed by Alshaikh in which the 2D K-Epsilon turbulence model achieved good correlation with experimental results when using the larger outlet has been reproduced as well as both the experimental and CFD work which has been used within this study. For larger outlets with significant downstream choking it is recommended therefore to use the 2D standard K-Epsilon model. However for smaller outlets which are typical of manufactured 5231BX fittings, the 3D K-Omega SST CFD model provides best performance. In addition, over the course of the validation study, differences between the performance of the 2D and 3D K-Omega SST based CFD model's have suggested a sensitivity to 3D flow effects which were previously neglected. These differences will be investigated in more detail in the following section.

5.2.6 Overview of Flow Features and Comparison of Flow Effects Between 2D and 3D Modelling for 5231BX PRV

As suggested from the validation results, significant differences for flow force prediction between 2D and 3D CFD modelling have been observed. Within figures 5.77 and 5.78 the differences in 2D and 3D correlation to experimental data are shown using the 5231BX modified gland PRV geometry. To achieve a fair comparison all previously validated modelling methods are maintained using the K-Omega SST turbulence model; therefore the only only variable within the data was the use of either a 2D or 3D computational domain.

From figure 5.77 it was clear that the disc force prediction of the 2D and 3D models at low lift were similar however significant differences became apparent for lifts greater than 2 mm. In addition, when comparing the mass flow rate predictions it could be appreciated that both the 2D and 3D models achieved in general very similar results for flowrate; as was previously found in research by both Alshaikh and Elmayyah. However at higher lift, there was also a slight reduction in accuracy for lifts greater than 3 mm; as mass flow rates were found to be overestimated when compared to experimental data. The results shown in figures 5.77 therefore suggest that the most significant differences between 2D and 3D modelling occur at higher disc lift values greater than 2 mm. It is suggested therefore that beyond 2 mm disc lift, the generation of 3D flow effects cause a significant reduction in accuracy for axisymmetric 2D modelling. This as a result challenges the validity of axisymmetric assumptions used in previous 2D PRV research for through flow PRV's. Figure 5.78 helps to supplement the results shown within figure 5.77 as the backpressure reported by CFD for both 2D and 3D simulations was found to be almost equivalent of each other. It could be suggested therefore that the flow regimes for the outlet facing section of the CFD models were similar with differences in force and 3D flow effects being generated within the disc/seat interface zone at the inlet facing side of the disc.

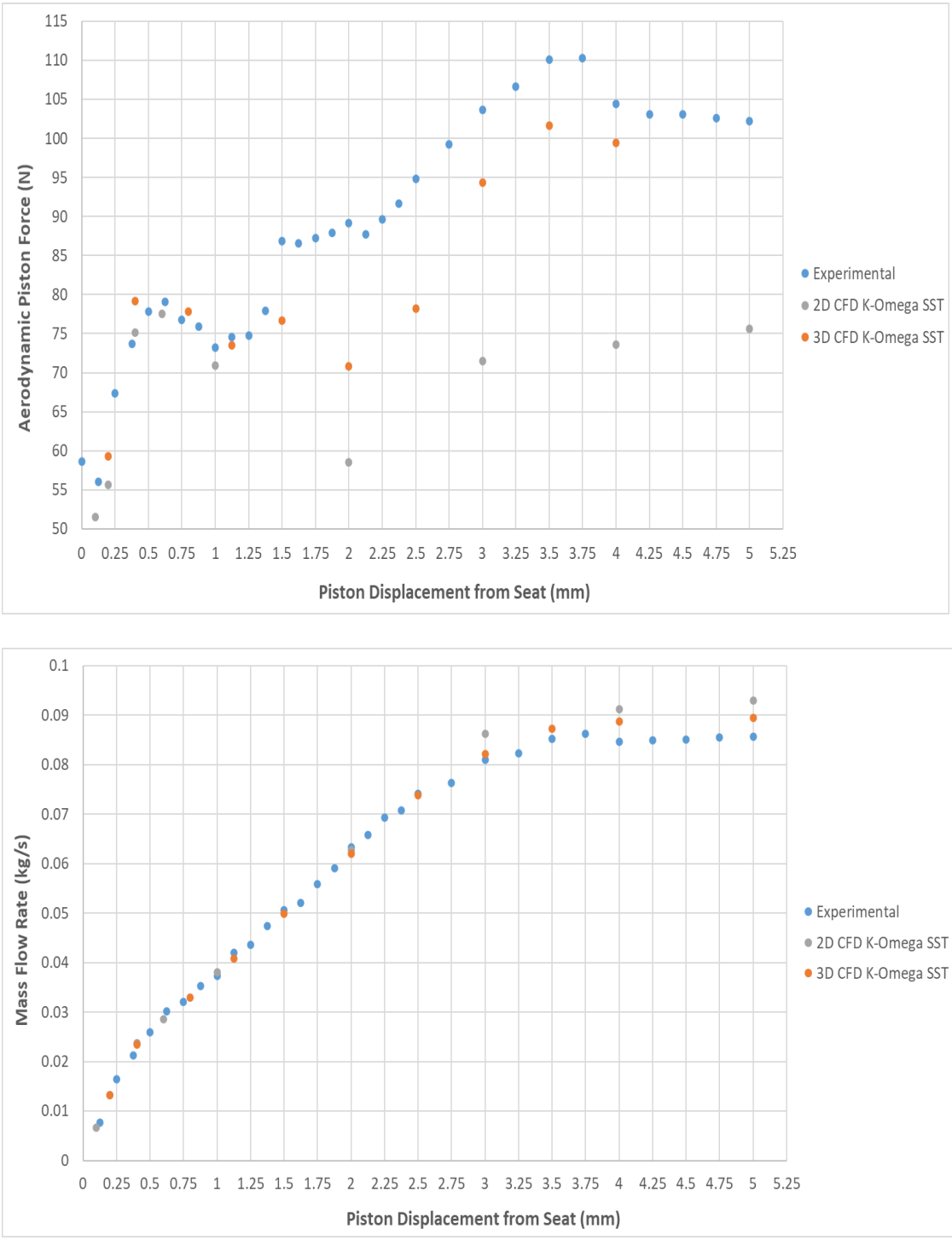

Figure 5.77 - Comparison of 2D and 3D K-Omega SST Disc Force (top) and Mass Flowrate (bottom) vs Lift Validation Results for 5231BX Modified Gland

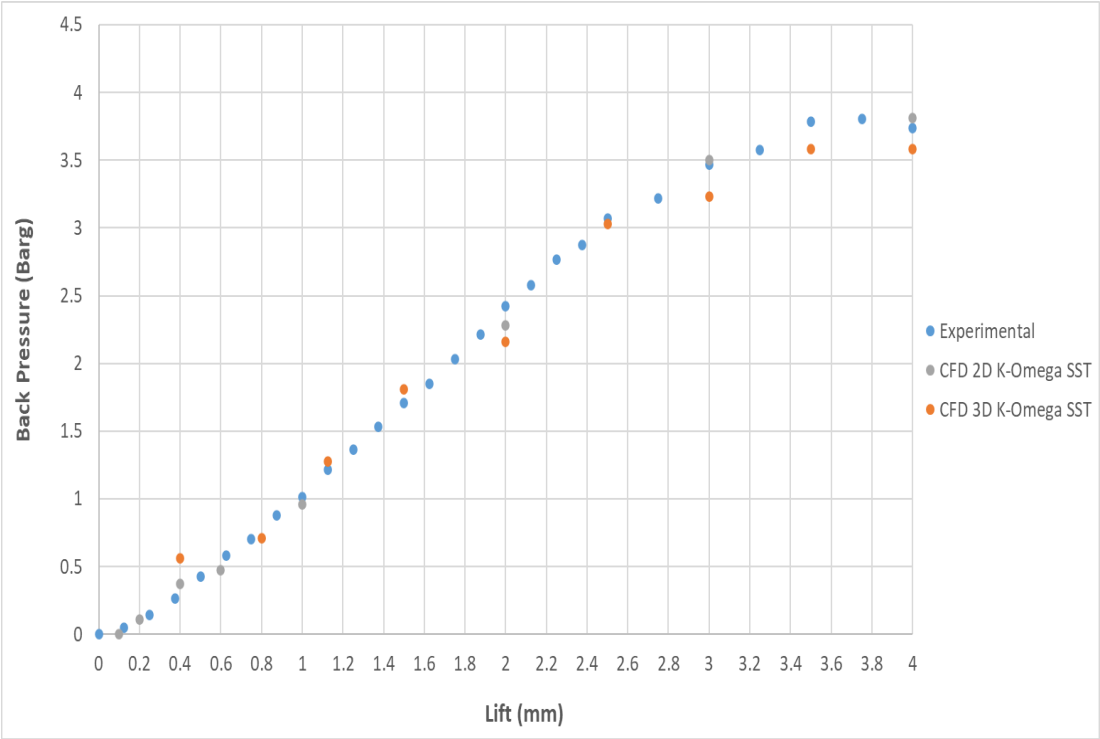

Figure 5.78 - Comparison of 2D and 3D K-Omega SST Back Pressure vs Lift Validation Results for 5231BX Modified Gland Geometry

The results indicated in Figure 5.78 for backpressure comparison allay the concerns in previous work by Elmayyah that the backpressure value would be the only source of differences between 3D and 2D modelling [11]. Elmayyah stated that he believed that the 2D model would produce a higher backpressure value when compared with the 3D model and that as a result would cause the 2D model to predict a lower disc force value. This is the case as shown within figure 5.77 however the results from figure 5.77 suggest that the backpressure is not the main source of difference between the two methods as the maximum percentage difference found between the two back pressure values at 3 mm was 8% and similar to the experiment. The disc force percentage difference between the two models at 3 mm however was 24%, therefore it was clear that there was a much more significant source of difference when using the K-Omega SST model for the standard 5231BX outlet. As indicated by figure 5.76 for the validation study of the Alshaikh outlet

geometry, there was a substantial difference in turbulence intensity at the inlet facing side of the disc at the outer face for both 2D and 3D models. This in turn was found to cause a noticeable variation in bulk flow features and static pressure distribution at the outer region of the disc as shown in figures 5.74 and 5.75 respectively. It was therefore concluded that the difference between the 2D and 3D models in the earlier identified disc/seat interface region was due to the generation of 3D flow effects below the disc.

From the 3D results for the quarter symmetry CFD model used for validation it was possible to use both the XZ and YZ symmetry planes to record both contours of mach number and static pressure to allow comparison to take place. If the use of axisymmetric 2D modelling was to be valid for the original outlet 5231BX PRV then the flow features found on both planes should be identical. However if differences are observed then the suggestion for the apparent generation of 3D flow effects in the disc/seat interface could be validated. Within figures 5.79 – 82, contours of Mach number are shown for both the XZ (left) and YZ (right) symmetry planes at disc lifts of 0.4 mm, 1.125 mm, 2.5 mm and 4 mm disc lift to allow the development of bulk flow features to be appreciated. Figures 5.83 – 86 also allow the appreciation in the development of static pressure at the disc/seat interface to be achieved.

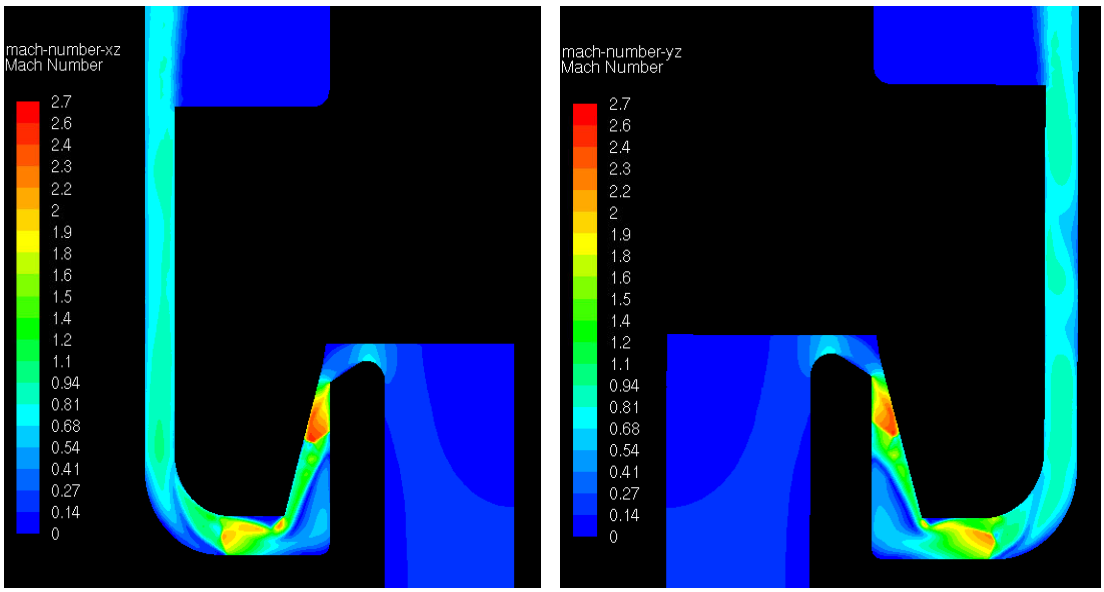

Figure 5.79 - Mach Number Comparison of XZ Plane (left) and YZ Plane (right) 3D K-Omega SST Model at 0.4 mm for 5231BX Modified Gland PRV

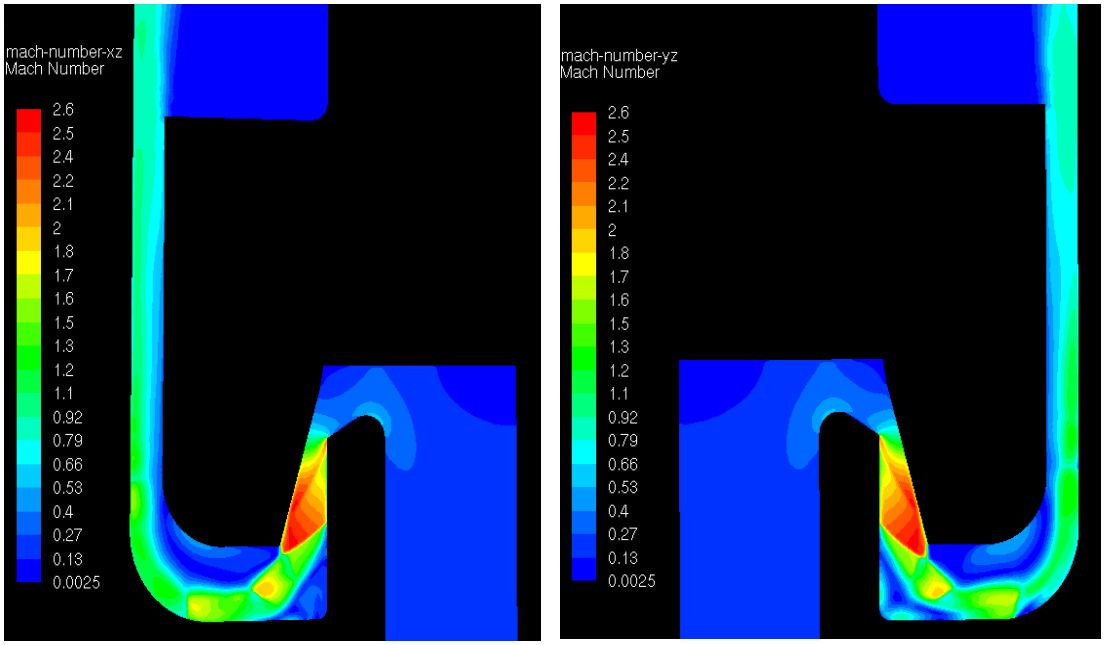

Figure 5.80 - Mach Number Comparison of XZ Plane (left) and YZ Plane (right) 3D K-Omega SST Model at 1.125mm for 5231BX Modified Gland PRV

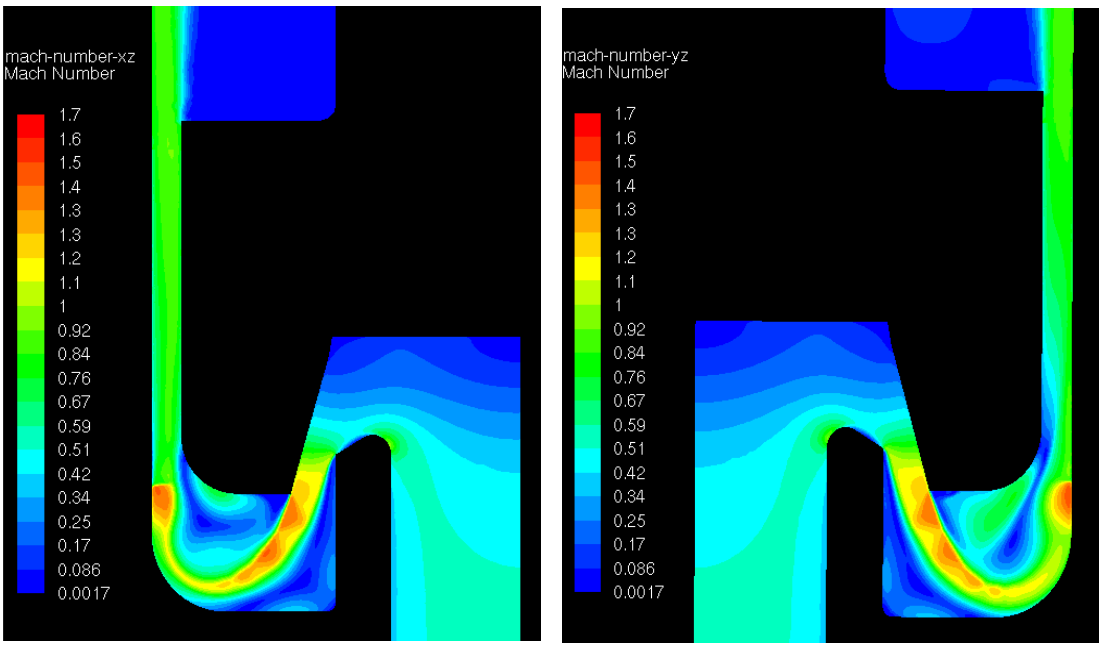

Figure 5.81 - Mach Number Comparison of XZ Plane (left) and YZ Plane (right) 3D K-Omega SST Model at 2.5 mm for 5231BX Modified Gland PRV

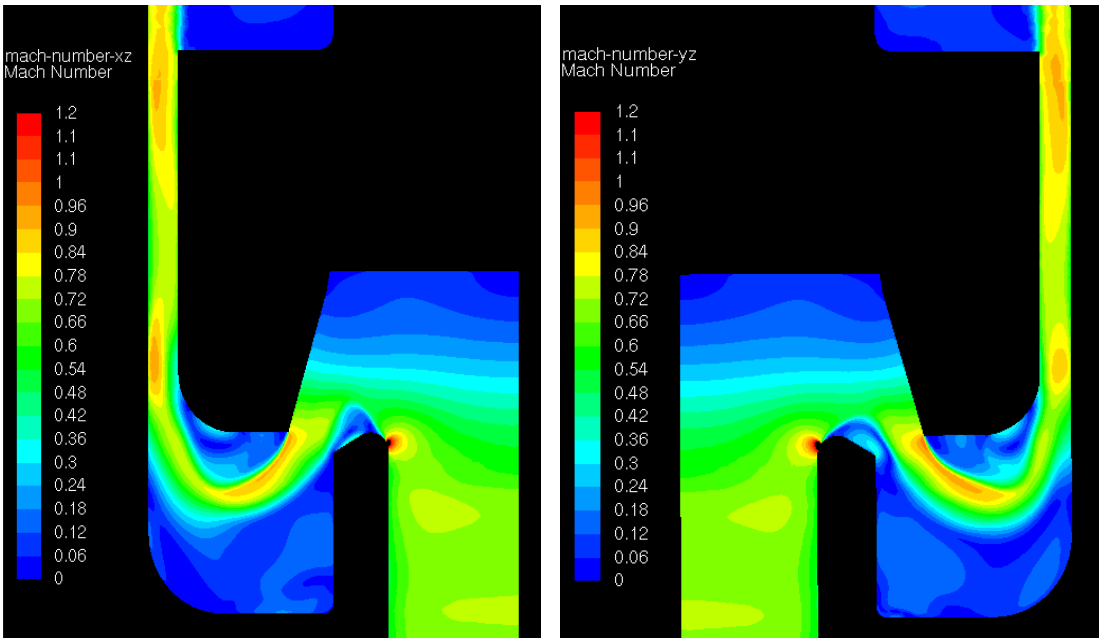

Figure 5.82 - Mach Number Comparison of XZ Plane (left) and YZ Plane (right) 3D K-Omega SST Model at 4 mm for 5231BX Modified Gland PRV

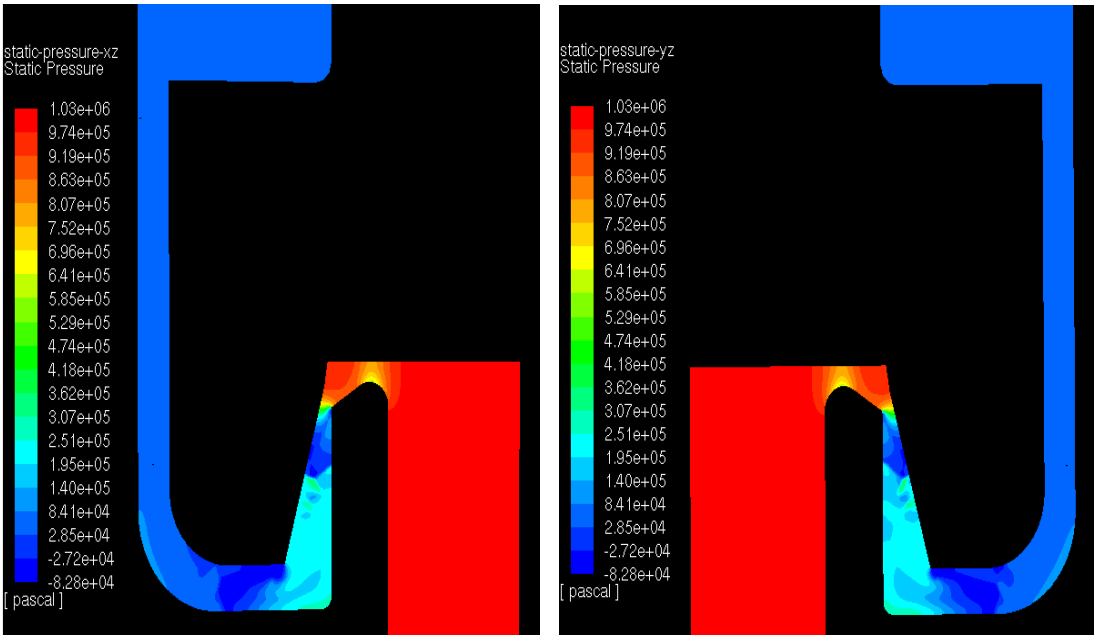

Figure 5.83 - Static Pressure Comparison of XZ Plane (left) and YZ Plane (right) 3D K-Omega SST Model at 0.4 mm for 5231BX Modified Gland PRV

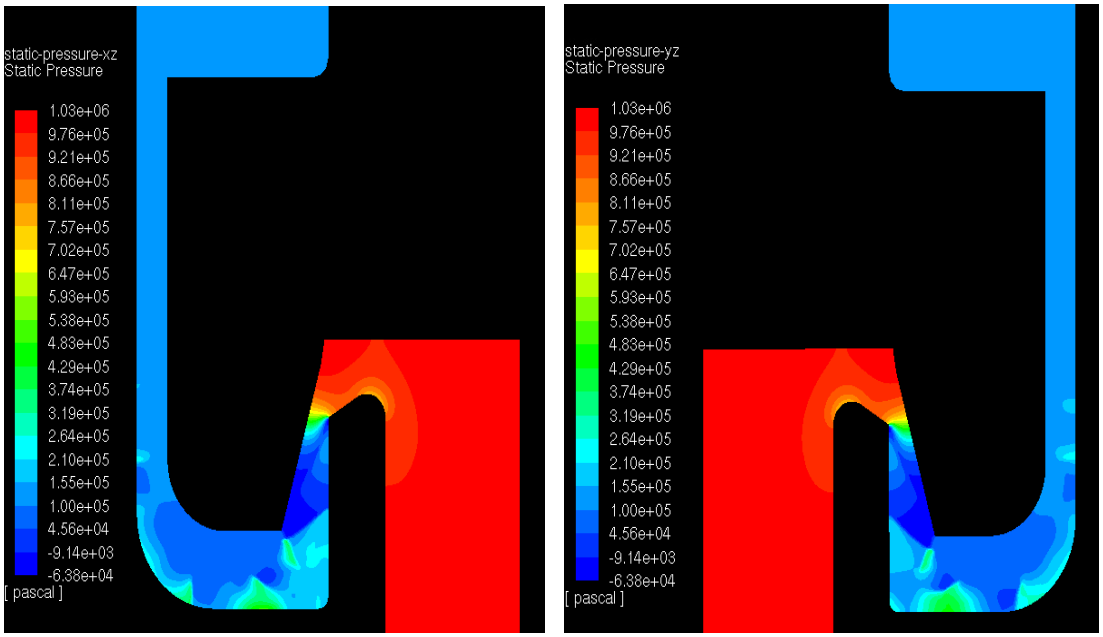

Figure 5.84 - Static Pressure Comparison of XZ Plane (left) and YZ Plane (right) 3D K-Omega SST Model at 1.125mm for 5231BX Modified Gland PRV

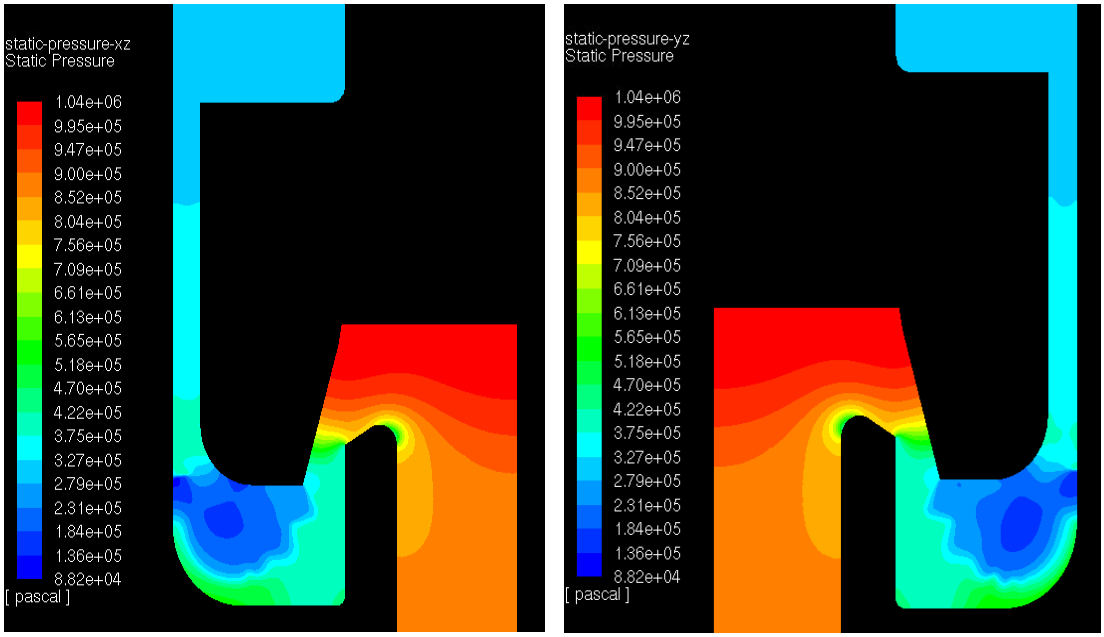

Figure 5.85 - Static Pressure Comparison of XZ Plane (left) and YZ Plane (right) 3D K-Omega SST Model at 2.5 mm for 5231BX Modified Gland PRV

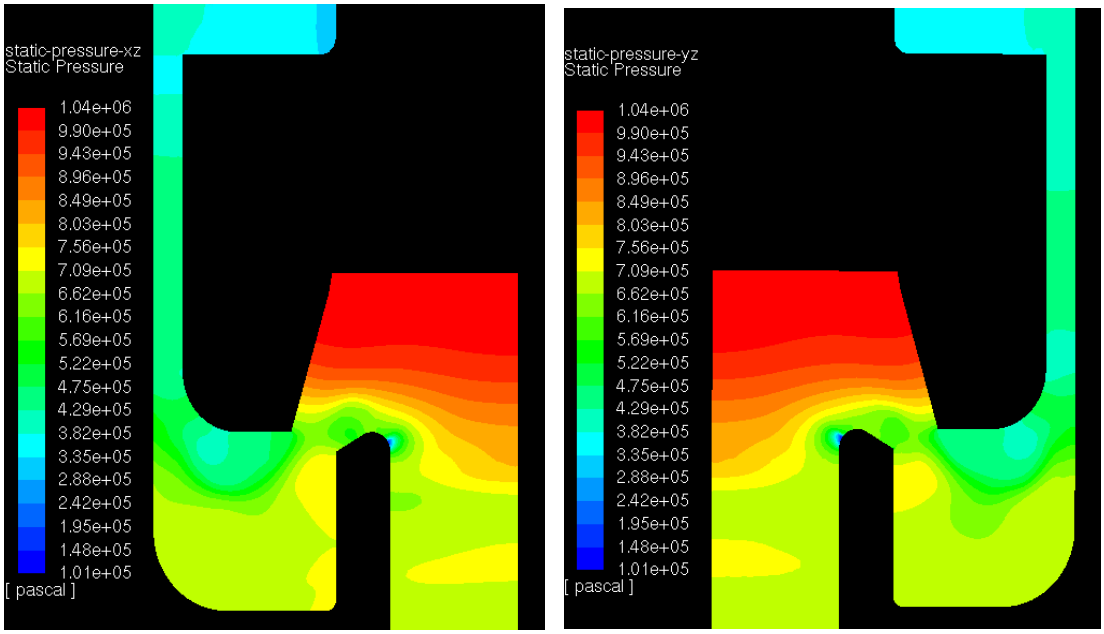

Figure 5.86 - Static Pressure Comparison of XZ Plane (left) and YZ Plane (right) 3D K-Omega SST Model at 4 mm for 5231BX Modified Gland PRV

As can be appreciated from figures 5.79 and 5.80 as well as figures 5.83 and 5.84, at low lift for 0.4 mm and 1.125 mm there is little difference in flow features between the XZ and YZ symmetry planes which confirms that there is little generation of 3D flow effects at low lift. This also helps to reinstate the reason as to why the results of both disc force and mass flow rate are in close agreement for both the 2D and 3D models at low lift as is shown within figures 5.77 and 5.78. By using figures 5.79 and 5.80, an understanding towards the bulk flow physics could be achieved. It can be seen that as flow enters through the inlet, it is initially turned and expanded using a Prandtl-Meyer expansion fan which results in the flow to reach a Mach number of up to 2.7 as it is expanded. The initial choking point for both 0.4 mm and 1.125 mm occurs at the seat geometry as the flow is initially turned 180 degrees however the choking point moves in the outlet direction as disc lift increases. Following the Prandtl- Meyer expansion the flow is then decelerated and turned once more towards the annular passageway between the disc and PRV body. Within this annulus it is clear that the flow is choked. From the static pressure plots it can be clearly seen that the majority of the high pressure which drives the disc force is acting in the central area of the disc with small gradients of static pressure change at the outlet region of the disc.

By comparing figures 5.80 and 5.81, it was clear that the bulk flow features between 1.125 mm and 2.5 mm had significantly transformed with the additional disc lift. The outer cavity between the PRV body and disc had noticeably increased in size as indicated in figure 5.81; which allowed the generation of a much more complex flow pattern at the outer disc region when compared with figure 5.80 for 1.125 mm. In addition it should also be noted that the initial choking point had moved to the outer edge of the seat protrusion. Figure 5.85 also highlights the effect the change in bulk flow features had on the static pressure distribution. It could be observed that a greater proportion of the disc surface was subjected to a higher pressure than at lower lifts which in turb would result in a greater disc force. On the other hand however the complex flow pattern within the outer disc region had induced the production

of a low pressure, recirculation region acting on the outer disc surface. Critically, within figure 5.81 a noticeable variation in bulk flow features within the low pressure recirculation region could be seen between the symmetry planes however the static pressure prediction remained fairly equal across both. The difference observed for the Mach number contour plots however highlighted the possibility of the generation of 3D flow effects within the outer cavity between the outer surface of the disc and PRV body.

Finally, from figure 5.82 at 4 mm disc lift the flow regime at maximum discharge rate and lift can be appreciated. As found in previous work by Elmayyah and Alshaikh [11, 12], the choking point of the flow at higher lifts moved to the annulus formed between the disc and body. The size of the cavity between the outer region of the disc and body was also significantly larger than at 2 mm where it can be seen that the bulk flow is no longer in contact with the bottom wall of the PRV body in the cavity. As a result, the change in direction of the jet is controlled by the recirculation region formed at the outer radial surface of the disc. The complex nature of the flow regime as can be seen in figure 5.82 results in a clear difference in flow features within the outer cavity highligting a break down in axisymmetric flow conditions. The symmetry breaking 3D flow effects also result in a slight variation in static pressure distribution at the outer surface of the disc as can be seen in figure 5.86. To provide a further appreciation in the differences of the flow regime across both symmetry planes, a contour plot showing turbulence intensity in the disc/seat interface area is shown within figure 5.87 at 4mm lift. It is clear from figure 5.87 that there is a difference in turbulence intensity between the symmetry planes affecting the bulk flow features and also confirms the generation of 3D flow effects in the outer cavity. The breakdown of axisymmetric flow conditions therefore results in the differences observed for both flowrate and disc force prediciton at higher lifts for both 2D and 3D modelling as has been shown within figures 5.77 and 5.78. However within figures 5.77 and 5.78, it is apparent that there is a reduction in accuracy for both the 2D and 3D models especially between 2-3 mm.

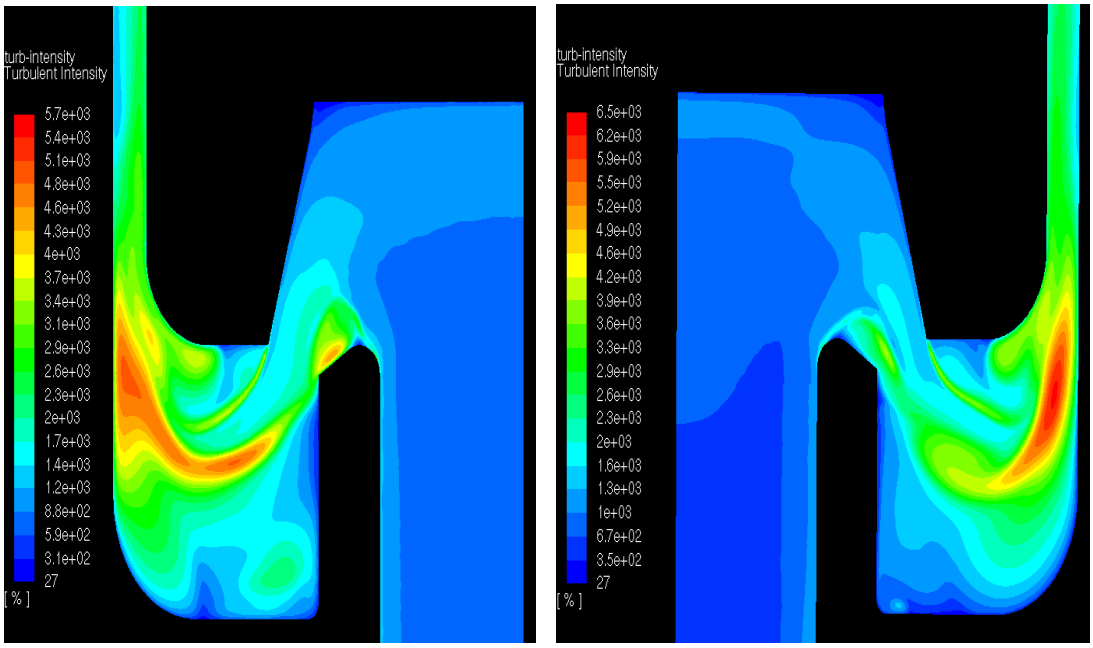

Figure 5.87 – Turbulence Intensity Comparison of XZ Plane (left) and YZ Plane (right) 3D K-Omega SST Model at 4mm for 5231BX Mod Gland PRV

In an attempt to identify the cause of inaccuracy between 2-3 mm from figures 5.81 and 5.85 at 2.5mm, it is clear that the jet is in contact with the wall of the PRV body within the outer cavity and there is the generation of a large low pressure area at the outer surface of the disc. The correlation error however reduces as disc lift increases towards 4 mm where the jet becomes detached from the wall of the PRV body at the cavity. Therefore it could be suggested that the prediction of the separation of the jet as well as the shear forces predicted at the walls could provide a source of error for the CFD model. This would result in a reduction in correlation with experimental data when compared with other data points at lower and higher disc lifts.

When referencing previous research performed by Padrón on the generation of symmetry breaking flow phenomena in axisymmetric domains, the flow conditions within the 5231BX meet the criteria set by Padrón for such flow bifurcations. This is due to the fact that at lifts greater than 2 mm the Reynolds

number of the flow with flow velocity reaching values greater than Mach 2. When the high Reynolds number flow is combined with an expansion of the inner disc/seat interface to the outer cavity, the ratio of domain heights is approximately three and continues to rise as the disc opens further. Padrón states that the combination of such flow and geometrical conditions at Reynolds number greater than 1500 can promote the generation of additional separation zones which are no longer symmetrical and exist within the turbulent flow regime. Therefore, the work performed for the 5231BX provide a suitable example of the suggestions by Padrón that symmetry breaking phenomena “constitute an outstanding challenge for CFD” as the region has displayed during validation sensitivity to both meshing and selection of turbulence model. Given the importance of accurately capturing the pressure distribution at the lower surface of the disc which is strongly affected by the 3D flow effects highlights the reason for CFD modelling difficulty in the cavity region and the requirement of a fine mesh to capture the significant flow gradients. In addition, it highlights the importance of using as little/no symmetry conditions at possible; however, this is not always feasible depending on computational constraints.

Interestingly however as has been shown in figure 5.79, the prediction of back pressure between 2D and 3D modelling remained similar. These results therefore suggested that the outlet side of the disc from the upper disc surface to the outlet wasn’t subjected to such flow bifurcations and generation of 3D flow effects as was found for the flow area below the disc. In order to fully appreciate the flow regimes at the outlet area, a series of contour plots for both static pressure and Mach number are shown for lifts of 0.4 mm, 1.125 mm and 4 mm. Figures 5.88 – 90 provide contour plots for Mach number and figures 5.91 – 93 provide contour plots for static pressure. It should be noted that for all figures, the YZ quarter symmetry plane from the 3D modified gland 5231BX PRV geometry was used as no differences were observed with the XZ plane.

From figures 5.88-90 it can be seen that in general, the flow pattern for Mach number across the full lift range remains similar with flow choking at the outlet. As a result there is little opportunity for the development of significant 3D flow effects across the full lift range. Therefore as can be seen from the earlier results, 2D modelling can easily capture the backpressure and flow pattern accurately downstream of the disc and little difference is found due to 3D modelling. In addition, the backpressure development from figures 5.91-93 highlight that the pressure gradients in general increase as flowrate and lift are increased. This therefore results in a higher backpressure to act on the upper surfaces of the disc to reduce the overall disc force at higher lifts. Hence as no significant differences in backpressure were found between 2D and 3D simulations as shown in figure 5.79, it could be concluded that the suggestion of Elmayyah of a reduction in backpressure for the 3D case would significantly affect the disc force was not valid. Rather the differences occur below the disc.

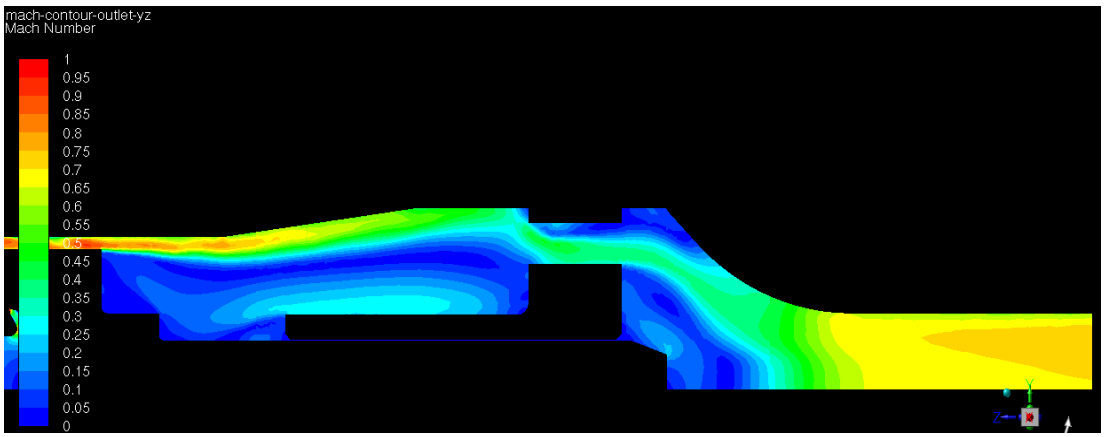

Figure 5.88 - Mach Number Contours of YZ Plane at Outlet Area for 3D K-Omega SST Model at 0.4 mm for 5231BX Modified Gland PRV

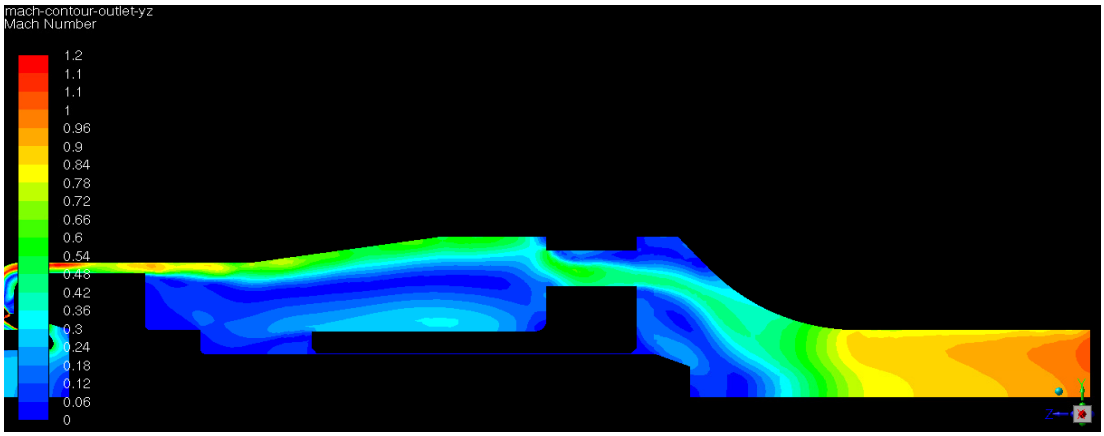

Figure 5.89 - Mach Number Contours of YZ Plane at Outlet Area for 3D K-Omega SST Model at 1.125 mm for 5231BX Modified Gland PRV

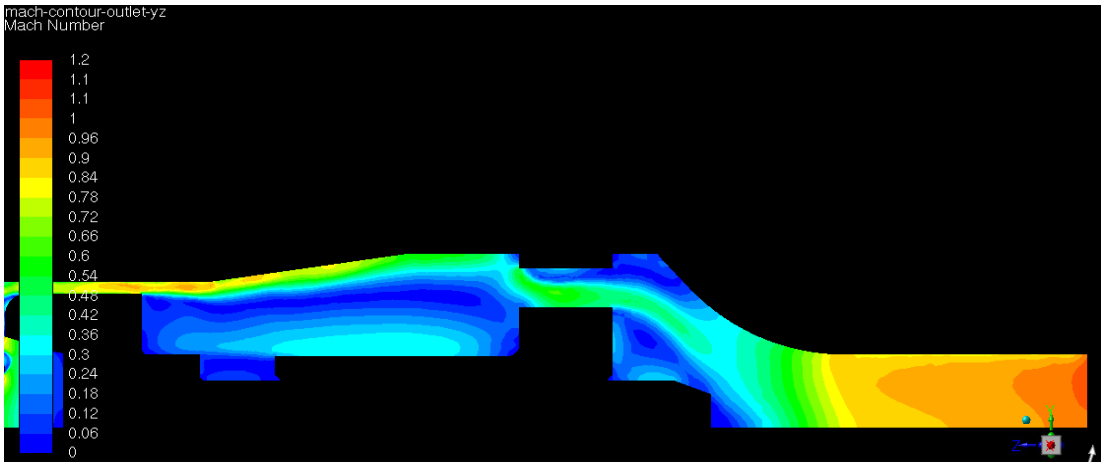

Figure 5.90 - Mach Number Contours of YZ Plane at Outlet Area for 3D K-Omega SST Model at 4 mm for 5231BX Modified Gland PRV

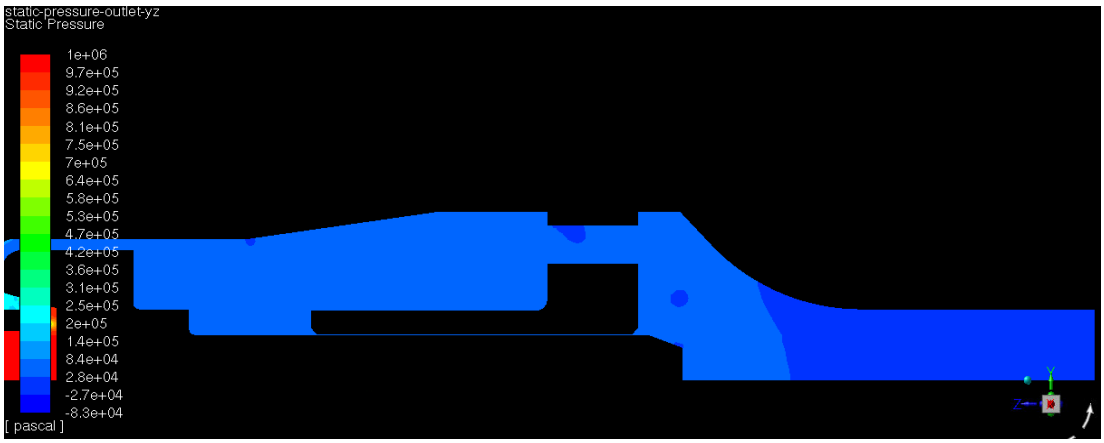

Figure 5.91 – Static Pressure Contours of YZ Plane at Outlet Area for 3D K-Omega SST Model at 0.4 mm for 5231BX Modified Gland PRV

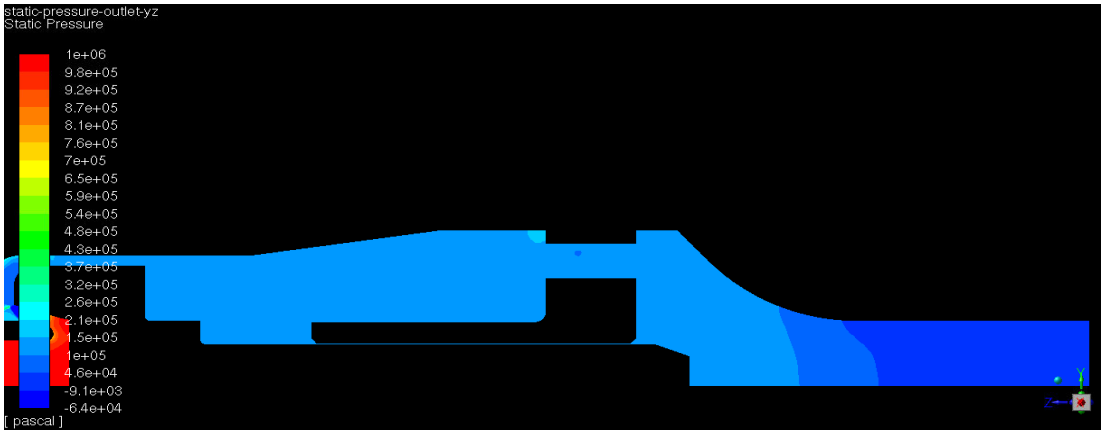

Figure 5.92 - Static Pressure Contours of YZ Plane at Outlet Area for 3D K-Omega SST Model at 1.125 mm for 5231BX Modified Gland PRV

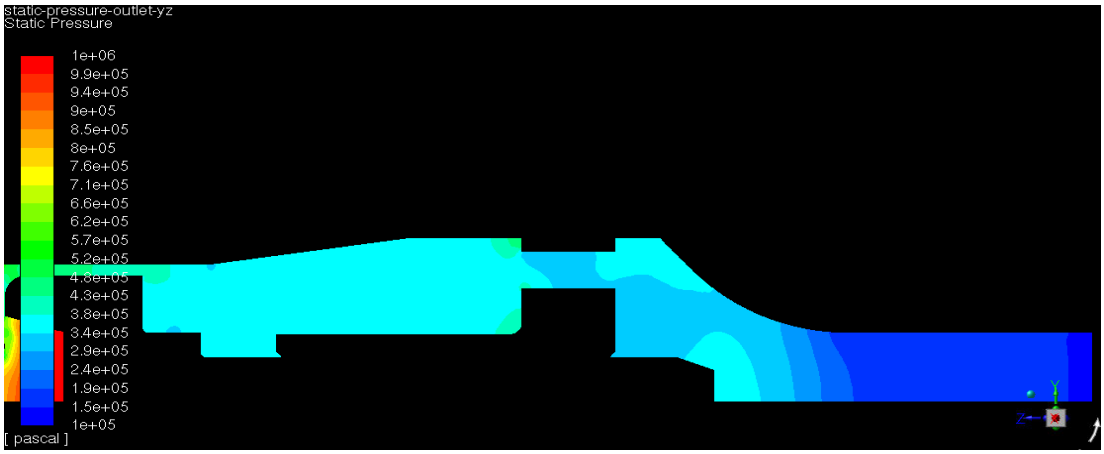

Figure 5.93 - Static Pressure Contours of YZ Plane at Outlet Area for 3D K-Omega SST Model at 4 mm for 5231BX Modified Gland PRV

5.3 Summary of Steady State CFD Validation Research for Both 3511E (Right Angled) and 5231BX (Through Flow) PRV's

Following an extensive CFD steady state validation study using ANSYS Fluent and Workbench for both the right angled type Broady 3511E PRV and through flow type Henry 5231BX PRV a number of conclusions could be established;

- For the Broady 3511E PRV, experimental data was provided for an inlet pressure of 3.3 barg during research by Taggart [9]. Data was provided at 15 discrete lifts from the almost closed position at 0.1 mm to fully open at 4mm. Both aerodynamic disc force and mass flow rate were recorded at each data point utilising the quasi steady assumption.

- For the Broady 3511E PRV, a half symmetry CFD model was developed using the K-Omega SST turbulence model at 3.3 barg inlet pressure. Over the course of the full lift range, an average percentage difference of the CFD results to experimental data for mass flow rate was found to be 1.6% for mass flow rate and 0.83% for disc force.

- Within the flow testing laboratory at the University of Strathclyde, an experimental rig for the Henry 5231BX PRV was developed to provide measurement of disc force and mass flow rate at lifts from 0.1 mm to 5 mm. Previous research at Strathclyde for through flow type PRV arrangements used 2D CFD modelling therefore a modified gland was manufactured and installed to achieve an axisymmetric domain suitable for 2D simulations. Experimental data was then generated for both the original gland and modified gland to validate that the flow rate was identical for both. However, a difference was observed for disc force; with the modified gland experiencing a higher force value due to a decrease in backpressure.

- As previous work used 2D CFD modelling for through flow PRV geometries, a 2D CFD model was developed for the 5231BX with modified gland. However, the 5231BX used in this study was different to the valves used in previous research as Alshaikh [12] used a 5231BX with a larger outlet during his validation study. It was shown during the CFD validation study that the 2D CFD models were unable to achieve the accuracy claimed during the validation work of Alshaikh using a 2D model with the standard K-Epsilon turbulence model. Both the standard K-Epsilon and K-Omega SST turbulence models were unable to achieve sufficient accuracy for disc force however the models were capable of good correlation for mass flow rate. In order to verify both the experimental and CFD methodologies within this research a test case was constructed using the PRV geometry used by Alshaikh during his research. During this work an experimental study and CFD study was performed using the larger outlet where it was also found that the 2D CFD K-Epsilon model provided the best performance and closest correlation to experimental data. As a result it could be concluded that the difference in outlet geometry was causing a significant modelling challenge for the smaller case. However, it was unclear whether or not the 2D CFD model provided the best accuracy for flow features, or the combined modelling error of the standard K-Epsilon model was resulting in false confidence of the CFD method.

- Due to the inaccuracy of the 2D CFD model for the 5231BX PRV, as suggested in previous work by Elmayyah [11] a 3D CFD model was developed to determine if an improvement in accuracy for disc force could be achieved. A quarter symmetry 3D CFD model was developed for both the original and modified gland 5231BX test cases as well as for the Alshaikh case with larger outlet modifications. For both gland cases, the 3D K-Omega SST turbulence model provided the best performance with an average correlation to experimental data of 1.67% for mass flow rate and 5.11% for disc force. In the case of the larger

outlet used in the work by Alshaikh, a significant improvement from the 2D K-Omega SST CFD model using the 3D K-Omega SST model was found however the 2D standard K-Epsilon model remained the best choice. This therefore validates the work found by Alshaikh [12] and highlights a sensitivity for outlet geometry on the use of both 2D and 3D modelling as well as turbulence model selection.

- Over the course of the Henry 5231BX validation study, significant differences in the performance of the 2D and 3D CFD models were found. As shown in the case for the modified gland, the 3D K-Omega SST turbulence model provided significant improvement to the 2D equivalent with close correlation to experimental data. It was found that the difference observed between the two models was due to the generation of 3D flow effects caused by symmetry breaking bifurcations. These bifurcations were due to the flow conditions within the PRV meeting criteria for both Reynolds number and geometrical expansion set in research by Padrón for symmetry breaking within axisymmetric domains. It was established by Padrón that when such conditions exist, additional separation zones are generated within the turbulent flow regime causing the flow to no longer be axisymmetric in an otherwise axisymmetric domain. It could therefore be concluded that for the 5231BX PRV geometry used within this study, which is representative of a typical production PRV that the use of axisymmetric boundary conditions within 2D CFD simulations were not valid. This challenges the recommendations previously established by both Elmayyah and Alshaikh for through flow PRV's.

- Both the validated 3D CFD models for the Broady 3511E PRV and modified gland 5231BX PRV using the K-Omega SST turbulence models will be used as a base for transient, dynamic mesh CFD models to be developed from.

CHAPTER 6

VALIDATION OF TRANSIENT MOVING MESH PRV CFD MODELS FOR SINGLE PHASE FLOW

In this chapter, the 3D steady state CFD models which were developed for both the Broady 3511E PRV at 4 notches and the Henry 5231BX PRV with modified gland will be extended for transient analysis using dynamic meshing techniques. The transient CFD analysis for single phase air flow required the development of a moving mesh fluid structure interaction model using the capability in FLUENT 17 and 18.1 to determine the position of the disc as inlet pressure changes. Such an approach therefore allows the effect of disc motion on the valve flow behaviour to be captured and assess the validity of quasi steady assumptions inherent in many design models. In addition to the development of transient CFD models, experimental techniques capable of capturing the dynamics of the PRV were developed to evaluate the accuracy of the CFD models.

6.1 Broady 3511E PRV Transient Validation

Within this section a transient moving mesh CFD simulation of the Broady 3511E PRV will be developed and validated against experimental data generated by Taggart [9] in a similar manner to the earlier steady state work. For all of the data generated both experimentally and computationally, a notch position of 4 for the blowdown ring was used as previously established in chapter 5.1, notch position 4 corresponded to the upper ring face being a height of 0.03mm above the datum seat position. Single phase air was used as the test medium for a set pressure for the PRV of approximately 3.3 barg.

6.1.1 Experimental Dynamic Testing for Broady PRV

The flow testing laboratory at Broady Flow Control was used by Taggart for dynamic testing however modifications were required to the steady state layout shown in figure 5.3 and table 5.1 in chapter 5.1. The load cell for the spindle was removed to allow an LVDT (Linear Variable Differential Transformer) to be installed to measure the linear displacement of the disc from the seat. This device would allow a time vs disc displacement (lift) relationship to be established as inlet pressure changes. Instead of maintaining a constant pressure of 3.3 barg for steady state, during dynamic testing it was necessary to slowly increase the pressure of the upstream vessel from below the set pressure (3.3 barg) to accurately capture the opening behaviour of the valve. Once the PRV was at full discharge capacity, the vessel pressure would drop significantly to allow the closing characteristics of the PRV to be captured. The set pressure of 3.3 barg was achieved by adjusting the pre-load of the spring until first audible leakage was identified as a marker for set pressure. This technique for identifying set pressure is recommended by ASME however it is subjective and can vary between PRV manufacturers causing a degree of ambiguity when defining set pressure.

Figure 6.1 shows the applied pressure profile established during the transient experiment which resulted in the valve opening and closing. The corresponding disc response is shown in Figure 6.2 where the disc position vs time curve is presented. Both the overpressure and blowdown values measured experimentally are shown in table 6.1.

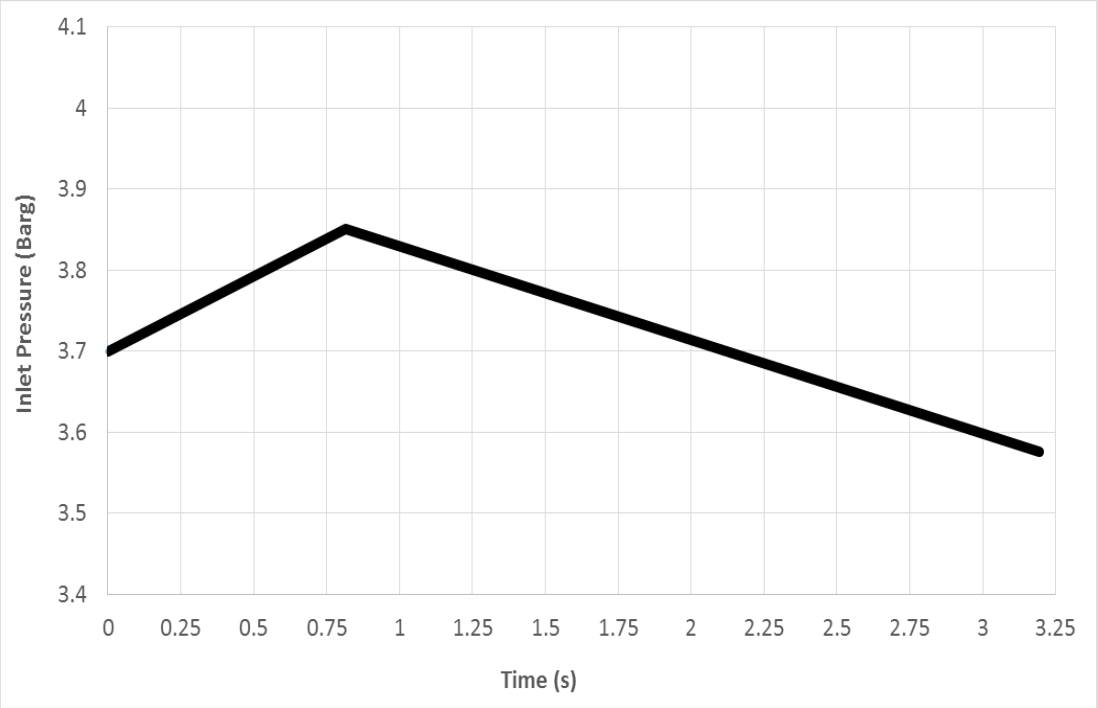

Figure 6.1 – Experimental Inlet Pressure Profile vs Time for Broady 3511E PRV at 4 Notches

The results for both over pressure and blowdown are shown within table 6.1 which meet the manufacturers expected performance for the notch position. It should be noted that the PRV performance shown in table 6.1 would not be considered operationally acceptable and could be improved by adjusting the notch position however notch 4 has been selected as a case for modelling. A total of 4 independent tests were carried out to obtain a mean value for over pressure and blowdown pressure reported within table 6.1 with a statistical error of 0.26% and 0.31% observed respectively.

The dynamic performance of the PRV can be appreciated from figure 6.2. During the initial phase, the PRV remains in a low lift huddling position of 0.1-0.25mm until 0.8s where the inlet pressure reaches a value of 3.85 barg. At this point the PRV popped open to a maximum disc displacement (lift) of 4 mm corresponding to an over pressure value relative to the set pressure of 16.67%.

After reaching maximum lift, as shown in figure 6.1 the inlet pressure decreased which allowed the disc to slowly close towards a disc lift of 2.75 mm at 2.85 s. The critical inlet pressure at this time was 3.6 barg (9.09% Blowdown Pressure) where the disc accelerated quickly to the closed position in order to reseal the system and prevent any further loss of vessel contents. In general, the dynamic behaviour of the 3511E PRV (notch 4) is stable with a clear opening and closing point with little oscillation. These characteristics are desirable to ensure that no damage is caused to the PRV and there are optimum conditions to initially relieve pressure and subsequently reseal the system to minimise loss of vessel contents once a safe pressure is reached.

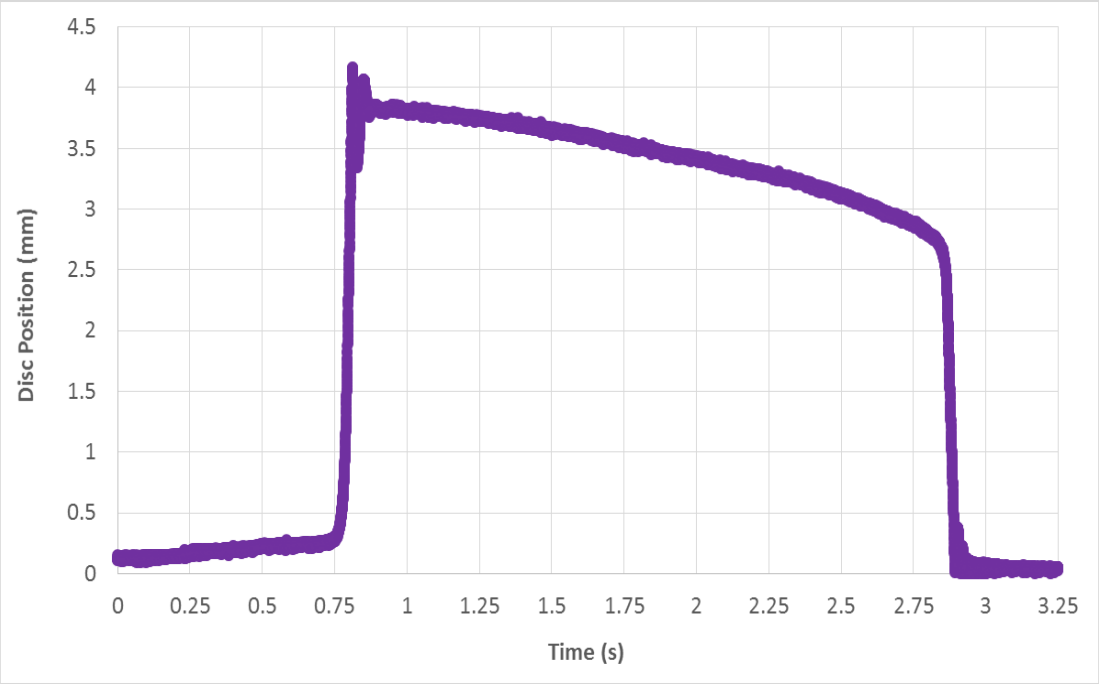

Figure 6.2 – Experimental Disc Position (Lift) vs Time for Broady 3511E PRV, (blowdown ring at Notch 4)

6.1.2 Development of Transient Moving Mesh CFD Model for Broady PRV

From the development of the 3D half symmetry steady state CFD model for the Broady 3511E PRV it was possible to establish an effective transient moving mesh 3D CFD methodology. This approach would allow a CFD based representation of the dynamic performance of the PRV during nominal operation to be achieved. The model was generated using the geometry and meshing tools available in ANSYS Workbench 17 and subsequently solved using ANSYS FLUENT 17. It should be noted that in order to utilise moving mesh methods for the transient CFD model, it was required for the PRV to not be fully closed with at least a single layer of cells to maintain the required mesh topology during mesh deformation. This therefore represented a source of inaccuracy for the CFD model as the initial contact would not be able to be captured using the dynamic mesh methods available within ANSYS FLUENT. As a result, the error was minimised through a series of design iterations of the computational model for an initial disc opening of 0.07 mm to be used (1.75% of maximum disc lift) as can be seen within figure 6.3. This therefore allowed the remaining 98.25% of PRV disc travel to be captured as well as remaining within the huddling region observed during experiments. The mesh design methodology utilised here was focussed on minimising the initial opening of the PRV in order to remove any induced error caused by the simulation starting from an open position. In real world application the PRV would remain closed with zero flow through the valve until the disc lifts from the seat. In reference to the experimental lift vs time curve shown in figure 6.2, an opening of 0.07 mm was deemed acceptable due to the nature of the Broady valve simmering with flow moving through the system at a lift greater than 0.07mm. In addition, when compared with maximum lift of 4mm it represents a gap of 1.75% maximum lift. The error induced by this assumption would therefore be expected to be insignificant as the CFD model would be operating within the simmering regime initially.

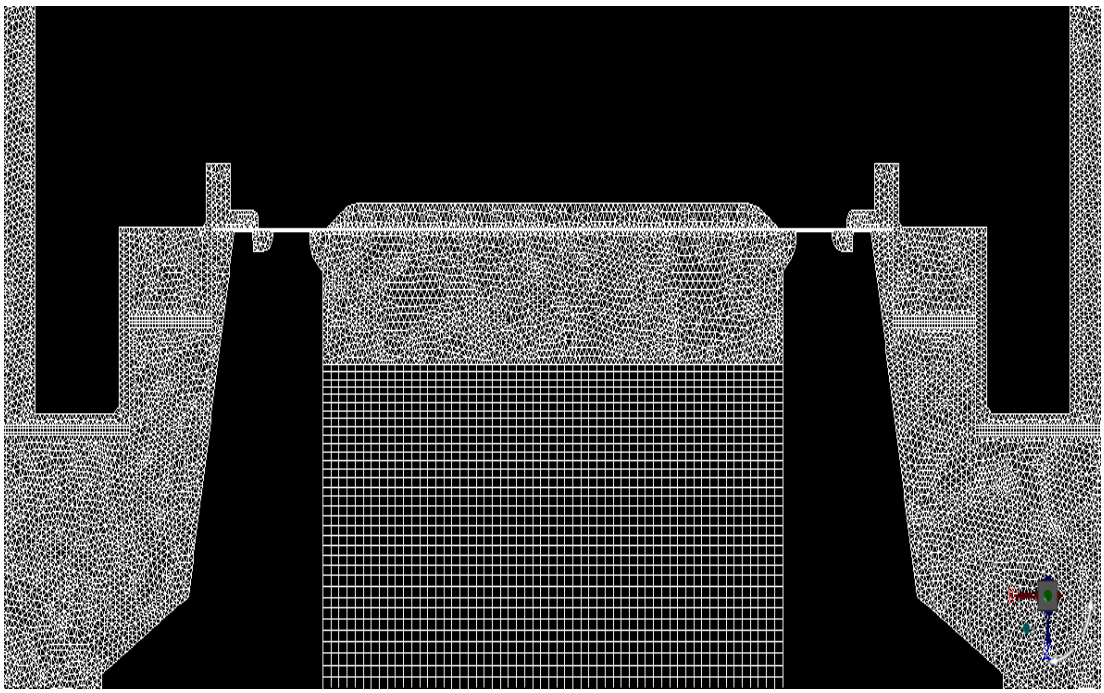

Figure 6.3 – 3D CFD Dynamic Mesh at Initial Lift of 0.07 mm for 3511E PRV

The overall half symmetry computational domain is shown on figure 6.4 where various changes could be observed from the mesh developed during the steady state validation process. It should be noted that the mesh density determined during the steady state validation study was maintained across the domain however due to the use of tetrahedral elements the total number of elements within the model at 0.07mm lift was 11.8 million compared to 9.1 million for steady state. The general bulk flow path across the PRV is marked using the yellow flow arrows in which flow originates from a pressure inlet marked in red and progresses towards both the atmospheric outlets marked in green.

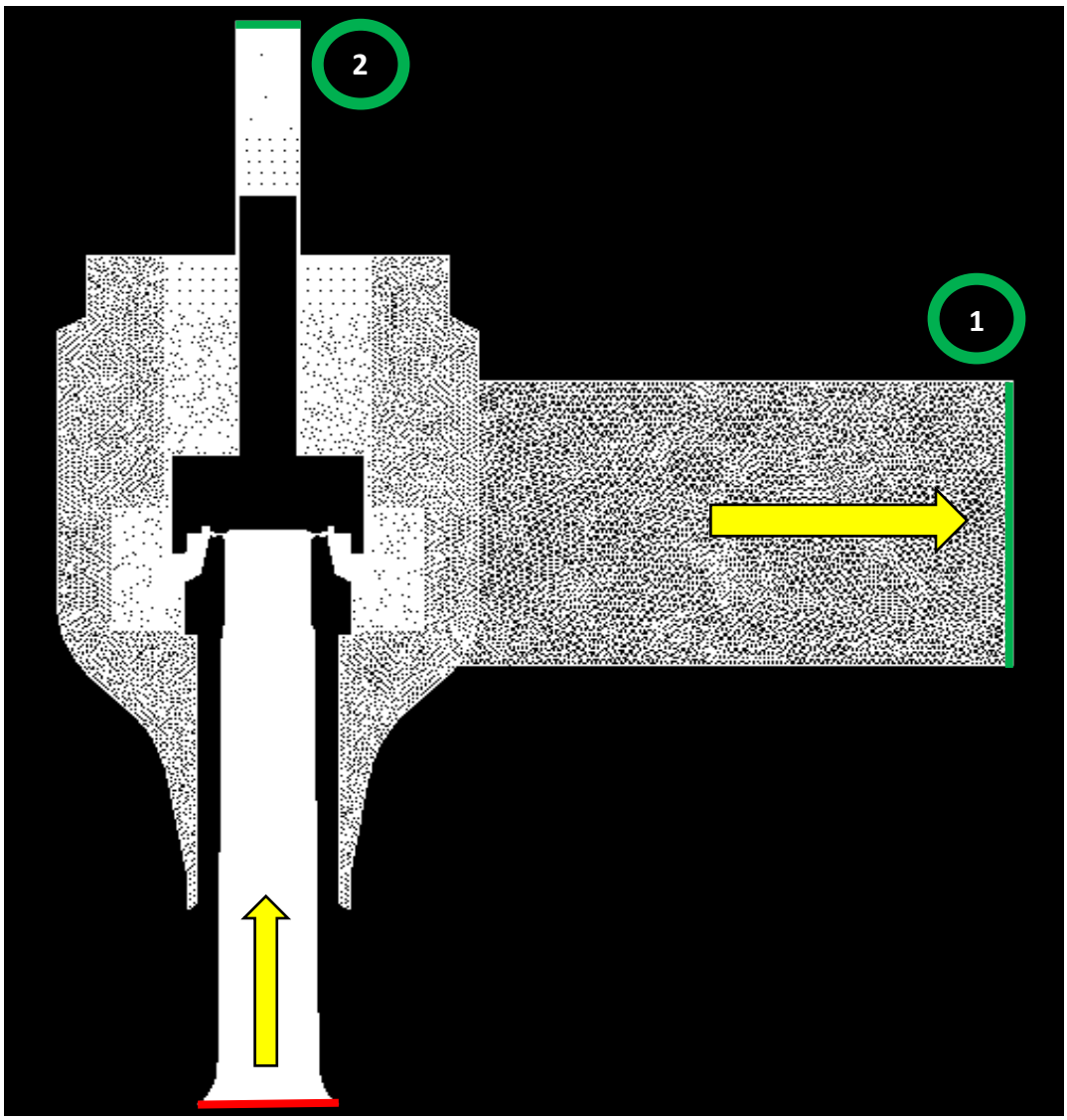

Figure 6.4 – Overall CFD Dynamic Mesh for Broady 3511E PRV (Notch 4)

An additional outlet (marked 2) was required directly above the disc in order to maintain an atmospheric pressure to act on the upper surface of the disc spindle as would occur in reality. This would therefore prevent any unrealistic change in surface pressure being caused due to flow effects at the disc surface and ensure that the pressure acting on the spindle was atmospheric. The narrow passage between the spindle and outlet wall was found to be suitably narrow and long to provide an effective seal for the top outlet to allow the majority of the flow to pass towards the flanged outlet (marked 1).

The overall mesh structure could also be appreciated from figure 6.4 in which it can be seen that the surrounding mesh consists of tetrahedral mesh elements however the structure remains unclear within the dense mesh regions. Figure 6.5 and 6.6 however help to illustrate the hybrid nature of the mesh developed for the transient, moving mesh CFD model. The discretisation shown is commonly known as the Domain Discretisation Method (DDM) where the use of a hybrid mesh was selected to accurately capture the complex geometry at the near disc/seat area and at the blowdown ring but allow the use of a structured mesh for dynamic layering. Dynamic layering was selected as the mode for mesh deformation as it would allow sufficient mesh quality to be maintained during mesh movement. During mesh deformation the structured zones would be discretized through cell layer creation/deletion which was achieved by defining a split and collapse factor based on the minimum cell height of a cell layer. From figures 6.5 and 6.6, it's clear that the mesh would allow dynamic layering in the red regions which are connected to unstructured mesh regions (blue) using conformal interfaces. The rigid motion of the blue zone was subjected to pre described motion within a User Defined Function (UDF); the operation of the UDF was described within the numerical methods chapter 4.5. It was also necessary for unstructured stationary zones (yellow) to be connected to the deforming mesh zones (red) to prevent further mesh deformation. Critically, non-conformal interfaces were required for the mesh zones surrounding the moving regions highlighted in red, yellow and blue to allow the rigid and deforming mesh zones to slide in reference to the surrounding mesh during mesh motion. This, as a result would prevent the generation of negative volumes and instability during computation. Due to the use of DDM, the deformation of the structured mesh within the deformation (red) zones could be controlled with the near wall mesh maintained during mesh movement.

The overall dynamic meshing strategy developed therefore represented a dynamic mesh system in which the unstructured rigid motion mesh zone (blue) would deform the structured mesh zone (red) using a conformal interface to

extend and retract the deforming zone as the value of disc lift changes. Conversely, the stationary (yellow) mesh zone would act as a physical stop to the mesh deformation at the conformal interface. This would therefore improve resilience of the simulation by helping to prevent the generation of poor quality and/or negative volume cells during mesh deformation.

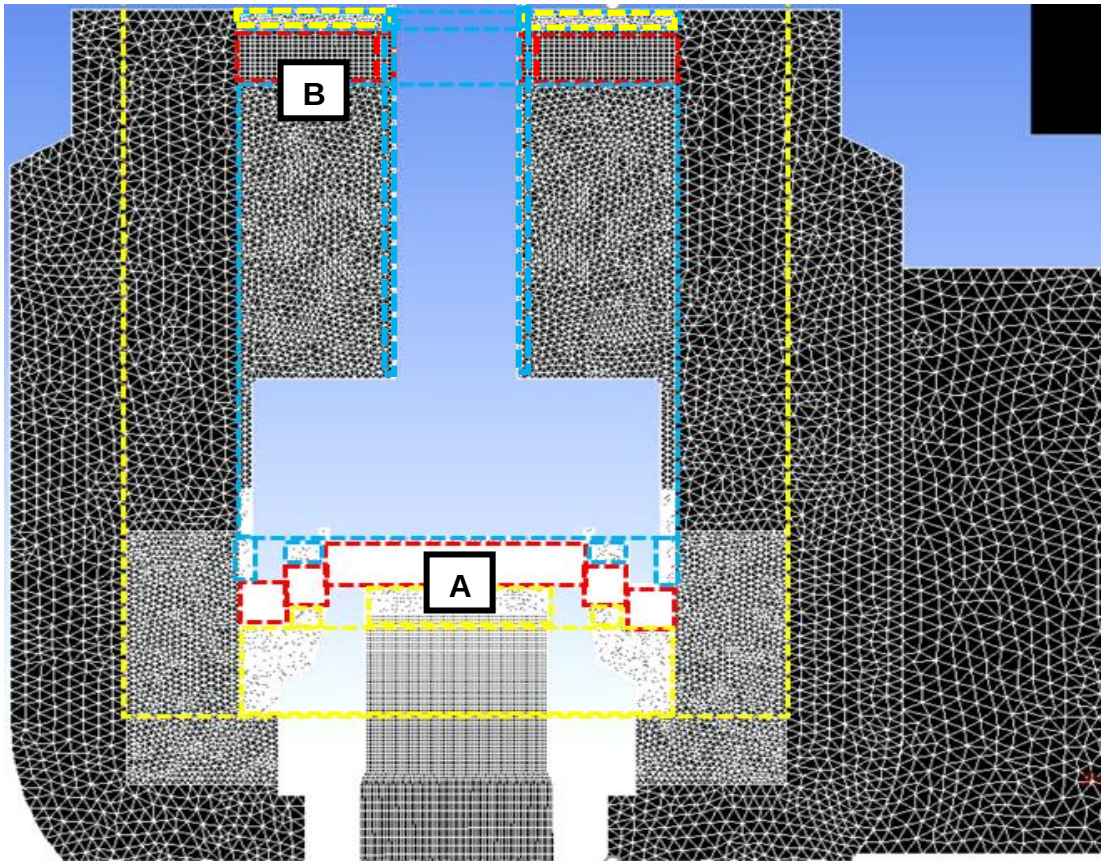

Figure 6.5 – CFD Dynamic Mesh Principle for 3511E PRV (Main Body)

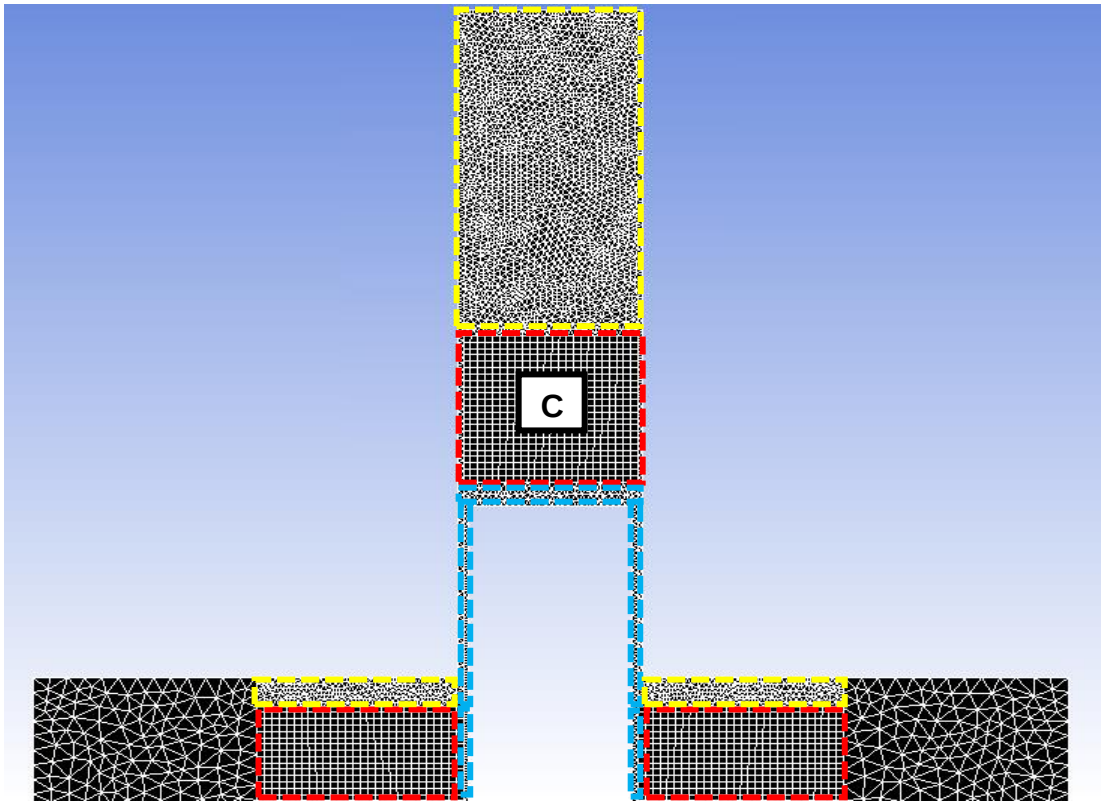

Figure 6.6 – CFD Dynamic Mesh Principle for 3511E PRV (Top Body)

As mentioned previously, the mesh density used for the transient model was based on the mesh independent values determined during the steady state study. The values used for the structured and unstructured mesh zones shown in figures 6.5 and 6.6 for regions A, B and C are shown in table 6.2.

Mesh Zone	**Structured Mesh Element Size (mm)**	**Unstructured Mesh Element Size (mm)**
A	0.0625-0.085 (increases outward)	0.135
B	0.4	0.55
C	0.4	0.35

Table 6.2 – Optimum Mesh Density for 3511E Dynamic Mesh Based on Steady State Validation

Broady 3511E Disc Motion and Inlet Pressure Profile for UDF

As described within the “User Defined Function” section within chapter 4, a general equation of motion for the Broady 3511E PRV is required to be input within the DEFINE_CG_MOTION and DEFINE_EXECUTE_AT_END macros. The equation of motion could be established from the free body diagram of the PRV disc shown within figure 6.7.

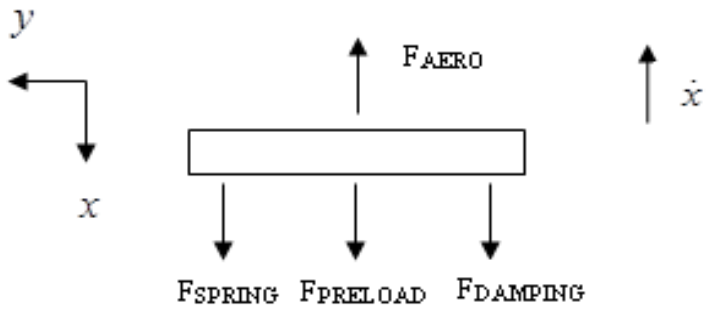

Figure 6.7 – Free Body Diagram of Broady 3511E PRV Disc

The force balance on the Broady 3511E PRV disc consists of several fundamental terms;

- Aerodynamic force due to static pressure acting on the disc (F_{AERO}). Shear forces are generally small. Within FLUENT the integration of static pressure across the disc’s wetted area is also performed by identifying the disc within the UDF. The integration is achieved using a DEFINE_ADJUST macro which determines the sum of the product of static pressure in each cell area located on the disc in the 3D domain.

- Spring force at displacement x_n (F_{SPRING}) and preload ($F_{PRELOAD}$) at displacement x_0 determined during the valve setting process at set pressure with spring constant k of 16 N/mm. The CFD preload used was

60.4N which was measured experimentally for 3.3 Barg set pressure in the notch position 4 blowdown ring configuration.

- Weight due to mass of moving parts, m (W_{MOVING}). It should be noted that this force is taken into account within $F_{PRELOAD} = F_{AERO} - W_{MOVING}$ at set pressure. The moving mass for the 3511E PRV included the disc/disc holder assembly, spindle, spring and spring carriers and was measured to be 0.687kg.

- Damping force ($F_{DAMPING}$) due to frictional contact and spring damping with damping constant c. For the Broady 3511E PRV, the damping was assumed to be zero due to the low friction design of the spindle.

Using Newton's 2nd law an expression for the net force F_x and general equation of motion at time n was derived from equation 6.1.

$$\sum F_x = -m\ddot{x}_n = kx_n + kx_0 + c\dot{x}_n - F_{AERO_n}$$
$$m\ddot{x}_n = F_{AERO_n} - kx_n - kx_0 - c\dot{x}_n \qquad \text{Equation 6.1}$$

From the general equation of motion, an explicit numerical scheme was derived to determine the disc velocity (equation 6.2) and displacement (equation 6.3) at time n+1 using a first order Eulerian method and time step Δt. The expressions derived within equations 6.1, 6.2 and 6.3 could then be input within the appropriate DEFINE_EXECUTE_AT_END macro to allow the DEFINE_CG_MOTION to apply rigid motion to the blue marked mesh zones.

When: $\ddot{x}_n = \frac{\dot{x}_{n+1} - \dot{x}_n}{\Delta t}$ and $F_{SPRING_n} = F_{PRELOAD} - kx_n$

$$\dot{x}_{n+1} = \dot{x}_n + \frac{\Delta t}{m}\left(F_{AERO_n} + F_{SPRING_n} + F_{DAMPING_n}\right) \quad \text{Equation 6.2}$$

$$x_{n+1} = (\dot{x}_n \times \Delta t) + x_n \quad \text{Equation 6.3}$$

The inlet pressure profile was defined using a linear pressure profile which would provide a representation of the vessel pressure with time which was observed experimentally within figure 6.1. The linear equations for both the overpressure and blowdown as well as the point of maximum pressure were input within the DEFINE_PROFILE macro with an IF conditional statement to select the correct equation dependant on the computational time. An example of the IF condition applied within the UDF macro to define the transient inlet pressure profile for the Broady 3511E PRV is shown within figure 6.8.

```
if (t >= 0 && t < 0.815)
{
        Pinlet = (18404.907975465 * t) + 370000;
}

if (t >= 0.815)
{
        Pinlet = (-11530.3983228571 * t) + 394408.805031457;
}
```

Figure 6.8 – UDF Inlet Pressure Profile for 3511E Broady PRV

Dynamic Mesh CFD Settings for Broady 3511E PRV Model

As demonstrated in figures 6.5 and 6.6, the deforming mesh zone highlighted in red was in the form of structured, hexahedral cells. By using the dynamic meshing tools available within ANSYS FLUENT it was possible to deform the red mesh zones by using dynamic layering to achieve structured hexahedral cell layer creation/deletion. As mentioned previously, this technique would provide the most robust dynamic mesh strategy available across the full lift range to maintain the required mesh metrics when compared with unstructured remeshing and/or smoothing. To allow the required dynamic meshing strategy to take place it was necessary for layering to be enabled via the mesh methods tab where with reference to chapter 4, the ratio based option was selected with a split factor of 0.05 and collapse factor of 0.4. These values ensured that sufficient mesh density was maintained during mesh deformation. The required dynamic mesh settings were applied within the “dynamic mesh zones” tab within FLUENT in which each mesh zone highlighted in yellow, blue or red in figures 6.5 and 6.6 were selected to be of either stationary, rigid body or deforming type. For the deforming mesh regions it was necessary to ensure that both the smoothing and remeshing methods were deselected to solely activate the dynamic layering mesh method. For each zone it was necessary to specify the appropriate minimum and maximum length scales of the mesh zone during deformation according to the mesh density set during mesh generation as well as maximum skewness which was set to 0.7.

In addition to the deforming zones, within the “dynamic mesh zones” tab the rigid body zones highlighted in blue were set with motion attributes according to the dynamic motion profile set within the UDF. From this it was also necessary to define the first layer cell height of the adjacent zones which was based on the mesh density set during mesh generation. The stationary mesh zones highlighted in yellow also required the definition of first cell height of the adjacent zone. To enable the required mesh deformation from the dynamic

layering model shown within figures 6.5 and 6.6, it was required to attribute either a stationary or rigid motion to the conformal interface with the adjacent zone. The conformal interfaces would then allow unified mesh motion across the three types of zones. On the other hand, the non-conformal interfaces created between the rigid motion/deforming mesh zones and the surroundings would allow a sliding interface to be achieved automatically during mesh movement. Figures 6.7 and 6.8 both highlight the use of conformal interfaces (green) and the use of non-conformal interfaces (purple) at the disc/seat interface. The step structure of the deforming zone shown in figure 6.8 was selected to capture the changes in disc/seat geometry and allow minimal interference of the deforming zone with the bulk flow. In addition, figure 6.7 highlights the very small deforming single layer height for the initial conditions at 0.07mm disc lift. It should be noted that in order to significantly reduce the time required to define the dynamic mesh properties of each individual zone and interface a journal was initially developed and used during the study.

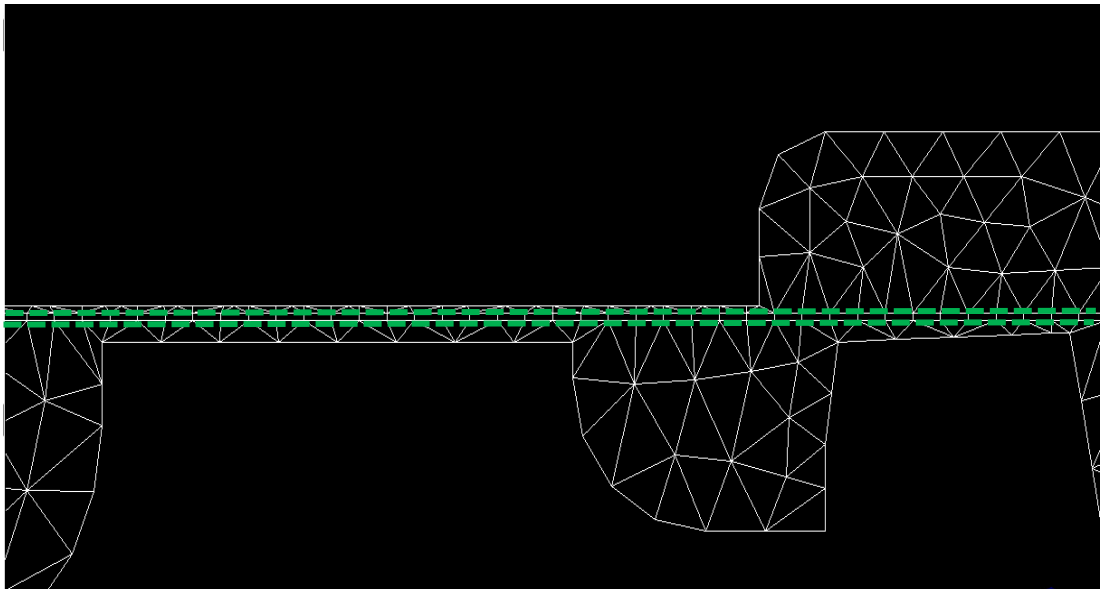

Figure 6.7 – Mesh Interfaces Required for Central Area of PRV Disc/Seat

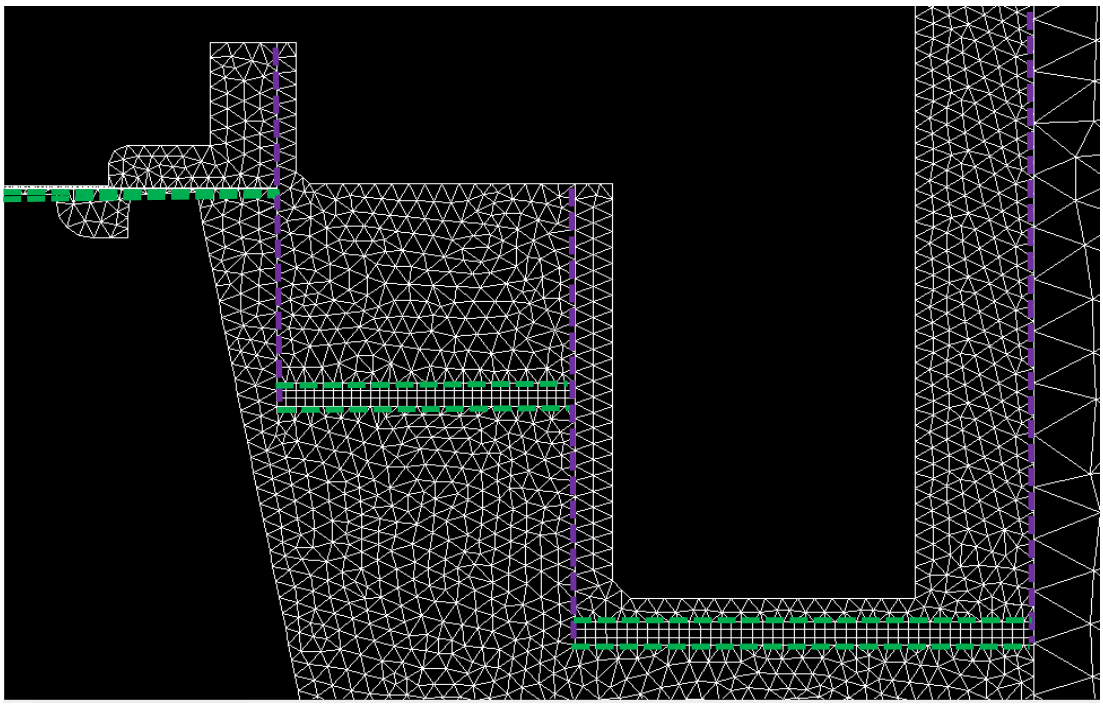

Figure 6.8 - Mesh Interfaces Required for Outer Area of PRV Disc/Seat

Broady 3511E Transient CFD Model Numerical Settings

In general, the numerical modelling procedure was similar to the methodology established during steady state validation of the Broady CFD model. Both the pressure based solver, Transition SST turbulence model and ideal gas law with the energy equation was used due to their strong performance during steady state testing. Key differences however were also present which required careful selection to maintain computational stability and accuracy.

As the transient solver was to be used, it was necessary to identify an appropriate time step to model the inlet pressure profile over the 3.25s time interval shown in figure 6.1. However due to the nature of the moving mesh, in order to prevent the generation of negative volumes during mesh deformation it was necessary for the time step to be less than the fraction of cell height to maximum disc velocity. This therefore represented the limiting factor of the

time step during both PRV opening and closure. In addition the time step would also affect the computational stability and accuracy therefore it was required to determine the most appropriate range of time step values to use during both opening and closing of the PRV. The final range of time steps developed are shown within figure 6.9 where it could be seen that 5 values were used over the course of the 3 second time period. These values were achieved following an iterative trial and error study as well as using experimental data to estimate disc velocity and general dynamic behaviour of the PRV. The planned time step values shown within figure 6.9 could either be set using a UDF or manually entered during simulation with reference to the flow time. It should also be noted that the maximum number of iterations/time step during all time steps was selected to be 15 to allow good convergence to be achieved.

Following the calculation of a steady state solution at the opening disc lift of 0.07mm at 3.7 barg to achieve an initial starting point for the transient solver it was necessary to use a time step value of 1e-3 ms for 100 iterations to ensure stability. Following the initial period, as can be seen from figure 6.9 the time step was increased to 0.15 ms until the PRV popped open at approximately 0.7s. During the initial phases of blowdown where the velocity of the disc would be expected to be low a larger time step value of 0.25 ms was used which was then increased to 0.45 ms until approximately 1.75s flow time. In preparation of the PRV disc closing with high velocity, the time step would be reduced to a value of 0.375 ms until closure and end of simulation would be achieved. The time step profile with flow time shown within figure 6.9 was found to be successful to ensure a stable solution and avoiding generation of negative volumes during mesh movement.

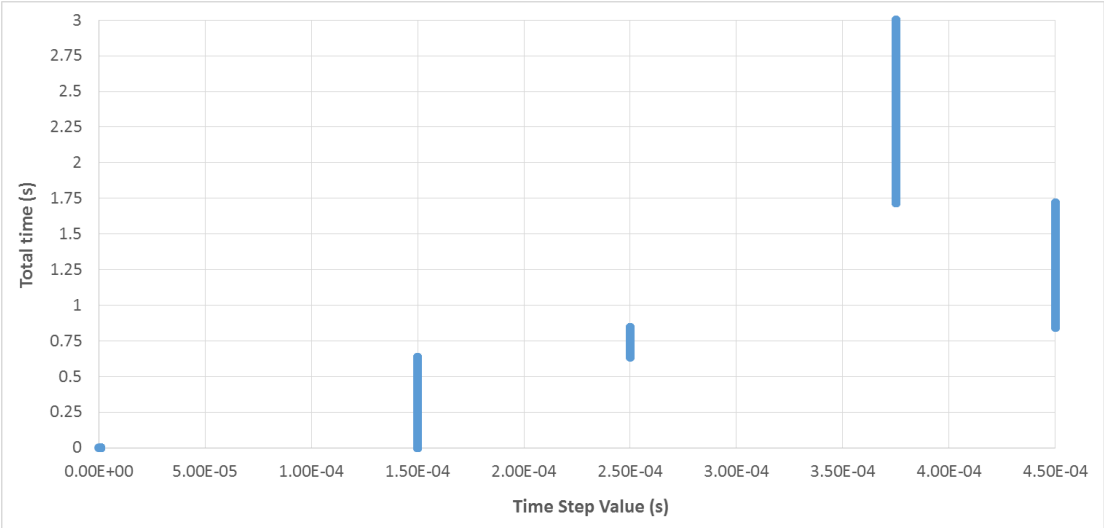

Figure 6.9 – Time Step Variation During Transient CFD Simulation for 3511E

In accordance with the methodology and justification developed during steady state analysis, similar modelling practices were adopted for the transient dynamic mesh case. Surface monitors were established for the aerodynamic force acting on the disc as well as for the mass flow rate at the inlet. All other numerical settings applied are shown within table 6.3 alongside the second order implicit transient formulation method available within FLUENT. The justification for the values shown in the recommended setting column were inherited from lessons learned during the steady state analysis discussed in chapter 5.1.

The boundary conditions for the transient model were identical to those established within the steady state research as shown within figure 6.11 with a pressure inlet, pressure outlet and half symmetry applied. For the transient moving mesh model, the inlet pressure was input using the UDF inlet pressure profile shown in figure 6.8 whereas the outlet pressure remained at atmospheric value. The temperature for both the inlet and outlet was applied as room temperature at 295K.

FLUENT Setting Type	**Recommended Setting**
Solver Type	Pressure Based
Turbulence Model	Transition SST
Air Density	Ideal Gas Law (Energy Equation ON)
Pressure-Velocity Coupling Scheme	Coupled
Spatial Discretisation - Gradient	Least Squares Cell Based Scheme
Spatial Discretisation (Pressure)	Second Order
Spatial Discretisation (Other Terms)	QUICK
Initial Flow Courant Number	7
Momentum, Pressure, Density and Energy URF's	0.2

Table 6.3 – Numerical Settings Required for Transient Moving Mesh CFD Model of 3511E PRV

6.1.3 Broady 3511E Transient CFD Model Results and Discussion

Following application of the aforementioned boundary conditions and dynamic mesh settings it was possible to generate a transient CFD solution for the dynamic performance of the Broady 3511E PRV for a set pressure of 3.3 barg. The HPC facility at Strathclyde was used to achieve a converged solution for the dynamic response of the PRV from initial opening to closure within approximately 4 days running time using 280 cores. The criteria for convergence was for residuals at the end of each time step to be either below 10e-6 for the energy equation and 1e-3 for all other terms or exhibit residual stability. The method for determining convergence was more challenging when compared to steady state modelling due to the introduction of a time step value and number of iterations per time step. Therefore care was required to ensure that the required convergence was achieved at all conditions during the motion of the PRV with mesh deformation.

For validation purposes, the following criteria will be utilised during the analysis;

- A comparison of the CFD values for both overpressure and blowdown prediction compared to experimental results.

- An evaluation of the similarities/differences observed for disc lift behaviour with time such as huddling, maximum lift, blowdown time and critical disc lift before valve closure.

- A direct comparison of the lift time curves generated by CFD to experimental data.

By following such criteria it would then be possible to achieve an appreciation of the capability of the transient moving mesh CFD model to accurately capture the dynamic behaviour of the PRV with varying inlet pressure. Within figure 6.10 the transient behaviour for disc lift with time when subjected to the pressure gradient representing the experimental pressure vessel (figure 6.1) is shown. From figure 6.10 it can be clearly observed that the overall correlation for the CFD model with experimental performance is very good when subjected to a pressure ramp boundary condition representative to experimental conditions. It can be appreciated that both the CFD model and experimental results huddle at a similar value of 0.15 mm lift after which the CFD model pops open.

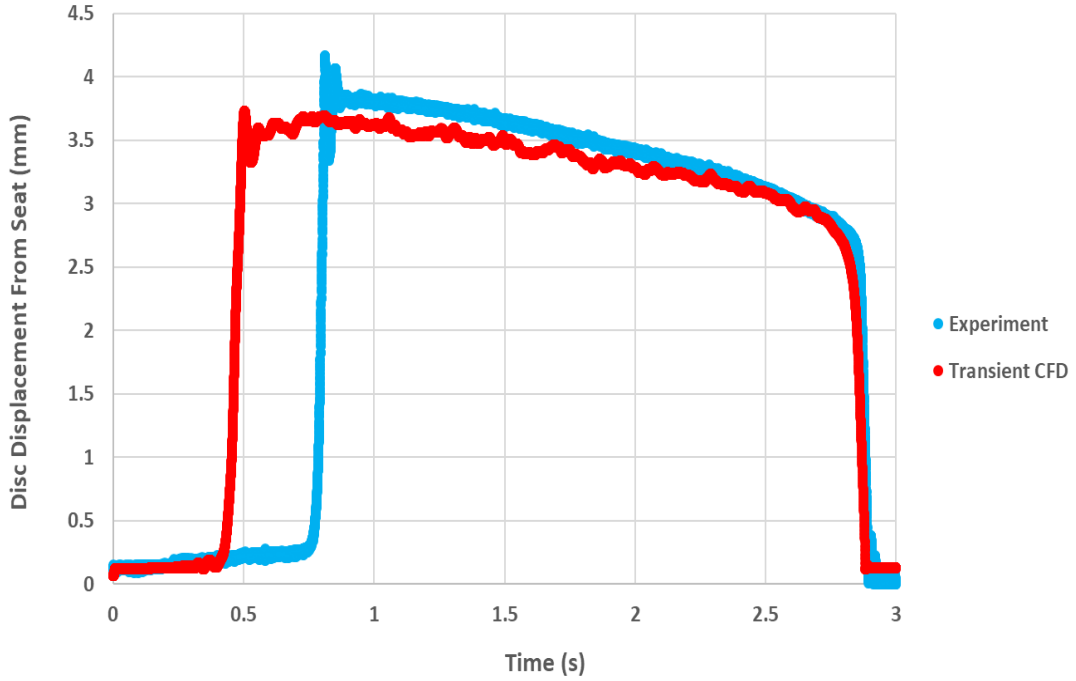

Figure 6.10 – Comparison of CFD to Experimental Disc Lift vs Time for Broady 3511E PRV for Inlet Pressure Profile in figure 6.1

The experimental results indicate however that in practice the PRV huddles until a lift value of 0.25 mm where the valve subsequently pops towards maximum lift. It could therefore be established that the dynamic mesh CFD model would pop open quicker when compared with experimental results which was consistent with the observations in the study by Budziszewski [42]. The value of maximum lift achieved by both the CFD model and experimental results without a physical stop was also in the region of 4 mm with a slight under prediction for the transient CFD model. In addition, the value of critical lift before PRV closure during blowdown was similar at approximately 3 mm where the CFD model was able to capture a stable blowdown similar to the experiment.

Furthermore, the results as indicated in table 6.4 show the strong performance of the CFD model to accurately predict both overpressure and blowdown values. Such a capability is of upmost importance for a PRV designer to

determine in order to achieve the desired pressure relieving performance for a given system. From table 6.4, it can be appreciated that the transient CFD model could predict overpressure and blowdown to the experiment with a relative error of 1.4% and 0.3% respectively. For opening there was also a small difference in opening time as the PRV was capable of opening within 60 ms during the experiment whereas the CFD model predicted an opening time of approximately 80 ms. It could be suggested that the use of a slight opening at the beginning of the process which was required for the dynamic mesh produced an instability which would result in premature PRV opening. Therefore, to reduce the error shown within table 6.4 and achieve a more "realistic" representation of the initial PRV flow conditions it would be necessary to use a smaller disc opening which would require a significant increase in mesh density or use an alternative dynamic mesh method such as chimera/overset meshing. In addition, the use of a vessel model to represent the inlet conditions would help to avoid a pressure condition mismatch between the experiment and CFD model inlet pressure.

	Overpressure	**Blowdown**
Experiment	3.85 Barg **(+16.7% Set P)**	3.6 Barg **(+9.1% Set P)**
Transient CFD	3.805 Barg **(+15.3% Set P)**	3.61 Barg **(+9.4% Set P)**

Table 6.4 – Comparison of CFD and Experimental Overpressure and Blowdown Values for 3511E PRV at 4 Notches

Figures 6.11- 6.22 utilise contours of both Mach number and static pressure for the overall PRV domain to illustrate the development of the flow regime and pressure profile during the opening process of the PRV as predicted by the transient moving mesh CFD model. A series of 6 discrete lift points of 0.15 mm, 0.5 mm, 1 mm, 1.75 mm, 2.5 mm and finally 3.7 mm at a simulation time of between 0.4 s-0.5 s will be used. Figures 6.11 and 6.12 represent the PRV

during the final stages of the huddling process shown within figure 6.10 for a disc lift of 0.15 mm above the seat. It can be clearly seen from figure 6.11 that a small leakage of flow occurred through the disc/seat area however the surrounding area in the proximity of the disc and outlet were predominantly unaffected. This as a result would produce a small effect on the static pressure distribution in the surrounding area as can be appreciated from figure 6.12 in which the highest static surface pressure acts on the central core region of the disc directly above the inlet. On the other hand it can be seen that a pressure loss occurs through the disc/seat flow interface towards atmospheric pressure conditions.

Figures 6.13 and 6.14 on the other hand highlight an increase in leakage through the PRV for a disc lift of 0.5 mm. At this point it can be clearly seen that a radial jet emanates from the central core which is in contact with the outer regions of the disc as the flow exhausts towards the outlet. The effect of this flow regime on the static pressure distribution is highlighted in figure 6.14 where pressurisation of the outer disc region occurs due to the impact and momentum change of the jet with the outer disc surface. As a result of the observable increase in pressure in this region above atmospheric conditions a greater aerodynamic force would be achieved to aid the opening process. Therefore as can be seen within figure 6.10, once pressurisation occurs within this region the opening pop process of the PRV is inevitable as an increased proportion of the disc surface becomes in contact with the jet to increase aerodynamic force which in turn overcomes the resistive spring force.

The development of the flow regime as the PRV opens to a lift of 1 mm is shown within figures 6.15 and 6.16. At this stage the jet is much more pronounced than that at 0.5 mm which is strongly coupled with the surface of the disc and surrounding area within the disc/seat interface. The static pressure highlights this observation as the entire lower surface of the disc has become pressurised above atmosphere due to contact of the jet with the disc.

In addition, at 1 mm it is clear from figure 6.15 that flow exhausted from the disc/seat interface was beginning to circulate in the body bowl around the upper surfaces of the disc towards the outlet. As a result, a slight increase in backpressure can be observed within the static pressure distribution shown in figure 6.16.

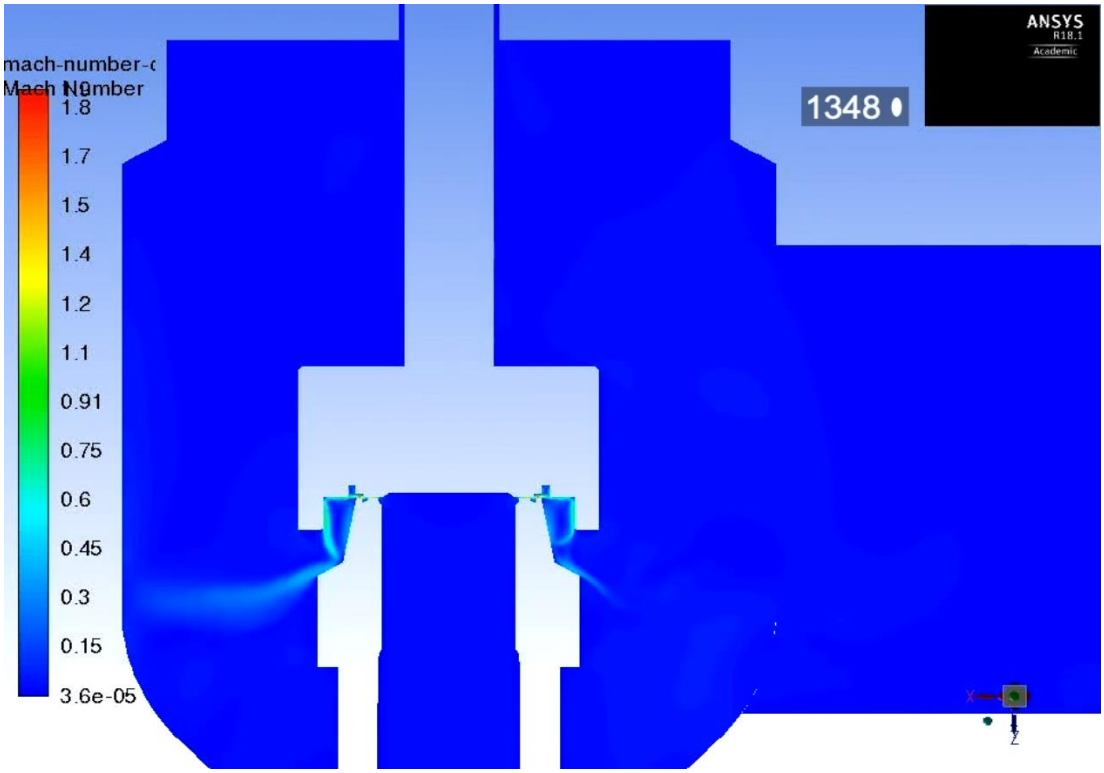

Figure 6.11 – Contours of Mach Number for 3511E at 0.15 mm Lift During Opening at t = 0.4 s-0.5 s

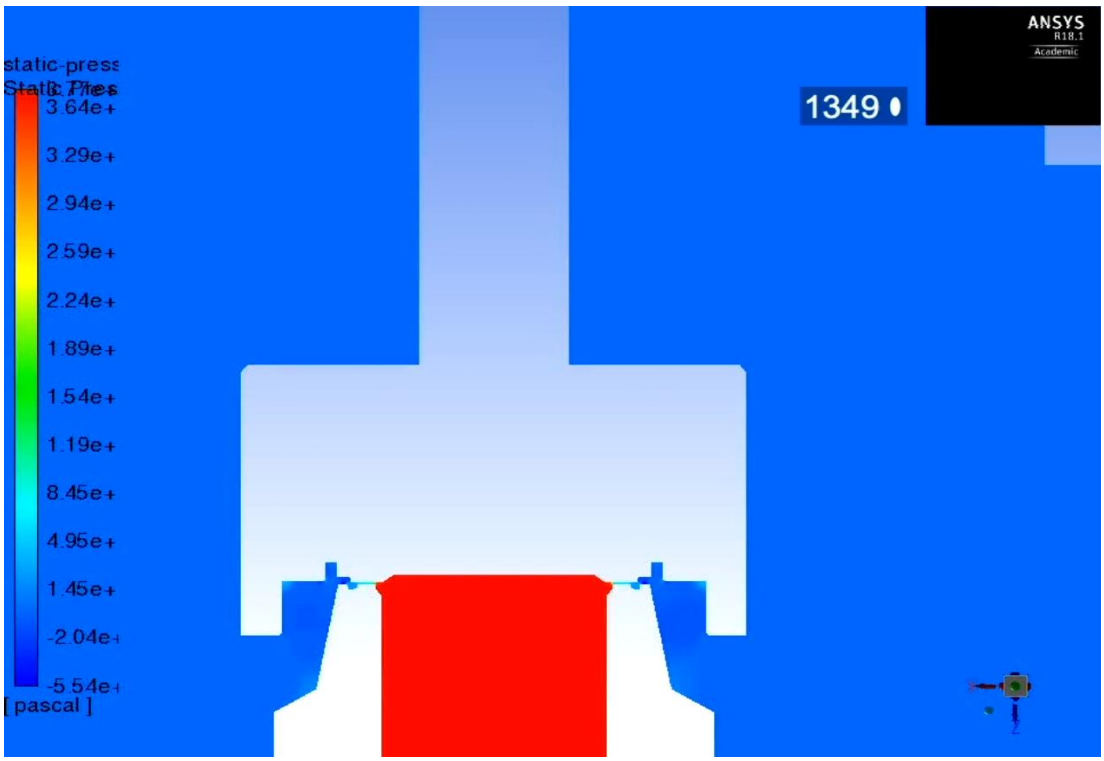

Figure 6.12 – Contours of Static Pressure in Barg for 3511E at 0.15 mm Lift During Opening at t = 0.4s-0.5s

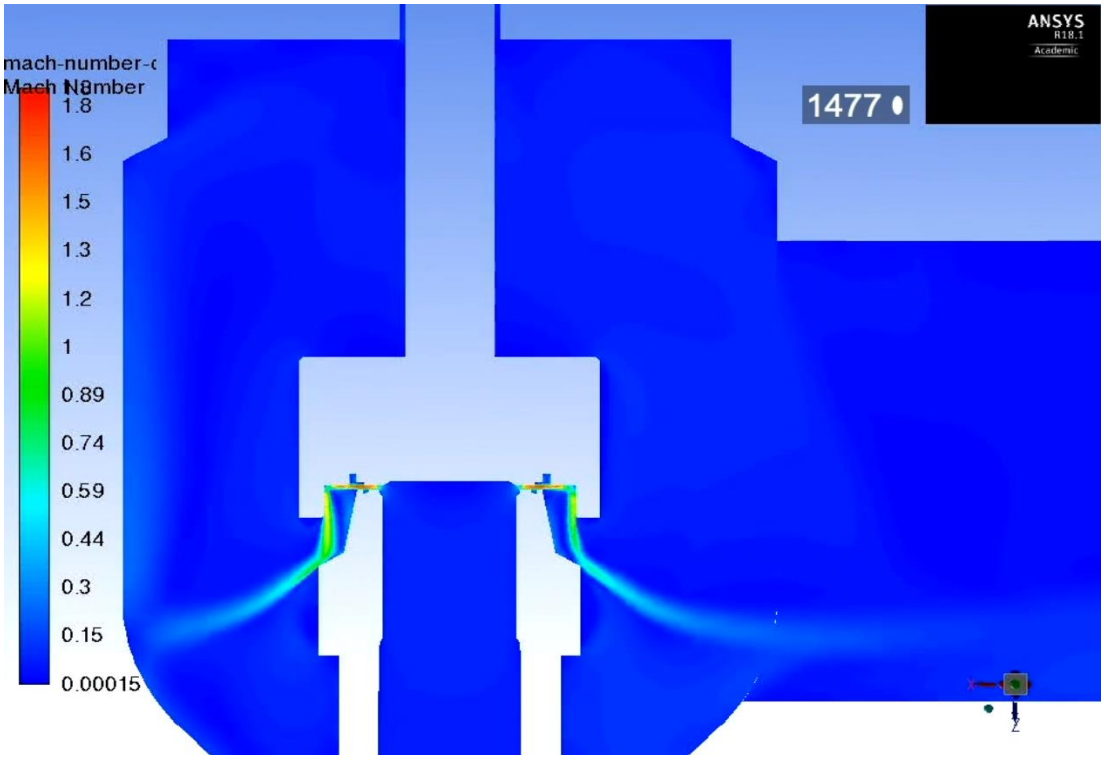

Figure 6.13 – Contours of Mach Number for 3511E at 0.5mm Lift During Opening at t = 0.4s-0.5s

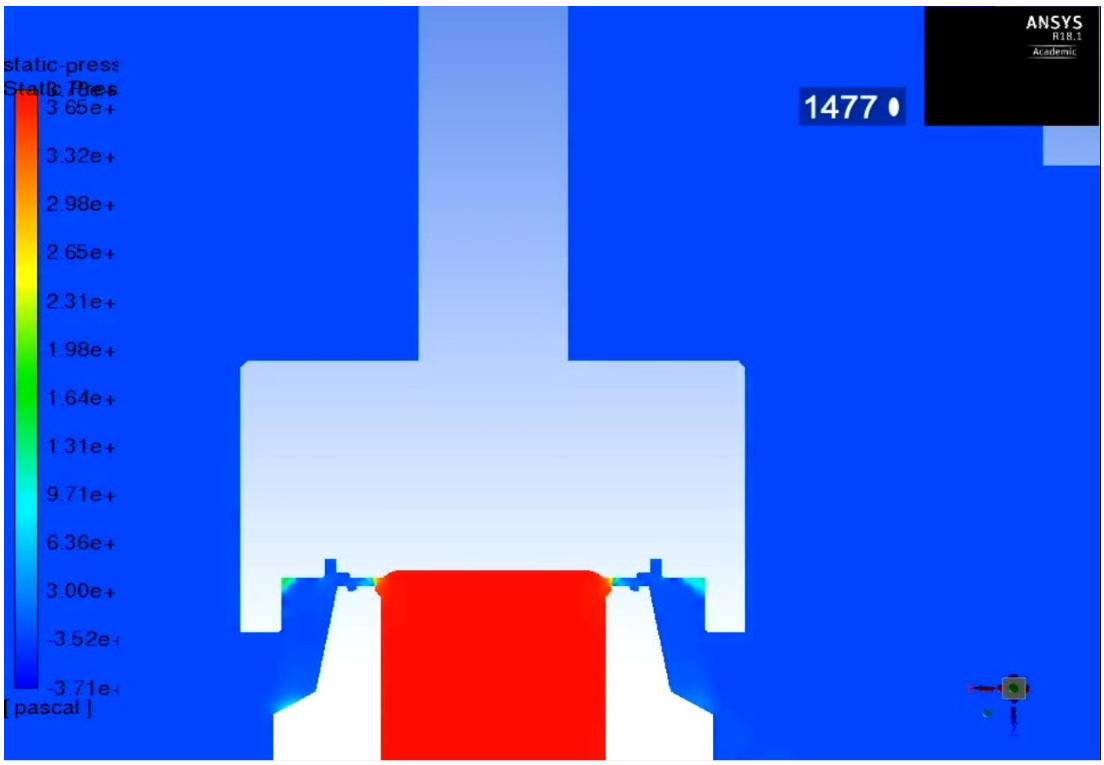

Figure 6.14 – Contours of Static Pressure in Barg for 3511E at 0.5mm Lift During Opening at t = 0.4s-0.5s

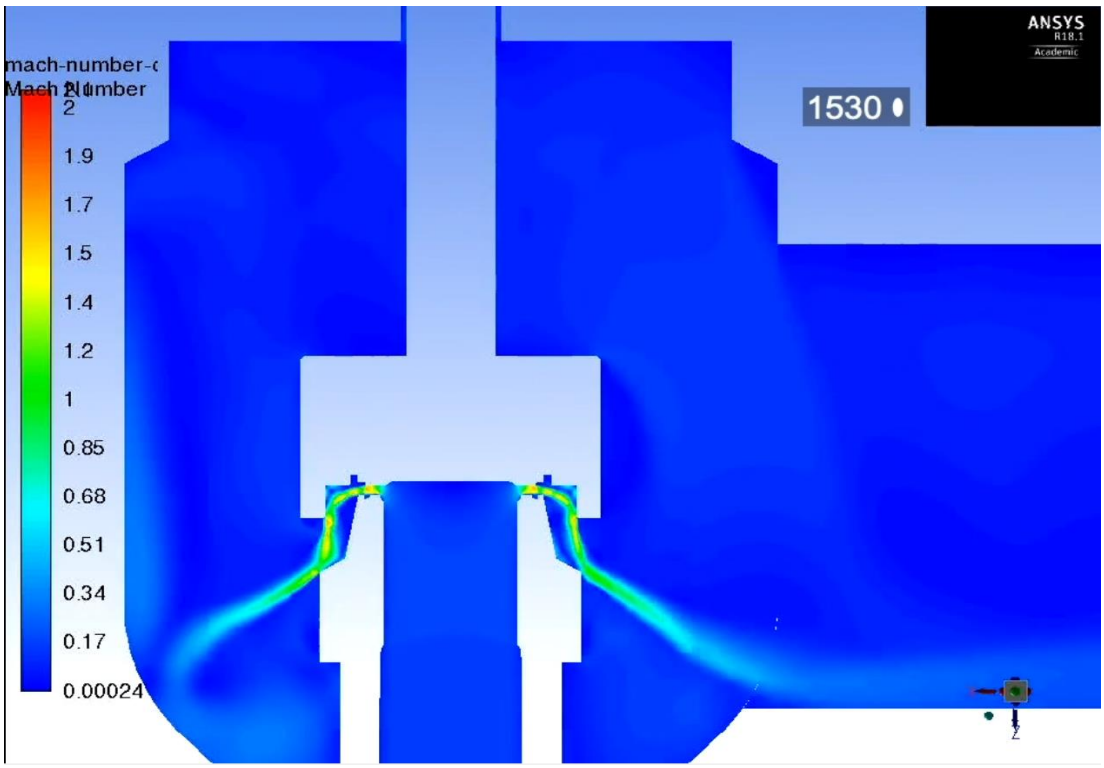

Figure 6.15 – Contours of Mach Number for 3511E at 1mm Lift During Opening at t = 0.4s-0.5s

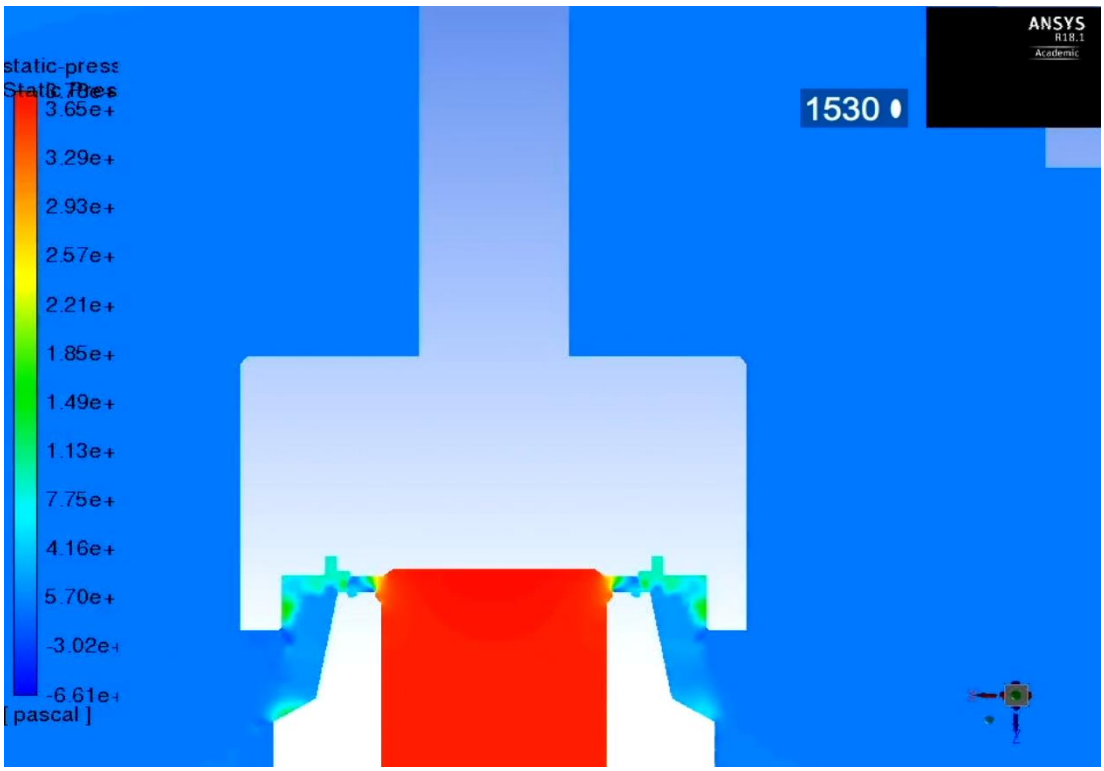

Figure 6.16 – Contours of Static Pressure in Barg for 3511E at 1mm Lift During Opening at t = 0.4s-0.5s

Figures 6.17 and 6.18 illustrate the flow conditions of the PRV during opening at a disc lift of 1.75 mm where it can be clearly observed that the flow has become much more developed throughout the entire domain with Prandtl Meyer expansion occuring within the disc/seat interface. In addition however the flow path surrounding the upper region of the disc has become more visible resulting in a further increase in back pressure as well as introducing a pressure gradient above the disc. Figure 6.18 also highlights the continuation of the entire lower disc surface becoming pressurised where a uniform static pressure could be observed across the middle area of the disc when compared with the patches of pressure observed within figure 6.16 at lower lifts. In general this is in agreement with the flow structure predicted during steady state simulation. A change however in the deflection angle of the jet with the blowdown ring could be seen when compared to figure 6.15 at 1 mm lift due to a slight shift in the bulk flow path towards the outlet. This effect was also

different to that observed in the earlier steady state research which suggested that a coupling of the disc motion with flow structure was taking place at this lift. As a result, the validity of the quasi steady assumption could be questioned and will be investigated in chapter 7.

The flow structure at a disc lift of 2.5 mm is shown in figures 6.19 and 6.20 where the general flow features observed in figures 6.17 and 6.18 are conserved but have become more pronounced due to the higher position of the disc and subsequent impact with the jet. Interestingly however as the disc opens further for the PRV to achieve maximum lift at approximately 3.7 mm disc lift, the mach number distribution in figure 6.21 remains similar to the 2.5 mm case however a greater value of back pressure can be measured within figure 6.22 as well as a more complex static pressure distribution at the lower surfaces of the disc. It could be measured that a much greater static pressure was required at the lower disc surfaces in order to allow the disc to overcome the spring force as well as the increase in backpressure at 3.7mm lift.

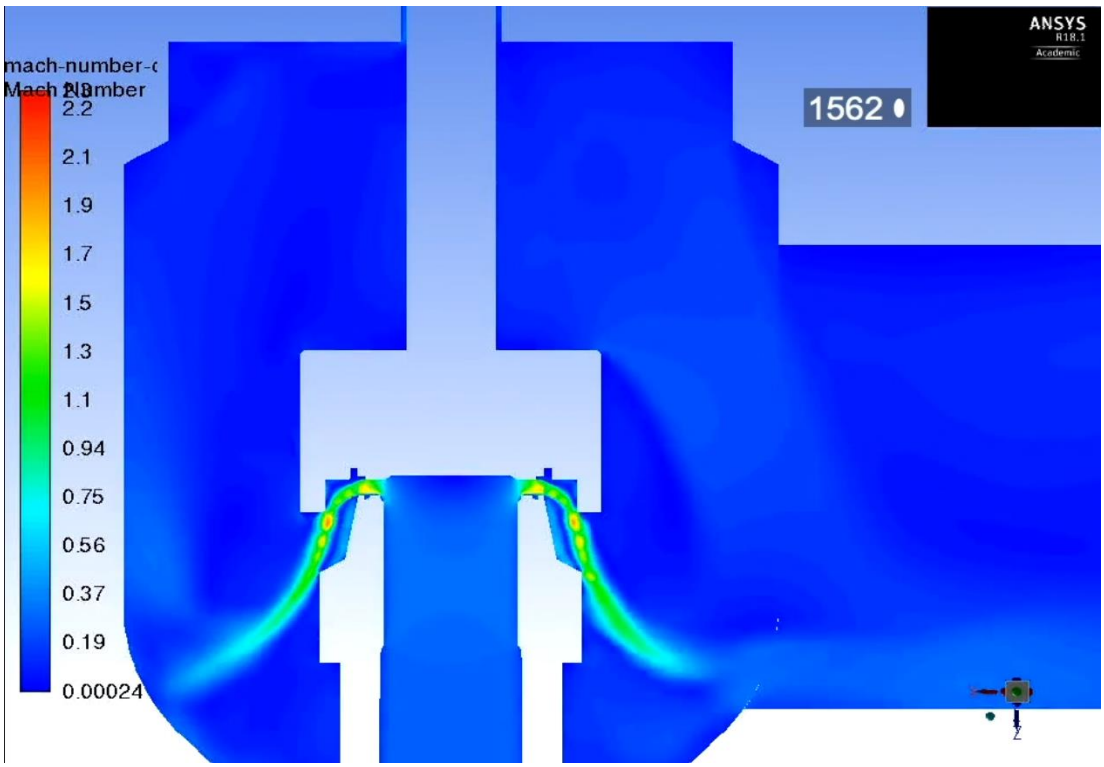

Figure 6.17 – Contours of Mach Number for 3511E at 1.75 mm Lift During Opening at t = 0.4s-0.5s

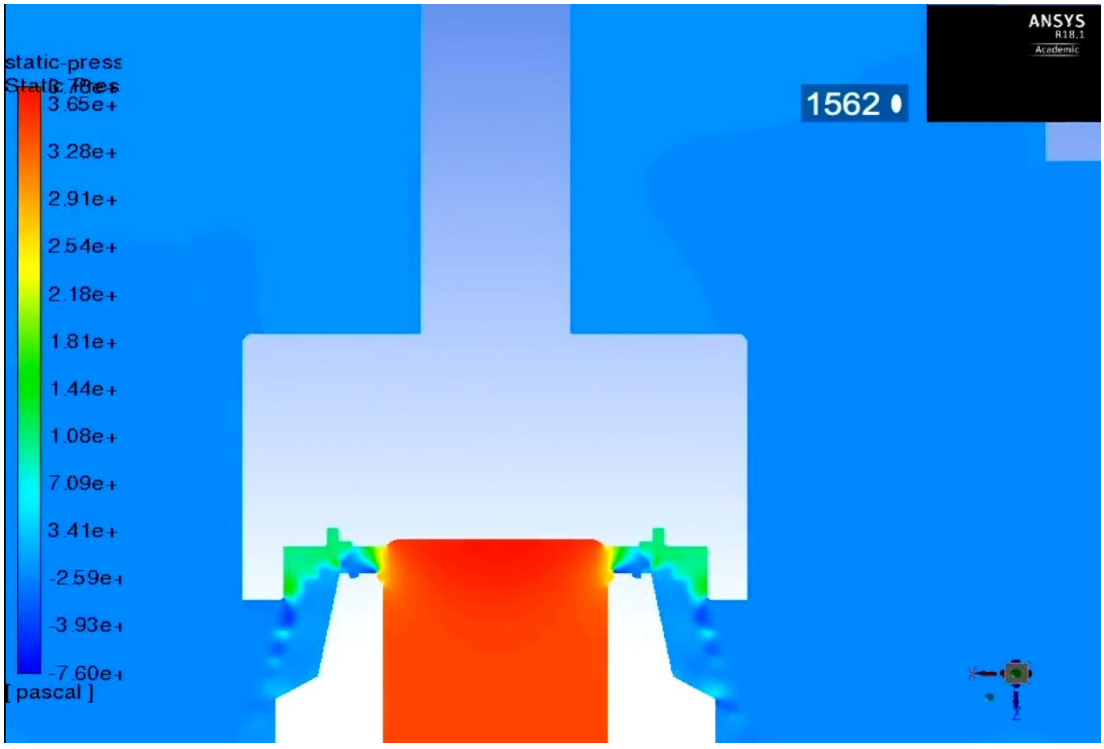

Figure 6.18 – Contours of Static Pressure in Barg for 3511E at 1.75mm Lift During Opening at t = 0.4s-0.5s

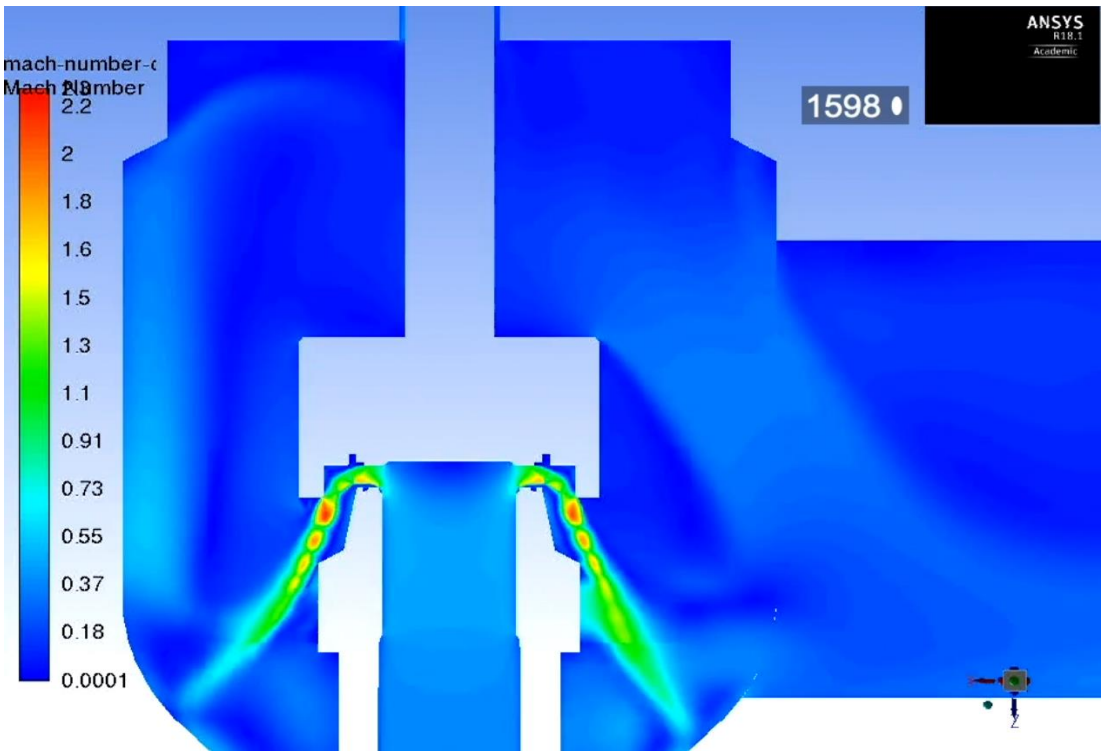

Figure 6.19 – Contours of Mach Number for 3511E at 2.5mm Lift During Opening at t = 0.4s-0.5s

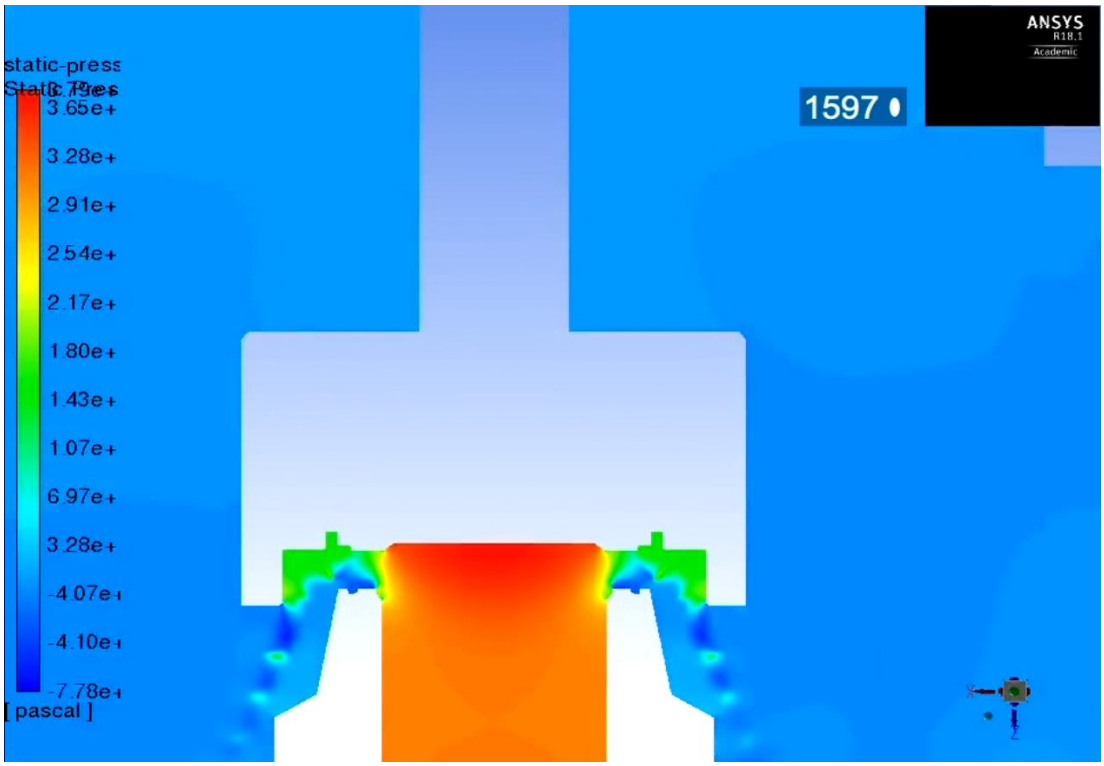

Figure 6.20 – Contours of Static Pressure in Barg for 3511E at 2.5mm Lift During Opening at t = 0.4s-0.5s

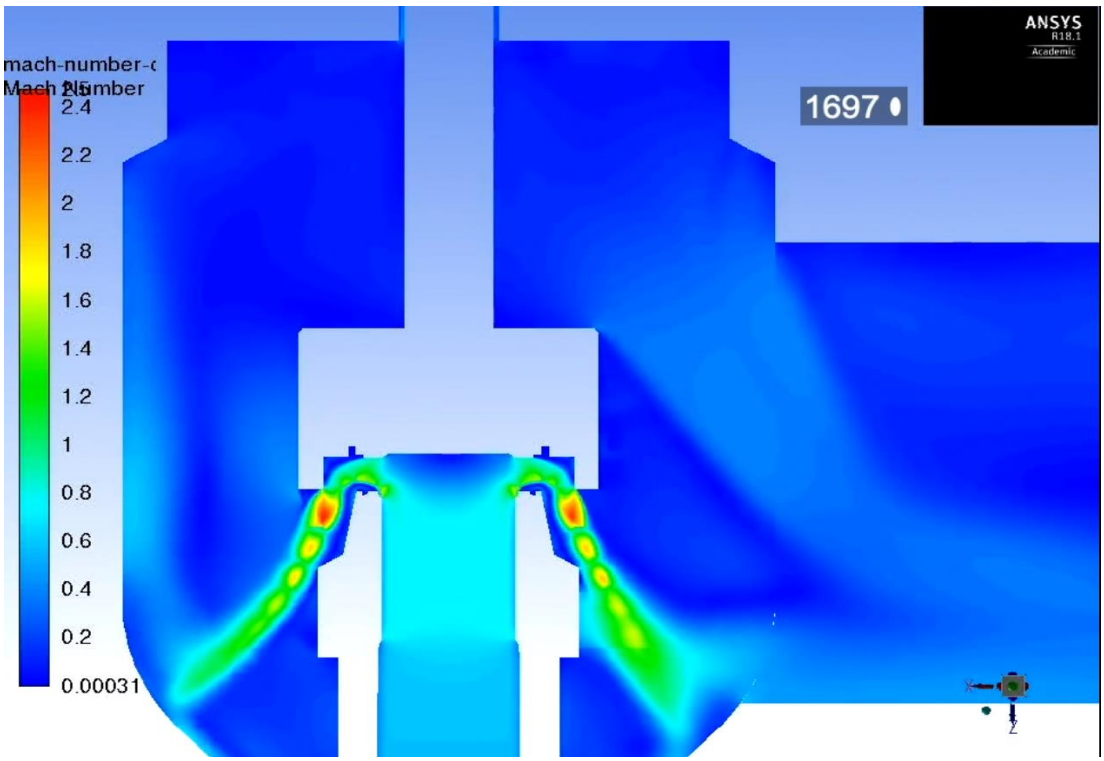

Figure 6.21 – Contours of Mach Number for 3511E at 3.7mm Lift During Opening at t = 0.4s-0.5s

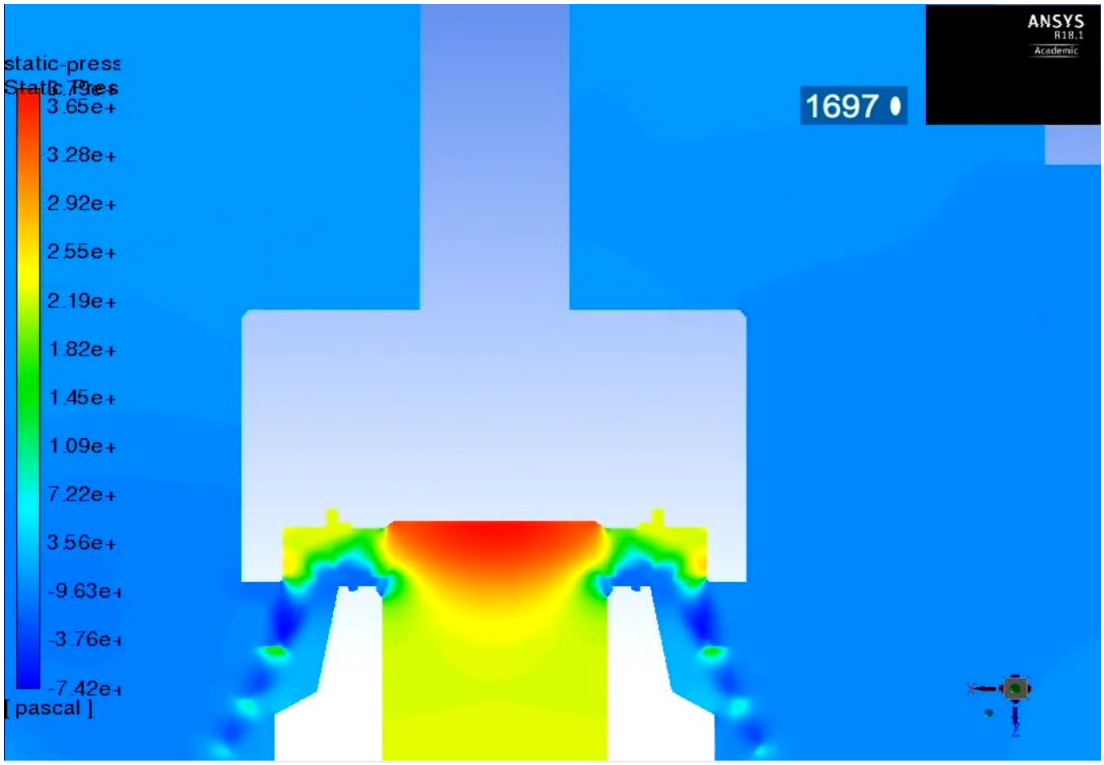

Figure 6.22 – Contours of Static Pressure in Barg for 3511E at 3.7mm Lift During Opening at t = 0.4s-0.5s

In addition to the opening process, figures 6.23-30 illustrate the closure process of the PRV during blowdown which occurred at a simulation time of 2.8s – 2.9s. For figures 6.23 and 6.24 for a disc lift of 2.75 mm it was observed that the Mach number profile and static pressure distribution was similar to the flow structure at an equivalent disc lift during opening. However as indicated within figure 6.10, as inlet pressure continues to fall, the aerodynamic force at this point is no longer able to remain open and begins to rapidly close. During the rapid closure, for a disc lift of 1 mm as shown in figures 6.25 and 6.26 there is a significant reduction in flow area as the disc closes which in turn reduces the size of the jet. Residual bulk flow can also be seen in the body bowl due to the sudden closure of the PRV causing a larger back pressure and gradient when compared with the opening case within figures 6.15 and 6.16. The bulk flow features at 1mm although are similar to the opening flow features.

Figures 6.27 and 6.28 display both Mach number and static pressure flow features at 0.5mm where significant differences with the opening profile could be identified when compared with figures 6.13 and 6.14. It could be observed from the Mach number profile for the closing case that there was a visible difference in the flow structure (Mach number plot) in the disc/seat interface region when compared with the opening case which resulted in a difference in static pressure distribution. However, the decompression profile at the lower surface of the disc was similar to that observed during opening where the central core was predominantly at a higher pressure with other regions of the lower disc surface at a pressure slightly above atmosphere. Further closure of the valve to the lowest value of 0.125mm maintained this decompression as can be seen in the static pressure plot within figure 6.30 where the outer regions of the lower surface of the disc as well as backpressure reached atmospheric conditions again to allow the PRV to return to its initial state. However a clear coupling of the rapid closure of the disc with the flow can be seen in figure 6.29 where the leakage flow was much more turbulent and followed a different flow path when compared to initial conditions during opening.

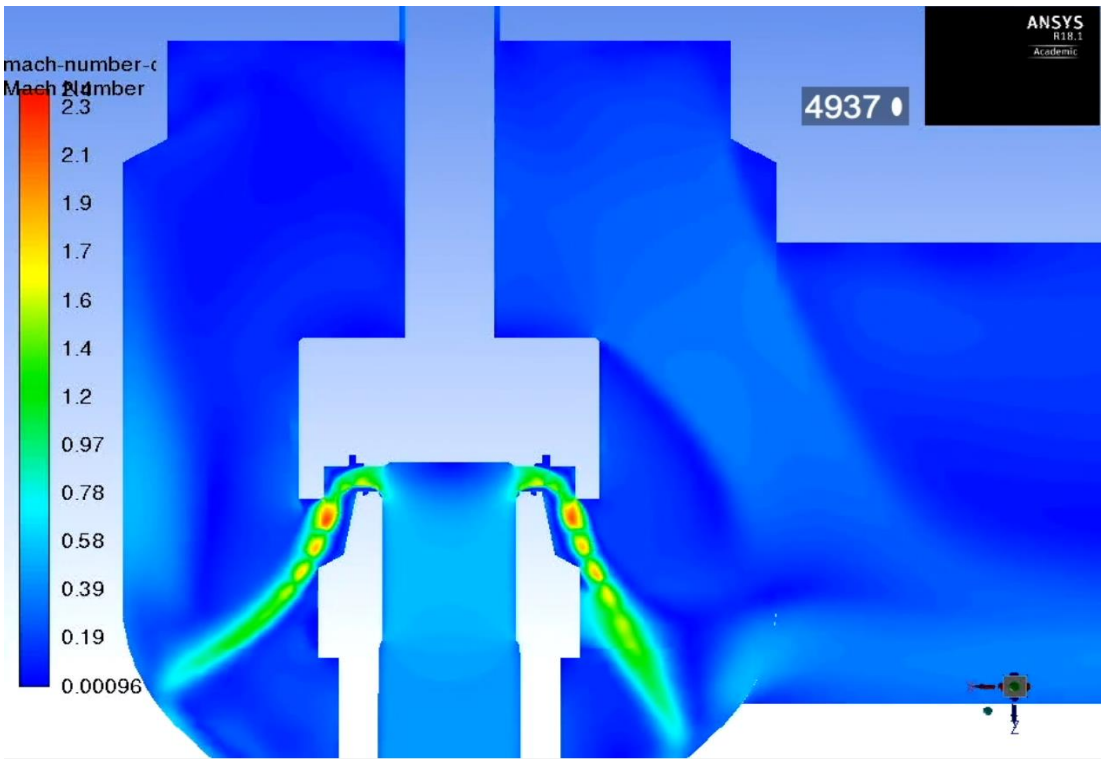

Figure 6.23 – Contours of Mach Number for 3511E at 2.75mm Lift During Blowdown at t = 2.8s-2.9s

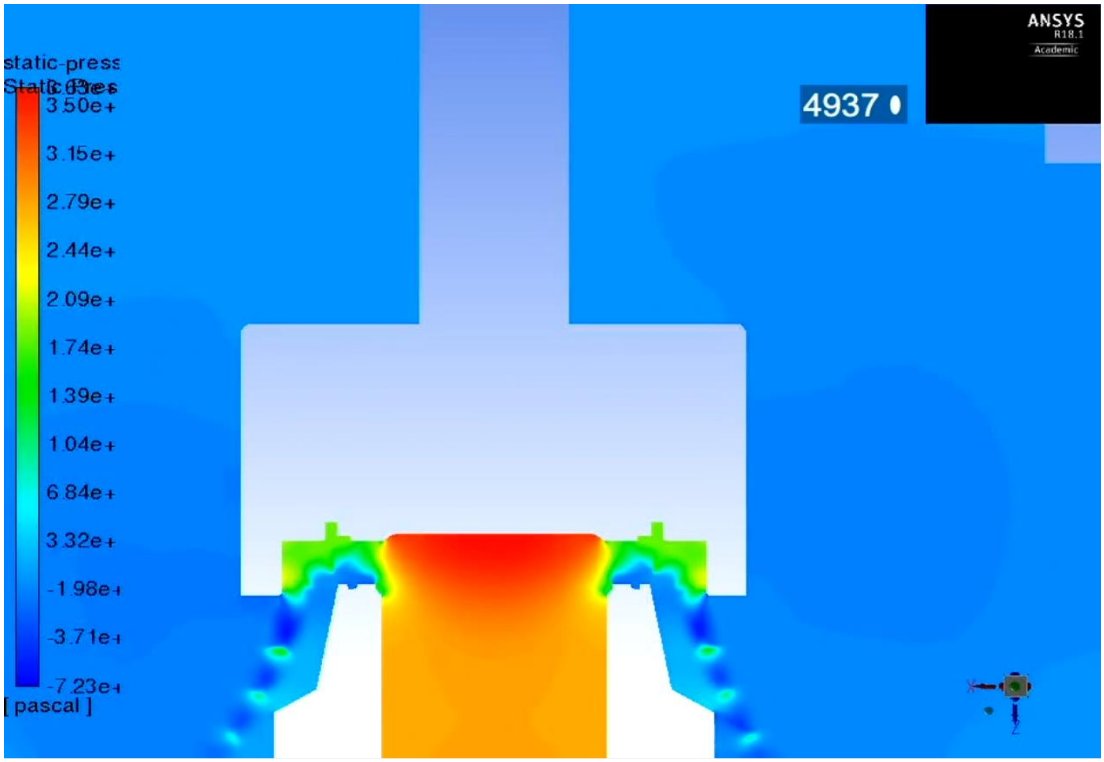

Figure 6.24 – Contours of Static Pressure in Barg for 3511E at 2.75mm Lift During Blowdown at t = 2.8s-2.9s

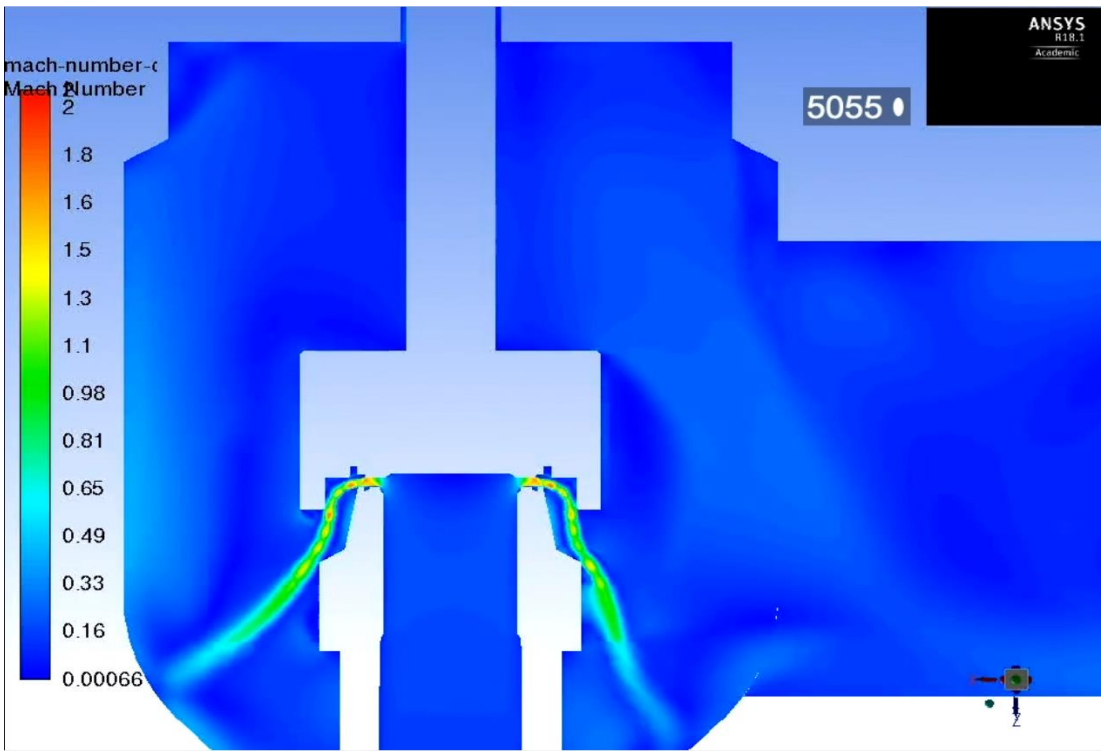

Figure 6.25 – Contours of Mach Number for 3511E at 1mm Lift During Blowdown at t = 2.8s-2.9s

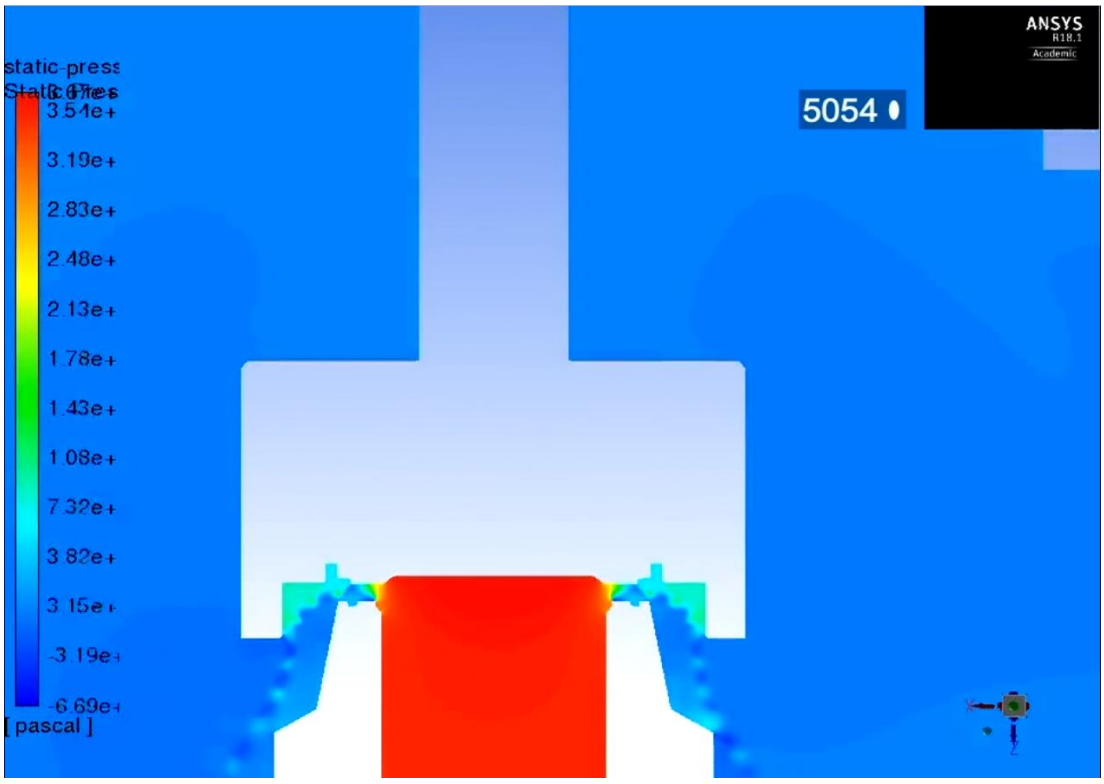

Figure 6.26 – Contours of Static Pressure in Barg for 3511E at 1mm Lift During Blowdown at t = 2.8s-2.9s

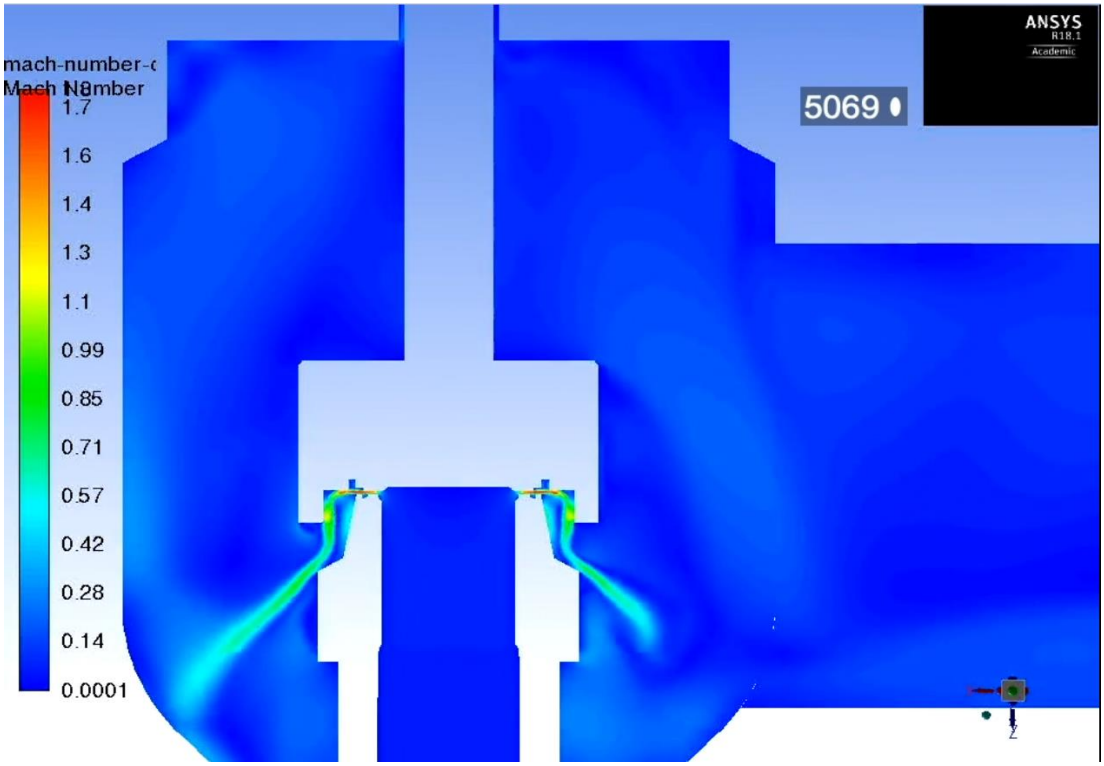

Figure 6.27 – Contours of Mach Number for 3511E at 0.5mm Lift During Blowdown at t = 2.8s-2.9s

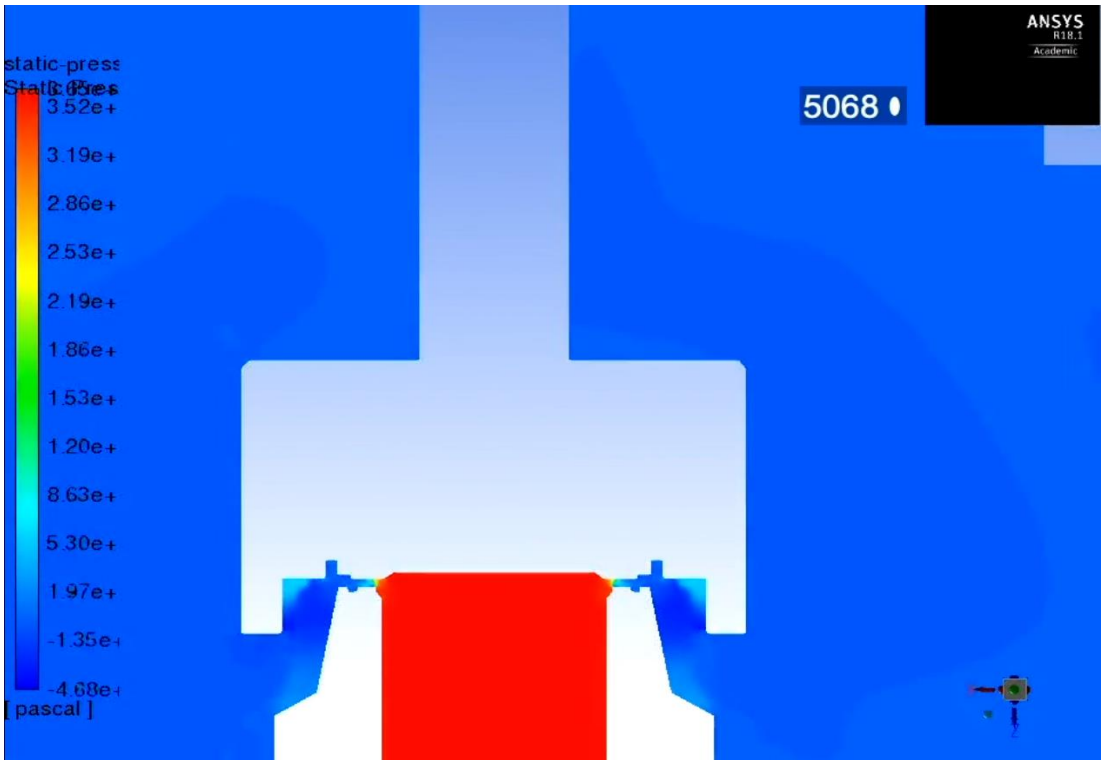

Figure 6.28 – Contours of Static Pressure in Barg for 3511E at 0.5mm Lift During Blowdown at t = 2.8s-2.9s

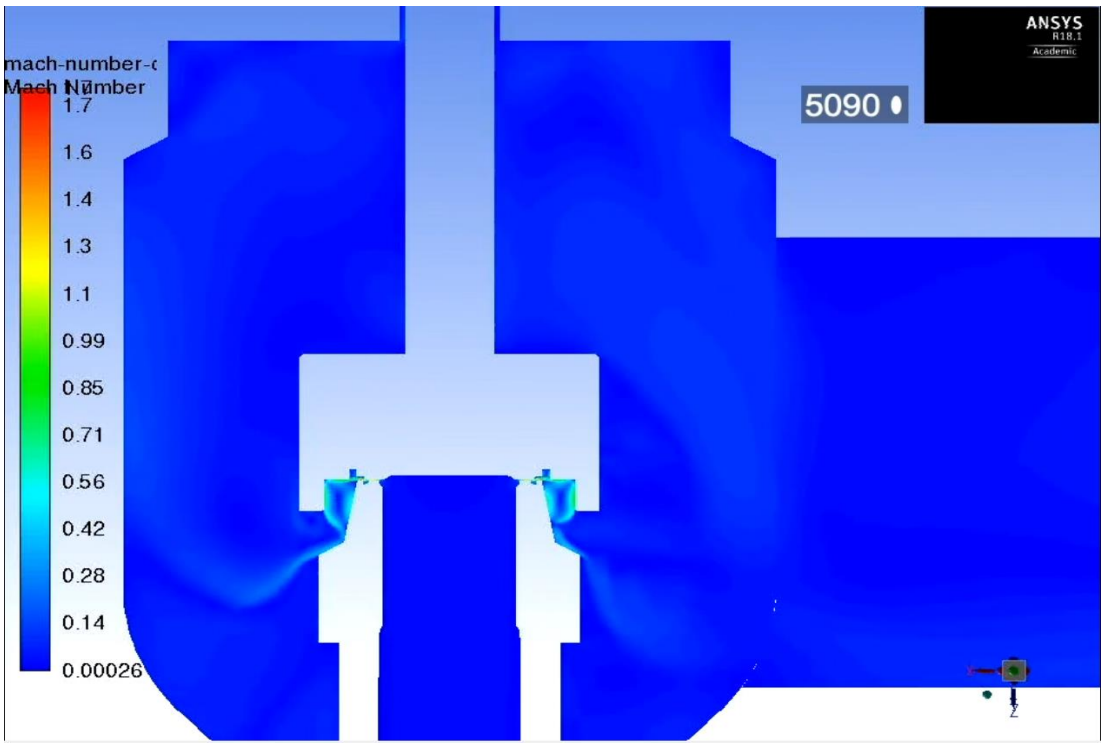

Figure 6.29 – Contours of Mach Number for 3511E at 0.125mm Lift During Blowdown at t = 2.8s-2.9s

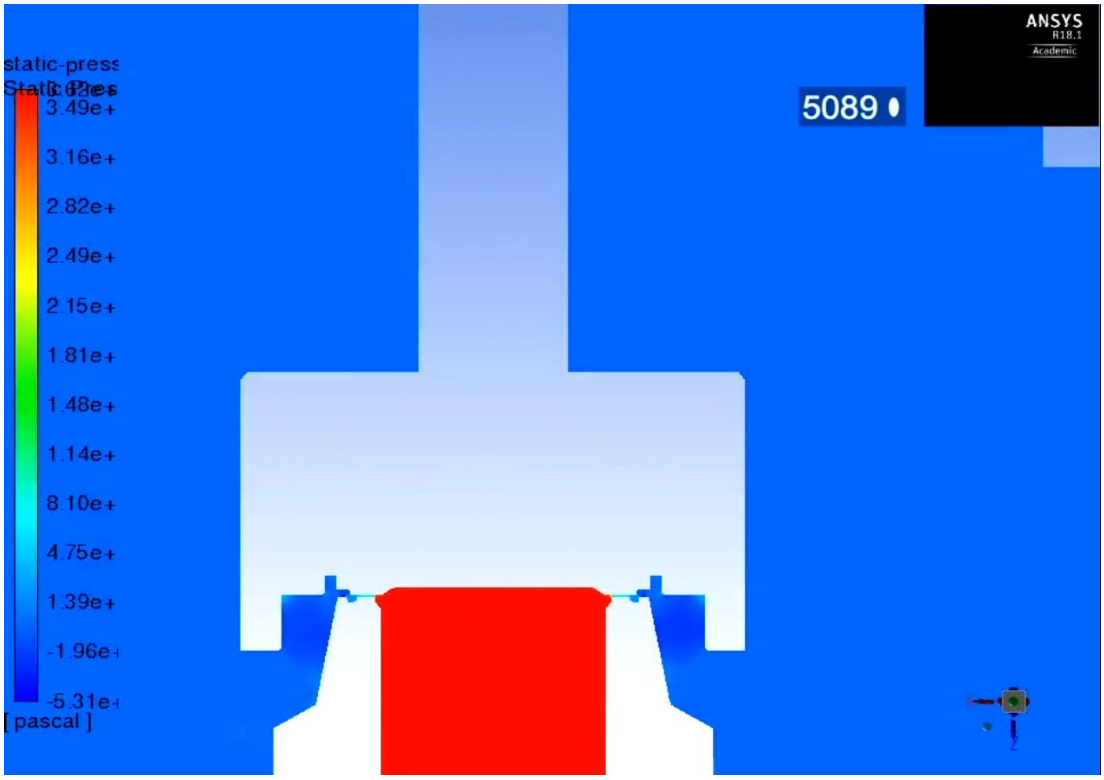

Figure 6.30 – Contours of Static Pressure in Barg for 3511E at 0.125mm Lift During Blowdown at t = 2.8s-2.9s

In order to appreciate the differences between the opening and closing flow features within the Mach number contour plots at lower lift a more detailed view of the disc/seat interface was generated in figures 6.31-34. In figures 6.31 and 6.32 at a disc lift of 0.15mm, figure 6.31 represented the opening process and figure 6.32 the closing process. Within the outer region of the disc/seat interface highlighted in red, a noticeable difference in the flow path and turbulence could be observed where the closing process produced a much more energetic flow regime due to flow history. This as a result confirms the observations of Beune [5, 20] who identified flow history effects during his transient studies which used a series of pre-defined meshes rather than a moving mesh.

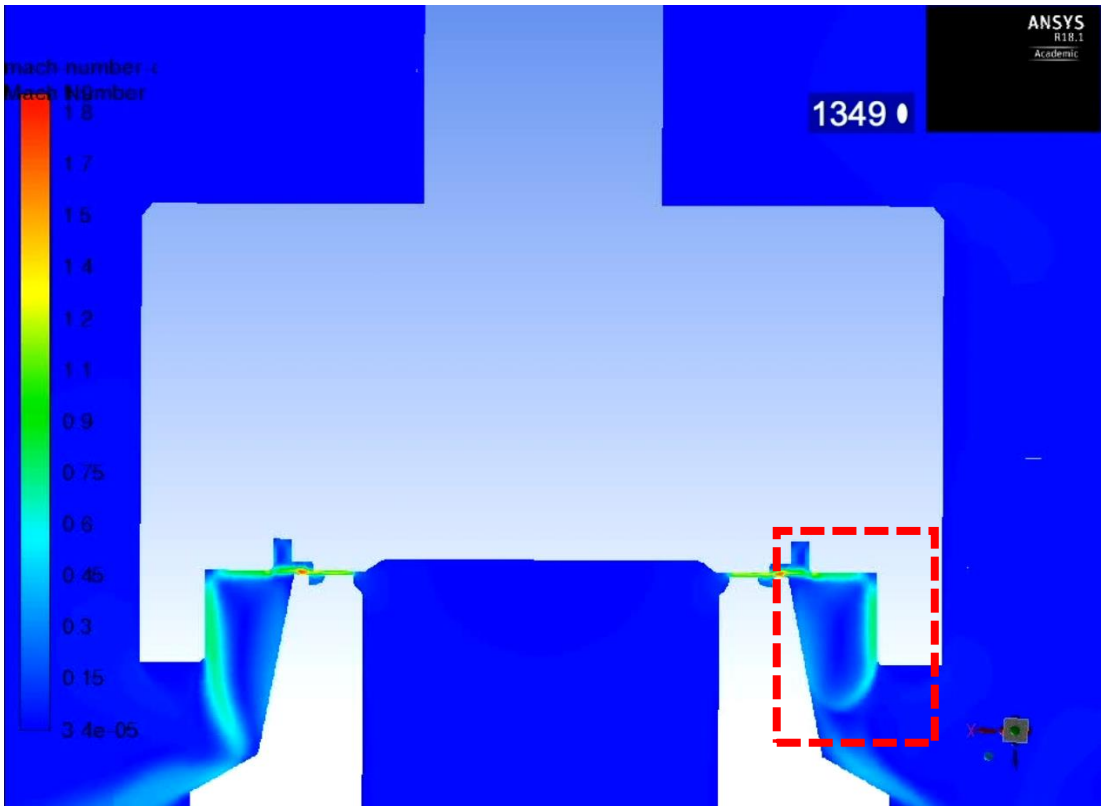

Figure 6.31 - Contours of Mach Number at Disc/Seat Interface for 3511E at 0.15mm Lift During Opening at t = 0.4s-0.5s

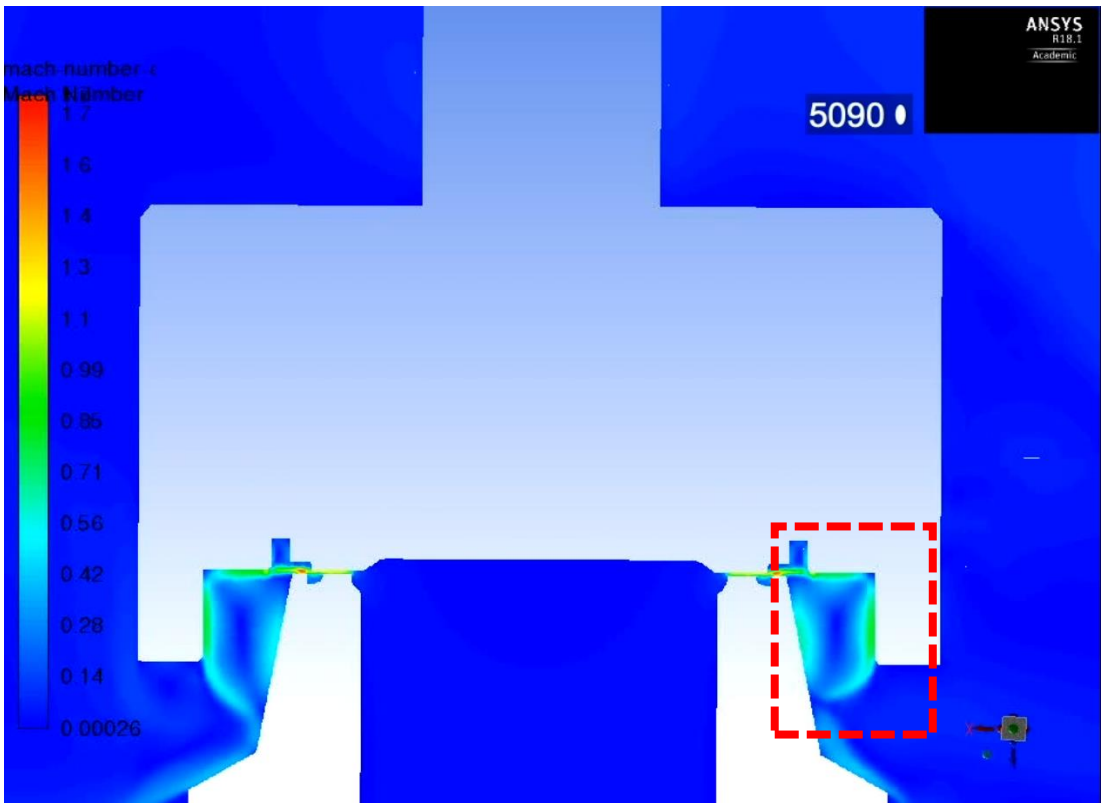

Figure 6.32 – Contours of Mach Number at Disc/Seat Interface for 3511E at 0.15mm Lift During Blowdown at t = 2.8s-2.9s

Figures 6.33 and 6.34 at 1 mm disc lift during PRV opening and closing respectively highlight that this effect is not as prominent at higher disc lift values where the bulk flow path of the jet as well as Prandtl Meyer expansion characteristics were similar. Small differences were evident at opening as recirculation was present in the vicinity of the outer disc surface when compared to closing however a similar degree of bulk flow differences to 0.15 mm lift wasn't evident. This therefore highlights that flow history effects for the Broady PRV are most obvious during opening/closing at lower lifts and care must be taken when applying quasi steady assumptions. In addition by identifying small flow differences during the opening and closing process, such flow mechanisms could be useful for PRV designers by utilising the flow visualisation capabilities of CFD to identify performance features which would normally be missed. The validity of the quasi steady assumptions for the Broady PRV will be investigated in the following chapter.

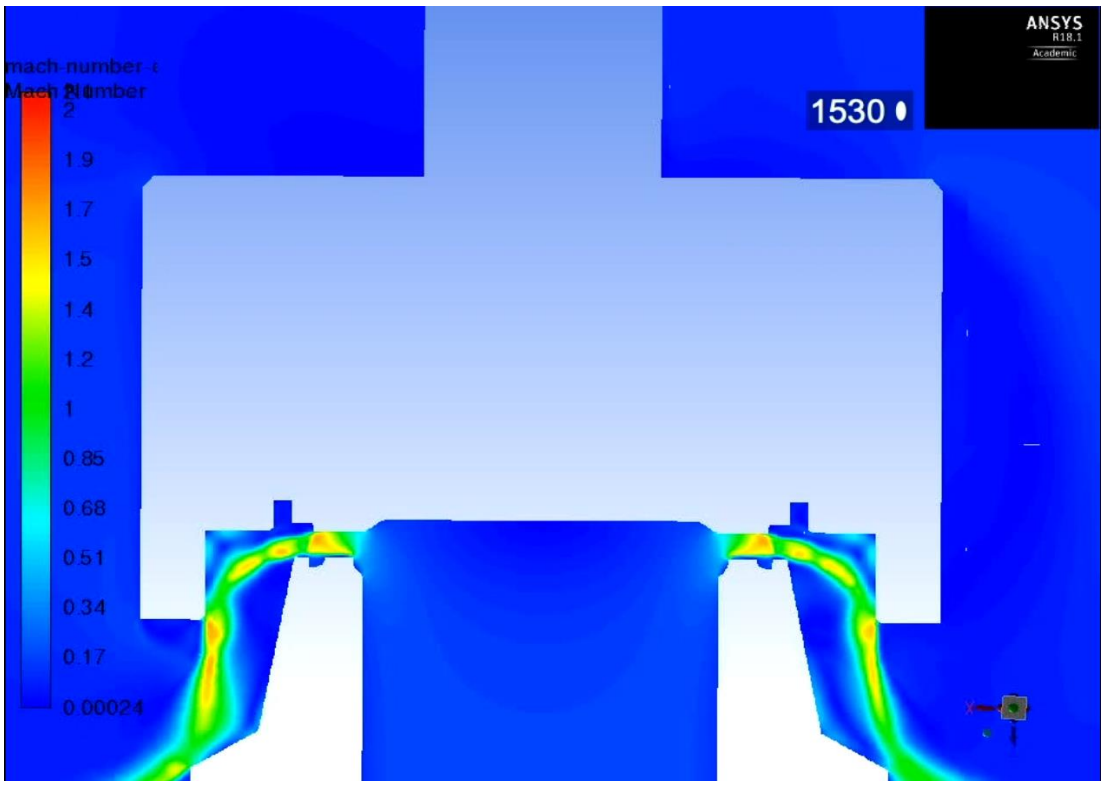

Figure 6.33 - Contours of Mach Number at Disc/Seat Interface for 3511E at 1mm Lift During Opening at t = 0.4s-0.5s

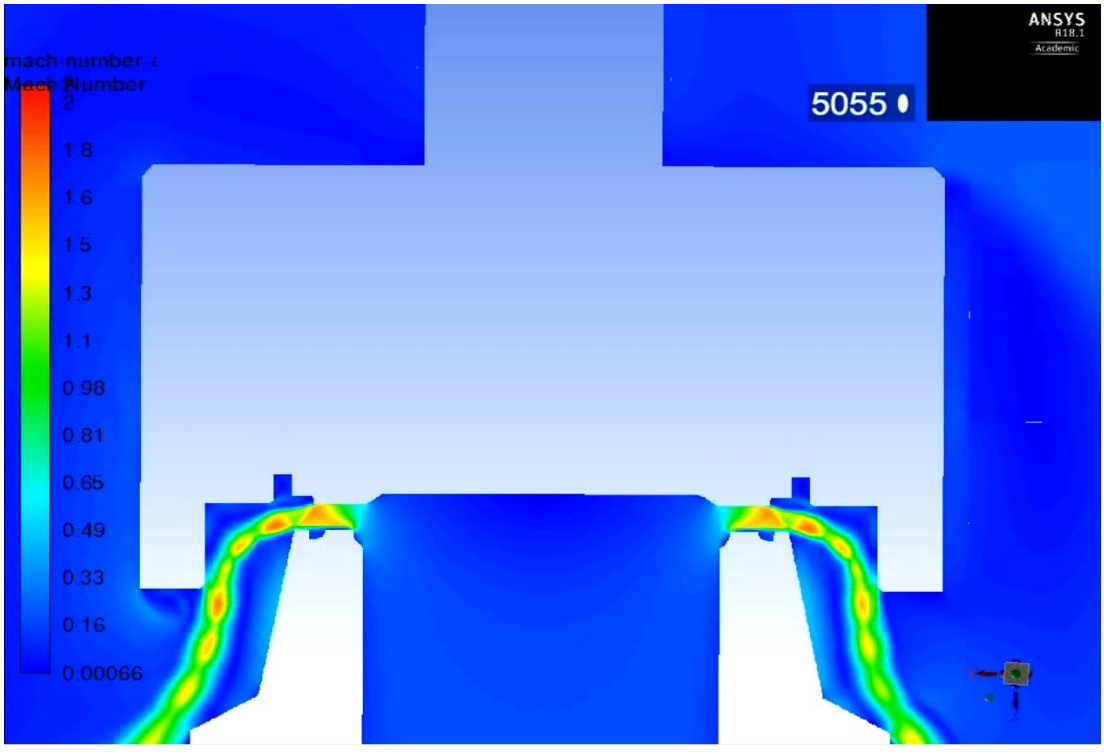

Figure 6.34 - Contours of Mach Number at Disc/Seat Interface for 3511E at 1mm Lift During Blowdown at t = 2.8s-2.9s

From figures 6.11 to 6.22 it could be seen that the lower surface of the disc as the disc lift increased during opening became increasingly pressurised in the radial direction. To achieve a greater understanding towards the static pressure distribution on the disc as lift increased figures 6.35, 6.36 and 6.37 were generated. These figures show the static pressure distribution predicted by CFD at the lower surface of the disc from 0.15mm lift to maximum lift at 3.7mm. Initially in figure 6.35 as was identified earlier, at 0.15mm the central core area of the disc which is directly above the inlet is subjected to the highest static pressure with a radial decay of static pressure towards atmospheric pressure at the outer regions of the disc. However at 0.5mm lift, the outermost edge of the disc results in an initial pressurisation of the surface to provide an additional aerodynamic force to help the disc to pop open as inlet pressure increases.

Once this initial area has become pressurised, as can be seen from figure 6.36 (lifts of 1mm and 1.75mm) the PRV pops open to allow further development of the static pressure profile across the disc between the central core and outer edge to further increase the force acting on the disc to overcome the spring force and preload. It should also be noted that the static pressure profile acting on the lower surface of the disc is axisymmetric which confirmed that there was no symmetry breaking flow bifurcations occurring similar to what was observed for the Henry 5231BX PRV. This as a result highlights the importance of CFD to evaluate the sensitivity between PRV geometry and Reynolds number (as discussed in chapter 3.4) in order to identify to PRV designers the criteria at which symmetry breaking flow processes would occur in the valve. At higher disc lifts of 2.5mm and maximum discharge position of 3.7mm it can be easily understood from figure 6.37 that the pressure profile remains axisymmetric where the pressure in the region between the centre and outside edge continues to increase. At maximum lift however it can be also observed that an additional gradient is produced with a lower pressure acting in the region immediately following the central core of the disc and therefore helps to reduce the total pressure force acting on the disc at maximum piston lift.

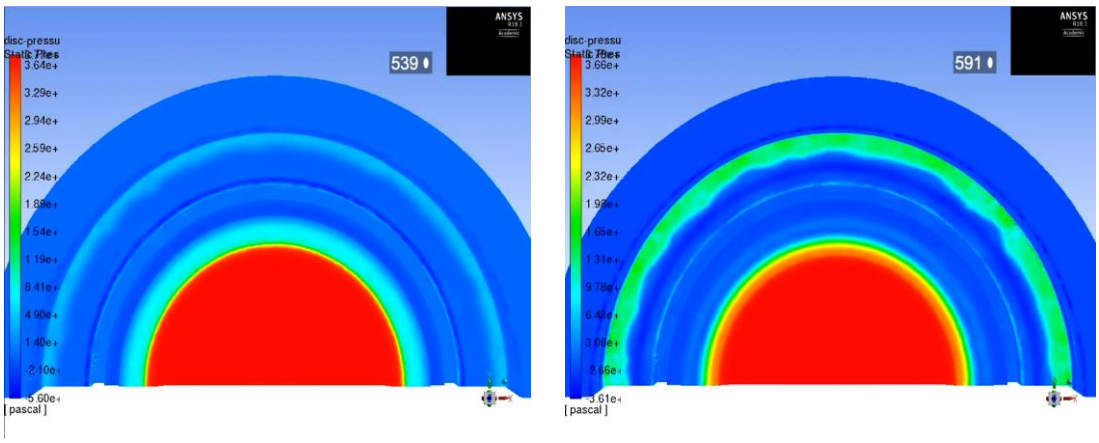

Figure 6.35 - Contours of Static Pressure on Disc Surface in barg for 3511E at Lifts of 0.15mm (left) and 0.5mm (right) During Opening at t = 0.4s-0.5s

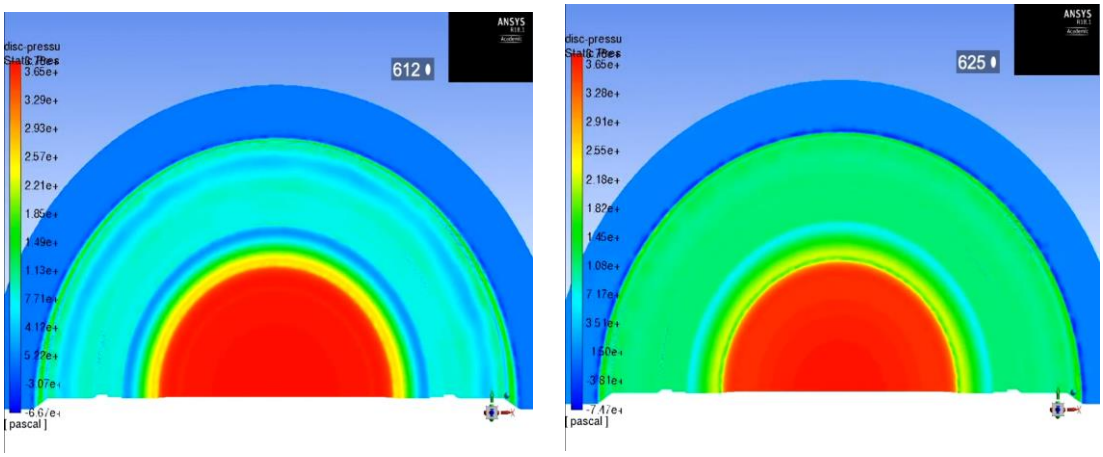

Figure 6.36 - Contours of Static Pressure on Disc Surface in barg for 3511E at Lifts of 1mm (left) and 1.75mm (right) During Opening at t = 0.4s-0.5s

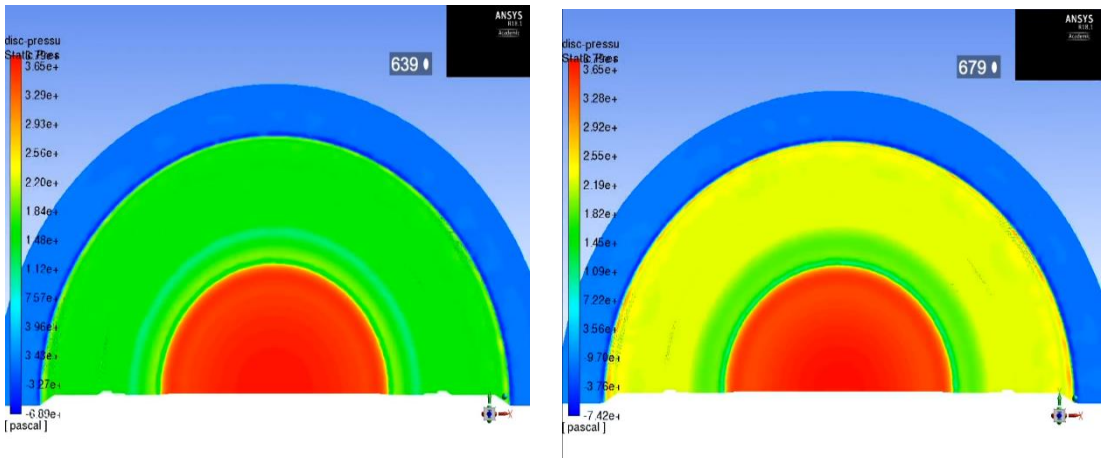

Figure 6.37 - Contours of Static Pressure on Disc Surface in barg for 3511E at Lifts of 2.5mm (left) and 3.7mm (right) During Opening at t = 0.4s-0.5s

6.2 Henry 5231BX (Modified Gland) PRV Transient Validation

Following on from both the steady state CFD model developed for the Henry 5231BX PRV as well as the dynamic mesh methodology used during the ASME valve validation it was possible to develop a transient moving mesh CFD model for the 5231BX. The variant used for the study was the modified gland with the original outlet as it represented an authentic form of the production valve. The modified gland was also used as it reduced the computational complexity of the gland geometry which was found during steady state validation to have no effect on the accuracy of the model. In this transient study, an experimental technique was developed to allow dynamic testing of the PRV in house at the University of Strathclyde. For all experimental and CFD data generated within this section; single phase air was used as the test medium for a set pressure for the PRV of 10.3 Barg.

6.2.1 Experimental Dynamic Testing for Henry PRV

An experimental assembly and measurement technique was developed within the flow testing laboratory at Strathclyde to measure the opening and closure behaviour of the Henry 5231BX PRV performance. The assembly developed is illustrated in figure 6.38 and table 6.5. It can be seen that a bespoke housing for both connection of the inlet to the supply piping (1) and outlet (3) to connect to the laser displacement sensor (7) was used [Keyence LK G87 Laser Displacement Sensor with LK GD500 Controller]. The laser in which a reference surface (5) connected to the disc was used to provide a measurement point; offered an alternate form of measuring disc lift when compared with an LVDT. The laser reference surface was connected to the PRV disc (4) via a thin spindle attached to the top surface of the disc. It was therefore possible to measure disc displacement directly to achieve a lift vs time relationship as the inlet pressure was varied. A transparent perspex shield (6) was adopted to protect the laser from the exhaust jet and any debris.

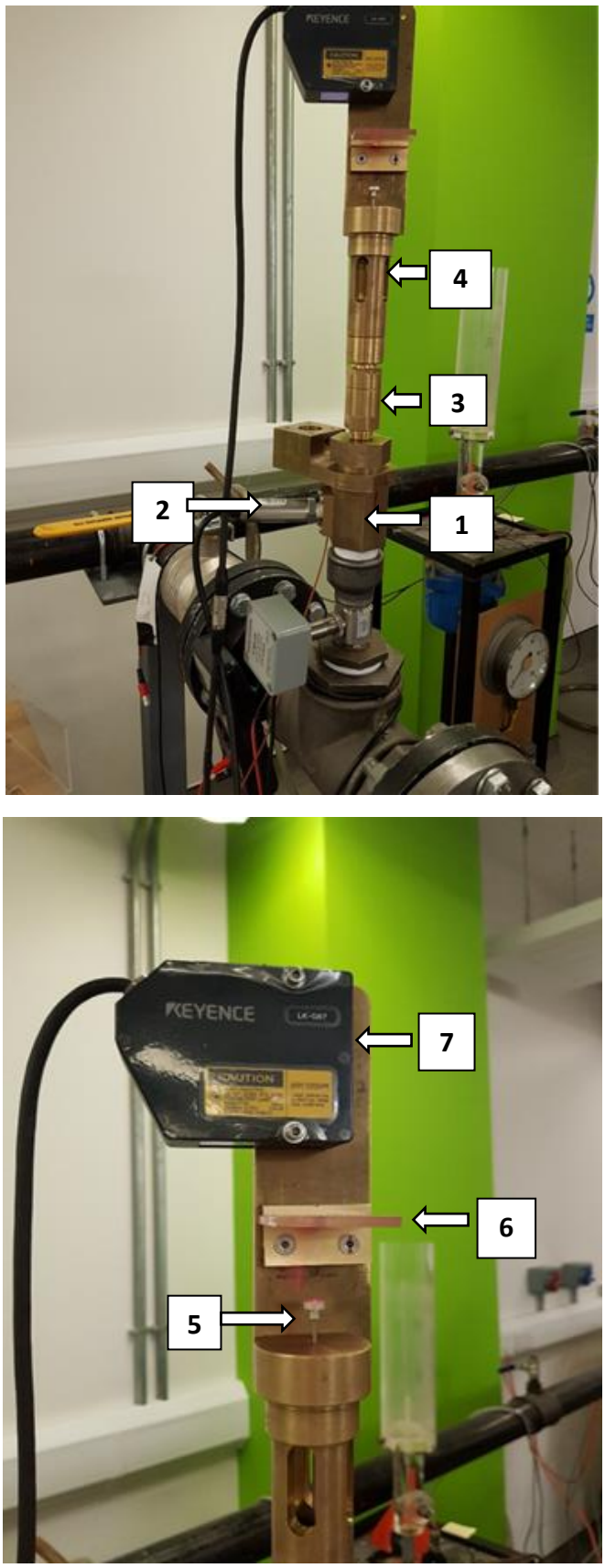

Figure 6.38 – Transient Experimental Rig for Henry 5231BX PRV

No.	**Experimental Part**	**Description**
1	PRV Inlet Assembly	Assembly to connect inlet of PRV to supply piping
2	Inlet Pressure Sensor	Sensor to measure inlet pressure to the PRV
3	5231BX PRV	PRV to be tested with modified gland assembly
4	PRV Outlet Assembly	Assembly to allow venting and visual check of spindle
5	Laser Reference Surface	Laser Reference surface to measure disc displacement
6	Perspex Shield for Laser	Shield to prevent laser damage and enable measurement
7	Keyence Laser Sensor	Laser to measure disc displacement (lift)

Table 6.5 – Description of Experimental Components in Figure 6.38

Property	**Transducer**	**Accuracy**	**Range**
Pressure	Electronic Pressure Gauge	0.08%	0-68 bar
Displacement	KEYENCE Laser Displacement	0.1%	-15 to +15 mm

Table 6.6 – Measurement Devices Required for Dynamic 5231BX Testing

During data collection, in-house developed software was used to collect inlet pressure from a sensor upstream of the PRV (2) [Omega Engineering PX409 pressure transducer] and disc displacement (lift) over time to determine overpressure, blowdown as well as monitoring the dynamic characteristics of the disc displacement during the general operation of the PRV. By monitoring these features it was possible to determine the effectiveness of an equivalent dynamic system established within a CFD model. It should be noted that the Broady first audible method of setting the PRV was used to establish the set pressure which was adjusted by changing the gland depth which due to contact with the spring affected spring preload by providing further spring compression. The gland depth used for the PRV during this study was 3.2 mm and would also be used for the CFD model as it provided the desired set pressure of 10.3 barg.

The general measurement procedure developed for dynamic measurement of the 5231BX PRV was as follows;

1. Before testing took place and flow was established it was crucial to ensure that the appropriate safety precautions were made within the laboratory such as securing of loose items in the vicinity of the jet, closing doors to public walking areas and wearing appropriate personal protection equipment (PPE) especially for ears, eyes and feet.

2. Initially by using digital Vernier calipers, the gland depth was measured and set pressure verified by increasing system pressure to 10.3 Barg to ensure first audible leakage was detected. This process required an iterative adjustment of the gland depth in order to achieve the desired set pressure. It should be noted that the original PRV outlet was used to provide easy adjustment of the gland as the outlet assembly (4) was not required during this process.

3. Once an appropriate spring preload and set pressure was achieved, the outlet assembly (4) was attached and it was critical to ensure again that no loose components or items were present in the vicinity of the jet.

4. As lab safety was ensured, the supply pressure was slowly increased by introducing flow to the system. Above an inlet pressure of 9.5 Barg, recording equipment was enabled to digitally measure both pressure and disc lift with time. As the supply pressure reached set pressure and overpressure the PRV would open and relieve the system pressure until subsequent closure at blowdown pressure. It should be noted that if the supply flow rate remained constant then a cyclic operating mode of the PRV would occur which would not be desirable to sustain for a long

period of time as it could cause damage to the seat and disc surfaces which would affect subsequent measurements. The total time taken for data capture was approximately 40s in which numerous cycles of the PRV opening/closing would take place.

5. Steps 1-4 of the experimental process were repeated numerous times in order to ensure repeatability of the results. The data was then collected for data processing to extract overpressure, blowdown and disc lift vs time. Overpressure and blowdown values were identified from the data once the PRV had reached its maximum opening lift value and fully closed position respectively.

To determine the overall uncertainty of the overpressure and blowdown readings it was required to identify the measurement errors in a similar manner to the analysis performed in chapter 5.2. The systematic measurement uncertainty of the devices used is shown in table 6.6. In addition, to effectively evaluate statistical uncertainty, 4 independent tests were carried out to quantify a statistical error of overpressure and blowdown pressure to be 0.13% and 0.19% respectively.

Figure 6.39 highlights the typical pressure profile established during the transient experiment for the Henry 5231BX PRV which corresponds to the disc position vs time curve shown within figure 6.40. The time taken for the cycle to complete from initial opening was approximately 3 seconds. Both the overpressure and blowdown values are determined from the experimental data and are shown within table 6.7.

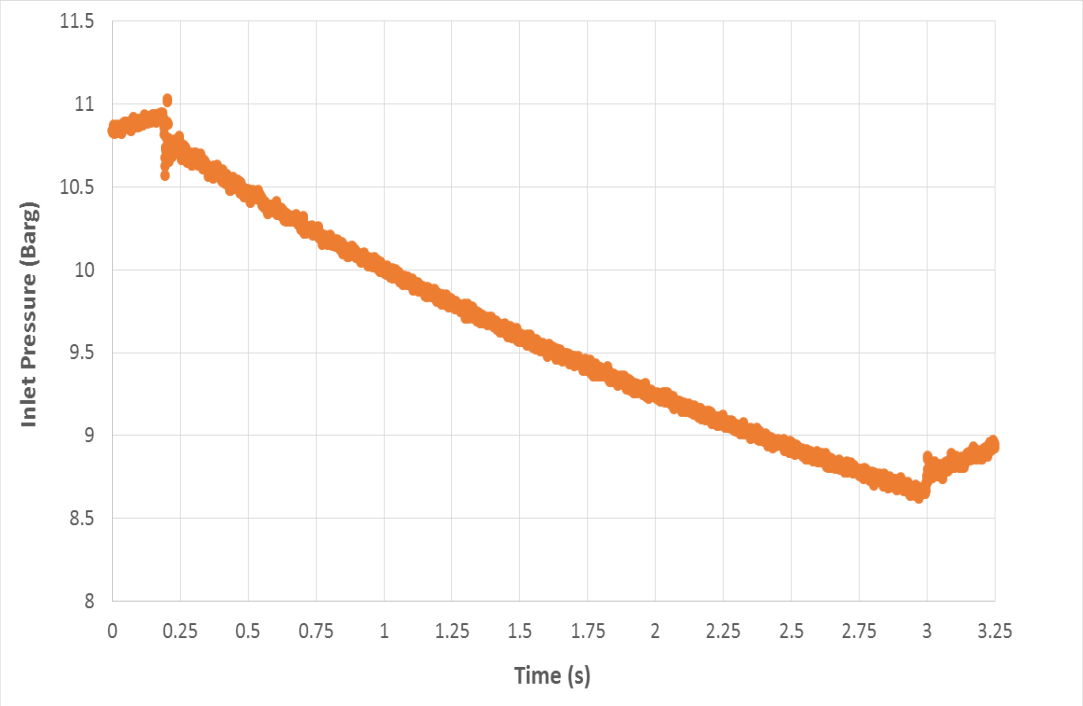

Figure 6.39 – Experimental Inlet Pressure Profile vs Time for Henry 5231BX PRV (Modified Gland)

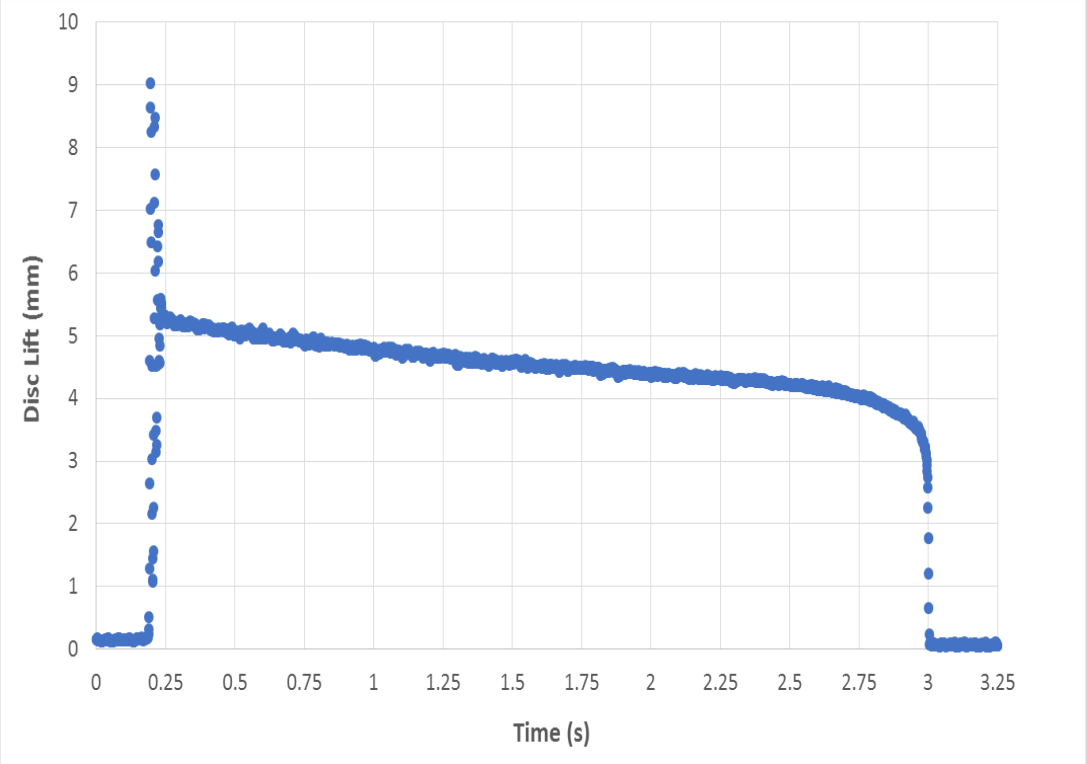

Figure 6.40 – Experimental Disc Position (Lift) vs Time for Henry 5231BX PRV (Modified Gland)

Over Pressure	**11.01 Barg** (+6.9% relative to set pressure)
Blowdown Pressure	**8.82 Barg** (-14.36% relative to set pressure)

Table 6.7 – Experimental Over Pressure and Blowdown Results for 5231BX PRV (Modified Gland) for Set Pressure of 10.3 Barg

The results for both over pressure and blowdown are presented in table 6.7 which meets the manufacturers expected performance of an allowable maximum of +10% over pressure and -15% blowdown relative to set pressure as specified within EN ISO 4126. The dynamic performance of the PRV can be appreciated from figure 6.40. During the initial phase, the PRV remains in an almost closed position with lower displacement for simmer/huddling when compared with the Broady 3511E PRV results shown in figure 6.2. This is because of the deformation occurring at the elastomer seal of the PRV as pressure increases.

Therefore as inlet pressure continued to increase to an over pressure value of 11.01 barg (6.9% over pressure) at 0.23s, the disc opens rapidly to a maximum value of 9 mm disc lift. However, within 0.1 s of maximum opening the disc quickly achieves an equilibrium position of approximately 5 mm once the aerodynamic forces between front face pressure and backpressure becomes balanced. The lift time behaviour shown also suggested a high amount of damping in the system with little significant oscillation following opening with no flutter detected.

Following reaching maximum lift of 5 mm, as shown in figure 6.40 the inlet pressure decreased which allowed the disc to slowly close towards a disc lift of 3.5 mm at 3 s. The critical inlet pressure at this time was 8.82 barg (-14.36% Blowdown Pressure) where the disc accelerated quickly to the closed position

in order to reseal the system and prevent any further loss of vessel contents. In general, the dynamic lift time behaviour of the Henry 5231BX PRV matched that of the Broady PRV however during opening the Henry PRV reached a much greater value and exhibited behaviour corresponding to high damping to return to a stable value of 5 mm lift from 9 mm initial opening.

6.2.2 Development of Transient Moving Mesh CFD Model for Henry PRV

Following on from the steady state CFD model developed for the Henry 5231BX PRV as well as the dynamic mesh model for the Broady PRV it was possible to achieve a transient CFD model for the Henry 5231BX valve. By using the quarter model geometry developed for the steady state testing of the modified gland 5231BX variant, only small adjustments were required to establish a computational domain suitable for a moving mesh model. The model was generated using the geometry and meshing tools available within ANSYS Workbench 18 and subsequently solved using ANSYS FLUENT 18.1.

Furthermore, as can be seen within figure 6.41 a small opening with a double layer of cells was required (as was the case for the ASME PRV) to allow mesh topology in the moving mesh region to be maintained as the PRV lift value fluctuates. A minimal initial disc opening of 0.05 mm (0.5% of maximum disc lift) was used following an iterative selection process which allowed the remaining 99.5% of disc travel to be captured by the CFD model. In contrast to the Broady valve, it was apparent from experimental results that less displacement occurred during the simmer phase as a result of the elastomer for the Henry PRV deforming. As a result it was deemed critical to minimise the initial opening for the Henry PRV to remain representative as possible. This is due to the required non-physical boundary condition of the PRV in an open state to maintain mesh topology during mesh deformation.

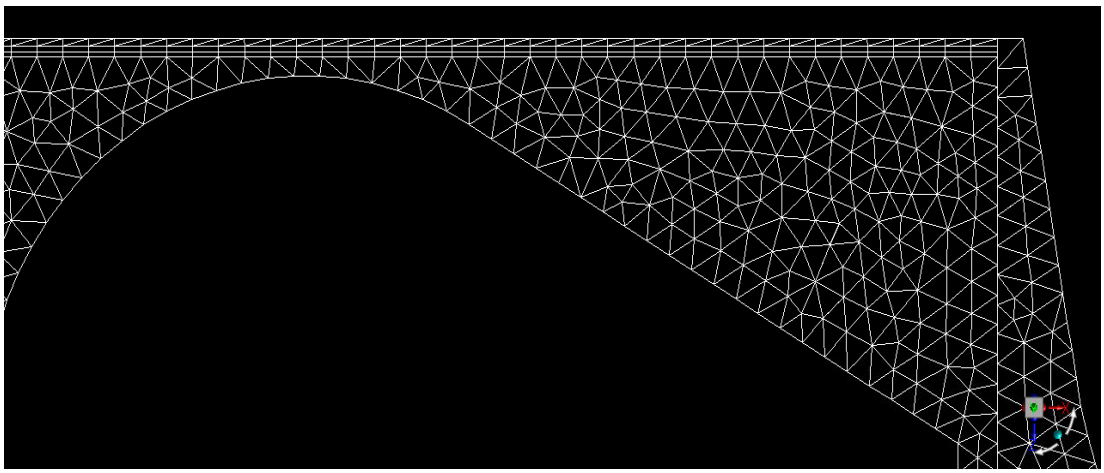

Figure 6.41 - 3D CFD Dynamic Mesh at Lift of 0.05mm for 5231BX PRV

The overall quarter symmetry CFD mesh developed for dynamic meshing in accordance to UDF commands is shown in figure 6.42. It should be noted that the mesh density determined during the steady state validation study was maintained however in a similar nature to the ASME valve, tetrahedral elements were required in addition to quadrilateral elements in order to capture the complex geometry of the PRV. This was also necessary to allow a suitable domain for dynamic layering to take place for the moving mesh to work effectively. The total number of elements within the model at 0.05 mm lift was 13 million elements with an average orthogonal quality of 0.78 and an average mesh skewness of 0.21. Within figure 6.42 the general bulk flow path across the PRV is marked using the yellow arrows in which flow originates from a pressure inlet marked as red towards the atmospheric outlet marked in green.

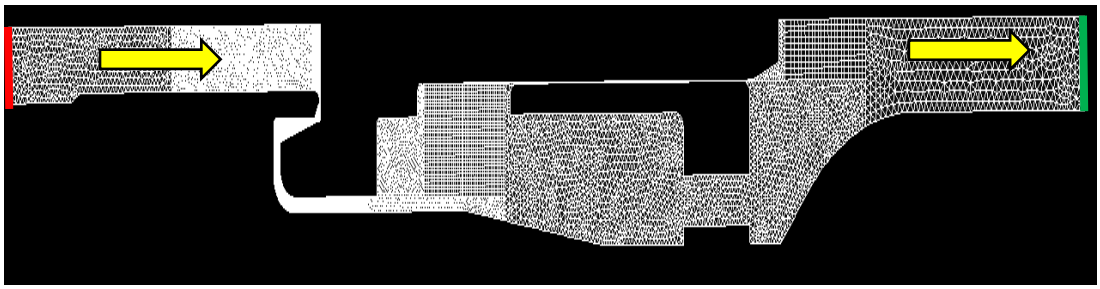

Figure 6.42 - Overall CFD Dynamic Mesh for Henry 5231BX PRV (Modified Gland)

The overall mesh structure could also be appreciated from figure 6.42 in which it can be seen that the mesh consists of a combination of structured and unstructured mesh regions using DDM. However the detail of the mesh remains unclear within figure 6.42 due to the high density of the mesh, especially in the near disc/seat area. Figures 6.43, 6.44 and 6.45 alleviate this issue by allowing the lower, middle and upper sections of the hybrid mesh to be clearly highlighted. In continuation with the moving mesh geometry and dynamic meshing methodology developed for the ASME PRV, the mesh shown within figures 6.5, 6.6 and 6.7 is consistent where the use of a structured mesh section would allow dynamic layering to take place and unstructured mesh area could capture the complex contours of the surrounding geometry. From figures 6.43, 6.44 and 6.45, it could be appreciated that the mesh would allow dynamic layering in the red regions which are connected to unstructured mesh regions (blue) using conformal interfaces. The UDF developed for the 5231BX PRV would allow the rigid motion of the blue zone to be controlled alongside appropriate dynamic mesh settings for the red regions. The unstructured stationary zones (yellow) were connected to the deforming mesh zones (red) to prevent further mesh deformation and generation of negative volumes.

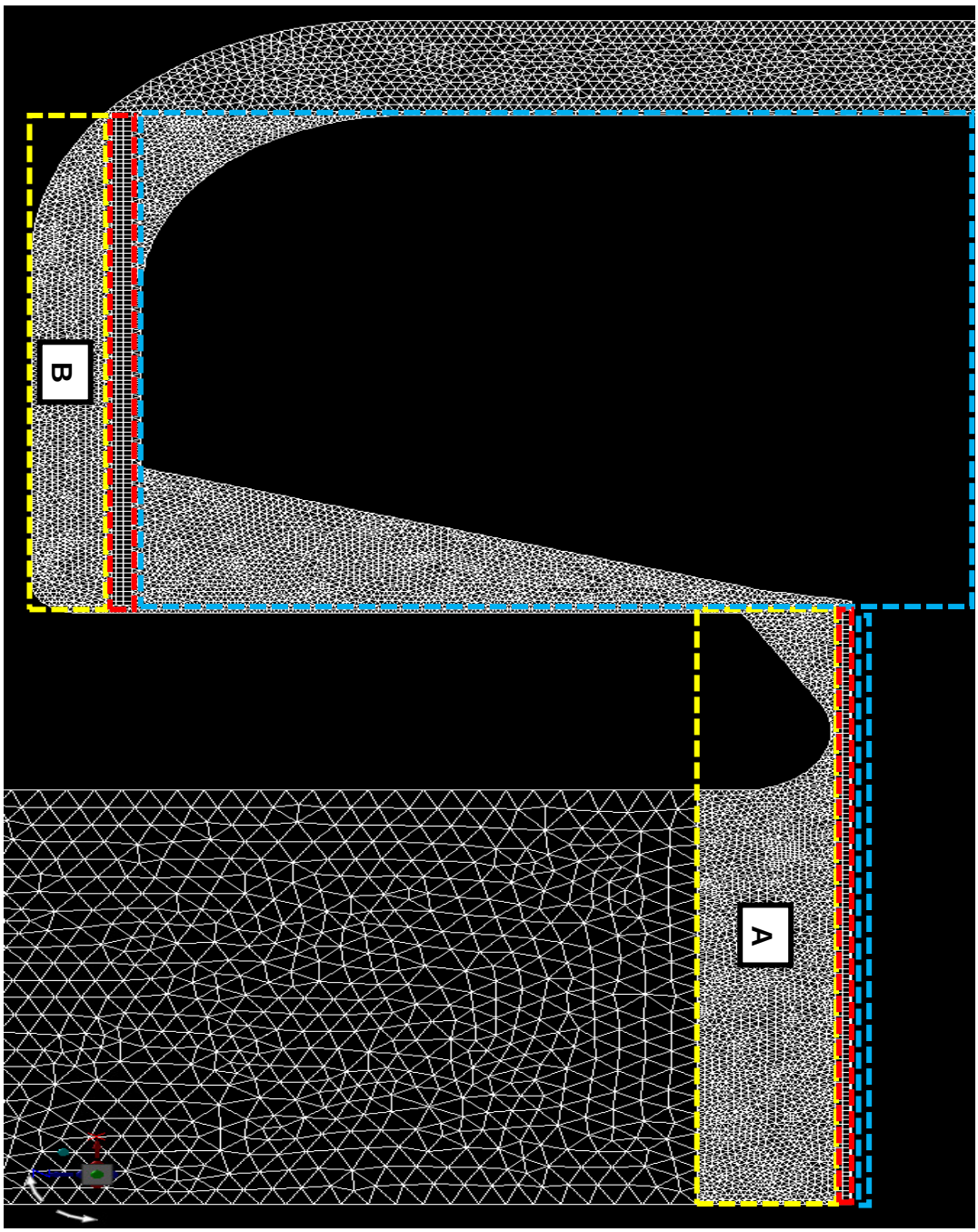

Figure 6.43 - CFD Dynamic Mesh Principle for 5231BX PRV (Disc/Seat)

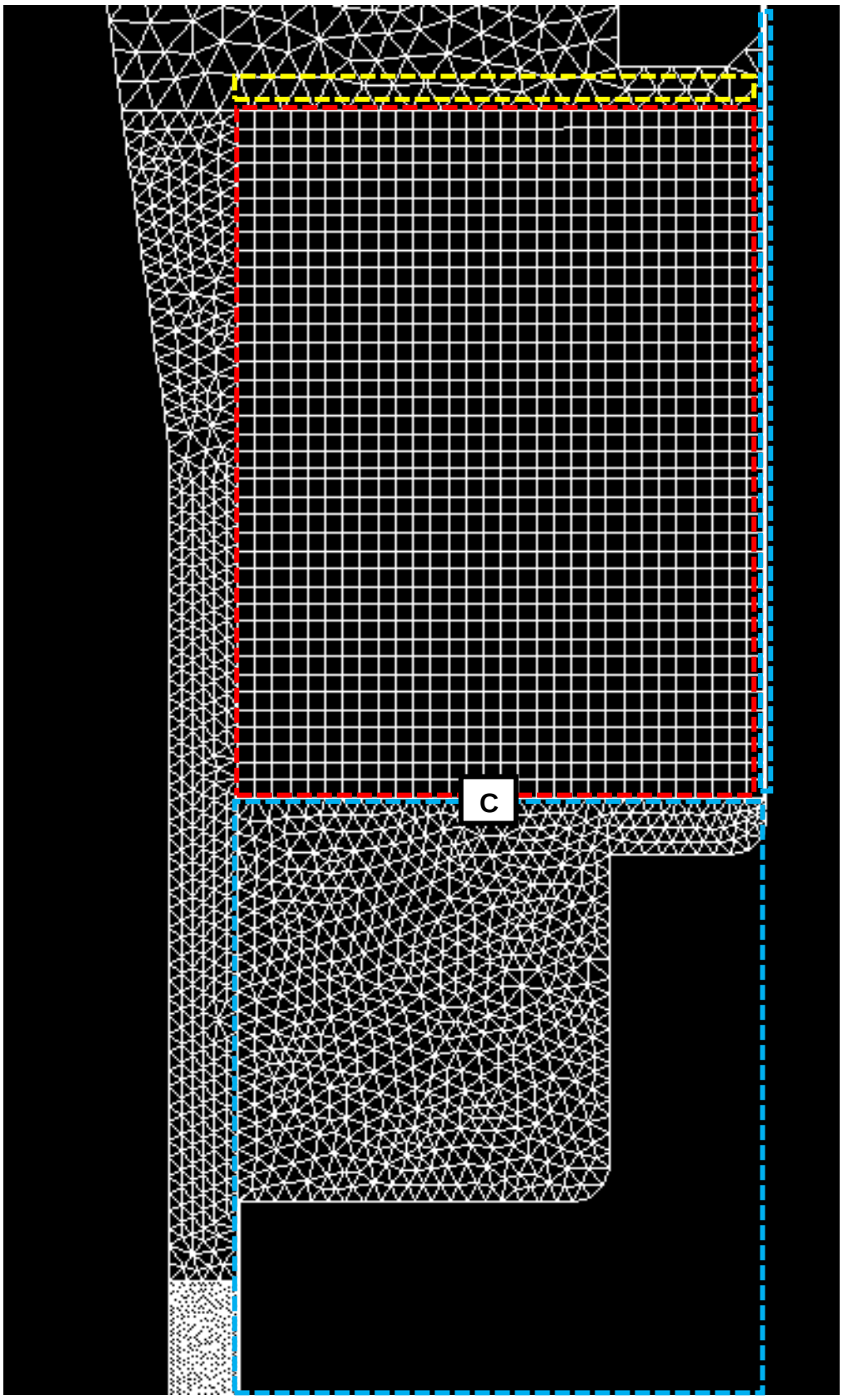

Figure 6.44 - CFD Dynamic Mesh Principle for 5231BX PRV (Upper Disc)

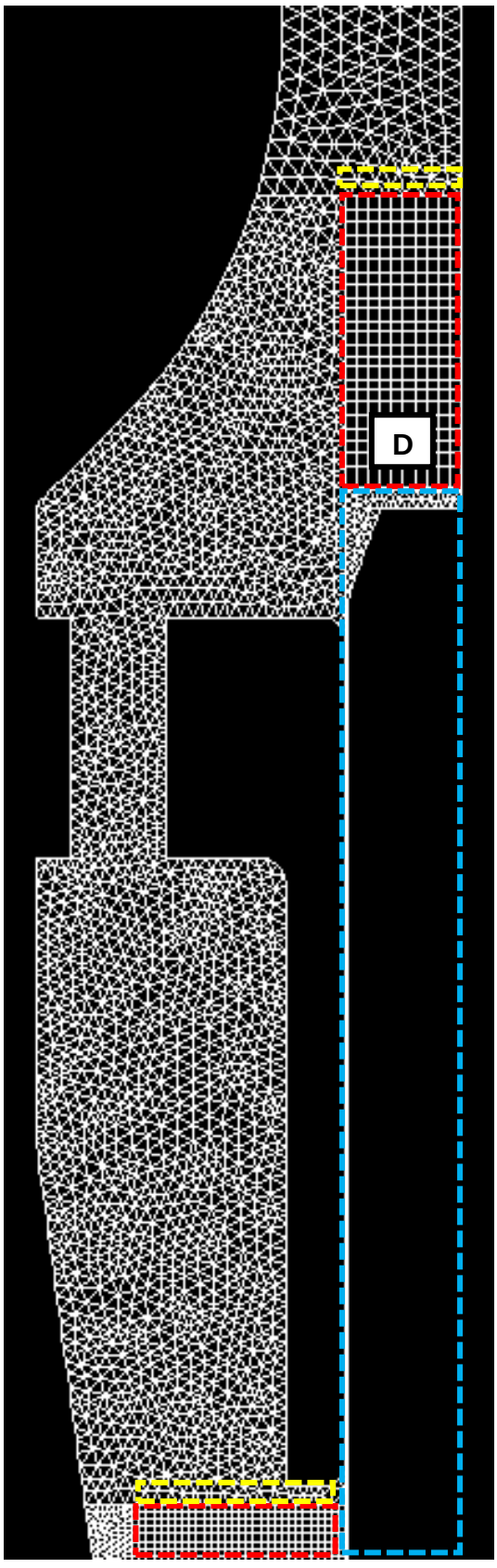

Figure 6.45 – CFD Dynamic Mesh Principle for 5231BX PRV (Gland/Outlet)

As mentioned earlier, the mesh density selected for the transient model shown in figures 6.43, 6.44 and 6.45 was based on the results of the steady state mesh independency study. The values used for the structured and unstructured mesh zones shown for regions A, B, C and D are shown within table 6.8.

Mesh Zone	**Structured Mesh Element Size (mm)**	**Unstructured Mesh Element Size (mm)**
A	4e-5	4e-5
B	4e-5	4e-5
C	2e-4	2e-4
D	3.5e-4	2.5e-4

Table 6.8 - Optimum Mesh Density for 5231BX Dynamic Mesh Based on Steady State Validation

Henry 5231BX PRV Disc Motion and Inlet Pressure Profile for UDF

Following on from the principles for the UDF developed during the ASME work an extension of the force balance shown in figure 6.7 was required for the Henry 5231BX PRV. The fundamental forces acting on the Henry 5231BX PRV were identified as follows;

- Aerodynamic force due to static pressure acting on the disc (F_{AERO}). Shear forces are generally small. Within FLUENT the integration of static pressure across the disc's wetted area is also performed by identifying the disc within the UDF. The integration is achieved using a DEFINE_ADJUST macro which determines the sum of the product of static pressure in each cell area located on the disc in the 3D domain.

- Spring force at displacement x_n (F_{SPRING}) and preload ($F_{PRELOAD}$) at displacement x_0 determined during the valve setting process at set pressure with spring constant k of 10.99 N/mm. The CFD preload used was 54 N which was measured experimentally for 10.3 Barg set pressure which was equivalent to a gland depth of 3.2 mm.

- Weight due to mass of moving parts, m (W_{MOVING}). This force is taken into account within $F_{PRELOAD} = F_{AERO} - W_{MOVING}$ at set pressure. The moving mass for the 5231BX PRV included the piston assembly and spring and was measured to be 0.03 kg.

- Damping force ($F_{DAMPING}$) due to frictional contact and spring damping with damping constant c. In contrast to the Broady PRV, due to the geometry of the Henry 5231BX PRV where the disc spindle is in close contact with the gland during valve motion, it was required to account for frictional contact between the two surfaces. As a result, following an iterative selection procedure a damping constant value of 5.45 Ns/m was identified as the most suitable value which corresponded to a damping ratio for the system of 0.15. This value was also verified using a logarithmic decrement analysis from experimental results alongside a realistic prediction of friction caused by spindle contact with gland.

The transient inlet pressure profile for the UDF of the Henry PRV was based on the experimental profile shown within figure 6.39. Due to the long duration (3s) of the experiment as well as the high mesh density it was required to compress the profile for the CFD profile to 1.5s to minimise computational expense. This would allow the HPC time of ARCHIE WeSt constraint of less than 2 weeks running time to be met. As this time period was representative of the time taken for the 3511E PRV to open and close fully, it was deemed sufficient to represent equivalent characteristics to experimental pressure profile. However, ideally both experimental and CFD pressure boundary

conditions should be equal. With further advances in computing resources this would be possible.

The resultant IF condition applied within the UDF macro to define the transient inlet pressure ramp for the Henry 5231BX PRV is shown within figure 6.46 alongside a visual representation of the pressure ramp within figure 6.47.

```
if (t >= 0 && t < 0.2)
{
        Pinlet = (51202.035709985200 * t) + 1091470.841429000000;
}

if (t >= 0.2 && t < 0.23)
{
        Pinlet = 1101711.249;
}

if (t >= 0.23)
{
        Pinlet = (-178119.09336295800 * t) + 1142678.64004449000;
}
```

Figure 6.46 - UDF Inlet Pressure Profile for 5231BX Henry PRV

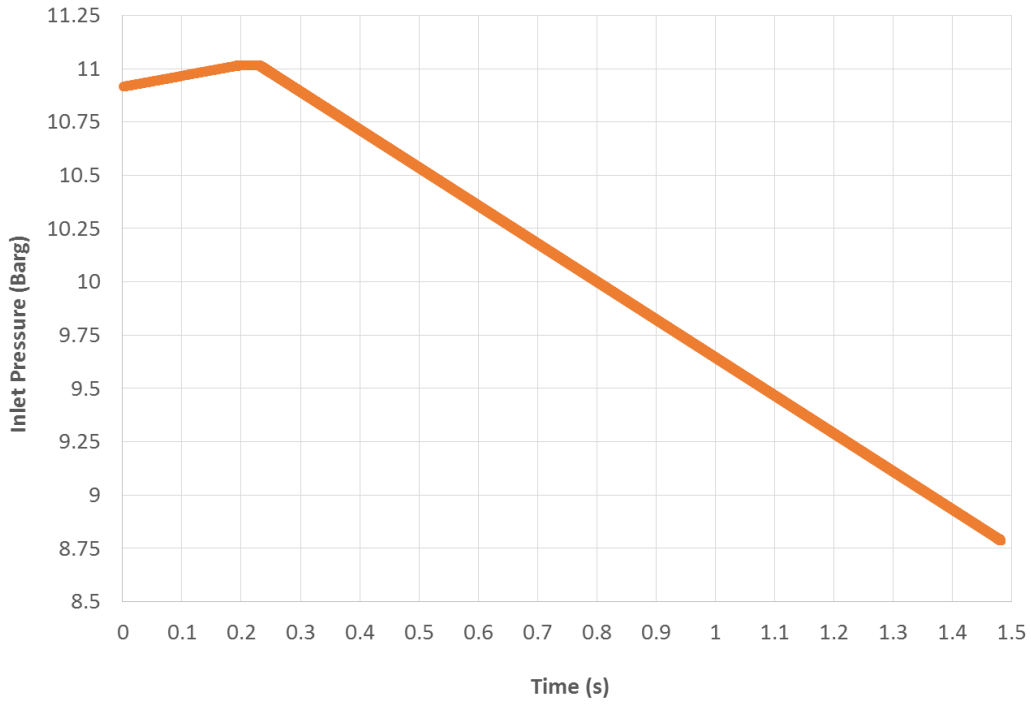

Figure 6.47 – Graph of 5231BX Inlet Pressure Ramp for Transient CFD

Dynamic Mesh CFD Settings for Henry 5231BX PRV Model

Similarly to the ASME valve it was required to enable layering as the primary dynamic meshing method. Furthermore, as established previously in the Broady PRV analysis the ratio based option was also selected for the Henry 5231BX valve with a split factor of 0.05 and collapse factor of 0.4 to ensure that sufficient mesh density was maintained during mesh deformation. The required dynamic mesh settings were applied within the “dynamic mesh zones” tab within FLUENT in which each mesh zone highlighted in yellow, blue or red within figures 6.43, 6.44 and 6.45 were selected to be of either stationary, rigid body or deforming type. Following this the procedure described earlier for the Broady dynamic mesh model was replicated to allow the appropriate dynamic mesh settings to be applied for the rigid body, stationary and deforming mesh zones.

The Henry model also required the use of both conformal and non-conformal interfaces to enable the dynamic mesh to work effectively as was described earlier. Figures 6.48 and 6.49 both highlight the use of conformal interfaces (green) and the use of non-conformal interfaces (purple) at the disc/seat interface where it can be seen that the structure of the interfaces was different to that generated for the ASME valve. It is therefore important to note that the creation of such zones is specific to each PRV and must be customised accordingly to allow a minimal initial disc opening to be achieved. Figures 6.48 and 6.49 highlight the very small deforming layers for the initial conditions at 0.05 mm disc lift. An elongated step can also be seen between the central and outer region of the 5231BX disc/seat interface which is significantly different to the geometry developed for the Broady 3511E PRV. A journal was also developed for the Henry PRV to define the dynamic mesh properties of each dynamic mesh zone and interface in order to reduce the time required during initial setting up of the simulation. As a result, the lengthy procedure is only required to be manually applied once.

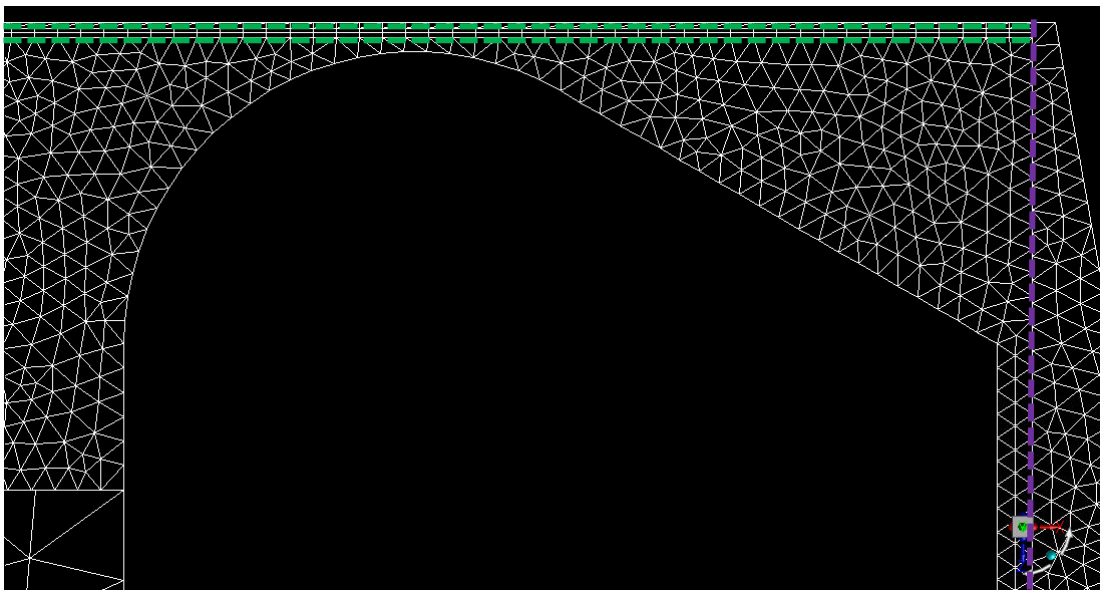

Figure 6.48 - Mesh Interfaces Required for Central Area of PRV Disc/Seat

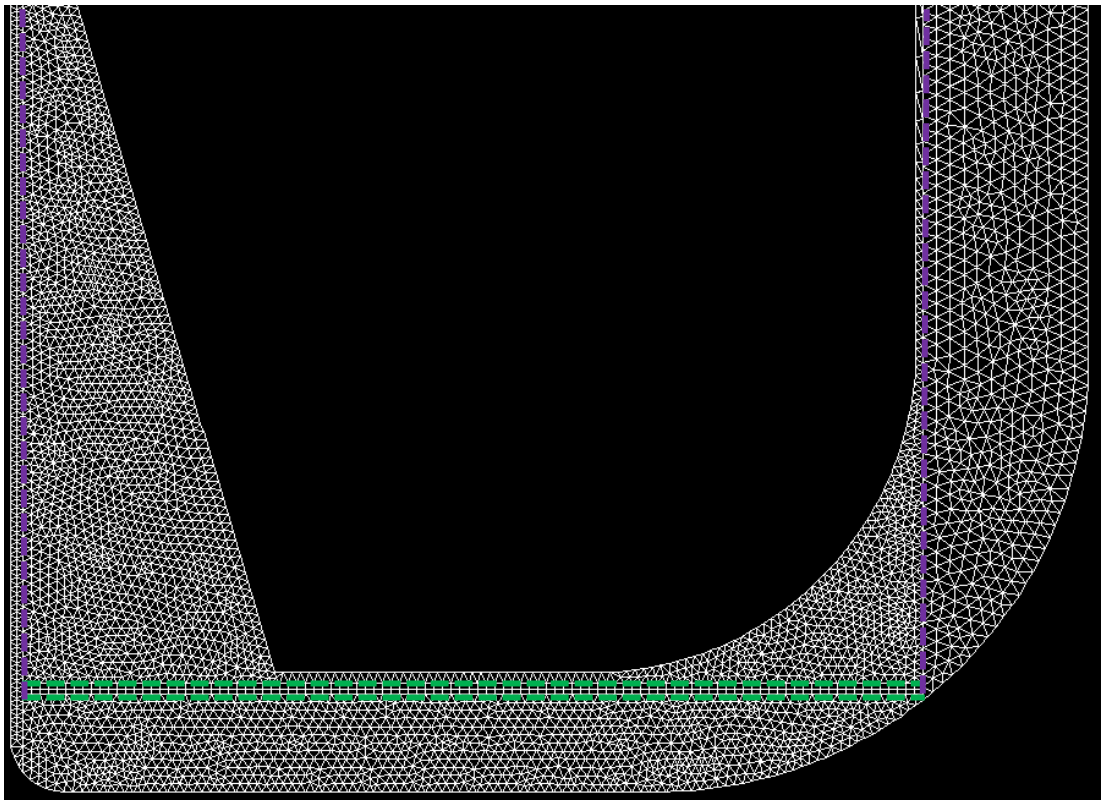

Figure 6.49 - Mesh Interfaces Required for Outer Area of PRV Disc/Seat

Henry 5231BX Transient CFD Model Numerical Settings

In general the numerical modelling procedure was similar to the methodology established during steady state validation of the Henry 5231BX CFD model. The pressure based solver, K-Omega SST turbulence model and ideal gas law with the energy equation was also selected for the transient model due to their strong performance during steady state testing. As the transient solver was to be used, it was necessary to identify an appropriate time step to model the inlet pressure profile over the 1.5s time interval shown in figure 6.47. The range of time steps which were developed to prevent the generation of negative volumes and ensured computational stability are shown within table 6.9. It can be appreciated that a series of 8 time step values were required compared to the 5 for the Broady PRV. This indicated a further aspect of dynamic mesh modelling which must be tailored specifically to the PRV which is being modelled. In a similar manner to the Broady ORV however the time step values were determined following an iterative trial and error study as well as using experimental data to estimate maximum disc velocity. It should also be noted that the maximum number of iterations/time step during all time steps was selected to be 15 to allow good convergence to be achieved

CFD Simulation Time Period (s)	**CFD Time Step Value Used (s)**
First 100 Iterations	1e-6
0-0.19	1.5e-5
0.19-0.26	1e-5
0.26-0.34	5e-5
0.34-0.85	7.5e-5
0.85-1.35	9.5e-5
1.35-1.47	1.5e-4
1.47-1.49	1e-5

Table 6.9 - Time Step Variation During Transient CFD Simulation for 5231BX

In general, the computational procedure for the Henry 5231BX PRV was as follows;

- Following the calculation of a steady state solution at the opening disc lift of 0.05mm at 10.9 Barg to achieve an initial starting point for the transient solver it was necessary to use a time step value of 1e-3 ms for 100 iterations to ensure stability. Following the initial period, as can be seen from table 6.9 the time step was increased to 0.015 ms until the PRV began to open significantly at approximately 0.19s.

- Once the disc began to open a time step value of 0.01 ms was selected from 0.19-0.26s due to the high velocity of the disc to prevent the generation of negative volumes/excessive mesh stretching as well as to ensure numerical stability. Following 0.26s once the vibration and maximum velocity of the disc began to dissipate a larger time step of between 0.05-0.075ms was used between the time of 0.26 s-0.85 s.

- During blowdown between 0.85s-1.35s where the velocity of the disc would be expected to be low a larger time step value of 0.095ms was used which was then increased to 0.15 ms until approximately 1.47s flow time. In preparation of the PRV disc closing with high velocity, the time step would be reduced to a value of 0.01 ms until closure and end of simulation would be achieved. The time step profile with flow time shown within figure 6.9, was found to be successful to ensure a stable solution and avoiding generation of negative volumes during mesh movement. It should be noted however that a smaller time step value was required on average across the full simulation period for the Henry model when compared with the ASME PRV due to vibration. This will be discussed in detail in the following section.

In accordance with the methodology developed during steady state analysis, surface monitors were established for the aerodynamic force acting on the disc as well as for the mass flow rate at the inlet. All other numerical settings applied are shown within table 6.10 alongside the second order implicit transient formulation method available within FLUENT.

FLUENT Setting Type	**Recommended Setting**
Solver Type	Pressure Based
Turbulence Model	K-Omega SST
Air Density	Ideal Gas Law (Energy Equation ON)
Pressure-Velocity Coupling Scheme	Coupled
Spatial Discretisation - Gradient	Least Squares Cell Based Scheme
Spatial Discretisation (Pressure)	Second Order
Spatial Discretisation (Other Terms)	QUICK
Initial Flow Courant Number	5
Momentum, Pressure, Density and Energy URF's	0.2

Table 6.10 - Numerical Settings Required for Transient Moving Mesh CFD Model of 5231BX PRV

The boundary conditions for the transient model were identical to those established within the steady state research as shown within figure 6.11 with a pressure inlet, pressure outlet and half symmetry applied. For the transient moving mesh model, the inlet pressure was input using the UDF inlet pressure profile shown within figure 6.42 whereas the outlet pressure remained at atmospheric value. The temperature for both the inlet and outlet was applied as room temperature at 295 K.

6.2.3 Henry 5231BX Transient CFD Model Results and Discussion

In a similar manner to the analysis performed for the ASME PRV, the criteria established for validation will be used for the 5231BX dynamic mesh PRV model with comparison to experimental results. Application of the boundary conditions alongside dynamic mesh settings described within the previous section was required within ANSYS FLUENT 18.1. The HPC facility ARCHIE WeSt was used with 280 cores to achieve a total calculation time of 5 days. A comparison of the transient results of the 5231BX PRV CFD model with experimental values for overpressure and blowdown is shown within table 6.11 and lift vs time within figure 6.50. It can be appreciated that the CFD model was capable of predicting the value of overpressure for a valve set at 10.3 barg to be 11.02 barg (6.96% above set pressure) with an opening time of 6 ms and blowdown to be 8.79 barg (14.7% below set pressure) with a blowdown time of 1.3s. These results were in accordance with the manufacturer's expectations of maximum discharge rate to be achieved within 10% overpressure and to be closed within 15% blowdown; as specified within EN ISO 4126. Therefore, it could be established that the dynamic mesh CFD model was capable of achieving accurate correlation of the opening and closing characteristics of the Henry PRV. In addition, the mass flow rate relationship with time is shown within figure 6.51 where the calculated discharge flowrate of 0.085 kg/s is in good agreement with the expected valve flowrate of 0.083 kg/s of air at 10.3 barg, as specified by the manufacturer.

	Overpressure	**Blowdown**
Experiment	11.01 Barg **(+6.9% Set P)**	8.82 Barg **(-14.36% Set P)**
Transient CFD	11.02 Barg **(+6.96% Set P)**	8.79 Barg **(-14.67% Set P)**

Table 6.11 - Comparison of CFD and Experimental Overpressure and Blowdown Values for 5231BX PRV (Mod Gland)

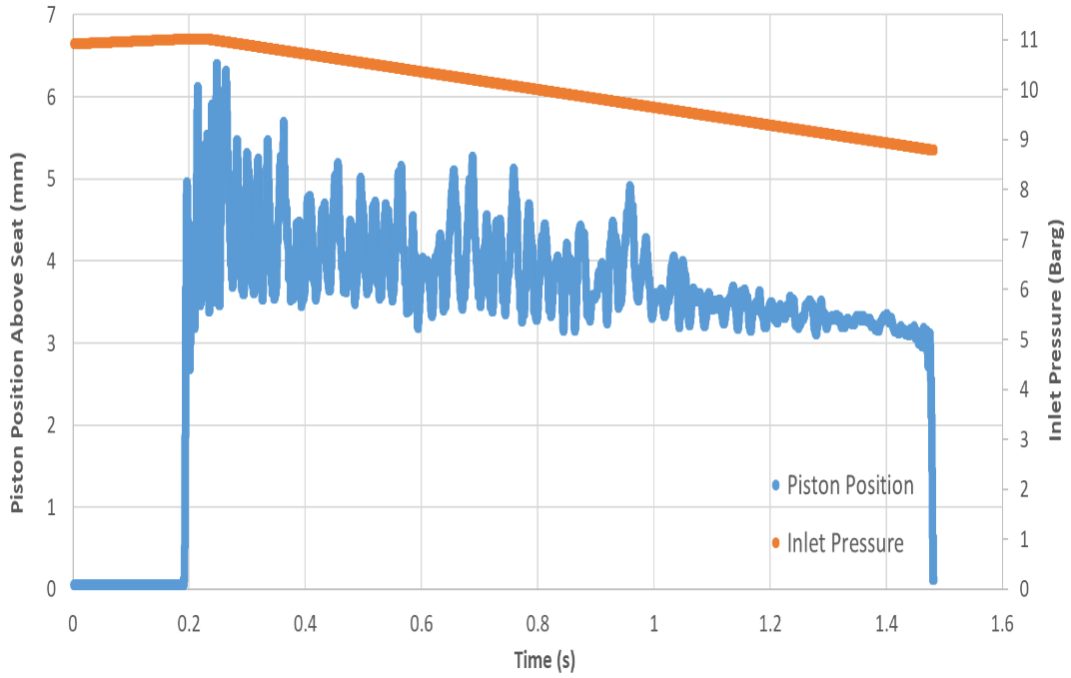

Figure 6.50 – CFD Results of Piston Disc Lift vs Time for Henry 5231BX PRV for Inlet Pressure Profile Described in Figure 6.47

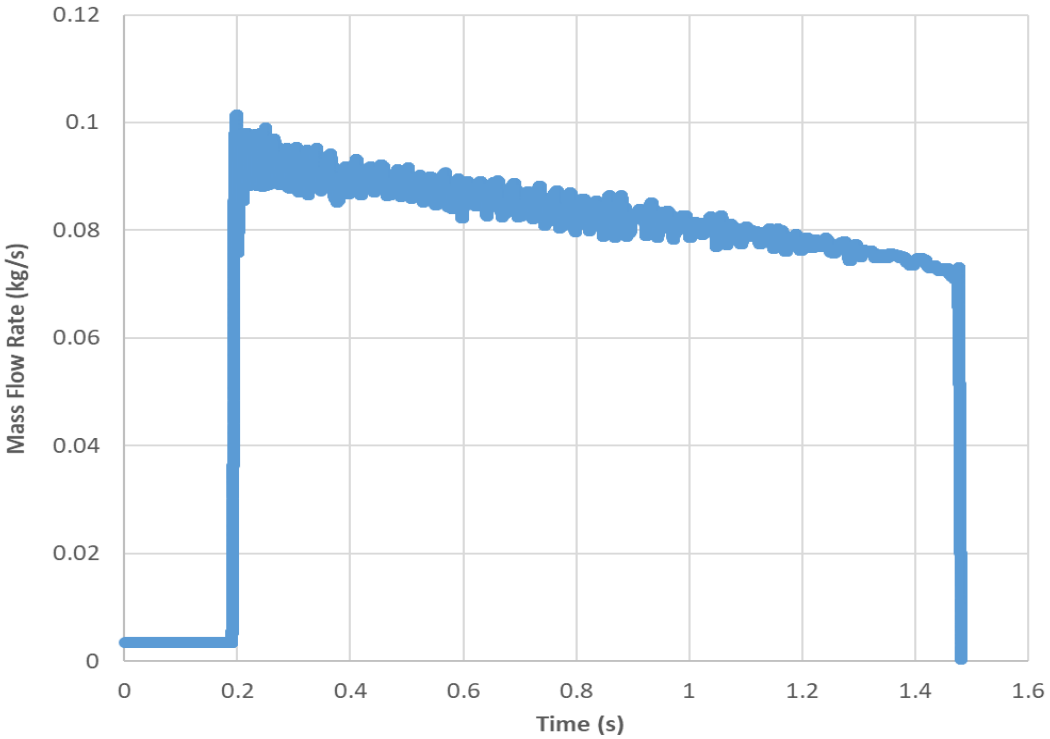

Figure 6.51 - CFD Results of Air Mass Flow Rate vs Time for Henry 5231BX PRV for Inlet Pressure Profile Described in Figure 6.47

The results presented in table 6.11 highlight the ability of the CFD model to accurately predict overpressure and blowdown which is in addition to the strong performance that the model demonstrated for the ASME 3511E PRV. This in turn highlights the capability of the dynamic mesh model developed within this study as a tool for analysis and/or initial PRV design. Interestingly however for the 5231BX it can be seen from figure 6.50 that there is oscillation after opening (0.2-1 s) which is damped over time due to the damping coefficient and further by fluid damping. This dynamic behaviour represents flutter however the PRV remains capable of achieving a stable transient response with a clear opening and closing point. From figure 6.50 it could also be seen that the PRV became stable at a lift value of approximately 3.5 mm during blowdown in which the flutter motion would dissipate. From experimental results shown earlier in figure 6.40 however the degree of oscillation in which the CFD model predicts is much higher suggesting that there is an inaccuracy with the CFD model which induces dynamic instability.

As shown in figures 6.52 and 6.53, a direct comparison has been made with the CFD model's opening disc lift vs time behaviour during both the opening and closing process. To achieve this, experimental and CFD data have been overlaid together to match the point of opening and closing irrespective of the pressure value. It would therefore be possible to directly compare the dynamic behaviour of the CFD model to experimental data to determine the capability of CFD to match real world transient performance. As can be appreciated from figure 6.52, the opening time of the experiment and CFD model is similar however differences could be observed with initial maximum lift of 9 mm for experimental data compared to 5-6 mm for the CFD model. In addition, the amplitude of vibration was much higher for the experimental data vs CFD performance however as mentioned previously, the experimental data for lift becomes constant by 0.23 s whereas the CFD model continues to oscillate. Similarity however could be found with both experimental and CFD data suggesting an initial equilibrium value of 5 mm disc lift by 0.23 s. No significant CFD error could be found from opening other than an under prediction of lift.

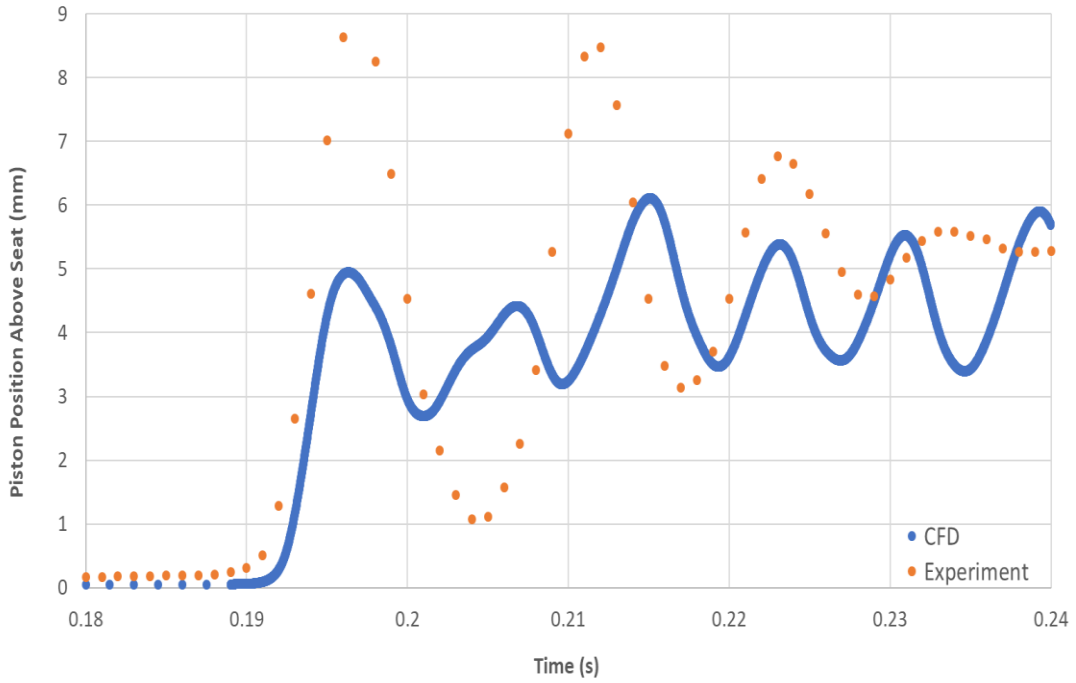

Figure 6.52 – Comparison of CFD to Experimental Disc Lift vs Time for Henry 5231BX PRV during opening

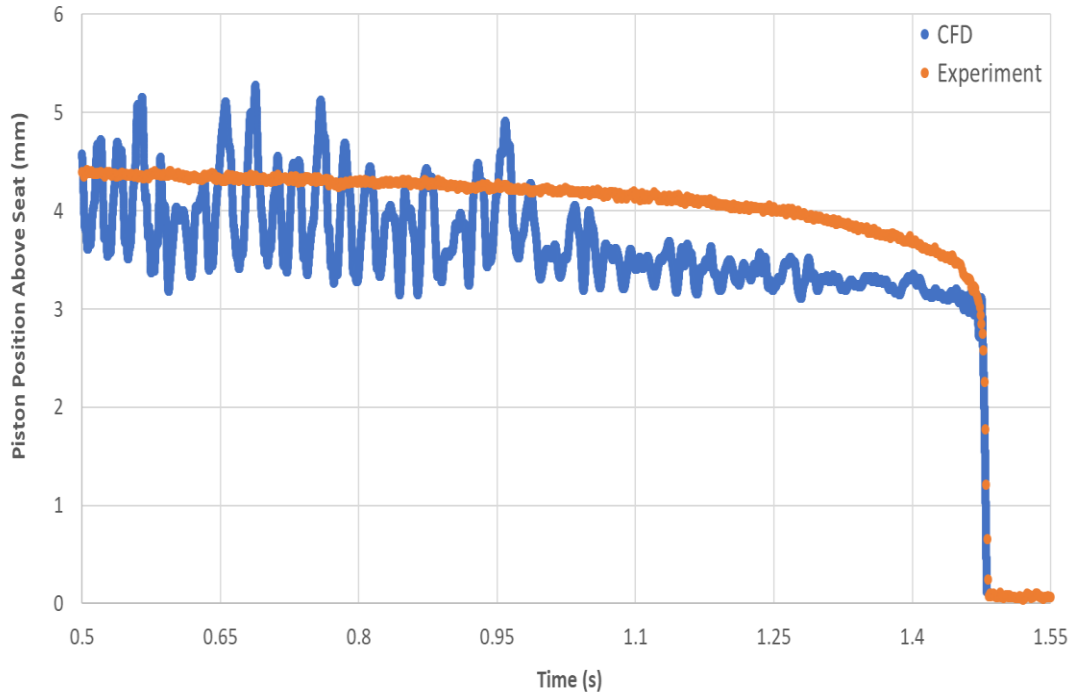

Figure 6.53 – Comparison of CFD to Experimental Disc Lift vs Time for Henry 5231BX PRV during closure

Comparison of the CFD model to experimental data for the closing process during blowdown could be appreciated from figure 6.53. Overall similarities could be found during the dynamic operation of the PRV as a general decrease of disc lift towards 3 mm during blowdown was captured by the CFD model which is in agreement with experimental data. At 3 mm, the PRV rapidly closes to the sealed position in an almost identical time frame for both the CFD model and experiment. This therefore provides confidence regarding the CFD model's capability to accurately capture the dynamics of the Henry 5231BX during blowdown. However as was observed during opening, significantly greater amplitudes of oscillation could be observed for the CFD model when compared to the experimental disc lift value. This phenomenon will be discussed further with use of contour plots for both pressure and Mach number from CFD to describe the transient flow characteristics predicted by the model.

Figures 6.54 to 6.69 utilise contours of both Mach number and static pressure for the overall PRV domain to illustrate the development of the flow regime and pressure profile during the opening process of the PRV as predicted by the transient moving mesh CFD model. A series of 8 discrete lift points of 0.05 mm, 0.25mm, 0.75mm, 2mm, 3mm, 4mm and 4.7mm will describe the initial opening process however a further lift point at 3.5mm during the initial vibration after maximum lift is achieved will also be used. The opening process took place during a simulation time of 0.189s-0.197s. Figures 6.54 and 6.55 represent the PRV during the final stages of the huddling process shown within figure 6.52 for a disc lift of 0.05mm above the seat. It should be noted that it was observed that the huddling process for the Henry valve was much shorter than the ASME valve as the 5231BX popped directly from the minimum lift of 0.05mm shown within the CFD model. Figure 6.54 highlights the nature of the flow regime with a small quantity of flow leaking through the disc/seat interface towards the outlet. The consequence of such a low flow rate can be seen in figure 6.55 where as expected the high pressure acts on the central core section of the disc in line with the inlet. Figures 6.56 and 6.57 however highlight the rapid development of the flow regime as by a lift value of 0.25mm there is

a noticeable increase in the size of the jet which subsequently causes a radial pressurisation from the central core. This as a result would significantly increase the aerodynamic force on the piston resulting in the rapid pop action observed within figure 6.50.

Figures 6.58 and 6.59 demonstrate a further increase in the static pressure value acting on the lower section of the disc once the disc lift increased to a value of 0.75mm. It could be observed in figure 6.59 that a high pressure region was established throughout the entire central lower region of the disc which as a result would further increase the aerodynamic force in order to overcome the increased spring force as the valve opened. In addition, noticeable pressurisation could also be found in the sloped region of the lower face of the disc which as a result would further increase surface area and hence aerodynamic force. There was similarity between the Mach number flow regime between figures 6.56 and 6.58 for 0.25mm and 0.75mm however for 0.75mm there was a significant increase in size of the jet between the cavity formed between the disc and seat. As a result, a visible difference in the pressurisation profile could be observed in figure 6.59.

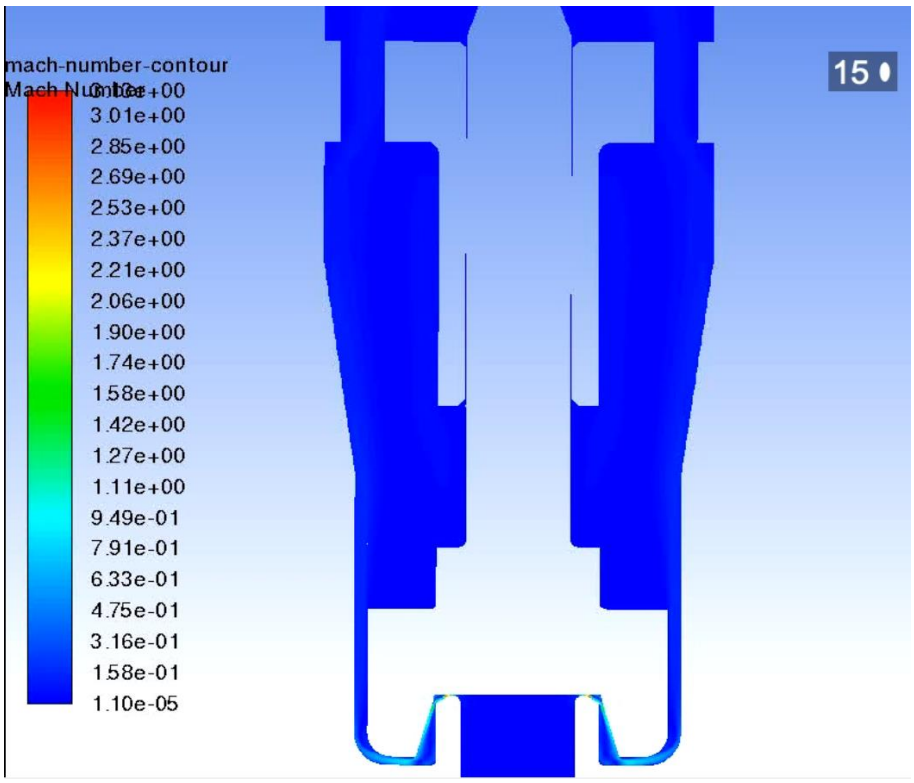

Figure 6.54 - Contours of Mach Number for 5231BX at 0.05mm Lift During Opening at t = 0.189s-0.197s

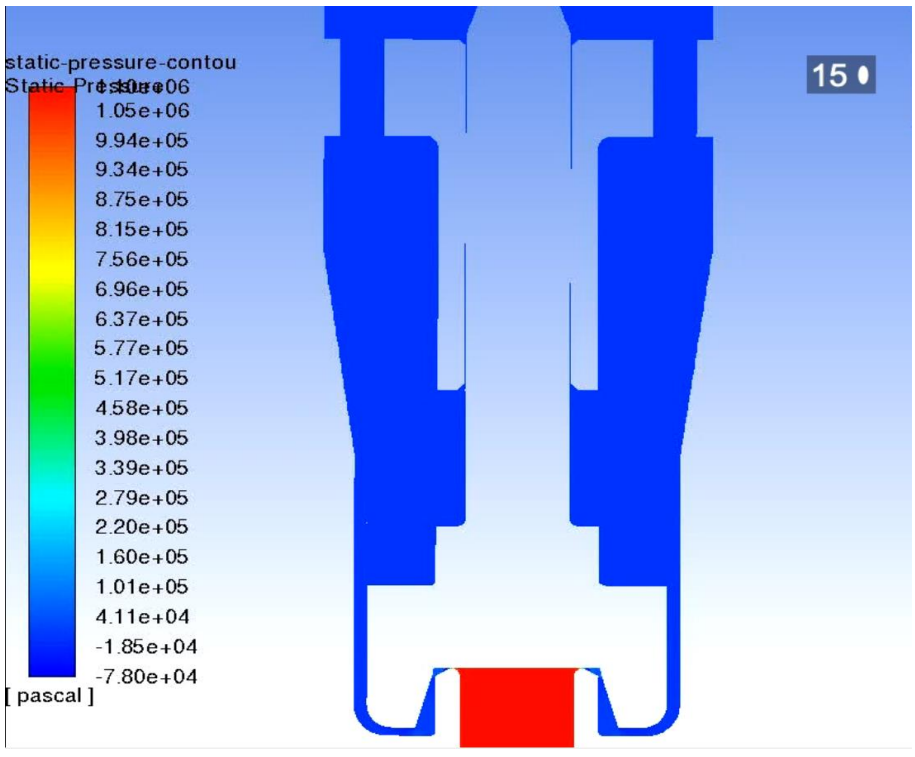

Figure 6.55 - Contours of Static Pressure (Pa) for 5231BX at 0.05mm Lift During Opening at t = 0.189s-0.197s

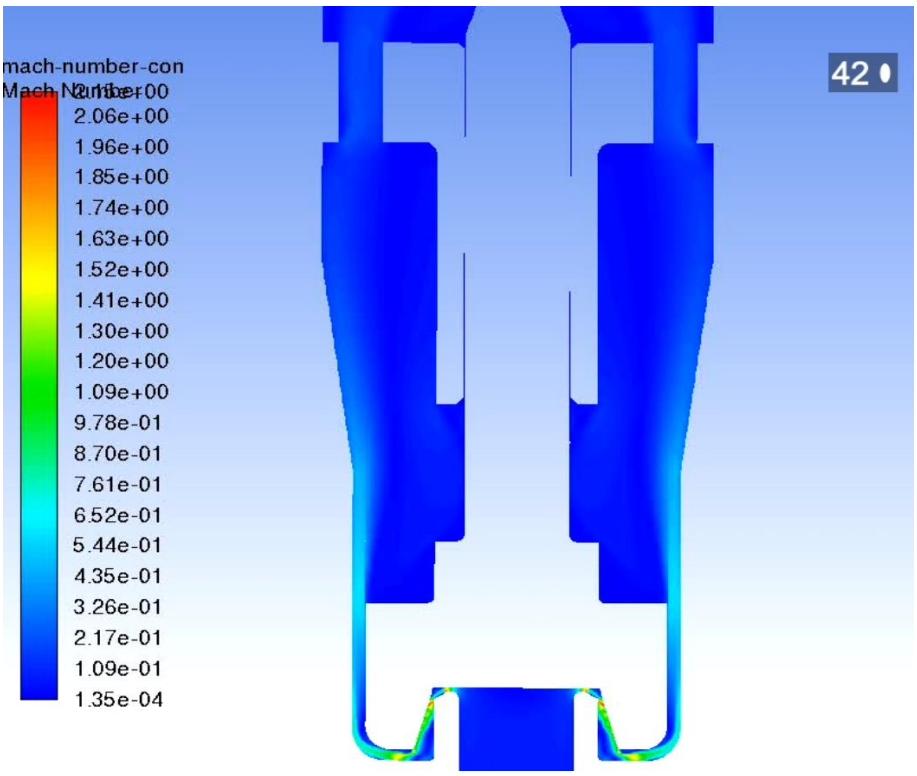

Figure 6.56 - Contours of Mach Number for 5231BX at 0.25mm Lift During Opening at t = 0.189s-0.197s

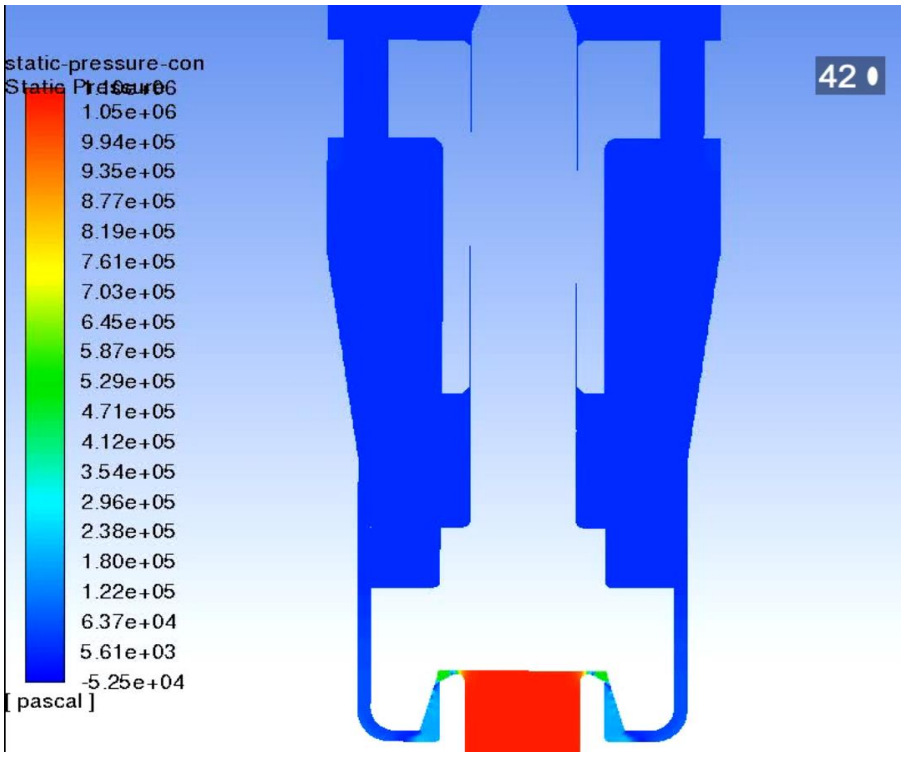

Figure 6.57 - Contours of Static Pressure (Pa) for 5231BX at 0.25mm Lift During Opening at t = 0.189s-0.197s

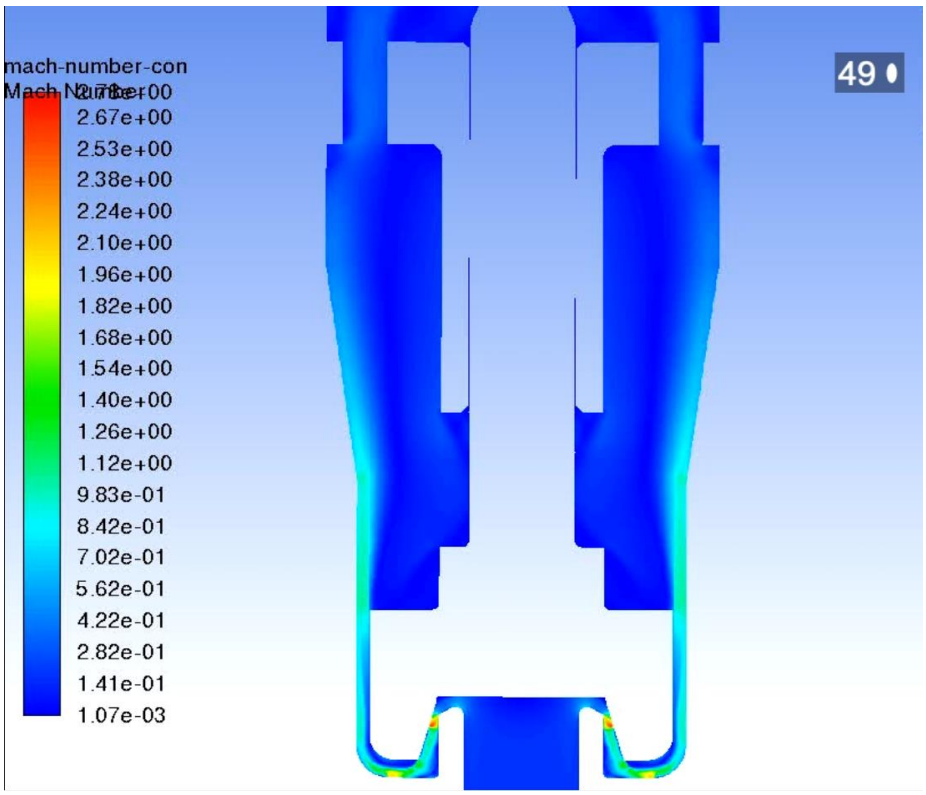

Figure 6.58 - Contours of Mach Number for 5231BX at 0.75mm Lift During Opening at t = 0.189s-0.197s

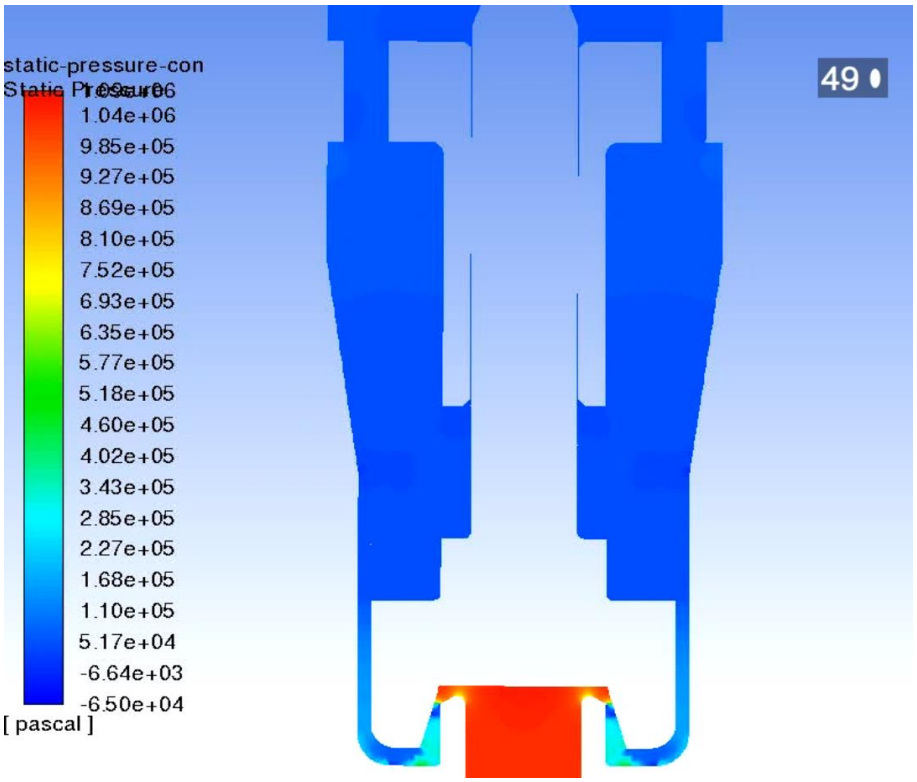

Figure 6.59 - Contours of Static Pressure (Pa) for 5231BX at 0.75mm Lift During Opening at t = 0.189s-0.197s

Figures 6.60 and 6.61 illustrate the flow conditions of the PRV during opening at a disc lift of 2mm where it can be clearly recognized that the size of the outer cavity between the disc and seat/valve body had significantly increased. Figure 6.60 highlights a further development in the size of the jet however a large area acting on the outer region of the disc is stagnant as the flow is redirected around it by the valve body.The effect of this is shown within the static pressure plot shown within figure 6.61 where the stagnant zone becomes slightly pressurised. Importantly however there is also an increase in back pressure at the upper region of the disc surfaces due to the development of the jet and increase in flowrate travelling through the PRV. In general this is in agreement with the flow structure predicted during steady state simulation.

A significant development in flow structure was found as the PRV opened further to 3mm (figure 6.62) at which the degree of turbulence for the jet visibly increased within the disc/seat interface due to the increase in size of the outer cavity. As a result of this turbulence, the flow regime was observed to become time-dependent with a larger deflection angle of the jet when compared with steady state results. This is in agreement with observations made during the Broady analysis which suggested an interdependence between the flow characteristics of the PRV and disc motion. Such an observation therefore casts doubt on the validity of the quasi steady assumption used during steady state analysis. The static pressure plot for a disc lift of 3mm shown within figure 6.63 highlights that due to the increased lift of the disc, the sloping section of the lower section of the disc was subjected to a greater area of the jets momentum change. As a result an increased value of static pressure could be observed in this region to further enhance the popping process of the PRV to ensure stability during opening. At a disc lift of 4mm, the flow regime shown within figure 6.64 highlights that the jet became detached from the lower region of the body at the outer cavity which in turn promoted further turbulence. Figure 6.65 depicts the result of this change in flow regime where the entire lower section had become pressurised however a large increase in backpressure could also be measured. This would limit further significant opening of the disc.

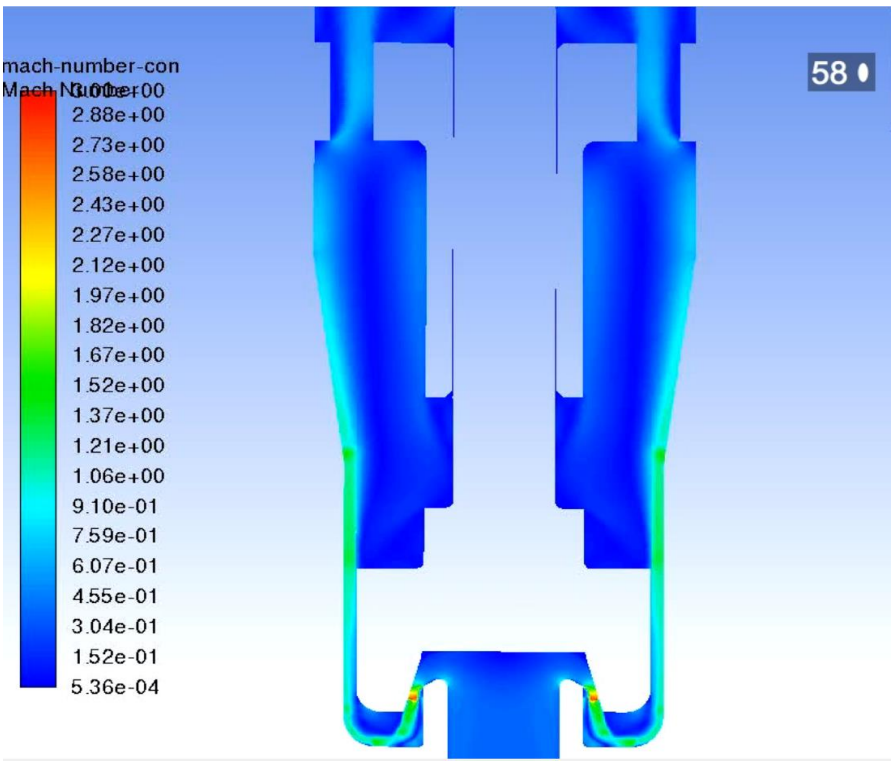

Figure 6.60 - Contours of Mach Number for 5231BX at 2mm Lift During Opening at t = 0.189s-0.197s

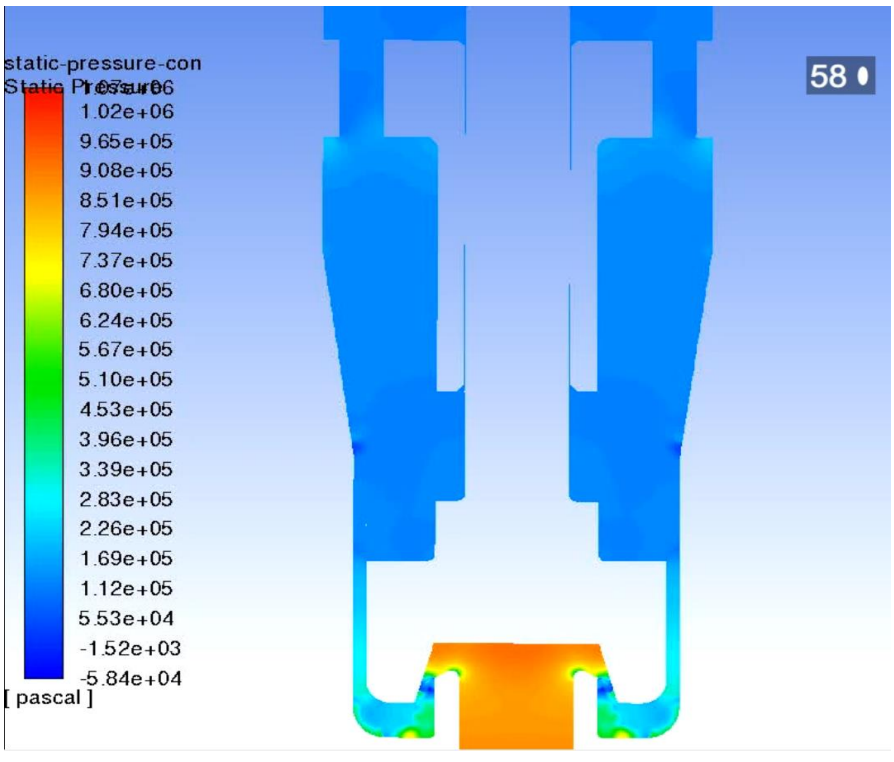

Figure 6.61 - Contours of Static Pressure (Pa) for 5231BX at 2mm Lift During Opening at t = 0.189s-0.197s

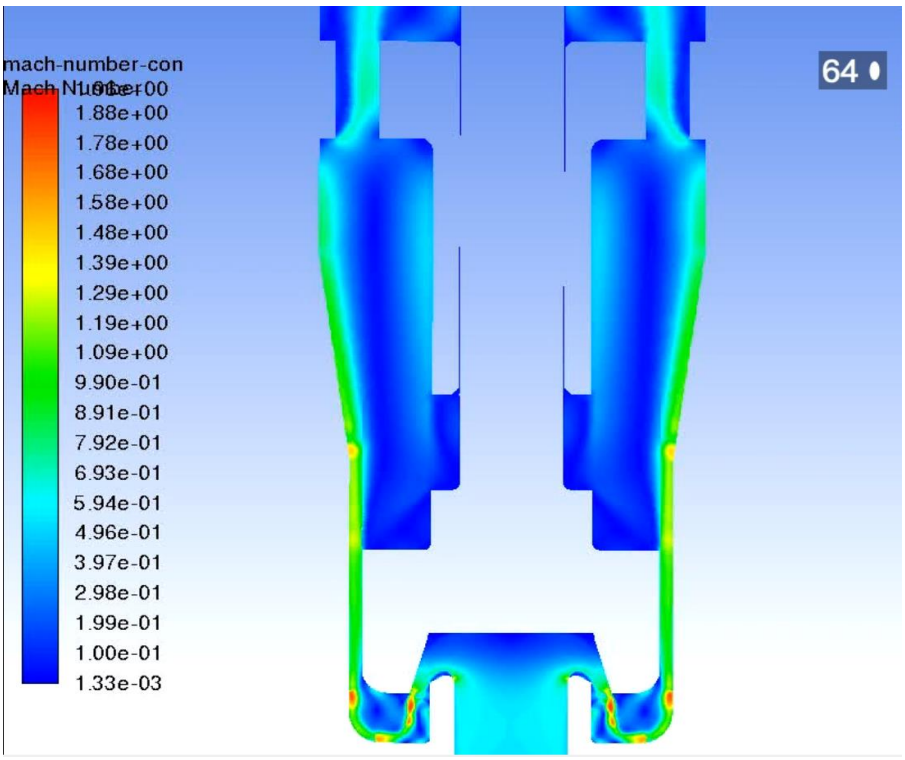

Figure 6.62 - Contours of Mach Number for 5231BX at 3mm Lift During Opening at t = 0.189s-0.197s

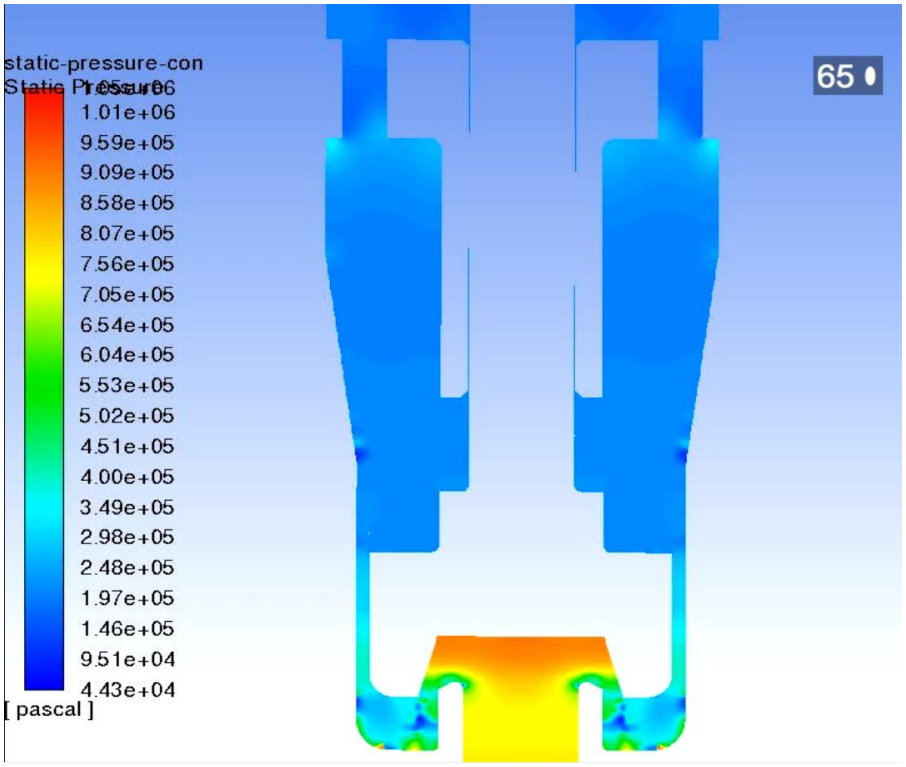

Figure 6.63 - Contours of Static Pressure (Pa) for 5231BX at 3mm Lift During Opening at t = 0.189s-0.197s

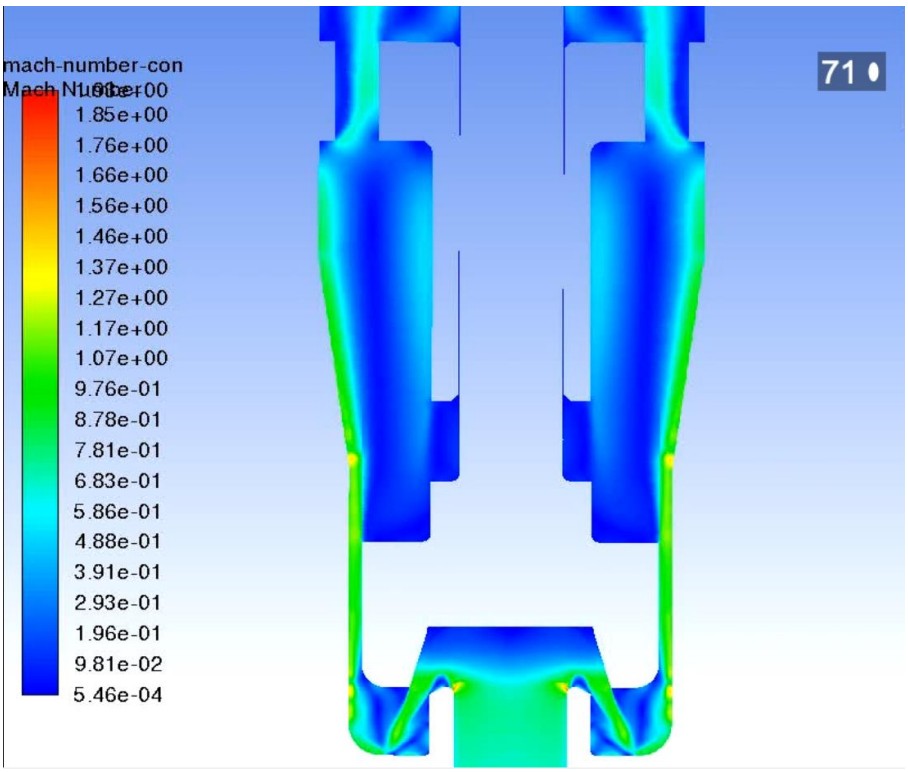

Figure 6.64 - Contours of Mach Number for 5231BX at 4mm Lift During Opening at t = 0.189s-0.197s

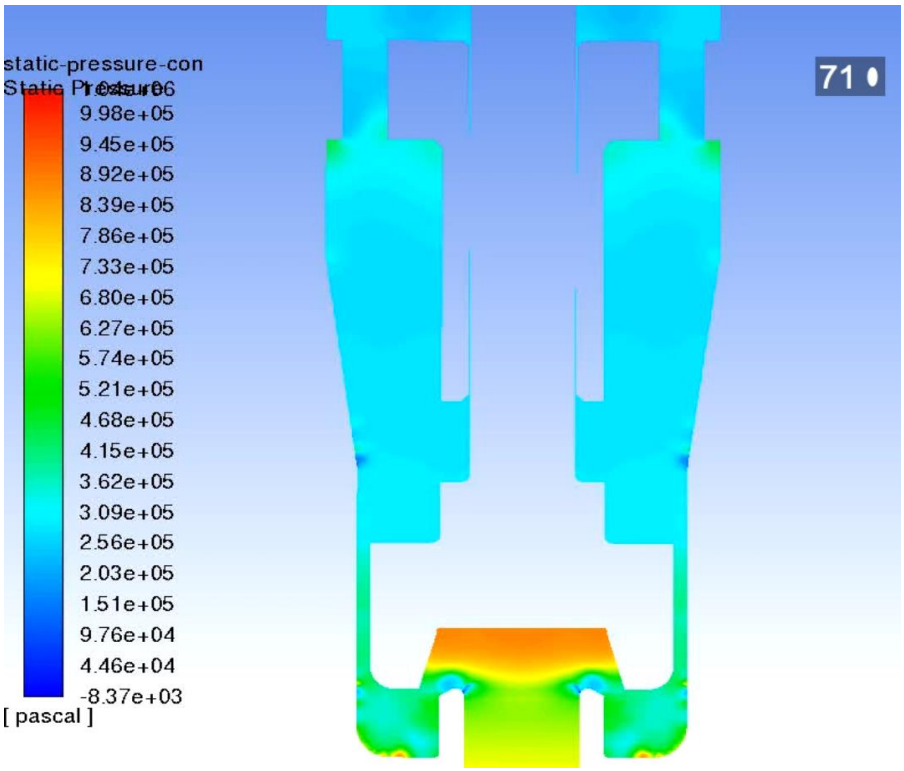

Figure 6.65 – Contours of Static Pressure (Pa) for 5231BX at 4mm Lift During Opening at t = 0.189s-0.197s

As observed in figure 6.65 at a disc lift of 4mm, the back pressure acting on the upper sections of the disc had significantly increased. This observation in combination with the majority of the lower disc surface exposed to a high pressure resulted in a deceleration of the disc. Figures 6.66 and 6.67 illustrate contours of Mach number and static pressure for the computational domain when the disc was at its maximum lift value of 4.7mm. Interestingly it could be seen from figure 6.66 that the jet in the outer cavity of the lower section of the disc had become fully detached from the lower body surface. In addition, the jet's orientation angle in the area marked in red moved in the horizontal direction from being almost vertical at 4mm as shown in figure 6.64. It is proposed that this change was caused by the deceleration of the disc as the effect of disc motion on the flow reduced. This is supported by the steady state Mach number contour plots shown earlier in which the jet remains in a similar horizontal configuration. The effect of the deceleration and change of flow regime on the static pressure distribution at the lower surfaces of the disc is shown within figure 6.67. In comparison with figure 6.65, it could be established that the area of low pressure at the outer section of the disc's lower surface was larger which would result in a further reduction in aerodynamic disc force.

Due to the further decrease of aerodynamic disc force at maximum lift, there is a significant vibration of the disc as shown in figure 6.52 in which the lift subsequently falls briefly to 3.5mm. Figures 6.68 and 6.69 present the flow regime at this stage of the oscillation in which further differences had occurred at the outer cavity highlighted in red. Due to the rapid downward movement of the disc, figure 6.68 illustrates that the jet at the outer cavity has become almost completely horizontal with a significant reduction in size of the recirculation zone which induced a low pressure zone shown in figures 6.65 and 6.67. The effect of this change in jet orientation is highlighted in figure 6.69 where the size of the low pressure section at the disc's lower surface has been significantly reduced which would increase the aerodynamic disc force. This process of self-excited oscillation/instability is the cause of vibration observed in figures 6.50, 6.52 and 6.53 and will be discussed in section 6.2.4.

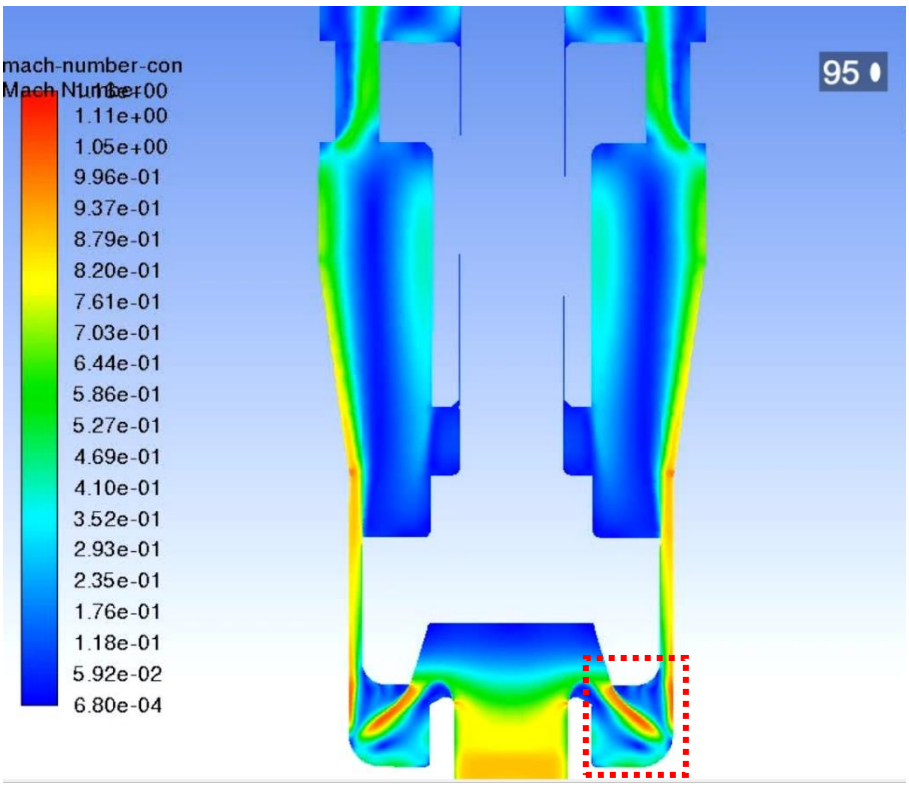

Figure 6.66 - Contours of Mach Number for 5231BX at 4.7mm Lift During Opening at t = 0.189s-0.197s

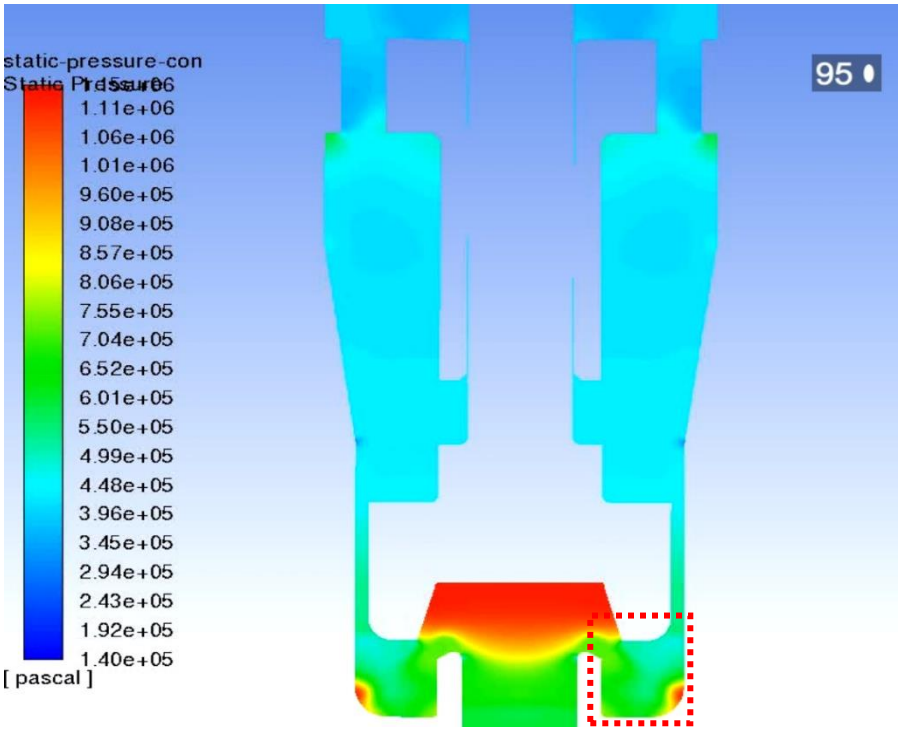

Figure 6.67 - Contours of Static Pressure (Pa) for 5231BX at 4.7mm Lift During Opening at t = 0.189s-0.197s

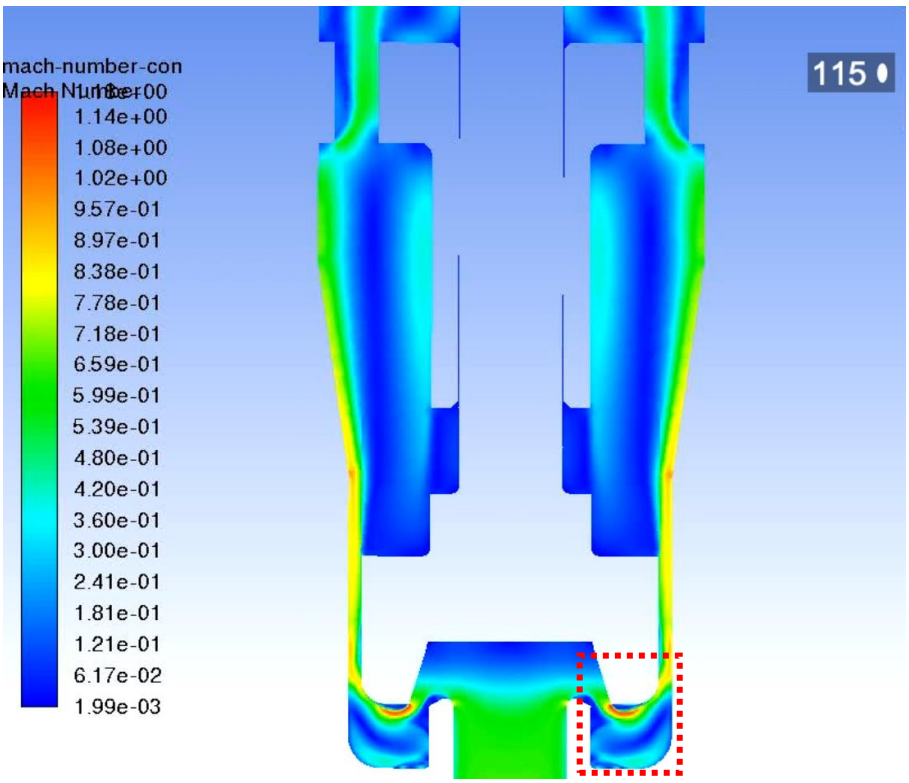

Figure 6.68 – Contours of Mach Number for 5231BX at 3.5mm Lift During Opening at t = 0.189s-0.197s

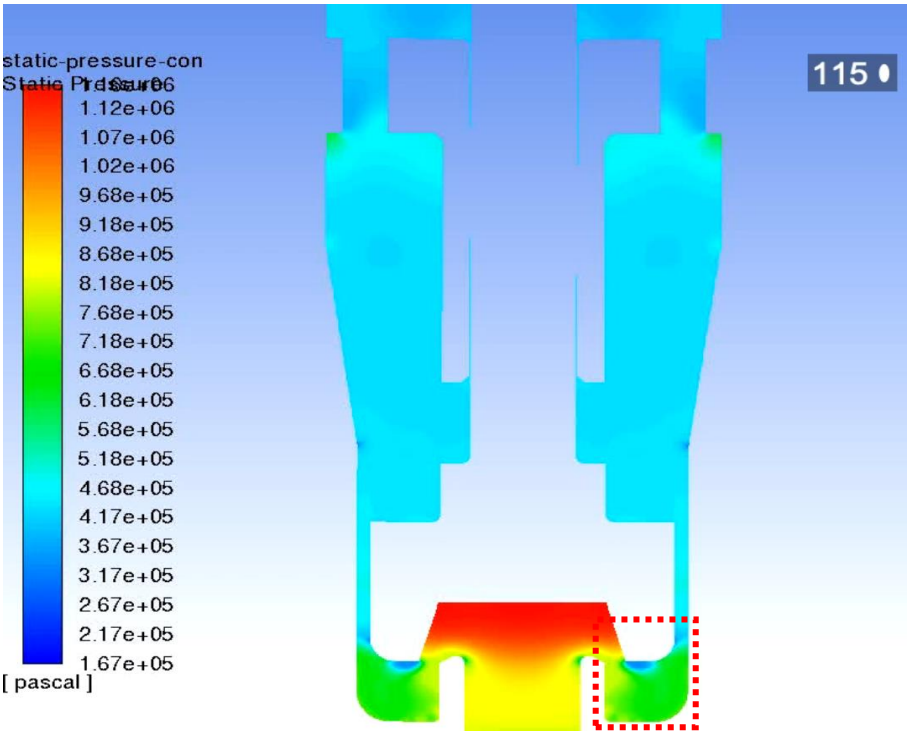

Figure 6.69 – Contours of Static Pressure (Pa) for 5231BX at 3.5mm Lift During Opening at t = 0.189s-0.197s

Figures 6.70-77 illustrate the final closure process of the 5231BX PRV during blowdown which occurred at a simulation time of 1.47-1.48s. For figures 6.70 and 6.71 for a disc lift of 3mm it can be seen that due to the low velocity of the disc, the flow regime is similar to that observed during steady state simulation. Interestingly the flow regime is also different in terms of the jet orientation within the outer cavity below the disc which was observed during opening at 3mm which further suggests the existence of a relationship between disc motion and the 3D flow structure. As was observed for the Broady PRV, as the inlet pressure falls the aerodynamic force is no longer able to support the disc so therefore the PRV begins to rapidly close. Figures 6.72 and 6.73 represent a disc lift of 2.5mm where it can be seen that the flow within the outer cavity as the PRV closes becomes very turbulent in the recirculation area. This as a result induces a further low pressure as was measured at 3mm which reduces the aerodynamic force. This effect in combination with the higher back pressure and spring force allows the PRV to further accelerate towards closure in a stable manner. In agreement with the observations captured during the analysis of the Broady PRV, the Henry 5231BX during closure also exhibits a gradual radial depressurisation towards the central core region of the disc.

Figures 6.74 and 6.75 show the flow regime during rapid closure at a disc lift of 1.5mm where it can be seen that the Mach number contours are consistent with that observed during opening and with steady state predictions. However, a much higher backpressure acts on the upper surface of the disc during closure which further enhances the rapid closure of the PRV. This theme is continued at the almost fully closed position and end point of the simulation at 0.3mm lift shown in figures 6.76 and 6.77. It can be seen that at this point the lower surfaces of the disc are almost completely depressurised with only the central core subjected to pressure from the inlet with low flow overall through the system. The observation of the flow regime during closure being different to opening at higher lifts and similar at lower lifts is a contradiction to the observations made during the Broady analysis. This suggests that geometry dictates the ability of a PRV to adhere to quasi-steady assumptions.

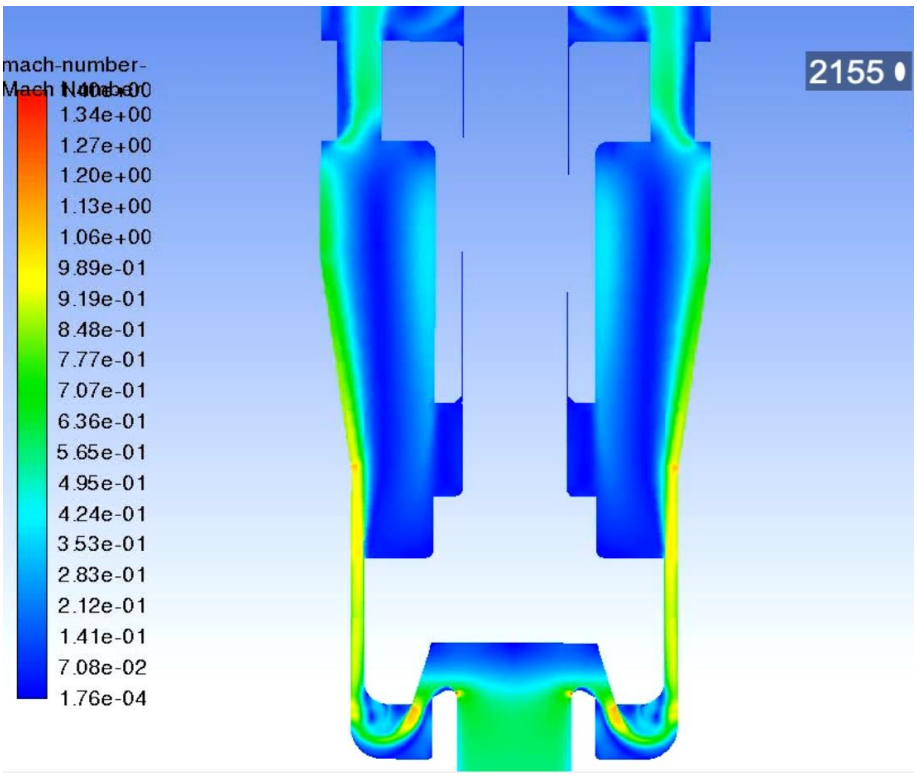

Figure 6.70 - Contours of Mach Number for 5231BX at 3mm Lift During Blowdown at t = 1.47s-1.48s

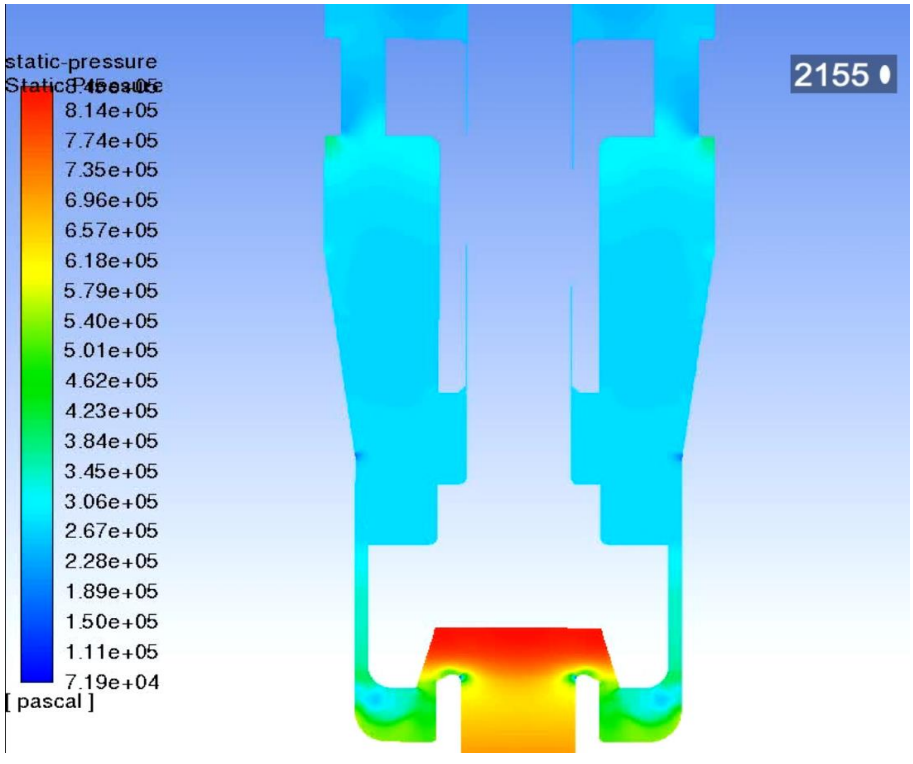

Figure 6.71 - Contours of Static Pressure (Pa) for 5231BX at 3mm Lift During Blowdown at t = 1.47s-1.48s

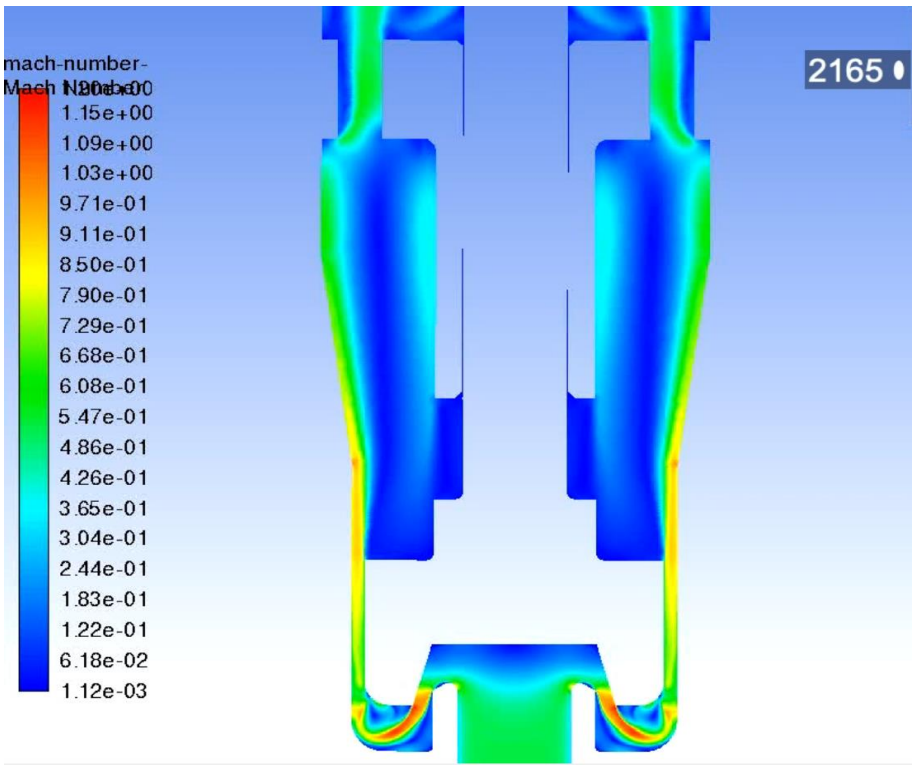

Figure 6.72 - Contours of Mach Number for 5231BX at 2.5mm Lift During Blowdown at t = 1.47s-1.48s

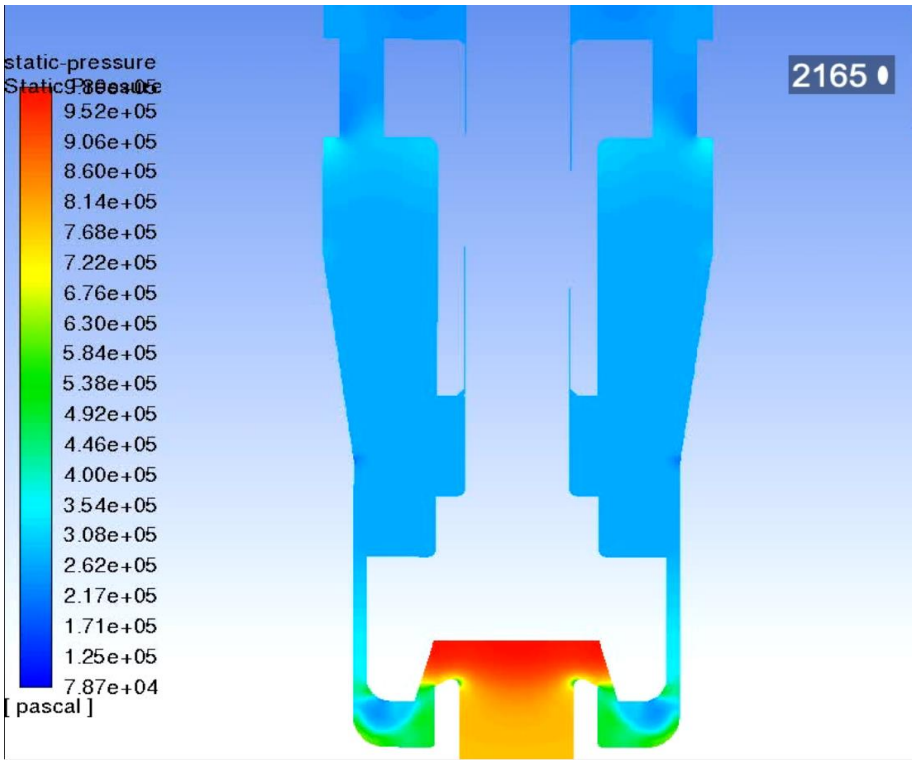

Figure 6.73 - Contours of Static Pressure (Pa) for 5231BX at 2.5mm Lift During Blowdown at t = 1.47s-1.48s

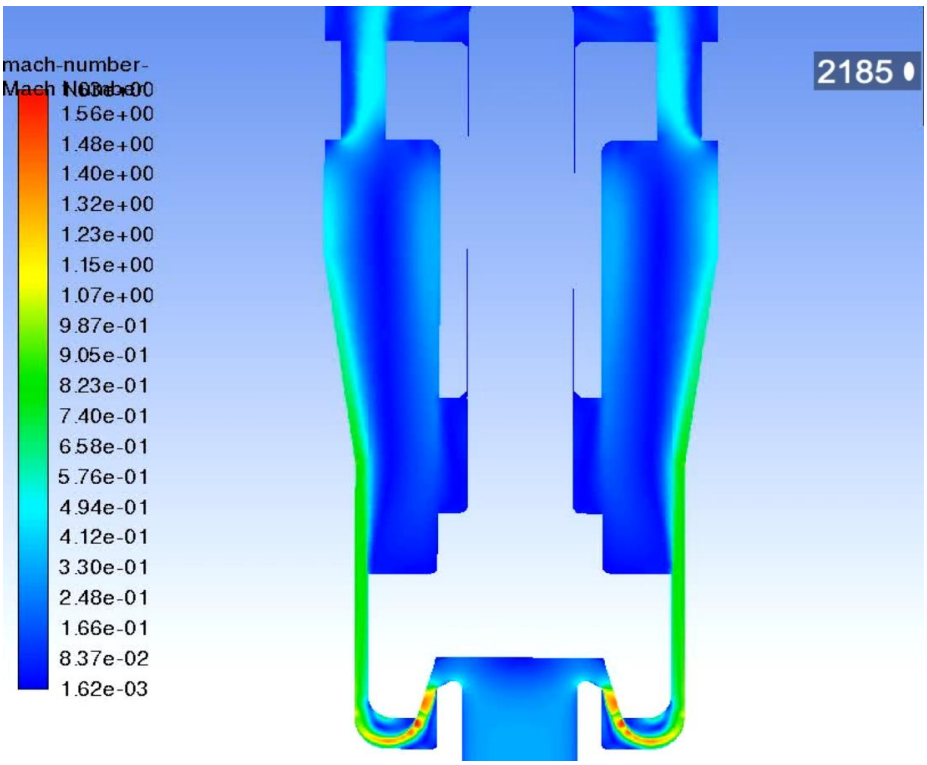

Figure 6.74 - Contours of Mach Number for 5231BX at 1.5mm Lift During Blowdown at t = 1.47s-1.48s

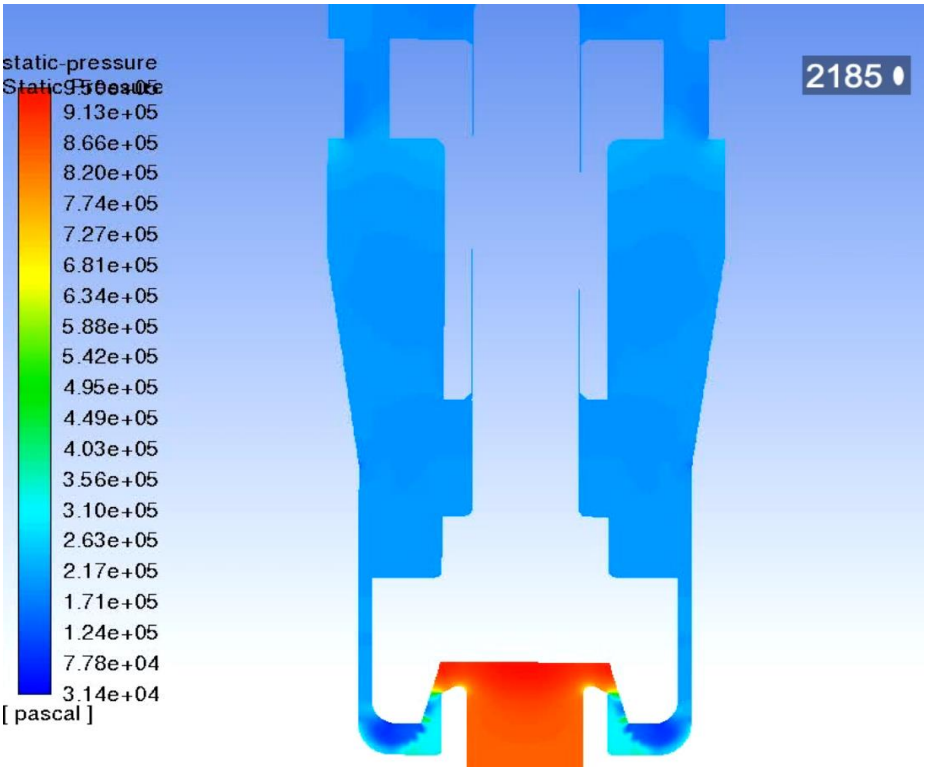

Figure 6.75 - Contours of Static Pressure (Pa) for 5231BX at 1.5mm Lift During Blowdown at t = 1.47s-1.48s

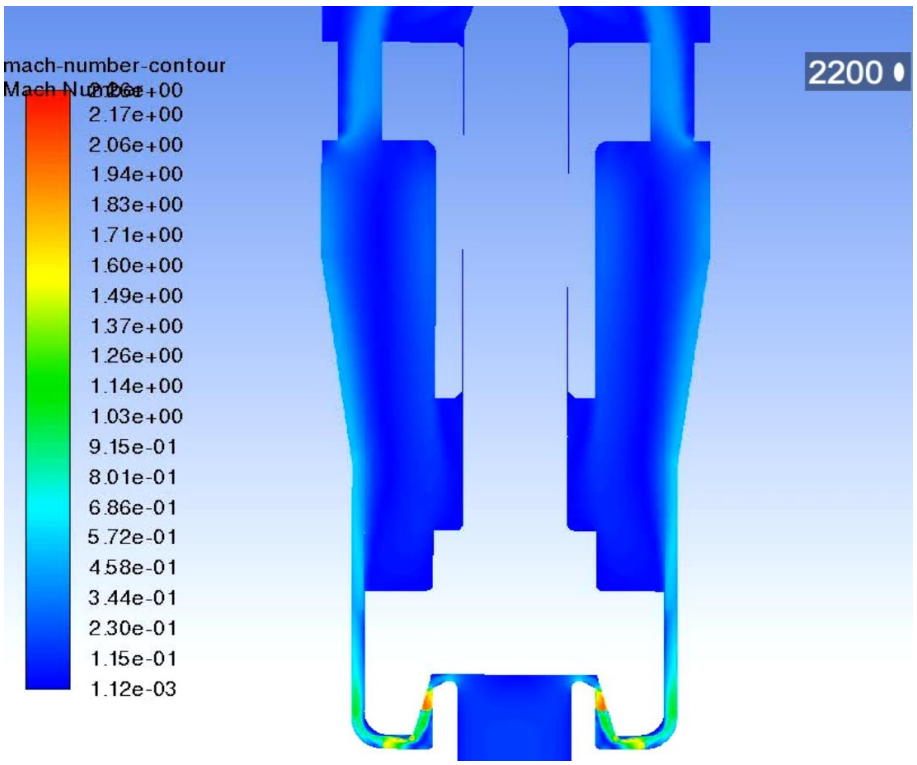

Figure 6.76 - Contours of Mach Number for 5231BX at 0.3mm Lift During Blowdown at t = 1.47s-1.48s

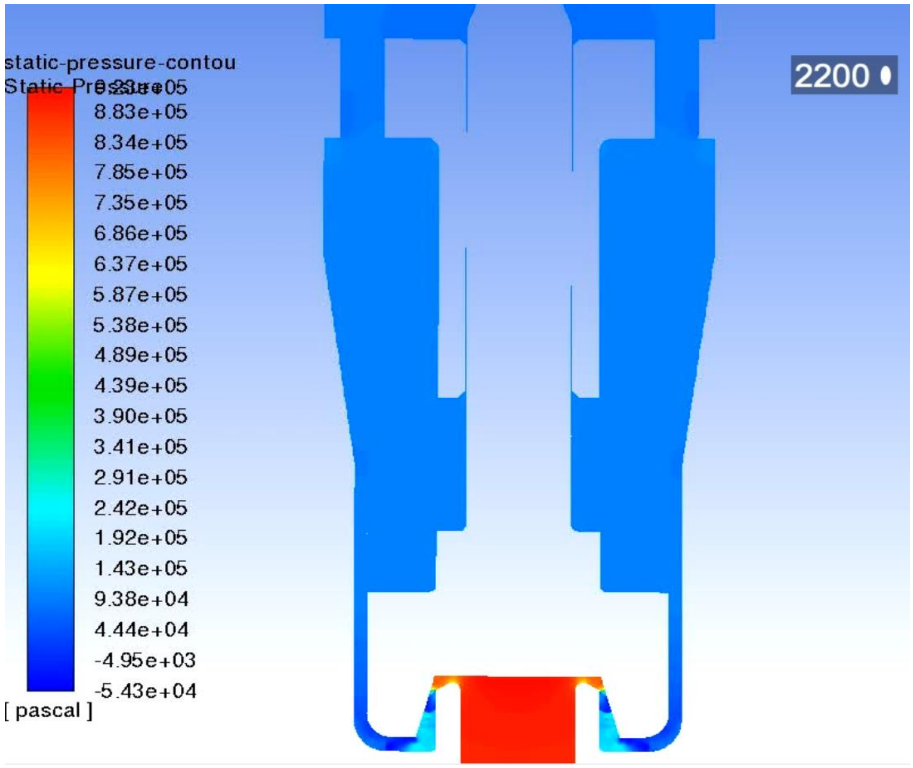

Figure 6.77 - Contours of Static Pressure (Pa) for 5231BX at 0.3mm Lift During Blowdown at t = 1.47s-1.48s

6.2.4 Discussion of the Instability Mechanisms Captured by the Henry 5231BX CFD Model in Comparison With Experiment

It was established earlier in section 6.2.3 that there was significantly more oscillation of the disc's position observed during blowdown for the CFD model when compared with experimental data. On the contrary however as shown in figure 6.52, within the initial 0.05s of the opening process the experimental data exhibited a greater amplitude of oscillation of the disc when compared with the CFD results. These results therefore suggest the potential presence of an instability mechanism which is present in the operation of the PRV and poses a source of CFD modelling inaccuracy. The use of CFD however is proposed in this study as a means to provide greater insight towards the flow characteristics in the near disc region which would otherwise be difficult to appreciate using experimental data only.

In terms of CFD results, as shown in figure 6.50 from the transient CFD model there is significant oscillation after opening (0.2s-1s). This oscillation is gradually reduced over time as the PRV moves out of the unstable region and allows the specified damping coefficient and fluid damping to act on the moving system and arrest the vibration. As shown within figures 6.54-69 the oscillatory behaviour was found to be caused by the production of vortices and centrifugal instability within the huddling chamber. As a result, an oscillation of a recirculation zone beneath the outer lower surface of the piston was found which directly affected the pressure distribution and therefore net force on the piston. A further observation was made with comparison of the transient response of mass flow rate shown in figure 6.51 compared to the displacement response; where the mass flow rate exhibited a smaller amplitude of oscillation. This is due to the choking point as seen within figure 6.62 at a piston displacement of 3 mm, where the flow is choked at the discharge area of the nozzle, thereby preventing piston geometry to cause a flow rate instability at higher lifts**.** The influence of pressure waves on the CFD model was also

checked by using a longer inlet length in order to increase the time taken for the pressure wave to return to the inlet and also the use of a non-reflecting boundary condition at the inlet was adopted. However, both techniques were unable to remove the oscillation observed in the CFD model which further increased the likelihood of the cause being a flow induced instability phenomena at the disc face.

Furthermore, in the analysis shown within figure 6.78 and in reference to figure 6.50, the transient response of the disc displacement becomes stable after passing the second cross over point of the transient force lift curve with the spring line at 3 mm. This observation validates the instability hypothesis of Borg [32] discussed in section 3.4. It can be seen from figure 6.53 that for a piston position greater than 3.2mm, the amplitude of oscillation was greater than for disc lift less than 3.2mm. This strongly suggests that a criterion of dynamic stability is dependent on the second crossover point shown at 3.2mm disc lift in figure 6.78.

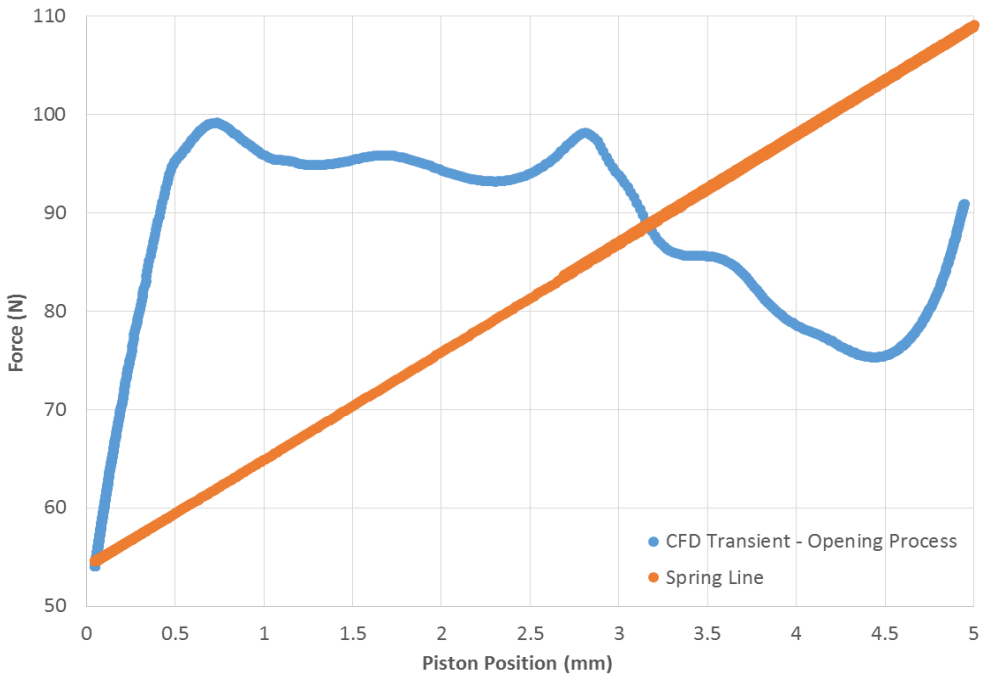

Figure 6.78 – Transient Force vs Lift Curve for 5231BX PRV with Spring Line

Therefore, it is likely that a combination of inaccurate CFD modelling of the lower face of the disc which causes significant fluctuation in pressure as well as systematic instability triggers shown in figure 6.78 highlights the likelihood of the oscillation observed during blowdown of the Henry 5231BX PRV. These conclusions also support the studies performed by Hos and Darby [22, 31] to identify likely instability triggers in dynamic PRV operation as well as Beune's conclusion that instability can't always be avoided in valve design [5]. In contrast to the 3511E right angled type PRV presented in chapter 6.1, the 5231BX through flow type PRV would appear to be much more unstable. This is a result of its design and more significant interaction of the disc/piston surfaces with the general flow path.

6.3 Summary of Transient Moving Mesh CFD Validation Research for Both Broady and Henry PRV's

Following an extensive single phase transient CFD study for both the right-angled type ASME 3511E PRV and through flow type Henry 5231BX PRV a number of conclusions could be established;

- It has been shown for both the ASME 3511E and 5231BX PRV's that the dynamic response of a PRV to a transient inlet pressure ramp can be accurately captured using moving mesh CFD methods. The overpressure and blowdown response of the Broady 3511E PRV was able to be accurately captured by CFD to a relative error of 1.4% and 0.3% respectively to experimental values. The 5231BX PRV with modified gland was also able to be captured by CFD to a relative error of 0.06% for overpressure and 0.31% for blowdown in reference to experimental data.

- Quasi Steady Observations – Variations in flow structure such as Mach number contours and static pressure distribution was found to exist between equivalent points of disc lift during opening and closing of the PRV. Differences could also be found when compared with flow structures predicted during steady state simulation. Larger differences were observed for the Henry PRV, in particular for the jet deflection angle and resulting regions of recirculating flow. It could therefore be suggested that an interdependence between disc motion and the flow regime exists during opening and closing which would challenge the validity of the quasi steady assumption commonly used in PRV design. This will be explored in the following chapter.

- Instability Observations - In general both the CFD representations of the dynamic characteristics of both the Henry and Broady PRV's were accurate to experimental values such as maximum lift and general blowdown behaviour. However in particular for the Henry 5231BX, a CFD induced instability was found which was not present in experimental data. This flutter was found to be caused by a self-excited flow phenomena induced by the rapid motion of the disc which in turn affected the static pressure distribution. This oscillation was reduced over time as the PRV moved out of the unstable region and allowed the specified damping coefficient and fluid damping applied within the UDF to act on the moving system and arrest the vibration. As the behaviour wasn't observed experimentally it could be suggested that the instability was a result of CFD inaccuracy using a RANS model therefore higher order computational methods such as LES should be explored if computationally feasible in the future.

CHAPTER 7

AN ASSESSMENT OF THE VALIDITY OF QUASI-STEADY BASED ANALYSIS OF PRV'S

In this chapter, the validity of the commonly used quasi-steady design approach to pressure relief valves (PRV) is examined. The study was achieved by using the results established within chapters 5 and 6 for both the Broady 3511E (Notch position 4) and Henry 5231BX (Modified Gland) PRV's. It should be noted that both of these PRV's conform to ASME VIII standards where quasi steady based design approaches are often used during the valve's early development. This chapter will utilise the validated steady state and transient CFD models which were developed using the commercial CFD package ANSYS FLUENT. As a result, it would be possible to compare the steady state simulations which utilised quasi steady conditions to high fidelity transient moving mesh simulations to allow the disc (piston) forces to be examined.

The premise of quasi steady state analysis techniques assumes that the influence of disc velocity on the flow is negligible, and the flow is not coupled with the opening time of the valve. As described earlier this assumption allows a series of steady state simulations at pre-defined values of disc displacement (lift) to calculate the aerodynamic force acting on the piston and to determine a valve characteristic force vs lift curve at a constant inlet pressure. As described by Beune [20] and Song [21], the results are converted to the time domain by solving equations of motion using a numerical solver package such as MATLAB which represents a simplified dynamic model of the PRV. This model represents an earlier defined type 1 model, (chapter 2) which will be utilised in this chapter to predict the overpressure and blowdown values of the PRV as well as its dynamic lift vs time characteristics. A comparison will then be made with the results from the transient CFD analysis in which the dynamics are governed by the flow conditions from the previous time step.

An in-house type 1 numerical model, which was developed at the University of Strathclyde and included in the work by Taggart [9] will be used to predict the opening and closing characteristics of both the Broady and Henry PRV's. Steady state experimental data for disc force vs lift will be input to the model to capture the dynamic response of the system as well as predict overpressure and blowdown values. As described in detail within the work by Taggart a set of additional equations are required in addition to the spring mass damper system described within equation 7.1. These equations include those to account for the change in pressure, temperature and mass flow rate through the PRV and supply pressure vessel. These second order ordinary differential equations are then subsequently solved using a Runge-Kutta solver (RK45) in MATLAB to provide a solution which could be compared to both transient CFD and experimental results. Equation 7.1 can be compared to an analytical solution using equation 7.2.

$$F(t) = m\ddot{x} + b\dot{x} + kx \qquad \text{Equation 7.1}$$

$$f(t) = Ae^{-\beta t}\cos(\omega t + \varphi) \qquad \text{Equation 7.2}$$

In his work [9], Taggart found that the Runge-Kutta RK45 solver could closely match the analytical solution. He found that by using the adaptive time-step control a maximum error of 1e-4 was found during each time step between the numerical and analytical solution. Taggart also extensively tested the MATLAB type 1 model where he determined that the accuracy of the model to capture the transient displacement of the disc was satisfactory with comparison to experimental data from an LVDT throughout the operating cycle of the PRV. Therefore it was deemed acceptable to utilise the type 1 model during this study in order to evaluate the effectiveness and accuracy of the quasi steady assumption for both the Broady 3511E and Henry 5231BX PRV's.

7.1 Discussion of Quasi Steady Assumption Effectiveness for 3511E PRV

As discussed in chapter 6 for the Broady 3511E PRV, differences in flow structure could be observed between opening and closing which suggested an interdependence between flow features and disc motion. To evaluate this further, the CFD calculated steady state disc forces presented in chapter 5 was compared with the transient CFD disc force calculated during opening across the full lift range. The results of this comparison is shown in figure 7.1 where both the steady state and transient disc forces used non dimensional values based on inlet pressure and area to remain independent of pressure and allow comparison to take place. It could be seen from figure 7.1 that the non-dimensional value of disc force for the transient model is slightly lower than the steady state value across the full lift range. However it was also apparent that the general disc force vs lift characteristics for the transient CFD followed a similar pattern and gradient to the quasi steady state CFD values.

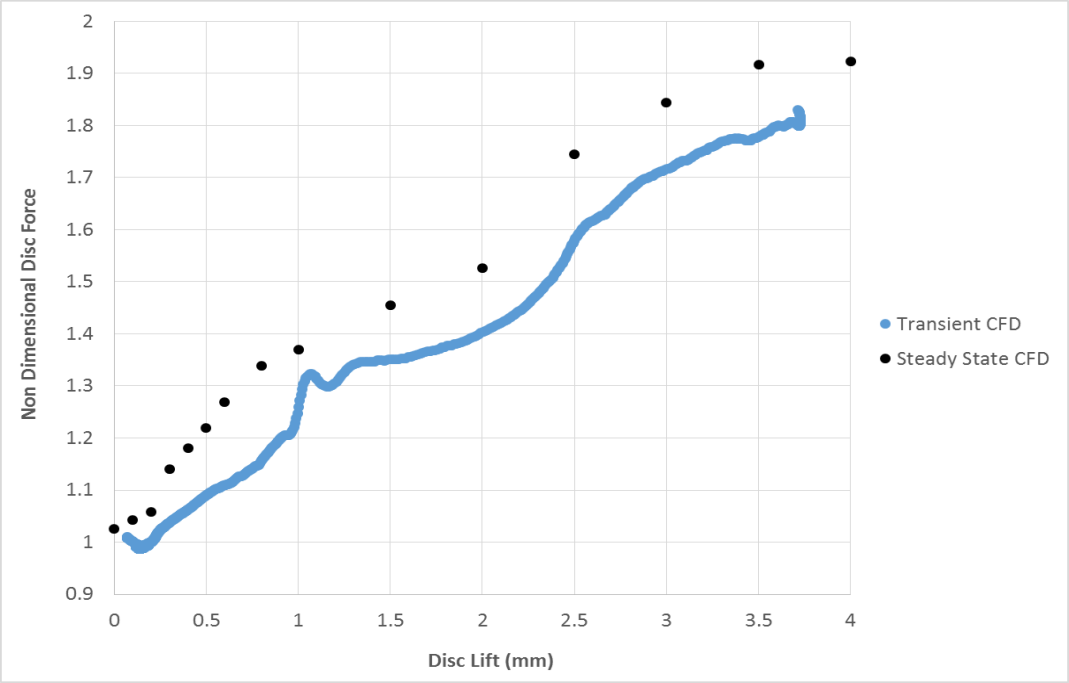

Figure 7.1 – Non-Dimensional Force vs Lift Comparison for 3511E PRV

Figure 7.1 indicates that at 1 mm for the transient CFD model during opening that there was a significant change in force gradient when compared with the steady state results. This region of disc lift represented the greatest variation between steady state and transient CFD force prediction therefore a comparison was made in figure 7.2 using Mach number contours to explore the differences.

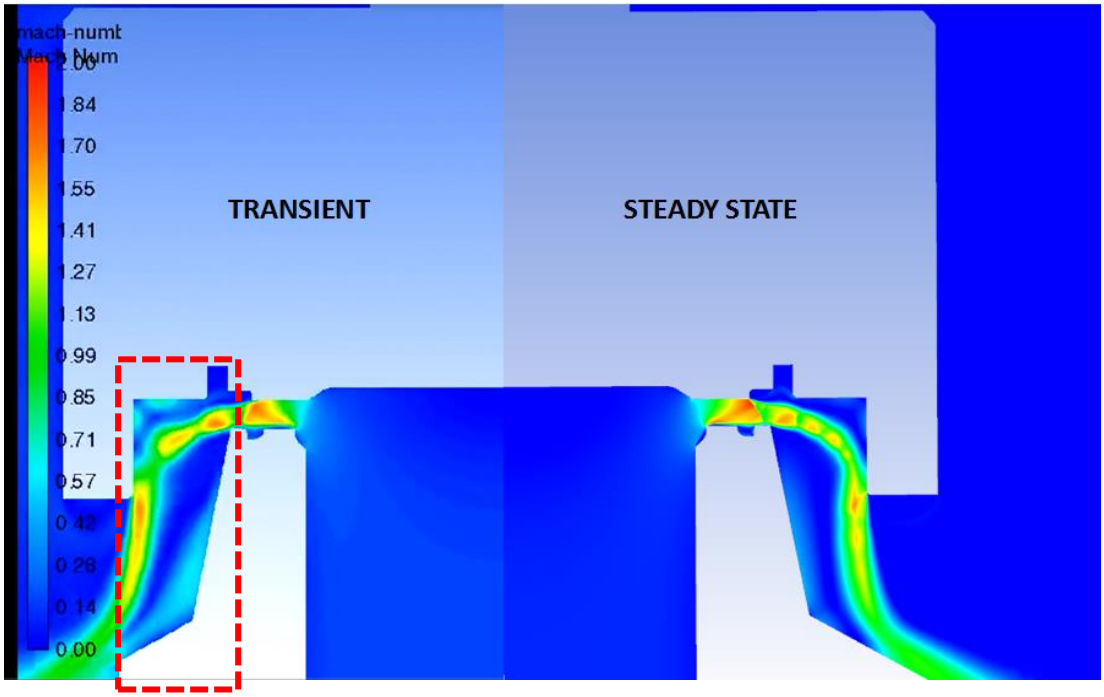

Figure 7.2 – Comparison of 3511E Transient and Steady State CFD at 1mm

It was apparent from figure 7.2 that there was significant variation in the region marked with the red hatched box for the transient model at 1 mm when compared with the steady state equivalent. It can be appreciated that the influence of disc motion has induced areas of higher flow velocity in the recirculation area above the jet of the bulk flow in contact with the lower surface of the disc. As a result the static pressure in this area would be greatly reduced when compared with the steady state profile which would result in a lower disc force as can be observed within figure 7.1. However at slightly above 1 mm a transition occurs to reduce the velocity of the recirculation area as was shown

in figure 6.17 at 1.75 mm which in turn allowed the disc force to dramatically increase and produce the gradient shown in figure 7.1. This observation is further supported in figures 6.33 and 6.34 in chapter 6 where at 1 mm an observable difference occurred between the Mach number contours recorded during opening compared to closing. For closing it could be seen that the flow regime was different to the opening distribution and represented a flow regime similar to the steady state distribution shown in figure 7.2. Therefore it could be concluded that as was predicted in the work by Beune [5, 20], flow features during the transient operation of a PRV are dependent on disc motion.

In order to evaluate the significance of the differences between steady state and transient flow regimes for the Broady 3511E PRV the MATLAB type 1 numerical model was used. In addition to providing an insight towards the effect of the differences between steady state and transient force-lift behaviour it would also allow the validity of the quasi steady assumption for the 3511E PRV to be determined. The results for the dynamic behaviour of the MATLAB quasi steady based model is shown alongside the transient CFD model within figure 7.3 and values of overpressure and blowdown in table 7.1.

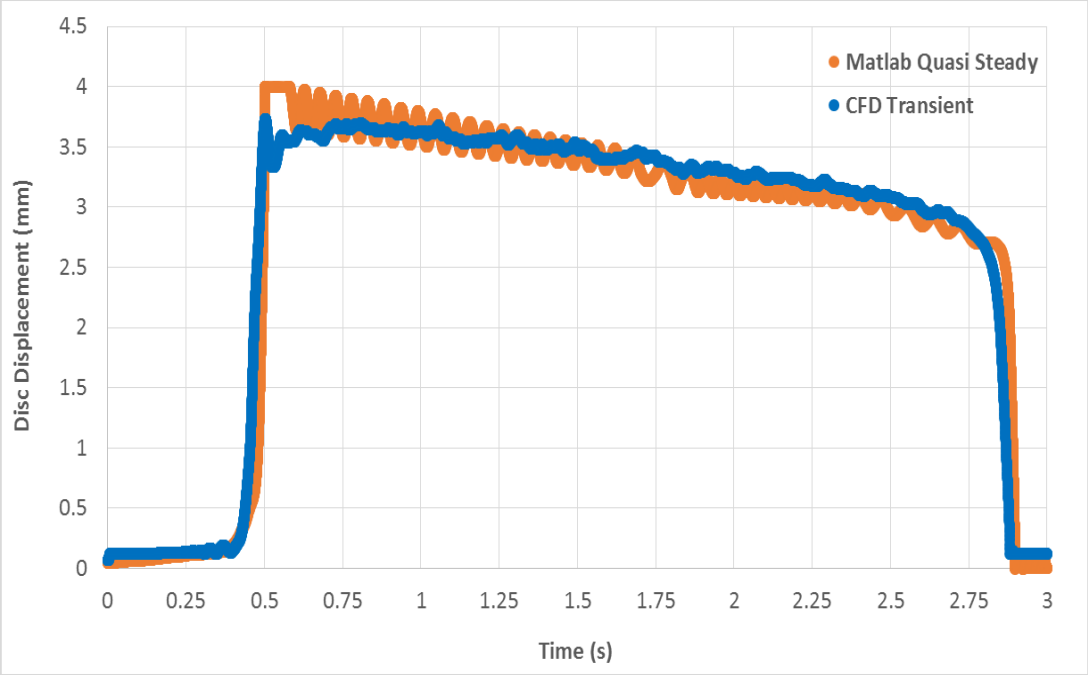

Figure 7.3 – Comparison of 3511E Transient CFD and MATLAB Type 1

	Overpressure	Blowdown
Experiment	3.85 Barg **(+16.7% Set P**)	3.6 Barg **(+9.1% Set P)**
Transient CFD	3.81 Barg **(+15.3% Set P)**	3.61 Barg **(+9.4% Set P)**
Matlab Type 1 Model	3.83 Barg **(+16.1 Set P)**	3.54 Barg **(+7.3 Set P)**

Table 7.1 – Comparison of 3511E PRV Overpressure and Blowdown Values

As can be seen from figure 7.3 and table 7.1, the quasi-steady based MATLAB type 1 model provided an accurate method of determining the dynamic characteristics of the 3511E PRV. The MATLAB model in particular was capable of predicting over pressure more accurately than the transient CFD which is likely due to the fact that a small opening is initially required for dynamic meshing as discussed earlier. For blowdown however there is a decrease in accuracy by approximately 2% however due to the reduced time and computational costs for the type 1 model it could provide a viable solution during initial design stages of the PRV. Figure 7.3 also illustrates the capability

of the type 1 model to accurately capture the dynamic characteristics of disc lift over time. Interestingly however, the MATLAB model predicts much more oscillation than the CFD model and also requires a stop at 4mm disc lift to prevent further disc displacement during opening. Therefore the transient CFD model would provide the most detailed information regarding the operating characteristics of the PRV however at a much greater time and computational cost. The CFD simulation for the Broady 3511E PRV took approximately 4 days using an HPC facility whereas the MATLAB model could be completed within 60 seconds using an i7 laptop. From this analysis for the Broady 3511E PRV (notch position 4) it was possible to establish that the use of the quasi steady assumption was generally suitable and effective for use.

7.2 Validity of the Quasi Steady Assumption for the 5231BX PRV

In chapter 6 it was also found that there were significant signs of an interdependence between disc motion and the flow regime, in particular in the disc/seat interface region. Therefore it's important to identify alongside the 3511E PRV if the quasi steady assumption would remain valid for the 5231BX PRV (modified gland). This would provide an insight towards whether or not the quasi steady assumption could be applied for all PRV's or in a case by case basis depending on PRV geometry as the 3511E PRV and 5231BX PRV contain significantly different features. The effectiveness of quasi steady state assumptions during the opening process of the Henry 5231BX PRV can be appreciated within figure 7.4, where steady state and transient CFD based non dimensional force vs disc displacement (lift) curves are compared during the opening process at 0.2 seconds. Non-dimensional disc force was calculated using equation 2.1.

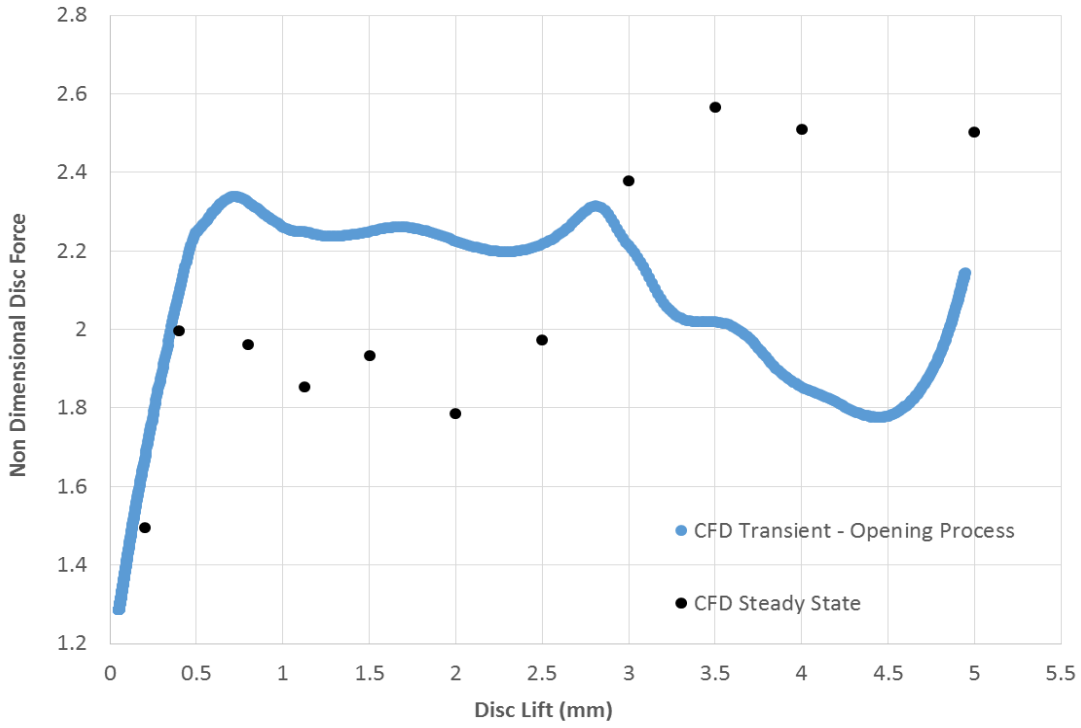

Figure 7.4 – Non-Dimensional Disc Force (eq 2.2) vs Lift for 5231BX PRV

From figure 7.4 it can be appreciated that there are significant differences in the disc force reported between the two approaches. The aerodynamic force predicted for transient simulation is much higher than the force predicted by steady state for lifts from 0-3 mm. However, for higher disc lifts of 3 mm or higher, the aerodynamic force is found to be considerably lower than the steady state equivalent. This difference observed for the 5231BX PRV is much larger than that measured for the 3511E PRV shown in figure 7.1 which suggests that the through flow type geometry used for the Henry PRV promotes a greater interdependence between disc motion and flow features. Such a distinctive difference therefore highlights the inability of quasi-steady state assumptions to capture transient flow effects and their influence on the aerodynamic force acting on the disc for the 5231BX PRV. It is therefore clear that the use of quasi steady state based design methods for the opening process of the 5231BX PRV would greatly underestimate the initial opening forces resulting in the opening dynamics being predicted incorrectly.

In order to achieve a greater understanding towards the degree of sensitivity of the measurement of disc force with disc motion the dynamic mesh CFD model described in chapter 6 was modified. The modification included a newly developed UDF for the dynamic mesh CFD model of the 5231BX which removed the fluid structure interaction element of the model and allowed a fixed disc velocity to be achieved at a constant inlet pressure of 10.3 barg. As a result, the velocity of the disc opening across the full lift range could be held constant to create numerous disc force vs lift curves for each value of piston velocity. During this analysis however it was critical to ensure an appropriate time step was used in order to meet convergence criteria set earlier for transient simulation and to also prevent generation of negative mesh volumes. The results of this study are shown in figure 7.5 where the disc force values at four fixed disc velocities (0.02m/s, 0.1m/s, 0.6m/s, 1m/s) are compared with steady state CFD values. From figure 7.5 it can be clearly established that there is an obvious influence of disc motion on the aerodynamic force acting on the disc and therefore a clear breach of quasi steady assumptions for the 5231BX PRV. It can be seen that the disc force vs lift characteristics of the disc at lower disc velocities such as 0.02m/s and 0.1m/s generally follow the steady state characteristics. However, a notable difference could be observed between both cases at lifts between 2.5mm – 4mm where the 0.1 m/s followed the steady state values more closely. At higher disc velocities such as 0.6 m/s and 1 m/s, the differences observed within figure 7.4 are confirmed as in general the transient disc force is much higher than steady state at low lift and lower than steady state at higher lifts. The reasoning for this difference will be explored later in this chapter.

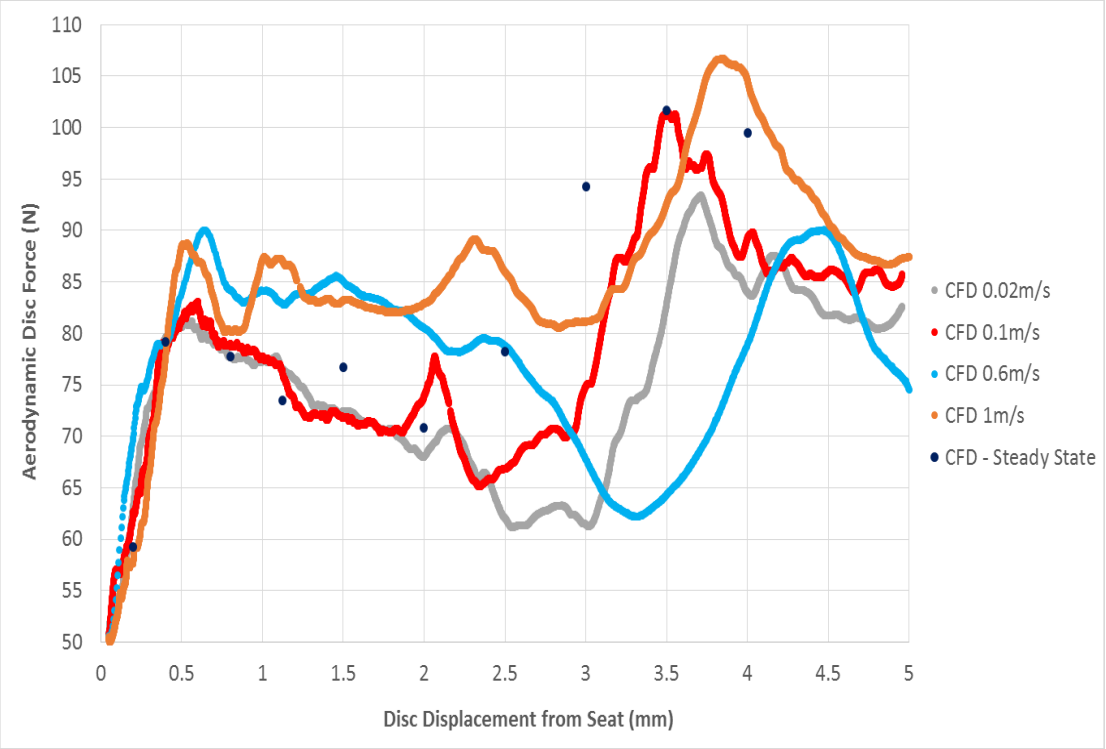

Figure 7.5 – Disc Force vs Lift for Several Fixed Disc Velocities at Constant Inlet Pressure of 10.3 Barg (5231BX)

As it was clear that there was a much greater sensitivity of the 5231BX PRV to disc motion to the 3511E it was important to develop a quasi-steady based MATLAB type 1 model to identify any differences in the predicted flow features. The results for the dynamic behaviour of the MATLAB model is shown in figure 7.6 and values of overpressure and blowdown within table 7.2. It could be established from figure 7.6 that the general dynamics of the PRV in terms of disc displacement at opening, blowdown and closure is consistent with transient CFD however there are noticeable differences during opening and closure. It could be seen that the opening process predicted by the MATLAB type 1 model was much more oscillatory than the CFD behaviour. A significant over prediction of overpressure can also be noted within table 7.2 which suggests that the MATLAB model is unable to accurately predict the opening process of the 5231 BX PRV. Closure for the MATLAB model also predicts the final blowdown process between 1.4s-1.5s to represent a step which is not

captured in the transient CFD model and experiment. However the blowdown pressure is accurately captured to be within 0.5% of the CFD value. As a result, from the results shown in figure 7.6 and table 7.2 the quasi steady model would not be suitable for accurately predicting over pressure and the opening process but would provide a suitable representation of the blowdown process for the 5231BX PRV.

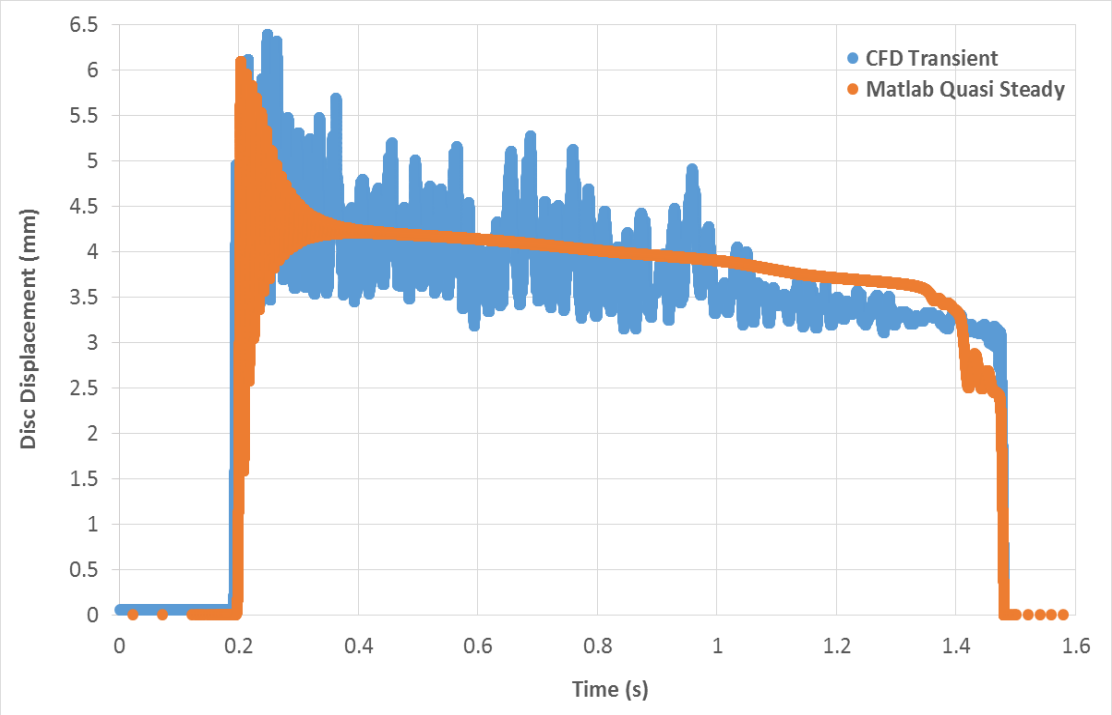

Figure 7.6 - Comparison of 5231BX Transient CFD and MATLAB Type 1

	Overpressure	**Blowdown**
Experiment	11.33 barg **(+10% Set P**)	8.75 barg **(-15% Set P)**
Transient CFD	11.02 barg **(+7% Set P)**	8.79 barg **(-14.7% Set P)**
Matlab Type 1 Model	10.52 barg **(+2.2% Set P)**	8.73 barg **(-15.2% Set P)**

Table 7.2 - Comparison of 5231BX PRV Overpressure and Blowdown Values

To achieve an understanding towards the differences observed from figure 7.4 between the transient moving mesh and steady state models for the 5231BX PRV; several Mach number contours at various lift points were generated. The flow characteristics at high lift (4mm) for both transient and steady state CFD simulation are shown within figure 7.7 using contours of Mach number.

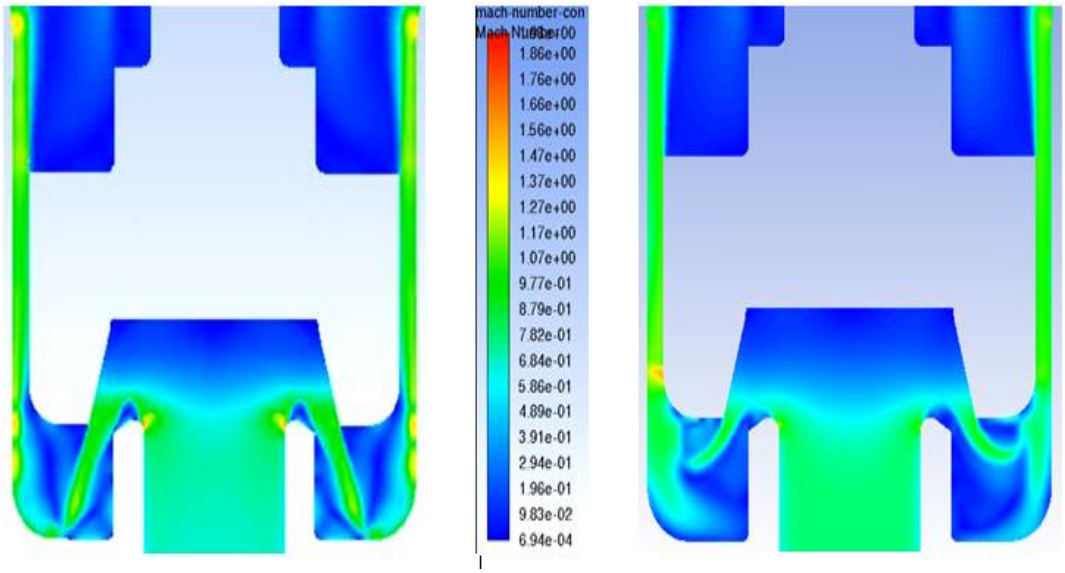

Figure 7.7 – Contours of Mach Number at 4 mm lift during PRV opening at t = 0.195s for transient (left) and steady state (right) simulation.

It can be seen within the Mach number plots that there is a considerable difference in bulk flow direction as has been observed by Beune [5, 20]. For transient simulations, the deflection angle of the fluid exiting the seat region, which represents the angle of the flow after contact with the piston has a greater downward orientation compared to the steady state results. By considering a simple momentum balance, the momentum transferred to the disc can be considered less for the transient simulation and will result in a significant reduction in flow force compared to steady state. It could therefore be suggested from the work performed so far that the flow differences observed in both figures 7.7 and 7.8 are due to the formation of temporal, short lived vortices at the piston surface which influence the bulk flow features as

the disc accelerates and decelerates. As a result, it can be established that for transient simulation during the opening process that there is a coupling of the flow through the valve and opening time (6ms). Therefore, the use of quasi-steady state assumptions during opening is largely invalid and results in poor prediction of piston forces for the 5231BX PRV. This has been confirmed in the results shown in figures 7.6 and table 7.2.

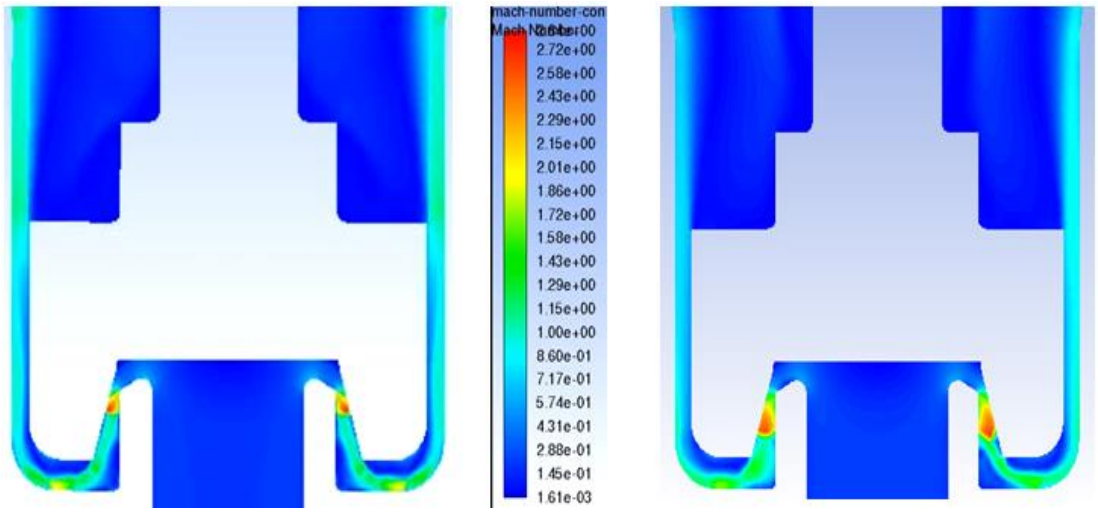

Figure 7.8 – Contours of Mach Number at 0.8mm lift during PRV opening at t = 0.192s for transient (left) and steady state (right) simulation.

Nonetheless, it is also important to note that while differences in the valve dynamics may occur between the different approaches; the choking points remain consistent between both models. The choking point controlling the mass flow depends on the lift; at low lift this occurs at the seat, while at higher lift it occurs at the exit from the annular piston/body region. This consistency in predicting the choking point at both high and low lifts explains the observation in figure 7.9, where the calculated mass flow rate through the valve using both steady state and transient simulation show good correlation. Therefore, the use of steady state methods to determine the dynamic mass flow characteristics of a PRV is appropriate for valves with similar geometry to the Henry 5231BX.

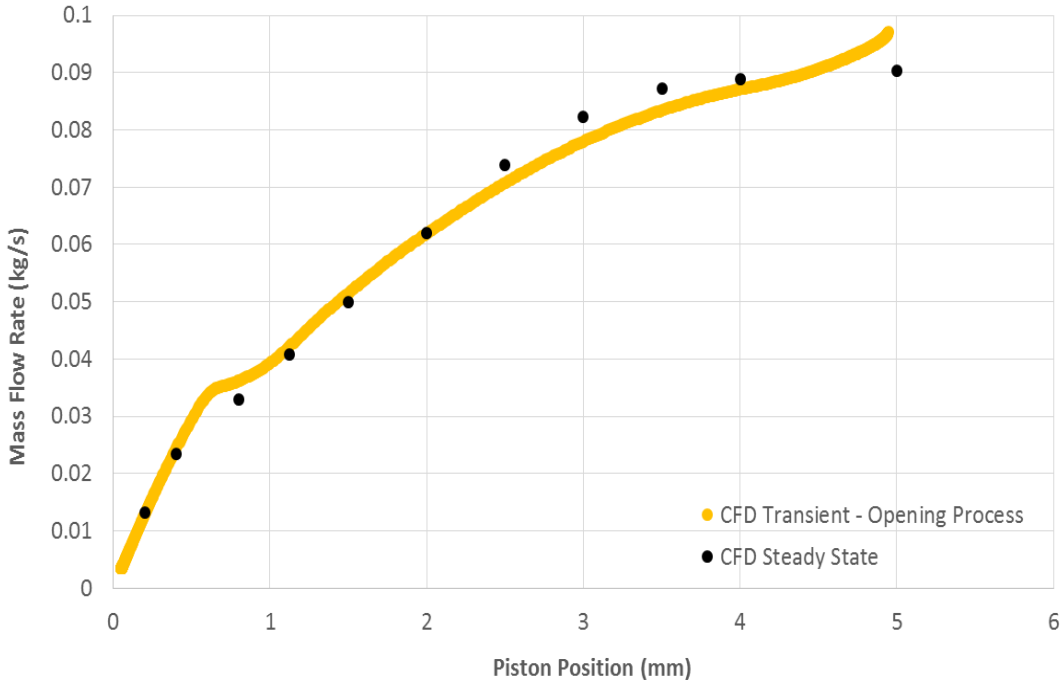

Figure 7.9 – Mass flow rate vs lift for transient and steady state during opening (overpressure) process of the PRV.

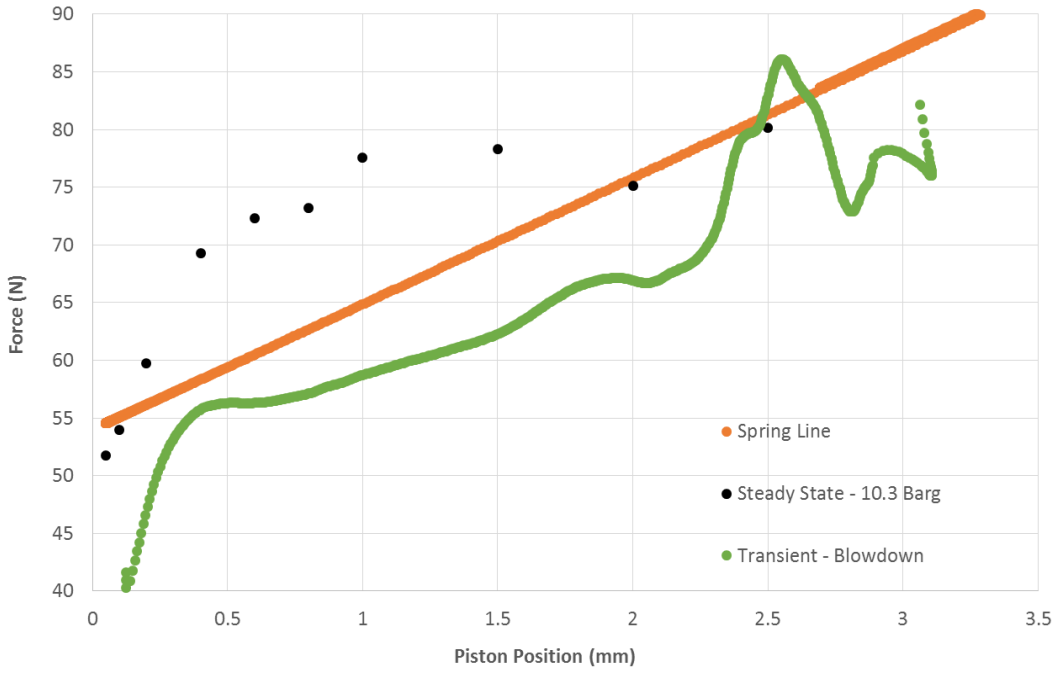

Figure 7.10 – Force vs lift curves for transient and steady state during closure (blowdown) process of the PRV.

In addition to understanding the differences between quasi steady state and transient simulation for opening, it was important to evaluate the effectiveness of quasi-steady assumptions during valve closure. The comparison is shown in figure 7.10, which shows the transient predicted forces at closing compared to the quasi steady forces at approximately 1.5 seconds. It should be noted that during closing in the transient case, the pressure is held approximately constant as closure takes place rapidly. The figure indicates differences between both approaches to predict flow force but smaller compared to the opening process. It can also be realized that the difference in force prediction improves as disc lift decreases. Figure 7.11 illustrates this observation using Mach number contour plots where it is clear that the bulk flow structure is similar for both modelling approaches. Therefore, it can be concluded that the use of quasi-steady design approaches during blowdown will be subjected to reduced error when compared to opening process when predicting blowdown. The results shown in figure 7.6 and table 7.2 for the MATLAB type 1 model confirmed this due to a decoupling of piston motion with the time scale of the blowdown process.

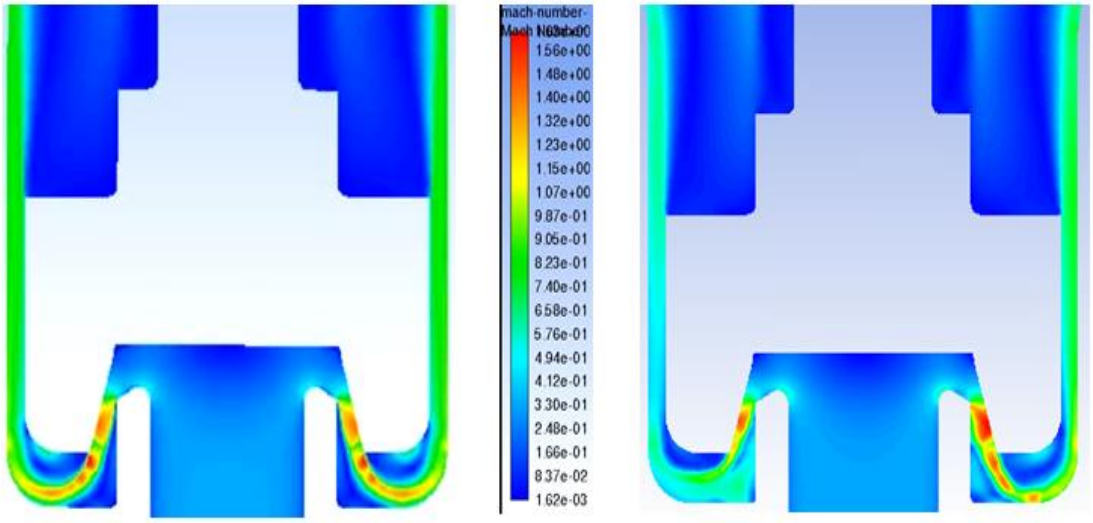

Figure 7.11 - Contours of Mach Number at 1.5 mm lift during PRV closure at t = 1.48s for transient (left) and steady state (right) simulation.

However, figure 7.12 highlights a deficiency of using quasi steady state assumptions during blowdown which is likely to cause the step effect exhibited by the MATLAB type 1 model within figure 7.6. It is shown that at the beginning of the blowdown process the transient force predicted by the solver has a maximum deviation of 20N when compared to steady state; at the corresponding blowdown pressure at a time of 0.34s. Such a difference in force as shown within figure 7.12 results in the transient force curve to dip below the spring line, which would result in a net force opposite to that of steady state.

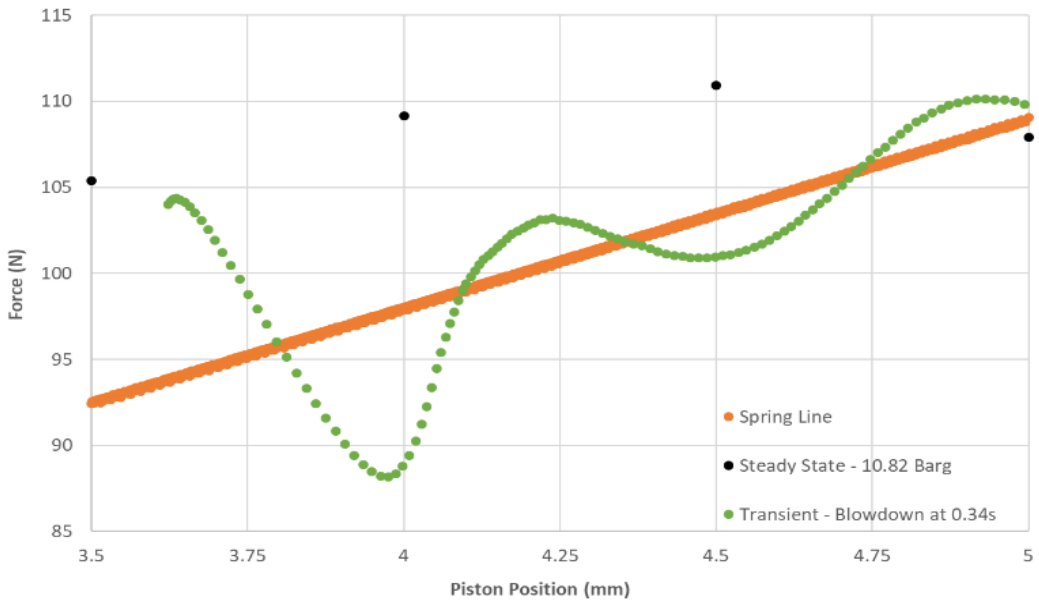

Figure 7.12 – Force vs lift curves for the transient blowdown process at t = 0.34s and corresponding steady state.

Therefore, it could be suggested that the quasi-steady state modelling approach would not be capable of accurately predicting the dynamics of the valve. It is proposed that this observation is caused by the rapid vibration of the valve (figure 7.6) at the start of the blowdown process which has a substantial impact on the formation of vortices within the transient simulation; resulting in a flow force which is coupled with piston motion. However, it is worth noting that while the quasi-steady forces during opening and blowdown

are quite different from the transient analysis their use shown in table 7.2 highlighted only a poor prediction of overpressure and good prediction for blowdown pressure. The blowdown pressure was captured accurately by quasi steady methods due to the relatively slow change in pressure compared to the opening and closing times. This is in contrast to the prediction of any oscillating flutter events shown in figure 7.12 which are unlikely to be credible if predicted by the quasi steady assumption due to the extended time period.

7.3 Summary of the Validity of Quasi Steady Assumption for both Broady 3511E and Henry 5231BX PRV's

A CFD study has been performed to determine the validity of the quasi-steady design approach for both the Broady 3511E and Henry 5231BX PRV's. Both steady state and moving mesh transient CFD based simulations was used to compare the flow characteristics of aerodynamic piston force and flow rate predicted using both approaches. In addition the use of a quasi-steady based MATLAB type 1 model was used and compared with transient CFD and transient experimental results. The following outcomes during the investigation have been established;

- It was found that for the Broady 3511E PRV a small effect of disc motion was caused on the flow characteristics of the PRV as the disc force was reduced due to an increase in flow velocity in the recirculation area below the lower disc surface. However following analysis using a quasi-steady based MATLAB type 1 model it was found that good correlation could be achieved in determining overpressure, blowdown and dynamic characteristics. Therefore the use of quasi steady models in the early design for PRV's such as the Broady 3511E PRV could provide a much more cost efficient solution in predicting the dynamic characteristics of a PRV. However care must be taken as the transient CFD model would be able to capture a much more accurate representation of the blowdown process as well as providing critical flow regime data.

- For the Henry 5231BX PRV, due to the formation of temporal, short lived vortices at the piston surface which influence the bulk flow features as the disc accelerates and decelerates, a significant difference in the prediction of aerodynamic force was found at both high and low lifts. It can be concluded that during a rapid piston displacement process that there is a coupling of the flow reducing the validity of the quasi-steady

state assumptions. This was confirmed using a series of transient moving mesh CFD simulations at various fixed values of disc velocity. It was found that at disc velocities greater than 0.6 m/s a significant difference was found between the prediction of the disc force for transient and steady state CFD.

- A consistency was found between transient and steady state simulation for the 5231BX PRV in predicting the choking point at both high and low lifts. As a consequence, the predicted mass flow rate through the valve using both numerical approaches displayed good agreement. Therefore, it was concluded that the use of quasi-steady design methods to determine the dynamic mass flow characteristics of a PRV with similar geometry to the 5231BX is appropriate.

- The differences in predicted force between steady state and transient simulation was found to not affect the final closure prediction of the MATLAB type 1 model due to the rapid changes. However, a greater influence is found during overpressure and vibration events during the blowdown process, where a prolonged influence of the error due to disc velocity will occur.

- It could therefore be concluded that the validity of the quasi-steady assumption for PRV design and modelling should be determined in a case by case basis as it was found to be valid for the 3511E PRV but had deficiencies for the 5231BX PRV. Care must be taken in particular for PRV's in which the disc is enclosed in a small cavity and complex flow paths exist around the disc similar in nature to the 5231BX. Whereby if the generation of vortices have a particular time scale and match with the disc opening time, a coupling will occur which as a result will detriment the validity of the quasi-steady assumption.

CHAPTER 8

TWO PHASE FLOW ANALYSIS OF HENRY 5231BX PRV

From the single phase analysis performed for the Henry 5231BX PRV in sections 5.2 and 6.2 it has been possible to generate an appreciation of the compressible flow characteristics for both steady state and dynamic operation. Therefore, due to the typical multiphase application of a PRV in service it is proposed to extend a similar methodology for two phase flow within this chapter. From previous studies carried out by both Elmayyah [11, 29, 30] and Alshaikh [12, 26-28] an understanding towards steady state experimental testing and CFD modelling of a through flow type PRV for a two phase flow regime has been achieved. This work has been summarized in chapter 3.2.

The multiphase flow regime used by both researchers was an air-water dispersed droplet regime , however in a similar manner to single phase, this research was limited to 2D CFD modelling. Therefore, the steady state 3D modelling CFD strategy utilised in chapter 5 will be extended with ANSYS FLUENT to include two phase flow (air-water) using a quarter symmetry model of the 5231BX with modified gland. The mixture model will be used with the previously validated k-omega SST turbulence model with the pressure based solver at 10.3 barg to achieve piston force vs lift and mass flow rate vs lift characteristics for validation with experimental data from an in-house developed two phase rig at Strathclyde. In addition, the two phase steady state experimental techniques and equipment used by Elmayyah and Alshaikh will be improved upon in order to achieve a more resilient and accurate means to measure PRV performance. It should be noted that water injection rates of 0.96 L/min, 2.1 L/min and 4.25 L/min will be used in order to gain an appreciation of the effects of various water content on performance. For a piston position of 4 mm, these injection rates correspond to a water mass fraction value of 0.18, 0.35 and 0.57 respectively. However, for CFD validation

only the 0.96 L/min and 2.1 L/min rates were selected as they were within the limits for the CFD mixture model to remain viable as discussed by Alshaikh [12]. It should be noted that for constant water injection rates, at lower lifts the water mass fraction would be greater than that at higher lifts due to a lower flow rate of air. Therefore, at low lifts the validity of the homogeneous mixture model is likely to break down as the corresponding water mass fraction will not remain within the mixture model's typical working range. This relationship will be investigated in further detail to appreciate it's influence on accuracy of the mixture model.

Furthermore, to extend the work discussed in chapter 6 a two-phase transient experimental methodology will be developed to gain an appreciation towards the implications of two-phase flow on dynamic PRV operation. A novel experimental method will be required to capture the dynamics of the through flow type Henry 5231BX PRV. As indicated in the literature, modelling and detailed experimental investigations of two-phase flow in safety relief valves are limited and the transient operation of a safety valve under two phase blowdown is considered unique to the literature.

8.1 STEADY STATE TWO PHASE FLOW

In this section a two phase (air-water) steady state experimental method will be described and the results compared to previous observations by Elmayyah [11] and Alshaikh [12]. Furthermore, the development of a two-phase 3D CFD model will be highlighted with predictions of piston force and mass flow rate vs lift l compared with the experimental data. This will enable a comparison to be made between the difference in modelling accuracy for 2D and 3D simulation for two phase flow using the mixture model. Observations will also be made in regards to symmetry breaking and if similar trends for symmetry breaking phenomena predicted for single phase CFD also occur for air-water

composition. In addition, a comparison will also be made by using various contour plots from CFD to study flow features such as Mach number, water volume fraction and static pressure against various water injection rates. As a result, it has been possible to gain an appreciation of the effect of increased water rates on PRV performance and compare this to single phase flow conditions.

8.1.1 Experimental Two Phase Steady State Tests

The lessons learned from previous research and development of an in-house two phase experimental facility at the flow laboratory in Strathclyde was used as a basis to develop a novel technique to capture steady state performance of the Henry 5231BX PRV. As developed in the single phase studies for the 5231BX PRV (section 5.2.1), the primary measurements required from the experiment were piston force, mass flow rate of air and back pressure vs lift at a specified inlet pressure of 10.3 barg where the flow testing laboratory air circuit described in section 5.2.1 was used. Therefore, the same platform which was described for the single phase steady state study was used for two phase testing with specific modifications. For two phase flow, the objectives were similar however the addition of a water injection rate was required to be monitored to ensure that the value of inlet water flow rate was controlled. This would therefore allow an appreciation of the influence of water mass fraction on results to be achieved.

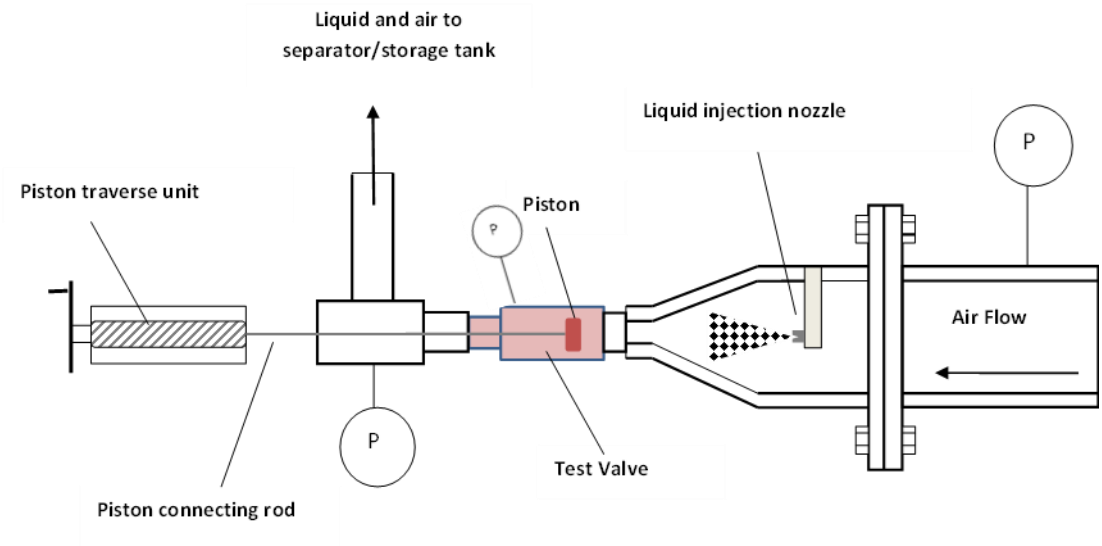

Figure 8.1 – Overview of Two Phase Steady State Experimental Rig

In concept, the experimental approach was similar to the set up developed by Elmayyah [11] and Alshaikh [12] and is shown in figure 8.1. Upstream of the PRV, water would be injected via a spray nozzle to allow the air-water mixture to develop before entering the inlet region of the valve. A converging nozzle was used in order to promote mixing of the two-phase flow to achieve an approximately mono dispersed droplet mixture of water in air. Following injection, it was required for a custom developed housing to be attached to the PRV outlet to facilitate the removal of water from the air/water mixture in order to allow recirculation of the water phase in the experimental system and prevent water egress to the surroundings. In a similar manner to the single phase testing, a piston traverse unit with a laser displacement measurement system would enable the value of piston lift to be measured and adjusted to the desired value. A load cell connected directly to the piston via a thin rod would also be used to measure piston force. Due to the tight tolerances required to achieve a good seal around the rod it was crucial to minimise any sources of friction caused by interaction of the rod with the seal/casing.

The water injection nozzle, highlighted in figure 8.1 is shown in operation in figure 8.2 where the PRV has been removed from the nozzle outlet in order to appreciate the spray formed. As described by Alshaikh in his thesis; “the droplets are injected via a spray nozzle that produced a full cone spray at a 30° spray angle and droplet diameters of the order of 400μm. The spray was injected into the air flow at the entrance of a converging nozzle with an area contraction ratio of 70 and under typical operating conditions would lead to the acceleration of the air flow from a negligible Mach number to one of 0.6, with velocities reaching 200 m/s”. As a result, Alshaikh assumed that the droplets would undergo breakup processes which would result in the critical Weber number being reached. In this case a droplet size of 1 μm represents homogeneous flow conditions where in accordance with previous research by Elmayyah and Alshaikh, it was concluded that for low liquid mass fraction flow the flow could be considered as homogeneous. This can be observed in figure 8.2 where the droplets are shown to be mono dispersed as the water droplets travel at a similar velocity to the bulk air flow.

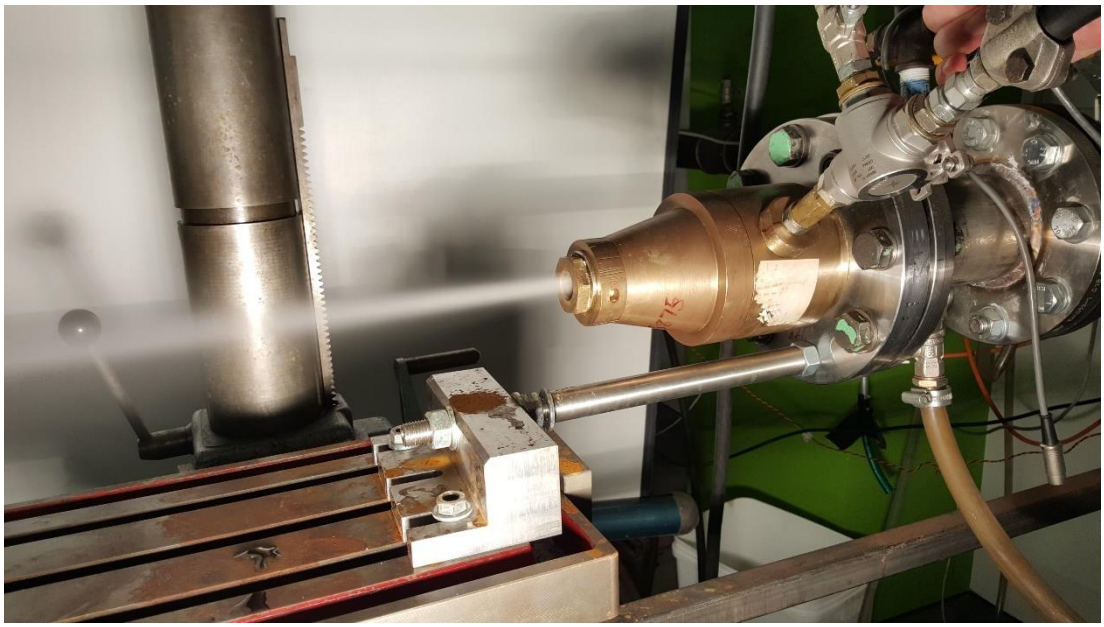

Figure 8.2 – Air/Water Mixture from Outlet of Water Injection Nozzle

A high level overview of the water circuit for the two phase experimental rig is shown in figure 8.3 and each component of the rig will be described in further detail from photographs in figures 8.4-9. It can be seen that water is supplied from a central water tank (A) to a positive displacement diaphragm pump (B) where the circuit is protected by a pressure relief valve (C) connected in parallel. A bladder accumulator (D) was used downstream of the pump which was subsequently connected to a turbine flow meter (E) to measure water rate. A bypass valve (F) allowed manual control of the water injection to the test PRV and separator for two phase flow experimentation of the 5231BX PRV to take place. From the separator, water which didn't return to the central tank (A) is stored within a smaller reservoir connected to the separator (G) to avoid loss of separation efficiency caused by accumulation.

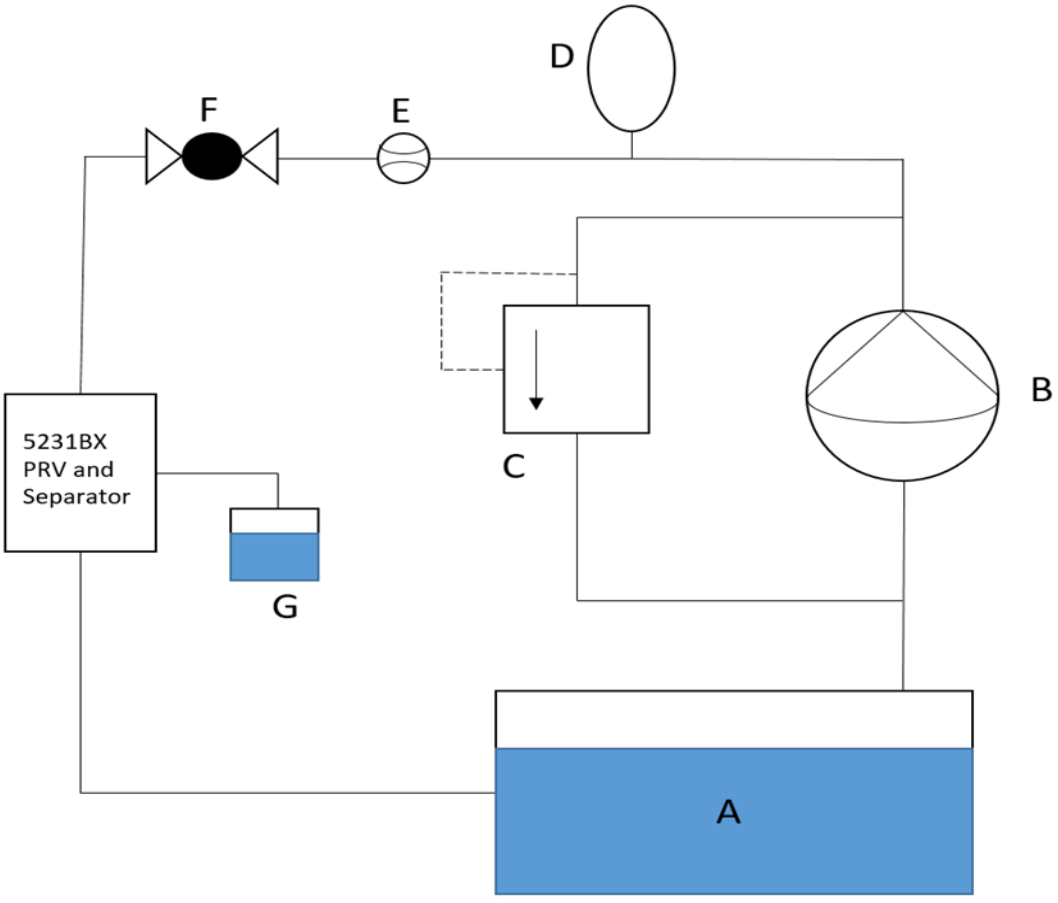

Figure 8.3 – Water Circuit for Two Phase Experimental Rig

The pump and accumulator setup within the laboratory is shown in further detail from figures 8.4 and 8.5. A positive displacement diaphragm water pump (Hydra Cell D/G-04 series) was used with a maximum rated flowrate of 11 L/min and delivered the flow independently of the downstream pressure up to 100 barg. The pump was driven by an AC motor controlled by a speed controller, which allows adjustment of the water flow rate (3). A correlation between pump speed and water rate is achieved through calibration by measuring the volume of water produced in a given time. A turbine flow meter (Omega Engineering FTB 1411) upstream of the injection nozzle is fitted to facilitate measurement of the water flow rate; it has a flow rate range of 0.4 - 10 l/min and has an accuracy of +/- 1% of the reading shown in (1). A compressed gas accumulator (bladder accumulator) (FlowGuard DS-20) is also attached to the pump outlet to ensure pulsations are removed from the pump (2).

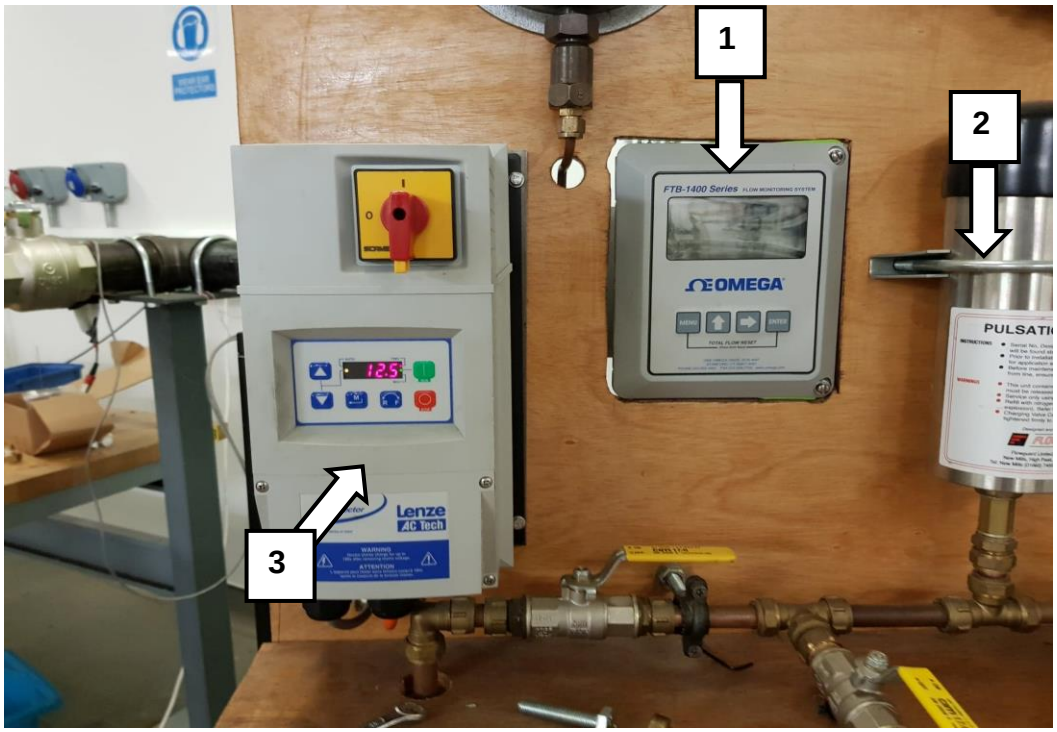

Figure 8.4 – Pump Controls for Two Phase Flow Experiment

With reference to figure 8.5, the operation of the water injector was controlled using the blue lever shown on (4) by regulating the shut off valve which was connected via a high pressure hose to the pump. Once the valve was opened, water would flow to the injector at (5) to allow the air-water mixture to enter the nozzle shown at (6).

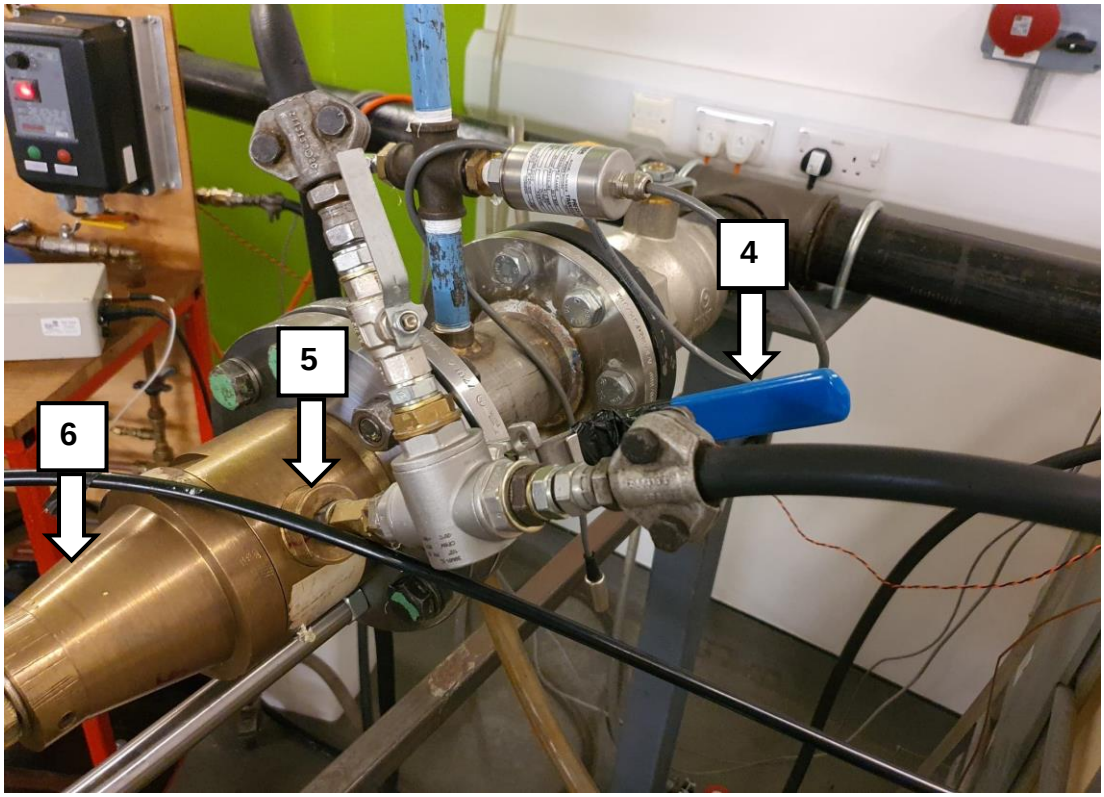

Figure 8.5 – Water Injection Unit

Figure 8.6 illustrates the connection of the Henry 5231BX PRV with modified gland (7) to the nozzle (6) and to the separator shown at (8). As described previously, the separator would allow the majority of the water flow to return by a main supply line to the water tank and prevent water egress to the surrounding environment. In addition to the brass housing of the separator shown in (8) an additional drainage cover was used at (9) which collected water at the bottom of the vessel. This water would subsequently flow to overflow containers via a hosed connection at (10).

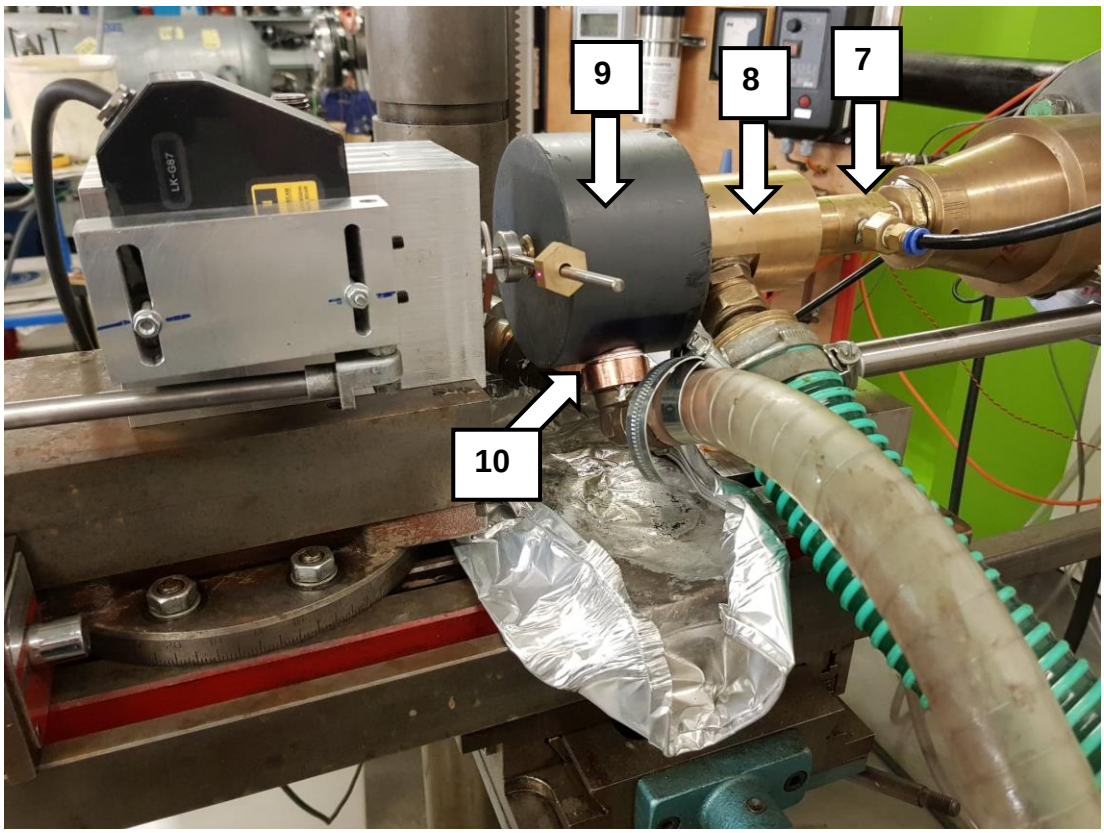

Figure 8.6 – Separator for Air-Water Flow from PRV

A cross section of the brass section of the separator (8) is shown within figure 8.7 in order to provide further detail of its operation. The device was designed to be modular to enable it to be used for a variety of PRV outlet dimensions by utilising a threaded connection piece called the PRV outlet connector. Following the PRV connector the flow enters a chamber whereby it is deflected towards the air-water outlet. The pressure in this chamber is monitored using a pressure gauge in order to ensure that there is no superimposed backpressure applied to the PRV which would affect accuracy of the experimental results. The connecting rod as described in the single phase study (5.2) then continues through the separator towards the connector rod seal which has a very tight tolerance at the outlet to minimise leakage. Water and air passing back along the rod is redirected radially in a perforated cylinder, dissipating the inertia as it enters a separation unit. The separator consisted of a porous element prompting droplet coalescence and gravitational

water drainage. This perforated cylinder was also designed to be modular in order to allow a range of rod diameters to be used. A detachable separator housing (9), secured by a push fit and sealed by O-Rings was also designed to allow ease of assembly. Separated water was allowed to drain from the separator via the hoses (10). Further barriers were also provided at the connecting rod/ housing cover interface in order to remove the formation of a jet which would impinge on the load cell.

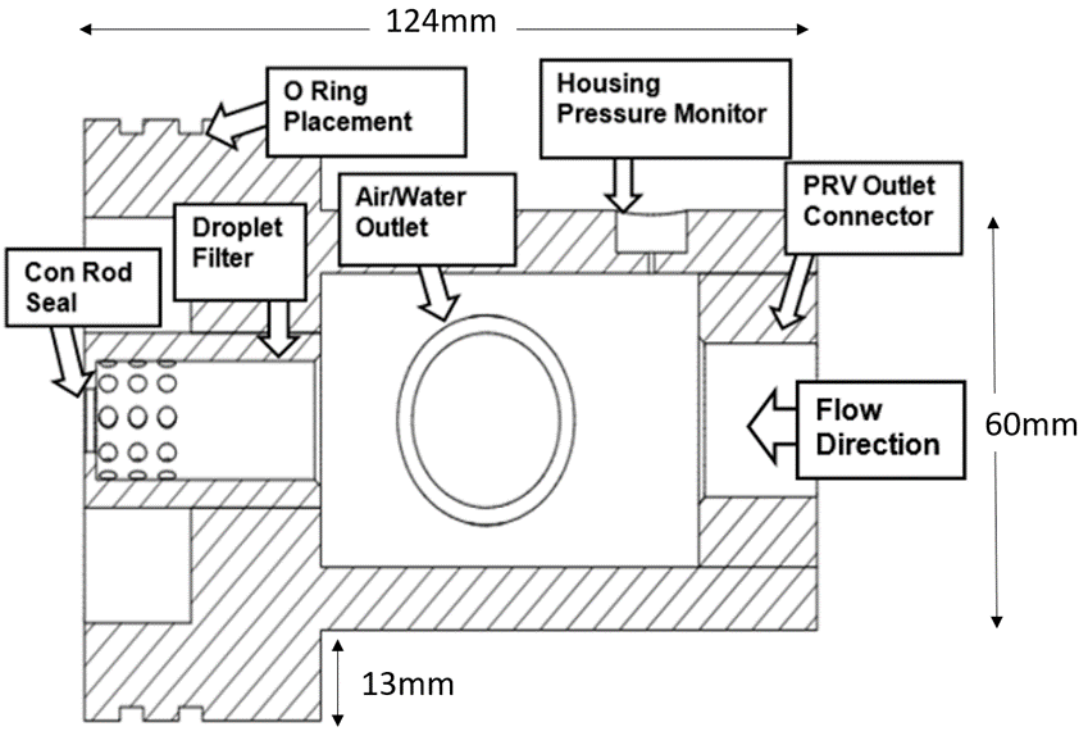

Figure 8.7 – Cross Section of Air-Water Flow Separator

The overall principle regarding water management and back pressure measurement for the two phase experimental rig is illustrated within figure 8.8. The backpressure of the PRV acting above the disc was measured using the bourdon gauge shown in (11) where the hose (12) to connect the air-water outlet for the separator to the water tank (13) provides a water circuit for the experimental rig. The hoses connected to the drainage cover are highlighted

at (14) where a minimal leakage flow would collect within overflow containers to be poured back in to the water tank at the end of a test.

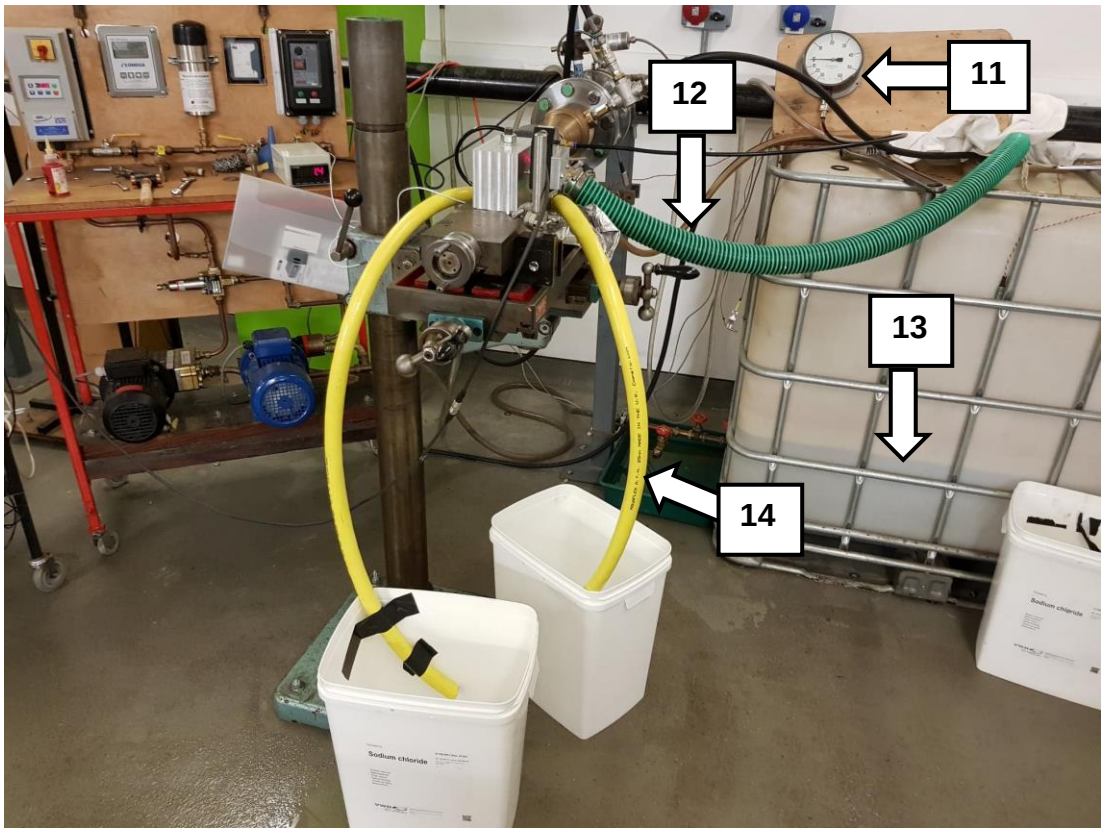

Figure 8.8 – Water Circuit for Two Phase Testing of PRV

The overall two phase steady state experimental set up for the Henry 5231BX PRV is shown in figure 8.9 which in general shares identical operational principles with the single phase rig described within section 5.2.1. The overall inlet pressure is monitored using the bourdon gauge shown at (15) and piston displacement (lift) measured using a laser displacement sensor (16) focussed on the reference surface structure at (20). The output from the laser sensor was measured at the monitor at (17) and piston lift changed by using the traverse table controls at (18). PRV backpressure was measured with the connector at (19) which was located above the rear piston face on the valve

body as described in the earlier single phase study (5.2). Piston force measured by the load cell was reported at (21).

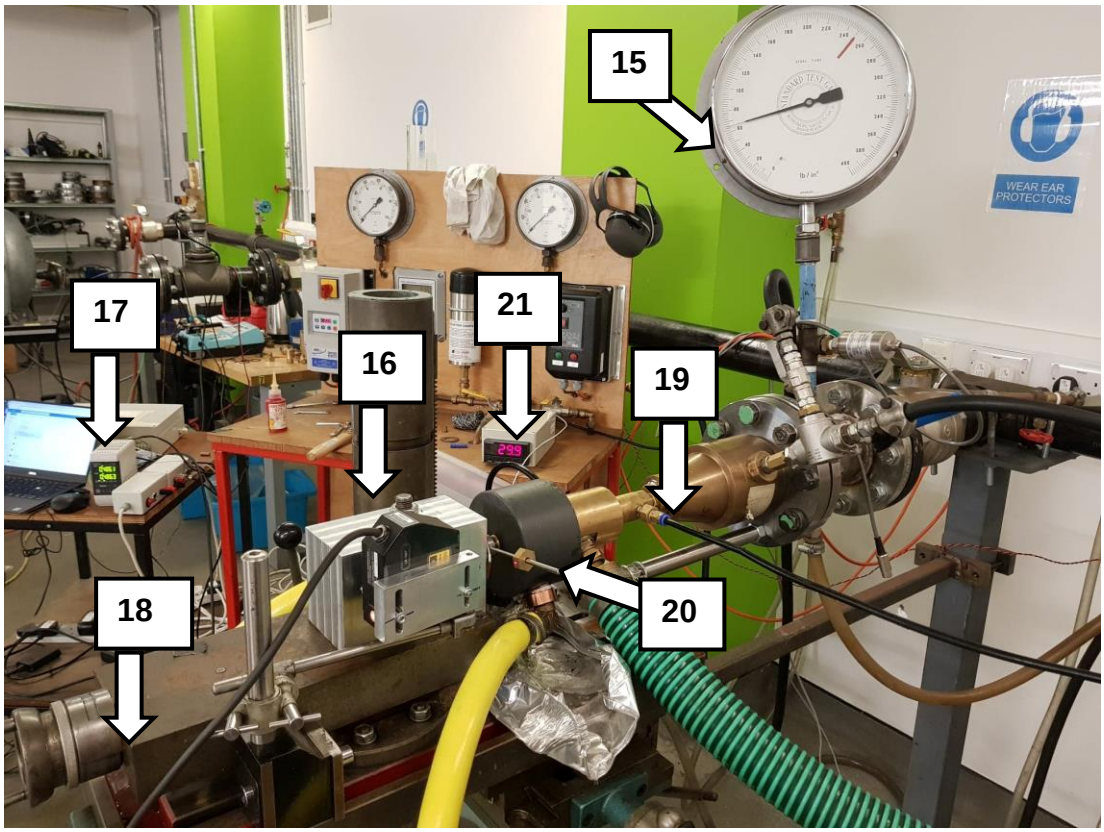

Figure 8.9 – Overall Two Phase Flow Experimental Rig for 5231BX PRV

Table 8.1 provides a look up table and description for the components shown in figures 8.3 - 8.9.

No.	**Experimental Part**	**Description**
1	Turbine Flow Meter	Provides measurement of water flowrate from pump
2	Bladder accumulator	Remove pulsations from water pump
3	Water pump controls	Positive displacement diaphragm water pump
4	Water Injection Shut Off Valve	To enable control of water injection from water pump to injection location

5	Water Injection Location	Position of water injection to main air supply for PRV
6	Water Injection Nozzle	Connection of PRV inlet to external piping to allow sufficient mixing of air-water to take place.
7	PRV	Henry 5231BX PRV with Modified Gland
8	Air-water Separator	Enables separation of air/water to water tank from PRV
9	Drainage Cover	Provides sealing and collects residual water from PRV
10	Drainage/Overflow Hose Connection	Provides means to drain water from drainage cover via 2x hoses at the base of the cover
11	Back Pressure Bourdon Gauge	Sensor to enable measurement of back pressure of the PRV at the outlet face of the piston
12	Main Air-Water Hose	Connection between main separator outlet and tank
13	Water Tank	Allows storage of water for injection
14	Drainage Hoses to Over Flow Containers	Hoses to connect drainage cover to over flow containers for reinjection to water tank
15	PRV Inlet Pressure Gauge	Sensor to enable measurement of inlet air pressure to the PRV
16	Laser Displacement Sensor	Measurement of piston lift
17	Laser Measurement Output	Reading of piston lift from zeroed position
18	Traverse Table Controls	Enable adjustment of piston lift
19	PRV Back Pressure Connection	Positioning of tubing for backpressure from PRV to Bourdon gauge
20	Laser Reference Structure	Structure to enable measurement of piston lift from a smooth/reflective surface
21	Load Cell Output	Reading of piston lift measured by load cell

Table 8.1 – Description of Rig Components in Figures 8.3 - 8.9.

In general, the single phase steady state experimental procedure described in section 5.2.1 was used for the 5231BX PRV for two phase (air-water) operation however specific modifications to the procedure were required. The adjustments took place in the following order;

1. Initially the system was cleared of any residual water by setting valve lift at a high value (3-4 mm) and increasing supply pressure to approximately 5 barg. This process would remove any water in the circuit remaining from a previous test and return it to the water storage tank.

2. To achieve a steady state two phase test at fixed pressure (usually 10.3 barg) an air flow was set by adjusting the air supply control valve until the set pressure upstream of the valve was achieved. By controlling the pump speed, the desired water flow rate was set, initially bypassing the test valve, flowing from the storage tank, via the pump to the three way valve and back to the storage tank. The three way valve was then used to direct the water flow into the test valve resulting in both a change in the upstream pressure and water flowrate due to the changed conditions. Both the air supply control valve and pump speed were changed to meet the desired conditions.

3. Once the required inlet pressure, piston position and water inlet rate were achieved; measurements were taken for piston force from the load cell alongside air flow rate and back pressure readings. This was repeated for each piston lift position. At each alteration of the valve lift, a change in the air flowrate would result, changing the upstream pressure and necessitating an adjustment of the air supply control valve to return the pressure to the desired value. Also note that measurements did not take place for lifts less than 0.5 mm due to the

flowmeters working range and to prevent water ingress to the compressed air system.

4. Steps 1-3 of the experimental process were repeated numerous times in order to ensure repeatability of the results and tests were conducted using both the original gland and modified gland.

5. For two phase experimental testing a water flowrate of 0.96 L/min, 2.1 L/min and 4.25 L/min was used at supply pressure of 10.3 barg for lifts greater than 0.5mm piston lift.

Similarly, to the uncertainty analysis used during single phase experimental studies the impact of measurement uncertainty was applied for the multiphase tests. The statistical error was quantified by using 10 tests at a fully open PRV position of 4mm lift for a pressure of 10.3 barg and a water flowrate of 1.1 L/min. A statistical error for flow force was determined for the modified gland experiment where the error was found to be 0.1%. For flow rate, a statistical error of 0.28% was found and 0.7% for backpressure measurement. This performance was deemed acceptable and highlighted the effectiveness and repeatability of the test rig for validation in two-phase operation.

The systematic measurement uncertainties for the various devices used in the two phase steady state experiment is shown within table 8.2 with statistical error presented at a lift of 4mm in table 8.3. It was therefore possible to gain an appreciation of the measurement error for each variable in the two phase experiment in which backpressure provided the greatest variance.

Device Uncertainty	Load Cell	Inlet Pressure	Laser	Air Flow Meter	Back Pressure	Water Injection
Disc Force	0.5-2%	0.25%	0.5%	N/A	N/A	1%
Air Mass Flow Rate	N/A	0.25%	0.5%	0.5%	N/A	1%
BackPressure	N/A	0.25%	0.5%	N/A	0.5%	1%

Table 8.2 –Measurement Device Uncertainty for Two Phase Experiment (Mod Gland)

	Statistical Uncertainty
Disc Force	0.1%
Air Mass Flow Rate	0.28%
BackPressure	0.7%

Table 8.3 - Calculation of Statistical Uncertainty at 4mm for Two Phase Steady State Experiment (Mod Gland)

The experimental results captured at 10.3 Barg inlet pressure across a lift range of 0.5mm-5mm for flow (piston) force, inlet air mass flow rate and back pressure for water injection rates of 0.96 L/min, 2.1 L/min and 4.25 L/min are shown in figures 8.10, 8.11 and 8.12 respectively. Single phase results for each variable have also been included which were measured using the two phase rig with the water injection pump switched off. This will enable easy comparison for single phase flow conditions to two phase (air-water flow) In addition, the inlet water mass fraction (defined in section 4.3) is shown in figure 8.13 to highlight the variation of water mass fraction with lift.

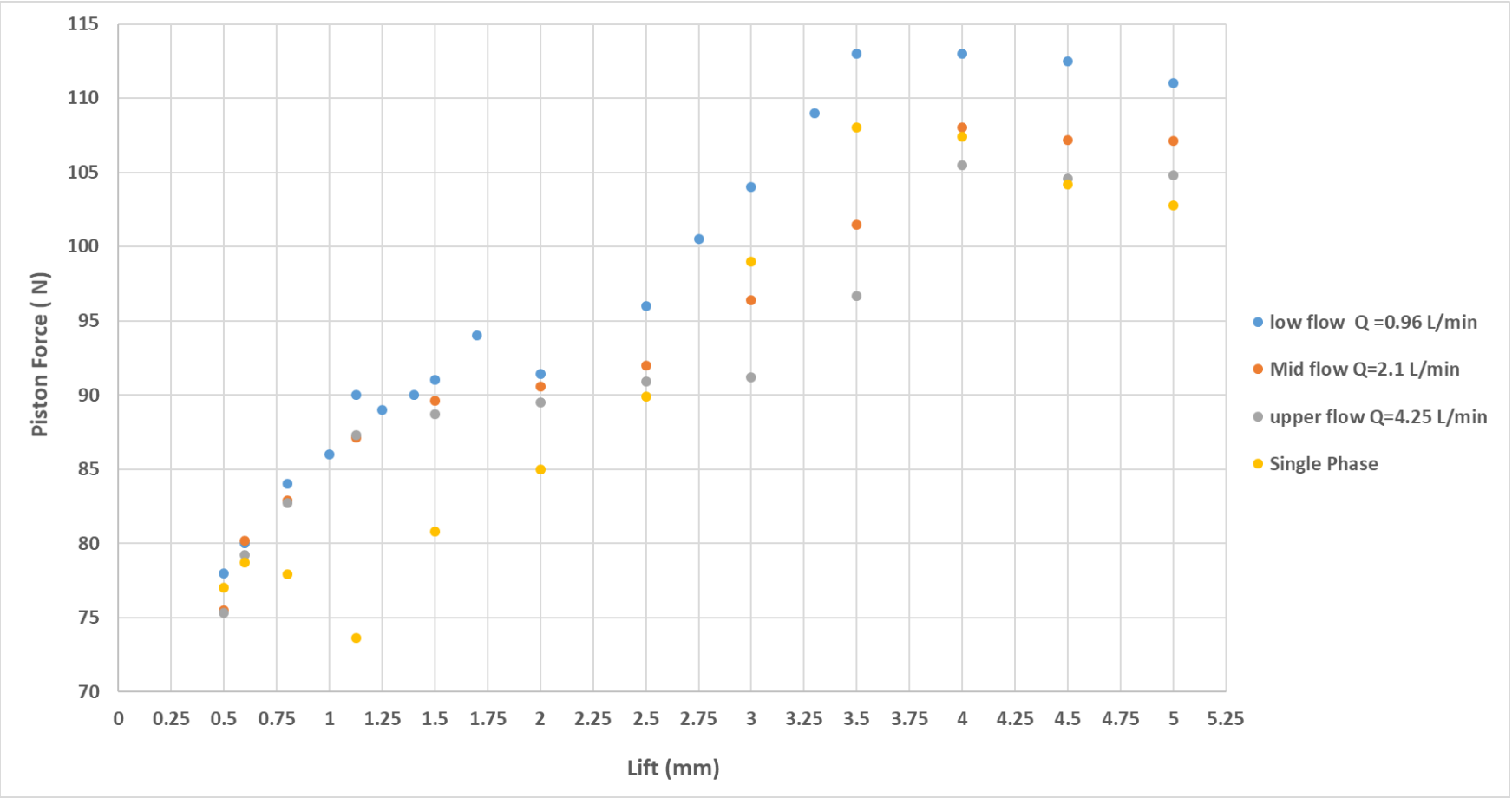

Figure 8.10 – Experimental Two Phase (Air-Water) Flow Force Results for 5231BX Modified Gland (10.3 barg)

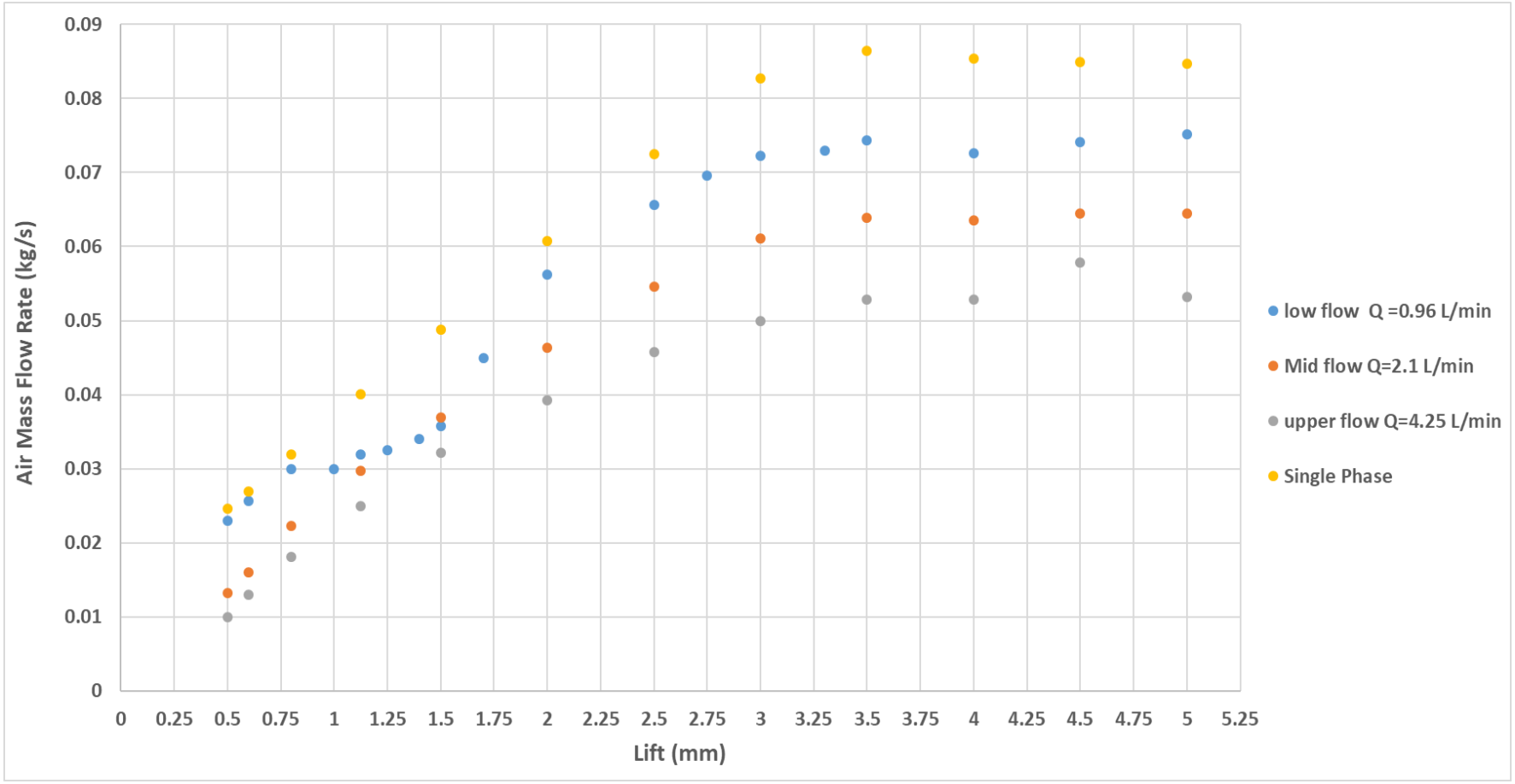

Figure 8.11 - Experimental Two Phase (Air-Water) Air Mass Flow Rate Results for 5231BX Modified Gland (10.3 barg)

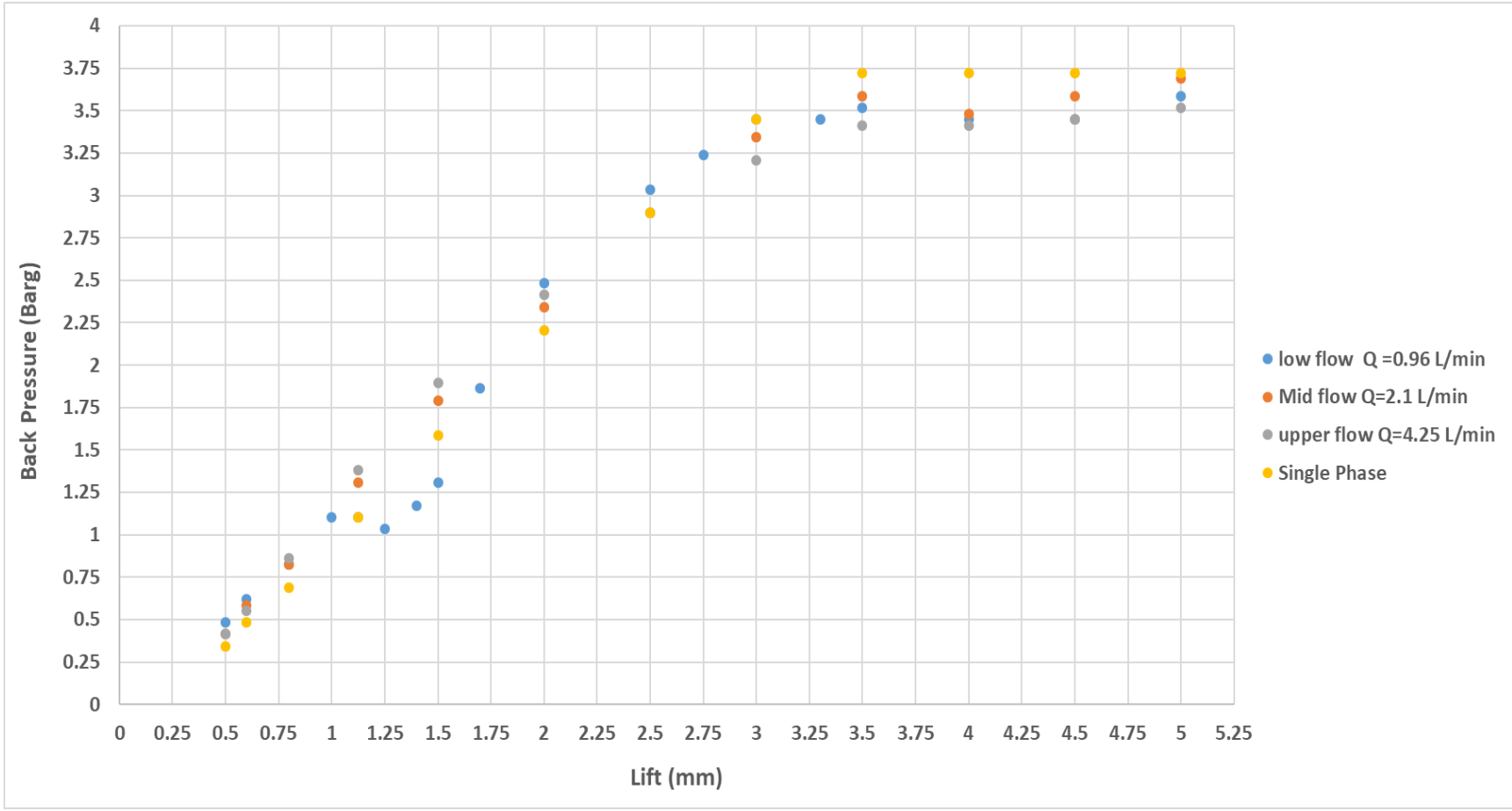

Figure 8.12 - Experimental Two Phase (Air-Water) Back Pressure Results for 5231BX Modified Gland (10.3 barg)

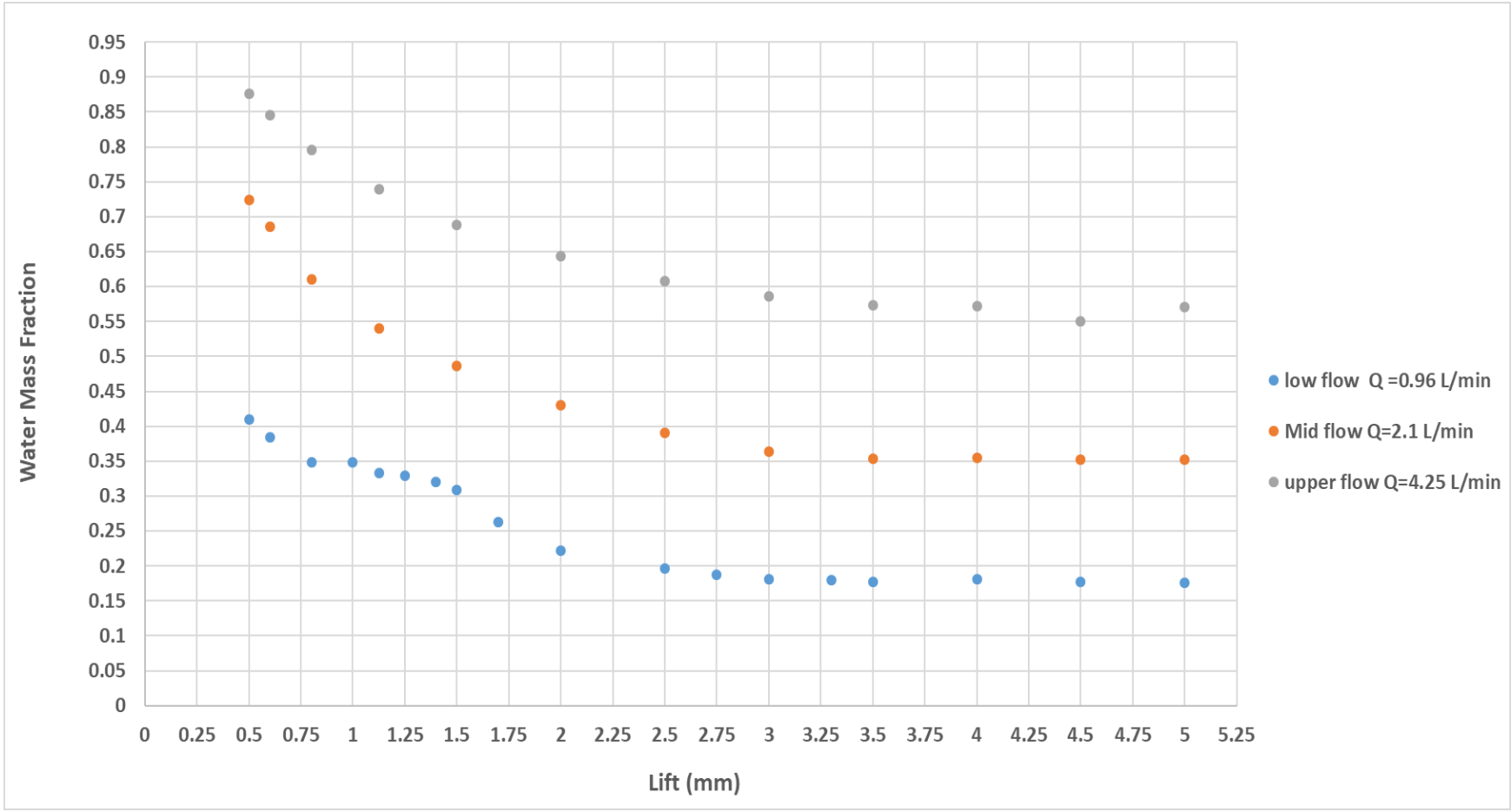

Figure 8.13 - Experimental Two Phase (Air-Water) Water Mass Fraction Results for 5231BX Modified Gland (10.3 barg)

From figure 8.10, the steady state characteristics of the piston force relationship with piston lift are presented for two phase flow conditions. For two phase flow in general, a similar trend is found for piston force as in single phase flow. This is due to a similar gradient for piston force increasing with disc lift until a maximum lift of 4 mm whereby piston force would remain constant or slightly decrease towards 5mm disc lift.

Notable differences however could be identified from 0.625 mm lift to 2.5 mm lift where the single phase disc force would decrease to a minimum value at 1.125 mm and return to an increasing gradient towards 4mm. All two phase results however did not exhibit this behaviour as piston force continued to increase from 0.5 mm to a point of inflection at 2 mm. Therefore at lower lifts, the two phase flow results indicated an increase in piston force of up to 25 N when compared with single phase. From the inflection point at 2.5 mm piston lift however, both the single phase and two phase flow disc force for all tested injection conditions generally matched each other. During the increase of piston lift from 0.5 mm to 2 mm lift the two phase flow piston forces were almost identical at all water injection rates. This therefore highlights that at low lift, water injection rate does not play a critical role to define the pressure distribution at the surface of the piston. However, the presence of water droplets does prevent the decrease of piston force at 1.125 mm observed for single phase air only conditions.

From the inflection point shown in figure 8.10 for the two phase flow results from 2-2.5 mm, subsequent significant variation of piston force with lift could be observed for various injection rates. For a low water flow rate of 0.96 L/min, a slight increase in piston force was found to occur over air only conditions whereas for higher water flow rates of 2.1 L/min and 4.25 L/min a slight decrease for piston force was measured. Therefore, it would appear that at higher disc lifts a strong relationship exists between piston force and water injection rate, with a decrease in disc force with increasing water injection. This

will be explored further in detail using CFD in section 8.1.4. In comparison with observations by both Elmayyah [11] and Alshaikh [12] the general relationship of water injection rate with disc force vs lift characteristics across the full lift region was consistent. Notable differences however could be found for the value of piston force due to both previous studies using modified versions of a through flow type PRV to suit experimental requirements. However, the PRV geometry used in this study remained true to the manufacturers original specification and differed from Elmayyah and Alshaikh's use of a modified outlet.

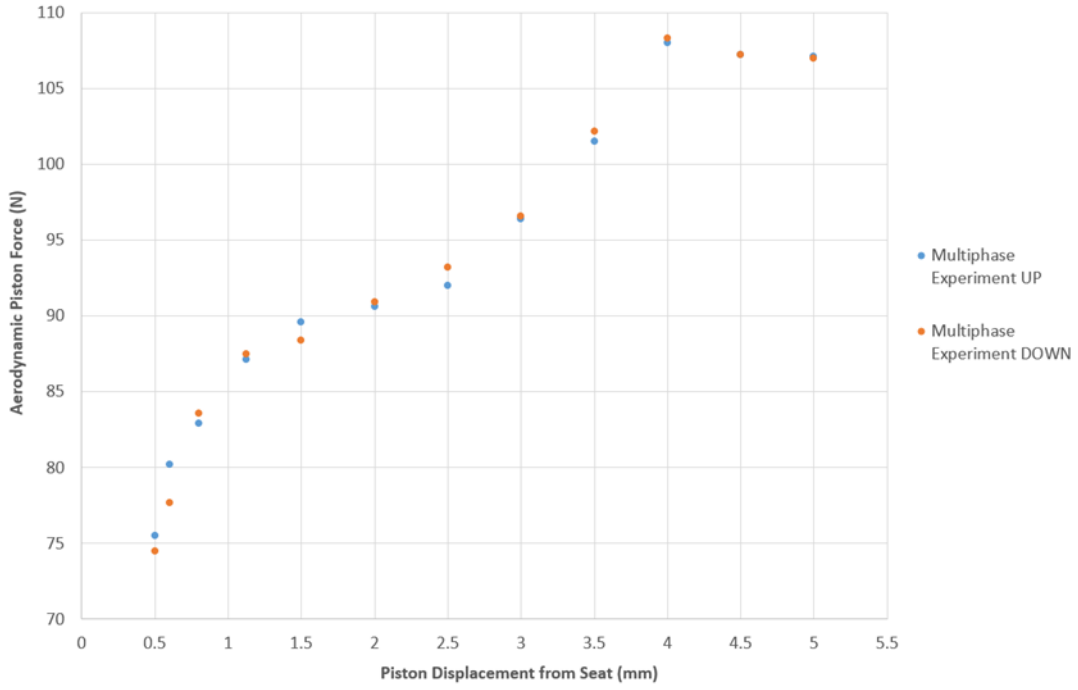

Figure 8.14 – Experimental Two Phase Hysteresis Study for Water Injection Rate of 2.1 L/min

As can be appreciated from figure 8.14; a hysteresis check was performed for air-water flow similar to that for single phase air only flow. This step was critical as it would allow an appreciation to be gained for the sensitivity of the experimental procedure i.e. initially measuring from closed position and

opening or vice versa. This was achieved by measuring piston force by taking measurements by opening the PRV from low lift (UP) and closing from high lift (DOWN). Interestingly however, the results shown in figure 8.14 highlight that the hysteresis found for single phase flow between 1 mm and 1.5 mm didn't occur for two phase flow at water injection rate of 2.1 L/min. This would therefore suggest that the flow structure in the flow region close to the piston was different from single phase flow to two phase conditions and as a result much less sensitive to hysteresis. In addition, it highlighted that consistent steady state measurement across the full lift range could be achieved regardless of opening/closing direction.

The relationship between air mass flow rate and piston lift was also shown in figure 8.11 where a clear relationship between water injection rate and air mass flow rate could be appreciated. It is clearly seen that as disc lift continued to increase at a constant pressure of 10.3 barg and water injection rate, that the corresponding air mass flow rate would decrease for higher water flow rates. This observation is also consistent with the experimental results generated in previous studies by Elmayyah [11] and Alshaikh [12]. This results in a variation in water mass fraction, as shown in figure 8.13 whereby higher values could be observed at lower lifts compared to that at higher lifts due to the increase in air flowrate with disc lift, as shown in figure 8.11.

In addition, the backpressure variation (i.e. the pressure at the rear of the piston) with disc lift for each flow condition is shown in figure 8.12. It can be appreciated that the back pressure remains approximately consistent for each flow condition, including between single phase and two phase operation. Small but higher values in pressure are observed at low lifts compared to single phase and small but lower pressures are observed at high lifts. These variations are of the order 0.2 bar and correspond to a back pressure force of approximately 3-4 N on the piston.

As a result, it could therefore be concluded that the differences observed for aerodynamic piston force would be caused by front face flow effects on the pressure distribution at the inlet facing side of the piston surface.

8.1.2 Development of 3D Two Phase Steady State CFD Model

For the two phase (air water) study, the 3D quarter symmetry computational domain (mesh) presented in section 5.2.4 for the 5231BX PRV valve with a modified gland will be used as a basis to develop a two phase CFD model with the mesh independent settings which was developed. This model will be used to perform a 3D CFD study to determine if an improvement in modelling prediction can be achieved over the 2D CFD models developed by Elmayyah and Alshaikh [11, 12]. Furthermore, the lessons learned from the single phase comparison will be carried over to the two phase analysis believing that the 3D models are better able to capture the flow physics (especially at the piston/seat interface).

For the two phase study, ANSYS FLUENT 18.1 was used in conjunction with a local desktop with 64GB of RAM and an Intel Xeon E5-1620 processor as well as the ARCHIE WeST HPC facility at the University of Strathclyde. As discussed for single phase, the HPC was required due to the significant mesh size used for the Henry 5231BX valve in addition to the more significant computational demands of a two phase CFD simulation. For all 3D simulations for the 5231BX valve on the ARCHIE WeST supercomputer, 280 Intel Xeon Gold 6138 cores with 192GB of RAM per node (40 cores) was utilized. A calculation time of approximately 18-36 hours depending on mesh size and piston displacement (lift) was necessary for a converged steady state solution to be achieved. In addition, the earlier validated K-Omega SST turbulence model will be applied to the two phase model to remain consistent with the

single phase study and allow comparison of flow features captured for each phase.

To remain consistent with the conclusions by both Elmayyah and Alshaikh, the mixture model will be applied for 3D modelling to minimize computational expense as it was deemed sufficiently accurate for the two phase conditions within the PRV. The mixture model was previously defined within section 4.3 where it represents a simplified model compared to the Euler-Euler multiphase model where the two phases are strongly coupled and therefore considered to be homogeneous. From the work of Elmayyah and Alshaikh [11, 12], the validity of the mixture model as an accurate modelling approach has only been demonstrated for low liquid mass fractions of less than 0.4 in 2D modelling.

8.1.3 Two Phase Steady State CFD Modelling Procedure

From the validated results of the 3D modelling approach for the single phase study of the 5231BX PRV, a group of similar boundary conditions were applied to the two phase model due to the use of the pressure based solver. The group of settings used for the two phase model within FLUENT is shown in table 8.4. Notably as previously mentioned, the mixture model has been selected alongside the no slip velocity condition for the homogeneous flow assumption to be valid and to improve computational convergence. Elmayyah [11] concluded that slip only needed to be accounted for at high water mass fraction flows and high lifts. In addition, the PRESTO! spatial discretisation model was used for pressure as recommended by the FLUENT user guide for two phase flow [56]. It should also be noted that to improve convergence of the two phase steady state CFD model, the pseudo-transient time stepping approach was used. This method is a form of implicit under-relaxation for steady-state cases where the time per iteration was higher, but the number of iterations required for convergence is typically dropped by an order of magnitude or more.

FLUENT Setting Type	**Recommended Setting**
Solver Type	Pressure Based
Multiphase Model	Mixture
Mixture Parameters	No Slip Velocity
Phases	Air-Water
Turbulence Model	K-Omega SST
Air Density	Ideal Gas Law (Energy Equation ON)
Solution Scheme	Pseudo-Transient
Pseudo Transient Time Step	Automatic
Pressure-Velocity Coupling Scheme	Coupled
Spatial Discretisation - Gradient	Least Squares Cell Based Scheme
Spatial Discretisation (Pressure)	Presto!
Spatial Discretisation (Other Terms)	Second Order
Initial Volume Fraction Courant Number	100
Momentum and Pressure ERF's	0.1
Density and Energy ERF's	0.1

Table 8.4 – Final 3D Two Phase Solver Settings for Use Across Full Lift Range

The previous justifications given in section 5.2.5 remain for the ideal gas law however the main differences shown in table 8.4 are the use of the second order spatial discretisation for all terms other than pressure and use of a volume fraction Courant number of 100 to promote quicker convergence. In addition, Pseudo transient Explicit Relaxation Factors (ERF's) of 0.1 was used for all variables to ensure computational stability.

For boundary conditions, the values used in the single phase study were adopted however a water volume fraction requires to be specified at the inlet in order to account for the liquid inflow via droplet spray formed by the nozzle

in the experiment. To achieve this, the method described by Alshaikh [12] was adopted where the inlet area is set to an inlet pressure of 10.3 barg and a volume fraction established to inject an appropriate amount of liquid corresponding to the water injection rates used in the experiment. The inlet area represented the full inlet area of the 5231BX PRV downstream of injection where it was assumed that a fully dispersed two phase flow regime was established. Alshaikh in his research found that this method was capable of setting the appropriate phase inlet boundary requirements to match the experiment and found good correlation. Conversely, Elmayyah [11] used a direct simulation of the nozzle injection however significant computational complexity was introduced which, especially for 3D modelling, would significantly increase mesh size and computational time. The set of boundary conditions which were applied for all lift conditions for the PRV two phase 3D CFD model for the validation study were applied as follows;

- **Inlet**
    - Mixture
        - Gauge Total Pressure Inlet of 10.3 barg – which represented vessel pressure, with the zone positioned at the inlet face of the model.
        - A turbulence intensity of 5% and 8.05 mm hydraulic diameter were also input to allow calculation of the inlet turbulence conditions.
    - Water Phase
        - Water volume fraction value consistent with water injection rate from experimental study (2.1 & 0.96 L/min).

Outlet

- Mixture
  - Gauge Pressure Outlet of 0 barg – which represented atmospheric exhaust, positioned at the outlet face of the model. This pressure was set to 0 barg as it was assumed that the flow within the outlet would be choked
  - A turbulence intensity of 5% and 10mm hydraulic diameter were also input to allow calculation of the outlet turbulence conditions.
- Water Phase
  - Backflow volume fraction of 0 to represent atmospheric conditions in experiment.

- Temperature at both inlet and outlet – 295K or 22 ^{0}C
- No slip shear condition on stationary, adiabatic valve walls
- Symmetry boundary condition applied on quarter symmetry planes XZ and YZ.
- Operating Conditions – 1 bar (to offset pressure boundary conditions to gauge)

The previous limitations of the pressure outlet condition identified in the single phase studies will also carry over to the two phase model. This will be further discussed for future recommended where the pressure outlet at the PRV be reconsidered by modelling the surroundings. Furthermore, the CFD best practice guidelines established for the single phase studies were followed by initialising the solution with first order upwind spatial discretisation terms before switching to a higher order scheme after 100-200 iterations. The hybrid initialisation scheme available within FLUENT was used for all cases. Residual requirements for a converged solution were to be below 10e-6 for the energy

equation and 1e-3 for all other terms and/or exhibit residual stability. To achieve a fully converged solution surface monitors for disc force and mass flow rate were used to ensure that a steady state result for both values would be valid.

Using the established mesh and modelling procedure, a two phase 3D validation study was performed for the 5231BX with Modified Gland valve model at 10.3 Barg. The results of the validation study are displayed in terms of percentage error of the CFD to experimental results in table 8.5 for a water injection flowrate of 0.96 L/min and table 8.6 for a water injection flowrate of 2.1 L/min. The comparison of CFD results of piston force, mass flow rate and backpressure vs lift curves to corresponding experimental values are shown in figures 8.15, 8.16 and 8.17 for a water injection of 2.1 L/min and figures 8.18, 8.19 and 8.20 for a water injection rate of 0.96 L/min respectively. In the 3D two phase validation study for the modified gland, disc lift from 0.5 mm to 4mm are studied over a total of 8 data capture points using the quasi steady assumption to incrementally determine the flow force and flow rate across the lift range.

From table 8.6 for a water injection rate of 2.1 L/min, it was shown that the two phase 3D CFD methodology developed could achieve an averaged accuracy across the full lift ranges of 3.6% for mass flow rate and 10.6% for disc force prediction compared to experimental values. Furthermore table 8.5 for a water injection rate of 0.96 L/min highlights that a correlation of CFD to experiment across the full lift ranges of 0.71% for mass flow rate and 14.09% for disc force prediction could be achieved. Therefore a degradation in accuracy for the two phase model can be appreciated when compared to single phase modelling. However it could also be established from the results that a representative 3D CFD model could be achieved for the Henry PRV in two phase conditions with good accuracy for air flowrate and reasonable accuracy for piston force prediction. In a similar manner to the single phase study, for both injection

rates the greatest deviation for piston force occurred within the 2-3 mm region which was earlier identified and discussed in section 5.2.6 where the piston force reported by CFD significantly under predcits compared to experimental results where errors of the order of 25% are observed.

From figures 8.17 and 8.20, an appreciation of back pressure correlation of the CFD model with the experimental results can be established. Interestingly, correlation with back pressure was very good for disc lifts greater than 2 mm. This as a result highlighted that the innacuracy from the CFD model to predict piston force between 2-3 mm is most likely caused by the CFD model's inability to capture the flow features for the inlet facing surfaces of the piston. However for lifts greater than 3 mm, the CFD model is capable of accurately capturing the flow characteristics in this region.

Inaccuracy for backpressure could also be found for piston lifts less than 2 mm with a significant over estimation of the backpresure by the CFD model. The degree of inaccuracy was found to be worse for the 0.96 L/min injection rate case when compared to a higher water flowrate of 2.1 L/min. With reference to figure 8.13, at lower lifts the water mass fraction in the system is greater therefore it would appear that a CFD model induced error occurs for lifts less than 2 mm when predicting back pressure. This supports the conclusions by both Alshaikh and Elmayyah of the limitations of the mixture model. The consequence of this inaccauracy for backpressure can be appreciated in the piston flow graphs shown in figures 8.15 and 8.18 where the piston force predicted is underestimated for lifts less than 2 mm.

Lift (mm)	Experiment Air Mass Flow Rate (Kg/s)	CFD Air Mass flow rate (Kg/s)	Error in Mass Flow Rate (%)	Experiment Disc Force (N)	CFD Disc Force (N)	Error in Disc Force (%)
0.8	0.0223	0.0200	-10.3	83.3	75.7	-9.1
1.125	0.0298	0.0257	-13.5	87.3	78.7	-9.9
1.5	0.0370	0.0337	-8.9	89	79.4	-10.8
2	0.0464	0.0439	-5.4	90.8	76.2	-16
2.5	0.0546	0.0539	-1.2	92.6	70.2	-24.2
3	0.0611	0.0615	0.8	96.5	83	-14
3.5	0.0639	0.0662	3.6	101.9	100.9	-1
4	0.0636	0.0677	6.5	108.2	108.3	0.1
Average % difference			**-3.6**			**-10.6**

Table 8.5 - Validation Results for Two Phase Henry 5231BX Modified Gland 3D CFD Model for Injection of 2.1 L/min

Lift (mm)	**Experiment Air Mass Flow Rate (Kg/s)**	**CFD Air Mass flow rate (Kg/s)**	**Correlation of Mass Flow Rate (%)**	**Experiment Disc Force (N)**	**CFD Disc Force (N)**	**Correlation of Disc Force (%)**
0.8	0.0300	0.0267	-11	84	70	-16.7
1.125	0.0320	0.0320	0	90	72.2	-19.8
1.5	0.0358	0.0395	10.2	91	77.3	-15.1
2	0.0562	0.0517	-8	91.4	81	-11.4
2.5	0.0656	0.0631	-3.8	96	73.4	-23.5
3	0.0723	0.0710	-1.8	104	92.7	-10.9
3.5	0.0743	0.0756	1.7	113	100.2	-11.3
4	0.0726	0.0776	6.9	113	108.5	-4
Average % difference			**-0.7**			**-14.1**

Table 8.6 - Validation Results for Two Phase Henry 5231BX Modified Gland 3D CFD Model for Injection of 0.96 L/min

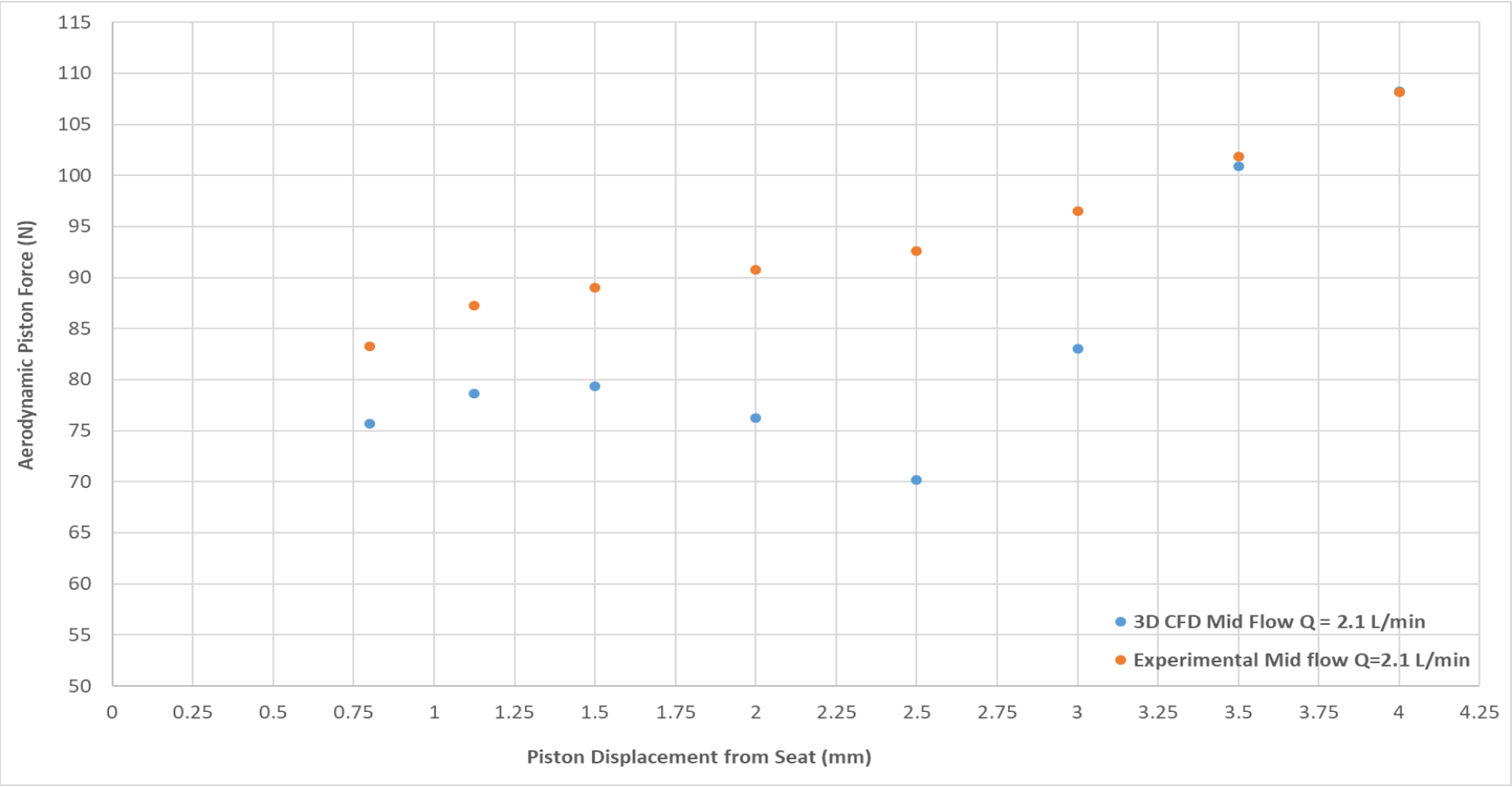

Figure 8.15 – Force vs Lift for Two Phase Henry 5231BX Modified Gland 3D CFD Model for Injection of 2.1 L/min

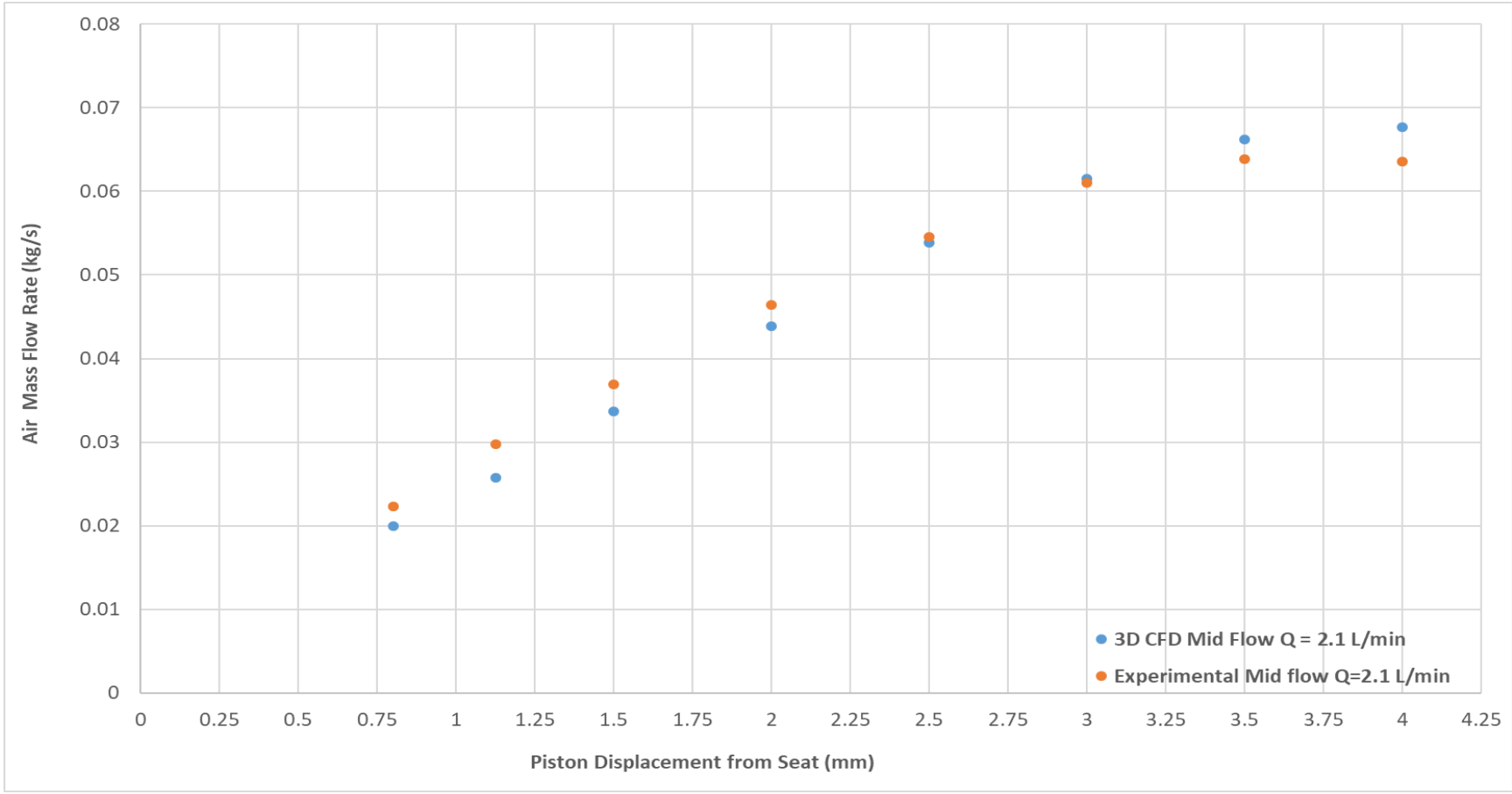

Figure 8.16 – Air Mass Flow Rate vs Lift for Two Phase 5231BX Modified Gland 3D CFD Model for Injection of 2.1 L/min

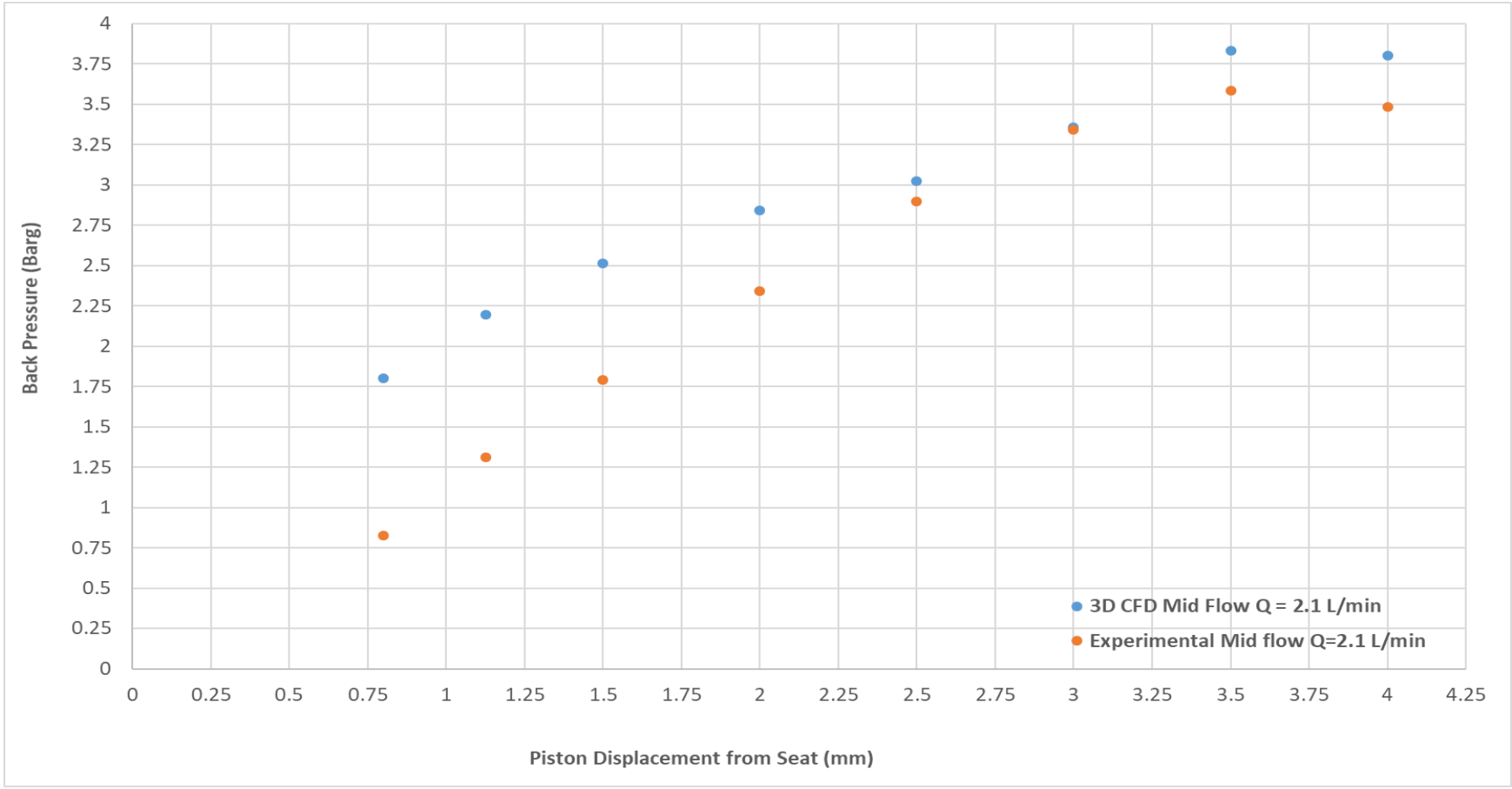

Figure 8.17 – Back Pressure vs Lift for Two Phase Henry 5231BX Modified Gland 3D CFD Model for Injection of 2.1 L/min

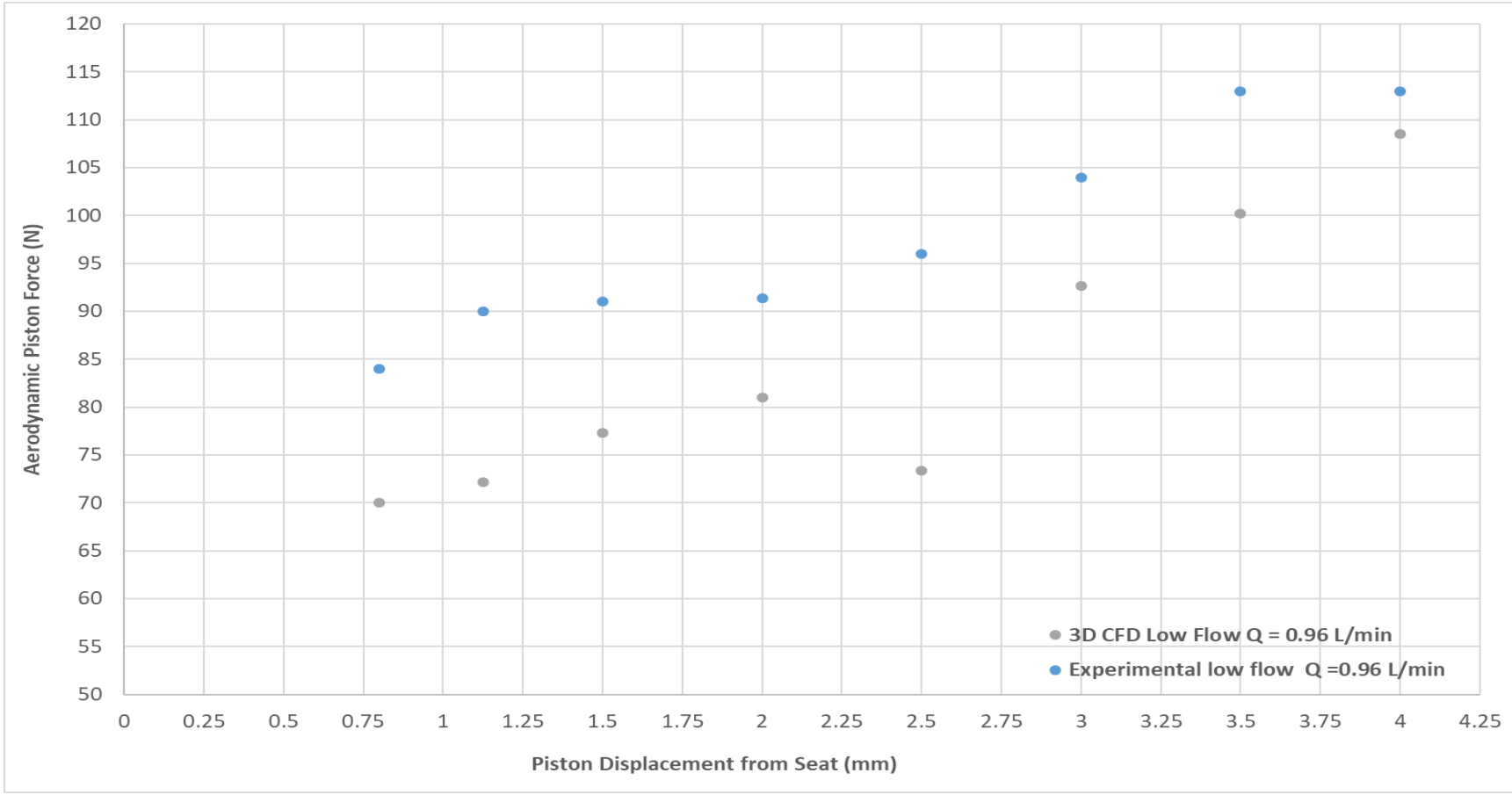

Figure 8.18 - Force vs Lift for Two Phase Henry 5231BX Modified Gland 3D CFD Model for Injection of 0.96 L/min

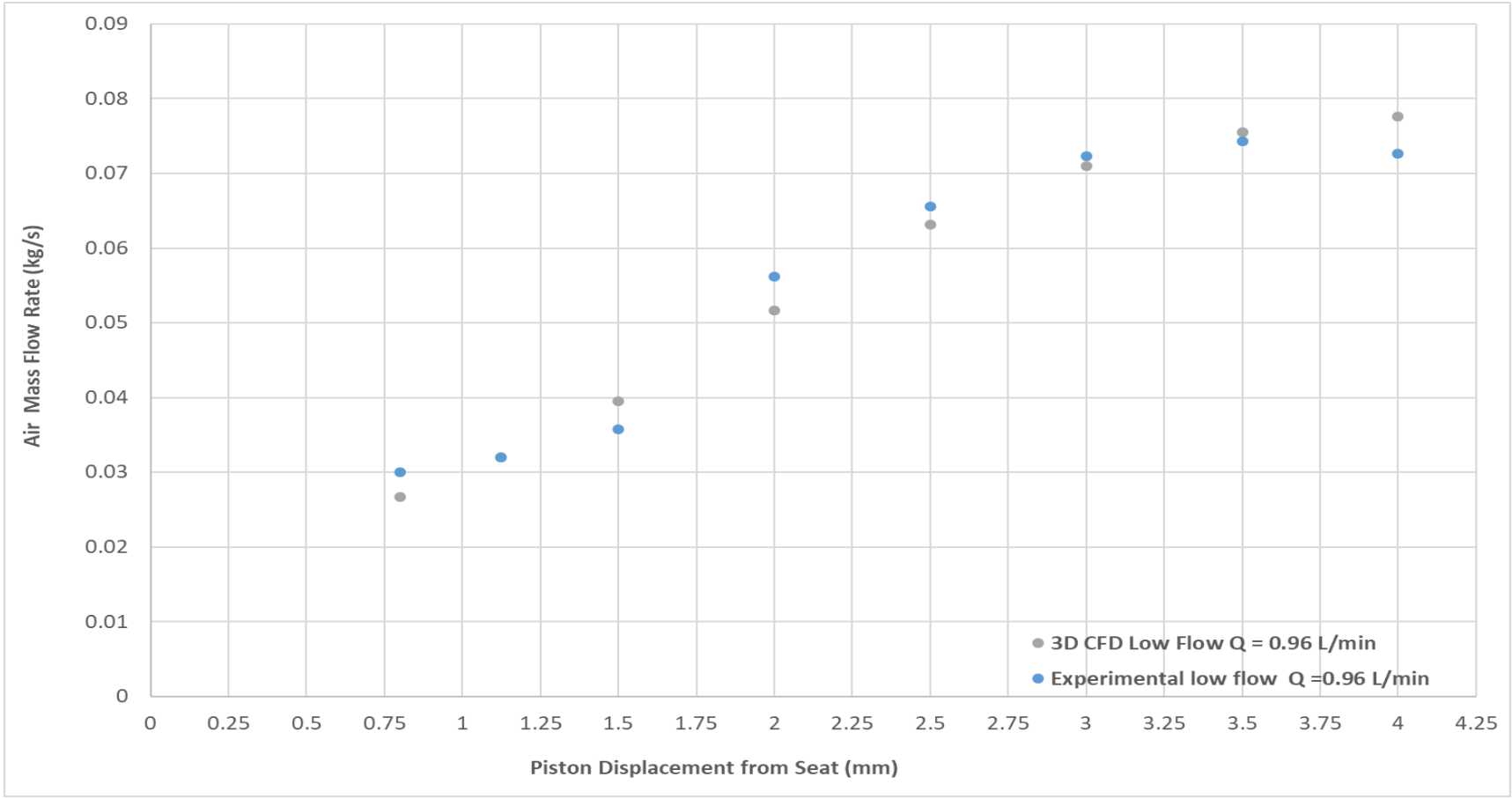

Figure 8.19 - Air Mass Flow Rate vs Lift for Two Phase 5231BX Modified Gland 3D CFD Model for Injection of 0.96 L/min

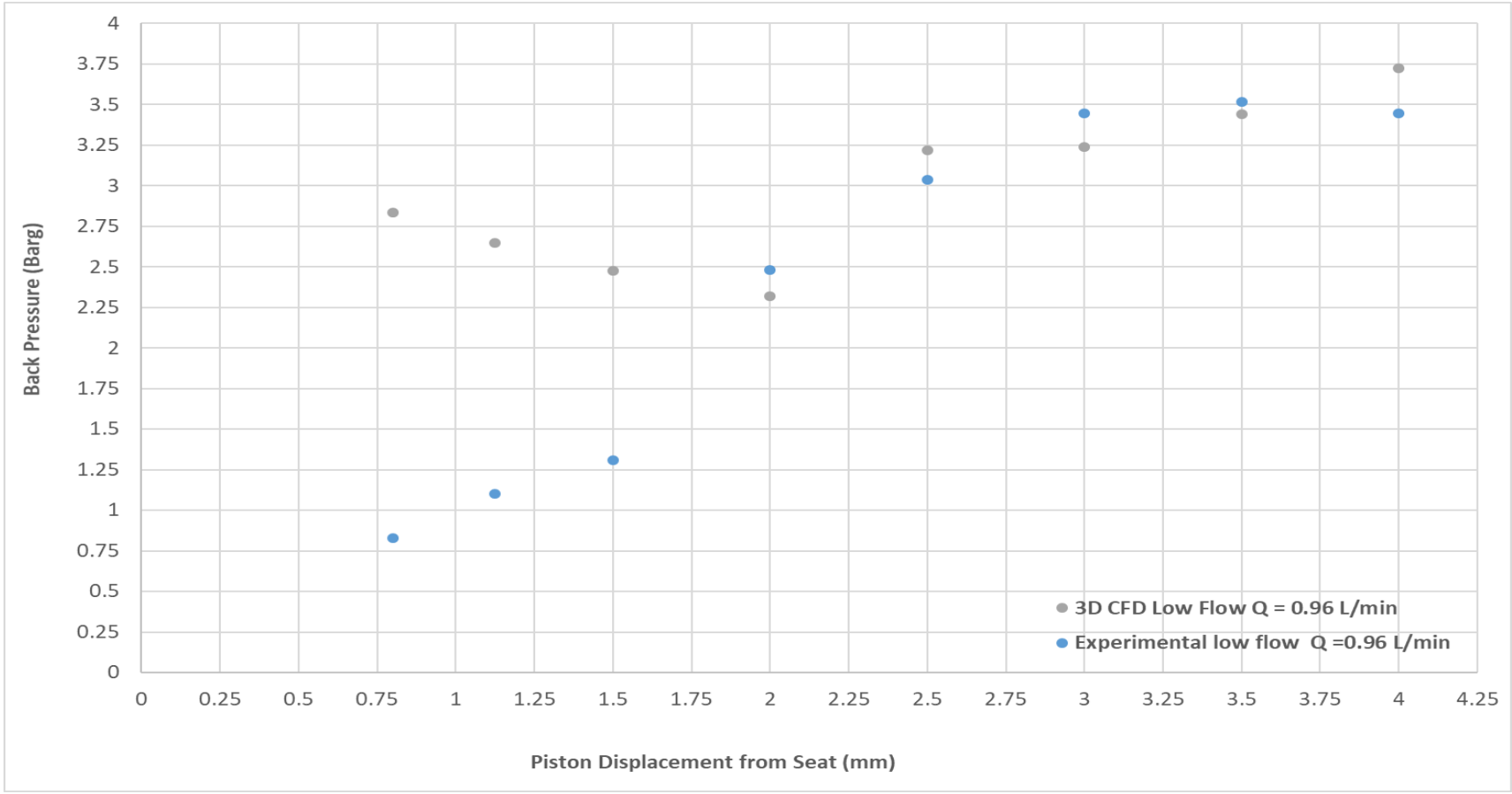

Figure 8.20 - Back Pressure vs Lift for Two Phase Henry 5231BX Modified Gland 3D CFD Model for Injection of 0.96 L/min

In general it could be concluded that in a similar manner to the single phase CFD model, the two phase CFD mixture model was capable of capturing the trends observed from the experimental results of the piston force. This behaviour is significantly different to the studies performed by both Elmayyah [11] and Alshaikh [12] where a monotonically increasing piston force vs lift curve was generated due to the use of a larger diameter, non-manufacturer specification outlet. Therefore, as established in section 5.2.5, this suggests that the outlet geometry of the Henry 5231BX PRV has a significant impact on the flow force behaviour of a PRV also in two phase operation. It should be noted that the peak force predicted by the CFD model for high disc lifts of 4mm exhibited correlation to experiment of 4% for 0.96 L/min injection rate compared to 1% for 2.1 L/min. From figures 8.16 and 8.19 the maximum mass flow rate prediction by CFD and experimental measurements was also in close agreement to within 7%; with the plateau for maximum flow rate being achieved at approximately 3.5mm.

8.1.4 Discussion of CFD Flow Features for Two Phase Model

From the two phase CFD validation results presented in section 8.1.3, it was necessary to understand the variation in accuracy across the 0.5 mm-4 mm lift range for piston force, air mass flow rate and back pressure. This would be achieved by comparing contour plots of mach number, static pressure and water volume fraction at lifts of 1.125 mm, 2.5 mm and 4 mm for both 2.1 L/min and 0.96 L/min water injection rates. In addition, for each plot a side by side comparison will be used for both the XZ and YZ planes of the quarter symmetry model to investigate if any occurrence of symmetry breaking was present in the CFD model and compared with the conclusions of the single phase study. Furthermore a comparison of flow features between both water injection rates and single phase conditions to determine the difference in flow characteristics caused by increasing water mass fraction.

It should be noted that for the mixture model used in ANSYS Fluent, the theory guide [48] does not sufficiently detail the determination of speed of sound for the mixture. However as discussed by Alshaikh [12] there is evidence which indicates that the reported Mach number is referred to the air phase velocity rather than the mixture velocity of the air-water flow. Alshaikh [12] highlighted that from the two fluid models of Städtke, the nonhomogeneous mixture acoustic speed was based on the Wallis model in which the air phase velocity is not equal to the water phase velocity for the calculation of the Mach number presented for an air volume fraction in the range 0.95-1. The effective/approximate Mach number was defined by Alshaikh [12] as follows in equation 8.1 using substitution from equation 8.2:

$$Mach\ Number = \frac{gas\ velocity\ (v_g)}{nonhomogeneous\ mixture\ sound\ velocity\ (a_{mixture})} \quad \textbf{Equation 8.1}$$

$$a_{nonhomogeneous\ mixture} = \sqrt{\frac{\alpha_g\rho_l + \alpha_l\rho_g}{\frac{\alpha_g\rho_l}{a_g^2} + \frac{\alpha_l\rho_g}{a_l^2}}} \quad \textbf{Equation 8.2}$$

Where:

ρ_l = liquid phase density, α_g = gas phase volume fraction,

ρ_g = gas phase density, α_l = liquid phase volume fraction.

a_g = sound velocity in air, a_l = sound velocity in water.

The definition of Mach number shown in equation 8.1 was checked by Alshaikh [12] against the data presented by the fluent code, using custom field functions (CFFs) provided in the fluent code. The Mach number values were found to give similar results presented by the fluent code which therefore validated the use of equation 8.1 as an appropriate representation of the code.

Figures 8.21 and 8.22 illustrate contours of water volume fraction for a water injection rate of 0.96 L/min and 2.1 L/min respectively. It could be appreciated

that for both cases an increase in water volume fraction could be found at the lower surface of the PRV body in the piston/seat interface region. This area is highlighted by a dashed red box within figure 8.21 and is located within a region of recirculation caused by the flow structure of the bulk flow moving through the channel between the piston and seat (piston/seat interface). It's also important to note that a difference in water volume fraction could be found at both injection rates for the XZ and YZ symmetry planes. This therefore highlights symmetry breaking flow characteristics found for single phase flow also occur for two phase CFD modelling.

When comparing figures 8.21 and 8.22, within the central area of the lower piston surface, the water volume fraction for the 2.1 L/min case is greater (0.017) than that of the 0.96 L/min case (0.008) which intuitively makes sense. However, within the dashed box region highlighted within figure 8.21, the water volume fraction in this region is greater for the 0.96 L/min case when compared to 2.1 L/min case. This therefore suggests that there is a greater build-up of water for the 0.96 L/min condition and as a result has a greater impact on the flow characteristics by limiting the bulk flow path through the piston/seat interface region at lower lifts. This conclusion is supported in the contour plots of Mach number in figures 8.23 and 8.24 where a significant variation of flow structure could be observed in the piston/seat region. The effect of symmetry breaking can also be observed by comparing the Mach number contours of the XZ and YZ planes for both injection rates. The corresponding effect on the static pressure distribution at the piston surfaces are shown in figures 8.25 and 8.26 where a greater area of low pressure is shown at the lower piston surface highlighted by the yellow dashed box. This as a result would generate a lower piston force for the 0.96 L/min condition when compared with 2.1 L/min for an equivalent back pressure.

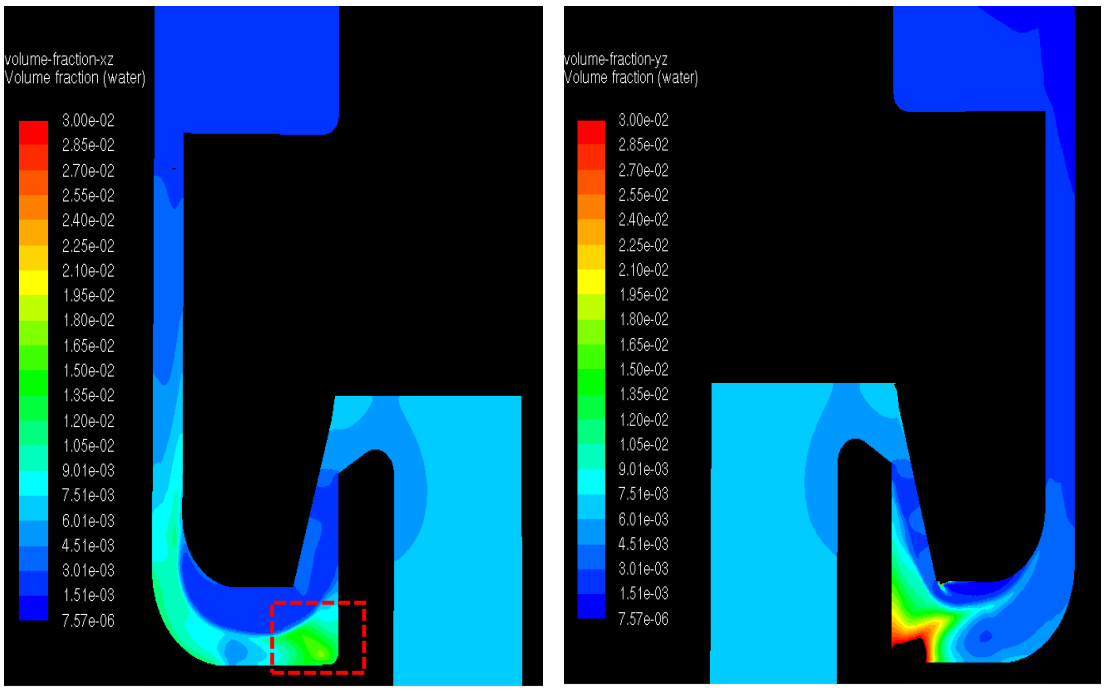

Figure 8.21 – Two Phase Water Volume Fraction Comparison of XZ Plane (left) and YZ Plane (right) at 1.125 mm for Water Injection Rate of 0.96 L/min

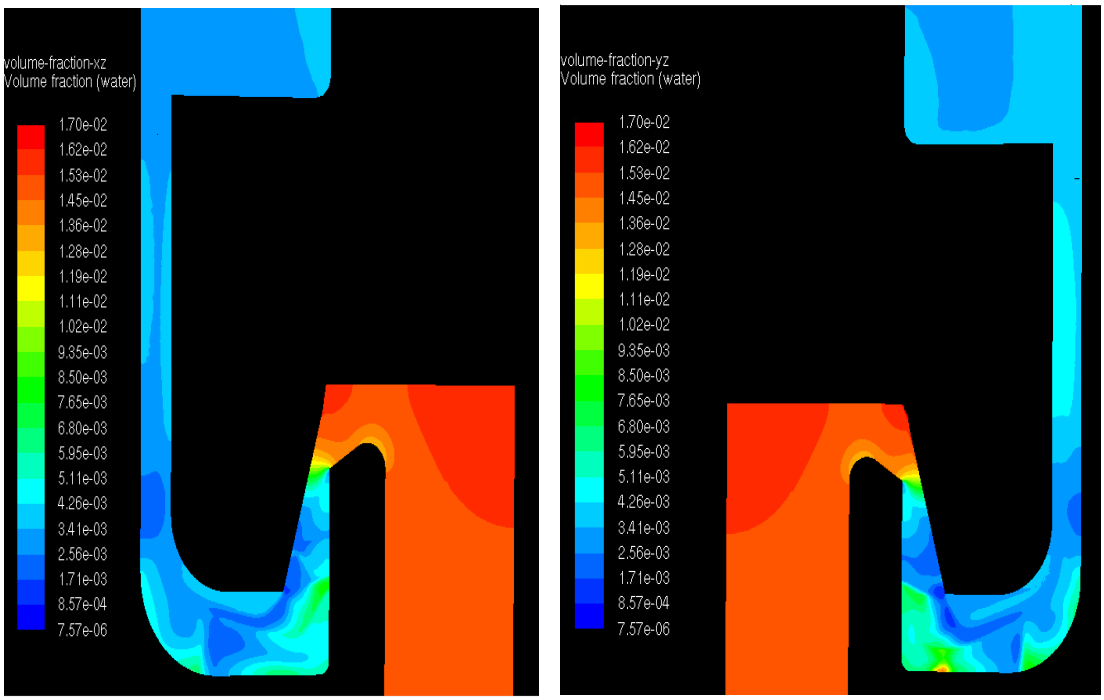

Figure 8.22 – Two Phase Water Volume Fraction Comparison of XZ Plane (left) and YZ Plane (right) at 1.125 mm for Water Injection Rate of 2.1 L/min

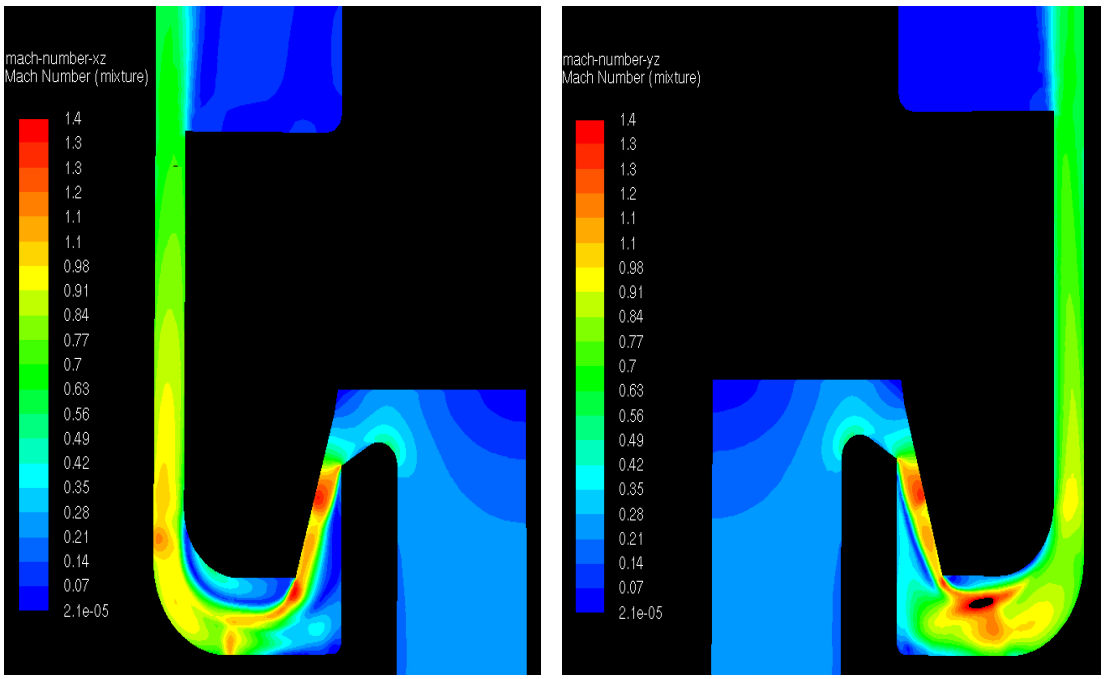

Figure 8.23 - Two Phase Mach Number Comparison of XZ Plane (left) and YZ Plane (right) at 1.125mm for Water Injection Rate of 0.96 L/min

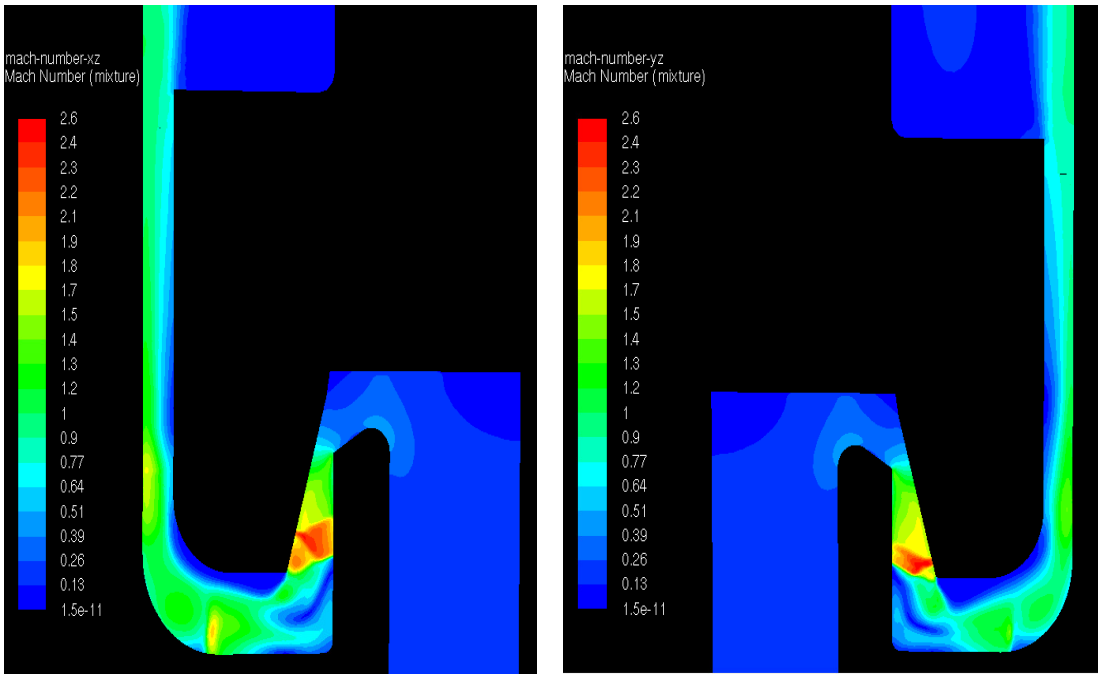

Figure 8.24 - Two Phase Mach Number Comparison of XZ Plane (left) and YZ Plane (right) at 1.125 mm for Water Injection Rate of 2.1 L/min

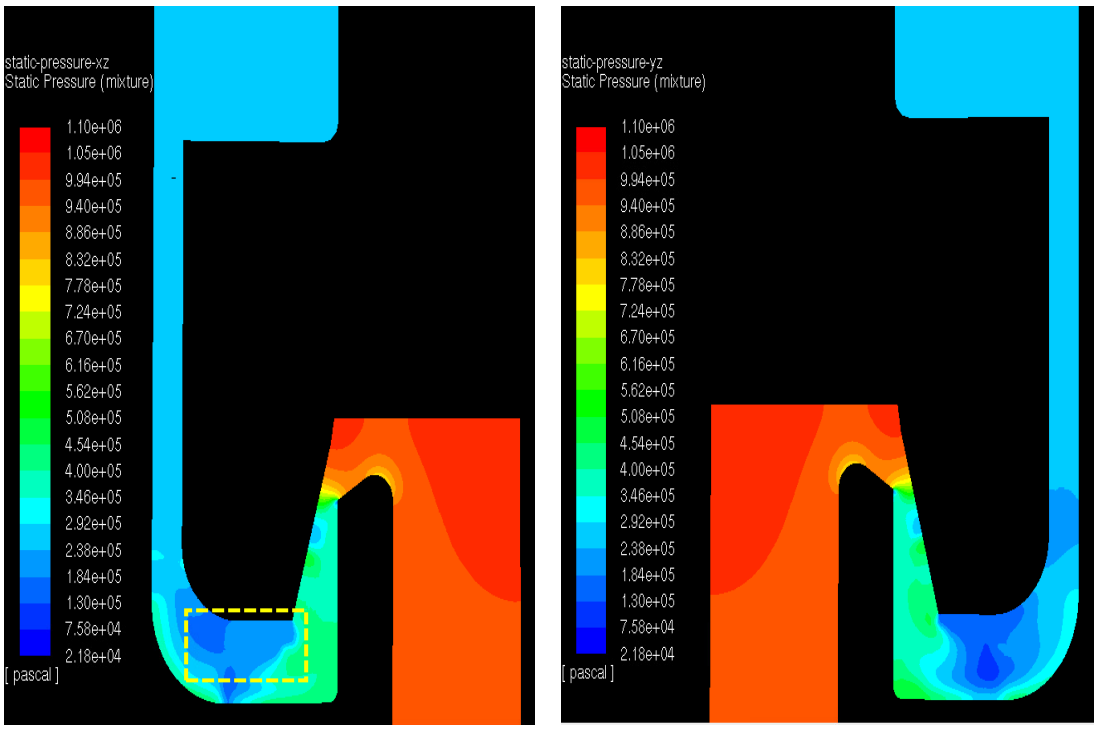

Figure 8.25 - Two Phase Static Pressure Comparison of XZ Plane (left) and YZ Plane (right) at 1.125mm for Water Injection Rate of 0.96 L/min

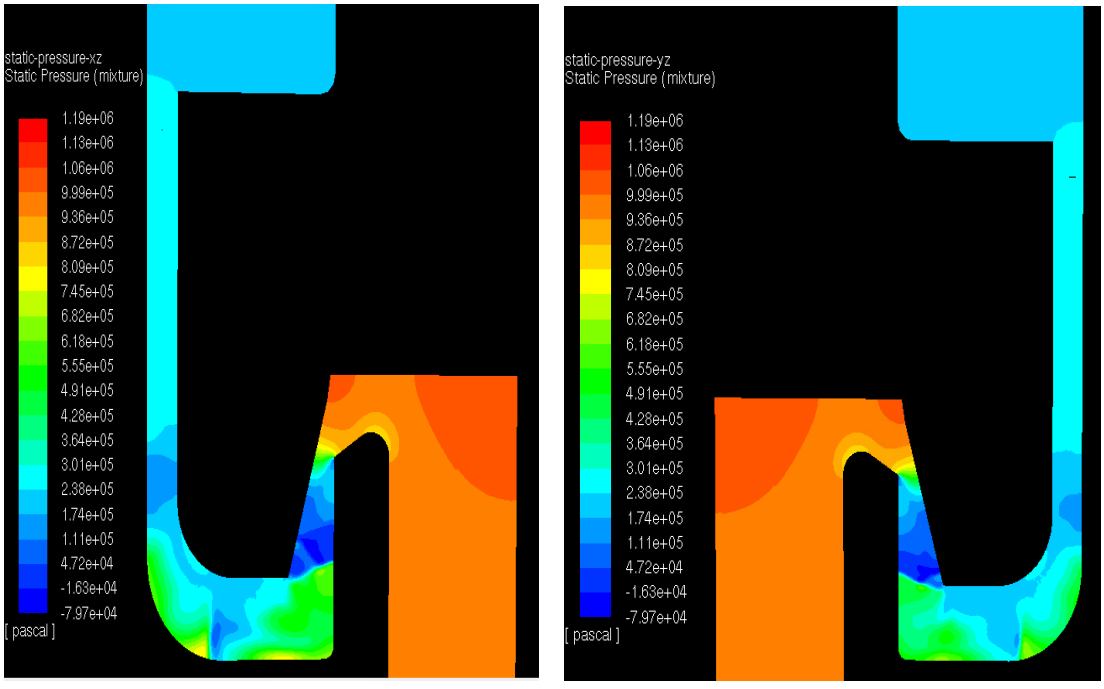

Figure 8.26 - Two Phase Static Pressure Comparison of XZ Plane (left) and YZ Plane (right) at 1.125mm for Water Injection Rate of 2.1 L/min

Interestingly from figures 8.23 and 8.24, it was clear that the Mach number reached in the annulus region between the piston and valve body was less than 1. When compared with single phase operation, this flow characteristic is different where the flow was found to choke in this region. As a result, it could be appreciated that when operating in two phase conditions, the choking points found during the single phase study are likely to change and hence static pressure distribution which would have a subsequent effect on piston force. In addition, as the choking point in two phase operation will move downstream towards the seat; there would be a change in flowrate due to a change in effective flow area.

Figures 8.27 and 8.28 represent the water volume fraction distribution at the piston/seat interface for a disc lift of 2.5 mm. This lift region was shown in tables 8.5 and 8.6 to exhibit the poorest correlation and greatest under prediction with the experimental piston force value therefore it's crucial to explore the potential causes of the inaccuracy within CFD with respect to the predicted flow structure. As can be appreciated from figures 8.27 and 8.28, the observation of water build-up for the 0.96 L/min condition at the lower seat surface was not evident where more intuitively the 2.1 L/min case exhibited higher water volume fractions. In addition, the effect of symmetry breaking appeared to be less apparent at 2.5 mm suggesting an axisymmetric flow structure. This is confirmed within the Mach number contours in figures 8.29 and 8.30 with similar flow behaviour across both the XZ and YZ symmetry planes. In addition, the general flow structure was consistent for both injection rates which results in a similar static pressure profile at the piston surface as shown in figures 8.31 and 8.32. From figures 8.29-32 a similar profile for both Mach number and static pressure could be observed at 2.5 mm with a large recirculation region forming below the outer radius of the front piston surface. This as a result reduces the piston force and as discussed earlier in section 5.2.6 is a likely source of the under estimation of the piston force by the CFD model at 2.5 mm – 3 mm lift region.

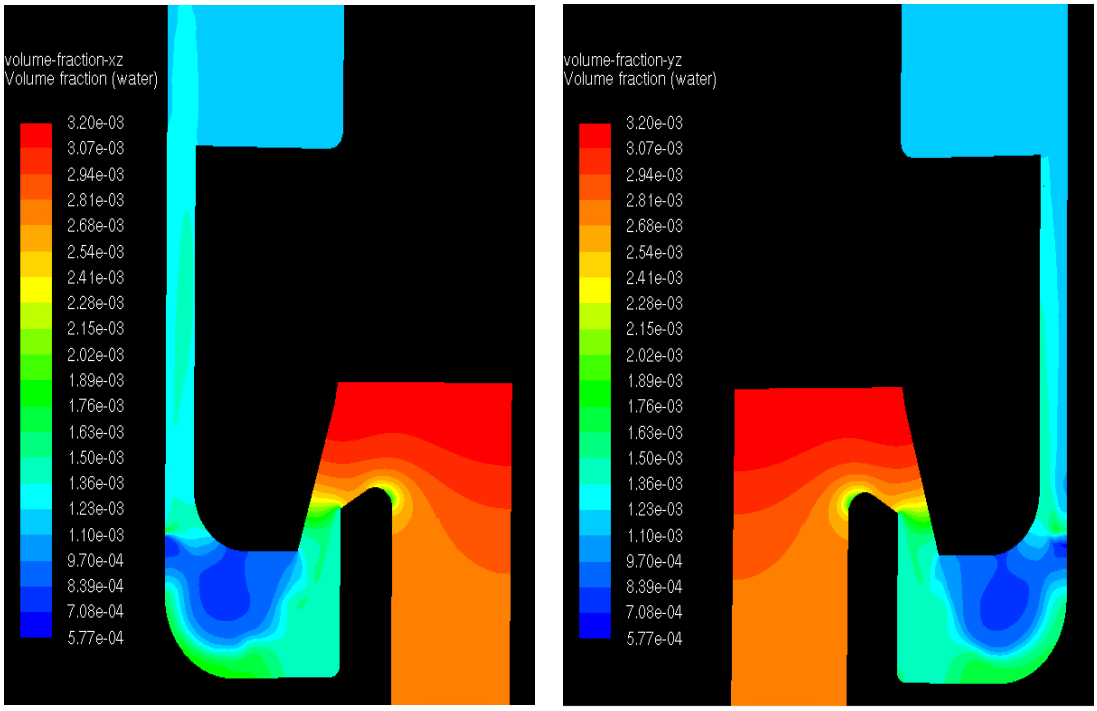

Figure 8.27 - Two Phase Water Volume Fraction Comparison of XZ Plane (left) and YZ Plane (right) at 2.5mm for Water Injection Rate of 0.96 L/min

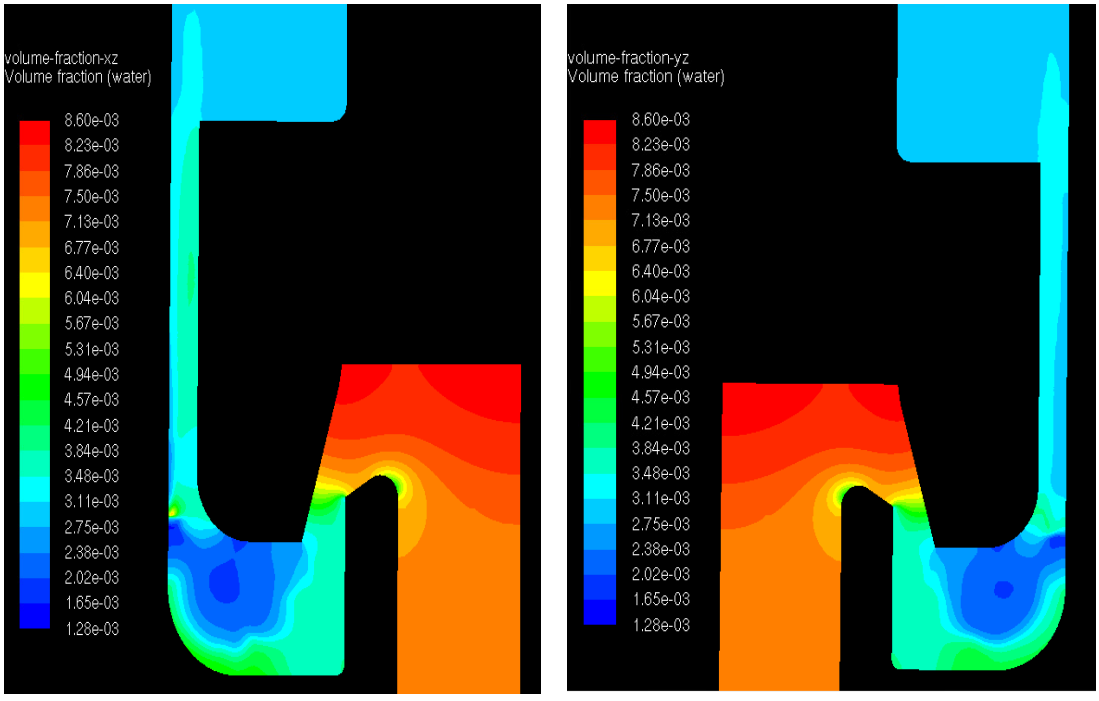

Figure 8.28 - Two Phase Water Volume Fraction Comparison of XZ Plane (left) and YZ Plane (right) at 2.5 mm for Water Injection Rate of 2.1 L/min

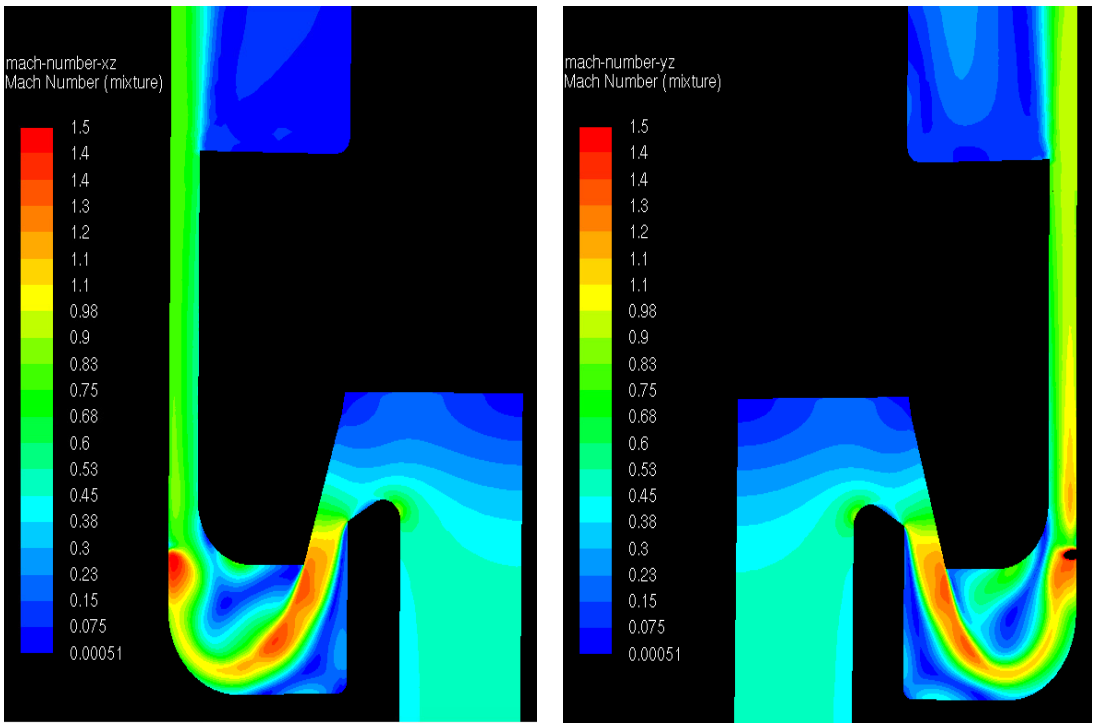

Figure 8.29 - Two Phase Mach Number Comparison of XZ Plane (left) and YZ Plane (right) at 2.5 mm for Water Injection Rate of 0.96 L/min

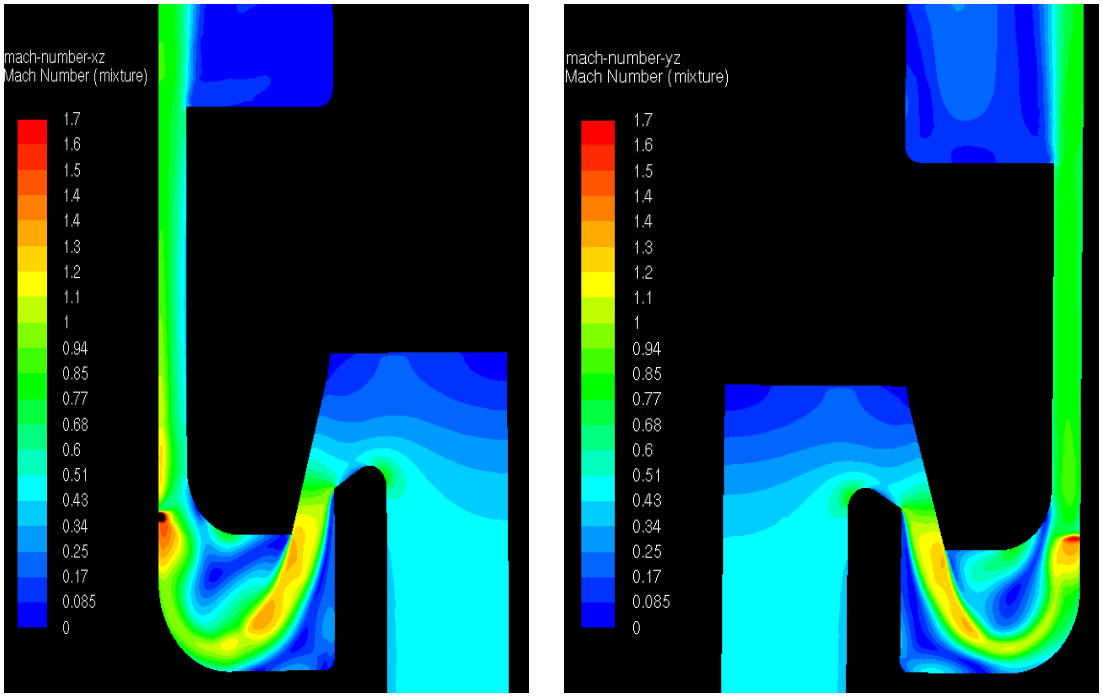

Figure 8.30 - Two Phase Mach Number Comparison of XZ Plane (left) and YZ Plane (right) at 2.5 mm for Water Injection Rate of 2.1 L/min

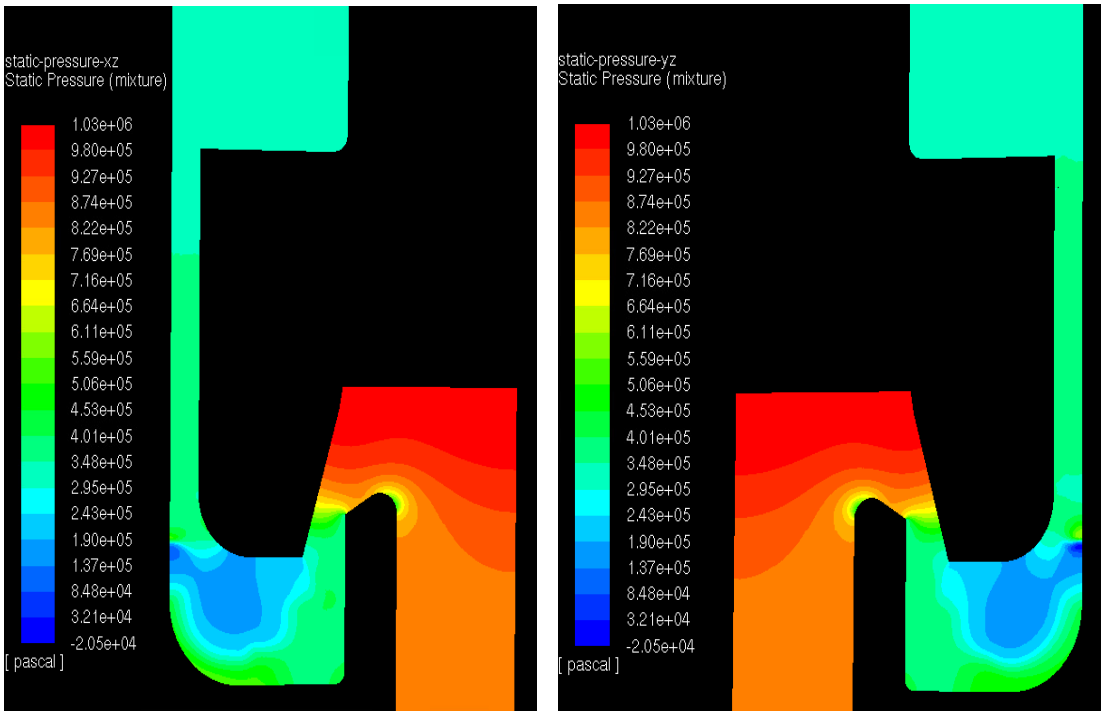

Figure 8.31 - Two Phase Static Pressure Comparison of XZ Plane (left) and YZ Plane (right) at 2.5mm for Water Injection Rate of 0.96 L/min

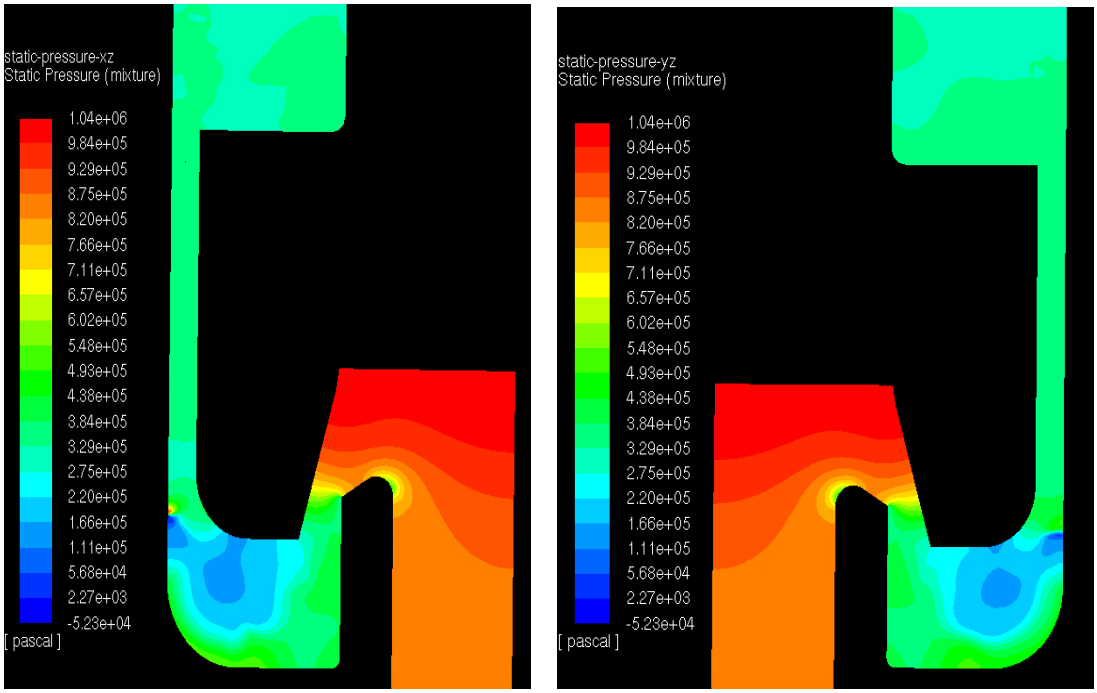

Figure 8.32 - Two Phase Static Pressure Comparison of XZ Plane (left) and YZ Plane (right) at 2.5mm for Water Injection Rate of 2.1 L/min

At a piston lift of 4 mm, the water volume fraction distribution for the steady state CFD model for both water injection rates is shown in figures 8.33 and 8.34. For the 2.1 L/min injection case a significantly greater liquid volume fraction could be found in the region marked by the red dashed box in figure 8.34 when compared with the 0.96 L/min case. In addition, the volume fraction distribution profile in this region was also found to be significantly different for both injection rates. A greater degree of symmetry breaking could also be identified for the 2.1 L/min condition. The corresponding contours of Mach number are shown within figures 8.35 and 8.36, however in general the flow characteristics were found to be similar in terms of choking point locations and recirculation region sizes. In accordance with the observations from figures 8.33 and 8.34, the 2.1 L/min injection case demonstrates more significant symmetry breaking for Mach number distribution at 4 mm when compared to 0.96 L/min which is likely caused by a greater volume of water in the recirculation regions.

The static pressure profiles at 4 mm for both injection rates are shown in figures 8.37 and 8.38 where conditions exhibit almost identical static pressure distribution at the piston surface with only slight differences in the region highlighted in yellow for 2.1 L/min. In general, the effect of symmetry breaking is not significant for static pressure distribution at 4 mm for the two phase flow regime.

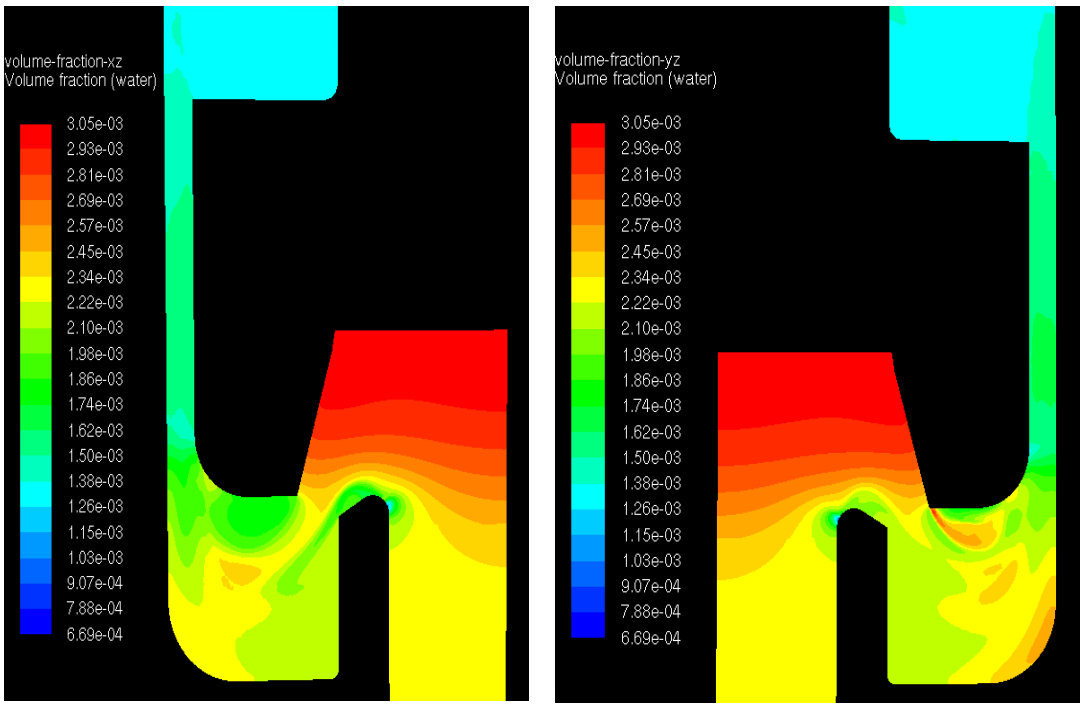

Figure 8.33 - Two Phase Water Volume Fraction Comparison of XZ Plane (left) and YZ Plane (right) at 4mm for Water Injection Rate of 0.96 L/min

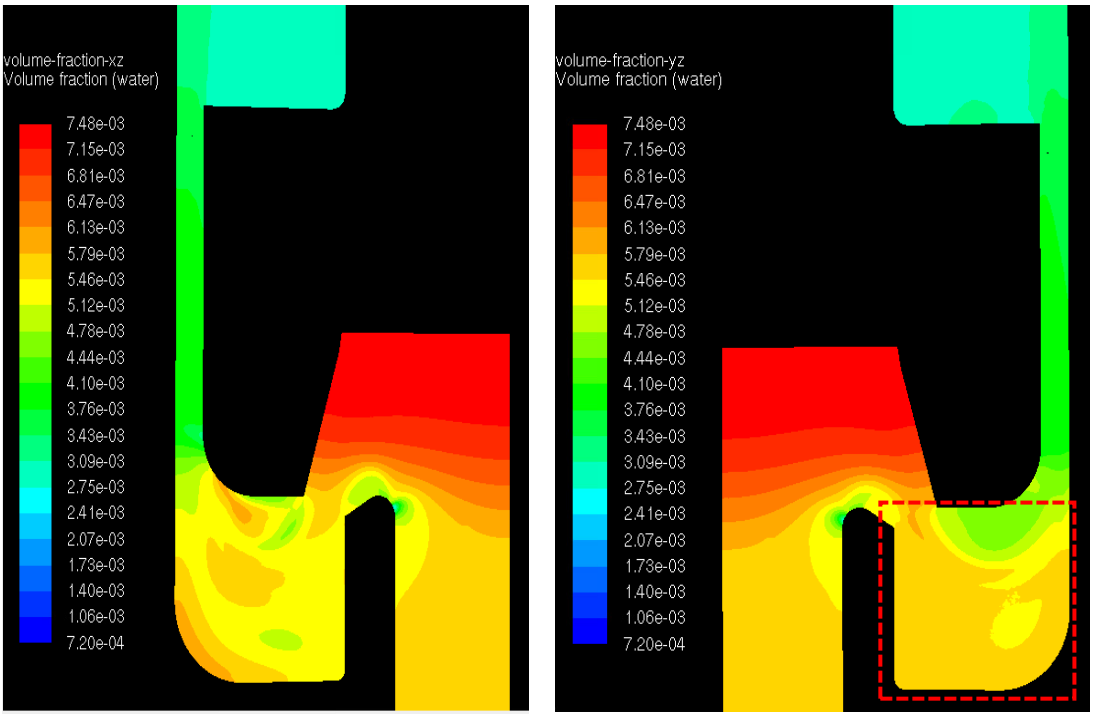

Figure 8.34 - Two Phase Water Volume Fraction Comparison of XZ Plane (left) and YZ Plane (right) at 4 mm for Water Injection Rate of 2.1 L/min

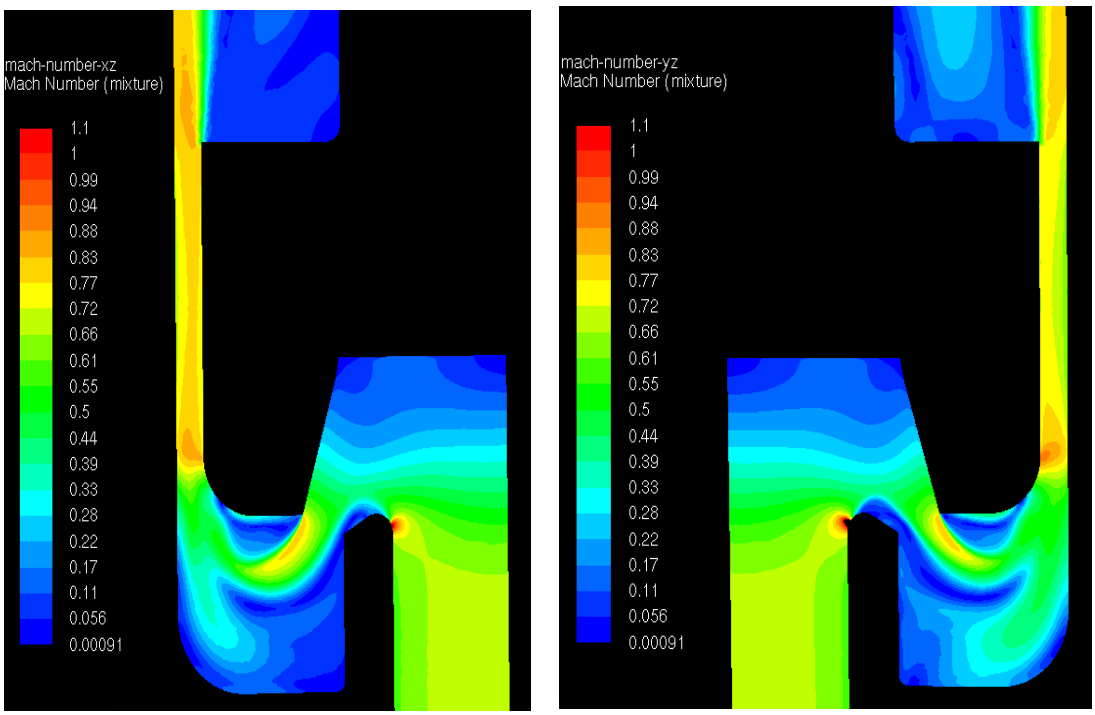

Figure 8.35 - Two Phase Mach Number Comparison of XZ Plane (left) and YZ Plane (right) at 4 mm for Water Injection Rate of 0.96 L/min

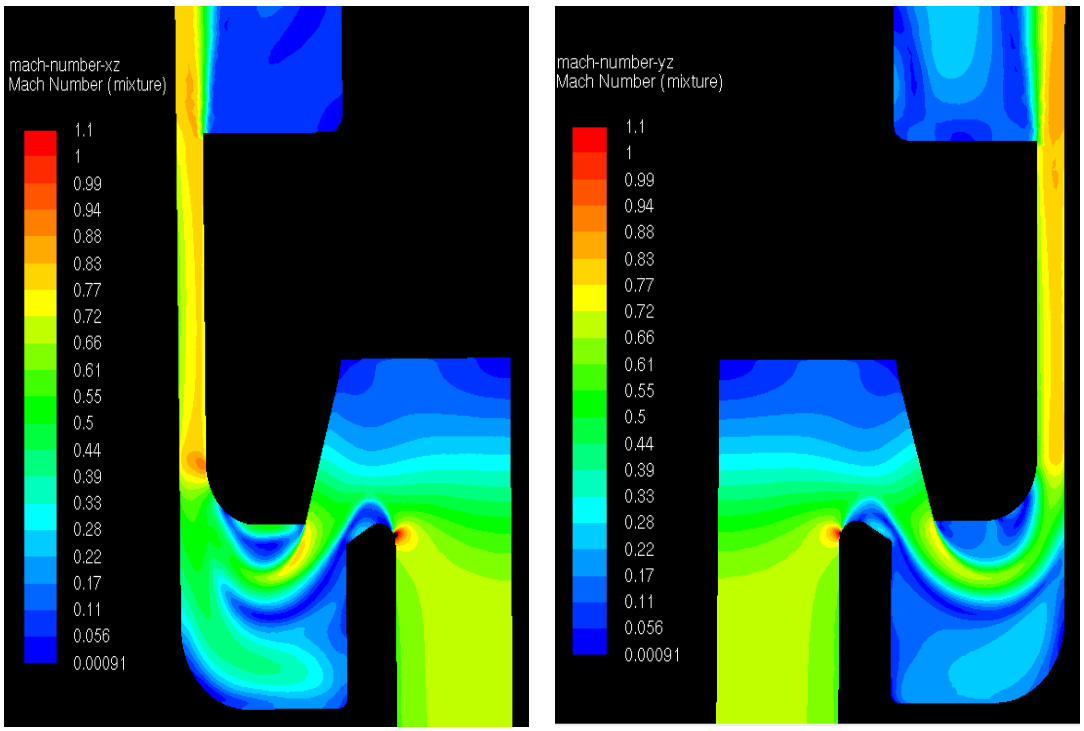

Figure 8.36 - Two Phase Mach Number Comparison of XZ Plane (left) and YZ Plane (right) at 4 mm for Water Injection Rate of 2.1 L/min

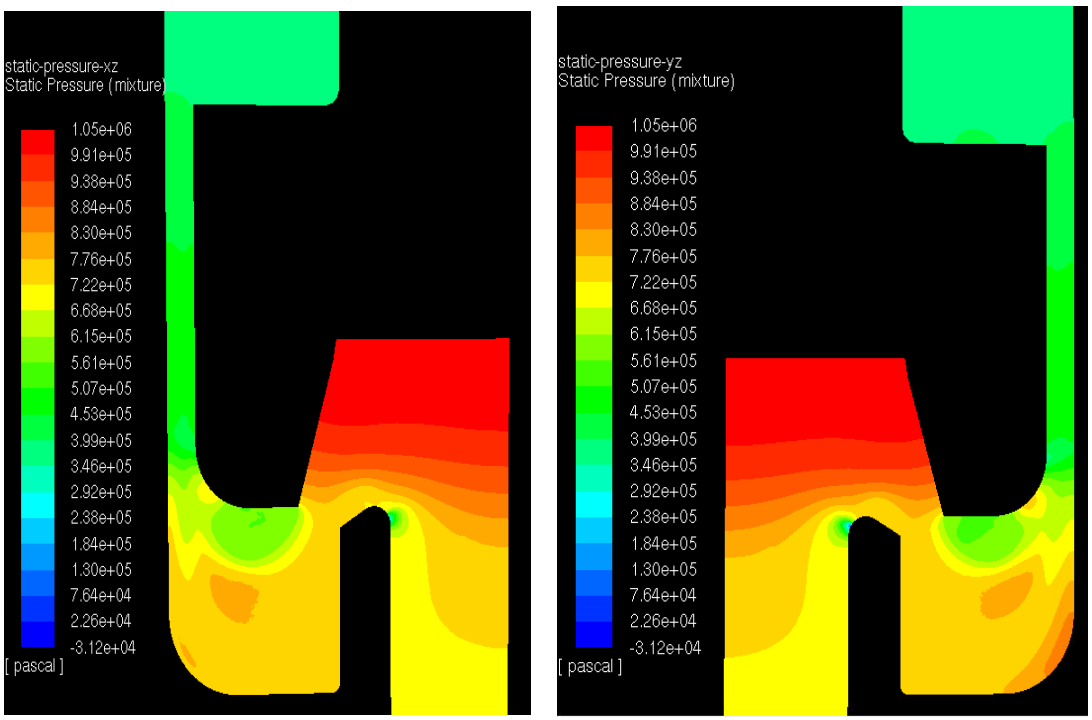

Figure 8.37 - Two Phase Static Pressure Comparison of XZ Plane (left) and YZ Plane (right) at 4 mm for Water Injection Rate of 0.96 L/min

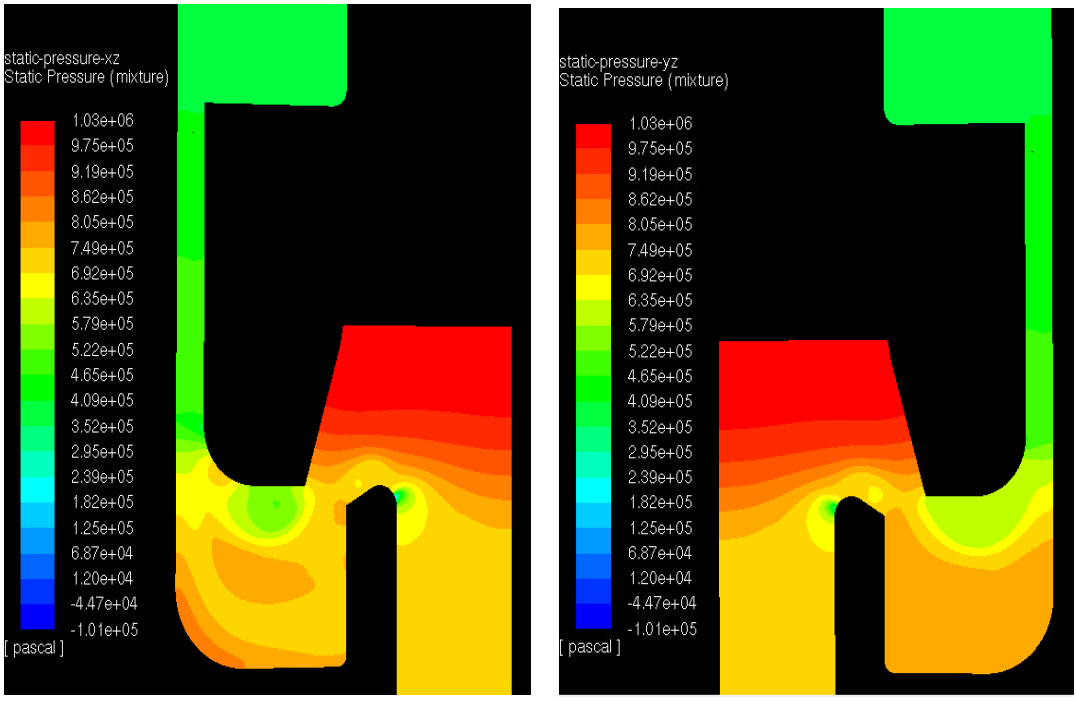

Figure 8.38 - Two Phase Static Pressure Comparison of XZ Plane (left) and YZ Plane (right) at 4 mm for Water Injection Rate of 2.1 L/min

The observations discussed from figures 8.33-38 are highlighted further in figures 8.40, 8.41 and 8.42 which compare the CFD reported values for piston force, air mass flow rate and back pressure for single phase and two phase air water flow with 0.96 L/min and 2.1 L/min water injection rates. From figure 8.40 several trends can be appreciated. In general, from a lift of 0.5 mm-4 mm the relationship established from the experiment is shown to be consistent with that predicted by CFD with single phase piston force being lower than that of two phase flow. From figure 8.40, it is also clear that an effect can be observed for increasing water injection rate on the CFD model for lifts lower than 3 mm. However, from 3 mm-4 mm disc lift results for both injection rates are similar which is not in agreement with experimental observations as increasing flow rate caused a noticeable reduction in piston force. This is likely to be caused by error induced by the mixture model in the peripheral piston/seat recirculation region discussed earlier. The cause of the differences in piston force at 4 mm could be appreciated from turbulence intensity plots shown in figure 8.39 which compares single phase CFD results to two phase. From evaluation of figure 8.39 it was clear that the cause of the reduction in piston force for single phase flow at 4 mm lift was due to a larger recirculation area shown within the red box which in turn resulted in a larger lower pressure region at the piston surface.

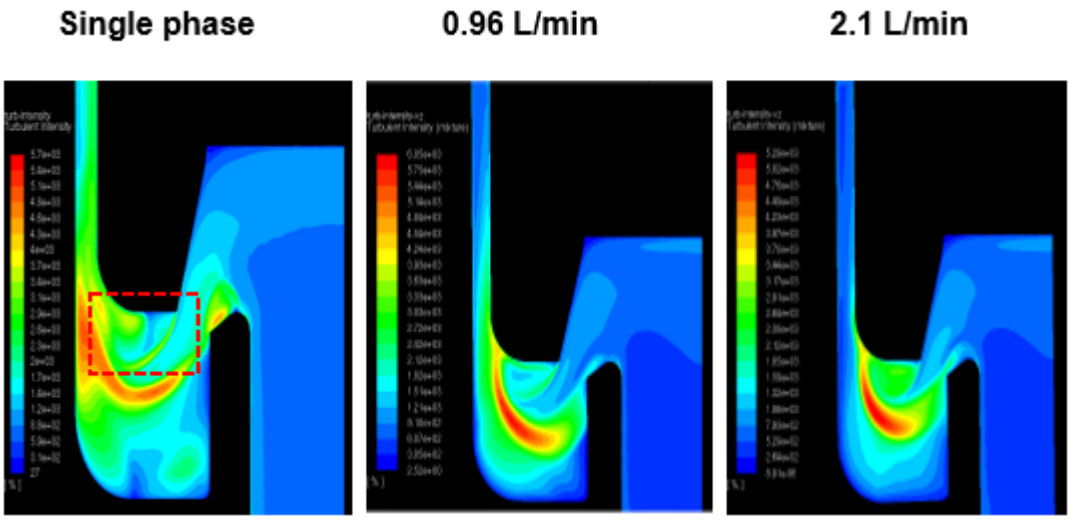

Figure 8.39 – Turbulence Intensity Comparison of CFD Single Phase vs Two Phase at 4 mm Lift for Henry 5231BX PRV

However, for the air mass flow rate relationships shown in figure 8.41 the experimental relationship defined in 8.1.1 is captured by the CFD model where with increasing water injection rate at a pressure of 10.3 barg; air mass flow rate would decrease. This therefore highlights the strong capability of the CFD model to capture the general flowrate characteristics caused by increasing water volume fraction from single phase flow.

Most significantly, for backpressure as shown in figure 8.42, the greatest deviation to the experimental trends stated in 8.1.1 could be found. For the experiment, backpressure for all water injection rates including single phase were approximately equal however from the values predicted by CFD, significant differences could be found. The error is most significant for lifts less than 2.5 mm where the backpressure predicted by the two phase CFD mixture model is significantly higher than single phase. To explore this observation further, contour plots of Mach number and static pressure were generated for the outlet section of the PRV; figures 8.43 and 8.44 correspond to a disc lift of 1.125 mm whereas figures 8.45 and 8.46 correspond to a disc lift of 4 mm.

As expected from figure 8.42, for a disc lift of 4 mm both the bulk flow features in the Mach number contour plot and static pressure plot (figures 8.43 and 8.44) are similar for all flow regimes which as a result allows an approximately equal value of backpressure to be achieved. However as can be seen from figure 8.43 despite the bulk flow features also being similar at 1.125 mm for the Mach number distribution; significant variation in static pressure could be observed in figure 8.44 with increasing back pressure as water injection rate increases and hence water volume fraction. From the two phase validation results presented earlier within tables 8.5 and 8.6 as well as figure 8.17 such an increase in backpressure with water volume fraction is not accurate and therefore an error induced by using the homogenous mixture model.

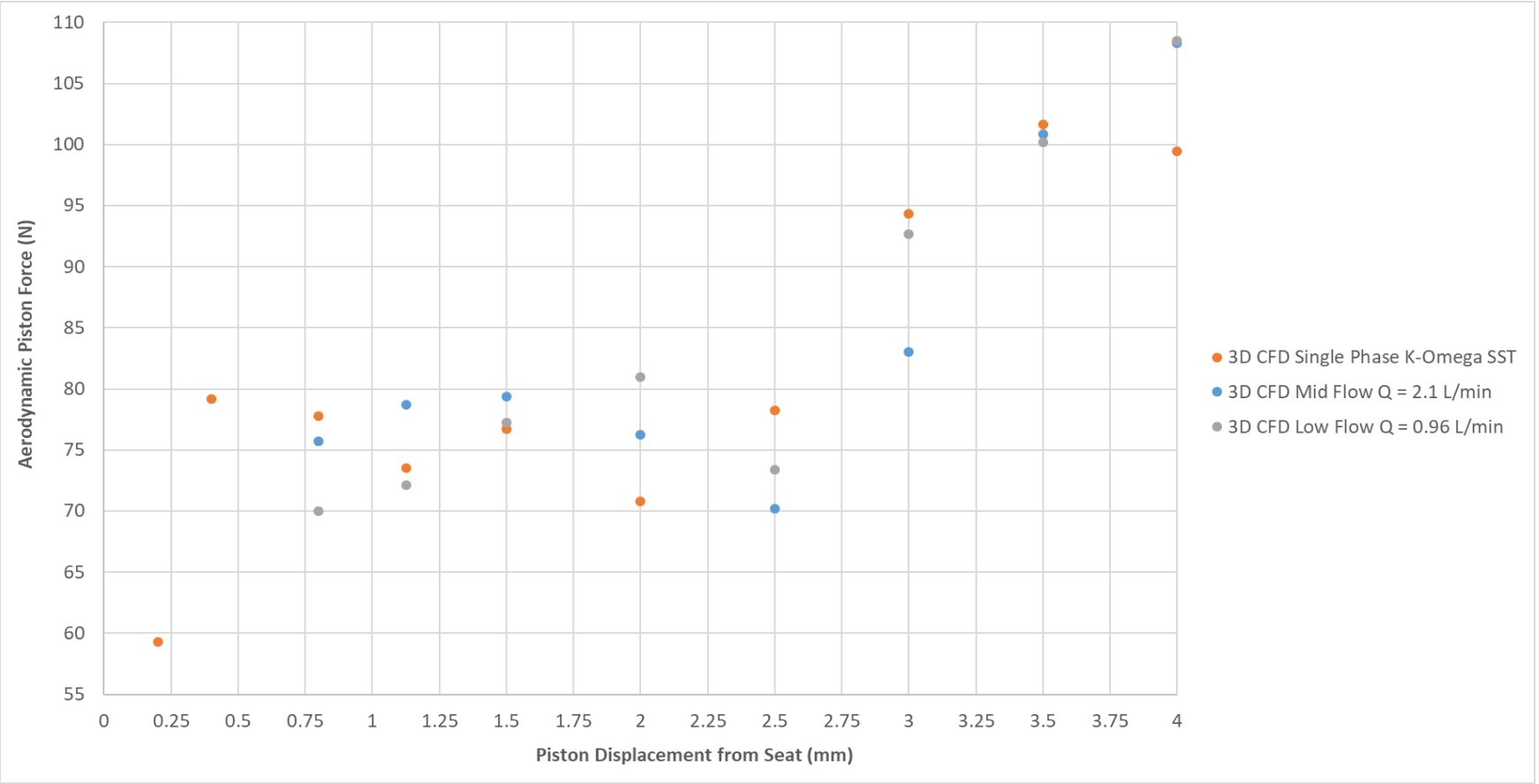

Figure 8.40 – Comparison of CFD Piston Force for Single Phase and Two Flow

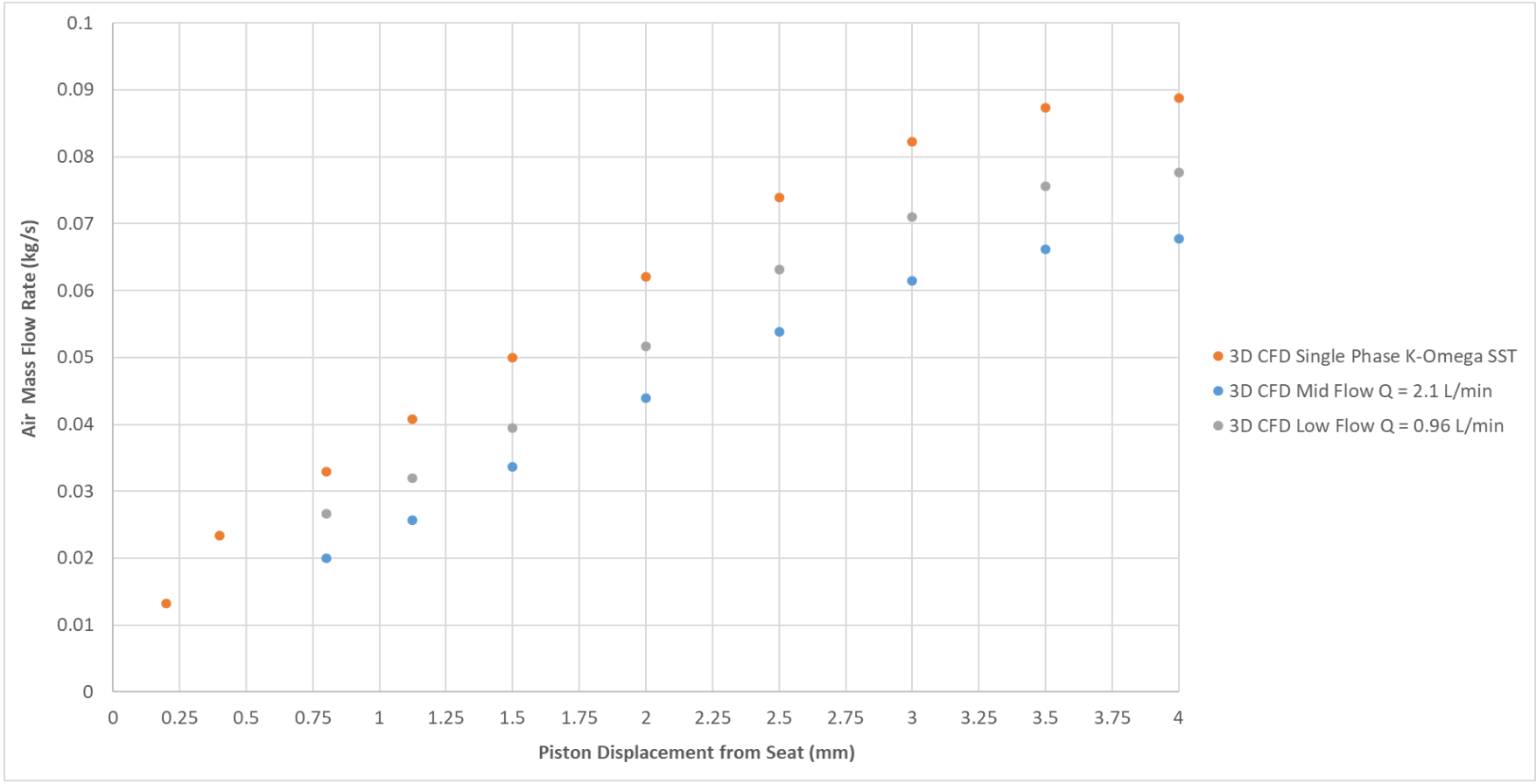

Figure 8.41 - Comparison of Air Mass Flow Rate for Single Phase and Two Flow

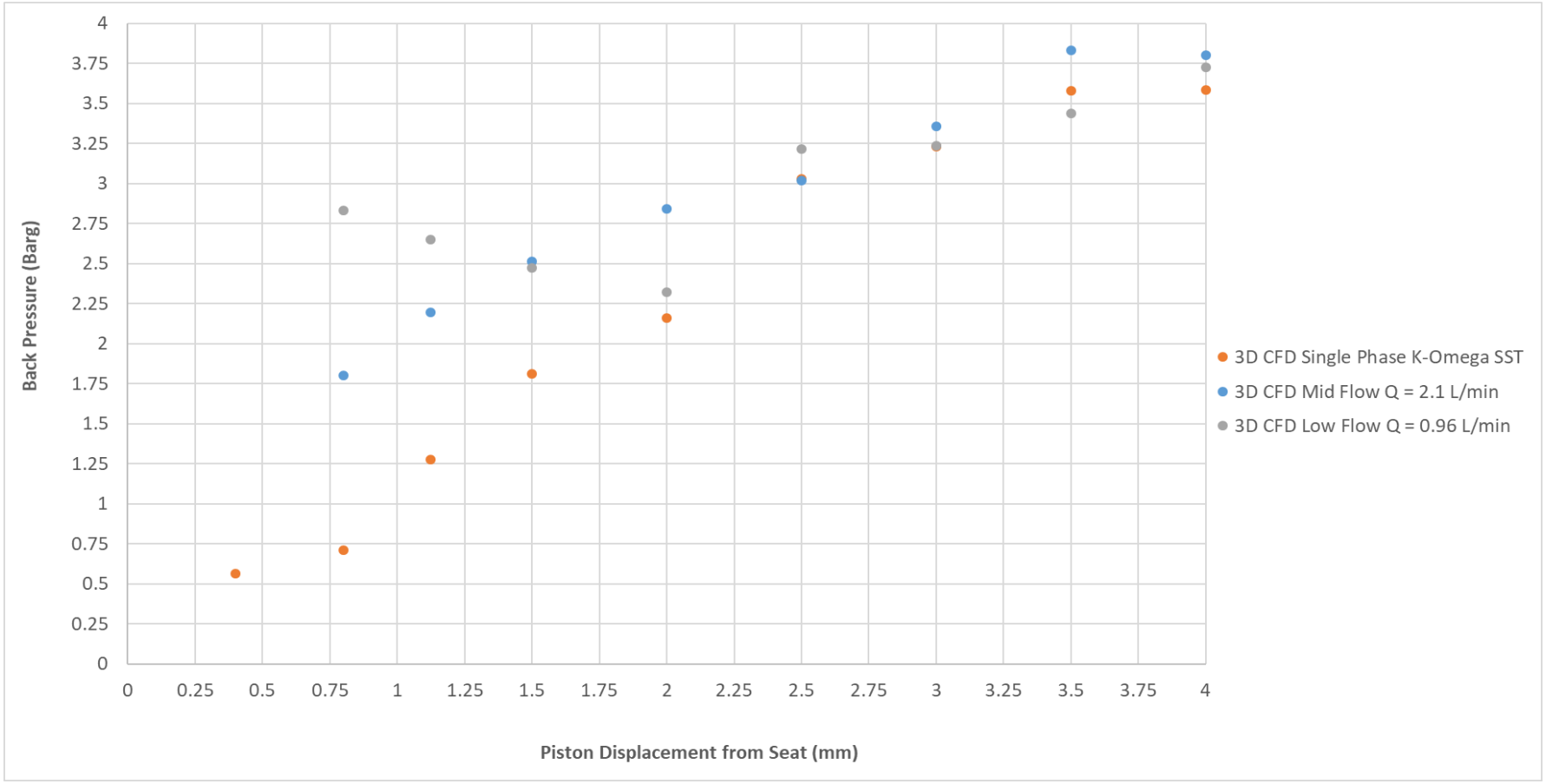

Figure 8.42 - Comparison of CFD Piston Force for Single Phase and Two Flow

1.125mm Piston Lift

Single Phase

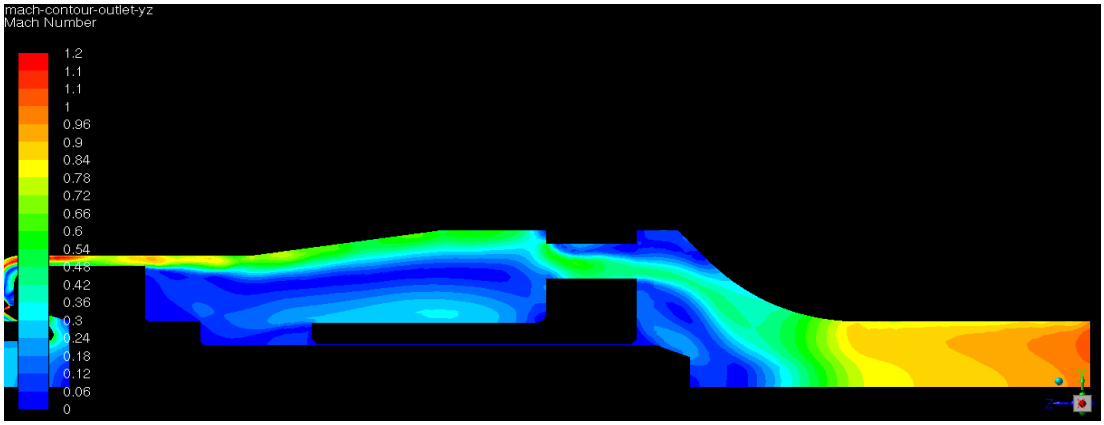

Water Injection Rate = 0.96 L/min

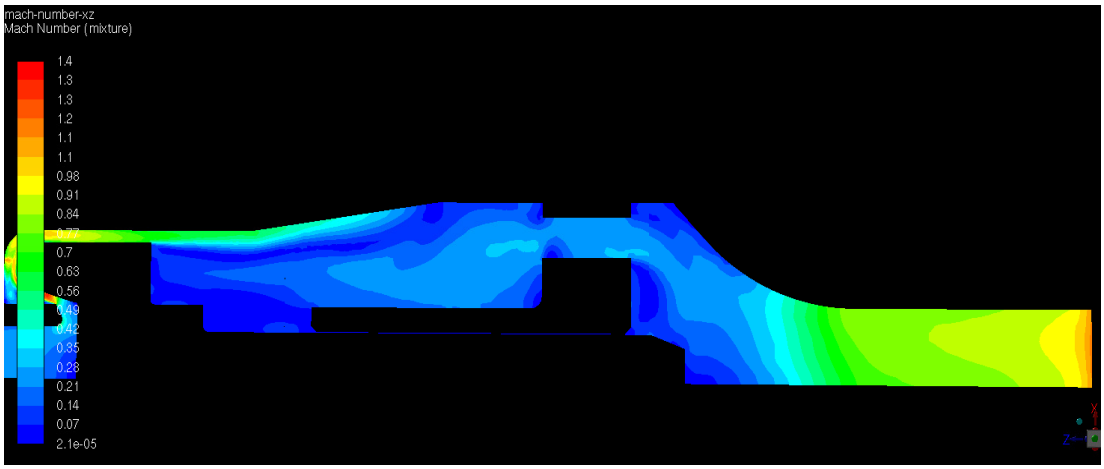

Water Injection Rate = 2.1 L/min

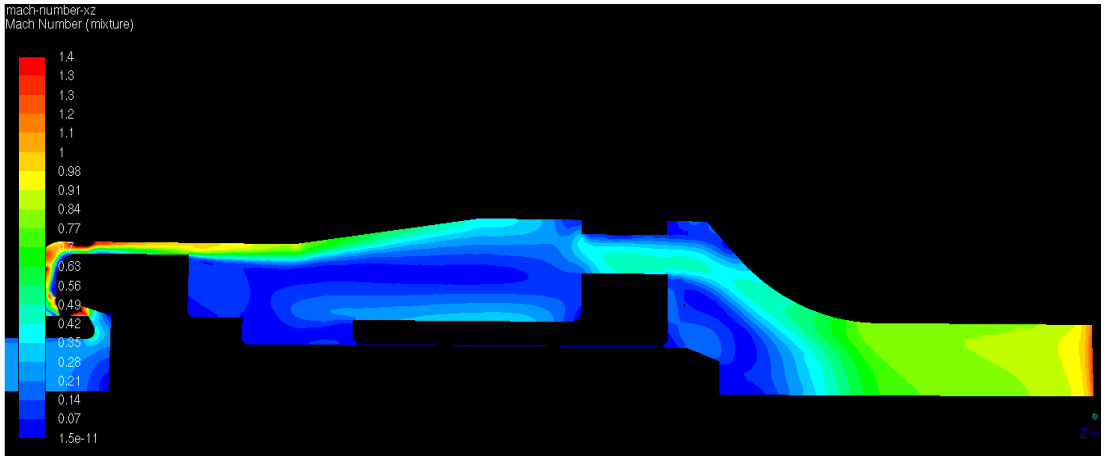

Figure 8.43 – CFD Comparison of Outlet Mach Number at 1.125mm Lift

1.125mm Piston Lift

Single Phase

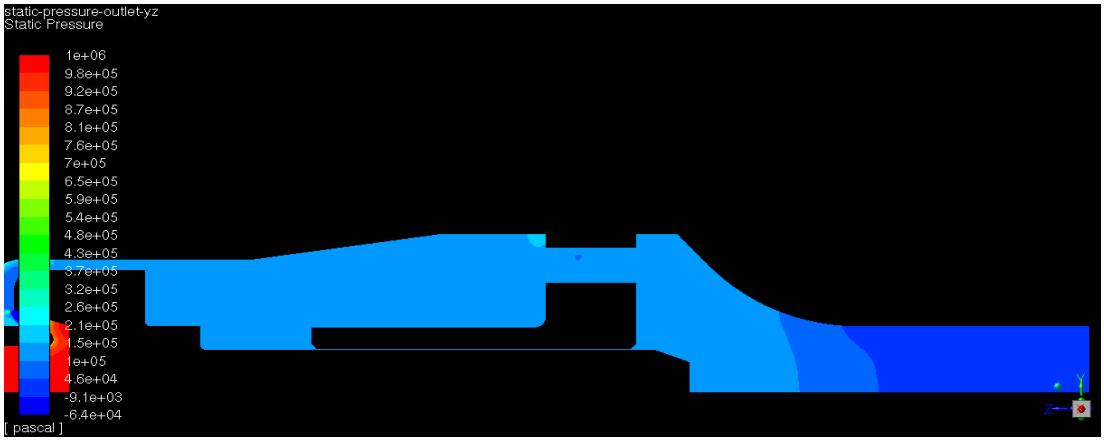

Water Injection Rate = 0.96 L/min

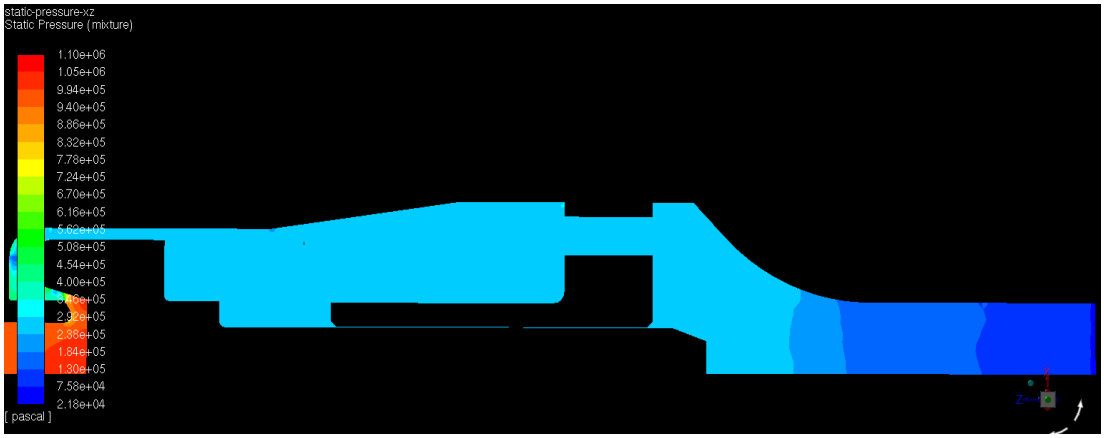

Water Injection Rate = 2.1 L/min

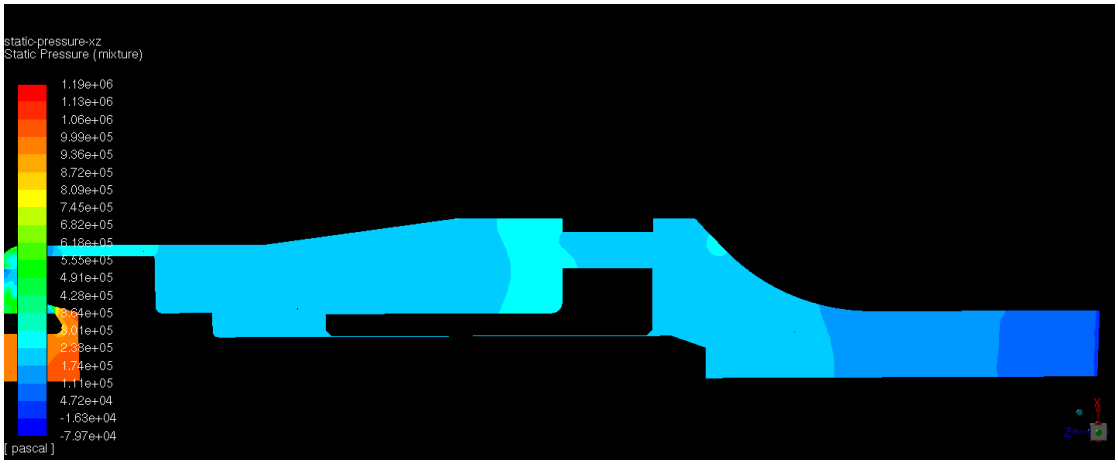

Figure 8.44 - CFD Comparison of Outlet Static Pressure at 1.125mm Lift

4mm Piston Lift

Single Phase

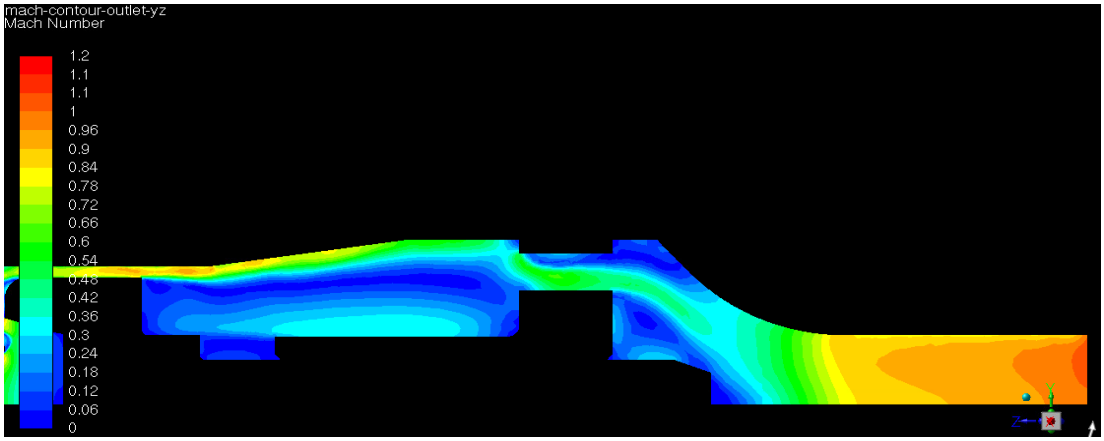

Water Injection Rate = 0.96 L/min

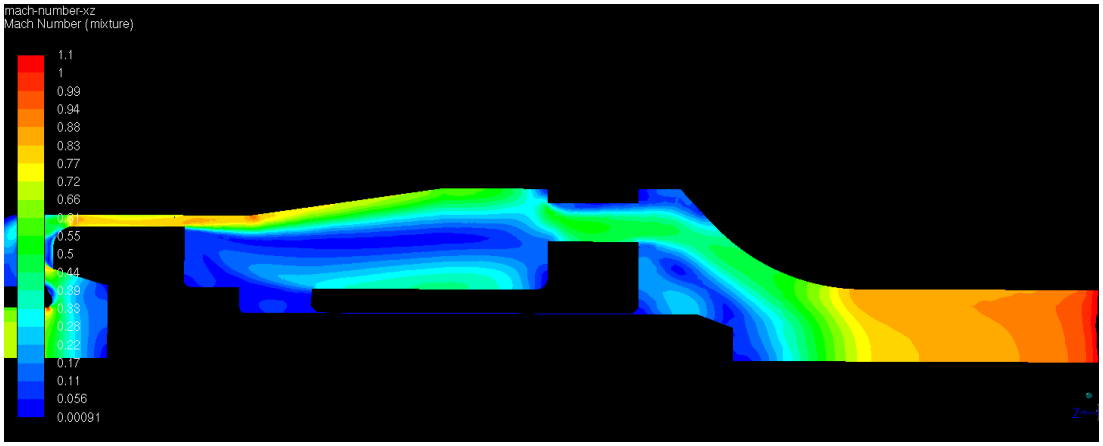

Water Injection Rate = 2.1 L/min

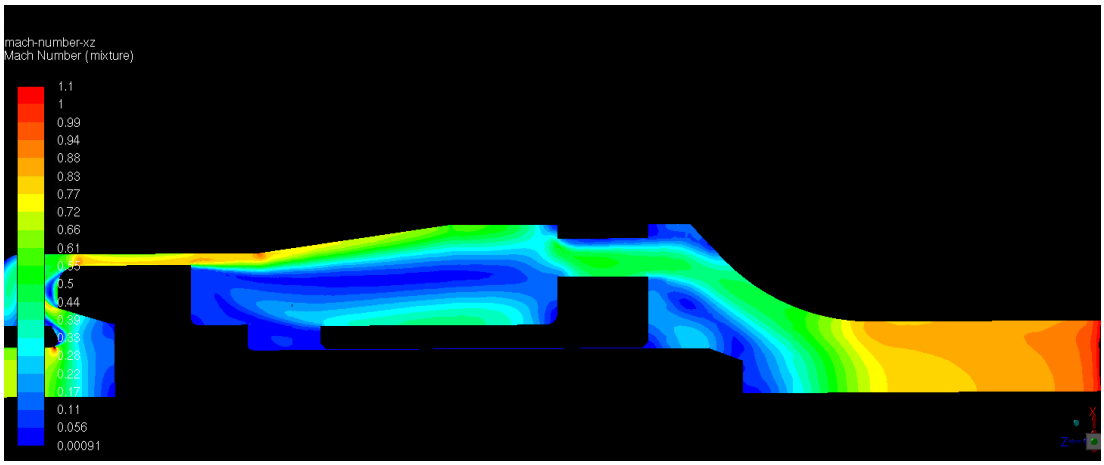

Figure 8.45 - CFD Comparison of Outlet Mach Number at 4mm Lift

4mm Piston Lift

Single Phase

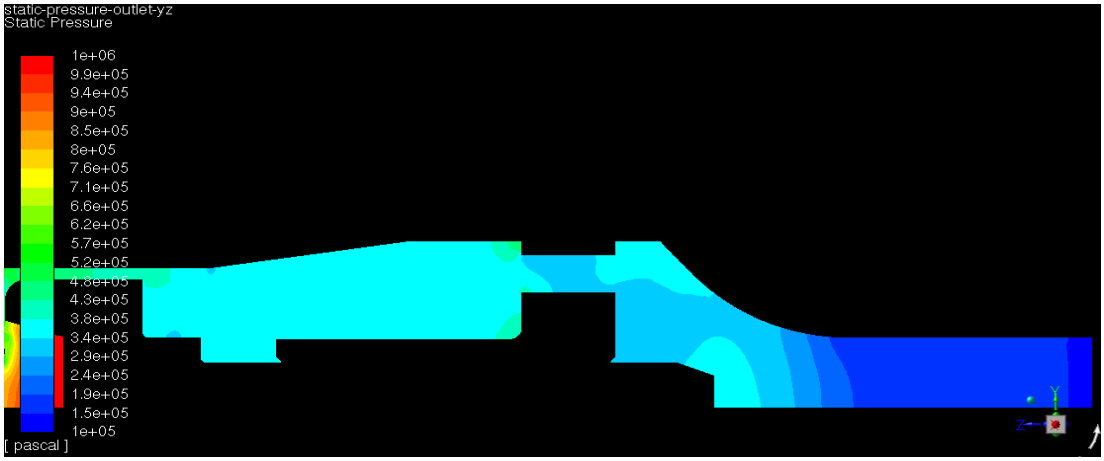

Water Injection Rate = 0.96 L/min

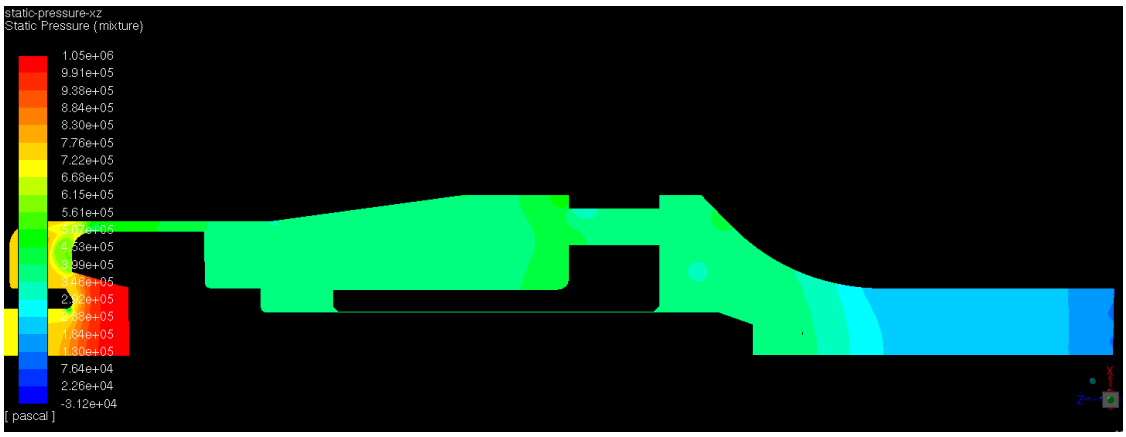

Water Injection Rate = 2.1 L/min

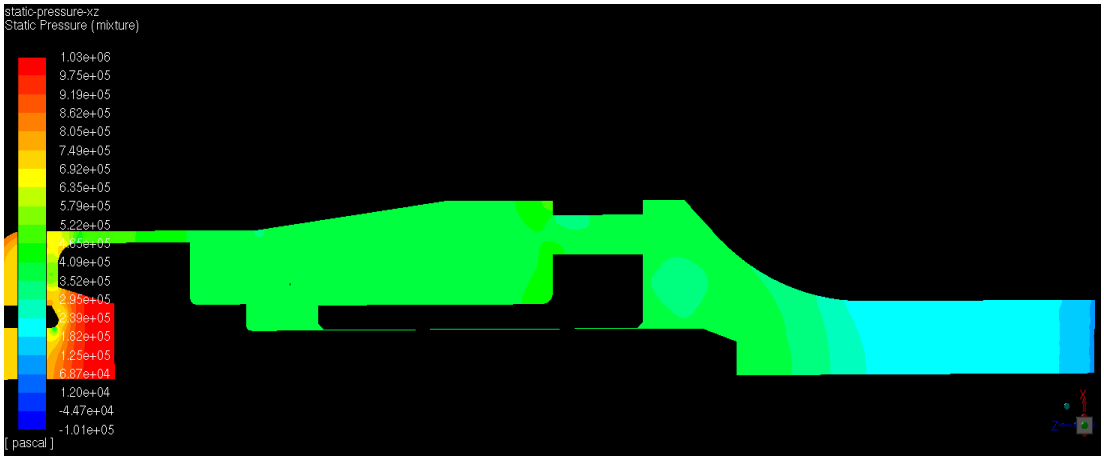

Figure 8.46 - CFD Comparison of Outlet Static Pressure at 4mm Lift

8.1.5 Summary of Two Phase Steady State CFD Validation Research for Henry 5231BX PRV

Following a two phase (air-water) CFD steady state validation study using ANSYS FLUENT and Workbench for the Henry 5231BX PRV with modified gland a number of conclusions could be established;

- By conducting two phase air water steady state tests, it could be concluded from the experimental results that there was a relationship for air mass flow rate and piston force with water injection rate however backpressure remained approximately constant for both single phase and two phase high lift operation. At low lift (0-2.5mm), piston force was found to be higher in two phase operation when compared to single phase with little difference in force observed with increasing water mass fraction. However, following an inflection point at 2.5mm for higher piston lifts between 2.5mm-5mm it was found that single phase piston force became comparable with two phase forces. Also with increasing water mass fraction in the higher lift regions, the value of piston force typically decreased in a linear manner. As would be intuitively expected, with increasing water injection rate; a decrease in air mass flow rate was observed across the full lift range. These experimental observations were generally in agreement with previous research performed by Elmayyah [11, 29, 30] and Alshaikh [12, 26-28].

- Previous two phase CFD modelling at Strathclyde for through flow type PRV's included only a 2D analysis for a larger non manufacturer specification outlet. Therefore, due to the identified inaccuracy of the 2D CFD model for the 5231BX PRV from the single phase study in 5.2 it was proposed to generate a 3D two phase (air-water) CFD model. A homogenous mixture model was used which was previously verified to

be effective [11, 12]; at lower water volume fractions. For water injection volumes of 2.1 L/min and 0.96 L/min. It was found that an average correlation to experimental data of 3.5% for mass flow rate and 10.6% for disc force could be achieved for 2.1 L/min and a correlation of 0.7% for mass flow rate and 14.1% for disc force could be achieved for 0.96 L/min.

- In general, the CFD trends for piston force, air mass flow rate and backpressure matched the experimental results especially for air mass flow rate. Although in conjunction with the conclusions from the single phase CFD model research, significant model induced error was found to occur for lifts between 2.5-3mm for piston force prediction due to the CFD model being unable to accurately resolve the recirculation region beneath the piston surface. Most significantly however, large differences for backpressure was found for the two phase CFD models for piston lift lower than 2.5 mm. Which as result caused the CFD models to suffer from an under-prediction of piston force at lower lifts.

- In addition, symmetry breaking phenomena could also be observed, especially at lower lifts of 1.5 mm for both injection rates and at high lift (4mm) at higher water volume fractions.

8.2 TWO PHASE TRANSIENT PRV PERFORMANCE: AN EXPERIMENTAL STUDY

In this section the operation of the Henry 5231BX PRV (modified gland) valve was investigated under transient two phase flow conditions. This would therefore allow the dynamic performance of the PRV to be understood when subjected to two phase (air-water) flow and be compared to the single phase dynamic operation presented in section 6.2. From the available literature, such

a transient two-phase study would be novel therefore it is hoped that the development of an experimental test would support future model validation work For all experimental data generated, a set pressure of the PRV of approximately 10.3 barg was used with an air-water mixture for a water injection rate of 1 L/min and 2.2 L/min as well as a reference single phase air test.

8.2.1 Experimental Two Phase Dynamic Testing of the Henry 5231BX PRV

A transient two-phase flow experimental assembly and measurement technique was required to be developed using the flow testing laboratory previously described at the University of Strathclyde. It was possible to use the water injection equipment and air-water separator from the steady state facility however this required the PRV to be installed in the horizontal position. This was different to the transient single phase study in which the PRV was installed vertically. In this case the existing two phase steady test arrangement was adapted to allow transient testing to be carried out. A drawing of the experimental set up required for the transient test is shown in figure 8.47 where the piston traverse unit was replaced with a laser displacement sensor which was focussed on a reference surface connected to the piston via a smaller diameter connecting rod than used in single phase testing.

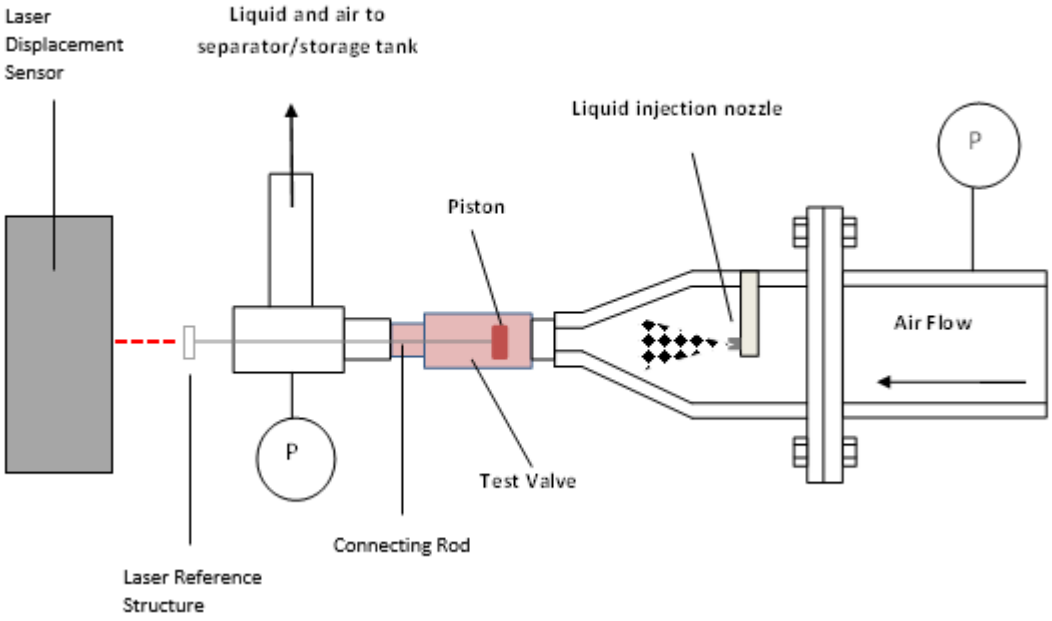

Figure 8.47 - Transient Two Phase Steady State Experimental Rig

In addition, for the separator it was required that the diameter of the droplet filter (shown in red dashed box in figure 8.48) should be reduced. This was due to the smaller diameter of the rod for the laser reference surface described in the single phase study when compared to the connecting rod used for the steady state analysis. In addition, for the two phase flow dynamic analysis only the blowdown process could be performed using water injection. This is due to the nature of water injection whereby if water was injected when the PRV was closed, water would ingress to the supply line which could cause damage to the laboratory air circuit and also possibly impair future experimentation. This assumption was deemed to have negligible error on the practical relevancy of the study, as during the rapid opening process of the PRV it could be assumed that the flow would be considered as single phase with two phase flow effects only occurring during the longer blowdown process.

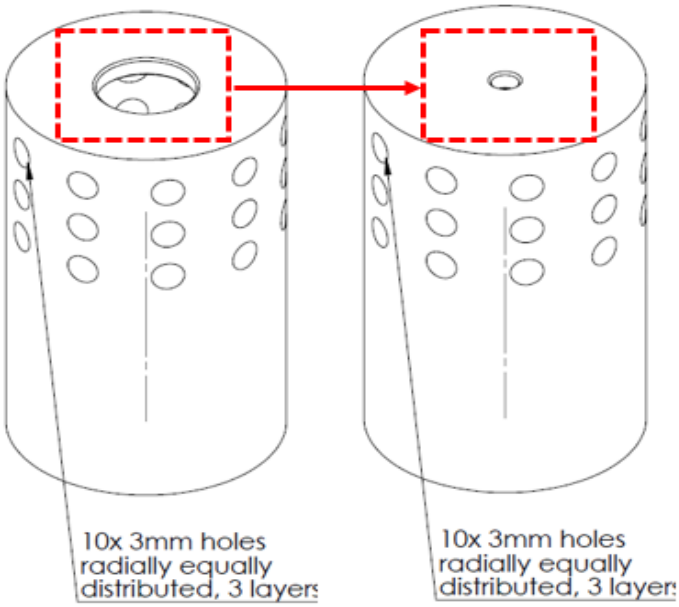

Figure 8.48 – Droplet Filter for Steady State (left) vs Transient (right)

The experimental assembly is shown in figures 8.49, 8.50 and 8.51 with further details given in table 8.7.The water injection nozzle (1) connected to the upstream compressed air supply circuit provides the desired air-water mixture to the inlet of the Henry 5231BX PRV (2). It should be noted that the same calibration technique for determining water injection rate was used for the transient dynamic testing. Furthermore, the separator (3) connected to the outlet of the PRV with the purpose of returning the air/water mixture to the water tank at atmospheric conditions as well as the drainage cover described in section 8.1.1. For the laser assembly it was critical to ensure the laser was positioned in the appropriate location for the full range of the displaced valve disc therefore the use of a laser arm structure (4) was necessary to hold the laser (5) in place and remain on target with the laser reference surface (6). It should be noted that the laser reference structure was also adapted from the single phase transient study in 6.2.1. A Perspex deflection shield (7) was also required to allow the laser beam to pass through the material and return to the sensor but also protect the laser from the exhaust jet, and droplet spray exiting the piston rod/separator inlet channel. As mentioned previously, the steady state horizontal rig described previously for both single phase and two phase

validation was utilised for two phase transient study due to the requirement of water injection, separation and water tank supply/connection which would require a significant adaptation to be held in a vertical position. This was deemed to be impractical for the outcomes of this study however could be investigated to test feasibility of a vertical arrangement of the PRV in future studies.

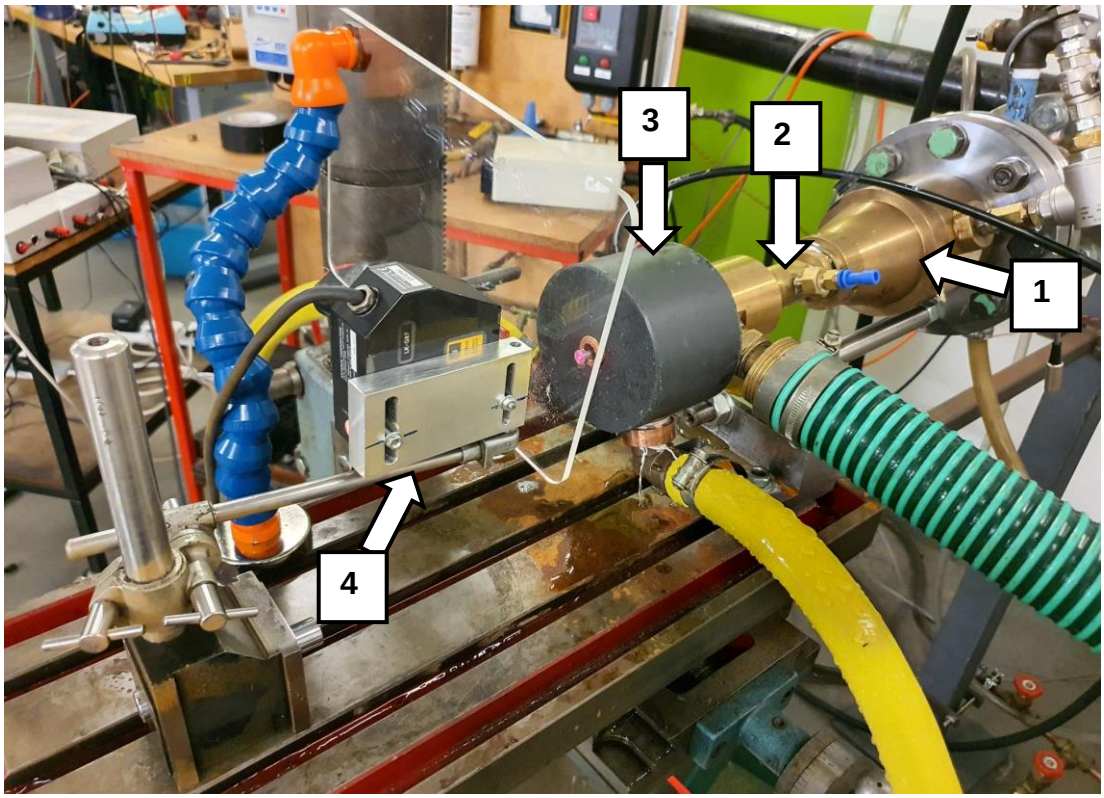

Figure 8.49 – Transient Two Phase Experimental Rig for Henry 5231BX PRV

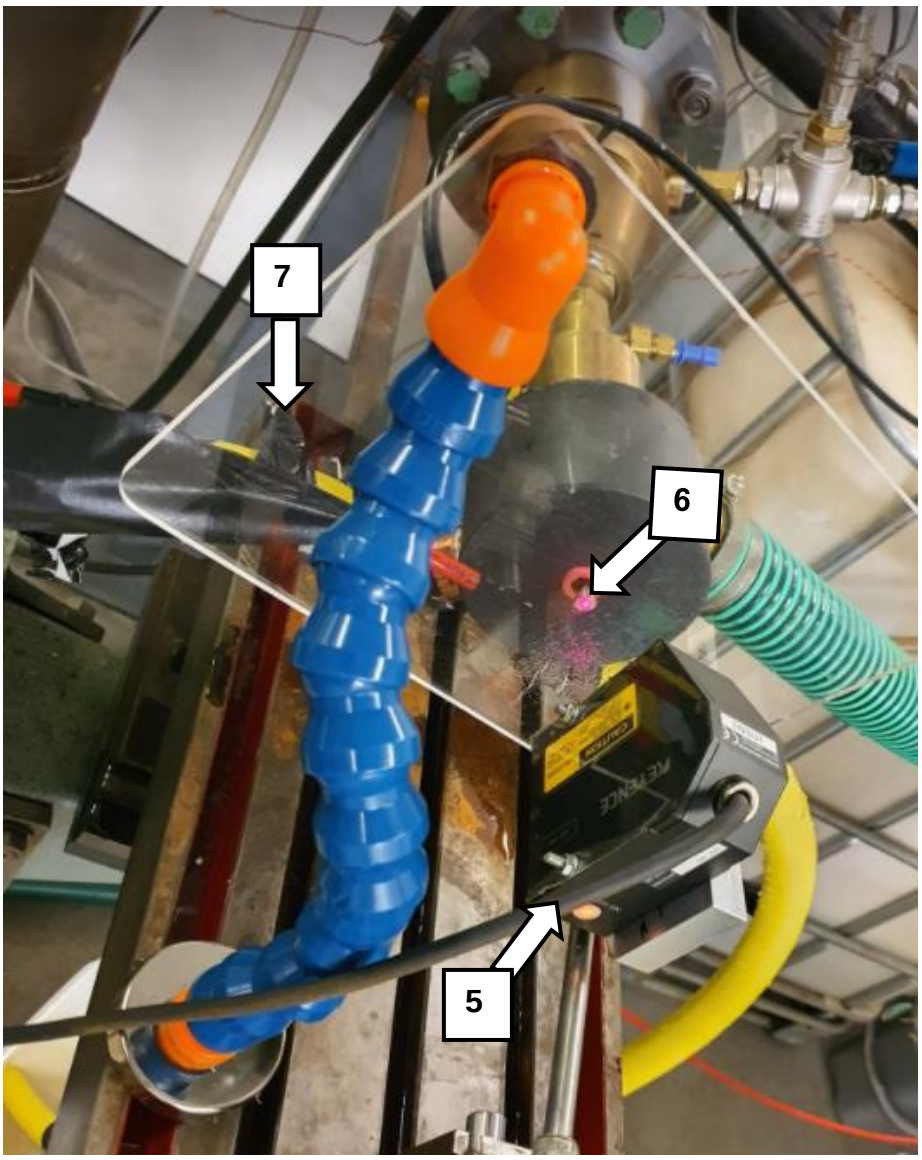

Figure 8.50 – Laser Displacement Sensor Arrangement Required for Transient Two Phase Experiment

For the water circuit, an identical principle was used to the steady state study where the shut off valve handle (8) was used to control water injection to the transient PRV test. This valve however could only be opened once the PRV was in the fully open position to prevent water from flooding the air supply pipework. Following water injection to the PRV, the main air-water hose returns the mixture to the water tank (11) and remaining leakage returns via the leakage hose connected to the drainage cover, to the overflow containers (10).

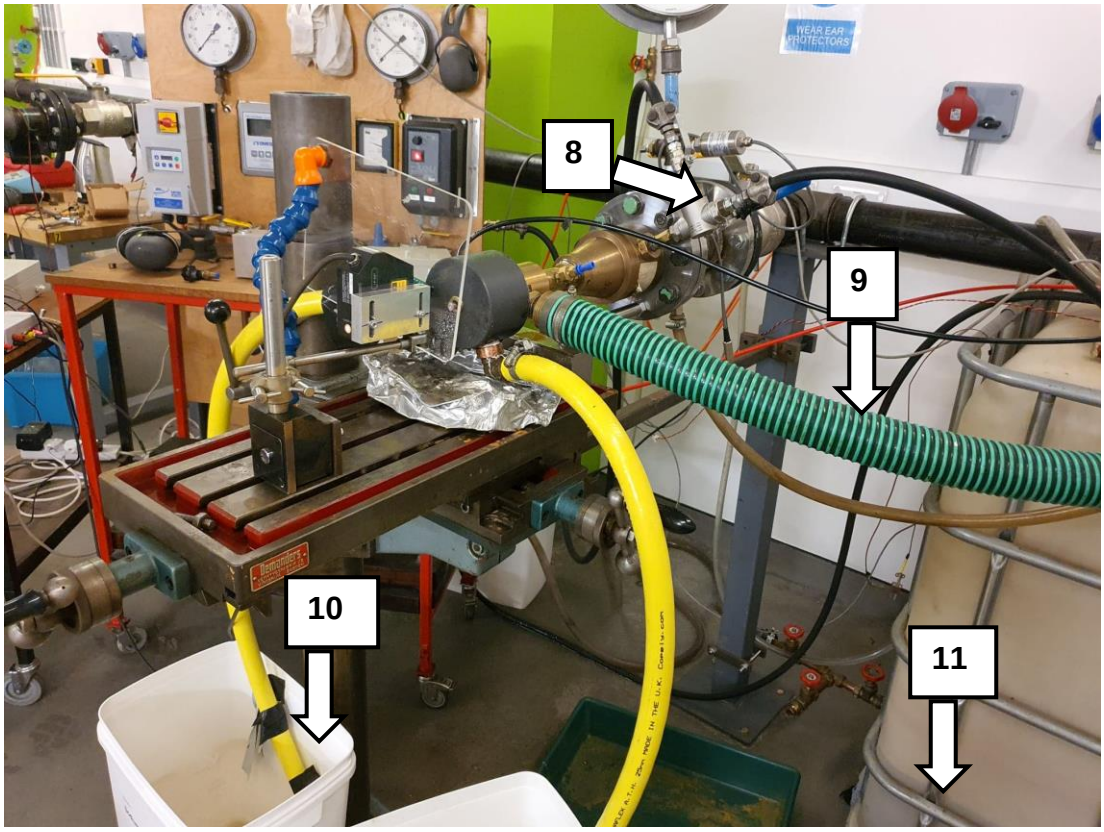

Figure 8.51 – Water Injection Circuit for Transient Two Phase PRV Experiment

Similarly, to the single phase transient test, during data collection an in-house developed software was used in order to collect inlet pressure from a sensor upstream of the PRV (2) and disc displacement (lift) over time from the laser (5) to determine blowdown pressure as well as monitoring the dynamic characteristics of the disc displacement during the general operation of the PRV for two phase flow. By monitoring these features it would be possible to compare the dynamic performance of the Henry 5231BX (modified gland) for two phase (air-water) flow and for single phase air only. In addition, the gland depth used for the PRV was consistent with the single phase study at 3.2 mm as it provided the desired set pressure of 10.3 barg

No.	**Experimental Part**	**Description**
1	Water Injection Nozzle	Connection of PRV inlet to external piping to allow sufficient mixing of air-water to take place.
2	PRV	Henry 5231BX PRV with modified gland
3	Separator	Air-Water separator with drainage cover
4	Laser Arm Structure	Structure required for laser positioning.
5	Laser Displacement Sensor	Sensor to measure transient piston displacement.
6	Laser Reference Surface	Surface connected to small diameter rod to piston for laser reference.
7	Jet Deflection Shield	Shield to protect laser from water spray.
8	Water Injection Shut Off Valve	To enable control of water injection from water pump to injection location.
9	Air-Water Outlet Hose	Connection between separator outlet and tank
10	Drainage Overflow Container	Overflow container for recycling of water leakage.
11	Water Tank	Allows storage of water for injection.

Table 8.7 – Description of Experimental Components in Figures 8.49 - 51

The general measurement procedure developed for dynamic measurement of the 5231BX PRV in two phase (air-water) operation was as follows;

1. Before testing took place and flow was established it was crucial to ensure that the appropriate safety precautions were made within the laboratory such as securing of loose items in the vicinity of the jet, closing doors to public walking areas and wearing appropriate personal protection equipment (PPE) especially for ears, eyes and feet.

2. Initially by using digital Vernier calipers, the gland depth was measured and set pressure verified by increasing system pressure to 10.3 Barg to ensure first audible leakage was detected for single phase air only. This

process required an iterative adjustment of the gland depth in order to achieve the desired set pressure. It should be noted that the original PRV outlet was used to provide easy adjustment of the gland as the air-water separator was not required at this stage.

3. Once an appropriate spring preload and set pressure was achieved, the separator assembly was attached and it was critical to ensure again that no loose components or items were present in the vicinity of the jet.

4. In accordance with the experimental procedure described in section 6.2.1. Single phase air only test took place to determine the performance of the PRV in the horizontal position.

5. For the two phase flow test (once the single phase test was completed) the supply pressure for single phase air only was once again slowly increased by introducing flow to the system with the water injection lever closed. As the supply pressure reached the set pressure and overpressure the PRV popped open where the air supply flow rate was adjusted until a steady state fully open position of the PRV could be achieved.

6. At the fully open position of the PRV in single phase, the corresponding pressure would then be noted as the overpressure value to allow an approximate calculation of the set pressure to be made based on the single phase performance. This in turn would allow a % blowdown value to be determined.

7. Following this, the recording equipment was enabled to digitally measure both pressure and disc lift with time. Once recording had started, the water injection shut off valve was opened to allow water to be pumped through the injection nozzle to the PRV inlet. The air supply control valve position was also closed. At this point the system pressure would relieve until subsequent closure at the blowdown pressure by which point the water injection valve would be immediately closed by the operator. The pressure in the system would then be relieved using an exhaust port via a silencer in the air supply pipework.

8. Steps 1-6 of the experimental process were repeated numerous times in order to ensure repeatability of the results. The data was then collected for data processing to extract blowdown and disc lift vs time. Blowdown values were identified from the data once the PRV had reached its fully closed position.

To determine the overall uncertainty of the overpressure and blowdown readings it was required to identify the statistical and systematic errors in a similar manner to the error analysis performed in chapter 5.2. The measurement uncertainty associated with each device is shown within table 8.8 with statistical uncertainty of blowdown evaluated by 3 tests to be 0.37%.

Property	**Transducer**	**Accuracy**	**Range**
Pressure	Bourdon Dial Pressure Gauge	0.2-2.5%	0-300 Psi
Displacement	KEYENCE Laser Displacement	<0.1%	-15 to 15 mm

Table 8.8 – Measurement Devices Required for Dynamic 5231BX Testing

Figure 8.52 highlights the typical pressure profile used during the single phase transient experiment for the Henry 5231BX PRV using the two phase equipment alongside the corresponding disc position vs time curve. Both the overpressure and blowdown values measured experimentally are shown within table 8.9. As established previously, for the single phase test shown in figure 8.52, the PRV was installed in a horizontal position which was different to the results discussed in section 6.2 where the PRV was in a vertical position.

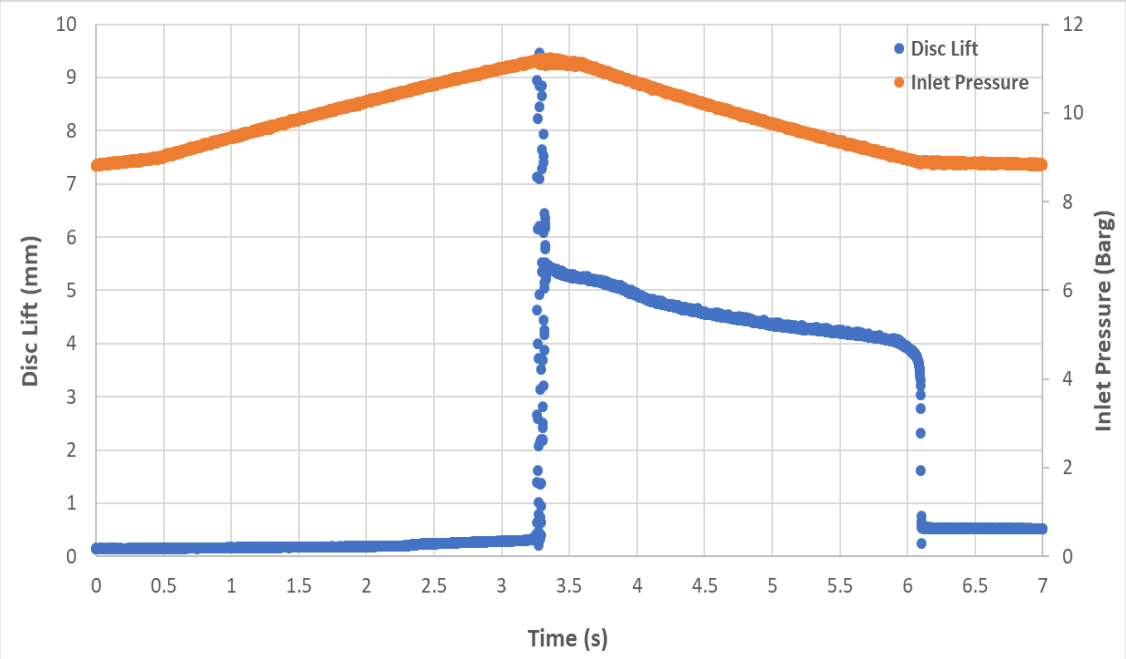

Figure 8.52 - Experimental Disc Position (Lift) vs Time for Henry 5231BX PRV (Modified Gland) for Air Only Flow in Two Phase Rig

Set Pressure	**10.36 barg**
Over Pressure	**11.2 barg** (+7.1% relative to set pressure)
Blowdown Pressure	**8.89 barg** (-15% relative to set pressure)

Table 8.9 - Experimental Over Pressure and Blowdown Results for 5231BX PRV (Modified Gland) for Air Only Flow in Two Phase Rig

The results shown in figure 8.52 highlight some slight differences to the transient experimental study performed when the PRV was installed in an upright orientation. From a time of 0-1 seconds the PRV remained in a fully sealed position as the inlet pressure increased; this behaviour is similar to that observed in section 6.2.1. However during the time period of 1-2 seconds the PRV begins to open and simmer at a disc lift of approximately 0.15 mm. Following this, from 2.25s to opening at 3.25s a further increase in disc lift was noted as inlet pressure increased as the PRV continued to simmer until popping open. This opening behaviour is distinctly different to what was measured during the transient study with the PRV in the upright position as an immediate popping action took place in that case. As a result it could be concluded that PRV orientation has an effect on the Henry 5231BX PRV's dynamic characteristics, particularly when the piston is contact with seat and should be investigated further in future studies to understand the reasons why. In general however, the dynamic characteristics were sufficiently similar to the study described in 6.2.1 with a maximum piston lift of 9 mm initially which settled to a lift of 5 mm during blowdown with the PRV closing once a disc lift of 3.5 mm was reached. Furthermore the overpressure value of 7.1% and 15% blowdown pressure correlated well with the earlier study. A difference however could be noticed at a time of approximately 6.2s where the PRV would not seal and would remain open slightly at a piston lift of 0.5 mm. This suggested that in the horizontal position the PRV was not able to generate a seal at a similar pressure to what the vertical orientation of the PRV was able to achieve. This is likely due to a loss of weight of the piston to provide a sealing force in the horizontal position and/or misalignment of the piston to prevent a complete seal being achieved. It should be noted however that with a further decrease in pressure, the piston would return to a fully closed, sealed position.

For two phase testing a similar approach to the single phase testing was followed but with water injection established after a steady single phase opening state had been established, as shown in Fig 8.53. This is due to the assumption that the flow regime during opening of the PRV would be single

phase. A likely installation would involve a PRV top fitted to a partially filled pressure vessel with gas on top of a liquid phase as shown in figure 1.1. Therefore, due to the rapid opening time, the PRV would open in a single phase manner by initially venting the gas space. Following the initial opening, two phase flow would subsequently become established once the PRV was at maximum lift with full flowing capacity to enable the pressurised vessel to blowdown to a safe pressure. As a result, for two phase testing it would be only necessary to test the blowdown of the PRV in two phase flow conditions.

This scenario has been implemented here and is shown in figure 8.53. Phase 1 represents the stabilisation period using air only with the water injection valve closed to achieve a steady state fully open condition. Once stability is reached, water is introduced to the system where after a further period of adjustment to account for reduced air flow takes place of the now two phase flow; the air supply control valve closed for blowdown to take place during phase 2. In phase 3, the PRV is closed and water injection shut off.

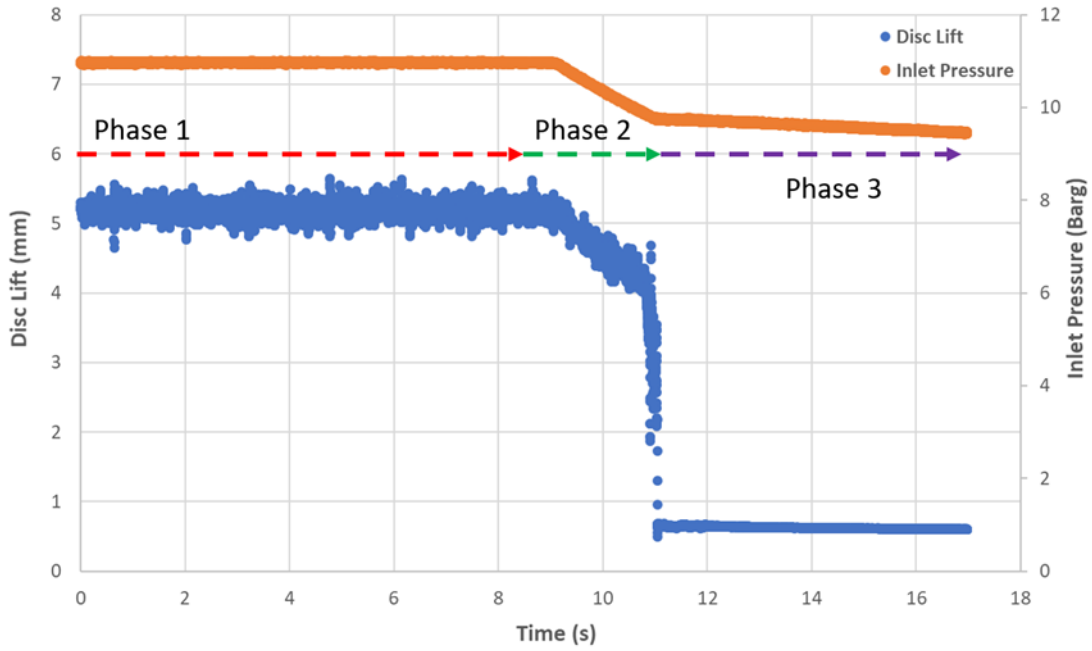

Figure 8.53 – Two Phase Transient Test Methodology

Two phase transient experimental results are shown in figures 8.54 and 8.55 for a water injection rate of 2.2 L/min and 1 L/min. The time set at 0 s corresponds to the moment when water injection was active and the air supply closed. It should also be noted that set pressure for both two phase flow cases was determined by assuming that the value of over pressure was 7.1% relative to set pressure as determined in table 8.9.

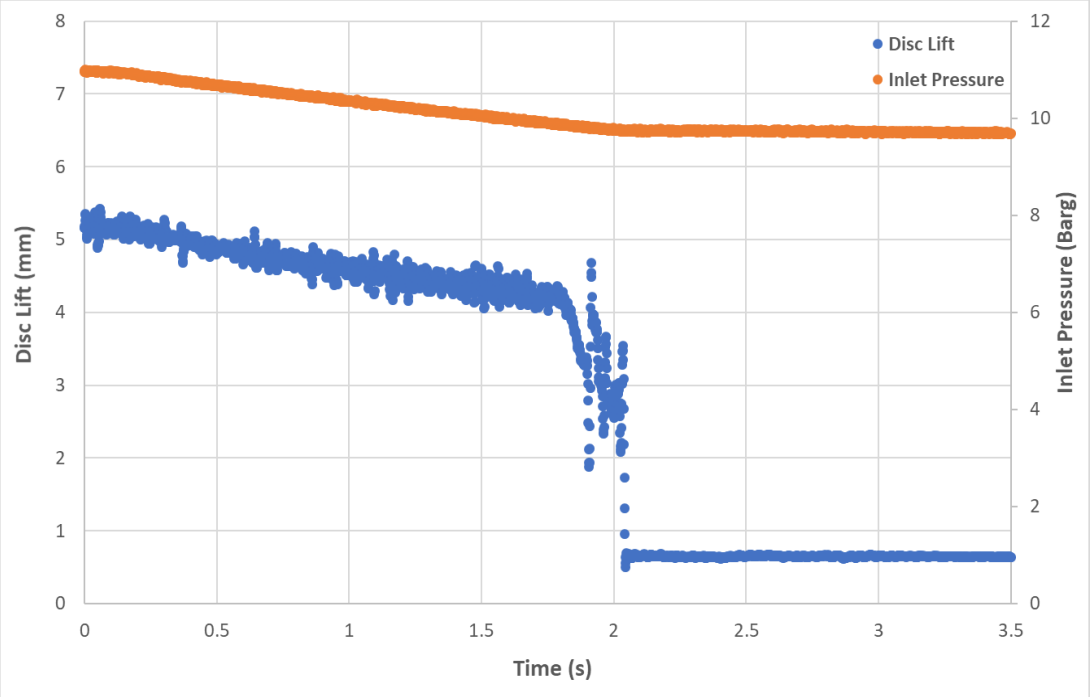

Figure 8.54 – Two Phase Experimental Disc Position (Lift) vs Time for Henry 5231BX PRV (Modified Gland) for Water Injection Rate of 2.2 L/min

Set Pressure	**10.25 barg**
Over Pressure	**10.98 barg** (+7.1% relative to set pressure)
Blowdown Pressure	**9.74 barg** (-5% relative to set pressure)

Table 8.10 – Two Phase Experimental Over Pressure and Blowdown Results for 5231BX PRV (Modified Gland) for Water Injection Rate of 2.2 L/min

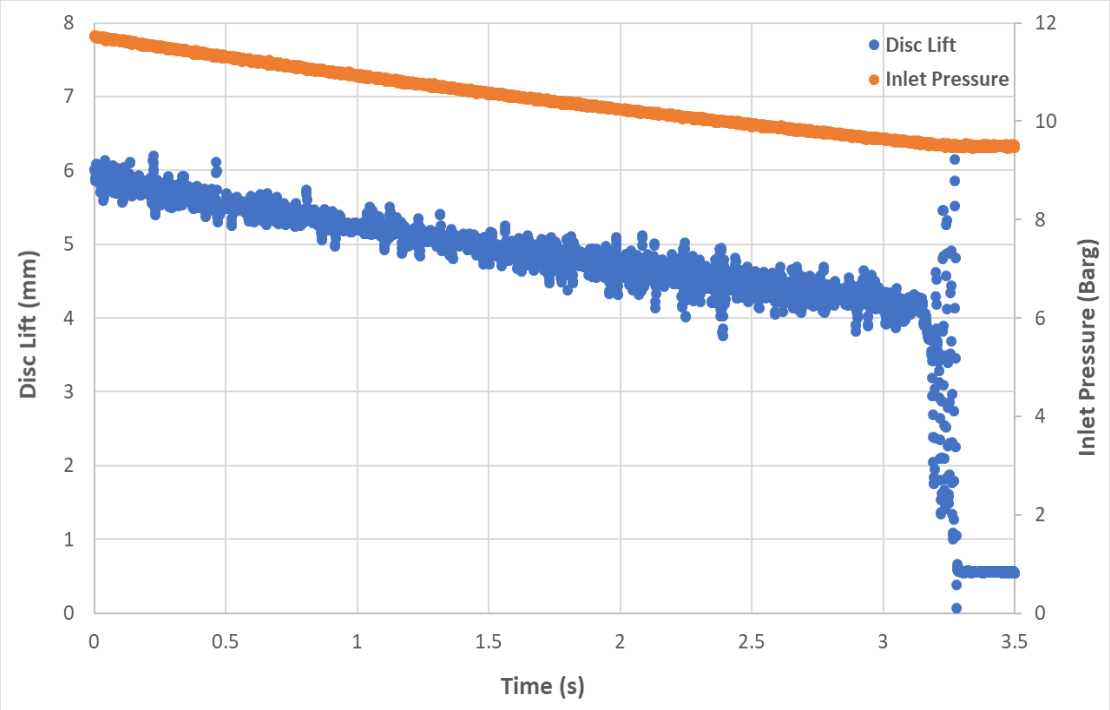

Figure 8.55 - Two Phase Experimental Disc Position (Lift) vs Time for Henry 5231BX PRV (Modified Gland) for Water Injection Rate of 1 L/min

Set Pressure	**10.94 barg**
Over Pressure	**11.71 barg** (+7.1% relative to set pressure)
Blowdown Pressure	**9.5 barg** (-13.13% relative to set pressure)

Table 8.11 - Two Phase Experimental Over Pressure and Blowdown Results for 5231BX PRV (Modified Gland) for Water Injection Rate of 1 L/min

As can be appreciated from figure 8.54 and table 8.10, a significant difference could be observed from the blowdown of the single phase test (table 8.9 and figure 8.52) to the two phase air water test at 2.2 L/min injection rate. The differences will be discussed further in detail in 8.2.2 however it was clear that in two phase operation the PRV was much more unstable in its operation with oscillation from 0-1.8 seconds across a disc lift range of 5 mm to 4 mm. At 4

mm the PRV rapidly closed however upon reaching a lift value of approximately 3.2 mm, the piston (disc) oscillated with a large amplitude until additional decrease in inlet pressure allowed the PRV to close further. In a similar nature to the single phase test however, the PRV was unable to achieve a fully closed (sealed) position due to the horizontal installation.

The results described in figure 8.55 and table 8.11 highlight the results of the transient experimental test of the PRV for a water injection rate of 1 L/min. A similar oscillation of disc lift could be observed from 0-3 seconds however the disc lift was initially 6 mm instead of 5mm at 0 seconds; this will be discussed in 8.2.2. From 6 mm during blowdown the PRV continued to close until 3.25 s where the disc rapidly closed to 1.5mm and oscillated significantly back to 6.5mm lift until further pressure decreases allowed the PRV to rapidly close. It should also be noted that as shown in figure 8.55, the PRV reached the fully closed position however immediately bounced and opened back to a steady lift value of approximately 0.5 mm in an unsealed position.

8.2.2 Comparison of Single Phase and Two Phase Transient PRV Experimental Performance for Henry 5231BX PRV

From the transient two phase results presented in 8.2.1, it was possible to identify notable differences for blowdown pressure and general dynamic characteristics from the single phase air only experiment shown in figure 8.52 and table 8.9. Principally in table 8.12, by comparing the % blowdown values determined from the three flow conditions it could be established that with an increased water injection rate; % blowdown value would increase. This therefore would result in the PRV closing at a higher system pressure with increasing water mass fraction. It could therefore be concluded that there was a direct relationship between dynamic operation of the PRV and the mass fractions of the two phase flow regime. The results also provide a strong

indication that the performance of the PRV varies depending on flow regime i.e. single phase vs two phase flow with more desirable operation occurring for two phase flow and increasing water mass fraction due to the decrease in piston force. However there would be a limit to desirability if the PRV shuts too early (near set pressure) therefore care must be taken to consider this effect.

Water Injection Rate	Blowdown %
0 L/min – Air Only	**-15%** relative to set pressure
1 L/min	**-13.13%** relative to set pressure
2.2 L/min	**- 5%** relative to set pressure

Table 8.12 – Comparison of % Blowdown vs Water Injection Rate for 5231BX

In addition to a direct relationship for blowdown pressure with the water injection rate, variation in the dynamic characteristics of the Henry 5231BX PRV during closure could also be established from figure 8.56. It should be noted that in figure 8.56, the graphs have been superimposed with each other in order to achieve the same time of closure. As a result, the inlet pressure for each flow condition would be different however figure 8.56 provides insight to understanding the variation in PRV closure dynamics.

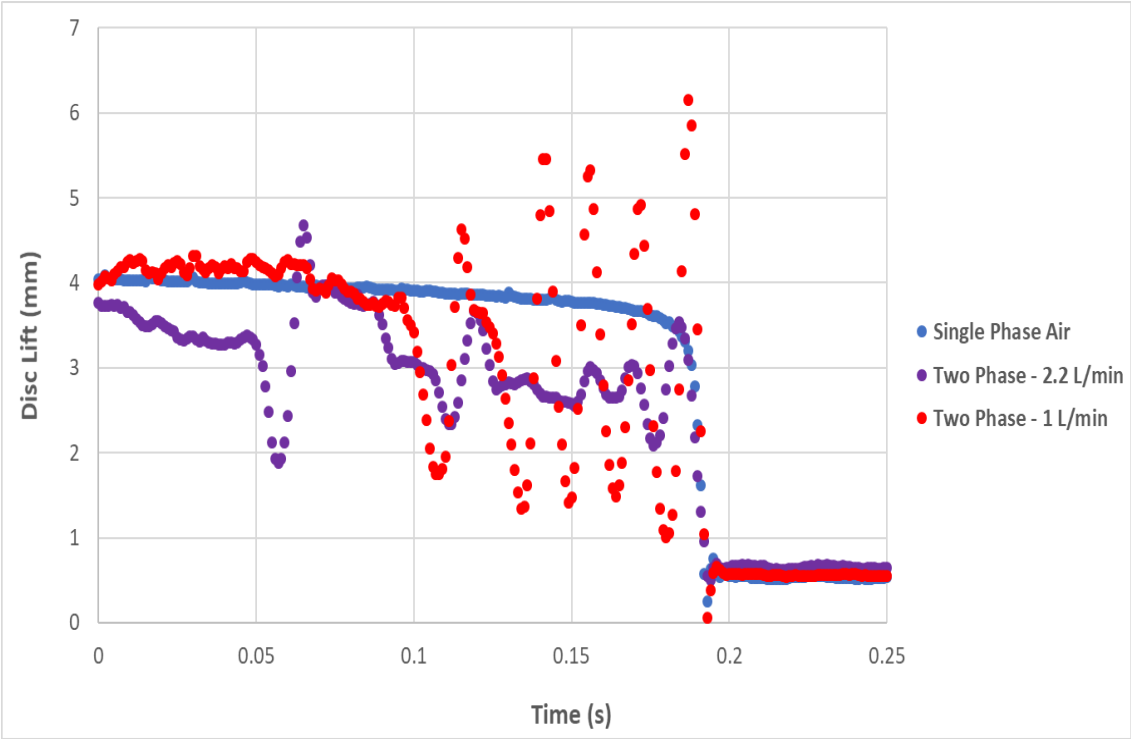

Figure 8.56 – Superimposed Graph of Disc Lift vs Time for Each Water Injection Condition (Point of PRV Closure Used as Reference Time)

From figure 8.56 it can be appreciated that for each flow condition at time equals to 0, the disc lift for each case was approximately 4 mm with a slight difference in the case of 2.2 L/min injection rate. However, a significant difference could be identified in the closure process for each injection rate. For the 2.2 L/min condition it can be seen that the closure process begins almost immediately with the PRV closing until approximately 3 mm at 0.05 seconds where a rapid closure event takes place. At this point however, significant piston instability could be observed at the PRV vibrated from a range of 4.5 mm to 2 mm (2.5mm amplitude) with a non-repeating pattern. In comparison, for the 1 L/min case, the disc lift followed the single phase trend until approximately 0.1 seconds whereby a similar vibration occurred however at a higher frequency than the 2.2 L/min condition and with a larger amplitude (4.5mm) between 1.5 mm and 6 mm disc lift. This behaviour for both of the two phase flow conditions is significantly different to the more stable dynamics

exhibited by the PRV when operating in single phase air only as the PRV approaches 3.5mm and closes immediately with no further vibration. Following closure, it could also be identified that the final position of the disc for the 2.2 L/min case was higher than that of the 1 L/min and single phase condition. This could be explained by the much higher inlet pressure at closure for the 2.2 L/min case which would result in the PRV to remain at a slightly higher lift due to the inability of the PRV to seal. In future work this should be investigated further with the PRV installed in a vertical position.

The instability events identified in figure 8.56 could be appreciated with reference to the steady state piston force vs lift graph (figure 8.10) and also water mass fraction vs lift graph (figure 8.13) generated within section 8.1. It was established that there was a clear connection between injection rate and piston force for each individual steady state lift data point. Therefore, during dynamic operation as shown within figure 8.56, as disc lift decreases the water mass fraction also changes in a logarithmic manner shown in figure 8.13 with an asymptote for disc lift of approximately 3.5 mm. As can be observed from figure 8.56, the instability behaviour exhibited for both two phase flow conditions occurred at approximately 3.5 mm disc lift whereby as the PRV continued to close further; water mass fraction would increase and piston force would change quickly. This rapid change in piston force would therefore result in an unstable dynamic relationship for the piston force and spring line resulting in the dynamic instability of the PRV shown in figure 8.56. In general, it could therefore be concluded that in addition to affecting blowdown pressure for the better, an undesirable increase in instability arises between single phase and two phase operation. These comments however at this stage can be only be defined as observations with further work required to understand the instability and generate appropriate conclusions.

8.2.3 Summary of Experimental Two Phase Transient Study

Following a novel two phase transient experimental study for the through flow type Henry 5231BX PRV, a number of conclusions could be established;

- The two-phase tests indicated that the closing of the PRV led to a reduction in blowdown pressure compared to single phase closure with higher liquid flowrates leading to an increased reduction in blowdown pressure. Thus for the tests examined, improved closure conditions was observed providing a more desirable PRV performance during two phase operation when compared with single phase air.

- When compared with single phase operation, the dynamic response of the valve was observed to undergo greater instabilities during two phase blowdown. With reference to the steady state two phase conclusions discussed in section 8.1, it can be postulated that the instability mechanism was caused by the relationship between piston force and water injection rate. Oscillation was therefore induced because of fluctuating piston force caused by changes in water mass fraction as the PRV disc lift reduced during closure.

CHAPTER 9

CONCLUSIONS AND FUTURE RECOMMENDATIONS

Throughout the work presented in this thesis, the research objectives have been pursued with the aim of providing a notable contribution to both PRV and applied CFD research fields. In general, the primary objective of this thesis was to perform an analysis of the complex single and two phase flow conditions often found in PRV's and establish the applicability of existing CFD modelling techniques using the commercial CFD package ANSYS FLUENT as a platform. It is hoped that this contribution has been achieved with reference to the gaps in knowledge and opportunities highlighted within the literature review to improve upon and develop a modern and sophisticated experimental and CFD modelling approach to the analysis of PRV performance. It should be noted that by tackling the thesis objectives to achieve the desired contribution it was necessary to overcome significant computational and practical challenges throughout the course of the project. By doing so it was possible to appreciate unexpected issues with experimental validation, measuring equipment, flow phenomenon and modelling issues in order to derive new conclusions and avenues for future research to take inspiration.

Furthermore, it is hoped that the demonstrated capabilities of both the experimental methods and partially validated computational models for various types of PRV geometries could be used in future research projects as well as by PRV manufacturers to improve upon their current research and development processes. Overall it could be concluded that the experimental and computational analysis techniques developed for both the Broady and Henry PRV's have been effective with the majority of the research objectives being met in order to provide a worthwhile contribution to the PRV research and industrial community. In the following subsections, the overall conclusions and contributions for each objective will be explored in more detail.

9.1 Single Phase CFD Validation Conclusions

In this study, the capability of current CFD techniques to model single phase flow for the two main types of PRV geometry for both 2D and 3D simulation has been investigated. By doing so the relevant literature has been reviewed to establish the current standard of both CFD and experimental validation techniques. It was found that a significant amount of work has been performed to develop accurate single phase steady state CFD models of PRV's which achieve good correlation with experimental data. Some work [11, 12] however in particular for through flow type PRV's was found to have been limited to a 2D axisymmetric approximation and although provided overall satisfactory results, anomalous predictions of back pressure were evident suggesting that the development of 3D CFD might resolve these inconsistencies. Furthermore, extensive validation of turbulence models and numerical discretization methods has not been widely performed for different types of PRV geometries. Therefore in this body of work a detailed validation study was performed for both an ASME Section VIII/API right angled PRV from Broady Flow Control and an ISO 4126 through flow PRV supplied by Henry Technologies. For both the Broady and Henry PRV's a bespoke experimental rig was constructed for steady state and transient testing using flow testing laboratories at Broady Flow Control and the University of Strathclyde.

For the Broady PRV, a half symmetry 3D CFD model was developed using the K-Omega SST turbulence model at 3.3 barg inlet pressure. Over the course of the full lift range, an average percentage difference of the CFD results to experimental data for mass flow rate was found to be 1.6% and 0.83% for disc force. For the Broady PRV, a 2D model was not used due to the asymmetry of the PRV geometry which would require significant geometrical changes in order to be suitable for 2D simulation. Such 2D models have been shown in work by Taggart to be valid at low lifts however are less accurate at larger lifts therefore are not suitable for dynamic mesh simulation.

The Henry PRV on the other hand was acceptable for the use of 2D CFD simulation which was in accordance with previous research performed at the University of Strathclyde. In order for the geometry to be valid for 2D simulation, the use of a modified gland was required which maintained the flow features of the original gland but maintained an axisymmetric domain. Experimental data was then generated for both the original gland and modified gland to validate that the flow rate was identical for both. However a difference was observed for disc force, with the modified gland experiencing a higher force value due to a decrease in backpressure. This was consistent with observations in previous research using a similar type gland.

For CFD modelling of the Henry 5231BX PRV, as previous work used 2D CFD modelling for through flow type PRV geometries, a 2D CFD model was developed for the PRV with modified gland. However, the 5231BX used in this study was different to the valve used in previous research as Alshaikh [12] used a 5231BX with a larger outlet during his validation study. It was shown here that during the CFD validation study the 2D CFD models were unable to achieve the accuracy claimed during the validation work of Alshaikh. Following investigation it was concluded that the difference in outlet geometry with the production PRV used in this thesis compared to the bespoke outlet used by Alshaikh caused a significant modelling challenge for the smaller production case. However it was unclear whether or not the 2D CFD model provided the best accuracy for flow features or the combined modelling error of the standard K-Epsilon model was resulting in false confidence of the CFD method.

Due to the inaccuracy of the 2D CFD model for the 5231BX PRV, as suggested in previous work by Elmayyah [11] a 3D CFD model was developed to determine if an improvement in accuracy for disc force could be achieved. A quarter symmetry 3D CFD model was developed for both the original and modified gland 5231BX test cases as well as for the Alshaikh case with larger outlet modifications. For both gland cases, the 3D K-Omega SST turbulence model provided the best performance with an average correlation to

experimental data of 1.67% for mass flow rate and 5.11% for disc force. In the case of the larger outlet used in the work by Alshaikh, a significant improvement from the 2D K-Omega SST CFD model using the 3D K-Omega SST model was found however the 2D standard K-Epsilon model remained the best choice. This therefore validates the work found by Alshaikh [12] and highlights a sensitivity for outlet geometry on the use of both 2D and 3D modelling as well as turbulence model selection.

Over the course of the Henry 5231BX steady state validation study, significant differences in the performance of the 2D and 3D CFD models were found. As shown in the case for the modified gland, the 3D K-Omega SST turbulence model provided significant improvement to the 2D equivalent with close correlation to experimental data. It was found that the difference observed between the two models was due to the generation of 3D flow effects caused by symmetry breaking bifurcations. It was postulated that these bifurcations were possibly caused due to the flow conditions within the PRV meeting criteria for both Reynolds number and geometrical expansion set in research by Padrón [47] for symmetry breaking within axisymmetric domains. It could therefore be suggested that for the 5231BX production PRV geometry used within this study, the use of axisymmetric boundary conditions within 2D CFD simulations were not valid. This challenges the recommendations previously established by both Elmayyah and Alshaikh for through flow PRV's.

Following on from the steady state validation work, as was identified within the literature there was a lack of validation data performed for various types of PRV geometry across their entire operating range from opening to closing. It was also found that most models available required significant geometrical simplification of the PRV to be suitable for dynamic meshing in CFD. Therefore within this thesis a dynamic mesh method was developed to accurately capture the geometrical details of various types of PRV geometries to predict the complete dynamic process of opening and closing of a PRV. Both the validated 3D CFD models for the Broady 3511E PRV and modified gland 5231BX PRV

using the K-Omega SST turbulence models was used as a template for transient, dynamic mesh CFD models to be developed from.

In order to allow transient validation to take place it was required to develop an effective transient experimental rig to capture the dynamics of each PRV during their operation. Experimental data for the 3511E PRV was provided by data generated during research by Taggart [9] at the testing facility at Broady Flow Control. A testing rig and method was constructed for the 5231BX at the flow testing laboratory at the University of Strathclyde. It has been shown for both the Broady and Henry PRV's that the dynamic response of a PRV to a transient inlet pressure ramp can be accurately captured using moving mesh CFD methods. The moving mesh method which was developed within this body of work utilised a hybrid mesh domain with dynamic layering occurring within the structured mesh regions. The deformation and dynamics of the PRV within the CFD model was controlled using a bespoke UDF which contained the characteristic information of the PRV required for modelling. It was found that the dynamic mesh approach was effective and provided an effective approach of dynamic meshing of a PRV when referencing available literature. The overpressure and blowdown response predicted by the moving mesh CFD model for the Broady 3511E PRV was able to be accurately captured to within 1.4% and 0.3% respectively. The 5231BX PRV with modified gland was also able to be captured to within 0.06% for overpressure and 0.31% for blowdown.

However, following on from the development and results of both the steady state and transient validation of the PRV's it was possible to appreciate flow mechanisms and features using the transient moving mesh CFD model in which the steady state model was not able to capture. As a result, instability mechanisms were able to be captured in particularly for the Henry PRV as well as flow features for both PRV's which questioned the validity of the generally assumed quasi steady behaviour of the PRV disc during operation. In general both the CFD representations of the dynamic characteristics of both the Henry and Broady PRV's were accurate when compared to experimental values such

as maximum lift and general blowdown behaviour. Variations in flow structure such as Mach number contours and static pressure distribution was found to exist between equivalent points of disc lift during opening and closing of the PRV. Differences could also be found when compared with flow structures predicted during steady state simulation with larger differences observed for the Henry PRV, in particular for the jet deflection angle and resulting regions of recirculating flow.

As a result of the observations of flow features which suggested differences between transient and steady state simulation a dedicated CFD study was performed to determine the validity of the quasi-steady design approach for both the Broady 3511E and Henry 5231BX PRV's. Both steady state and moving mesh transient CFD based simulations was used to compare the flow characteristics of aerodynamic piston force and flow rate predicted using both approaches. In addition the use of a quasi-steady based MATLAB type 1 model was used and compared with transient CFD and transient experimental results. For the Broady PRV it was found that a small effect of disc motion was caused on the flow characteristics of the PRV as the disc force was reduced. However following analysis using a quasi-steady based MATLAB type 1 model it was found that the quasi steady assumption was valid for the Broady PRV as good correlation could be achieved in determining overpressure, blowdown and dynamic characteristics.

On the other hand, for the Henry 5231BX PRV, it was found that due to the formation of temporal, short lived vortices at the piston surface which influence the bulk flow features as the disc accelerates and decelerates, a significant difference in the prediction of aerodynamic force was found at both high and low lifts. It can be concluded that during a rapid piston displacement process for the 5231BX PRV that there is a coupling of the flow reducing the validity of the quasi-steady state assumptions. This was confirmed using a series of transient moving mesh CFD simulations at various fixed values of disc velocity. It was found that at high piston velocities within an enclosed valve body such

as the 5231BX; a significant difference was found between the prediction of the piston force for transient and steady state CFD. From experimental and CFD results, the piston velocity for the 5231BX was found to be significant during opening and final closure which further suggested the likelihood of a breakdown of the quasi steady flow conditions. A consistency however was found between transient and steady state simulation for the 5231BX PRV in predicting the choking point at both high and low lifts. As a consequence, the predicted mass flow rate through the valve using both numerical approaches displayed good agreement. Therefore, it was concluded that the use of quasi-steady design methods to determine the dynamic mass flow characteristics of a PRV with similar geometry to the 5231BX is appropriate but care should be taken for piston force.

It was therefore established that the validity of the quasi-steady assumption for PRV modelling should be determined in a case by case basis as it was found to be valid for the ASME 3511E PRV but had deficiencies for the through flow 5231BX PRV. Care must be taken in particular for PRV's in which the disc is enclosed in a small cavity and complex annular flow paths exist around the disc similar in nature to the 5231BX. In addition the use of a transient CFD model would be able to capture a much more accurate representation of the opening and blowdown processes compared to a typical type 1 numerical modelling approach using quasi steady assumptions. CFD could therefore be used by PRV designers to provide visualization and in depth data regarding the flow regimes in the PRV.

Overall, it could be concluded that the research objectives for single phase CFD validation were met within this thesis with future recommendations outlined within section 9.4.

9.2 Two Phase CFD Validation Conclusions

The current literature indicates there has been development of two phase experimental and modelling techniques in 2D for through flow PRV geometry, in particular for previous research performed at Strathclyde. Furthermore, the effectiveness of CFD has been compared to simpler analytical type 2 models suggested in standards however little CFD work has been performed for two phase analysis for 3D domains and therefore an opportunity was identified to possibly provide improvement in accuracy for modelling two phase flow through a PRV by using improved 3D geometrical representation. In addition, no previous studies were identified for transient two phase experimental testing of a through flow type PRV in order to determine the effects of two phase flow on the dynamic performance of a PRV when compared to single phase conditions.

A number of conclusions can be made following a two phase (air-water) CFD steady state validation study using ANSYS FLUENT for the Henry 5231BX PRV. Within the flow testing laboratory at the University of Strathclyde, a two phase (air-water) experimental rig for the Henry 5231BX PRV with modified gland was developed to provide measurement of piston force, mass flow rate and backpressure at piston lifts from 0.5 mm to 5 mm. To achieve this, an improved experimental rig was developed in order to improve accuracy and operation of the experiment. Experimental tests were conducted for water injection rates of 0.96 L/min, 2.1 L/min and 4.25 L/min to produce a mono-dispersed jet of water droplets with air. From the steady state experimental results, it could be concluded that injection rate influenced both valve air mass flowrate and piston force. However backpressure was not influenced significantly between single phase and two phase operation. This was in contrast to previous conclusions by Elmayyah [11]. Furthermore, the two phase analysis performed previously at Strathclyde by Elmayyah [11, 29, 30]

and Alshaikh [12, 26-28] included analysis only for a larger non manufacturer specification outlet.

A 3D two phase steady state model was developed using ANSYS FLUENT 18.1 by applying the lessons learned from the single phase steady state study presented in section 5.2. The 3D CFD model utilised a two phase mixture model in order to minimise computational expense and was verified in previous studies to be effective [12] at lower mass fractions. A quarter symmetry 3D CFD model was developed for the modified gland through flow 5231BX valve for water injection volume flowrates of 2.1 L/min and 0.96 L/min. It was found that an average correlation to experimental data of 3.5% for mass flow rate and 10.6% for disc force could be achieved for 2.1 L/min and a correlation of 0.7% for mass flow rate and 14.1% for disc force could be achieved for 0.96 L/min.

In general, the CFD trends for piston force, air mass flow rate and backpressure matched the experimental results especially for air mass flow rate. Although in conjunction with the conclusions from the single phase CFD model research, significant model induced error was found to occur for lifts between 2.5-3 mm for piston force prediction due to the CFD model being unable to accurately resolve the recirculation region beneath the piston surface. Most significantly however, large differences for backpressure was found for the two phase CFD models for piston lift lower than 2.5 mm. Which as result caused the CFD models to suffer from an under-prediction of piston force at lower lifts. In addition, symmetry breaking phenomena could also be observed, especially at lower lifts of 1.5 mm for both injection rates and at high lift (4mm) at higher water volume fractions.

In addition to the two phase steady state analysis a novel two phase transient experimental study for Henry 5231BX PRV (modified gland) was carried out.

It was necessary that in order to obtain an understanding towards the effect of two phase (air-water) flow on the dynamic operation of the Henry 5231BX PRV (modified gland). It was necessary to develop an in-house, two phase transient experimental rig to capture the dynamics of the 5231BX PRV during its typical operation for a range of water injection rates.

From the transient experimental two-phase flow results it was shown that the dynamic response of the 5231BX PRV for two-phase flow could be captured. As a result, it was possible to establish that an increase in water injection rate will lead to a more rapid closure of the valve with subsequent reduction in blowdown pressure when compared to single phase air only operation. In addition, it was found that an instability mechanism was present during rapid closure of the PRV for two phase flow caused by the relationship between piston force and water injection rate. An oscillation was therefore induced because of fluctuating piston force caused by changes in water mass fraction as the PRV disc lift reduced during closure.

9.3 Evaluation of CFD as a Design Tool for PRV Development

The project overview previously discussed in chapter 1 proposed that a CFD model of a PRV once validated to an acceptable degree of accuracy, could provide valve manufacturers with an inexpensive theoretical solution when compared to experimental testing. This is especially true during the initial design stages of PRV design which is often the most time consuming stage of the development process and where significant cost reductions for the PRV manufacturer could be achieved by utilizing CFD. In fact this has already been shown in the studies of Taggart [9] where CFD combined with optimization processes can lead to improved valve designs in typical single phase operation

This study has shown that both the steady state CFD models are generally accurate at capturing the overall flow features of both ASME and the generic through flow type PRV's to predict both disc forces and flow rates. However, a limitation of the quasi steady state assumption was observed for the through flow Henry PRV which would reduce the effectiveness of a type 1 numerical model to predict the dynamic characteristics of the PRV. As a result of the ability of steady state CFD to capture flow characteristics of both the through flow (Henry) and ASME (Broady) PRV's accurately it is clear that the visualization tools available from CFD could provide designers with a useful design tool. This is due to the fact that CFD allows for diagnosis of design issues and flow performance which would normally be difficult to appreciate from experimental tests for force and mass flow rate alone could be achieved. This was also observed in the conclusions of research performed by Taggart [9] who utilized optimization tools alongside CFD to improve PRV performance in a much more timely and efficient manner than by physical testing only.

Furthermore, in the case of dynamic moving mesh CFD simulations, it has been demonstrated that the transient characteristics during both overpressure and blowdown for the Henry and Broady PRV's has been accurately captured. Therefore, especially in the case of the Henry PRV where the quasi steady assumption was found to be invalid, dynamic mesh CFD models could be used to replace type 1 numerical models in order to allow designers to achieve a greater understanding of the transient characteristics of the PRV. This is due to the fact that the moving mesh CFD results would provide greater information regarding the transient performance of the PRV when compared to the type 1 model and identify any flow issues which may arise during operation. This allows further refinement of PRV design before physical prototypes are required to be machined and helps to improve overall safety. As a result of both steady state and transient CFD simulations it would therefore be hoped that fewer physical design iterations would be required which would significantly reduce manufacturing and testing cost.

Following discussion with engineers from both Henry and Broady and evaluating the CFD costs involved in this thesis by referencing the access fees required for the HPC facility ARCHIE WeST it was possible to produce the data shown within table 9.1. Within the table an approximate cost per each physical design iteration is provided for each manufacturer alongside an estimated cost for both steady state and transient CFD simulation using non-academic access of the ARCHIE WeST HPC.

	Steady State CFD Cost/Simulation (£)	**Moving Mesh CFD Cost/Simulation (£)**	**Manufacturing Cost/Design Iteration (£)**
Broady	2772	1344	4000
Henry	3696	1680	1000

Table 9.1 – Cost Comparison of Both Steady State and Moving Mesh CFD Simulation vs Manufacturing Cost per Each Physical Design Iteration

From the results it is clear that if CFD is used correctly in the early design phase, especially in the case of the Broady PRV, significant financial benefits could be achieved when compared to producing physical test valves. In addition, a hidden benefit could also be found by the reduction in use of machining and workshop staff to manufacture the test valves as those valuable resources could be used elsewhere. Interestingly from table 9.1 it could also be appreciated that in the case of the Henry PRV analysis, a transient moving mesh CFD analysis would be much more cost effective than a steady state study due to the large meshing requirements of the 5231BX model. This is especially true as the quasi-steady assumption is not valid. On the other hand, for the Broady PRV both a steady state and moving mesh CFD simulation could be performed at a similar cost to producing a physical prototype of a design iteration for testing. Furthermore, the use of a two phase flow CFD

analysis could help to identify flow features which would otherwise have been discounted using single phase CFD techniques alone.

9.4 Novel Contributions

When evaluating the thesis overall, several novel contributions from this body of work have been identified.

- When reviewing chapter 5 and the extensive single-phase, steady state CFD modelling and validation work which was performed for both the Broady and Henry PRV geometries; it was evident that a clear numerical modelling approach had been identified to be resilient for both types of PRV's. This primarily included the use of 3D modelling, with a well refined, mesh independent region at the disc/seat interface. In addition, the use of the K-Omega SST turbulence model was identified to provide better accuracy when compared with K-Epsilon where in previous literature this had not been clearly demonstrated. In addition, the limitations of 2D modelling were explored in some detail within chapter 5 to provide a much deeper understanding towards the limitations of utilizing 2D CFD models for PRV's which were previously only postulated. This step was also crucial in providing a basis in which the single-phase transient moving mesh CFD model would be developed upon. It is hoped that these novel insights will therefore provide a foundation of CFD modelling to assist in future PRV research.

- In chapter 6, there were several novel contributions which could be identified. Initially, the meshing procedure which was used was proven to be resilient across both the Broady and Henry PRV geometry to achieve a dynamic mesh CFD model capable of accurately capturing the dynamic features of PRV operation such as overpressure and

blowdown. This dynamic meshing procedure had been previously demonstrated to be effective in modelling pumps, however this was the first time such an approach had been modified and used in the case of PRV's. Furthermore, it was also demonstrated that the numerical modelling used within the single phase, steady state 3D models could be successfully extended to transient dynamic mesh modelling with the use of an HPC. In addition, a bespoke method of transient, dynamic experimental testing was developed to allow model validation.

- In the case of the Henry 5231BX transient dynamic mesh CFD model, the insights generated from the observed disc instability and associated flow features were novel and had not been previously documented in literature for a through flow type PRV. As a result, this work has helped to provide a significant leap in understanding and documenting the limitations and capability of CFD to capture the complex flow phenomena which occur during the dynamic operation of a PRV similar in geometry to the through flow type Henry 5231BX PRV.

- Furthermore, chapter 7 helps to gain a greater appreciation and explore the limitations of the quasi-steady assumption for PRV's. Such an analysis had been discussed in literature previously however had not been explored for both right angled and through flow type PRV's and had not utilized a transient, dynamic mesh model to do so. Therefore, the insights generated within this chapter were especially novel in nature and it is hoped will help better inform of the limitations for using the quasi-steady assumption for PRV design/analysis in the future.

- Finally, chapter 8 within this thesis provided a novel extension of the 2D two-phase work found in literature for through flow type PRV's to 3D; which as a result generated a vast array of insights in to the capability of the homogenous CFD mixture model. Achieved alongside this was the development of a bespoke two phase (air/water) steady state and transient experimental testing process and equipment. This approach

was particularly novel in terms of the methodology used, especially for transient experimental measurement of two-phase flow in a through flow type PRV where no such previous work was identified in literature. The experimental insights generated for the dynamic performance of a through flow type PRV in two-phase are therefore incredibly valuable to the industry in achieving a better understanding of PRV performance in such flow conditions.

9.5 Future Work and Recommendations

Following the significant amount of validation and analysis performed for both steady state and transient moving mesh CFD simulations; a number of proposals for future work and recommendations could be made to compliment the research presented within this thesis;

- To test the robustness and accuracy of both steady state and transient CFD models developed at much higher pressure for both PRV's. The pressures tested for both the ASME 3511E PRV and Henry 5231BX PRV were relatively low to ensure that experimental validation could take place. However, as validation has been performed, the work demonstrated within this thesis could be extended to appreciate flow characteristics at higher pressures and understand any CFD modelling challenges which may arise from doing so.

- Investigate the use of models other than RANS such as RSM and LES as readily available computational resources continue to increase to determine if an improvement in correlation can be achieved. This is in order to better understand the poor performance of RANS based models to capture the flow characteristics of the Henry 5231BX PRV below the piston face.

- The use of overset meshing and zero gap technology to achieve a more accurate representation of opening for transient CFD modelling. This is due to the ever-developing nature of CFD models and the potential benefits which using overset meshing may provide to capture the initial phases of opening. Where the current methodology presented within this thesis includes a small opening during transient CFD modelling to maintain mesh topology.

- To develop an automatic time step routine within the UDF for the transient moving mesh CFD model to maintain computational stability and avoid the generation of negative volumes.

- To develop an optimization routine similar to that of Taggart [9] for the transient dynamic mesh model in order to achieve the desired dynamic performance such as overpressure and blowdown by modifying critical geometry at the disc and seat areas.

- To develop an experimental rig which would allow Particle Image Velocimetry (PIV) to take place to validate areas of recirculation and symmetry breaking suggested in this research for the Henry 5231BX PRV. This would therefore open a possible avenue of further investigation for validating the RANS CFD models used in this thesis and understand their limitations. In addition, it would be useful to understand the effect of such flow characteristics on the typical operation of the PRV such as instability. In addition, a representative section of the disc/seat geometry of the 5231BX PRV could be used to remove the remaining flow regions of the PRV which are not of interest.

- To develop a two-phase dynamic mesh transient CFD model and validation study to experimental measurements. This will allow a greater understanding of the effect of two-phase flow on the transient operation performance of a PRV when compared to single phase operation only.

REFERENCES

1. Hellemans, M., *Chapter 3 - Terminology*, in *The Safety Relief Valve Handbook*, M. Hellemans, Editor. 2010, Butterworth-Heinemann: Oxford. p. 27-52.

2. Malek, M.A., *Pressure relief devices : ASME and API code simplified*. 2006, New York: New York : McGraw-Hill.

3. American Institute of Chemical Engineers. Center for Chemical Process, S., *Guidelines for pressure relief and effluent handling systems*. Pressure relief and effluent handling systems. 1998, New York, N.Y.: New York, N.Y. : The Institute.

4. Hellemans, M., *Chapter 4 - Codes and Standards*, in *The Safety Relief Valve Handbook*, M. Hellemans, Editor. 2010, Butterworth-Heinemann: Oxford. p. 53-77.

5. Beune, A., *Analysis of high-pressure safety valves*. 2009.

6. Kourakos, V., et al., *Flowforce in a Safety Relief Valve Under Incompressible, Compressible, and Two-Phase Flow Conditions (PVP-2011-57896).* Journal of Pressure Vessel Technology, 2013. **135**.

7. Scuro, N.L., et al., *A CFD analysis of the flow dynamics of a directly-operated safety relief valve.* Nuclear Engineering and Design, 2018. **328**: p. 321-332.

8. Song, X., et al., *A CFD analysis of the dynamics of a direct-operated safety relief valve mounted on a pressure vessel.* Energy Conversion and Management, 2014. **81**: p. 407–419.

9. Taggart, S., *Design Optimisation of a Safety Relief Valve to Meet ASME Section I Performance Requirements*. 2020.

10. Hellemans, M., *Chapter 1 - History*, in *The Safety Relief Valve Handbook*, M. Hellemans, Editor. 2010, Butterworth-Heinemann: Oxford. p. 1-5.

11. Elmayyah, W., *Theoretical and Experimental Investigations of Multiphase Flow in Safety Relief Valves*. 2010.

12. Alshaikh, M., *Theoretical and Experimental Investigations on Critical Multiphase Flows in Safety Relief Valves and Nozzles*. 2015.

13. Matthews, C., *A quick guide to pressure relief valves (PRVs)*. Pressure relief valves. 2004, London: London : Professional Engineering Publishing.

14. Clement, C., *Fault Tree Analysis of the Three Mile Island (TMI) Nuclear Reactor Partial Nuclear Melt Down*. 2014.

15. Hellemans, M., *Chapter 2 - Overpressure Protection*, in *The Safety Relief Valve Handbook*, M. Hellemans, Editor. 2010, Butterworth-Heinemann: Oxford. p. 6-26.

16. Hellemans, M., *Chapter 7 - Sizing and Selection*, in *The Safety Relief Valve Handbook*, M. Hellemans, Editor. 2010, Butterworth-Heinemann: Oxford. p. 158-189.

17. Dossena, V., et al., *Reynolds number effects on the performance of safety valves operating with incompressible flows.* Journal of Loss Prevention in the Process Industries, 2017. **49**: p. 525-535.

18. Yang, L., et al., *Experiments and transient simulation on spring-loaded pressure relief valve under high temperature and high pressure steam conditions.* Journal of Loss Prevention in the Process Industries, 2016. **45**.

19. Beune, A., J. Kuerten, and J. Schmidt, *Numerical Calculation and Experimental Validation of Safety Valve Flows at Pressures up to 600 bar.* Aiche Journal - AICHE J, 2011. **57**.

20. Beune, A., J. Kuerten, and M. Heumen, *CFD analysis with fluid–structure interaction of opening high-pressure safety valves.* Computers & Fluids, 2012. **64**: p. 108–116.

21. Song, X.-G., Y.-C. Park, and J.-H. Park, *Blowdown prediction of a conventional pressure relief valve with a simplified dynamic model.* Mathematical and Computer Modelling, 2013. **57**(1): p. 279-288.

22. Darby, R., *The dynamic response of pressure relief valves in vapor or gas service, part I: Mathematical model.* Journal of Loss Prevention in the Process Industries, 2013. **26**: p. 1262-1268.

23. Darby, R. and A.A. Aldeeb, *The dynamic response of pressure relief valves in vapor or gas service. Part III: Model validation.* Journal of Loss Prevention in the Process Industries, 2014. **31**: p. 133-141.

24. Hellemans, M., *Chapter 5 - Design Fundamentals*, in *The Safety Relief Valve Handbook*, M. Hellemans, Editor. 2010, Butterworth-Heinemann: Oxford. p. 78-128.

25. Dempster, W., S. Taggart, and C. Doyle, *Limitations in the Use of Pressure Scaling for Safety Relief Valve Design*. 2018. V03AT03A002.

26. Alshaikh, M. and W. Dempster, *A CFD Study on Two-Phase Frozen Flow of Air/Water Through a Safety Relief Valve.* International Journal of Chemical Reactor Engineering, 2015. **13**.

27. Dempster, W. and M. Alshaikh, *An Investigation of the Two Phase Flow and Force Characteristics of a Safety Valve.* Procedia Engineering, 2015. **130**: p. 77-86.

28. Dempster, W. and M. Alshaikh, *CFD Prediction of Safety Valve Disc Forces Under Two Phase Flow Conditions*. 2018. V03AT03A003.

29. Dempster, W. and W. Elmayyah, *Two phase discharge flow prediction in safety valves.* International Journal of Pressure Vessels and Piping, 2013. **110**: p. 61-65.

30. Elmayyah, W. and W. Dempster, *Prediction of two-phase flow through a safety relief valve.* Proceedings of the Institution of Mechanical Engineers, Part E: Journal of Process Mechanical Engineering, 2013. **227**: p. 42-55.

31. Hős, C.J., et al., *Dynamic behaviour of direct spring loaded pressure relief valves connected to inlet piping: IV review and recommendations.* Journal of Loss Prevention in the Process Industries, 2017. **48**: p. 270-288.

32. Borg, A., *On the stability of pressure relief valves - a numerical study using CFD*. 2014.

33. Zheng, F., et al., *Dynamic Instability Analysis of a Spring-Loaded Pressure Safety Valve Connected to a Pipe by Using CFD Methods.* Journal of Pressure Vessel Technology, 2021. **143**.

34. Elmayyah, W., *Computational Fluid Dynamics Investigations of Shock Waves in Safety Relief Valves.* International Conference on Aerospace Sciences and Aviation Technology, 2013. **15**: p. 1-11.

35. Dempster, W. and W. Elmayyah, *A computational fluid dynamics evaluation of a pneumatic safety relief valve.* The International Conference on Applied Mechanics and Mechanical Engineering, 2008. **13**.

36. Srikanth, C. and C. Bhasker, *Flow analysis in valve with moving grids through CFD techniques.* Advances in Engineering Software, 2009. **40**(3): p. 193-201.

37. Zhan, J.-M., et al., *Numerical study on the six-DOF anchoring process of gravity anchor using a new mesh update strategy.* Marine Structures, 2017. **52**: p. 173-187.

38. Saha, B.K., et al., *Dynamic simulation of a pressure regulating and shut-off valve.* Computers & Fluids, 2014. **101**: p. 233-240.

39. Song, X., L. Wang, and Y. Park, *Transient Analysis of a Spring-Loaded Pressure Safety Valve Using Computational Fluid Dynamics (CFD).* Journal of Pressure Vessel Technology, 2010. **132**: p. 054501.

40. Zhang, J., et al., *Prediction of blowdown of a pressure relief valve using response surface methodology and CFD techniques.* Applied Thermal Engineering, 2018. **133**.

41. Iannetti, A., M. Stickland, and W. Dempster, *A CFD and experimental study on cavitation in positive displacement pumps: Benefits and drawbacks of the 'full' cavitation model.* Engineering Applications of Computational Fluid Mechanics, 2016. **10**: p. 57-71.

42. Anna Budziszewski, L.T., *CFD simulation of a safety relief valve for improvement of a one-dimensional valve model in RELAP5*. 2012.

43. Couzinet, A., et al., *Experimental Study and Numerical Modeling of Incompressible Flows in Safety Relief Valves*. 2015.

44. Arnulfo, G., C. Bertani, and D.S. Mario, *Prediction of two-phase choked-flow through safety valves.* Journal of Physics: Conference Series, 2014. **501**: p. 012016.

45. Doyle, C., W. Dempster, and S. Taggart, *An Assessment of the Validity of Quasi-Steady Analysis of Pressure Relief Valves*. ASME 2019 International Mechanical Engineering Congress and Exposition, Volume 7:Fluids Engineering. 2019.

46. *11 Annular- and leakage-flow-induced instabilities*, in *Fluid-Structure Interactions*, M.P. Païdoussis, Editor. 2003, Academic Press. p. 1221-1420.

47. Padron, F., *Study Of Symmetry-Breaking Instabilities In Axisymmetric Geometries*. 2016.

48. *ANSYS Fluent Theory Guide 15.0*. 2013.

49. Fung, Y.C. and J.L. Sanders, Jr., *A First Course in Continuum Mechanics (Second Edition).* Journal of Applied Mechanics, 1978. **45**(4): p. 969-969.

50. Aris, R., *Vectors, Tensors and the Basic Equations of Fluid Mechanics*. Dover Books on Mathematics. 1990: Dover Publications.

51. Versteeg, H.K. and W. Malalasekera, *An Introduction to Computational Fluid Dynamics: The Finite Volume Method*. 2007: Pearson Education Limited.

52. Wintergerste, T., M. Casey, and A. Hutton, *The Best Practice Guidelines for CFD: A European Initiative on Quality and Trust (Keynote)*. 2002.

53. Kleinstreuer, C., *Two-Phase Flow: Theory and Applications*. 2003: Taylor & Francis.

54. Flows, S. and M. Sommerfeld, *Best Practice Guidelines for Computational Fluid Dynamics of Dispersed Multi-Phase Flows*. 2008.

55. *ANSYS Fluent Customization Manual 18.0*. 2017.

56. *ANSYS Fluent User Guide 18.1*. 2017.

57. Gronkowski, J., *Integration of Computational Fluid Dynamics and Transient Analysis Methods into Relief Valve Design* 2010.

APPENDIX

Appendix A1 – Transient CFD Dynamic Mesh Animations for 3511E and 5231BX PRV's. These files are hosted as unlisted videos on YouTube and can be accessed by clicking on the links below.

Broady 3511E PRV - https://youtu.be/nE5fJ4FEqEQ

Henry 5231BX PRV - https://youtu.be/9QzbaNeRO6k

Appendix A2 – Example UDF for Transient CFD Model within ANSYS FLUENT for Henry 5231BX PRV (modified gland)

```
/************************************************************
* UDF for 3D Transient Simulation of Henry Technologies Pressure Relief Valve Using Dynamic Meshing for use within ANSYS FLUENT - CHRIS DOYLE
************************************************************/
#include "udf.h"
#include "mem.h"

/*global variables*/
static real k = 10990; /*spring constant*/
static real gravity = 9.81; /*gravity constant*/
static real z max = -0.006; /*the maximum lift is 5 mm*/
static real f0 = 54; /*initial spring force */
static real mass = 0.03; /*spindle mass - preload already incorporates moving mass value so gravity force is not included*/
static real c = 5.4473;
real total_force = 0.0;
real pressure force = 0.0; /*the total hydraulic force over the entire spindle*/
real pressure_force1 = 0.0; /*hydraulic force on disc*/
real pressure_force2 = 0.0;
real pressure force3 = 0.0;
real pressure_force4 = 0.0;
real spring_force = 0.0;
real damping force = 0.0;
real z = -0.00005; /*NEED TO MEASURE THIS ON FLUENT simulation starts with an opening of 0.05 mm*/
real velocity1 = 0.0;
real velocity2 = 0.0;
real massflow = 0.0;
real total_area1 = 0.0;
real total area2 = 0.0;
real total_area3 = 0.0;
real mass_flow1 = 0.0;
real mass flow2 = 0.0;
real mass_flow3 = 0.0;
real timestep = 0.0;
real dz = -0.00595; /* real dz = real z_max - realz */
real velocity = 0.0;
real total_time = 0.0;
real time step = 0.0;
real pressure = 0.0;
real inlet_pressure = 0.0;
/*****************************************************************************/


DEFINE_ADJUST(force_calculation, domain)
{
    /* This function calculates the hydraulic forces acting on the spindle*/
    int surface thread id1 = 79;
    int surface thread id2 = 80;
    int surface_thread_id3 = 81;
    int surface_thread_id4 = 82;

    pressure_force1 = 0.0;
    pressure_force2 = 0.0;
    pressure force3 = 0.0;
    pressure_force4 = 0.0;

#if !RP HOST
    Thread *thread1; /*structure data type that stores data that is common to the
                       group of cells or faces that it represents*/
    Thread *thread2;
    Thread *thread3;
    Thread *thread4;

    face_t face; /* an integer data type that identifies
                 a particular face within a face thread*/
    real area[ND_ND];

    /*get the thread pointer for which this motion is defined*/
    thread1 = Lookup Thread(domain, surface thread id1);
    thread2 = Lookup_Thread(domain, surface_thread_id2);
    thread3 = Lookup_Thread(domain, surface_thread_id3);
    thread4 = Lookup_Thread(domain, surface_thread_id4);

```

```
    /*compute pressure forces on body by looping through all faces*/
    begin f loop(face, thread1)
        if (PRINCIPAL_FACE_P(face, thread1)) /* test if the face is the principle face*/
        {
            F AREA(area, face, thread1);
            pressure_force1 += area[2] * F_P(face, thread1);
        }
    end_f_loop(face, thread1)

    begin_f_loop(face, thread2)
        if (PRINCIPAL_FACE_P(face, thread2)) /* test if the face is the principle face*/
        {
            F_AREA(area, face, thread2);
            pressure_force2 += area[2] * F_P(face, thread2);
        }
    end_f_loop(face, thread2)

    begin_f_loop(face, thread3)
        if (PRINCIPAL_FACE_P(face, thread3)) /* test if the face is the principle face*/
        {
            F_AREA(area, face, thread3);
            pressure_force3 += area[2] * F_P(face, thread3);
        }
    end_f_loop(face, thread3)

    begin f loop(face, thread4)
        if (PRINCIPAL_FACE_P(face, thread4)) /* test if the face is the principle face*/
        {
            F AREA(area, face, thread4);
            pressure_force4 += area[2] * F_P(face, thread4);
        }
    end_f_loop(face, thread4)


        pressure_force = pressure_force1 + pressure_force2 + pressure_force3 + pressure_force4;
#endif

#if RP NODE
    /*the value from all nodes are summed*/
    pressure_force = PRF_GRSUM1(pressure_force);
    pressure force1 = PRF GRSUM1(pressure force1);
    pressure_force2 = PRF_GRSUM1(pressure_force2);
    pressure_force3 = PRF_GRSUM1(pressure_force3);
    pressure_force4 = PRF_GRSUM1(pressure_force4);

#endif

    /*the data from the nodes is sent to the host*/
    node_to_host_real_5(pressure_force, pressure_force1, pressure_force2, pressure_force3,
    pressure_force4);
}
/*****************************************************************************/

DEFINE_ADJUST(velocity_calculation, domain)
{
    int surface_thread_id1 = 77; /*Inlet*/
    int surface thread id2 = 107; /*Nozzle Outlet - Nozzle_oface*/
    int surface_thread_id3 = 78; /*Outlet*/

    total area1 = 0.0;
    total_area2 = 0.0;
    total_area3 = 0.0;
    mass flow1 = 0.0;
    mass_flow2 = 0.0;
    mass_flow3 = 0.0;

#if !RP_HOST

    Thread *thread1;
    Thread *thread2;
    Thread *thread3;
    face t face;
    real area[ND_ND];
```

```
144
145     thread1 = Lookup Thread(domain, surface thread id1);
146     thread2 = Lookup_Thread(domain, surface_thread_id2);
147     thread3 = Lookup_Thread(domain, surface_thread_id3);
148
149     begin_f_loop(face, thread1)
150         if (PRINCIPAL_FACE_P(face, thread1))
151         {
152         F_AREA(area, face, thread1);
153         total_area1 += NV_MAG(area);
154         mass_flow1 += F_FLUX(face, thread1);
155         }
156     end_f_loop(face, thread1)
157
158     begin_f_loop(face, thread2)
159         if (PRINCIPAL_FACE_P(face, thread2))
160         {
161         F_AREA(area, face, thread2);
162         total_area2 += NV_MAG(area);
163         mass_flow2 += F_FLUX(face, thread2);
164         }
165     end_f_loop(face, thread2)
166
167     begin_f_loop(face, thread3)
168         if (PRINCIPAL_FACE_P(face, thread3))
169         {
170         F_AREA(area, face, thread3);
171         total_area3 += NV_MAG(area);
172         mass_flow3 += F_FLUX(face, thread3);
173         }
174     end_f_loop(face, thread3)
175
176 #endif
177
178 #if RP_NODE
179     mass_flow1 = PRF_GRSUM1(mass_flow1);
180     mass_flow2 = PRF_GRSUM1(mass_flow2);
181     mass_flow3 = PRF_GRSUM1(mass_flow3);
182     total_area1 = PRF_GRSUM1(total_area1);
183     total_area2 = PRF_GRSUM1(total_area2);
184     total_area3 = PRF_GRSUM1(total_area3);
185 #endif
186
187     massflow = mass_flow1;
188
189     node_to_host_real_1(massflow);
190
191 }
192 /*****************************************************************************/
193
194 DEFINE_CG_MOTION(spindle, dt, vel, omega, time, dtime)
195 {
196     /*reset velocities*/
197     NV_S(vel, = , 0.0);
198     NV_S(omega, = , 0.0); /*no angular motion*/
199
200     /*set z-component of velocity*/
201     vel[0] = 0;
202     vel[1] = 0;
203     vel[2] = velocity;
204
205     /*variable needed in execute_at_end*/
206     timestep = dtime;
207 }
208 /*****************************************************************************/
209
210 DEFINE_EXECUTE_AT_END(Velocity)
211 {
212     /*Calculation of velocity*/
213     real dv = 0;
214     /*real gravity_force = 0.0; */
215     spring_force = 0.0;
216     damping_force = 0.0;
```

```
217
218     /* calculate the total force acting on the spindle*/
219     /*gravity_force = mass*gravity; commented out as preload incorporates gravity force*/
220
221     /*calculate the spring force*/
222     spring_force = -k*z + f0; /*added a negative sign for Hooke's Law*/
223
224     /*calculate the total hydraulic force since quarter symmetry is used*/
225     pressure_force = pressure_force * 4;
226
227     damping_force = -c * velocity;
228
229     total_force = pressure_force + spring_force + damping_force; /*taken out gravity_force*/
230
231     dv = timestep * total_force / mass;
232     velocity += dv;
233
234     /*Restriction: stop at lift = 4 mm*/
235     if (dz > 0)
236     {
237         Message("\nThe valve is fully open!");
238     }
239
240     /*Restriction: stop if the valve is closed*/
241     if (dz < -0.00587) /*NEEDS CHANGED always 0.00001 less than real dz!!!!!!!!!!!***add additional
        correction factor to prevent negative volume during simmer***CHANGE FOR VARIOUS LIFTS*/
242     {
243         if (total_force > 0)
244         {
245             velocity = 0;
246             Message("\nThe valve is fully closed");
247         }
248     }
249 }
250     /************************************************************************/
251
252 DEFINE_EXECUTE_AT_END(lift_movement)
253 {
254     /*Calculation of the spindle position*/
255     z += timestep*velocity;
256     dz = z_max - z;
257
258     Message("\nThe spindle has moved %f\n", z);
259
260     total_time += timestep;
261 }
262     /************************************************************************/
263 DEFINE_EXECUTE_AT_END(saving_values)
264 {
265 #if RP_NODE
266     if (myid == 0)
267     {
268     FILE *data;
269     data = fopen("DampingNEW140319DynSimResults.txt", "a");
270     fprintf(data, "%f\t %f\t %f\t %f\t %f\t %f\t %f\t %f\t %f\t %f\t %f\t %f\t %f\t %f\t %f\n",
        total_time, velocity, z, pressure_force1, pressure_force2, pressure_force3, pressure_force4,
        pressure force, spring_force, damping_force, total_force, inlet_pressure, velocity1, velocity2,
        massflow);
271     fclose(data);
272     }
273 #endif
274 }
275 /************************************************************************/
276
277 DEFINE_PROFILE(inlet_pressure_profile, thread, P)
278 {
279 #if RP_NODE
280
281     face t f;
282     real Pinlet;
283     real t = CURRENT_TIME;
284
285     if (t >= 0 && t < 0.2)
```

```
286     {
287         Pinlet = (51202.035709985200 * t) + 1091470.841429000000; /*NEEDS CHANGED!!!!!!!!!!*/
288     }
289
290     if (t >= 0.2 && t < 0.23)
291     {
292         Pinlet = 1101711.249; /*NEEDS CHANGED!!!!!!!!!!*/
293     }
294
295     if (t >= 0.23)
296     {
297         Pinlet = (-178119.09336295800 * t) + 1142678.64004449000; /*NEEDS CHANGED!!!!!!!!!!*/
298     }
299
300     begin_f_loop(f, thread)
301     {
302         F_PROFILE(f, thread, P) = Pinlet;
303     }
304
305     end_f_loop(f, thread)
306
307         inlet_pressure = Pinlet;
308
309 #endif
310 }
311
312
313 /*************************************************************************/
314
```

Appendix A3 – Example of MATLAB script for TYPE 1 numerical model used in quasi steady analysis for 5231BX PRV

```
function [F, c, ceq] = SRV



%V=0.1; %% volume
tspan=[0,10]; %% time span
ic=[10e5,295,0,0,0,0,54]; %% initial conditions
options=odeset('AbsTol',1e-8,'RelTol',1e-11,'InitialStep',0.00000001); %% error limits to control time step

[t,y]=ode45(@(t,y)  SRV_model(t,y(1),y(2),y(3),y(4),y(5),y(6),y(7),tspan(2)),tspan, ic,options);

P = y(:,1);
x = y(:,5);
nf = y(:,6);

BD = (((10.3e5 -  (P(end)))/ 10.3e5)*100);

P_max=max(P);
OP = ((((P_max) - 10.3e5) / 10.3e5)*100);
%csvwrite('x_data_CFD.txt', x);
%csvwrite('p_data_CFD.txt', P);
%csvwrite('t_data_CFD.txt', t);

%F(1) = BD;
%F(2) = OP;
F =abs(BD+OP);


c = [];
ceq  = F;

 fprintf ('\n');
 fprintf ('Blowdown : %.3f',BD);
 fprintf ('\n');
 fprintf ('Overpressure : %.3f', OP);
 fprintf ('\n');


% % Lift Graph
    figure('color','w')
    plot(t,y(:,5),'-k')
    grid on
    grid minor
    xlabel('Time (s)')
    ylabel('Lift (m)')
    title(' Lift v Time ' )
    %xlim([20 30])
```

```
    %ylim([-0.1 0.1])
%
% % Net Force Graph
%figure
%hold on
%plot(t,y(:,7),'-k')
%xlim([10 20])
%grid on
%xlabel('Time (s)')
%ylabel('Net force (N)')
%title('Net force on disc holder assembly' )
%hold off

% Velocity Graph
% hold on
% figure
% plot(t,y(:,3),'-k')
% grid on
% xlabel('Time (s)')
% ylabel('Velocity (m/s)')
% title(' Velocity v time' )
% hold off

% % Temperature Graph
% hold on
% figure
% plot(t,y(:,2),'-k')
% grid on
% xlabel('Time (s)')
% ylabel('Temperature (K)')
% title(' Temperature v time' )
% hold off

% Pressure Graph
   figure
   hold on
   plot(t,y(:,1),'-k')
   grid on
   xlabel('Time (s)')
   ylabel('Pressure (Pa)')
   title(' Pressure v Time ' )
   hold off


end % end function, objectiveFunction
```

```
function y = SRV_model(t,P,T,~,~,x,ve,~,tfinal)

%Timer
fprintf('TIME: %.3f of %.3f\n',t,tfinal)

%constants
V = 0.2;          %% tank volume
g = 9.81;         %% gravitational constant
R=287;            %% ideal gas constant
Cp=1005;          %% specific heat capacity of air
gamma=1.4;        %% heat capacity ratio
d=0.007;       %% Inlet diameter
A_i=pi*(d/2)^2; %% Inlet area
P_atm=101000;    %% atmospheric pressure
P_set=10.9e5;       %% set pressure
T_atm=293;       %% atmospheric temperature
T_o=295;         %% Inlet gas temperature
ma=0.03;        %% mass of moving parts
k=10990;         %% spring stiffness
c=1.183;             %%Damping coefficient 5.4473

%%Discharge coefficient and flow area

CD=0.789;
A=3.14*d*x;
if A>A_i
    A=A_i;
end

if A <0
    A = 0;
end

%choked/subsonic conditions

if P_atm/P>0.5283
    P_prime=P_atm;
    T_prime=T_atm;
else
    P_prime=0.5283*P;
    T_prime=0.833*T;
end



%Mass flow rate(algebraic eqn) and conditions

m_e=A*CD*(P_prime/(R*T_prime))*(2*Cp*T*(1-(P_prime/P)^((gamma-1)/gamma)))^0.5;  %%mass↙
outflow rate
```

```
if (1-P_prime/P)<=0
    m_e=0;
end

m_i=0.08;
if t>2 %%16.4
    m_i=0;
end

m_v=m_i-m_e; %%mass rate of change of vessel

%odes

dP=(1/V)*(Cp*(gamma-1)*(m_i*T_o-m_e*T)); %% change in pressure
dT=(T/P)*dP-((R*T^2)/(P*V))*(m_v);%% change in temperature
dm_e=m_e; %% amount of mass to leave vessel
dm_v=m_v; %% mass change of vessel
dx=ve; %% rate of change of position

%Valve opening and closing limits

if x>0.0051
    if dx>0
        dx=0;
    end
end

if x<1e-10
    if dx<0
        dx=0;
    end
end

%Force constants

x_1 = [0    0.00005  0.0001  0.00015 0.0002  0.00025 0.0003  0.00035 0.0004  0.0005 ↙
0.0006  0.0007  0.0008  0.0009  0.001   0.001125    0.00125 0.001375    0.0015 ↙
0.001625    0.00175     0.001875    0.002   0.002125    0.00225 0.002375    0.0025 ↙
0.002625    0.00275 0.002875    0.003   0.003125    0.00325 0.003375    0.0035 ↙
0.003625    0.00375 0.003875    0.004   0.004125    0.00425 0.004375    0.0045 ↙
0.004625    0.00475 0.004875    0.005];
y_1 = [1.362293153  1.392566334  1.508613528 1.581773716 1.712957501 1.834050226 ↙
1.81134534  1.876937233 1.942529125 2.000552722 2.025780373 1.960188481 1.917301474 ↙
1.917301474 1.831527461 1.803777045 1.846664051 1.897119353 1.977847836 2.086326736 ↙
2.098940561 2.114077152 2.146873098 2.164532454 2.182191809 2.358785366 2.421854494 ↙
2.44960491  2.482400856 2.517719567 2.555561044 2.585834225 2.633766762 2.676653769 ↙
2.701881419 2.729631836 2.694313124 2.689267594 2.643857822 2.603493581 2.532856158 ↙
2.507628507 2.505105742 2.502582977 2.492491916 2.487446386 2.502582977];
```

```
f_1 = pchip(x_1,y_1,x);



F=(f_1*P*A_i)-54;

nf = F;


dve=(F-c*ve-k*x)/(ma); %% rate of change of disc velocity


if x < 1e-10
    if dve < 0
        dve = 0;
    end
end


%matrix/vector
y=[dP;dT;dm_e;dm_v;dx;dve;nf];

end
```

Appendix A4 – Assembly Drawing for Broady 3500 Type PRV's

Item	Description	Material (C/S)	Material (S/S)
1	Body	Carbon Steel	Stainless Steel
2	Nozzle	Stainless Steel	Stainless Steel
3	Cap	Carbon Steel	Stainless Steel
4	Disc	Stainless Steel	Stainless Steel
5	Spindle	Stainless Steel	Stainless Steel
7	Disc Holder	Stainless Steel	Stainless Steel
8	Blowdown Ring	Stainless Steel	Stainless Steel
10	Bonnet	Carbon Steel	Stainless Steel
12	Collar	Stainless Steel	Stainless Steel
13	Adjusting Screw	Stainless Steel	Stainless Steel
14	Locknut	Stainless Steel	Stainless Steel
15	Screwed Pin	Stainless Steel	Stainless Steel
16	Clampscrew	Stainless Steel	Stainless Steel
17	Spring Carrier	Stainless Steel	Stainless Steel
18	Locknut	Stainless Steel	Stainless Steel
19	Pin, Small	Stainless Steel	Stainless Steel
20	Pin, Large	Stainless Steel	Stainless Steel
21	Bellows	Stainless Steel	Stainless Steel
23	Stud	Stainless Steel	Stainless Steel
24	Nut	Stainless Steel	Stainless Steel
26	Guide	Stainless Steel	Stainless Steel
28	Drain Plug	Stainless Steel	Stainless Steel
29	Spring	Stainless Steel	Stainless Steel
30	Joint, Bellows	Stainless Steel	Non Asbestos
31	Joint, Guide	Non Asbestos	Non Asbestos
32	Joint, Cap	Non Asbestos	Non Asbestos
33	Joint, Clampscrew	Non Asbestos	Non Asbestos
34	Joint, Plug	Non Asbestos	Non Asbestos
35	Circlip, Disc	Stainless Steel	Stainless Steel
36	Plug	Stainless Steel	Stainless Steel

These Items are recommended spares.

Typical Flanged Type 3500

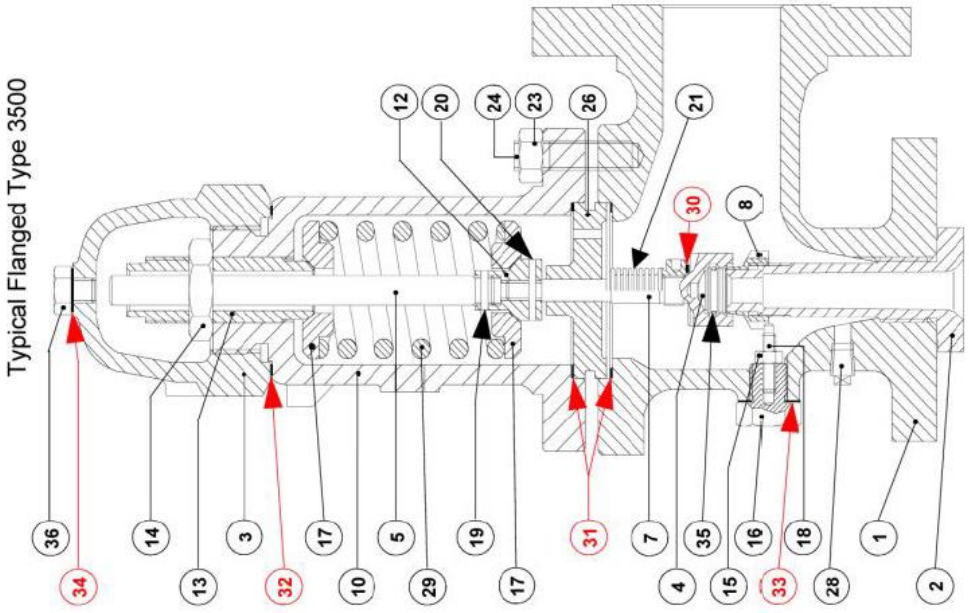

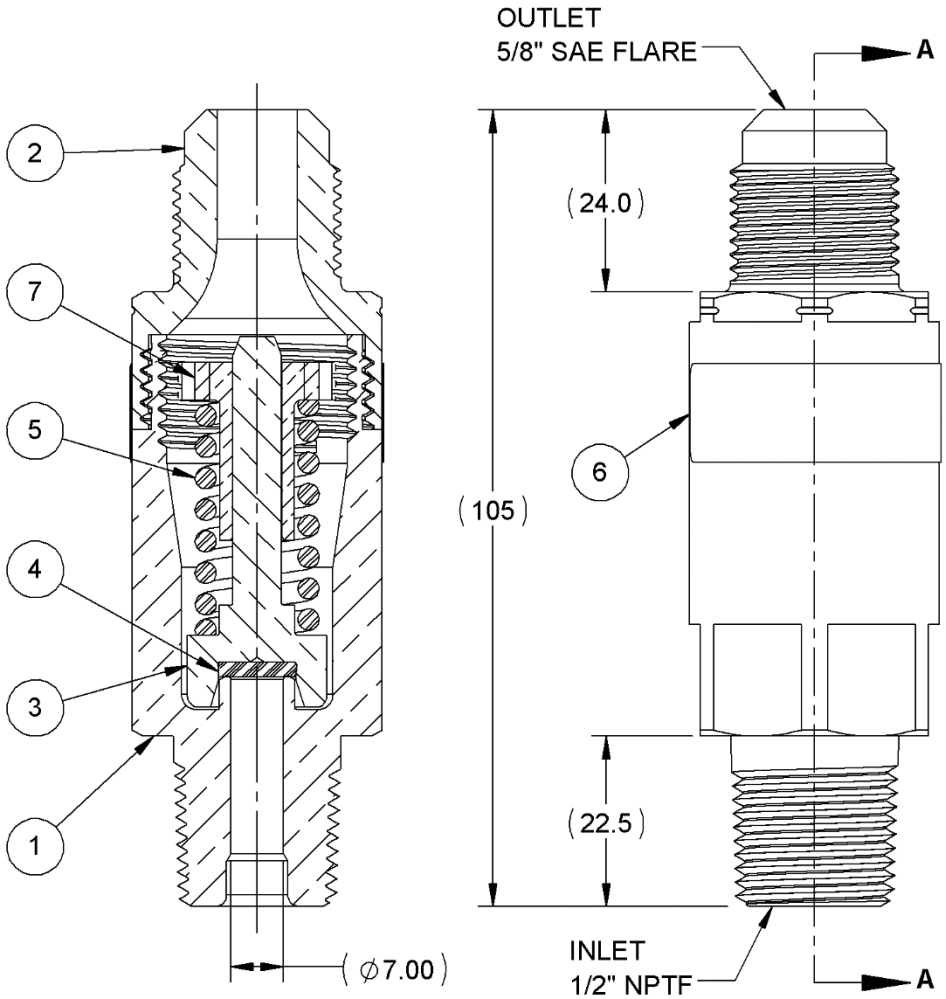

SECTION A-A

ITEM NO.	DESCRIPTION	QTY
1	Main Body	1
2	Outlet Connection	1
3	Piston	1
4	Seal	1
5	Spring	1
6	Tamper-Proof Seal	1
7	Adjusting Gland	1

All Dimensions in mm

Appendix A6 – Manufacturing Drawings for Laser Reference Structure Designed for Steady State Experimental Tests of the 5231BX PRV

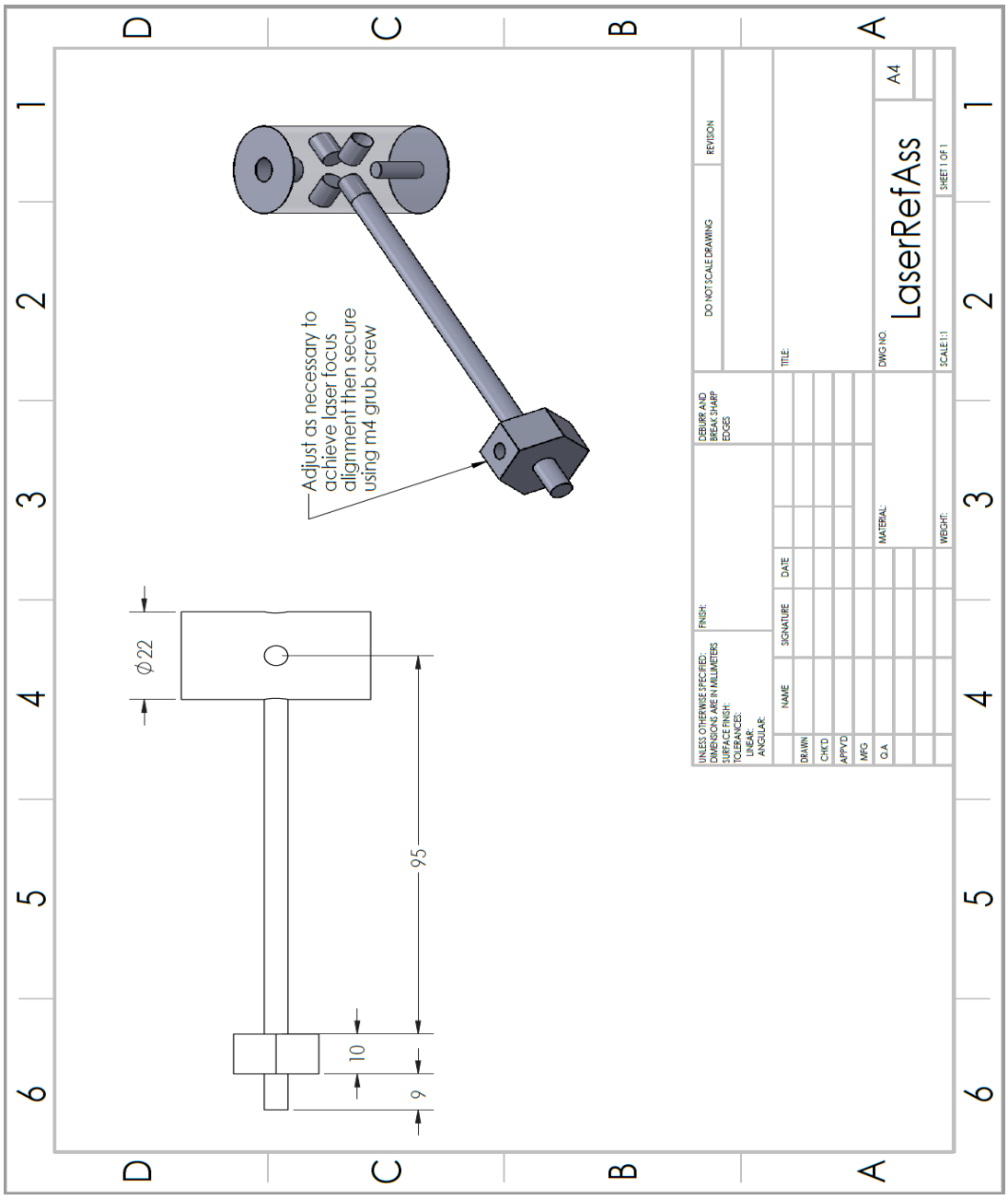

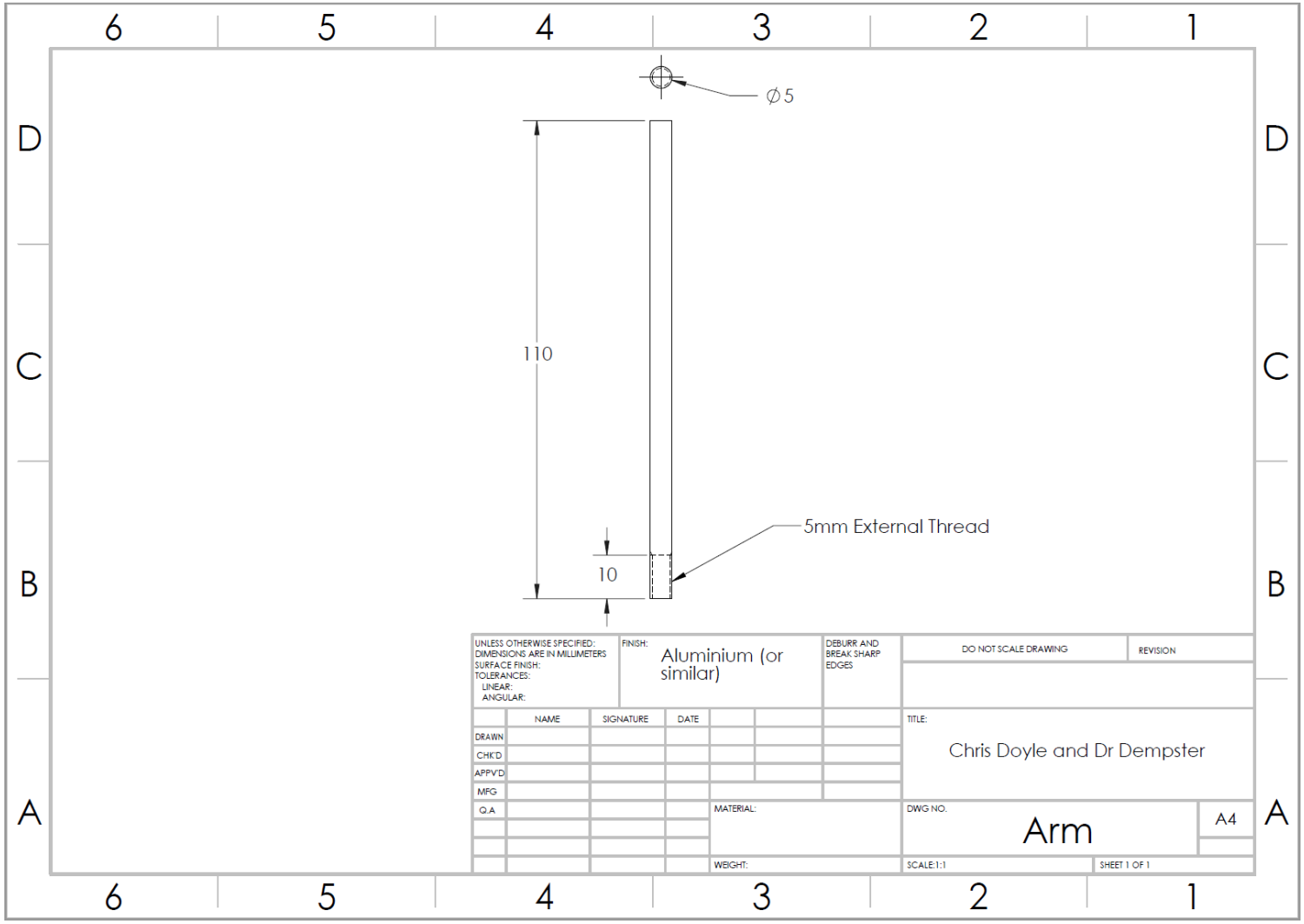
6
5
4
3
2
1
D
C
B
A
ϕ5
110
10
5mm External Thread
UNLESS OTHERWISE SPECIFIED:
DIMENSIONS ARE IN MILLIMETERS
SURFACE FINISH:
TOLERANCES:
LINEAR:
ANGULAR:
FINISH:
Aluminium (or similar)
DEBURR AND BREAK SHARP EDGES
DO NOT SCALE DRAWING
REVISION
NAME
SIGNATURE
DATE
DRAWN
CHK'D
APPV'D
MFG
Q.A
TITLE:
Chris Doyle and Dr Dempster
MATERIAL:
DWG NO.
Arm
A4
WEIGHT:
SCALE:1:1
SHEET 1 OF 1

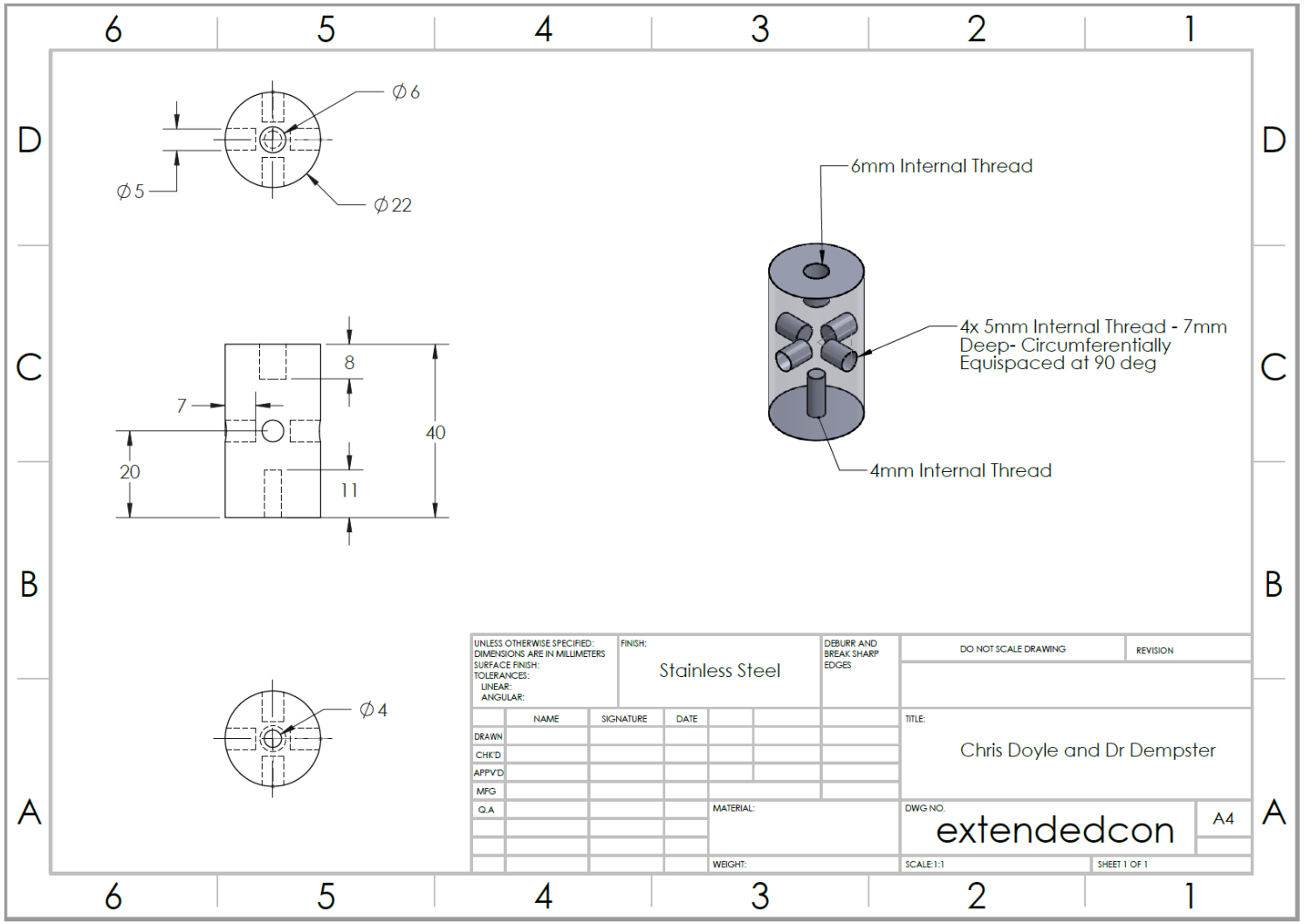
6
5
4
3
2
1
D
C
B
A
Ø6
Ø5
Ø22
8
7
40
20
11
Ø4
6mm Internal Thread
4x 5mm Internal Thread - 7mm Deep- Circumferentially Equispaced at 90 deg
4mm Internal Thread
UNLESS OTHERWISE SPECIFIED:
DIMENSIONS ARE IN MILLIMETERS
SURFACE FINISH:
TOLERANCES:
LINEAR:
ANGULAR:
FINISH:
Stainless Steel
DEBURR AND BREAK SHARP EDGES
DO NOT SCALE DRAWING
REVISION
NAME
SIGNATURE
DATE
DRAWN
CHK'D
APPV'D
MFG
Q.A
MATERIAL:
WEIGHT:
TITLE:
Chris Doyle and Dr Dempster
DWG NO.
extendedcon
A4
SCALE:1:1
SHEET 1 OF 1

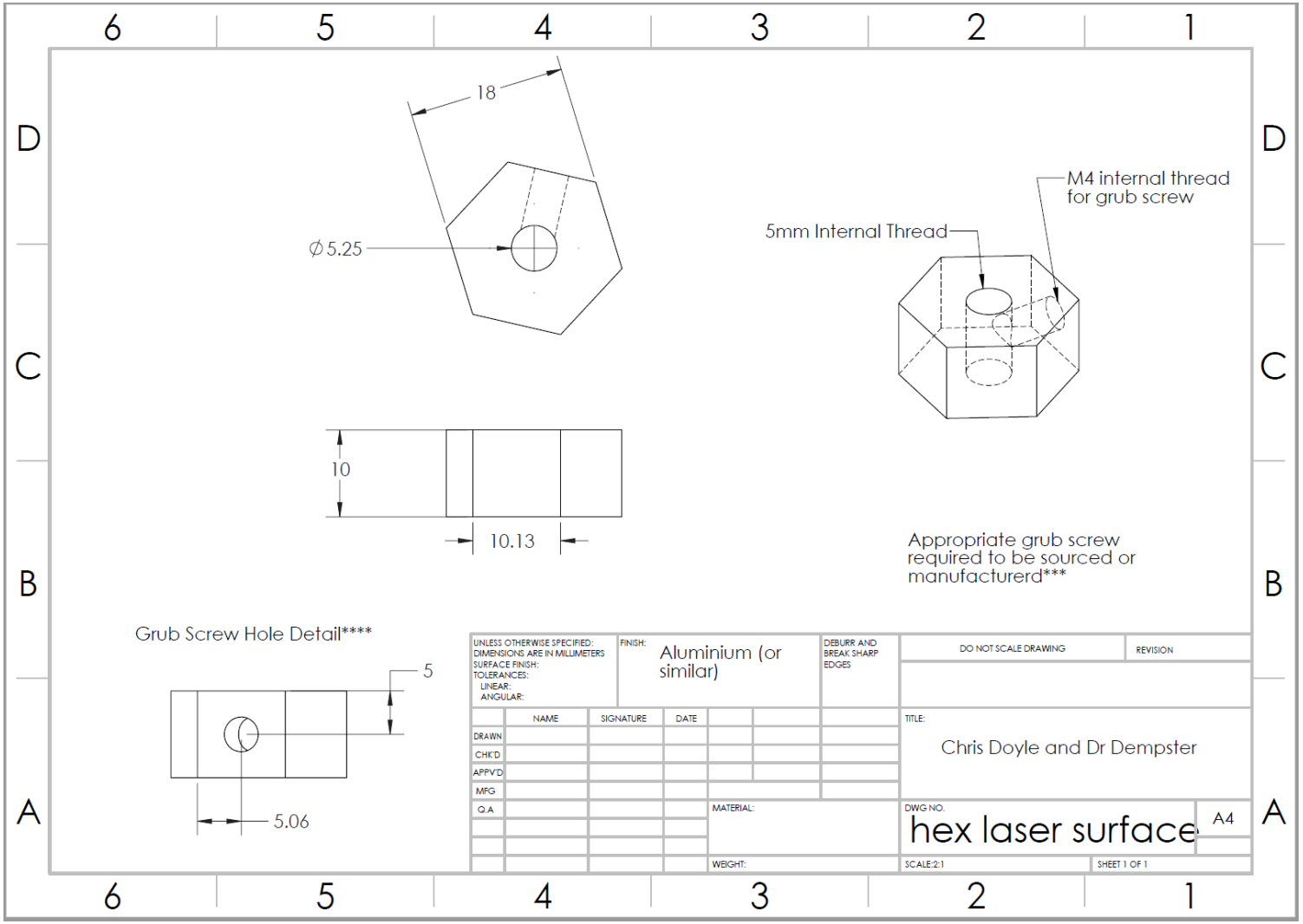
18
∅5.25
10
10.13
5mm Internal Thread
M4 internal thread for grub screw
Appropriate grub screw required to be sourced or manufacturerd***
Grub Screw Hole Detail****
5
5.06
UNLESS OTHERWISE SPECIFIED:
DIMENSIONS ARE IN MILLIMETERS
SURFACE FINISH:
TOLERANCES:
LINEAR:
ANGULAR:
FINISH:
Aluminium (or similar)
DEBURR AND BREAK SHARP EDGES
DO NOT SCALE DRAWING
REVISION
NAME
SIGNATURE
DATE
DRAWN
CHK'D
APPV'D
MFG
Q.A
MATERIAL:
WEIGHT:
TITLE:
Chris Doyle and Dr Dempster
DWG NO.
hex laser surface
A4
SCALE:2:1
SHEET 1 OF 1

Appendix A7 – Manufacturing Drawings for Laser Support Structure Designed for Steady State Experimental Tests of the 5231BX PRV

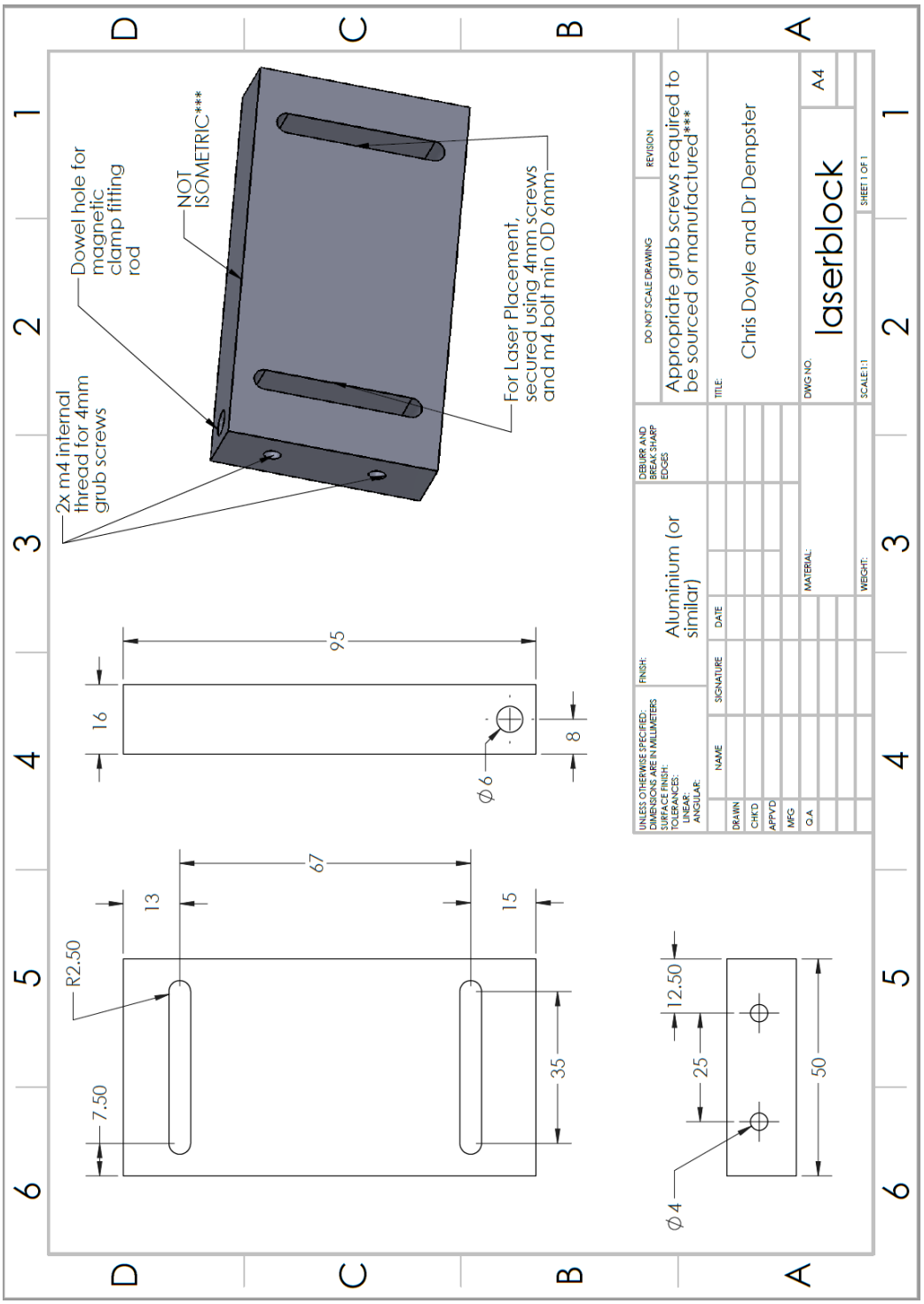

Appendix A8 – Manufacturing Drawings for Backpressure Monitoring Port Designed for Steady State Experimental Tests of the 5231BX PRV

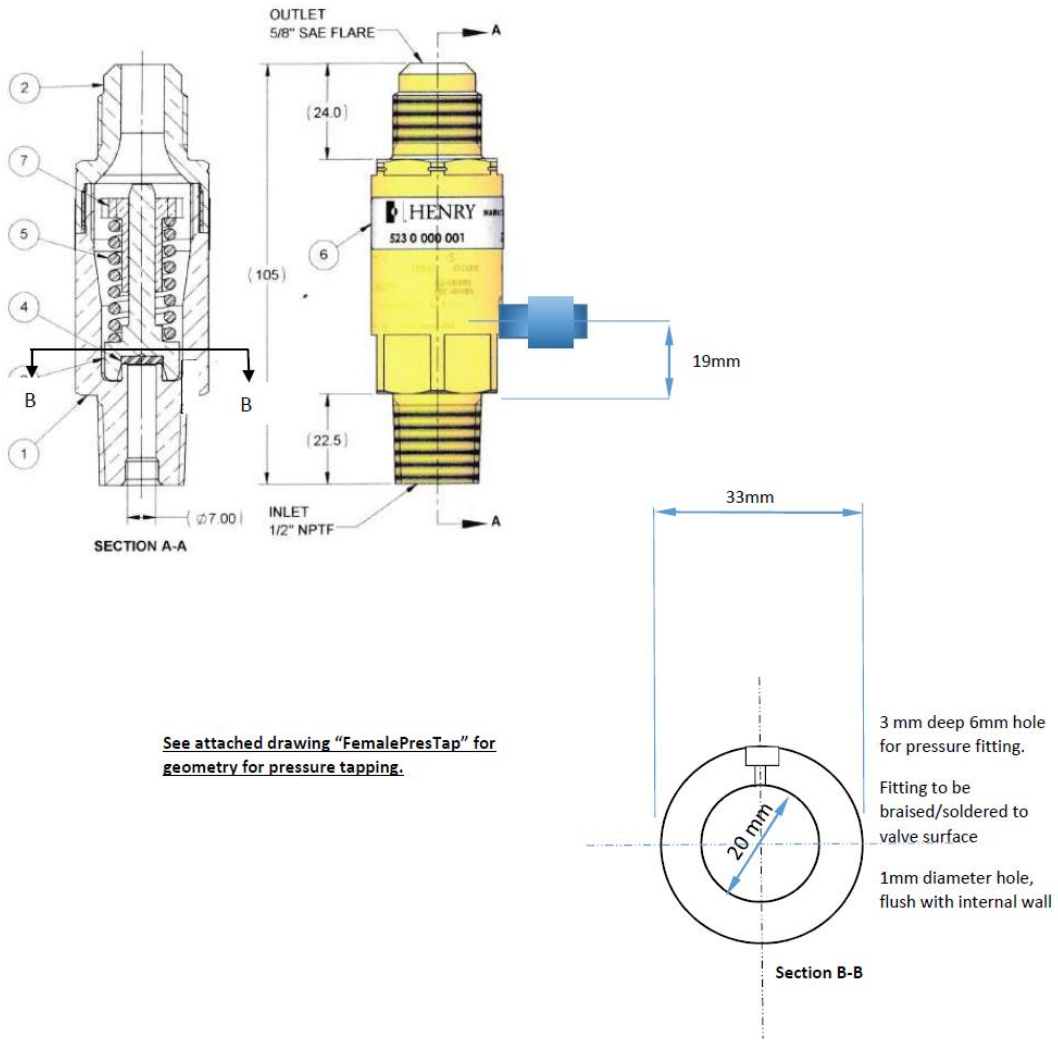

Henry Technologies Valve: Pressure tapping and fittings

(see Bill Dempster for example)

Appendix A9 – Manufacturing Drawings for Modified Gland Designed for Steady State and Transient Experimental/CFD Tests of the 5231BX PRV

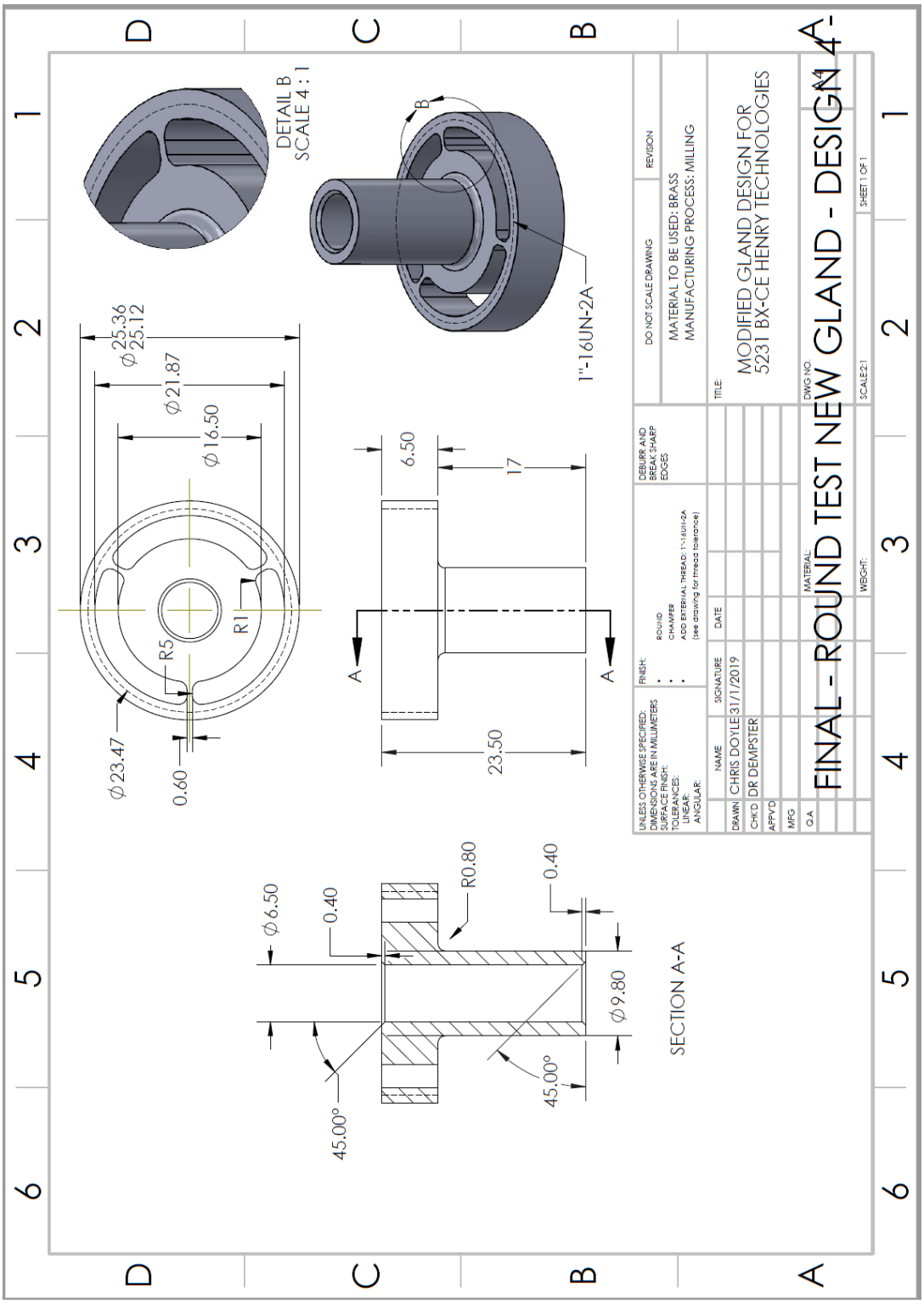

Appendix A10 – Manufacturing Drawings for Separator Designed for Transient Two Phase Experimental Tests of the 5231BX PRV

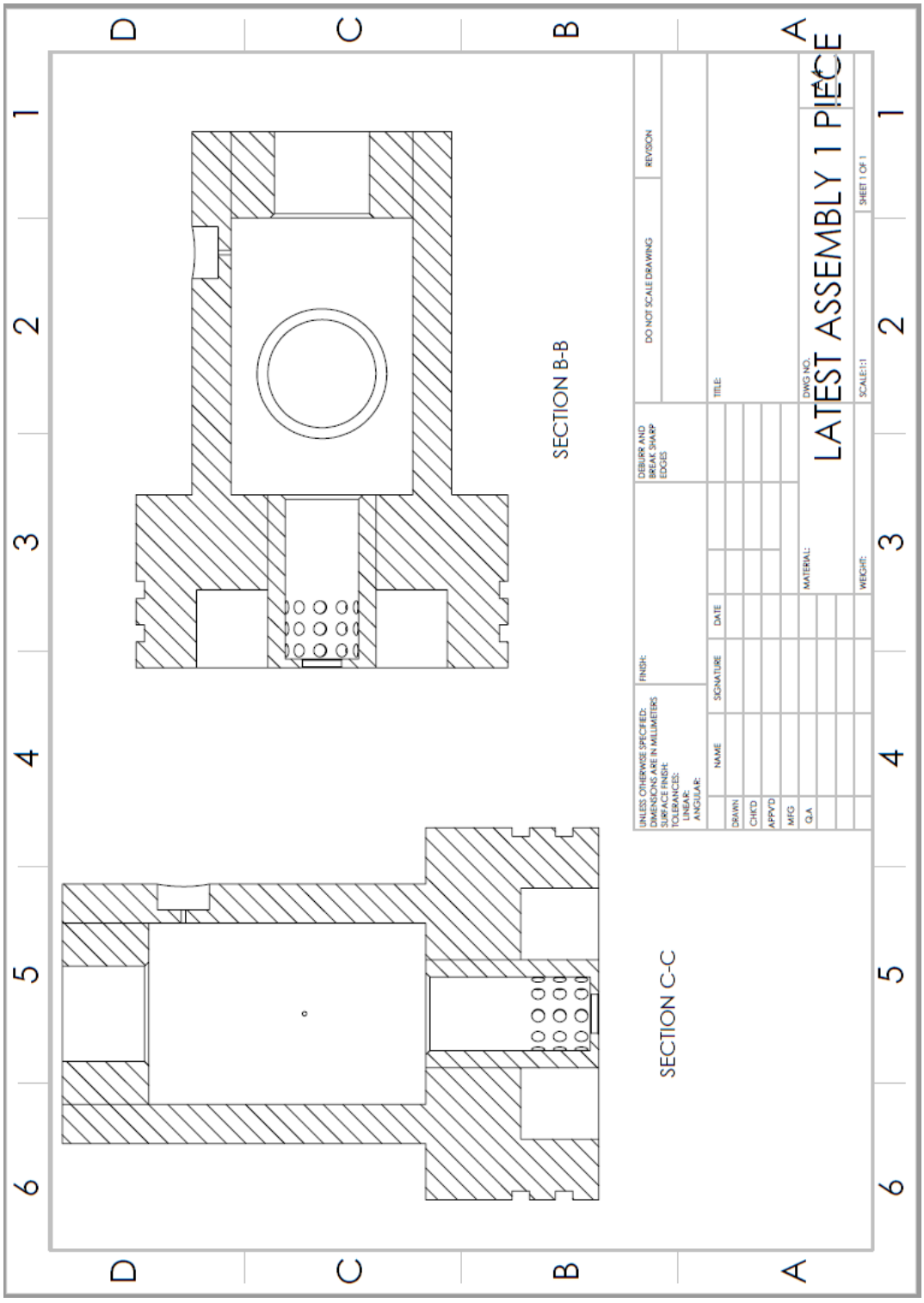

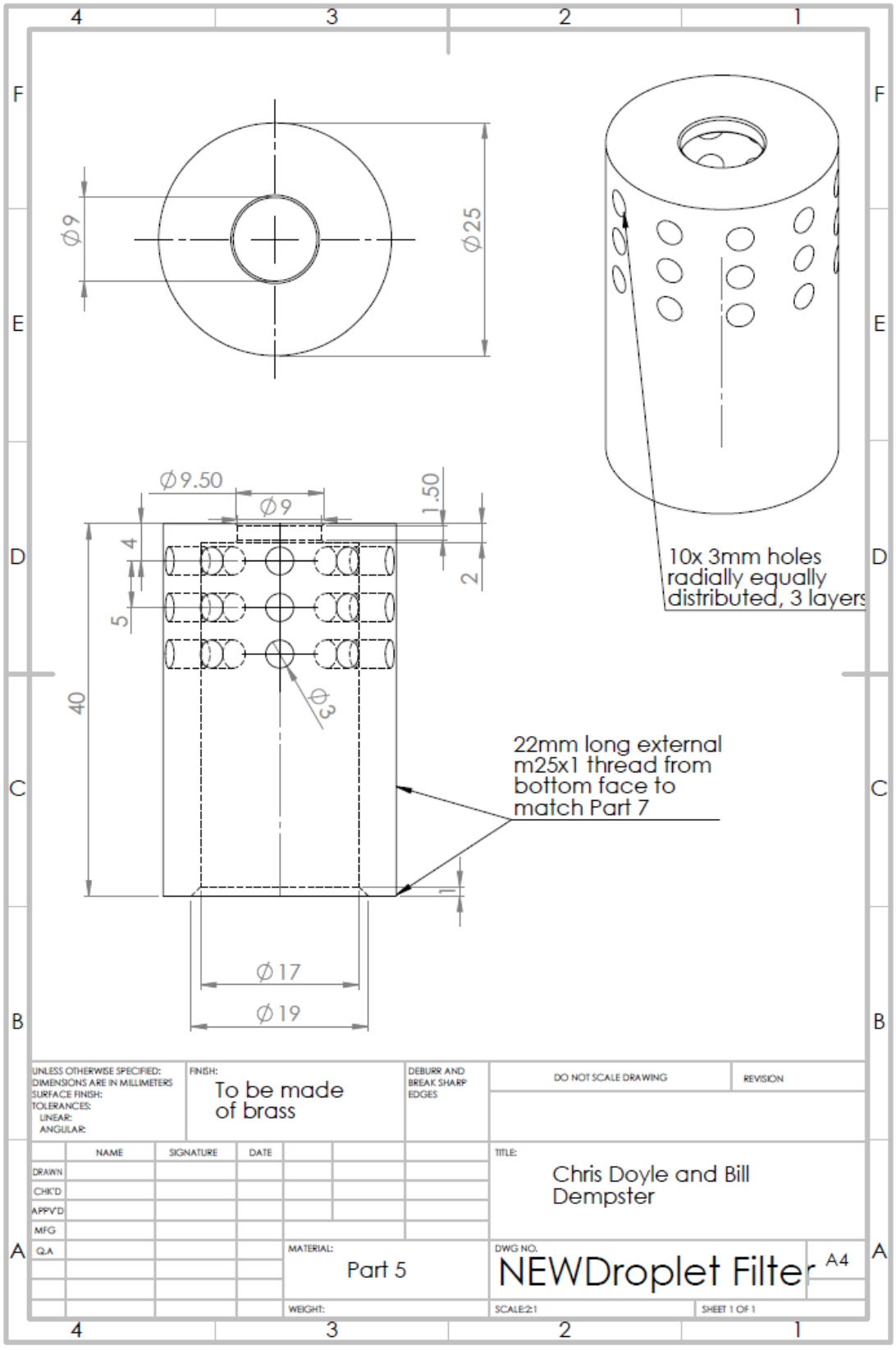
4
3
2
1
F
E
D
C
B
A
Ø9
Ø25
Ø9.50
Ø9
1.50
4
5
2
40
Ø3
1
Ø17
Ø19
10x 3mm holes radially equally distributed, 3 layers
22mm long external m25x1 thread from bottom face to match Part 7
UNLESS OTHERWISE SPECIFIED:
DIMENSIONS ARE IN MILLIMETERS
SURFACE FINISH:
TOLERANCES:
LINEAR:
ANGULAR:
FINISH:
To be made of brass
DEBURR AND BREAK SHARP EDGES
DO NOT SCALE DRAWING
REVISION
NAME
SIGNATURE
DATE
DRAWN
CHK'D
APPV'D
MFG
Q.A
TITLE:
Chris Doyle and Bill Dempster
MATERIAL:
Part 5
DWG NO.
NEWDroplet Filter
A4
WEIGHT:
SCALE:2:1
SHEET 1 OF 1

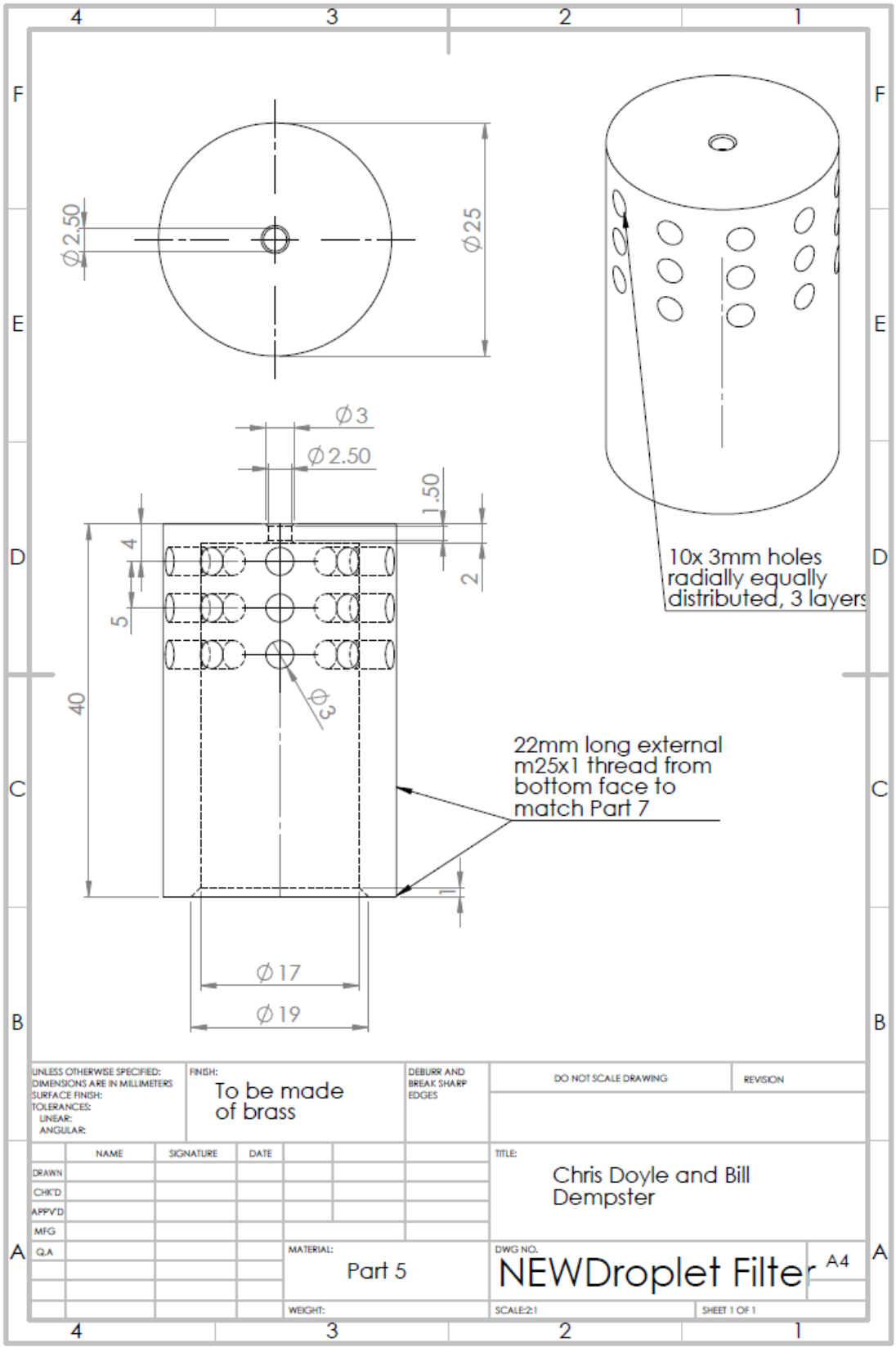
Ø2.50
Ø25
Ø3
Ø2.50
1.50
4
5
2
40
Ø3
1
Ø17
Ø19
10x 3mm holes radially equally distributed, 3 layers
22mm long external m25x1 thread from bottom face to match Part 7
UNLESS OTHERWISE SPECIFIED:
DIMENSIONS ARE IN MILLIMETERS
SURFACE FINISH:
TOLERANCES:
LINEAR:
ANGULAR:
FINISH:
To be made of brass
DEBURR AND BREAK SHARP EDGES
DO NOT SCALE DRAWING
REVISION
NAME
SIGNATURE
DATE
DRAWN
CHK'D
APPV'D
MFG
Q.A
TITLE:
Chris Doyle and Bill Dempster
MATERIAL:
Part 5
DWG NO.
NEWDroplet Filter
A4
WEIGHT:
SCALE:2:1
SHEET 1 OF 1

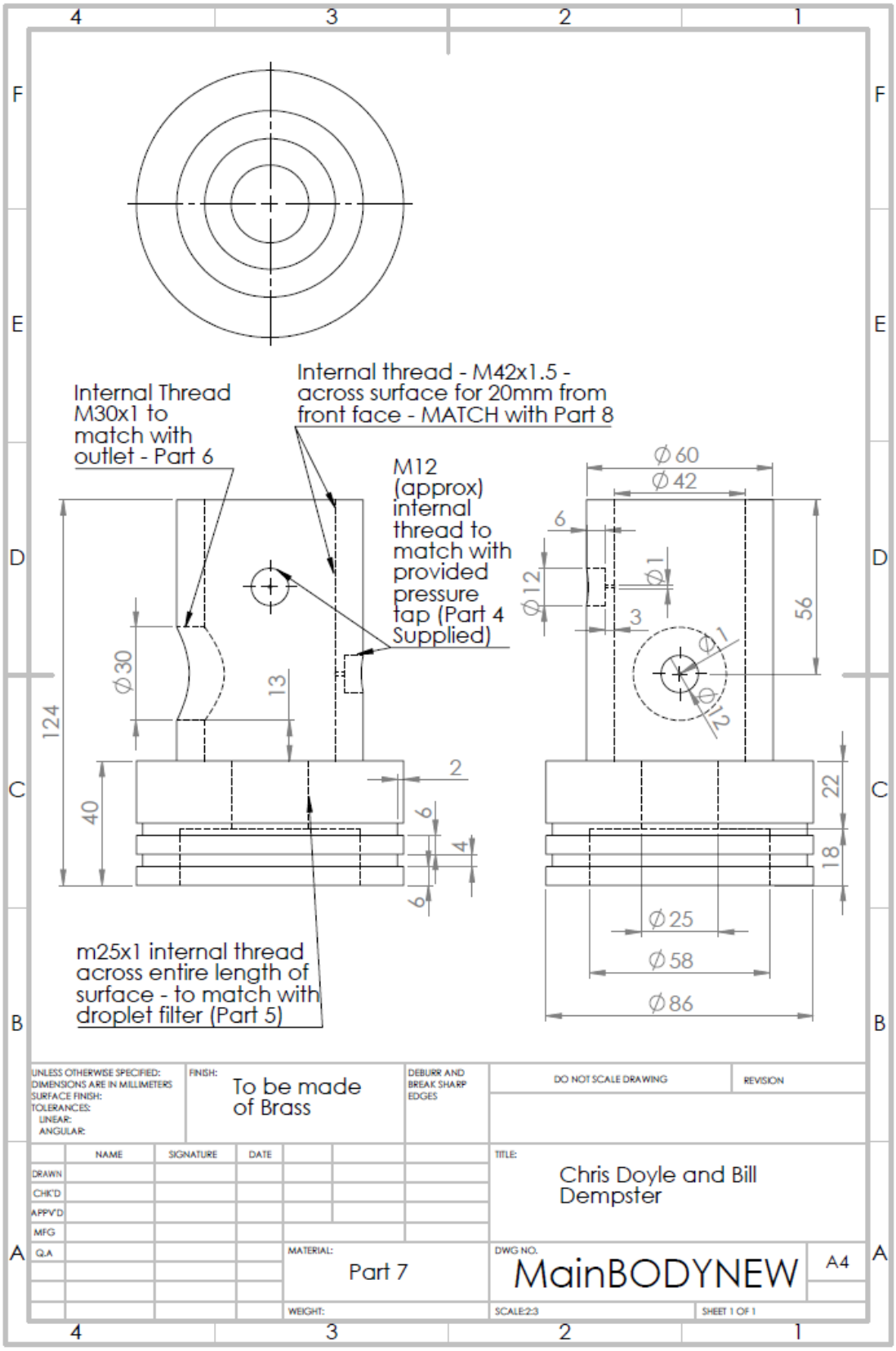
Internal Thread M30x1 to match with outlet - Part 6
Internal thread - M42x1.5 - across surface for 20mm from front face - MATCH with Part 8
M12 (approx) internal thread to match with provided pressure tap (Part 4 Supplied)
m25x1 internal thread across entire length of surface - to match with droplet filter (Part 5)
Ø60
Ø42
Ø30
Ø25
Ø58
Ø86
124
40
13
2
6
4
22
18
56
3
UNLESS OTHERWISE SPECIFIED:
DIMENSIONS ARE IN MILLIMETERS
SURFACE FINISH:
TOLERANCES:
LINEAR:
ANGULAR:
FINISH:
To be made of Brass
DEBURR AND BREAK SHARP EDGES
DO NOT SCALE DRAWING
REVISION
NAME
SIGNATURE
DATE
DRAWN
CHK'D
APPV'D
MFG
Q.A
TITLE:
Chris Doyle and Bill Dempster
MATERIAL:
Part 7
DWG NO.
MainBODYNEW
A4
WEIGHT:
SCALE:2:3
SHEET 1 OF 1

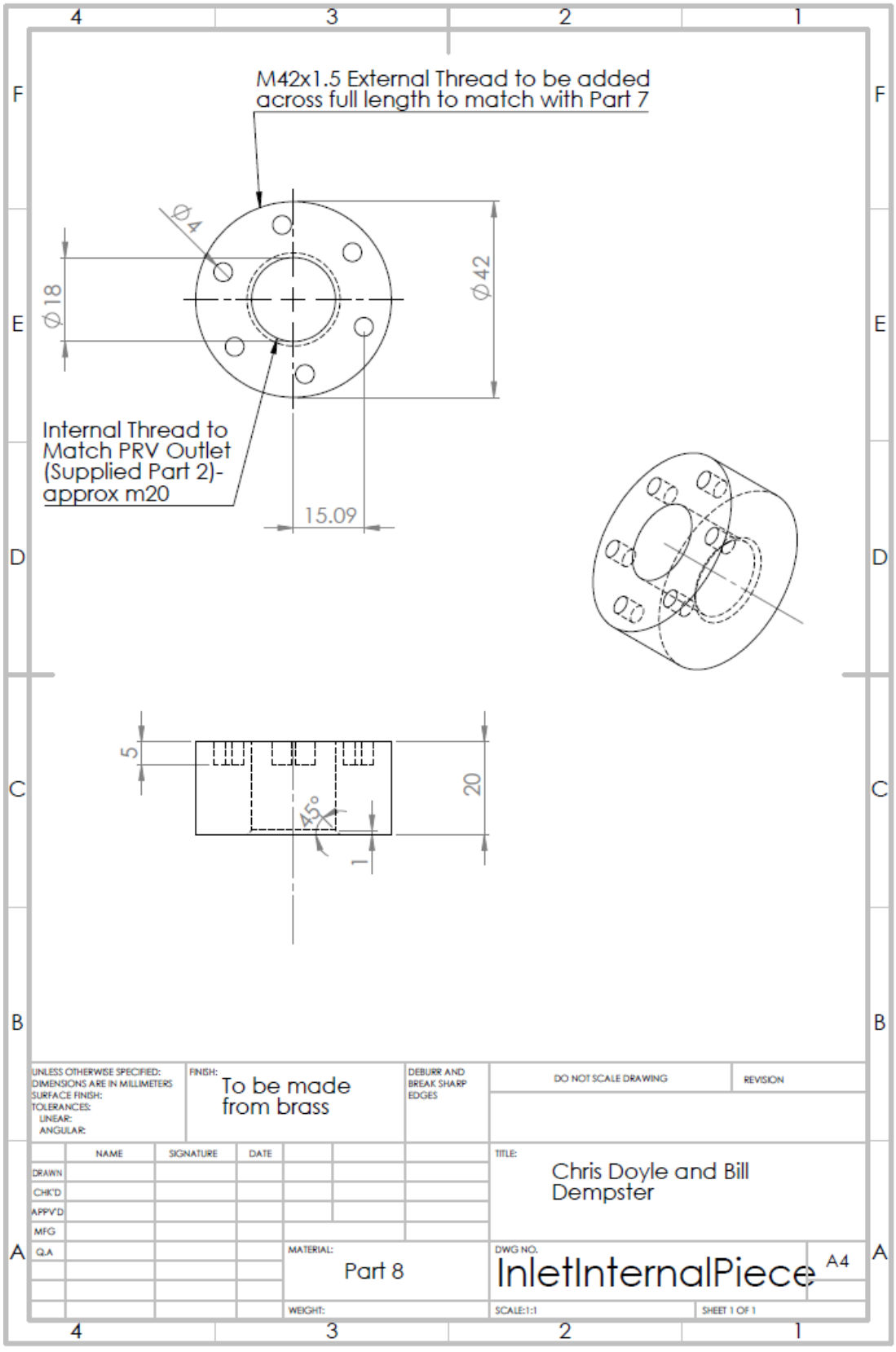
M42x1.5 External Thread to be added across full length to match with Part 7
Ø4
Ø18
Ø42
Internal Thread to Match PRV Outlet (Supplied Part 2)- approx m20
15.09
5
20
45°
1
UNLESS OTHERWISE SPECIFIED:
DIMENSIONS ARE IN MILLIMETERS
SURFACE FINISH:
TOLERANCES:
LINEAR:
ANGULAR:
FINISH:
To be made from brass
DEBURR AND BREAK SHARP EDGES
DO NOT SCALE DRAWING
REVISION
NAME
SIGNATURE
DATE
DRAWN
CHK'D
APPV'D
MFG
Q.A
TITLE:
Chris Doyle and Bill Dempster
MATERIAL:
Part 8
DWG NO.
InletInternalPiece
A4
WEIGHT:
SCALE:1:1
SHEET 1 OF 1